WOODHEAD PUBLISHING IN MATERIALS

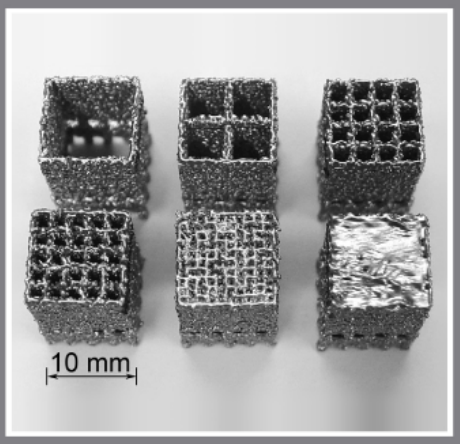

Metals for biomedical devices

Edited by Mitsuo Niinomi

CRC

WP

Metals for biomedical devices

Related titles:

Joint replacement technology: new developments
(ISBN 978-1-84569-245-2)
Increasing numbers of joint revision and replacement operations drive the demand for improved prostheses. This book comprehensively reviews developments in joint replacement technology, covering the most pertinent materials science and engineering issues, specific joints, clinical trial results and sterilisation techniques. Part I discusses biomechanics, tribology, the chemical environment of the body and an overview of materials and engineering of joint replacement. The second part reviews specific materials, bearing surfaces and bone cements, in addition to the failure mechanisms and lifetime prediction of joints. Part III discusses the biological environment and interaction of replacement joints. Specific joints are analysed in detail in Part IV.

Shape memory alloys for biomedical applications
(ISBN 978-1-84569-344-2)
Shape memory metals are suitable for a wide range of biomedical devices including applications in dentistry, bone repair, urology and cardiology. This book provides a comprehensive review of shape memory metals and devices for medical applications. The first part of the book discusses the materials, primarily Ti–Ni based alloys. Chapters cover the mechanical properties, thermodynamics, composition, fabrication of parts, chemical reactivity, surface modification and biocompatibility. Medical and dental devices using shape memory metals are reviewed in the following section: chapters cover stents, orthodontic devices and endodontic instruments. Finally, future developments in this area are discussed, including alternatives to Ti–Ni based shape memory alloys.

Dental biomaterials: imaging, testing and modelling
(ISBN 978-1-84569-296-4)
Dental biomaterials: imaging, testing and modelling focuses on the techniques required to undertake research in dental biomaterials. The text forms an instructive and practical review of the scientific methods applied to dental biomaterials, with appropriate case studies. The book includes chapters discussing the practicalities of working on dental biomaterials, such as reviewing the mechanisms of cutting tooth tissue and methods for characterising dental hand piece performance. Chapters review optical and electron imaging techniques for biomaterial interfaces. Specific materials, applications and experimental techniques are discussed in addition to the development and application of computer models to this complex area.

Details of these and other Woodhead Publishing materials books can be obtained by:

- visiting our web site at www.woodheadpublishing.com
- contacting Customer Services (e-mail: sales@woodheadpublishing.com; fax: +44 (0) 1223 893694; tel.: +44 (0) 1223 891358 ext. 130; address: Woodhead Publishing Limited, Abington Hall, Granta Park, Great Abington, Cambridge CB21 6AH, UK)

If you would like to receive information on forthcoming titles, please send your address details to: Francis Dodds (address, tel. and fax as above; e-mail: francis.dodds@woodheadpublishing.com). Please confirm which subject areas you are interested in.

Metals for biomedical devices

Edited by
Mitsuo Niinomi

CRC Press
Boca Raton Boston New York Washington, DC

WOODHEAD PUBLISHING LIMITED
Oxford Cambridge New Delhi

Published by Woodhead Publishing Limited, Abington Hall, Granta Park, Great Abington, Cambridge CB21 6AH, UK
www.woodheadpublishing.com

Woodhead Publishing India Private Limited, G-2, Vardaan House, 7/28 Ansari Road, Daryaganj, New Delhi – 110002, India
www.woodheadpublishingindia.com

Published in North America by CRC Press LLC, 6000 Broken Sound Parkway, NW, Suite 300, Boca Raton, FL 33487, USA

First published 2010, Woodhead Publishing Limited and CRC Press LLC

British Library Cataloguing in Publication Data
A catalogue record for this book is available from the British Library.

Library of Congress Cataloging in Publication Data
A catalog record for this book is available from the Library of Congress.

Woodhead Publishing ISBN 978-1-84569-434-0 (book)
Woodhead Publishing ISBN 978-1-84569-924-6 (e-book)
CRC Press ISBN 978-1-4398-3107-6
CRC Press order number: N10188

The publishers' policy is to use permanent paper from mills that operate a sustainable forestry policy, and which has been manufactured from pulp which is processed using acid-free and elemental chlorine-free practices. Furthermore, the publishers ensure that the text paper and cover board used have met acceptable environmental accreditation standards.

Typeset by Replika Press Pvt Ltd, India
Printed by TJ International Limited, Padstow, Cornwall, UK

Contents

Contributor contact details

(* = main contact)

Editor and Chapter 5

Professor Mitsuo Niinomi
Department of Biomaterials Science
Institute for Materials Research
Tohoku University
2-1-1, Katahira
Aoba-ku, Sendai 980-8577
Japan

Email: niinomi@imr.tohoku.ac.jp

Chapter 1

Professor Takao Hanawa
Department of Metals
Institute of Biomaterials and Bioengineering
Tokyo Medical and Dental University
2-3-10 Kanda-surugadai
Chiyoda-ku
Tokyo 101-0062
Japan

Email: hanawa.met@tmd.ac.jp

Chapter 2

Dr Yoshimitsu Okazaki
Advanced Biomaterial Group
Institute for Human Science and Biomedical Engineering
National Institute of Advanced Industrial Science and Technology
1-2-1 Namiki
Tsukuba
Ibaraki 305-8564
Japan

Email: y-okazaki@aist.go.jp

Chapter 3

Professor Takayoshi Nakano
Course of Materials Science & Engineering
Division of Materials & Manufacturing Science
Graduate School of Engineering
Osaka University
2-1, Yamada-Oka
Suita, Osaka 565-0871
Japan

Email: nakano@mat.eng.osaka-u.ac.jp

Chapter 4

Dr Sachiko Hiromoto
Biomaterials Center
National Institute for Materials Science
1-1 Namiki
Tsukuba
Ibaraki 305-0044
Japan

Email: hiromoto.sachiko@nims.go.jp

Chapter 6

Dr Norio Maruyama
Biomaterials Center
National Institute for Materials Science
1-1 Namiki
Tsukuba
Ibaraki 305-0044
Japan

Email: maruyama.norio@nims.go.jp

Chapter 7

Dr Yu Yan
Institute of Thermofluids,
Surfaces and Interfaces (iETSI)
School of Mechanical Engineering
University of Leeds
Leeds
LS2 9JT
UK

Email: Y.Yan@leeds.ac.uk

Chapter 8

Professor Chunxiang Cui
School of Materials Science and Technology
Hebei University of Technology
No. 8, Road No. 1
Dingzigu
Hongqiao District
Tianjin 300130
China

Email: hutcui@hebut.edu.cn

Chapter 9

Dr Margam Chandrasekaran
Chief Scientist
Bio-scaffold International Pte Ltd
61, Science Park Road
THE GALEN
#02-01
Science Park III
Singapore 117525

Email: chandram@bio-scaffold.com

Chapter 10

Prof. Dr-Ing. Roger Thull
Em. Head of the Chair of Functional Materials for Medicine and Dentistry
University of Würzburg
Pleicherwall 2
D-97070 Würzburg
Germany

Email: rthfmz@mail.uni-wuerzburg.de

Chapter 11

Professor Toshihiro Kasuga
Department of Frontier Materials
Graduate School of Engineering
Nagoya Institute of Technology
Gokiso-cho
Showa-ku
Nagoya 466-8555
Japan

Email: kasuga.toshihiro@nitech.ac.jp

Chapter 12

Dr Kazuhiko Ishihara* and Jiyeon Choi
Department of Materials Engineering
School of Engineering and Center for NanoBio Integration (CNBI)
The University of Tokyo
7-3-1, Hongo, Bunkyo-ku
Tokyo 113-8656
Japan

Email: ishihara@mpc.t.u-tokyo.ac.jp

Chapter 13

Dr Sophie Lerouge
Department of Mechanical Engineering
Ecole de Technologie Supérieure (ÉTS)
1100 Notre-Dame West
Montreal
Quebec, H3C 1K3
Canada

Email: sophie.lerouge@etsmtl.ca

Adjunct Professor
Department of Radiology
University of Montreal
Canada

Chapter 14

Professor Tomiharu Matsushita
College of Life and Health Sciences
Chubu University
1200 Matsumoto-cho
Kasugai, Aichi 487-8501
Japan

Email: matsushi@isc.chubu.ac.jp

Chapter 15

Professor Takayuki Narushima
Department of Materials Processing
Tohoku University
6-6-02 Aza Aoba
Aramaki, Aoba-ku
Sendai 980-8579
Japan

E-mail: narut@material.tohoku.ac.jp

Chapter 16

Professor Diego Mantovani
Laboratory for Biomaterials and Bioengineering
Department of Mining, Metallurgy and Materials Engineering & Hospital Research Center
Pavillon Adrien-Pouliot, room 1745-E
Laval University
1065 Ave de la Médecine
Québec City
QC, G1V 0A6
Canada

Email: diego.mantovani@gmn.ulaval.ca

Introduction

Metallic materials are used as structural materials for medical devices in the fields of orthopedic surgery, blood circulatory system and dentistry. Approximately 70% of the structural materials employed in implants are found to be metallic materials. The elderly population (over 65 years old) is rapidly increasing all over the world, as shown in Fig. 0.1 (Yanno Tsunetarou Memorial Foundation, 2009). The elderly population (over 60 years old) over the world is increasing by approximately 2–3% per year, although the total population over the world is decreasing, as shown in Fig. 0.2 (Population Division of the Department of Economic and Social Affairs of the United Nations Secretariat, 2009). In some countries such as Japan, Italy, and Germany, the ratio of the elderly population to the total population

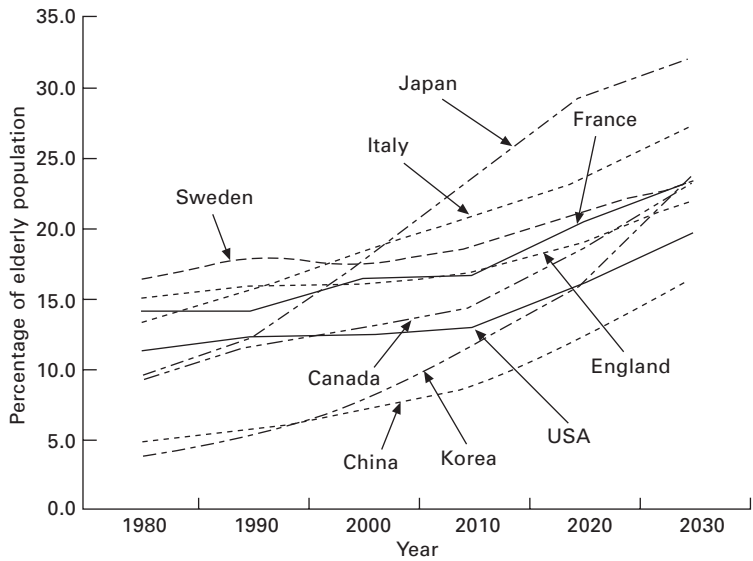

0.1 Change and estimation of elderly (over 65 years old) population (%).

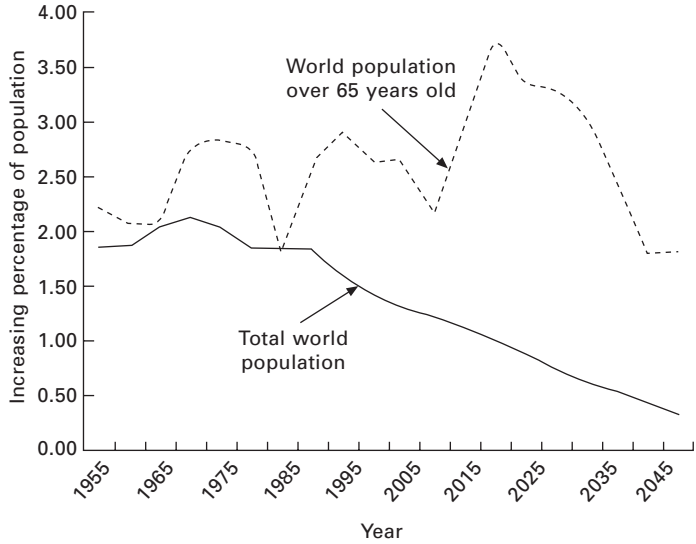

0.2 Change in increasing percentage of world population over 65 years old and total world population with year.

is already over 20%, especially in Japan where it is approximately 22%; Japan is already the super aged society. Therefore, the number of elderly people with failed tissue needing replacement with artificial instrumentations made of metallic biomaterials is growing.

The metallic biomaterials are roughly grouped into stainless steels: mainly SUS 316L stainless steel, cobalt (Co)–chromium (Cr) alloys, titanium (Ti; pure titanium) and its alloys; mainly pure titanium and Ti-6mass% aluminum (Al)-4mass% vanadium (V), and precious alloys (gold (Au) based, silver (Ag) based or platinum (Pt) based alloys). The implant materials used for fabricating artificial hip joints, other artificial joints, bone plates and screws, and artificial tooth roots are mainly stainless steel, Co–Cr alloys, titanium and titanium alloys. Precious alloys are mainly used as dental materials, for fabricating dental products such as dentures, crowns, inlays and bridges. In the early stage of the usage of the metallic materials as biomaterials, general structural metallic materials were used. Now we are seeing a large number of metallic materials composed of nontoxic and allergy-free elements and exhibiting mechanical biocompatibility being proposed or under development.

The metallic materials used in biomaterials, namely metallic biomaterials, do not possess bio-functionalities such as bone conductivity, bioactiveness and blood compatibility. Hence, surface modification of metallic biomaterials using bioactive ceramics, such as hydroxyapatite and biopolymers, is required. The integration and harmonization of metals, ceramics, and polymers are very important for developing metal-based bio-functional biomaterials;

these integrated materials should be called biometals. The harmonization of metals, ceramics and polymers also leads to the harmonization of metallic biomaterials and living tissues. If these sorts of metallic biomaterials are established, then metallic biomaterials will become the scaffold used for artificial organs

This book begins with an overview of metals used for biomedical applications, including metal selection for biomedical devices. Part II contains a discussion of mechanical behaviors, degradation and testing of metals used for biomedical devices, including physical, mechanical, and corrosion properties, fatigue and failure properties, mechanical testing and wear testing, and biocompatibility of metallic biomaterials. Part III has chapters on metal processing techniques used for biomedical applications, including forging metals and alloys used for biomedical applications, surface treatment of metallic biomaterials, coatings used for metallic biomaterials, biocompatible polymer assembly on metal surfaces, and sterilization/cleaning of metallic biomaterials. Part IV focuses on specific applications of metals used for biomedical devices, including orthopedic applications of metallic biomaterials, new-generation metallic biomaterials, and degradable metallic biomaterials, made of Mg and Fe, used in cardiovascular stents and orthopedic fixation devices.

Every chapter in this book is contributed by distinguished experts in the biomaterials field. The editor (M.N. Mitsuo Niinomi) is grateful to all the authors for their outstanding efforts. The editor is also grateful to the staff of Woodhead Publishing Limited for their help and encouragement in publishing this book.

References

Population Division of the Department of Economic and Social Affairs of the United Nations Secretariat, World Population Prospects: The 2008 Revision, http://esa.un.org/unpp, (2009).

Yano Tsunetarou Memorial Foundation, Sekai-kokusei-zue, Kokusei Co. Ltd, (2009), pp. 75–76.

1
Overview of metals and applications

T. HANAWA, Tokyo Medical and Dental University, Japan

Abstract: This chapter discusses characteristics such as composition, mechanical properties, corrosion resistance and surface properties, of metals and alloys widely used for medical and dental devices. It first reviews the advantages of metals and the properties required for medical devices, as well as the application of metals to the devices, followed by an explanation of the characteristics of each material as well as advanced future materials from the biomedical viewpoint. The chapter will impart a basic knowledge of metallic biomaterials.

Key words: metal, alloy, biomaterial, implant, medical device.

1.1 Introduction

The use of metals as raw materials has a long history and it can be said that materials science and engineering have been based on research into metals. However, metals are sometimes thought of as 'unfavourite materials' for biomaterials because of memories of the environmental and human damage caused by heavy metals. Since an improvement in the safety of metals for medical use is vital, strenuous efforts have been made to improve corrosion resistance and mechanical durability. In addition, metals are typically artificial materials and have no biofunctions, which makes them fairly unattractive as biomaterials. This viewpoint is short-sighted and is caused by misunderstandings. On the other hand, the fast technological evolution of ceramics and polymers has made it possible to apply these materials to medical devices over the last three decades. In particular, because of their excellent biocompatibility and biofunctions, ceramics and polymers show useful properties as biomaterials; in fact, many devices made from metals have been replaced by others made from ceramics and polymers. In spite of this fact, over 70% of implant devices are still made from metals and this percentage remains unchanged because of their high strength, toughness, and durability. Therefore current metallic biomaterials cannot be replaced with ceramics or polymers at present. In addition, research into their use in regenerative medicine will not be completed for at least another few decades. In other words, artificial materials such as metals will continue to be used as biomaterials in the future.

This chapter looks at the utilization and types of metals employed in medicine and dentistry. The properties and problems or the advantages and disadvantages of metals used for medical devices are then explained. In

addition, new alloys are introduced that are currently being researched and developed.

1.2 General properties required for metals in medical devices

1.2.1 Biological environment

The biological environment that influences the durability of metals is summarised in Fig. 1.1. The concentrations of chloride ions in serum and interstitial fluid are 113 and 117 mEq L^{-1}, respectively, which is 1/3 of the concentration in brine and a seriously corrosive environment for metallic materials (Fig. 1.1). Body fluids contain various amino acids and proteins that influence metallic corrosion (Merritt and Brown, 1998; Williams *et al.*, 1988) because they are electrolytes. In addition, the concentration of dissolved oxygen in venous blood is 1/4 that of air and in intercellular spaces 1/80–1/4 that of air (Black, 1984), which accelerates the corrosion of metallic materials. Changes in the pH of body fluids are small because the fluids are buffered solutions and the pH usually remains between 7.0 and 7.35 (Black, 1984). The pH of the hard tissue into which a material is implanted decreases to approximately 5.2 and then recovers to 7.4 within two weeks (Hench and Ethridge, 1975). However, the local pH may change according

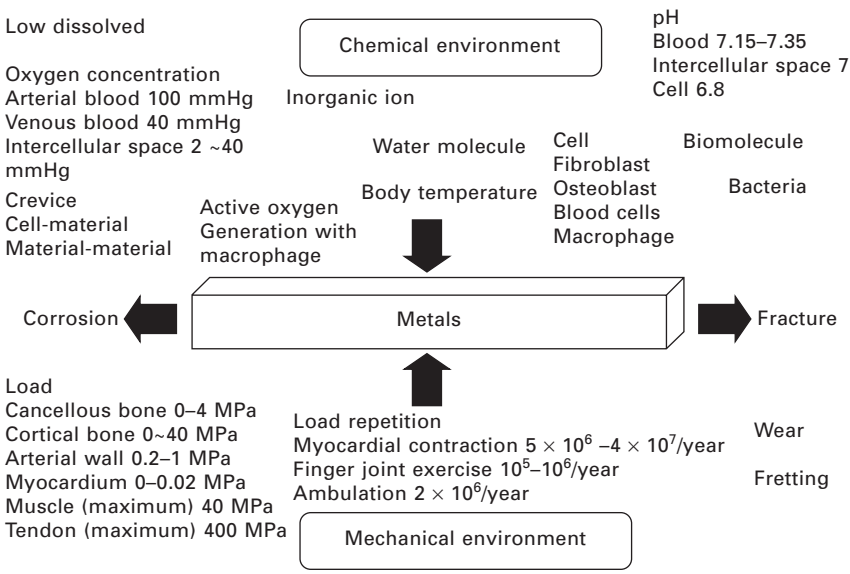

1.1 Biological environment of metallic materials implanted into human body.

to the dissociation of protein in the body fluid and the isoelectric point of protein (usually 5–7). The pH in an oral cavity may decrease to about 2 if carbonated drinks and foods are ingested. The cell is also a kind of charging body that may influence the corrosion of metallic materials.

Materials implanted in the human body are intermittently stressed with loads due to weight and activity (Fig. 1.1). In particular, materials in the lower extremities are intermittently loaded with stressors several times heavier than body weight. In addition, loading is repeated a great number of times. Such loads are applied in the chemical environment described above.

Under these conditions, material properties such as strength, toughness, rigidity, elasticity, wettability, bioinertness, bioactivity, biodegradability and X-ray imaging are required according to their purpose. Since biomaterials are used in contact with living tissues, they need to be absolutely safe for the human body. Moreover, it must be possible to sterilize biomaterials. Needless to say, durability in the human body is also important. In particular, corrosion resistance is required in metals.

1.2.2 Properties required for metals in medicine and dentistry

Materials are categorised as metals, ceramics, and polymers (Fig. 1.2). Metallic materials generally have a multi-crystal body consisting of metal bonds. However, metal oxides, metal salts, metal complexes, etc. contain metal elements, but since these are compounds consisting of ionic bonds or covalent bonds, their properties are completely different from those of metals consisting of metal bonds.

In the field of materials engineering, ceramics and metals are clearly distinguished, despite the fact that both of them are categorised as inorganic compounds. Each material has its own advantages and disadvantages, and applications are determined according to their properties.

Metals have been utilised for dental restoration and bone fixation for the past 2500 years and have a long history as biomaterials. The properties of metals derive from their metal bonds and their advantages as biomaterials are as follows:

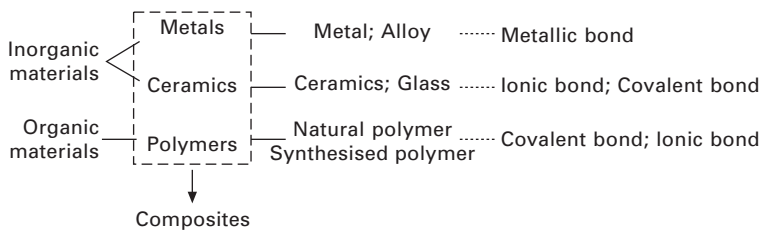

1.2 Category of materials and their chemical bonding.

- high strength
- high ductility; easy working
- high fracture toughness
- suitable elasticity and stiffness
- high electroconductivity.

Metals and alloys are widely used as biomedical materials and are indispensable in the medical field. The advantages of metals compared with ceramics and polymers are their great strength and resistance to fracture. In particular, toughness, elasticity, rigidity, and electrical conductivity are essential properties for metals used in medical devices. The metals used for such devices are listed in Table 1.1. Conventionally, metals have been essential for orthopaedic implants, bone fixators, artificial joints, external fixators, etc., because they can substitute for the function of hard tissues in orthopaedics. Stents and stent grafts are placed at stenotic blood vessels for dilatation. Therefore, these devices require elasticity or plasticity for expansion and rigidity for maintaining dilatation. In dentistry, metals are used for restorations, orthodontic wire, and dental implants. For mechanical reliability, metals must be used and cannot be replaced with ceramics or polymers. The most important property of biomaterials is safety. Therefore, corrosion-resistant materials such as stainless steel, cobalt (Co)–chromium (Cr)–molybdenum (Mo) alloys, metallic titanium (Ti), and Ti alloys are employed. Noble-metal-based alloys, such as gold (Au) alloys and silver (Ag) alloys, are also used in dentistry.

Safety to the human body is essential in biomaterials; therefore, no toxic material is used for biomaterials. Metals implanted in tissues do not show any toxicity unless there is metal ion dissolution from corrosion and/or the generation of debris from wear. Therefore, corrosion resistance is absolutely essential for metals in biomedical use, necessitating the use of noble or corrosion-resistant metals and alloys for medicine and dentistry. Of the noble metals and alloys, Au markers are used for the imaging of stents, Pt is used for embolic coils, and Au alloys and Ag alloys for dental restoratives. Of the base metals and alloys, austenitic stainless steels, Co–Cr alloys, Ti and Ti alloys, whose corrosion resistance is maintained by a passive film of surface oxide, are utilised for implant materials. In addition, wear resistance is required to reduce the generation of wear debris. Co–Cr–Mo alloys have good wear resistance and are used for sliding parts of artificial joints. A comparison of the various properties of metals used for implants is summarised in Table 1.2. The positions of the component elements of metals in biomedical use on the periodic element table are shown in Fig. 1.3.

Table 1.1 Metals used for medical devices

Clinical division	Medical device	Material
Orthopaedic surgery	Spinal fixation	316L stainless steel; Ti; Ti–6Al–4V; Ti–6Al–7Nb
	Bone fixation (bone plate, screw, wire, bone nail, mini-plate, etc.)	316L stainless steel; Ti; Ti–6Al–4V; Ti–6Al–7Nb
	Artificial joint; bone head	Co–Cr–Mo; Ti–6Al–4V; Ti–6Al–7Nb
	Spinal spacer	316L stainless steel; Ti–6Al–4; Ti–6Al–7Nb
Cardiovascular medicine and surgery	Implant-type artificial heart (housing)	Ti
	Pace maker (case)	Ti; Ti–6Al–4V
	(electric wire)	Ni–Co
	(electrode)	Ti; Pt–Ir
	(terminal)	Ti; 316L stainless steel; Pt
	Artificial valve (frame)	Ti–6Al–4V
	Stent	316L stainless steel; Ti–N; Ta; Co–Cr–Mo
	Guide-wire	316L stainless steel; Ti–Ni; Co–Cr
	Embolization wire	Pt
	Clip	Ti–6Al–4V; 630 stainless steel; Co–Cr
Otorhinology	Artificial inner ear (electrode)	Pt
	Artificial eardrum	316L stainless steel
Dentistry	Filling	Au foil; Ag–Sn(–Cu) amalgam
	Inlay, crown; bridge; clasp; denture base	Au–Cu–Ag; Au–Cu–Ag–Pt–Pd; Ti; Ti–6Al–7Nb; Co–Cr; 304 stainless steel; 316L stainless steel
	Thermosetting resin facing crown; porcelain-fused-to-metal	Au–Pt–Pd; Ni–Cr
	Solder	Au–Cu–Ag; Au–Pt–Pd
	Dental implant	Ti; Ti–6Al–4V; Ti–6Al–7Nb; Au
	Orthodontic wire	316L stainless steel; Co–Cr; Ti-Ni; Ti-Mo
	Magnetic attachment	Sm–C; Nd–Fe–B; Pt–Fe–Nb; 444 stainless steel; 447J1 stainless steel; 316L stainless steel
General surgery	Treatment device (bar, scaler, periodontal probe, dental tweezers, raspatory, etc.)	304 stainless steel
	Needle of syringe	304 stainless steel
	Scalpel	420J1 stainless steel
	Catheter	Ni–Ti; 304 stainless steel; 316L stainless steel; Co–Cr; Au; Pt–In
	Staple	630 stainless steel

Table 1.2 Comparision of properties of metals for implants

Materials		Mechanical property Tensile strength	Workability			Corrosion resistance Pitting
			Wear resistance	Plasticity	Machinability	
Stainless steel	Type316L	Good	Excellent	Excellent	Excellent	Excellent
Co–Cr alloy	Cast Annealed	Good Excellent	Good Good	Poor Good	Poor Good	Good Fair
Ti; Ti alloy	CP Ti Ti–6Al–4V	Excellent Excellent	Excellent Excellent	Fair Fair	Fair Excellent	Excellent Excellent

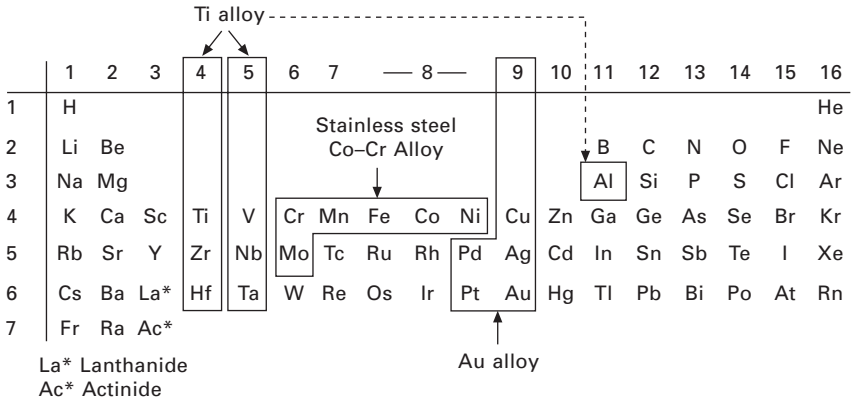

1.3 Position of elements constituting metallic biomaterials in periodic table.

1.3 Stainless steels

1.3.1 Definition and category

'Stainless steel' is defined as an iron-based alloy containing over 12–13mass%Cr and other elements, provided that the content of iron (Fe) is not over 50mass%. Stainless steel is not corroded under an oxygen-containing atmosphere, but is locally corroded and sometimes forms pits in chloride solutions such as body fluids. Nickel (Ni), Mo, copper (Cu), Ti, niobium (Nb), nitrogen (N), etc. are added to stainless steels to improve their corrosion resistance, heat resistance, strength, and workability. The metallurgical structure, strength, and corrosion resistance of stainless steels depend on the concentrations of Ni and Cr they contain and stainless steels are categorised as ferritic (Fe–Cr system), martensitic (Fe–Cr system), and austenitic (Fe–Cr–Ni system), according to their crystal phase. Austenitic-type stainless steels have outstanding corrosion resistance, but do not have great

strength. Therefore, austenitic stainless steels are strengthened by working and heat treatment, and hardened with the addition of nitrogen (N). The addition of Mo improves their corrosion resistance, because their passive film becomes more stable. The categories of popular stainless steel series are summarised in Fig. 1.4, according to their development history. In AISI numbering, the 200s represent Fe–Cr–Ni–manganese (Mn) alloy systems, the 300s represent Fe–Cr–Ni alloy systems, and the 400s represents Fe–Cr systems. Recently, the stainless steels used for the stems of artificial hip joints and bone fixators have been replaced by Ti alloys. However, stainless steel is still used for internal bone fixators that are retrieved after healing, and for sternal wire and bone fixation wire, because of its excellent torsion property and elongation. Major stents are made from austenitic stainless steel. Stainless steels are also used for treatment and operating equipment and instruments. Type 304 stainless steel is used for medical equipment such as scalpels, forceps and dental tweezers.

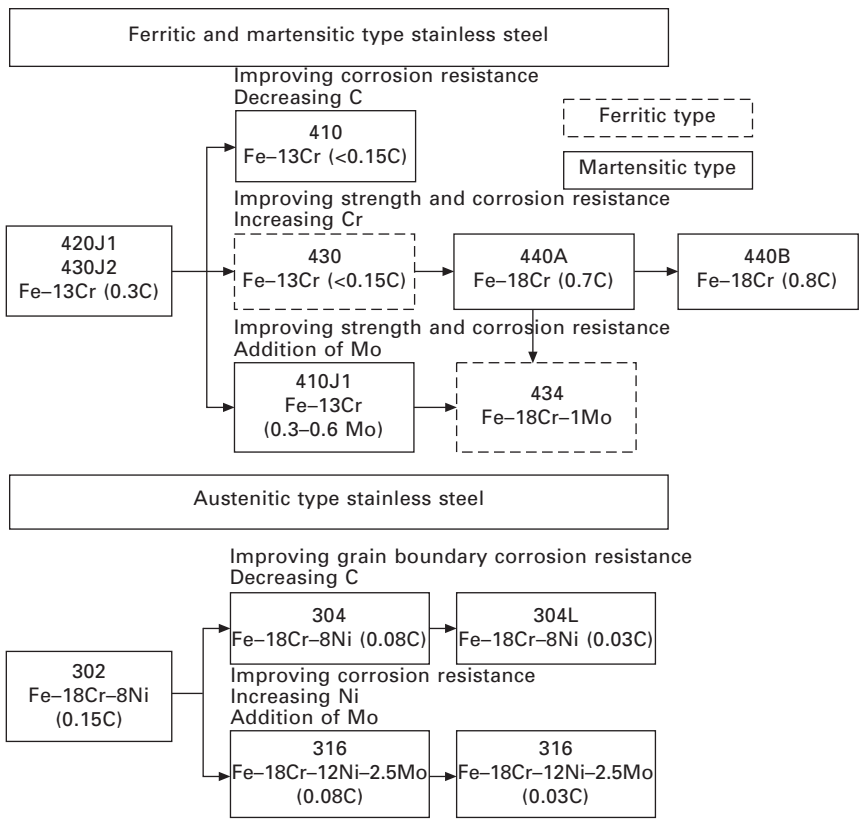

1.4 Concept of design of predominant stainless steels.

1.3.2 Type 316L stainless steel

The design of type 316L stainless steel is based on type 302 stainless steel. Its corrosion resistance is improved by adding 2.0–3.0mass% of Mo, increasing Ni from 8.0–10.0mass% to 12.0–15.0mass%, and reducing C to less than 0.030%. 'L' means 'low carbon content'. The presence of Mo as an alloying element in stainless steel reduces both the number and the size of nucleations and metastable pits. This is because bonds in the oxide film are strengthened and active sites caused by the formation of molybdates or of molybdenum oxyhydroxides are eliminated (Ilevbare and Burstein, 2001). The composition and mechanical properties of this alloy are summarised in Tables 1.3 and 1.4.

In the case of type 316L stainless steel, solution treatment is carried out, followed by rapid cooling (such as water cooling) after the products have been heated to 1010–1150 ºC. This form of heat treatment causes dissolution of precipitates during the manufacturing process, as well as the release of strains which were induced during rolling. The release of strain energy causes recrystallization of the structures. Metallic biomaterials must possess essential prerequisite properties such as corrosion resistance, strength, toughness, and ductility. As discussed above, these properties can be achieved through

Table 1.3 Composition of representative stainless steel and Co–Cr alloys

Material		C	Si	P	S	Mn	Cr	Ni	Mo	W	Co	Fe
Stainless steel	Type 316L	<0.03	<0.045	<0.03	<1.0	<2.00	16.0 –18.0	12.0 –15.0	2.0 –3.0			Bal.
Co–Cr alloy	Cast ASTM F75–92	<0.35	<1.0			<1.0	27.0 –30.0	<1.0	5.0 –7.0		Bal.	<0.75
	Wrought ASTM F90–92	0.05 –0.15	<0.4	<0.04	<0.03	1.0 –2.0	19.0 –21.0	9.0 –11.0		14.0 –16.0	Bal.	<3.0

Table 1.4 Mechanical properties of representative stainless steel and Co–Cr alloys

Materials		Tensile strength (MPa)	Proof strength (MPa)	Elongation (%)
Stainless steel	Type 316L Solution treatment and annealing	>480	>175	>40
Co–Cr alloy	Cast ASTM F75–92	655	450	8
	Wrought ASTM F90–92 Annealed	860	310	30–45

chemical composition, heat treatment, and working such as forging and rolling.

The surface oxide film on type 316L steel polished mechanically in de-ionised water consists of oxide species of iron, chromium, nickel, molybdenum and manganese, and its thickness is about 3–4 nm (Hanawa *et al.*, 2002). The surface film contains a large amount of OH^- – the oxide which is hydrated or oxyhydroxidised. In pins and wires made from 316L austenitic stainless steel, calcium and phosphorus are present in the surface oxide. Calcium phosphate is formed for specimens immersed in Hanks' solution and in a cell culture medium, as well as incubated with culture cells. Sulfate is adsorbed by the surface oxide film and reduced to sulfite in the cell culture medium and with the cultured cells. The surface oxide changes into iron and chromium oxides, when a small amount of molybdenum oxide is present.

1.3.3 Nickel-free austenitic stainless steel

Nickel is a high-risk element from the viewpoint of allergic problems. Thus, Ni-free austenitic stainless steel is required. Schaeffler's phase diagram can be used for the development of high-performance austenitic stainless steels (see Fig. 1.5). The y-axis corresponds to the Ni-equivalent for the elements which stabilise the austenitic microstructure; the x-axis corresponds to the Cr-equivalent for the elements which stabilise the ferritic microstructure.

Nitrogen, which is one of the austenitizing elements, is an important alloying element for austenitic stainless steels in terms of corrosion resistance and strength (Ornhagen *et al.*, 1996). Nitrogen dissolved in austenitic stainless

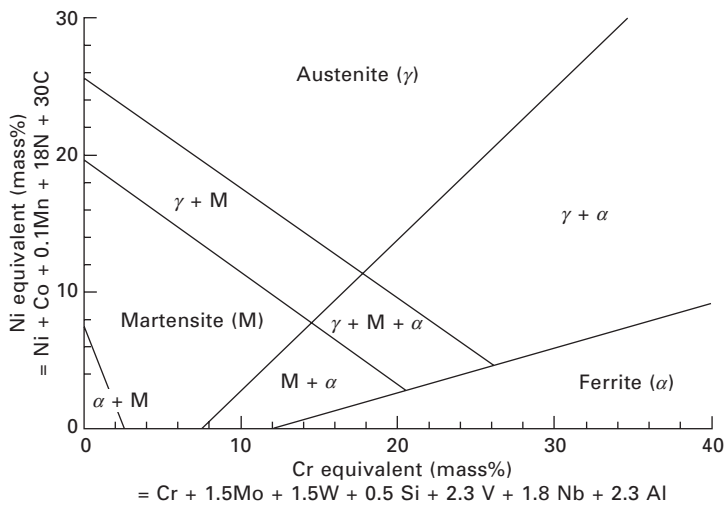

1.5 Schaeffler's phase diagram.

steel acts to increase its strength and improve its resistance to pitting corrosion and crevice corrosion in solutions containing chloride ions. The mechanisms have been summarised as follows (Baba *et al.*, 2002):

- N in solid solution is dissolved and produces NH_4^+, hence depressing oxidation inside a pit;
- concentrated N at the passive film/alloy surface stabilises the film and prevents attack from anions (Cl^-);
- nitrate ions are produced to improve resistance to pitting corrosion;
- N addition stabilises the austenitic phase; and
- N blocks kink and controls the increase of electric current for pit production.

Therefore, austenitic high-nitrogen stainless steels containing over 0.3mass%N are used.

As an alternative, nickel-free austenitic stainless steel, having a high concentration of nitrogen with N and Mn instead of Ni and displaying high strength and corrosion resistance, has been developed (Sumita *et al.*, 2004). Fe–(19–23)Cr–(21–24)Mn–(0.5–1.5)Mo–(0.85–1.1)N (BioDur® 108) in the United States (Gebau and Brown, 2001), Fe–18Cr–18Mn–2Mo–0.9N in Germany (Menzel *et al.*, 1996), and Fe–(15–18)Cr–(10–12)Mn–(3–6) Mo–0.9N in Switzerland (Uggowitzer *et al.*, 1996) have been developed for medical use. These alloys are fabricated with an electro-slug remelting process where N is absorbed into the alloy during melting under a high-pressure N atmosphere. A new manufacturing process, where N is absorbed into ferritic stainless steel after forming at 1200 °C, has also been developed (Kuroda *et al.*, 2003).

1.4 Cobalt–chromium-based alloys

1.4.1 Properties of Co–Cr alloys

Co–Cr alloys were originally developed for aircraft engines and heat-resistant materials. Co–Cr alloys show excellent mechanical properties such as strength and toughness, castability, corrosion resistance, and wear resistance. Their corrosion resistance is better than that of stainless steel; their wear resistance is better than that of stainless steel and Ti alloys; but their plasticity and workability are lower than those of stainless steel and Ti alloys. They were initially used for cast alloys because working them was difficult.

For biomedical use, cast Co–Cr–Mo alloys are better known as 'Vitallium.' Cast Co–Cr alloys are resistant to pitting and crevice corrosion. In particular, Co–Cr alloys have excellent wear resistance, so they are used for sliding parts of artificial joints. Good castability makes it possible to use them for denture bases. Wrought Co–Cr alloys have been designed to avoid the cast

defects in cast Co–Cr alloys, and their strength and elongation increase with solution heat treatment and cold working to almost the same level as those of stainless steel. The corrosion resistance of wrought Co–Cr alloy is less than that of cast Co–Cr alloy and more than that of stainless steel. Therefore, wrought alloys are used for guide wire, clips, orthodontic arch wire, and catheters. The heads of artificial hip joints and the sliding parts of artificial knee joints consist of Co–Cr alloys and their replacement with other alloys is difficult, because of the lack of corrosion resistance in stainless steel and the lack of wear resistance in Ti alloys. Initially, stents were made from a 40Co–20Cr–15Ni–7Mo–Mn alloy named 'Elgiloy', which had been developed as a heat-resistant alloy, and at present it is used for orthodontic arch wire. Current stents consist of stainless steel and Ni–Ti alloy. The composition and mechanical properties of a typical Co–Cr alloy are listed in Tables 1.3 and 1.4.

The surface oxide film of a Co–Cr–Mo alloy was characterised as containing oxides of cobalt and chromium without Mo, and the film on another Co–Cr–Mo alloy, polished mechanically in de-ionised water, consisted of oxide species of cobalt, chromium and molybdenum and had a thickness of about 2–3 nm (Hanawa *et al.*, 2001). This surface film contains a large amount of OH^- – the oxide which is hydrated or oxyhydroxidised. Cobalt was dissolved in a Co–Cr–Mo alloy during immersion in Hanks' solution and in a cell culture medium, as well as during incubation in a cell culture (Hanawa *et al.*, 2001). After dissolution, the surface oxide consisted of chromium oxide (Cr^{3+}) which contained molybdenum oxides (Mo^{4+}, Mo^{5+} and Mo^{6+}). Calcium phosphate was also formed on the upper surface.

1.4.2 Ni-free Co–Cr alloys

The allergy problem of Ni mentioned previously is also a problem in Co–Cr alloys. Thus, Ni-free Co–Cr alloys are required. The Co–Cr–Mo alloy contains a small amount of Ni and this may preferentially dissolve under wear conditions. However, since the plastic workability of the Co–Cr–Mo alloy decreases in the absence of Ni, it is necessary to add strength and ductility to the Ni-free Co–Cr–Mo alloy by grain refinement. A Ni-free Co–(16–29) Cr–6Mo alloy has been developed (Kurosu *et al.*, 2007). The grain size of this alloy is controlled by the forging ratio.

1.5 Titanium-based alloys

Ti and Ti alloys were developed for aerospace materials and have also been used for medical and dental implants, because they show good corrosion resistance and great specific strength. Their Young's modulus is about half that of stainless steel and Co–Cr alloys, and this low Young's modulus makes

them the preferred material for use in bone fixators. Ti materials form stable titanium oxide films on their surfaces, with the result that their corrosion resistance is better than that of stainless steel and Co–Cr alloys. Ti and most of the Ti alloys show high corrosion resistance and are safe for use in the human body; moreover, they exhibit good tissue compatibility, especially for hard tissue. On the other hand, Ti and Ti alloys are not suitable for bone fixation wires and sternal wires that require ligatures because of their low torsion strength (torque) and torsion angle to fracture.

Although Ti is seen as suitable for dental restoratives because of its good corrosion resistance and biocompatibility, the application of Ti to dentistry was initially difficult because Ti has a high melting point, low fluidity, and a high reactability with moulds. However, Ti is now utilised for dental castings as a result of the development of casting machines and special moulds.

1.5.1 Properties of Ti

Titanium is an extremely active element, causing a low standard electrode potential of –1.63 V vs. NHE in the reaction, $Ti \rightarrow Ti^{2+} + 2e^{-}$. This activity is the basis of the chemical properties of titanium, such as the difficulty in smelting it, its high corrosion resistance, and safety (Fig. 1.6). The corrosion resistance of Ti is very high, in spite of the high activity of the titanium element, because Ti immediately reacts with water molecules in aqueous solutions and moisture in the air, and forms a very thin titanium oxide film on its surface. This oxide film is immediately repaired even when it is ruptured

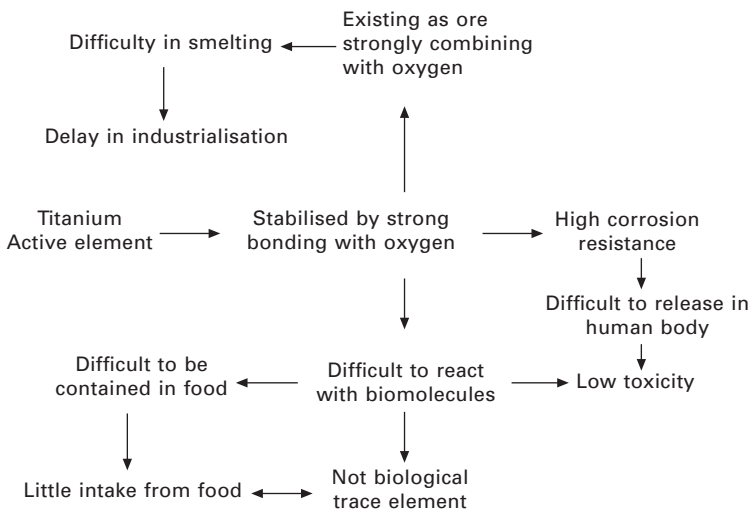

1.6 Properties of titanium induced by thermodynamical activity of titanium.

by scratching, and thus the reaction of Ti with the external environment is inhibited, causing the apparent inactivity of Ti. This property directly contributes to its corrosion resistance and its safety.

Pure Ti is composed of hcp crystals (α phase) at ambient temperatures, but is composed of bcc crystals (β phase) over 882 °C. Real pure Ti does not exist, because Ti easily dissolves oxygen, carbon, and nitrogen and contains them as impurities. Ti containing these impurities is described as commercially pure Ti (CP Ti). CP Ti is classified into four grades, according to its impurity content and mechanical properties (Table 1.5). The higher the grade number, the higher the impurity, tensile strength, and offset yield stress, and the lower the elongation (Fig. 1.7). In other words, CP Ti is a type of alloy, from the viewpoint of the definition of an alloy and the general effects of alloying. CP Ti is used for maxillofacial prosthetic plates, sternal wire, dental implants, dental restoratives, and dental denture bases. Sometimes, CP Ti containing more impurities than grade 4 displays almost the same strength as Ti alloys, and since the tensile strength greatly increases with cold working, bone screws that are exposed to a large load are sometimes made of CP Ti.

The surface oxide film on Ti consists mainly of amorphous or low-crystalline and non-stoichiometric TiO_2, and can withstand chloride ions. Since a considerable portion of oxidised titanium remains as Ti^{2+} and Ti^{3+} in the surface film, the oxidation process can be fully completed only on the uppermost part of the surface film. When Ti which has been surgically implanted into the human jaw is characterised using Auger electron

Table 1.5 Compositions and mechanical properties of commercially pure titanium (CP Ti)

	Grade 1	Grade 2	Grade 3	Grade 4
Element		Composition (mass%)		
Fe	<0.15	<0.2	<0.25	<0.3
O	<0.18	<0.25	<0.35	<0.45
N	<0.03	<0.03	<0.05	<0.05
H	<0.0125	<0.0125	<0.0125	<0.0125
C	<0.1	<0.1	<0.1	<0.1
Ti	Balance	Balance	Balance	Balance
		Mechanical property		
Tensile strength (MPa)	275–412	343–510	481–618	>550
0.2% Proof strength (MPa)	170	275	380	>440
Elongation (%)	>27	>23	>18	>15
Young's modulus (GPa)	114			

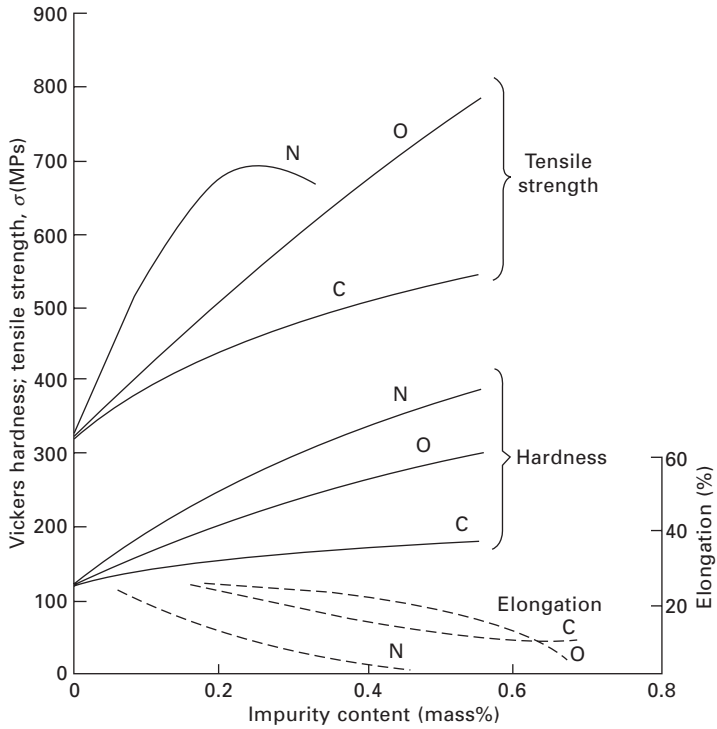

1.7 Changes of tensile strength, hardness, and elongation of titanium with impurities.

spectroscopy (AES), its surface oxide film reveals constituents of calcium, phosphorus, and sulfur (Sundgren *et al.*, 1986; Espostito *et al.*, 1999). Immersing Ti and its alloys in Hanks' solution and other solutions (Hanawa and Ota, 1992; Healy and Ducheyne, 1992) causes the formation of calcium phosphate on their surfaces. Extrapolating from this, it can be assumed that bone formation is faster on Ti implanted in hard tissue simply because the surface oxide film is titanium oxide.

1.5.2 Ti alloys

Ti alloys at ambient temperatures are categorised as α-type, $\alpha + \beta$-type, and β-type alloys, according to the quantities and types of their alloying elements. Many kinds of alloys have been developed (Table 1.6) but the Ti-6 aluminium (Al)-4 vanadium (V) alloy, an $\alpha + \beta$-type alloy, is the most conventional one for medical use. This alloy show good workability, heat treatment ability, and weldability, as well as corrosion resistance, strength, and biocompatibility. The extra low interstitials (ELI) grade alloy, containing small amounts of

Table 1.6 Specificated titanium alloys

Composition (mass%)	Type	UNS	ASTM	ISO
Ti–3Al–2.5V	$\alpha + \beta$	R56320	ASTM B 348	–
Ti–5Al–2.5Fe	$\alpha + \beta$	–	–	ISO 5832-10
Ti–6Al–4V	$\alpha + \beta$	R56400	ASTM F 1472	ISO 5832-3
Ti–6Al–4V ELI	$\alpha + \beta$	R56401	ASTM F 136	ISO 5832-3
Ti–6Al–7Nb	$\alpha + \beta$	R56700	ASTM F 1295	ISO 5832-11
Ti–15Mo	β	R58150	ASTM F 2066	–
Ti–13Nb–13Zr	β	R58130	ASTM F 1713	–
Ti–12Mo–6Zr–2Fe	β	R58120	ASTM F 1813	–
Ti–45Nb	β	R58450	AMS 4982	–
Ti–35Nb–7Zr–5Ta	β	R58350	–	–
Ti–55.8Ni	Metallic compound	–	ASTM F 2063	–

interstitial impurities, oxygen (O), carbon (C), N, and hydrogen (H), is used for biomaterials. The Ti–6Al–4V ELI alloy shows great toughness, because the impurities decrease the fatigue strength with the notch effect. ELI alloy is used for bone fixation plates and the stems of artificial hip joints. Ti–6Al–4V alloy has an extremely large 0.2% offset yield strength of 895 MPa, which is much larger than that of stainless steel and Co–Cr-Mo alloys, making plastic deformation difficult even under a large load.

The Ti–6Al–7Nb alloy (Semlitsch *et al.*, 1985) has been developed as a replacement for the Ti–6Al–4V alloy, mainly used in Europe, because the V contained in the Ti–6Al–4V alloy shows strong toxicity, although there are no reports of accidents when using Ti–6Al–4V alloy implants. The Ti–6Al–7Nb alloy has been created by substituting the V with Nb at the same atomic concentration. Its corrosion resistance and safety are greater than those of Ti–6Al–4V. Elsewhere, the Ti–6Al–2.5Fe alloy developed in Europe, Ti–13Zr–13 tantalum (Ta) alloy (nearly β) developed in the United States, and Ti–6Al–2Nb–1Ta alloy and Ti–15 zirconium (Zr)–4Nb–4Ta alloy developed in Japan, have been specified. These are $\alpha + \beta$-type alloys. However, Young's modulus could decrease to about 60 GPa in a β-type alloy. Various β-type alloys, Ti–12Mo–6Zr–2Fe alloys (Wang *et al.*, 1993), T–15Mo (Zardiackas *et al.*, 1996) and Ti–15Mo–2.8Nb–0.2Si–0.28O (Fanning, 1996) have been developed in the United States and Ti–15Mo–5Zr–2Al alloy has been specified. The mechanical properties of β-type alloys are shown in Fig. 1.8.

Ti alloys consisting of elements with low toxicity have been developed. The basic design of the alloys is the substitution of V and Al with Nb, Ta, Zr, and hafnium (Hf), which are in groups 4 and 5 in the periodic table (Fig. 1.3). On the other hand, β-type alloys show a low Young's modulus and may prevent stress shielding as used for bone fixators; for this reason, Ti–29Nb–13Ta–4.6Zr has been developed as a β-type alloy (Kuroda *et al.*,

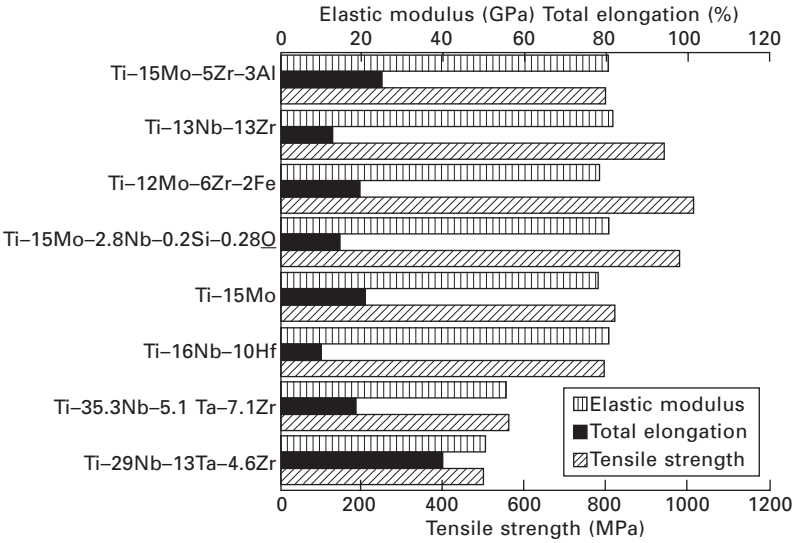

1.8 Mechanical properties of β-type titanium alloys.

1988). This alloy is transformed to the β phase by heat treatment and forging, and shows the smallest Young's modulus among β-type alloys. Elsewhere, the Ti–Nb–Sn alloy system is in the process of development (Ozaki *et al.*, 2004).

1.6 Shape memory and superelastic alloys

Ti–Ni alloys consisting of equal atomic amounts of Ti and Ni (49–51mol%Ni) show unique mechanical properties such as shape memory, superelasticity, and dumping. With the shape memory effect, the original shape can be recovered after deformation by heating; with superelasticity, any apparent plastic deformation can be returned to the original shape by releasing the load. Because of these unique properties, the Ti–Ni alloy is used for guide wires, stents, orthodontic arch wires, endodontic reamers and files.

The range of composition for the Ti–Ni alloy displaying these properties is very narrow, nearly a 1:1 atomic ratio. This Ti–Ni alloy has a specific transformation temperature as a biomaterial. An austenitic phase (A phase) appears at a higher temperature and a martensitic phase (M phase) appears at a lower temperature according to a heat-elastically martensitic transformation. As shown in Fig. 1.9(a), when the temperature of the alloy is decreased from the A phase, the martensitic transformation begins at M_s (1) and all phases transform to the M phase at M_f (2). On the other hand, when the temperature is increased from the M phase, austenitic transformation begins at A_f (3) and all phases transform to the A phase at A_f (4). From the viewpoint of

the crystal structure, as shown in Fig. 1.9(b), when the alloy in the A phase is cooled under M_s, the phase transforms to the M phase; however, the apparent morphology is not changed, although the crystal lattice is somewhat strained. When external stress is loaded onto the crystal, the crystal deforms by the formation of a twin, not by slip, and the relative configuration of the atoms is not changed. Therefore, when the temperature is again increased, the crystal returns to the original crystal structure and original morphology. The twin deformation compensates for 8% of the deformation in tensile strain; slip deformation will occur above this strain and it is then impossible to recover the original morphology. This transformation is caused by the change in temperature. However, superelasticity is caused by stress, not by a change in temperature, and is known as a stress-induced transformation. The

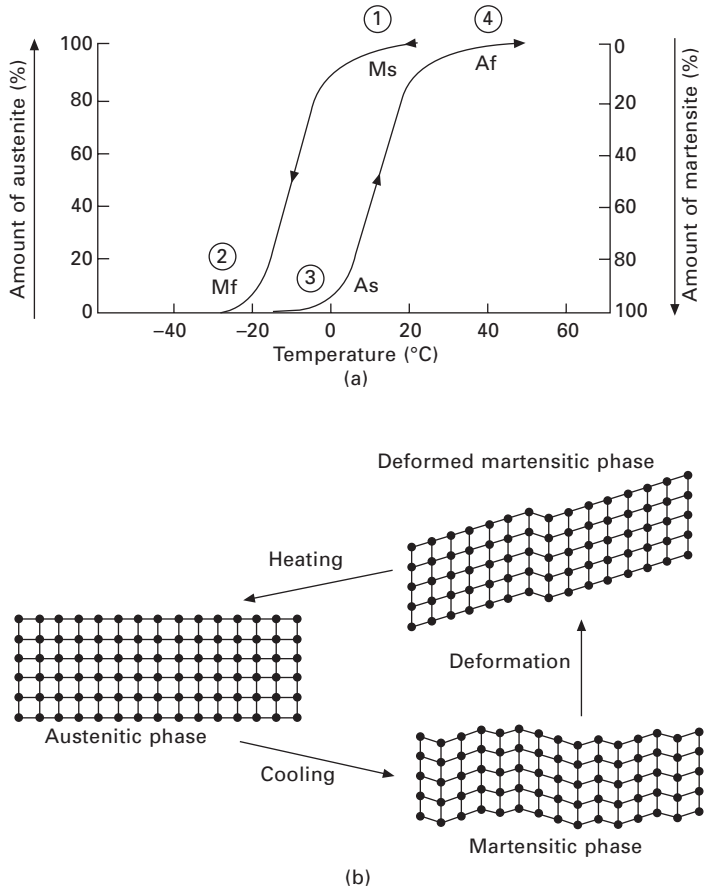

1.9 Transformation of Ni–Ti alloy and mechanism of shape memory effect.

transformation between the A phase and M phase is caused by stress: the A phase transforms to the M phase by stress and the M phase transforms to the A phase by the release of stress. The characteristics of the Ti–Ni alloy change according to the transformation temperature and the service temperature, with the transformation temperature being influenced by composition, impurity, and heat history.

The safety level of the Ti–Ni alloy is lower than that of Ti, but is the same as that of stainless steels and Co–Cr alloys, because the Ti–Ni alloy is covered by a surface oxide film, consisting mainly of titanium oxide and nickel hydroxide. However, the Ti–Ni alloy contains about 50mol%Ni and its use in medicine is limited from the viewpoint of safety. Therefore, there is a great demand for Ni-free shape-memory and superelastic alloys. Ti–Sn–Nb (Takahashi *et al.*, 2002), Ti–Nb–Al (Hosoda *et al.*, 2003), Ti–Mo–Ga (Kim *et al.*, 2004), Ti–Mo–Sn (Maeshima and Nishida, 2004), Ti–Nb–O (Kim *et al.*, 2004b), Ti–Nb–Zr (Kim *et al.*, 2005) alloy systems are reported to have a good shape-memory effect and superelasticity, while the recovery strain and superelastic deformation stress of these alloys are still smaller than those of the Ti-Ni alloy. It is possible to improve the shape memory effect and superelasticity by changes in the transformation temperature, martensite-induced stress transformation, and critical slip stress due to alloy composition and working heat treatment.

1.7 Noble metals and alloys

Au alloys, Ag alloys, CP Ti, and Ti alloys are used for dental restoratives such as inlays, crowns, bridges, and clasps. Dental casting Au alloys are the Au–Ag–Cu system alloys, which have high corrosion resistance, high ductility, good castability, and cast fitness. Au alloys are categorised into four types, according to their Au content and mechanical properties (Tables 1.7 and 1.8). A type 1 alloy contains the most Au and is used for simple inlays; a type 2 alloy is used for complex inlays and crowns; a type 3 alloy is used for crowns and bridges; and a type 4 alloy is used for denture bases, clasps,

Table 1.7 Properties of dental casting gold alloys

Type	Heat treatment	Vickers hardness (HV)	Proof strength (MPa)	Elongation (%)	Liquidus temperature (°C)
I	Softened	50–90	>80	>18	<1050
II	Softened	90–120	>180	>12	
III	Softened	120–150	>240	>12	
IV	Softened Hardened	>150 >220	>300 >450	>10 >2	

Table 1.8 Composition ranges of dental casting gold alloys

Type	Composition (mass%)					
	Au	Ag	Cu	Pd	Pt	Zn
I	80.2 ~ 95.8	2.4 ~ 12.0	1.6 ~ 6.2	0 ~ 3.6	0 ~ 1.0	0 ~ 1.2
II	73.0 ~ 83.0	6.9 ~ 14.5	5.8 ~ 10.5	0 ~ 5.6	0 ~ 4.2	0 ~ 1.4
III	71.0 ~ 79.8	5.2 ~ 13.4	7.1 ~ 12.6	0 ~ 6.5	0 ~ 7.5	0 ~ 2.0
IV	62.4 ~ 71.9	8.0 ~ 17.4	8.6 ~ 15.4	0 ~ 10.1	0.2 ~ 8.2	0 ~ 2.7

Table 1.9 Representative composition of gold alloy for porcelain-fused-to-metal (mass%)

Au	Pt	Pd	Ag	Others
85	8	4	1	2

and bridges that require strength. Type 3 and 4 alloys could be hardened by heat treatment. Zn is added to them as a deoxidiser.

The composition of Au alloy used for porcelain-fused-to-metal repairs to teeth is listed in Table 1.9. This alloy has a high melting temperature, because the porcelain is sintered during casting. In and Sn are also added to increase the bonding strength with the porcelain. This alloy system contains no Cu and only a small amount of Ag, because these elements stain the alloy after porcelain sintering.

In the case of bridges connecting several teeth, the cast parts are soldered together. Dental solders have a basic composition of Au–Cu–Ag with 58–84% Au, and Zn and Sn are added to lower the melting point. Solder for porcelain-fused-to-metals contains Pt and Pd to raise the melting point, inhibiting deformation during sintering of the porcelain.

1.8 Other metals

1.8.1 Tantalum

Tantalum (Ta) is used for skull implants and X-ray image markers for stents. Ta is ductile and produces good X-ray imaging, because of the heavy metal. Ta is easily oxidised and passivated. Ta_2O_5, as a passive film, is very stable and difficult to corrode in a biological environment. Ta also shows low magnetic susceptibility.

1.8.2 Magnesium alloys

Magnesium (Mg) alloys are expected to be biodegradable metals for use in stents and artificial bones. Mg has the lowest density of all the metals used. At least one of Al, Zn, Mn, Zr, rare earth metals, etc. is added to form a

Mg alloy, because pure Mg cannot be utilised as a structural material due to its low strength. Mg alloys used as stents in Germany contain Al, Y, Ce, Nd and/or rare earth metals. The addition of rare earth metals improves castability and pressure resistance, but their strength at ambient temperature is lower. Controlling degradation and corrosion of Mg in the human body is difficult due to its extreme activity. In addition, hydrogen evolution occurs when it dissolves. Control of the degradation rate, so that it is safe for the human body, is a key factor for enabling the utilisation of Mg alloys for medical devices.

1.8.3 Amorphous alloys

Amorphous alloys do not have a specific atomic configuration, grain boundary, crystal segregation and defect. Therefore, an amorphous alloy exhibits a higher corrosion resistance, wear resistance, tensile strength, and fatigue strength than a crystalline alloy with the same composition. Medical devices may be miniaturised by the utilization of amorphous alloys. The Young's modulus of an amorphous alloy is as low as 75 GPa in a Zr-based amorphous alloy, much lower than that in a Ti alloy. These properties may reduce the size of implant devices. Zr-based amorphous alloys are being investigated for biomaterials (Hiromoto *et al.*, 2001).

1.8.4 Permanent magnetic materials

Permanent magnetic alloys are utilized for magnetic attachments in dental restoratives (Takada and Okuno, 2005). Samarium (Sm)–Co and Nb–Fe–boron (B) alloys are used as magnetic materials, and type 444-grade stainless steel and type 447J1-grade stainless steel are used as keepers in dental attachments. It is difficult to simultaneously fulfil the qualities of strong magnetism, high corrosion resistance and miniaturisation.

1.9 References

Baba H, Kodama T and Katada Y (2002), 'Role of nitrogen on the corrosion behavior of austenitic stainless steels', *Corros Sci*, 44, 2393–2407.

Black J (1984), *Biological Performance of Materials*, Plenum, New York.

Espostito M, Lausmaa J, Hirsch J M and Thomsen P (1999), 'Surface analysis of failed oral titanium implants', *J Biomed Mater Res Appl Biomater*, 48, 559–568.

Fanning J C (1996), 'Properties and and processing of a new metasatable beta titanium alloy for surgical implant applications', in Blenkinsop P A, Evans W J and Flower H eds., *Titanium '95: Science and Technology*, Cambridge, The University Press, 1800–1807.

Gebau R C and Brown R S (2001), 'Biomedical implant alloy', *Adv Mater Process*, 159, 46–48.

Hanawa T, Hiromoto S and Asami K (2001), 'Characterization of the surface oxide film of a Co–Cr–Mo alloy after being located in quasi-biological environments using XPS', *Appl Surf Sci*, 183, 68–75.

Hanawa T, Hiromoto S, Yamamoto A, Kuroda D and Asami K (2002), 'XPS characterization of the surface oxide film of 316L stainless samples that were located in quasi-biological environments', *Mater Trans*, 43, 3088–3092.

Hanawa T and Ota T (1992), 'Characterization of surface film formed on titanium in electrolyte', *Appl Surf Sci*, 55, 269–276.

Healy K E and Ducheyne P (1992), 'The mechanisms of passive dissolution of titanium in a model physiological environment', *J Biomed Mater Res*, 26, 319–338.

Hench L L and Ethridge E C (1975), 'Biomaterials – The interfacial problem', *Adv Biomed Eng*, 5, 35–150.

Hiromoto S, Tsai A P, Sumita M and Hanawa T (2001), 'Corrosion behaviour of $Zr_{65}Al_{7.5}Ni_{10}Cu_{17.5}$ amorphous alloy for biomedical use', *Mater Trans*, 42, 656–659.

Hosoda H, Fukui Y, Inamura T, Wakashima K, Miyazaki S and Inoue K (2003), 'Mechanical properties of Ti-base shape memory alloys', *Mater Sci Forum*, 426–4, 3121–3125.

Ilevbare G O and Burstein G T (2001), 'The role of alloyed molybdenum in the inhibition of pitting corrosion in stainless steels', *Corros Sci*, 43, 485–513.

Kim HY, Ohmatsu Y, Kim JI, Hosoda H and Miyazaki S (2004a), 'Mechanical properties and shape memory behavior of Ti–Mo–Ga alloys', *Mater Trans*, 45, 1090–1095.

Kim JI, Kim HY, Hosoda H and Miyazaki S (2004b), 'Shape memory behavior of Ti–22Nb–(0.5–2.0)O(at%) biomedical alloys', *Mater Trans*, 45, 852–857.

Kim JI, Kim HY, Inamura T, Hosoda H and Miyazaki S (2005), 'Shape memory characteristics of Ti–22Nb–(2–8)Zr(at.%) biomedical alloys', *Mater Sci Eng*, A403, 334–339.

Kuroda D, Hanawa D, Hibaru T, Kuroda S, Kobayashi M and Kobayashi T (2003), 'New manufacturing process of nickel-free stainless steel with nitrogen absorption treatment', *Mater Trans*, 44, 414–420.

Kuroda D, Niinomi M, Morinaga M, Kato Y and T. Yashiro T (1988), 'Design and mechanical properties of new B type titanium alloys for implant materials', *Mater Sci Eng*, A243, 244–249.

Kurosu S, Nomura N and Chiba A (2007), 'Microstructure and mechanical properties of Co–29Cr–Wo alloy aged at 1023K', *Mater Trans*, 48, 1517–1522.

Maeshima T and Nishida M (2004), 'Shape memory properties of biomedical Ti–Mo–Ag and Ti–Mo–Sn alloys', *Mater Trans*, 45, 1096–1100.

Menzel J, Kirschner W and Stein G (1996), 'High nitrogen containing Ni-free austenitic steels for medical applications', *ISIJ Int*, 36, 893–900.

Merritt K and Brown S A (1998), 'Effect of proteins and pH on fretting corrosion and metal ion release', *J Biomed Mater Res*, 22, 111–120.

Ornhagen C, Nilsson J O and Vannevik H (1996), 'Characterization of a nitrogen-rich austenitic stainless steel used for osteosynthesis devices', *J Biomed Mater Res*, 31, 97–103.

Ozaki T, Matsumoto H, Watanabe S, Hanada S (2004), 'Beta Ti alloys with low Young's modulus', *Mater Trans*, 45, 2776–2779.

Semlitsch, Staub F and Weber H (1985), 'Titanium-aluminum-niobium alloy, development for biocompatible, high strength surgical implants', *Biomed Technik*, 30, 334–339.

Sumita M, Hanawa T and Teoh S H (2004), 'Development of nitrogen-containing nickel-free austenitic stainless steels for metallic biomaterials — review', *Mater Sci Eng*, C24, 753–760.

Sundgren J E, Bodo P and Lundstrom I (1986), 'Auger electron spectroscopic studies of the interface between human tissue and implants of titanium and stainless steel', *J Colloid Interface Sci*, 110, 9–20.

Takada Y and Okuno O (2005), 'Effect of heat history on the corrosion of ferritic stainless steels used for dental magnetic attachments', *Dent Mater J*, 24, 391–397.

Takahashi E, Sakurai T, Watanabe S, Masahashi N and Hanada S (2002), 'Effect of heat treatment and Sn content on superelasticity in biocompatible TiNbSn alloys', *Mater Trans*, 43, 2978–2983 (2002).

Uggowitzer P J, Magdowski R and Speidel M O (1996), 'Nickel free high nitrogen austenitic steels', *ISIJ Int*, 36, 893–900.

Wang K, Gustavson L and Dumbleton J (1993), 'Low modulus, high strength, biocompatible titanium alloy for medical implants', in Froes F H and Caplan H L eds., *Titanium '92: Science and Technology*, Warrenda, TMS, 2697–2704.

Williams R L, Brown S A and Merritt K (1988), 'Electrochemical studies on the influence of proteins on the corrosion of implant alloys', *Biomaterials*, 9, 181–186.

Zardiackas L D, Mitchell D W and Disegi J A (1996): 'Characterization of Ti-15Mo beta titanium alloy for orthopaedic implant applications', in Brown S A and Lemons J E eds., *Medical Applications of Titanium and Its Alloys*, West Conshohoken, PA, ASTM, 60–75.

2
Material selection

Y. OKAZAKI, National Institute of Advanced Industrial Science and Technology, Japan

Abstract: Metal material principles of orthopaedic implants are integrated in understanding the factors affecting the performance and durability. This chapter reviews aspects governing biocompatibility such as corrosion resistance and mechanical compatibility, and the related testing methods. The future perspective regarding materials and testing methodology are also considered.

Key words: orthopaedic implant, metallic materials, microstructure, corrosion resistance, fatigue property, mechanical compatibility, durability of device, testing method.

2.1 Introduction

Many types of metallic biomaterial devices have widely been used to replace failed hard tissues; namely, bone screws, bone plates, compression hip screws (CHS), intramedullary fixations, short femoral nails, artificial hip joints, artificial knee joints, spinal instruments, and dental implants. Orthopaedic implants require biomechanical and biochemical compatibilities, as well as biological safety. Therefore, many types of metallic orthopaedic devices, manufactured from metallic materials with excellent mechanical properties and structural stability, are used worldwide in the orthopaedic field. In order to determine biomechanical and biochemical properties, as well as biological safety, many mechanical, chemical and biological tests are conducted during device developments. This chapter will provide the test methods for characterising the appropriate materials for metallic orthopaedic devices such as osteosynthesis and artificial joints. Recent topics on the mechanical, chemical, and biological test results of the new biocompatible materials will be introduced, with the developments of new orthopaedic devices.

2.2 Standardised implantable metals

Stainless steels, cobalt (Co)–chromium (Cr)–molybdenum (Mo) alloys, commercially pure titanium (CP Ti), and Ti alloys are widely used in orthopaedic surgery. Many types of these alloys have been standardised on the basis of international and national standards; for example, International Organisation for Standardisation (ISO), American Society for Testing and Materials (ASTM), and Japanese Industrial Standard (JIS). As well as the

alloy specifications, main corrosion test methods and corrosion testing solutions for metals used for orthopaedic implants are also standardised as guides (Table 2.1).[1–19] In the orthopaedic field, given that mechanical compatibility has an effect on the long-term clinical result, materials for these devices should have excellent mechanical strength and ductility. Figure 2.1 shows the correlations between minimum values of ultimate tensile strength (σ_{UTS}) and total elongation (T. E.) of these materials specified in ISO and JIS, namely, stainless steel, high-nitrogen stainless steel, Co–Cr–Mo alloys, and Ti materials (CP Ti and Ti alloys). The T. E. of various materials continuously decreases with increasing σ_{UTS}. The σ_{UTS} of the cold-worked CP Ti grade 4 containing small amounts of oxygen (O) and iron (Fe) is close to those of the Ti alloys. The main applications of these alloys are shown in Table 2.2. Stainless steel (ISO 5832-1 and ISO 5832-9), CP Ti and Ti alloys are widely used in osteosynthesis devices, while Co–28Cr–6Mo alloys are used in artificial joint bearing parts. Artificial hip joints, consisting of two types of stems and immobilising bones, with or without cement, are widely used in many countries. However, for the cement-type stem, the consumed

Table 2.1 Implantable metals and the testing methods specified in ISO and JIS standards

Standard	Metals and testing methods
ISO 5832-1	Wrought 18Cr–14Ni–2Mn–2.5Mo stainless steel
ISO 5832-9	Wrought high-N 21Cr–10Ni–3Mn–2.5Mo stainless steel
ISO 5832-4	Co–28Cr–6Mo casting alloy
ISO 5832-5	Wrought Co–20Cr–15W–10Ni alloy
ISO 5832-6	Wrought Co–35Ni–20Cr–10Mo alloy
ISO 5832-7	Forgeable and cold-formed 41Co–20Cr–16Ni–7Mo–Fe alloy
ISO 5832-8	Wrought Co–20Ni–20Cr–3.5Mo–3.5W–5Fe alloy
ISO 5832-12	Wrought Co–28Cr–6Mo alloy
ISO 5832-2	Unalloyed titanium
ISO 5832-3	Wrought Ti–6Al–4V alloy
ISO 5832-11	Wrought Ti–6Al–7Nb alloy
ISO 5832-14	Wrought Ti–15Mo–5Zr–3Al alloy
JIS T 7401-4	Wrought Ti–15Zr–4Nb–4Ta alloy
ISO 16428	Test solutions and environmental conditions for static and dynamic corrosion tests on implantable materials and medical devices
ISO 16429	Measurements of open-circuit potential to assess corrosion behaviour of metallic implantable materials and medical devices over extended time periods
JIS T 0302	Testing method for corrosion resistance of metallic biomaterials by anodic polarisation measurement
JIS T 0304	Testing method for metal release from metallic biomaterials
JIS T 0305	Testing method for galvanic corrosion in pseudo-physiological solution
JIS T 0306	Analysis of state for passive film formed on metallic biomaterials by X-ray photoelectron spectroscopy

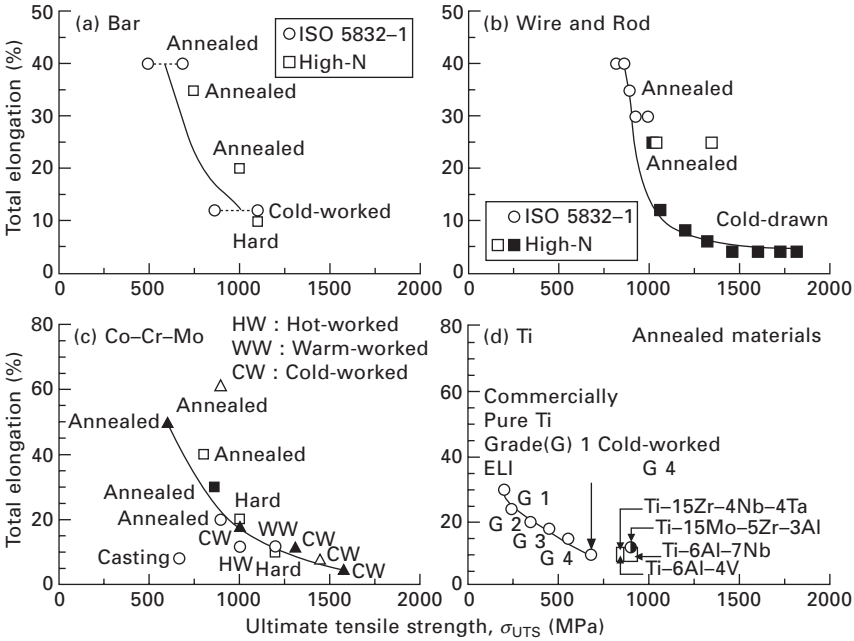

2.1 Relationship between minimum values for ultimate tensile strength and total elongation of implantable metals specified in ISO and JIS. (a), (b) Stainless steel (ISO 5832-1: 18Cr–14Ni–2Mn–2.5Mo), high–N stainless steel (21Cr–10Ni–2.5Mo–3Mn–0.3N),
(c) Co–Cr–Mo (○: Co–28Cr–6Mo, □: Co–35Ni–20Cr–10Mo, ■: Co–20Cr–15W–10Ni, ▲: 41Co–16Ni–20Cr–7Mo–16Fe, △: Co–20Ni–20Cr–3.5Mo–3.5W–5Fe)
(d) Ti materials (commercially pure Ti grade 1, grade 2, grade 3, grade 4 and cold-worked grade 4, and annealed Ti–6Al–4V, Ti–6Al–7Nb, Ti–15Mo–5Zr–3Al and Ti–15Zr–4Nb–4Ta alloys).

Table 2.2 Main metallic materials used in orthopaedic implants

	Devices	Used materials
Osteosynthesis		
	• Bone plates	• Commercially pureTi, Ti alloy
	• Screws	• Ti alloy, stainless steel
	• Compression hip screws	• Ti alloy
	• Short femoral nails	• Stainless steel, Ti alloy
	• Intramedullary nails	• Stainless steel, Ti alloy
Hip joints		
	• Cemented stem	• Hot-forged Co-28Cr-6Mo, cold-worked stainless steel
	• Cementless stem	• Ti alloy
Knee joints		
	• Femoral components	• Co-28Cr-6Mo casting
	• Tibial plates	• Ti alloy

amount of Ti alloys has tended to decrease recently. This is due to corrosion caused by micromotion between the stem and the cement mantle (formed by cement inserted into bone), particularly when less-stiff Ti alloy is used for the artificial hip stem.[20] In contrast, the Co–28Cr–6Mo alloy and high-nitrogen (N) stainless steel, with high strength and stiffness, has become the most popular cement-type stem material. On the other hand, for the cementless stem, the use of Ti alloy with high biocompatibility has become popular. Figure 2.2 shows the relationship between σ_{UTS} and Vickers hardness with tensile test specimens (diameter: 1.5 or 3 mm, gauge length: 9 or 15 mm) taken from orthopaedic devices: bone plates, compression hip screws (CHS), intramedullary rods, short femoral nails, artificial hip stems, artificial knee femoral components, and tibial stems. The σ_{UTS} of forged Co–28Cr–6Mo alloys and stainless steels used for artificial hip stems is very high. Figure 2.3 shows typical optical micrographs and transmission electron microscopy (TEM) images of the hot-forged Co–28Cr–6Mo alloy and cold-worked high-nitrogen stainless steel (ISO 5832-9) used for the cement-type stem. In the TEM images of hot-forged Co–28Cr–6Mo alloys, much finer fcc γ (gamma) structures are observed. For high-carbon Co–28Cr–6Mo alloys, $M_{23}C_6$ carbide precipitates in the γ matrix.[21] In cold-worked high-nitrogen stainless steel, CrNbN precipitation is observed in the fine austenitic (γ) phase in Fig. 2.3(d).[22]

2.3 Biocompatibility of various metals

The relationship between cytocompatibility and polarisation resistance of various pure metals is summarised in Fig. 2.4.[23–26] Cr toxicity appears to

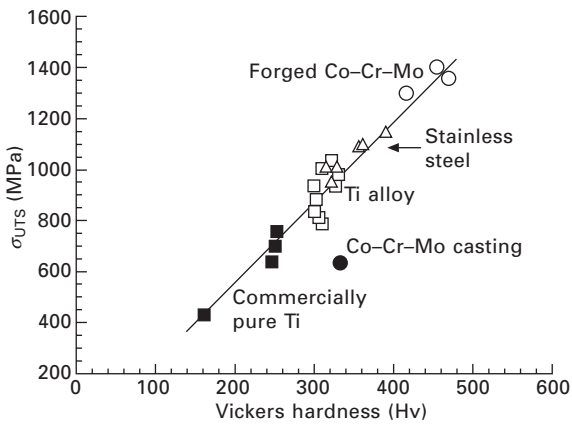

2.2 Relationship between ultimate tensile strength (σUTS) and Vickers hardness (10 N) with specimens taken from osteosynthesis devices, and artificial hip and knee joints.

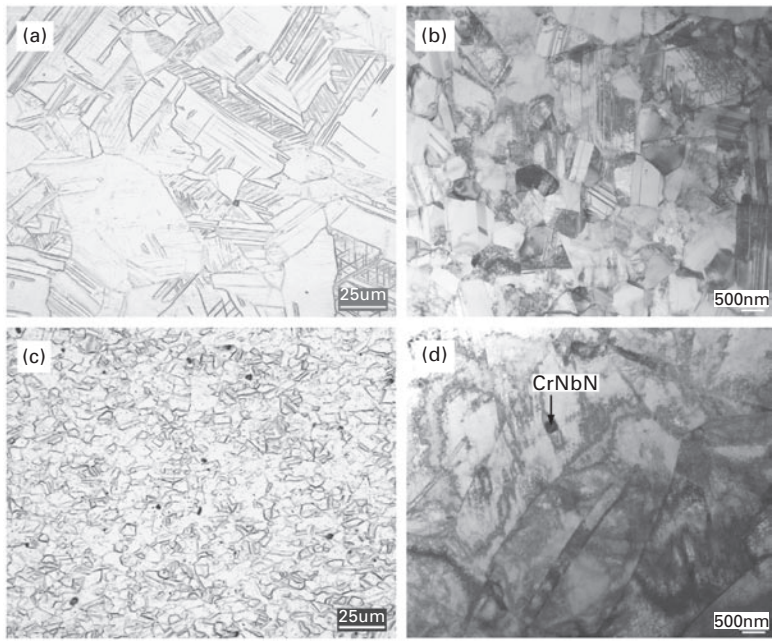

2.3 Optical micrographs (a), (c), and TEM images (b), (d) of hot-forged Co–28Cr–6Mo alloy (a), (b), and cold-worked high-N stainless steel (c), (d).

be closely related to the Cr valence state, unlike toxic elements such as Co, nickel (Ni), and vanadium (V). Co toxicity is strongly dose-related.[27] It has been reported that zirconium (Zr), niobium (Nb), and tantalum (Ta) exhibit excellent corrosion resistance and biocompatibility, and all of those belong to the loose connective vascularised (vital) group with regard to tissue reaction.[23] Among 70 metals in the periodic table of elements, only Ti and Zr show excellent cytocompatibility to both soft tissue-derived mouse fibroblast cells and bone-derived mouse osteoblast cells.[24] Adding a small amount of alternative metal elements improves the quality of the alloy. However, too much addition of Nb and Ta to Ti alloy may increase the manufacturing cost and lessen biocompatibility (Fig. 2.4(b)). In particular, fabrication of an alloy that has greater than 5 mass percent Ta content requires a special melting apparatus; conventional vacuum arc-melting is not applicable. The cytotoxicity of V ion is seen from the medium concentration of 0.1 mass ppm.

2.4 Highly biocompatible $\alpha + \beta$-type Ti alloy

Among the metallic materials used for implants today, CP Ti and Ti alloys have warranted particular focus as materials, owing to their better biomechanical

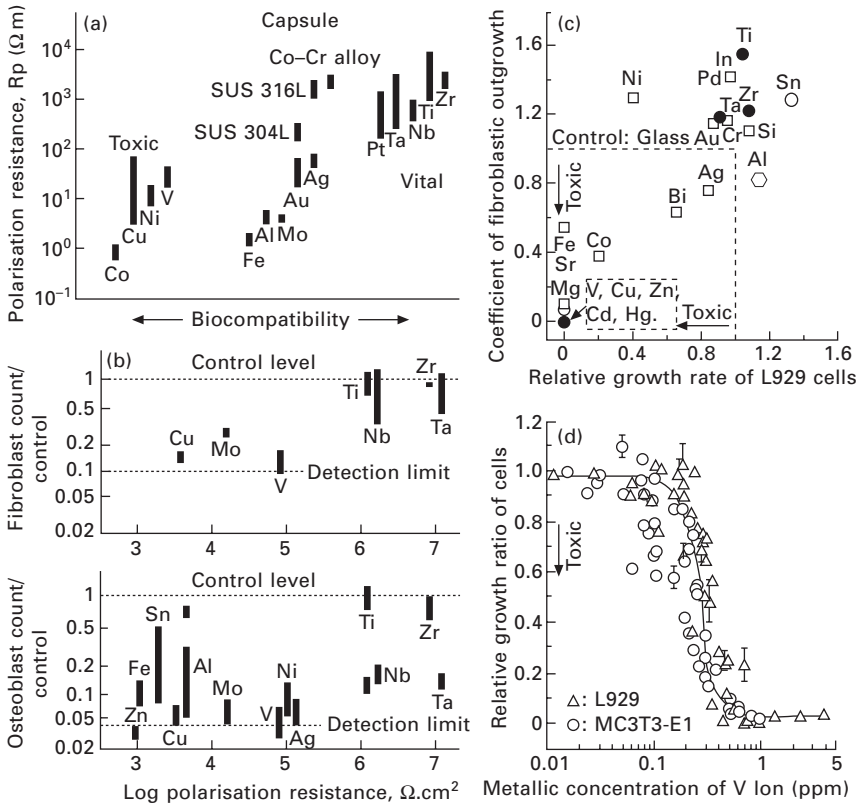

2.4 Relationship between the polarisation resistance and biocompatibility of various pure metals and alloys, (a), (b). Cytotoxicity of various pure metals (c) and V ion (d).

and biochemical compatibilities than conventional materials such as stainless steel and Co-based alloys. Recently, studies on Ti alloys have been carried out, assuming their long-term use in the human body and possible long-term health problems associated with the release of toxic ions and fatigue fractures.[28–38] The results confirmed that Ti alloys are valuable orthopaedic metallic materials having the desired characteristics such as long-term high biocompatibility, excellent corrosion resistance and fatigue strength.

2.4.1 Role of alloying elements

As summarised in Fig. 2.5, Ti alloys specified in JIS, ISO, and ASTM are categorised into three types according to their microstructural differences: α (alpha) type alloy having hexagonal close-packed structure: hcp, β (beta)-type alloys having body centred cubic structure: bcc, and $\alpha + \beta$-type alloys having the mixed structure α and β phases.[39–42] Recently, the metastable β type

Alpha structure (Hcp)	Mixed alpha-beta structure	Beta structure (Bcc)
← Alpha-stabilising elements [Al, O, Zr etc.]		Beta-stabilising elements → [Mo, Fe, Nb, Ta, etc.]
	← Higher fatigue strength	
	Improved fabricability →	
Unalloyed titanium (ISO 5832–2)	Ti–6Al–4V (ISO 5832–3) Ti–6Al–7Nb (ISO 5832–11) Ti–6Al–2Nb–1Ta (JIS T 7401–3) Ti–15Zr–4Nb–4Ta (JIS T 7401–4) Ti–13Zr–13Nb (ASTM F 1713) Ti–15Mo–5Zr–3Al (ISO 5832–14)	Ti–15Mo (ASTM F 2066) Ti–12Mo–6Zr–3Fe (ASTM F 1813)

2.5 Effects of alloying elements on Ti alloy structure, and microstructures of Ti alloys specified in ISO, ASTM and JIS.

Ti–15molybdenum (Mo)–5Zr–3aluminium (Al) alloy has been standardised in ISO 5832-14. ASTM-standardised alloy (like near-β-type Ti–13Zr–13Nb alloy and β-type alloys such as Ti–15Mo and Ti–12Mo–6Zr–2Fe) has slightly lower Young's modulus than $\alpha + \beta$-type alloys. Among the $\alpha + \beta$-type alloys, Ti–6Al–4V alloy has been extensively used for various orthopaedic applications, as seen in Table 2.2. The $\alpha + \beta$-type alloy demonstrates better fatigue characteristics than the β type alloy. Another $\alpha + \beta$-type alloy, the Ti–15Zr–4Nb–4Ta alloy has been developed in Japan as a highly biocompatible alloy for long-term biomedical applications[43–59] and is standardised in JIS T 7401-4.[13]

The microstructural change of the latest $\alpha + \beta$ type Ti–15Zr–4Nb–4Ta alloy can be expected with Al equivalence ([Al]eq) and Mo equivalence ([Mo]eq). [Al]eq and [Mo]eq are calculated using the following formula with mass percent of each element.[60] As [Al]eq increases, the volume fraction of the α phase increases. Likewise, with an increase in [Mo]eq, the volume fraction of the β phase increases. With the Ti–15Zr–4Nb–4Ta alloy not containing Al, oxygen had an effective role.

$$[\text{Al}]\text{eq} = [\text{mass\%Al}] + 1/6[\%\text{Zr}] + 10[\%\text{O}] \quad [2.1]$$

$$[\text{Mo}]\,\text{eq} = [\%\text{Mo}] + 1/3.6[\%\text{Nb}] + 1/5[\%\text{Ta}] + 2.5\,[\%\text{Fe}] + 1/1.5[\%\text{V}] + 1/2.5[\%\,\text{W}] \quad [2.2]$$

2.4.2 Forging process and heat treatment

Ti–15Zr–4Nb–4Ta alloy ingot is homogenised at approximately 1200 °C for more than 3h (hours), and β-forged at the same temperature to a forging

ratio (cross-section before forging/cross-section after forging) of more than 3. Secondly, β-forging while controlling the grain growth of the β phase is conducted to make the β phase as minimal as possible at 1000 to 1150 °C, in proportion to the size of the billet and forging ratio. Afterwards, α–β forging at β phase transformation temperature (β-transus: T_β)-(35–50 °C) is conducted to obtain α and β structures, by decoupling the fine β phase. After the α–β forging, annealing is generally conducted at 500 to 700 °C (Fig. 2.6(a)). To obtain higher strength, ageing treatment at high-/low-temperature is conducted after the solution treatment. In addition, an advanced manufacturing process such as die-forging is introduced to improve the durability.

In the Ti–15Zr–4Nb–4Ta alloy, a correlation between T_β and each element (percent by mass) is expressed using the following formula.[25] This predicts the effect of elements that increase or decrease T_β.

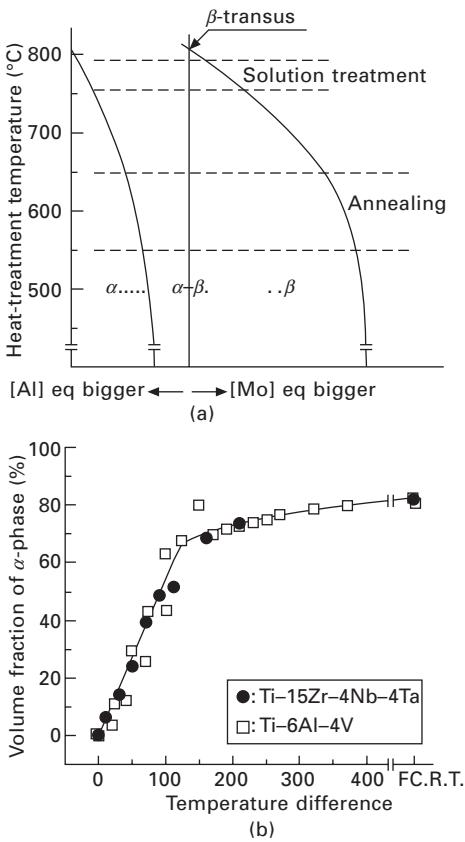

2.6 Schematic illustrations of microstructural change of α–β Ti alloy (a) and change in volume fraction of α-phase of Ti alloys as a function of temperature difference between β-transus and heat-treatment temperature (b).

$$T_\beta/°C = 848–4.2[\%Zr]–5.5[\%Ta] –6.3[\%Nb]–76[\%Pd] + 343\ [\%O] + 600\ [\%N] \quad [2.3]$$

Figure 2.6(b) shows the change in volume fraction of α phase with temperature difference between T_β and each heat-treatment temperature. Recorded changes in the volume fraction of the α phase for both Ti–15Zr–4Nb–4Ta and Ti–6Al–4V alloys were almost the same.

The annealing process of the Ti–15Zr–4Nb–4Ta alloy is generally the removal of internal stress, heat treatment at 500–700 °C for 2 h to optimise the microstructure, and then air-cooling. As the annealing temperature increases, grain coarsening and decrease in strength tend to appear. Heat treatment over the T_β decreases the ductility following the formation of acicular structure. Solution treatment could generally be conducted at the T_β-(30–50 °C), in which the volume fraction of the primary α phase is 15 to 20 vol% for 1 h, and then is water-quenched. Ageing treatment to obtain optimum balance of strength and ductility is conducted at a relatively high temperature (over-ageing temperature, which is between 500 to 700 °C) for 2 h. Further improvement of strength is obtained with the lower ageing treatment at 400 °C over 8 h.[56]

2.4.3 Microstructure of α + β-type alloy

Figure 2.7 shows optical micrographs, scanning electron microscopy (SEM) and transmission electron microscopy (TEM) images of the Ti–15Zr–4Nb–4Ta alloy after annealing at 650 or 700 °C for 2 h and air-cooling, and over-ageing treatment (600 °C, 2 h, followed by air-cooling) or ageing treatment (400 °C, 8 h, followed by air-cooling) after solution treatment (800 °C, 1 h, followed by water-cooling), respectively. The annealed Ti–15Zr–4Nb–4Ta alloy mostly consisted of α phase matrix with approximately 25 vol% β phase (Fig. 2.7(a)). TEM observation and electron beam diffraction analysis confirm the β phase at grain boundaries of the α phase. In the optical micrographs and TEM images of aged Ti–15Zr–4Nb–4Ta alloy (Figs 2.7(e) and (f)), precipitations of fine α phase precipitated by ageing are observed in addition to the primary α phase precipitated by solution treatment. Figures 2.8(a) and (b) indicate that the annealed Ti–6Al–4V alloy consists of an α phase matrix with approximately 20 vol% β phase. As shown in Fig. 2.8(c) and (d), solution-annealed Ti–15Mo–5Zr–3Al alloy features β phase matrix containing a small amount of the α phase.

2.4.4 Mechanical properties of α + β alloy

The following formulae are used to express the correlations between tensile strength of annealed Ti–15Zr–4Nb–4Ta alloy rods and the Vickers hardness,

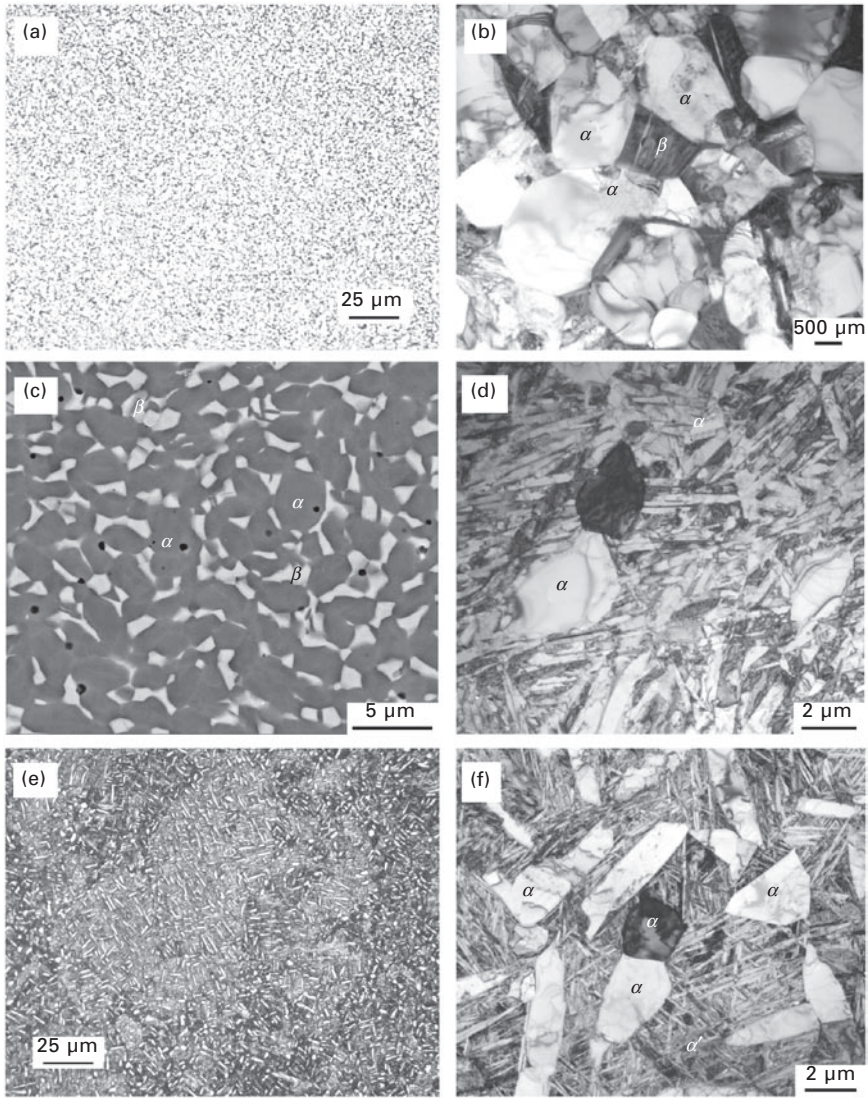

2.7 Optical micrographs, SEM and TEM images of annealed and aged Ti–15Zr–4Nb–4Ta alloys. Optical micrograph (a) and TEM image (b) of alloy annealed at 700 °C for 2 h, SEM image (c) of alloy annealed at 650 °C for 2 h, TEM image (d) of alloy over-aged at 650 °C for 2 h, optical micrograph (e) and TEM image (f) of alloy aged at 400 °C for 8 h.

and the tensile strength and each alloying element (percent by mass).[49]

$$0.2\%\ \text{proof strength (MPa)} = -160 + 3.4[\text{Hv}] \quad [2.4]$$

$$\text{Ultimate tensile strength (MPa)} = -91 + 3.5[\text{Hv}] \quad [2.5]$$

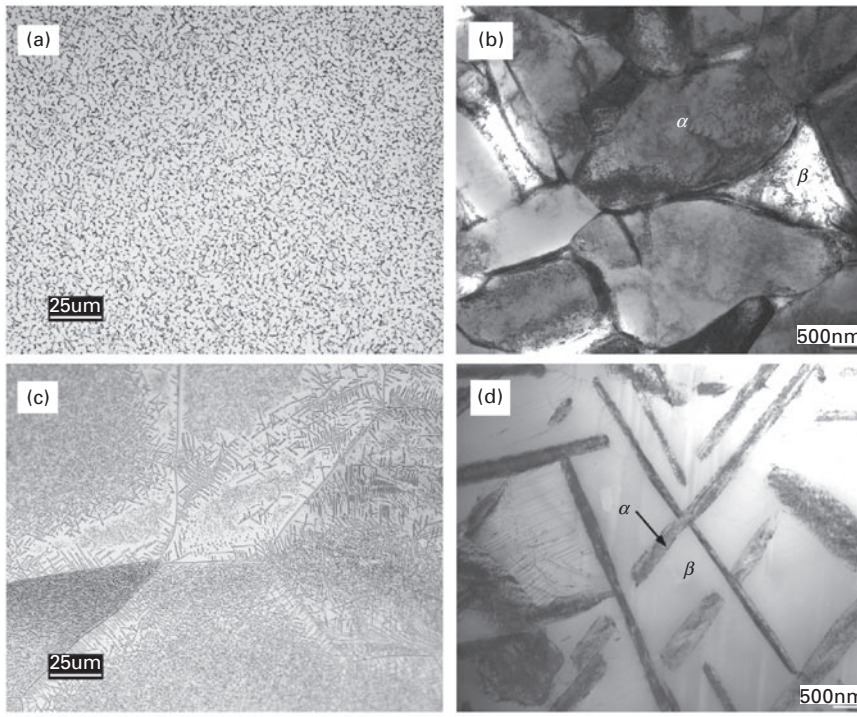

2.8 Optical micrographs and TEM images of Ti–6Al–4V and Ti–15Mo–5Zr–3Al alloys. Optical micrograph (a) and TEM image (b) of annealed Ti–6Al–4V, optical micrograph (c) and TEM image (d) of solution-annealed Ti–15Mo–5Zr–3Al.

$$0.2\%\ \text{proof strength (MPa)} = 472 + 9.8[\%\text{Zr}] - 3.2[\%\text{Nb}] + 10.7[\%\text{Ta}] + 335[\%\text{O}] + 1611[\%\text{N}] \quad [2.6]$$

$$\text{Ultimate tensile strength (MPa)} = 487 + 10.9[\%\text{Zr}] + 4.9[\%\text{Nb}] + 2.9[\%\text{Ta}] + 514[\%\text{O}] + 1491[\%\text{N}] \quad [2.7]$$

Ti alloy can be strengthened by adding trace amounts of iron and oxygen. Figure 2.9 shows the effect of solution treatment temperature, ageing temperature and ageing time on the mechanical properties of the Ti–15Zr–4Nb–4Ta alloy at room temperature. The solution treatment temperature is in the neighbourhood of T_β (at 795 °C). Each ageing condition of the alloy is (a) ageing at 400 °C for 10 h, followed by solution treatment at each temperature in the neighbourhood of T_β for 1 h and then quenching in water, (b) ageing in the range from 350 to 450 °C for 10 h, and (c) ageing at 400 °C for 5 to 15 h after solution treatment at 775 °C for 1 h. The reductions of area and α phase in volume percent gradually decrease with increasing solution

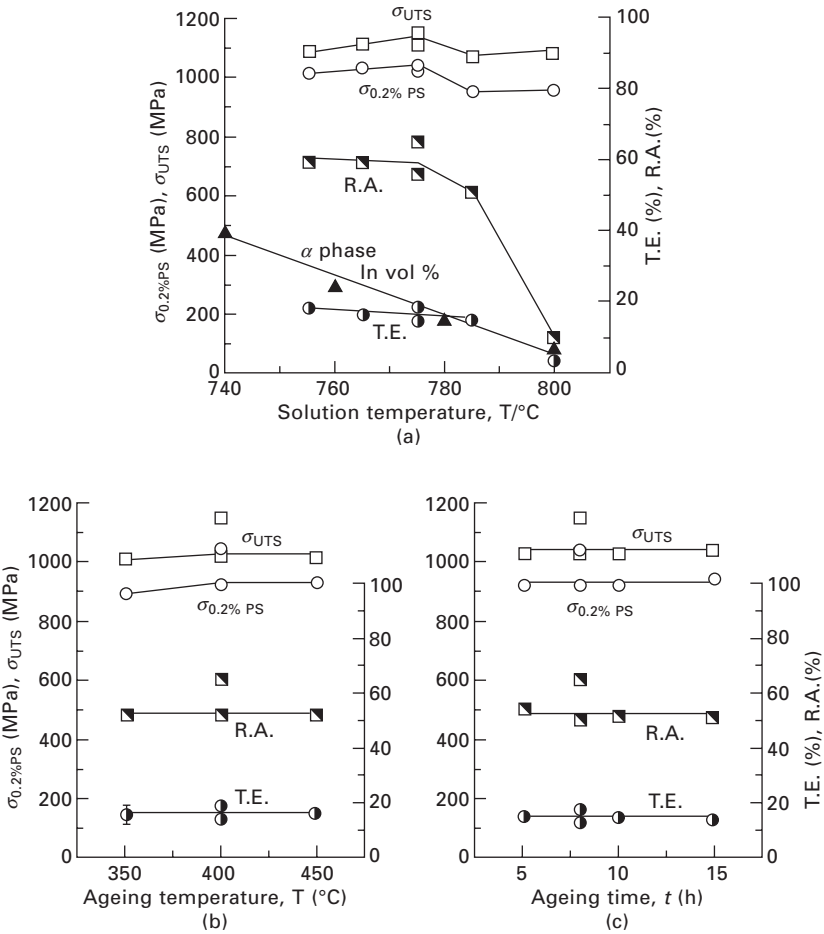

2.9 Effects of solution treatment temperature (a), ageing temperature (b), and ageing time (c) on mechanical properties of Ti–15Zr–4Nb–4Ta alloy at room temperature: 0.2% proof strength (σ0.2PS), ultimate tensile strength (σUTS), total elongation (%), and reduction of area (%).

temperature, while the tensile strength remains fairly stable. When the alloy is solution-treated at over the T_β, the values decline sharply. However, as demonstrated in Fig. 2.9(b) and (c), the effects of the ageing time and ageing temperature on the mechanical properties are negligible. Table 2.3 shows the mechanical strength of the Ti–15Zr–4Nb–4Ta alloy annealed at 700 °C for 2 h, over-ageing treatment at 600 °C for 2 h after solution treatment at 775 °C for 1 h, and ageing treatment at 400 °C for 8 h after the solution treatment. Solution treatment and over-ageing (STOA) do not transform the equiaxed granular structure to acicular structure, but change the mechanical characteristics. Primary α phase and acicular α phase that resulted from the

Table 2.3 Effect of heat treatments on mechanical properties of Ti-15Zr-4Nb-4Ta alloy

Heat treatment	$\sigma_{0.2\%PS}$(MPa)	σ_{UTS}(MPa)	T.E.(%)	R.A.(%)
Annealed	840	915	21	55
Over-aged	855	945	19	55
Aged	895	1020	15	48

over-ageing treatment are shown in the optical micrograph in Fig. 2.7(d). It also has a good combination of strength, ductility and toughness. Solution treatment and ageing (STA) affect the strength and ductility depending on the amount and grain size of the α and β phases, which are shown in Fig. 2.7(c) and (d).

2.5 Stability of passive film formed on metals

Many studies have shown the strong relationship between metal ion release from implants and clinical failure.[61–69] Previous reports indicate that several metal ions are released into the surrounding tissues owing to various mechanisms such as corrosion and mechanically-accelerated electrochemical processes such as stress corrosion, corrosion fatigue, and fretting corrosion.[68] Metal ion release into the body is an inevitable consequence of implanting metal into the body. Therefore, studying the cytotoxicity and corrosion resistance is a paramount concern with regards to biocompatibility, as shown in Fig. 2.4.

A surface oxide film, referred to as a passive film formed on metallic materials, plays an important role as an inhibitor of ion release.[70] Metallic materials with strong passive films exhibit lower quantities of metal ions released from implants. Thus, the quantity of metal ions released changes depending on the nature and strength of the metal–oxide bond, structure, role of alloying elements, composition, and thickness of oxide films.[71]

The electrochemical strength and stability of the oxide films formed on the surface of the various alloys implanted into a living body can be examined via an anodic polarisation test. The anodic polarisation test is performed in accordance with the JIS T 0302 standard.[16] In this test, a specimen is initially held at –1 V for 300 s and then at an open circuit potential for 300 s. The test is conducted from –1 to 2 V at a sweep rate of 20 mV/min. The counter and reference electrodes are platinum and saturated calomel electrodes (SCE), respectively.

2.5.1 Passive film formed on stainless steel and Co–Cr–Mo alloy

The role of alloying elements in passive films formed on SUS 316L stainless steel and Co–Cr–Mo alloys in a calf serum solution has been examined by

X-ray photoelectron spectroscopy (XPS). The XPS spectra of the passive films exhibit peaks corresponding to Cr_2O_3, CoO, Fe oxide and Mo oxide.[45] Further XPS examination revealed that metal release from various grades of stainless steel into synthetic body fluids changes owing to the Cr content in the oxide film. The rate of metal release from stainless steel into artificial lysosomal fluid decreases with increasing Cr/(Cr + Fe) ratio of the oxide film, which clearly indicates that Cr is attributed to passive film formation.[72–74]

Examination of the effect on the element Cr in the passive and transpassive behaviours of Co–Cr–Mo alloys in biological solutions clearly shows that the passive and transpassive behaviour of the alloy is markedly affected by the alloying element Cr. Furthermore, the active dissolution behaviour is mainly affected by Co.[75] Another study with XPS and Auger electron spectroscopy supports this observation, indicating the effect of Cr_2O_3/Cr ratio on Co and Cr releases from high/low carbon Co–Cr–Mo alloys into phosphate-buffered saline (PBS) and synovial fluid.[76]

2.5.2 Passive films formed on Ti alloys

The oxide film formed on Ti alloys consists mainly of TiO_2 which is thinner and stronger than Cr_2O_3 film.[45] Figure 2.10 shows the anodic polarisation curves of Ti–6Al–4V and Ti–15Zr–4Nb–4Ta alloys tested in Ringer's solution, Eagle's medium, and 0.9% NaCl. In the case of Ti–6Al–4V alloy, the change in current density is small at potential 2 V or lower, and then starts to increase. Meanwhile, the current density of the Ti–15Zr–4Nb–4Ta alloy film did not increase until reaching potential 4 V, revealing that the passive Ti–15Zr–4Nb–4Ta film has even higher strength and stability than the Ti–6Al–4V alloy. In terms of the polarisation behaviour, the Ti–15Zr–4Nb–4Ta alloy showed a passive zone nearly double that of the Ti–6Al–4V alloy. Figure 2.11 shows the change in the critical current density for passivation (Ic) and the potential (E^{10} vs. SCE) at 10 μA/cm^2 for Ti–6Al–4V and Ti–15Zr–4Nb–4Ta alloys. The critical current density of the Ti–6Al–4V alloy gradually decreases with increasing pH, and it becames stable from pH 3, accounting for 2 μA/cm^2. On the other hand, the Ic of Ti–15Zr–4Nb–4Ta alloy remains stable throughout the pH range from 1 to 8. The E^{10} of Ti–15Zr–4Nb–4Ta alloy is 4–5 V, which is double that of the Ti–6Al–4V alloy. Thus, the Ti–15Zr–4Nb–4Ta alloy has the most stable passive film, compared with the Ti–6Al–4V alloy. The Ic and E^{10} for the Ni–Ti alloy show a relationship with pH in Fig. 2.12. Ic increased with decreasing pH, and it levelled off after reaching 1.4 μA/cm^2 at pH 4. Figure 2.12(b) shows that the potential (E10 vs SCE) at 10 μA/cm^2 rapidly increases up to pH 2.[77]

This indicates the long-term excellent biocompatibility of Ti alloys, presumably owing to the formation of a highly dense and more stable

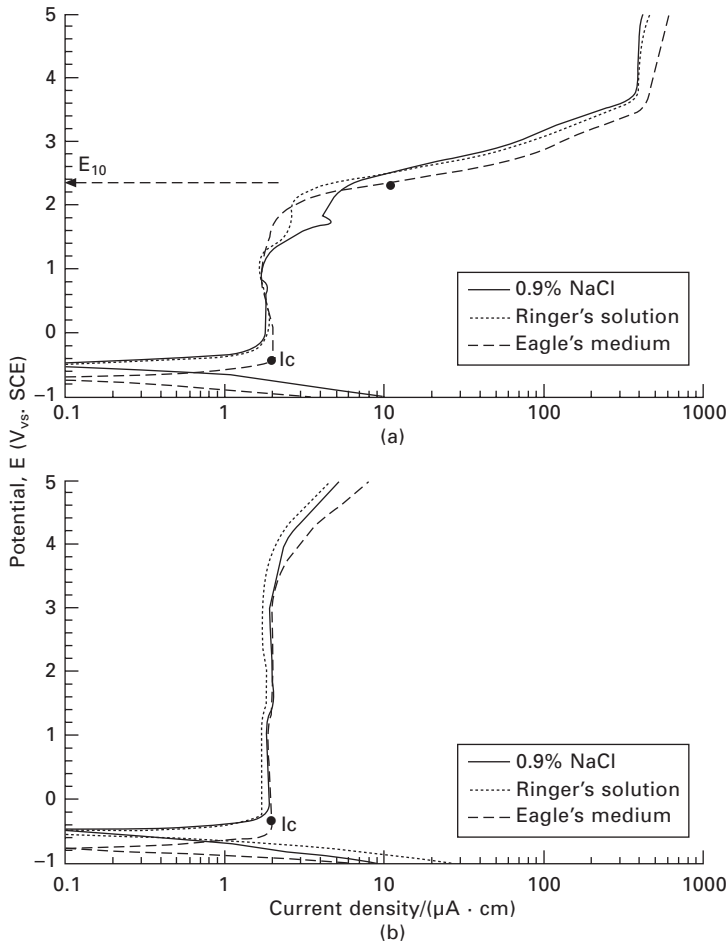

2.10 Comparison of anodic polarisation curves of Ti–6Al–4V (a) and Ti–15Zr–4Nb–4Ta (b) alloys in 0.9%NaCl, Ringer's solution and Eagle's medium at 37 °C.

TiO_2 passive film that is deposited after being damaged, even in solutions which have low oxygen content or are under fretting corrosion. The anodic polarisation curbs highlight the stability difference of two types of Ti alloy, Ti–6Al–4V and Ti–15Zr–4Nb–4Ta alloys; Zr, Nb, and Ta are very significant supplementary metals for Ti alloys. When Zr, Nb or Ta is added, the resultant ZrO_2, Nb_2O_5, or Ta_2O_5 formed in the TiO_2 passive film strengthens the TiO_2 passive film on the Ti alloy itself.[44, 49] The corrosion resistance provided by advanced passive film influences functional performance and durability, and is a primary factor governing biocompatibility of the implant material.

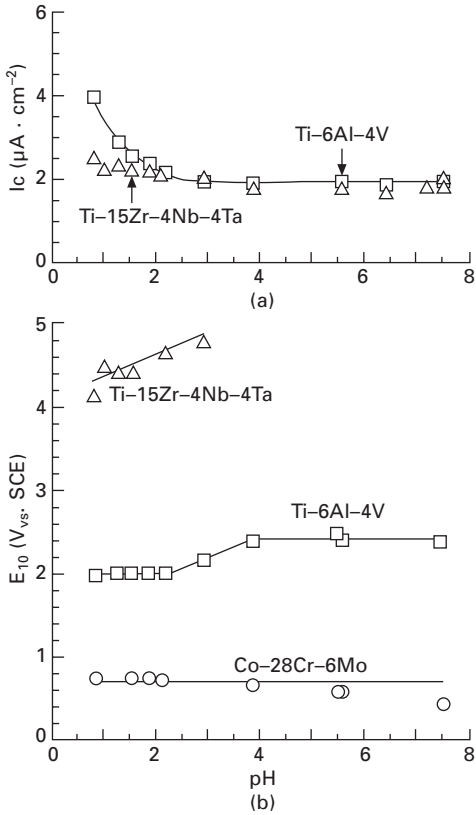

2.11 Changes in critical current density for passivation (Ic), and potential (E_{10}) (b) at a point of current density 10 μA/cm^2 obtained from anodic polarisation curves in various solutions with different pH values, shown in Table 2.4.

2.6 Metal ion release

Concerns such as metal sensitivity remain, considering the long-term exposure to metal ions released from metal implants into the body. However, no long term detrimental effects of metal ion release from the devices have been validly confirmed in the literature. Nonetheless, many useful specifications for testing methods are defined in international standards.

JIS T 0304 standard specifies the static immersion test using various solutions.[17] The solutions used are shown in Table 2.4. Ringer's solution and 0.9% NaCl are recommended solutions for corrosion testing in ISO 16428 and ISO 16429 standards. ISO 16428 also defines that 0.9% NaCl solution adjusted to pH 2 by adding HCl meets the rigorous testing conditions.[14] The definitions of 0.9% NaCl+HCl solutions at lower pHs prepared by adding HCl (pH = 2, 3, 4, 5, and 6) and NaCl solutions with higher concentrations

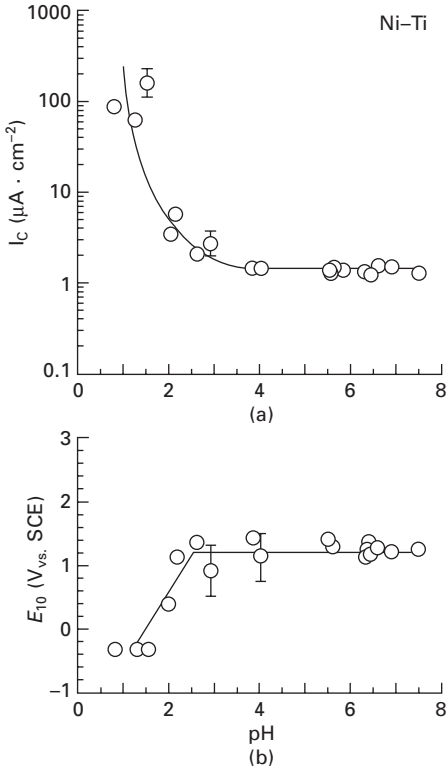

2.12 Changes in critical current density for passivation (Ic) (a), and potential (E_{10}) (b) at a point of current density 10 μA/cm^2 obtained from anodic polarisation curves of Ni–Ti alloy in various solutions with different pH values.

of NaCl (1.8, 2.7, 3.6, and 4.5% NaCl) are all indicated in ISO 16429.[15] Bottles of each solution, without a specimen, are prepared as blanks. The weekly quantity of each metal released (μg/cm^2) is estimated using the following formula:

$$\text{(amount of solution: 50 ml)} \times [\text{(metal concentration in each solution)} - \text{(mean metal concentration of three blank bottles)}]/\text{(surface area of specimen)} \quad [2.8]$$

2.6.1 Metal ion released from stainless steel and Co–Cr–Mo alloys

The effect of pH on the metal release rate in various solutions is examined with the aim of reducing the toxicity risk due to metal ion release. Figure 2.13 shows the effect of pH on the quantities of metals released from three

Table 2.4 Solutions used in the immersion test

Solutions	pH	Composition (g/L)
α-medium	7.5	NaCl: 6.8, KCl: 0.4, Na_2HPO_4: 1.15, $NaH_2PO_4{\cdot}H_2O$: 0.2, Amino acids and vitamins: 0.27, Fetal bovine serum (10 vol%), 7.5% $NaHCO_3$ solution (1 vol%)
PBS (–)	7.5	NaCl: 8, KCl: 0.2, NaH_2PO_4: 0.14, KH_2PO_4: 0.2
Calf serum	7.4	
Artificial saliva*	6.4	NaCl: 0.844, KCl: 1.2, $CaCl_2$: 0.146, $MgCl_2$: 0.052, K_2PO_4: 0.342
Ringer's solution	6.1	NaCl: 8.36, KCl: 0.3, $CaCl_2$: 0.15
0.9/4.5% NaCl	5.6/5.4	NaCl: 9/45
0.9% NaCl + HCl	2/3/4/5	NaCl: 9, HCl added to adjust pH
4.5% NaCl + HCl	2	NaCl: 45, HCl added to adjust pH
0.01/0.05/1% Lactic acid	3.5/3/2.2	
1.2% L-cysteine	2.1	$HSCH_2CH(NH_2)COOH{\cdot}HCl{\cdot}H_2O$: 17.6
0.01% HCl (0.05 vol% Concentrated HCl)	2	

*Contains trace amounts of thickener and benzoic acid to adjust the viscosity to 6 mPa·s.

types of solution-treated stainless steel. The quantities of Fe, nickel (Ni), and total metals (Fe + Cr + Ni + Mo + Mn) released from the stainless steel linearly decreased with increasing pH (pH 2–7.5), while the quantity of Cr released gradually increased with decreasing pH (pH ≤ 6) and plateaued at pH 6. The quantity of Mo released is slightly higher in Ringer's (pH 6.1) and 4.5% NaCl (pH 5.5) solutions than in the other solutions. The quantity of total metal released depends on pitting resistance equivalent (PRE).[78]

$$\text{PRE} = \%\text{Cr} + 3.3\%\text{Mo} + 16\%\text{N} \qquad [2.9]$$

The PRE values of ISO 5832, 316L, and high-N stainless steels are approximately 24, 32, and 35, respectively. Therefore, the weekly quantity of total metal released from high-N stainless steel is the lowest among the three stainless steels.

Figure 2.14 shows the pH effects on metal release from three types of Co–Cr–Mo alloy: as-cast, annealed, and hot-forged. The trends of the effect of pH on Co, Cr, and Mo releases are nearly the same in the Co–Cr–Mo alloys. In particular, the pH effect on Co release is very small. The quantity of Cr released gradually increases as pH decreases (pH ≤ 6) and is stably low throughout the pH range. The quantity of Mo released is also very low at a pH of approximately 3 and higher. The results indicate that heat treatment and hot forging have negligible effects on metal ions released from the Co–Cr–Mo alloys. Retrospectively, there have been many studies on metal ion release from orthopaedic implants, particularly those focusing

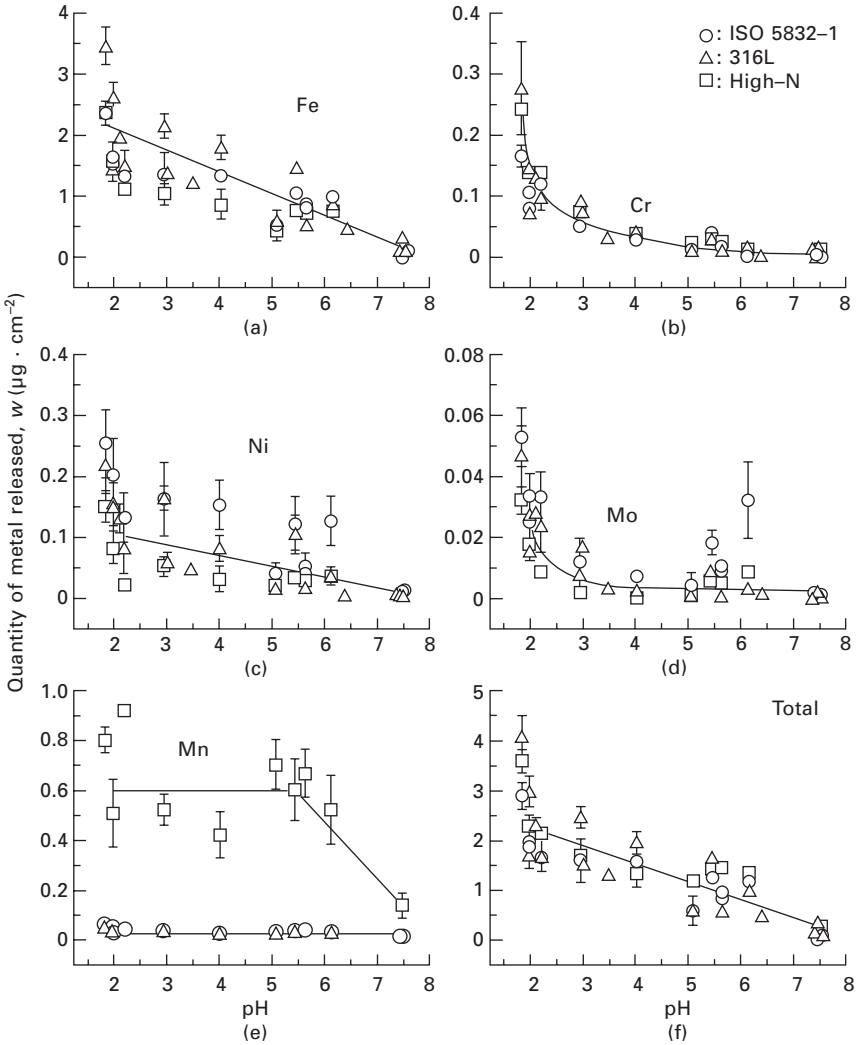

2.13 Effect of pH on quantities of each metal element released from the three kinds of solution-treated stainless steels (ISO 5832-1, 316L, and high-N) at 37 °C for one week: (a) Fe, (b) Cr, (c) Ni, (d) Mo, (e) Mn, and (f) total.

on metal-on-metal bearing hip joints made of Co–Cr–Mo alloys in recent years.[79–90] The average percentages of metal sensitivity (Co, Cr, and nickel (Ni)) are approximately 10% for the general population, 22% for patients with well-functioning implants, and 60% for patients with poorly functioning metal-on-metal bearing hip implants.[62]

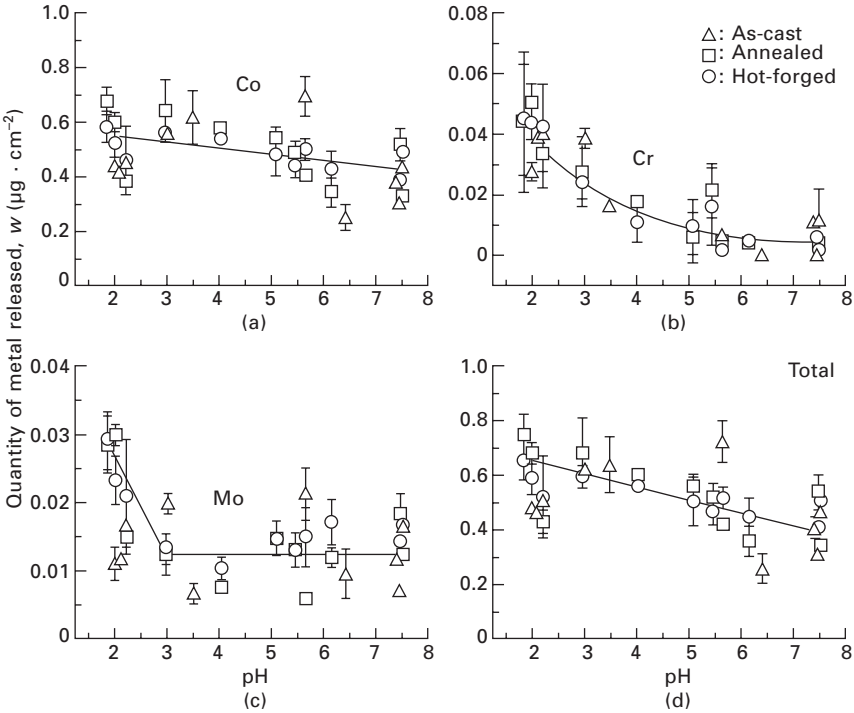

2.14 Effect of pH on quantities of each metal element released from three types of Co–28Cr–6Mo alloy (as-cast, annealed, and hot-forged) at 37 °C for one week: (a) Co, (b) Cr, (c) Mo, and (d) total.

2.6.2 Metal ion released from Ti alloys

Figure 2.15 shows the amounts of released Ni and Ti ions from Ni–Ti alloy in relation to pH.[77] The quantities of both Ni and Ti released markedly increases with decreasing pH, particularly at about pH 2, and levels off from pH 4. In terms of the clinical application, the amount of Ni ion release is within the permissible range for *in vivo* application, and that satisfies the requirements for spinal implants, biliary stent, coronary stent, and stent graft for abdominal and thoracic aorta. Therefore, Ni–Ti alloy has been intensively developed for clinically applied devices because it possesses brilliant superelasticity and is now specified in ASTM F 2063.[91]

According to the commission directive 2004/96/EC released by the European Community on 27 September 2004, in all post-assemblies intended to be inserted into pierced ears and other pierced parts of the human body, the rate of Ni release should be less than 0.2 μg/cm^2/week in an artificial sweat solution.[92] As shown in the results, the rate of Ni release from stainless steel and Ni–Ti alloys is less than 0.2 μg/cm^2/week.

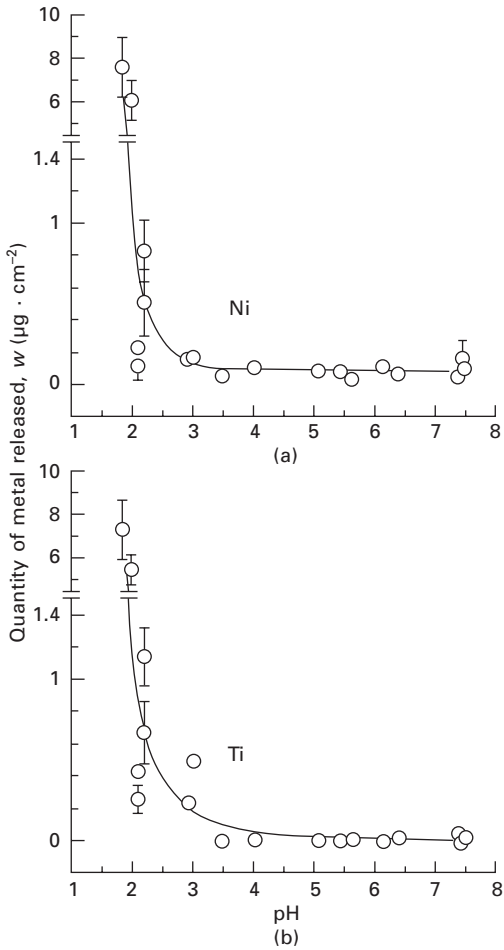

2.15 Effect of pH on quantities of Ni and Ti released from Ni–Ti alloy at 37 °C for one week: (a) Ni, and (b) Ti.

Figures 2.16 and 2.17 show the effect of pH on the quantities of metal released from Ti–6Al–4V and Ti–15Zr–4Nb–4Ta alloys. The effect of pH becomes evident in Ti–6Al–4V alloy; the amounts of metals released rapidly increase along with the pH decrease in the pH range of 2 to 3 or 4, although at pH higher than 3, the releases are almost zero. On the other hand, even low pH has virtually no effect on metal releases in Ti–15Zr–4Nb–4Ta alloy, except on Ti. Ti release starts to increase, although more gradually than in Ti-6Al-4V alloy, when the pH decreases to around 3.5. The other elements, Zr, Nb, and Ta, are barely released regardless of the pH level. It is evident that the metal release of Ti–15Zr–4Nb–4Ta alloy is much less than that of Ti–6Al–4V alloy. The series of results obtained through several analyses have

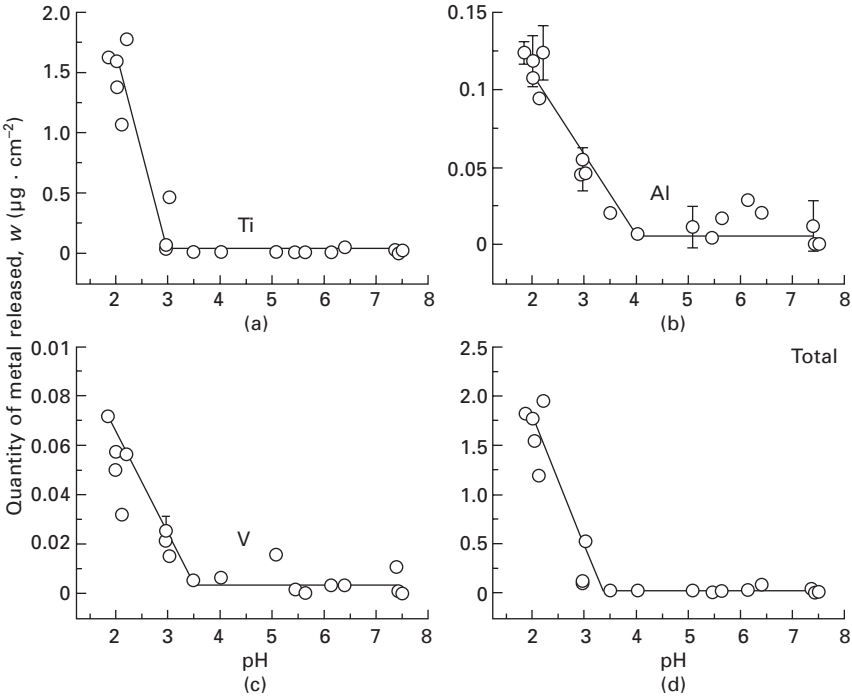

2.16 Effect of pH on quantities of each metal element released from Ti–6Al–4V alloy at 37 °C for one week: (a) Ti, (b) Al, (c) V and (d) total.

also confirmed that 0.9% NaCl+HCl solution adjusted to pH 2 is appropriate as an accelerated immersion test solution.

2.7 Evaluation of biological properties

2.7.1 Osteocompatibility of Ti alloys

The parameters for newly formed bone tissues around implants can be calculated using the following four formulae.[58]

$$\text{new bone formation rate (\%)} = (\text{total length of new bone formed around implant})/(\text{surrounding length of implant}) \quad [2.10]$$

$$\text{bone contact rate (\%)} = (\text{total length in direct contact with implant as determined from} \times 100 \text{ optical micrograph})/(\text{surrounding length of implant}) \times 100 \quad [2.11]$$

$$\text{thickness of new bone} = (\text{total area of new bone})/(\text{total length of new bone formed around implant}) \quad [2.12]$$

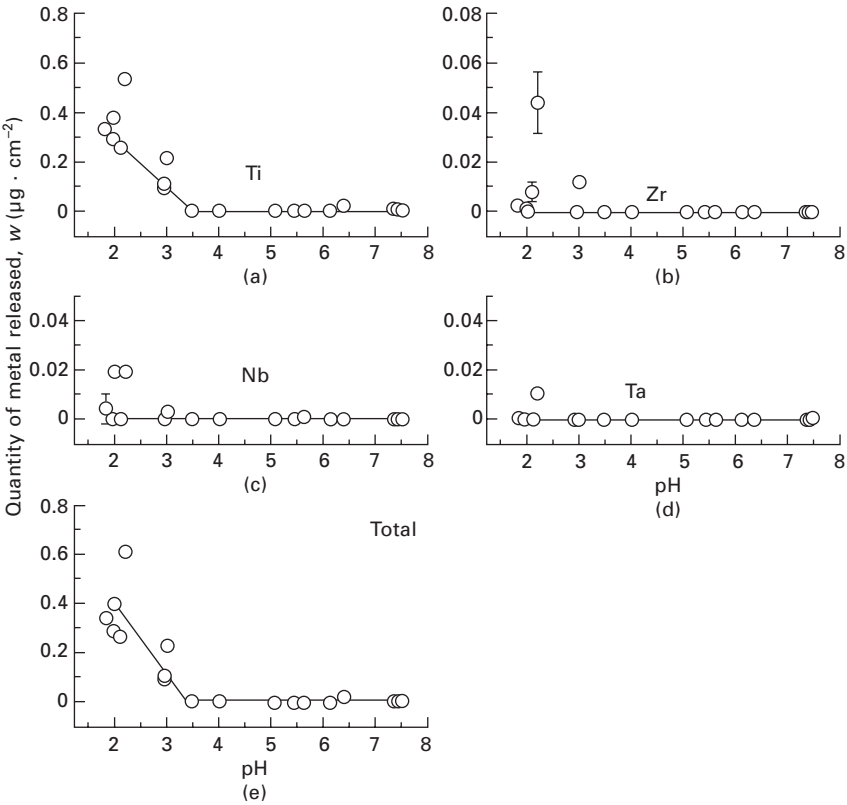

2.17 Effect of pH on quantities of each metal element released from Ti–15Zr–4Nb–4Ta alloy at 37 °C for one week: (a) Ti, (b) Zr, (c) Nb, (d) Ta and (e) total.

osteoid formation rate (%) using villanueva stain = [(total area of osteoid bone)/total area of new bone (osteoid plus calcified bone)] [2.13]

Figure 2.18 shows an optical micrograph of the new bone formed around Ti–15Zr–4Nb–4Ta alloy implants. The newly formed bone is stained with toluidine blue 48 weeks after implantation (a), and decalcified bone is stained with hematoxilen eosin (H.E.) 12 weeks after implantation (b). The Ti–15Zr–4Nb–4Ta alloy implant is completely surrounded by the new bone. Figure 2.19 summarises each value of Ti–6Al–4V and Ti–15Zr–4Nb–4Ta alloys implants obtained from the four morph metrical parameters. The new bone formation rates are more than 90% in the early implantation period for all the alloy implants. The bone contact rates gradually increase to approximately more than 75% at 24 weeks after implantation, and thereafter, remain almost

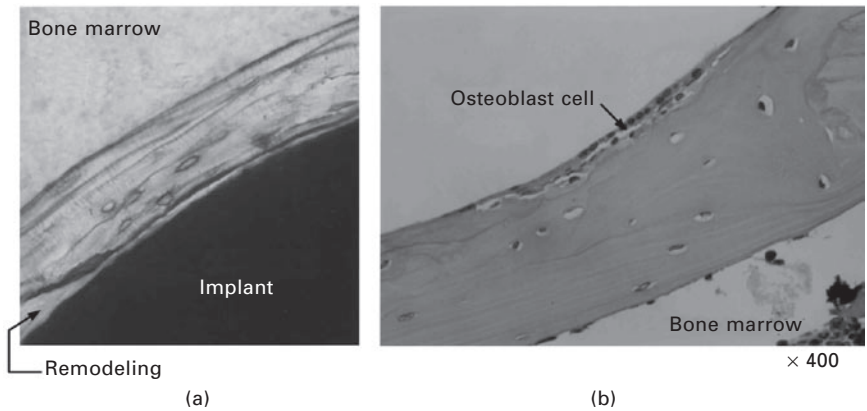

2.18 Optical micrographs of non-decalcified bone stained with toluidine blue around Ti–15Zr–4Nb–4Ta implant 48 weeks after implantation (a), and that decalcified bone stained with H.E. 12 weeks after implantation (b).

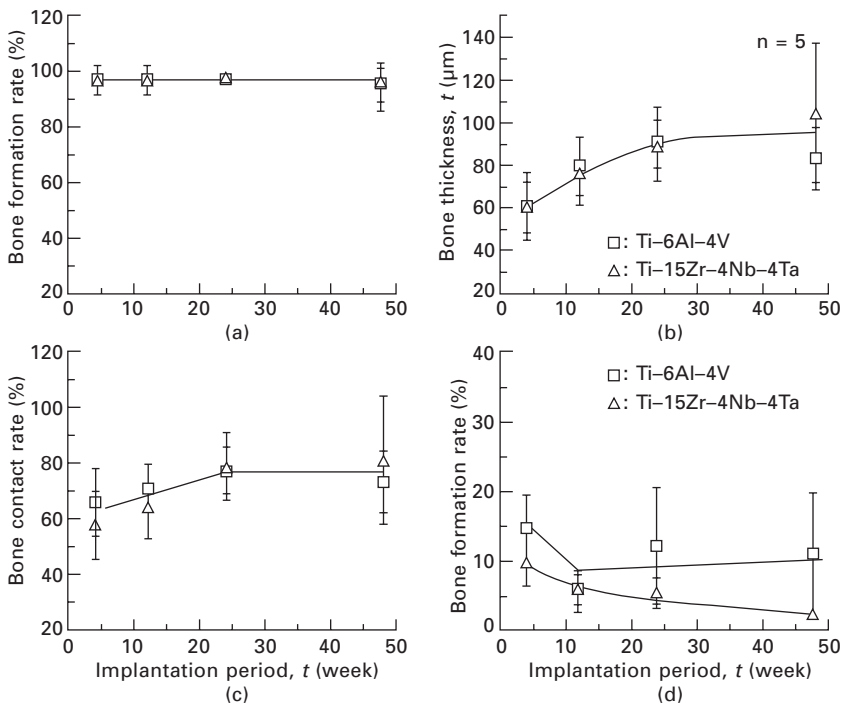

2.19 Changes in newly formed bone around implants during implantation period: (a) bone formation rate, (b) bone thickness, (c) bone contact rate, and (d) osteiod formation rate.

unchanged. No difference in new bone thickness between the Ti–6Al–4V and Ti–15Zr–4Nb–4Ta alloy implants is observed. As compared in Fig. 2.19(d), in the case of the Ti–15Zr–4Nb–4Ta alloy implant, the osteoid formation rates are 10 ± 4, 6 ± 3, 6 ± 2, and 3 ± 1% at 4, 12, 24, and 48 weeks after implantation, respectively. In contrast, in the case of the Ti–6Al–4V alloy implants, the osteoid formation rates slightly increase from 24 up to 48 weeks after implantation, and the values are 9 ± 6 and 12 ± 8% at 48 weeks.[58] The effect of a different surface treatment on Ti–6Al–4V and Ti–15Zr–4Nb–4Ta alloy implants was investigated by implantation into rabbit femur. The pullout strength shows no statistical differences within blasted/machined implants at any stage after implantation, showing a linear increase between 4 and 24 weeks followed by a slight decrease at 48 weeks. By comparing the effect of treated surfaces within the same alloy implants, blasted show significantly higher pullout strength than machined counterparts (Fig. 2.20).[93]

2.7.2 *In vivo* metal release

The metal concentration in the solution containing the dissolved bone tissues is determined by Inductively Coupled Mass Spectrometry (ICP-MS). The concentrations (μg/g) of various metals in the bone tissues can be calculated by dividing each metal quantity (μg) in the dissolved bone tissue solution by the lyophilized bone tissue weight (g).[59] As seen in Fig. 2.21, the Ti concentration in the rat tibia tissues with the Ti–15Zr–4Nb–4Ta implant is considerably lower than that in the tibia tissue with the Ti–6Al–4V implant.

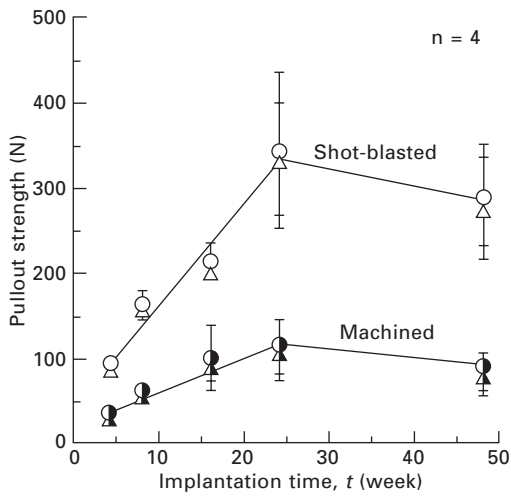

2.20 Pullout strengths after rabbit implantation of Ti–6Al–4V and Ti–15Zr–4Nb–4Ta alloys, surface treated (machined or shot-blasted).

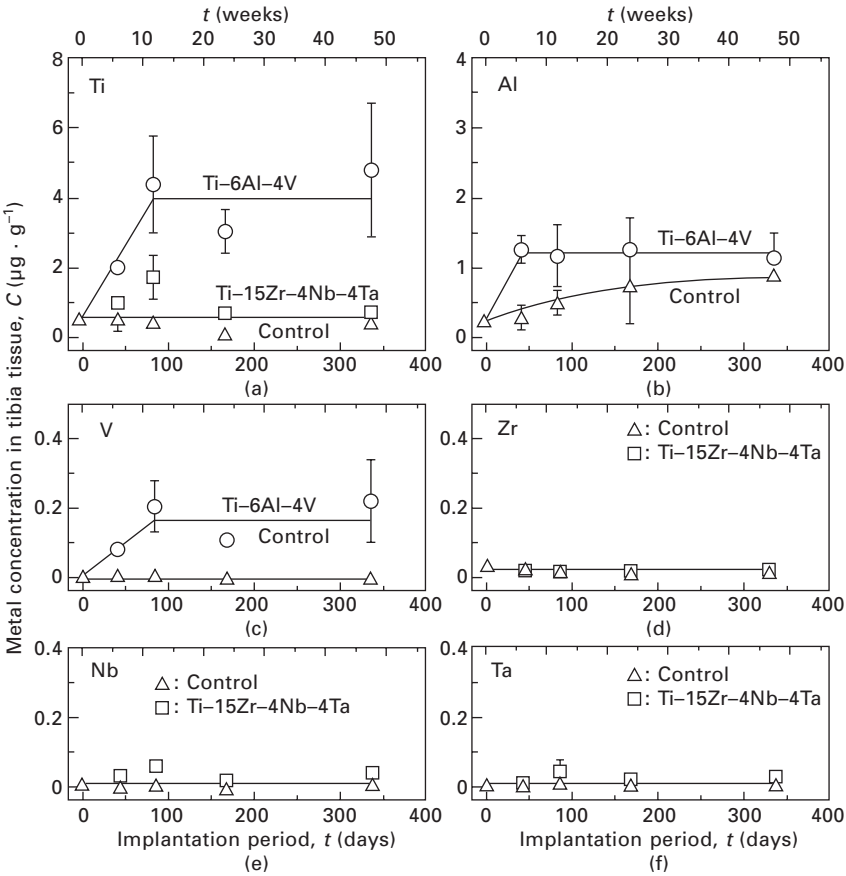

2.21 Changes of metal concentration in lyophilized tibia tissue with Ti–6Al–4V or Ti–15Zr–4Nb–4Ta implants during implantation period: (a) Ti released from Ti–6Al–4V or Ti–15Zr–4Nb–4Ta, (b) Al released from Ti–6Al–4V, (c) V released from Ti–6Al–4V, (d) Zr released from Ti–15Zr–4Nb–4Ta, (e) Nb released from Ti–15Zr–4Nb–4Ta, and (f) Ta released from Ti–15Zr–4Nb–4Ta.

The Zr, Nb, and Ta concentrations do not increase markedly compared with those of the control sample (without implant). The ratio of Ti concentration or the total concentration of each alloying element in the tibia tissue with the Ti–15Zr–4Nb–4Ta implant to that in the tibia tissue with the Ti–6Al–4V implant is estimated in Fig. 2.22. The Ti concentration in the tibia tissue with the Ti–15Zr–4Nb–4Ta implant is approximately 40% lower than that in the tibia tissue with the Ti–6Al–4V implant. The (Zr+Nb+Ta) concentration is 20% less than the (Al+V) concentration.

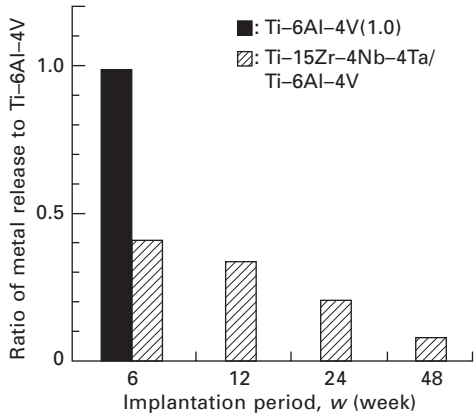

2.22 Ratios of Ti ions released from Ti–15Zr–4Nb–4Ta alloy and Ti–6Al–4V alloy (Control: 1.0) into rat bone tibia tissue with implants.

2.7.3 Evaluation of biological properties under Good Laboratory Practice regulation

The quantity of released metal ion affects biocompatibility, including cytotoxicity, sensitisation, and genotoxicity. In cytotoxicity tests performed under the GLP (Good Laboratory Practice) regulation, cell line V79 is cultured directly on Ti–15Zr–4Nb–4Ta alloy discs for a colony formation test. The aim is to evaluate the cytotoxicity of released substances and interaction with the material surface such as cell adhesion. The result yielded neither an increase in the cell adhesiveness and colony forming ratio nor cytotoxicity. This result is the same as that obtained previously with Ti–6Al–4V alloy that was used as a control sample. No sensitisation is detected by maximisation test using guinea pigs. In a reverse mutation test with bacteria and a chromosomal aberration test with CHL/IU cells, concerning genotoxicity, the clastogenic property is negative and both tests showed no genetic mutation induction. In implantation tests in rabbit tibia and femur for 4, 12, 26, and 52 weeks, no degeneration in the bone marrow tissue around the implantation sites is observed under all implant conditions. Aggregates, degeneration, and necrosis are not induced by inflammatory cells such as macrophage, heterophil, and leukocyte. New bone is formed from 4 weeks, which is the same as in the case using the reference material, Ti–6Al–4V alloy.

2.8 Fatigue assessment

Fatigue resistance is one of the most important mechanical characteristics of structural biomaterials, because biomaterials are generally used under cyclic loading conditions. An electro-hydraulic-servo testing machine is

popularly used in Ringer's solution, which is considered to be an appropriate solution for corrosion testing in ISO 16428.[14] The specimen is fitted into a polyethylene testing cell containing Ringer's solution and then set on a fatigue testing machine. The solution temperature inside the cell is maintained at 37 °C using heated water circulating around the cell. The tests are carried out mainly in the tension-to-tension mode with a sine wave. Testing conditions are as follows: stress ratio (R = (minimum stress)/(maximum stress)) of 0.1, frequency of 10 Hz. To obtain the profiles of maximum stress vs. number of cycles (S–N curves), the specimens are cycled with a constant load amplitude for a maximum of 10^9 cycles or until they fail.[94]

2.8.1 Effect of specimen shape on S-N curves

As shown in Fig. 2.23(a), the effect of specimen thickness with annealed Ti–15Zr–4Nb–4Ta alloy plates is small, and fatigue strength at 1×10^8 cycles is approximately 485 MPa. Figure 2.23(b) shows S–N curves obtained using different specimen types of annealed Ti–15Zr–4Nb–4Ta alloy rods (uniform specimen) in Ringer's solution at 37 °C. The effect of specimen diameter is small at 3 mm or longer diameter. The fatigue strength at 1×10^8 cycles is approximately 730 MPa. In a uniform specimen, fatigue fracture occurs at different positions owing to the effect of machining; however, hourglass-shaped specimens fracture at the same position (at the position of minimum diameter). Plate-shaped specimens also exhibit lower fatigue strength than rod-shaped specimens.

2.8.2 Comparison of fatigue strengths for Ti alloys

As shown in Fig. 2.24(a), the fatigue strengths of annealed Ti–6Al–7Nb, Ti–6Al–4V, and Ti–6Al–2Nb–1Ta hourglass-shaped rods (minimum diameter: 4.5 mm) at 1×10^8 cycles in Ringer's solution at 37 °C are approximately 600, 685, and 700 MPa, respectively. Figure 2.24(b) shows the S–N curves for annealed and aged Ti–15Zr–4Nb–4Ta hourglass-shaped rods (minimum diameter: 4.5 mm) in Ringer's solution at 37 °C. Aged specimens yield much higher fatigue strength than annealed ones.

Mechanical properties and the ratios of fatigue strength at 1×10^8 cycles to ultimate tensile strength are compared in Table 2.4. The ratios for all the materials except Ti–15Mo–5Zr–3Al alloy were higher than approximately 65%. Aged Ti–15Zr–4Nb–4Ta rod, in particular, exhibits a high rate of approximately 75%. The ratios at 1×10^7 cycles reported in the literature are summarised in Table 2.5. Ti–15Mo, Ti–12Mo–6Zr–2Fe, and Ti–24Nb–4Zr–8Sn alloys, which have β phase matrix and exhibit high ultimate tensile strength, show lower ratios than CP Ti. To improve the fatigue strengths of these β-type alloys, studies on the ageing condition, which follows solution

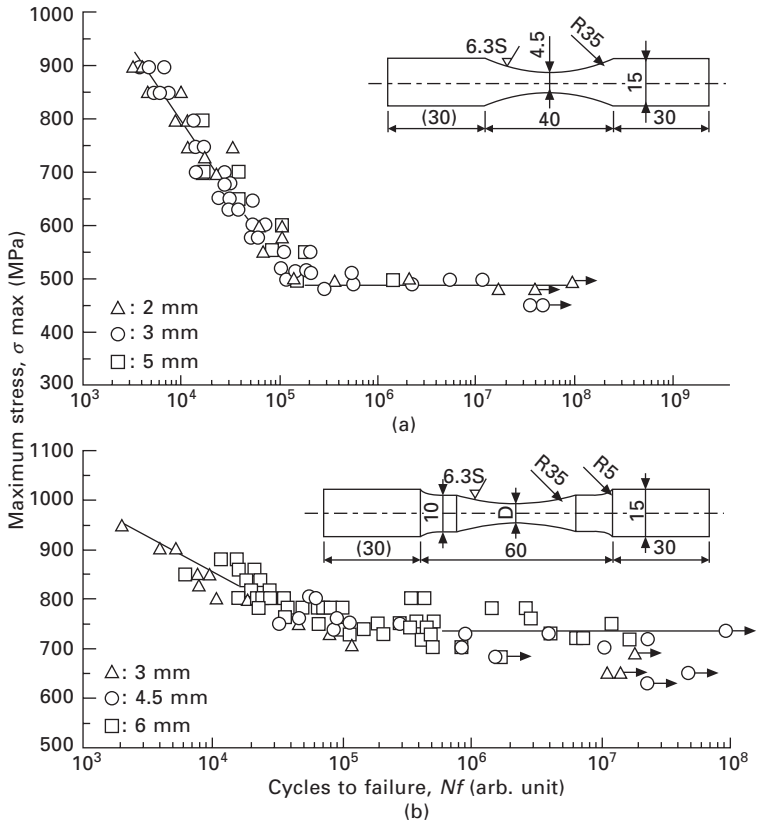

2.23 S–N curves obtained from tension-to-tension fatigue test with sine wave (10 Hz) in Ringer's solution at 37 °C for annealed Ti–15Zr–4Nb–4Ta alloy plates or rods: (a) effect of plate specimen thickness, and (b) effect of specimen diameter.

treatment or cold working, were carried out, and it has been clarified that their fatigue strengths are heightened following a number of treatments. However, the relatively high fatigue strength can be achieved by annealing in Ti–15Zr–4Nb–4Ta alloy, which is $\alpha + \beta$ type alloy.

2.9 Orthopaedic implant device failure: Analysis of adverse clinical cases

One of the considerable issues concerning implant devices is the failure of surgically implanted examples. Retrospective analyses of 17 000 clinical device adverse cases in orthopaedics between 1992 and 2001 on the Food and Drug Administration database (Manufacturer and User Facility Device Experience Database, USA) have yielded increasing failure cases in bone

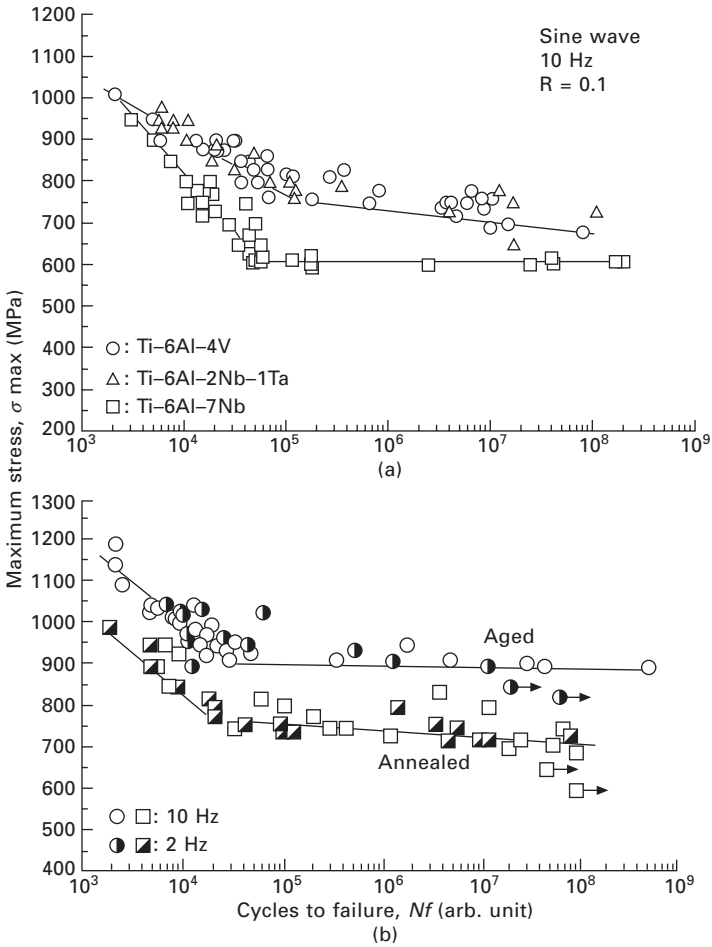

2.24 S–N curves obtained from tension-to-tension fatigue test in Ringer's solution at 37 °C for annealed Ti–6Al–7Nb, Ti–6Al–4V, Ti–6Al–2Nb–lTa alloy rods (a), and annealed and aged Ti–15Zr–4Nb–4Ta alloy rods (b).

screws, bone plates, compression hip screws, intramedullary fixations, short femoral nails, and artificial hip/knee joints. The percentage of breakage is approximately 70% in osteosynthesis devices. However, the percentage of breakage in artificial hip/knee joints is below 20%. The applied points of the broken bone screws are mostly in lower limbs such as hip joint and femur, followed by spine. In the cases of bone plate breakages, the femur is the most reported. The breakage points of CHS are mostly on the side plates, followed by lag screw and screw of the side plate. Breakage of the intramedullary nail is more in rods than in screws; the points occur more on

proximal screw holes than on the distal screw holes. Approximately 60% of the breakage is in the position of the screw hole. Likewise, breakage of the rod with screw hole of short femoral nail accounts for about 90% of the total cases. Figure 2.25 shows the adverse analysis of artificial hip joints. Breakage is approximately 45% of the total. The most common parts of loosening are cups, followed by stems and components of cups; the most common parts of breakages are stems, followed by liners and ceramic heads. The most common parts of stem breakage are the neck part and the middle of the stem. For artificial knee joint, wear is the most common reason for the failure, accounting for 25% of all failures. Breakage and loosening follow. One-third of the common breaking points is in the fibula insert, then fibula base plate and followed by the patella. It was found to be important to evaluate not only simple strengths, such as mechanical strength, but also durability in fatigue tests.

2.10 Performance evaluation for orthopaedic devices

Mechanical testing machines on bone plates, CHS, short femoral nails, intramedullary nails, screws, artificial hip joints, artificial knee joints, and spine fixtures have been developed over time. For bone plates and intramedullary nails, methods of evaluating the bending strength, bending stiffness, and durability using the four-point bending test have been developed, as shown in Figs 2.26(a) and (b).[95–96] For CHS and short femoral nails, compression strength, compression stiffness, and durability are evaluated using the

Table 2.5 Mechanical properties of commercially pure Ti (CP Ti) and various Ti alloys, and comparison of ratio of fatigue strength at 108 cycles (σFS) with ultimate tensile strength (σUTS)

Alloys	$\sigma_{0.2\%PS}$(MPa)	σ_{UTS}(MPa)	T.E.(%)	R.A.(%)	E(GPa)	σ_{FS}/σ_{UTS}
Ti–15Zr–4Nb–4Ta						
Annealed (plate)	800±14	910±10	19±2			0.54
Annealed (rod)	848±2	915±3	21±2	55±3	94±2	0.80
S.T.+Aged (rod)	894±5	1020±8	15±2	48±3	98±2	0.89
C.P.Ti Grade 2	276±6	410±4	40±2	60±6	106±2	0.68
C.P.Ti Grade 3	380±2	540±2	32±2	54±2	108±3	0.66
C.P.Ti Grade 4	600±6	701±8	26±2	46±3	118±2	0.69
Ti–6Al–4V	849±1	934±1	16±1	42±3	102±4	0.73
Ti–6Al–7Nb	845±8	960±10	18±2	47±3	108±2	0.63
Ti–6Al–2Nb–1Ta	842±2	900±3	18±3	43±4	110±1	0.81
Ti–15Mo–5Zr–3Al						
Solution annealed	910±10	930±8	19±2	50±2	92±2	0.38
Hot-forged	963±12	988±10	18±2	50±6	102±2	0.71
Ti–15Mo [34]		1420	2			0.46
Ti–12Mo–6Zr–2Fe [33]		1080	20		80	0.54
Ti–24Nb–4Zr–8Sn [28]		1020	9		70	0.40

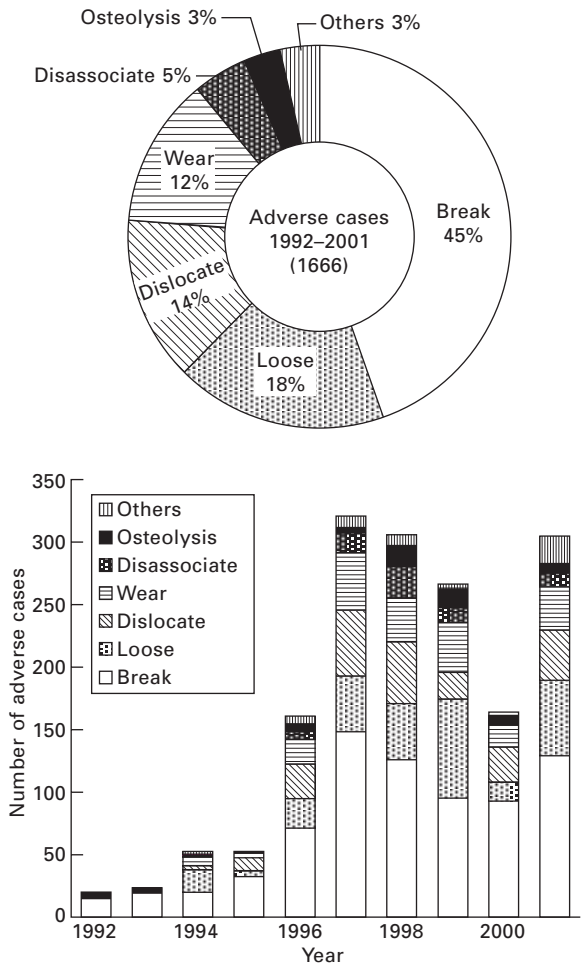

2.25 Analysis for hip joints in adverse clinical cases with FDA D.B.

compression bending test (Fig. 2.26(d)). For screws, a torsional breaking test, an evaluation of durability by the 4-point bending, a driving force test into artificial (model) bones, and a pullout test from model bones are examined (Figures 2.26(c) and 2.27).[97] For artificial hip joints, methods are examined mainly to evaluate the durability of stems and wearing parts; for artificial knee joints, methods are examined mainly to evaluate the durability of tibial components and polyethylene liners.[98]

2.10.1 Mechanical properties for osteosynthesis devices

To evaluate the bending strength, bending structural stiffness, and fatigue properties of osteosynthesis devices, 4-point and 3-point bending tests on

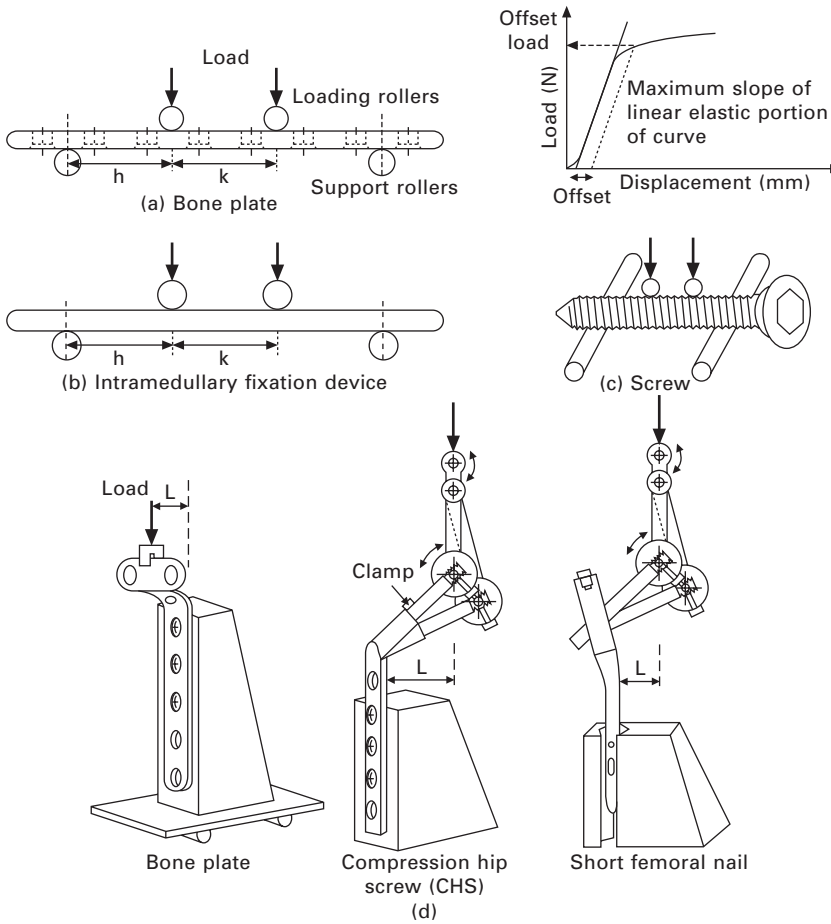

2.26 Static 4-point bending and 4-point bending fatigue tests (a), (b), (c). Loading rollers are placed at one-third points between the two support rollers. Schematic illustration of compression bending tests (d).

bone plates, intramedullary nail rods, and bone screws are conducted. Load versus displacement (L-D) curves in all tests are determined at a crosshead speed of 10 mm/min (Fig. 2.26).[97] The bending strength and bending structural stiffness are determined using the following expressions:

bending strength (N·m) on 4-point and 3-point bending tests

$$= Ph/2 \qquad [2.14]$$

bending structural stiffness (N·m^2) on 4-point bending test

$$= (2h+3k)Mh^2/12 \qquad [2.15]$$

(in the case of 3-point bending test, the value of h is 0)

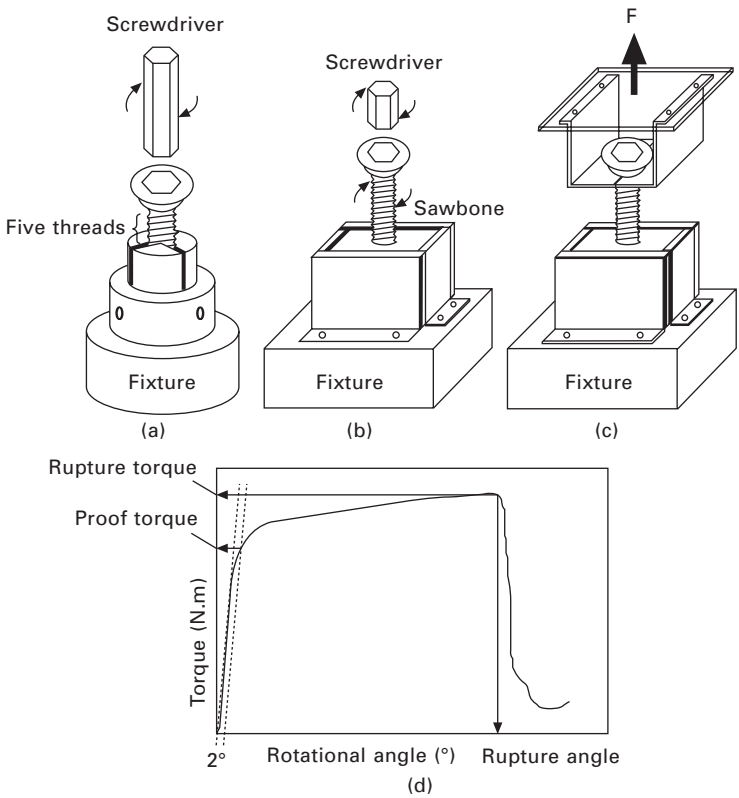

2.27 Schematic illustration of (a) torsional breaking, (b) driving force, and (c) pullout tests. (d) Torque versus rotational angle curve.

where:
P = offset load for 0.2% or 2% offset displacement
h = distance between loading roller and support roller
k = loading span distance
M = bending stiffness estimated from the maximum slope of the linear portion of the L-D curve

The design and composition of the devices affect the test results. The difference in bending strength of the bone plate on 3-point and 4-point bending tests appears after the bending strength exceeds 20 N·m; the values on the 3-point bending test are higher than those on the 4-point bending test. On the 4-point bending test for bone plates, it is recommended that two support rollers be used, and also two screw holes from the outside of the loading rollers. The offset displacement is 0.2% of the distance between the support rollers and loading rollers. On the basis of the 4-point bending fatigue test on bone plate, it is found that the frequency can be accelerated to 5 Hz. The fatigue

property of the bone plate measured in Eagle's medium, is almost the same as that measured in air. The fatigue properties of all tested devices are affected more by their design than by the composition of materials. Likewise, the intramedullary nail rod shows excellent fatigue properties. The fatigue properties of a screw made of Ti materials markedly changes with the core diameter of 3 to 3.5 mm.

The compression bending tests on CHS, short femoral nails, and T-shaped metal plates (T-plates) are conducted to evaluate the compression bending strength, compression bending stiffness, and fatigue properties. Load versus displacement (L–D) curves are measured at a crosshead speed of 10 mm/min. Bending stiffness (N/m) is estimated from the maximum slope of the linear elastic portion of the L–D curve. Bending strength (N·m) is defined as:

$$\text{bending strength (N·m)} = \text{lever arm} \times \text{offset load} \qquad [2.16]$$

To estimate offset load, 0.2% or 2% of the lever arm is used as the offset displacement. The design and composition of the devices affects the test results. The compression bending strength of CHS with all screw holes of the side plate anchored is approximately 1.3 times higher than that with the top screw hole unanchored. The bending stiffness decreased as the lag screw became longer, although the bending strength is not affected by the lag screw length. Short femoral nails show higher bending stiffness and strength than CHS. T-plate shows higher bending strength and fatigue property than the T-buttress plate in all tests. As the maximum load in fatigue test (R = 0.1) of CHS became smaller, the starting point of the fracture shifted from the lag screw to the side plate. The fatigue properties of the sliding-type CHS are markedly lower than those of the tube type. The effect of jig fixation on the fatigue properties of CHS is small. The fatigue properties of short femoral nails are higher than those of CHS. The effect of diameter of the proximal nail on its bending stiffness and strength is large, whereas the effect of proximal shaft angle is small. Its fatigue properties decrease with decreasing proximal shaft angle and diameter of the nail.

2.10.2 Performance properties for metallic bone screw

To evaluate the torsional breaking and performance properties of cortical, cancellous, and locking screws widely used in thigh bones, a torsional breaking test (rotational speed: 1 rpm), a screw driving force test into cortical sawbone (Solid Rigid Polyurethane Foam, 15 pcf) or cancellous sawbone (Cellular Rigid Polyurethane Foam, 20 pcf) with a loading of 100 N, and a pullout test (crosshead speed: 10 mm/min) on screws driven and left in sawbone in the driving force test are conducted (Fig. 2.27).[96] It is shown that the 2° proof and rupture torques of screw estimated from torque versus rotational angle

curves increased with increasing core diameter of the screw. The 2° proof torque of a stainless steel screw is higher than that of screws made from Ti materials. Rupture torque is not affected by different materials. Cortical double-threaded screws show the highest rupture torque among all cortical screws. The maximum pullout load tends to increase with the driving torque indicated in a driving force test. The effects of screw shapes, namely, the height of the screw [(thread diameter-core diameter)/2], the pitch, and the aspect ratio (height of screw/pitch) on driving torque are small while the maximum pullout load increases with those values. In general, the maximum pullout load of the pre-tap screw is larger than that of the self-tap screw.

2.10.3 Performance evaluation for artificial hip joints

Testing machines are developed, which are based on a 4-axis control, to evaluate wear properties of artificial hip and knee joints under the simulation of human movement (Fig. 2.28).[97] In the artificial hip joint test, the load of human body weight and angles of human femoral movement (angles of flexion or extension, adduction or abduction, and inward or outward rotation) are simulated using two samples. The samples are subjected to a load either with or without rotation. The findings sufficiently show consistent patterns between the command waves, adjusted using the system, and the measured waves. This shows that the machine is sustainable to function continuously. The developed machine for artificial knee joints is used under two standard testing conditions: load control and displacement control. The system is able to independently optimise each applied 4-axis force action, namely, axial force, flexion, tibial rotation, and anterior posterior (AP) force. The control also minimises the effect caused by the surface shapes of the femur component and tibia insert when all four axes are loaded at the same time. A series of wear characteristic test results showed little wear loss of a clinically-used artificial hip joint, which consisted of a cross-linked ultrahigh molecular weight polyethylene (UHMWPE) liner and Co–Cr–Mo articular head. Wear loss of an artificial knee joint, composed of a UHMWPE liner and Co–Cr–Mo alloy femoral components, increased linearly with wear cycles. The wear loss of UHMWPE per million cycles was approximately 10–20 mg.

2.11 Future trends

Many measurement techniques have been used to study biomaterials and have contributed to the improvement of orthopaedic devices over the years. Effective test strategies are necessary for evaluating novel technologies, making suitable design decisions and gathering data to standardise and monitor devices in clinical use. In other words, they enable a broader understanding of corrosion resistance and long-term stability, fatigue assessment, capability

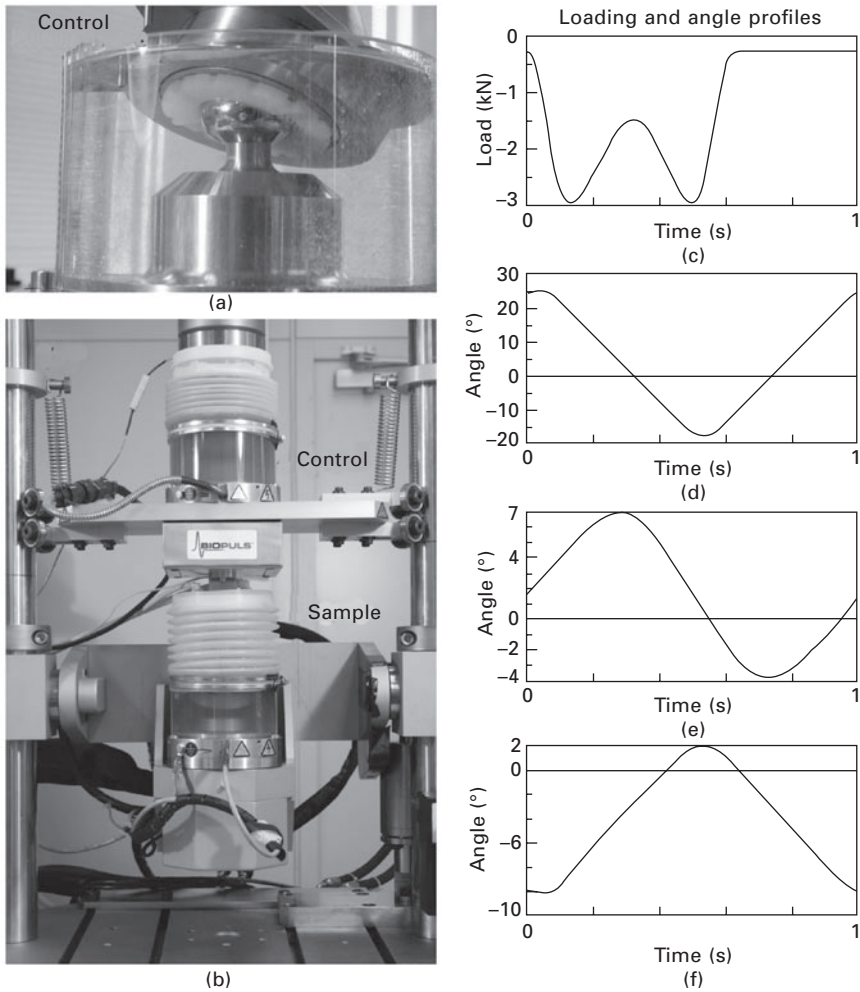

2.28 (a), (b) Test system for the wear property evaluation of artificial hip joint. (c) Applied load, (d) angle of flexion (+) or extension (–), (e) angle of adduction (+) or abduction (–), and (f) angle of inward (+) or outward (–) rotation.

of being processed, and manufacturing cost–efficiency. In the future, more technologies are expected to be applied to facilitate development of new biocompatible devices. As we have seen, a better understanding of material properties highlights the importance of advanced material selection, which reduces failure of metallic orthopaedic devices. From this perspective, commercially pure Titanium and Ti alloy, stainless steel and cold-worked CP Ti grade 4, are likely to gain future significance due to their characteristics. Subsequently, prospective use of the Co–28Cr–6Mo alloy will become more

pervasive for artificial joint bearing parts. However, the general trend of usage differs according to the application. As for the cement-type artificial hip stem material, Ti alloys are not likely to be used in the future, and will be replaced by the Co–28Cr–6Mo alloy and cold-worked high-nitrogen stainless steel with high strength and stiffness. On the other hand, the importance of the highly biocompatible Ti alloy should be emphasised as a cementless hip stem material. Taking into account the annealing process and the characteristic change, annealing treatment of $\alpha + \beta$-type Ti alloy will result in relatively high fatigue strength. The further development of alloys with high fatigue strength will be expected, just like hot-forged Co–28Cr–6Mo and cold-worked stainless steel which have gained rapid attention as orthopaedic materials. Thus, the introduction of solution treatment and over ageing (STOA) treatment or die-hot forging techniques are deemed promising for the mechanical property improvement of the Ti alloy.

However, the detrimental health outcomes of metal ion release from the devices should not be neglected. In particular, the long-term effect is an issue of concern. Two standardised tests may provide an impetus to raise this issue: the static immersion test in JIS T 0304 and the evaluation method for electrochemical strength and stability of the oxide film formed on the metal surface in JIS T 0302.

In terms of the metallic elements, Ti and Zr exhibit excellent cytocompatibility to both soft tissue-derived mouse fibroblast cells and bone-derived mouse osteoblast cells. Thus, Zr, Nb, and Ta as alloying elements for Ti alloys are important to attain long-term superior corrosion resistance and biocompatibility in the long-term. Furthermore, the oxides ZrO_2, Nb_2O_5, and Ta_2O_5 strengthen the passive film and prevent metal ion release, via the compound addition of Zr, Nb and Ta. However, recall that too large an addition of Nb and Ta to Ti alloy leads to higher manufacturing costs and lower biocompatibility. The most suitable alloy with the most favourable properties is the Ti–15Zr–4Nb–4Ta alloy, which has better room-temperature strength and fatigue properties with higher biocompatibility. In fact, the biological safety of this alloy has already been proven in cytotoxicity tests, sensitivity tests, genetic damage tests and rabbit implantation tests. This creates high expectations for the long-term future use of this alloy as a viable implant material.

2.12 References

1 ISO 5832-1, Implants for surgery – Metallic materials – Part 1: Wrought stainless steel, 2007.
2 ISO 5832-2, Implants for surgery – Metallic materials – Part 2: Unalloyed titanium, 1999.
3 ISO 5832-3, Implants for surgery – Metallic materials – Part 3: Wrought titanium 6-aluminium 4-vanadium alloy, 1996.

4 ISO 5832-4, Implants for surgery – Metallic materials – Part 4: Cobalt-chromium-molybdenum casting alloy, 1996.
5 ISO 5832-5, Implants for surgery – Metallic materials – Part 5: Wrought cobalt-chromium-tungsten-nickel alloy, 2005.
6 ISO 5832-6, Implants for surgery – Metallic materials – Part 6: Wrought cobalt-nickel-chromium-molybdenum alloy, 1997.
7 ISO 5832-7, Implants for surgery – Metallic materials – Part 7: Forgeable and cold-formed cobalt-chromium-nickel-molybdenum-iron alloy, 1994.
8 ISO 5832-8, Implants for surgery – Metallic materials – Part 8: Wrought cobalt-nickel-chromium-molybdenum-tungsten-iron alloy, 1997.
9 ISO 5832-9, Implants for surgery – Metallic materials – Part 9: Wrought high nitrogen stainless steel, 2007.
10 ISO 5832-11 Implants for surgery – Metallic materials – Part 11: Wrought titanium 6-aluminium 7-niobium alloy, 1994.
11 ISO 5832-12, Implants for surgery – Metallic materials – Part 12: Wrought cobalt-chromium-molybdenum alloy, 2007.
12 ISO 5832-14 Implants for surgery – Metallic materials – Part 14: Wrought titanium 15-molybdenum 5-zirconium 3-aluminium alloy, 2007.
13 JIS T 7401-4, Titanium materials for surgical implant applications. Part 4: Wrought titanium 15-zirconium 4-niobium 4-tantalum alloy, 2002.
14 ISO 16428, Implants for surgery – Test solutions and environmental conditions for static and dynamic corrosion tests on implantable materials and medical devices, 2005.
15 ISO 16429, Implants for surgery – Measurements of open-circuit potential to assess corrosion behaviour of metallic implantable materials and medical devices over extended time periods, 2004.
16 JIS T 0302, Testing method for corrosion resistance of metallic biomaterials by anodic polarization measurement, 2000.
17 JIS T 0304, Testing method for metal release from metallic biomaterials, 2002.
18 JIS T 0305, Testing method for galvanic corrosion in pseudo physiological solution, 2002.
19 JIS T 0306, Analysis of state for passive film formed on metallic biomaterials by X-ray photoelectron spectroscopy, 2002.
20 Thomas S R, Shukla D, Latham P D, 'Corrosion of cemented titanium femoral stems', *J Bone Joint Surg*, 2004, 86B, 974–978.
21 Okazaki Y, 'Effects of heat treatment and hot forging on microstructure and mechanical properties of Co–Cr–Mo alloy for surgical implants', *Mater Trans*, 2008, 49, 817–823.
22 Okazaki Y, 'Effects of solution treatment and cold rolling on microstructure and mechanical properties of stainless steel for surgical implants', *Mater Trans*, 2008, 49, 1423–1427.
23 Steinemann S G, 'Corrosion of surgical implants – *in vivo* and *in vitro* tests'. In: Winter G D, Leray J L, de Groot K, ed. (1980), *Evaluation of Biomaterials*, Chichester, Wiley, 1–34.
24 Steinemann S G 'Compatibility of titanium in soft and hard tissue – the ultimate is osseointegration'. In: Stallforth H, Revell P, ed. (1999) *Materials for Medical Engineering*, Weinheim, Wiley–VCH, 199–203.
25 Okazaki Y, Ito Y, Ito A, Tateishi T, 'Effect of alloying elements on mechanical properties of titanium alloys for medical implants', *Mater Trans JIM*, 1993, 34, 1217–1222.

26 Okazaki Y, Rao S, Asao S, Tateishi T, Katsuda S, Furuki Y, 'Effects of Ti, Al and V concentrations on cell viability', *Mater Trans JIM*, 1998, 39, 1053–1062.
27 Wapner K L, 'Implications of metallic corrosion in total knee arthroplasty', *Clin Orthop Relat Res*, 1991, 271, 12–20.
28 Li S J, Cui T C, Hao Y L, Yang R, 'Fatigue properties of a metastable β-type titanium alloy with reversible phase transformation', *Acta Biomaterialia*, 2008, 4, 305–317.
29 Lin C W, Ju C-P, Lin J-H C, 'A comparison of the fatigue behavior of cast Ti–7.5Mo with c.p. titanium, Ti–6Al–4V and Ti–13Nb–13Zr alloys', *Biomaterials*, 2005, 26, 2899–2907.
30 Akahori T, Niinomi M, Fukui H, Ogawa M, Toda H, 'Improvement in fatigue characteristics of newly developed beta type titanium alloy for biomedical applications by thermo-mechanical treatments', *Mater Sci Eng*, 2005, 25C, 248–254.
31 Niinomi M, Akahori T, Hattori Y, Morikawa K, Kasuga T, Fukui H, Suzuki A, Kyo K, Niwa S, 'Super elastic functional β titanium alloy with low Young's modulus for biomedical applications', *J ASTM International*, 2005, 2(6), 135–150.
32 Niinomi M, 'Fatigue characteristics of metallic biomaterials', *Int J Fatigue*, 2007, 29, 992–1000.
33 Wang K K, Gustavson L J, Dumbleton J H, 'Microstructure and properties of a new beta titanium alloy, Ti–12Mo–6Zr–2Fe, developed for surgical implants'. In: Brown S A, Lemons J E, ed. (1996) *Medical Applications of Titanium and its Alloys: The Material and Biological Issues*, ASTM STP 1272, 76–87.
34 Marquardt B, Shetty R, 'Beta titanium alloy processed for high strength orthopedic applications', *J ASTM International*, 2005, 2(9), 71–82.
35 Gaebler C, Stanzl-Tschegg S, Laube W, Vécsei V, 'The fatigue strength of small diameter tibial nails', *Injury Int J Care Injured*, 2001, 32, 401–405.
36 Amel-Farzada H, Peivandi M T, Yusof-Sani S M R, 'In-body corrosion fatigue failure of a stainless steel orthopaedic implant with a rare collection of different damage mechanisms', *Eng Fail Anal*, 2007, 14(7), 1205–1217.
37 Chao J, López V, 'Failure analysis of a Ti6Al4V cementless HIP prosthesis', *Eng Fail Anal*, 2007, 14(5), 822–830.
38 Heim C S, Postak P D, Greenwald A S, 'Femoral stem fatigue characteristics of modular hip designs'. In: Marlowe D E, Parr J E, Mayor M B, ed. (1997) *Modularity of Orthopedic Implants*, American Society for Testing and Materials Special Technical Publication, 1301, 226–243.
39 ASTM F 1713, Standard Specification for Wrought Titanium-13Niobium-13Zirconium Alloy for Surgical Implant Applications.
40 ASTM F 1813, Standard Specification for Wrought Titanium-12Molybdenum-6Zirconium-2 Iron Alloy for Surgical Implant Applications.
41 ASTM F 2066, Standard Specification for Wrought Titanium-15Molybdenum Alloy for Surgical Implant Applications.
42 JIS T 7401-3, Titanium materials for surgical implant applications. Part 3: Wrought titanium 6-aluminium 2-niobium 1-tantalum alloy, 2002.
43 Okazaki Y, Ito A, Tateishi T, Ito Y, 'Effect of alloying elements on anodic polarization properties of titanium alloys in acid solutions', *Mater Trans JIM*, 1994, 35, 58–66.
44 Okazaki Y, Kyo K, Ito Y, Tateishi T, 'Effects of Mo and Pd on corrosion resistance of V-free titanium alloys for medical implants', *Mater Trans JIM*, 1997, 38, 344–352.

45 Okazaki Y, Tateishi T, Ito Y, 'Corrosion resistance of implant alloys in pseudo physiological solution and role of alloying elements in passive films', *Mater Trans JIM*, 1997, 38, 78–84.
46 Ito A, Okazaki Y, Tateishi T, Ito Y, '*In vitro* biocompatibility, mechanical properties, and corrosion resistance of Ti–Zr–Nb–Ta–Pd and Ti–Sn–Nb–Ta–Pd alloys', *J Biomed Mater Res*, 1995, 29 , 893–900.
47 Okazaki Y, Ito Y, Ito A, Tateishi T, 'New titanium alloys to be considered for medical implants'. In: Brown S A, Lemons J E, ed. (1996) *Medical Applications of Titanium and its Alloys: The Material and Biological Issues*, ASTM STP 1272, 45–59.
48 Okazaki Y, Rao S, Tateishi T, Ito Y, 'Cytocompatibility of various metal and development of new titanium alloys for medical implants', *Mater Sci Eng*, 1998, A 243, 250–256.
49 Okazaki Y, Rao S, Ito Y, Tateishi T, 'Corrosion resistance, mechanical properties, corrosion fatigue strength and cytocompatibility of new Ti alloys without Al and V', *Biomaterials*, 1998, 19, 1197–1215.
50 Okazaki Y, Ito Y, 'New Ti alloy without Al and V for medical implants', *Advanced Eng Mater*, 2000, 2, 278–281.
51 Okazaki Y, Nishimura E, 'Effect of metal released from Ti alloy wear powder on cell viability', *Mater Trans JIM*, 2000, 41, 1247–1255.
52 Okazaki Y, 'A new Ti–15Zr–4Nb–4Ta alloy for medical applications', *Current Opinion in Solid State and Materials Science*, 2001, 5, 45–53.
53 Okazaki Y, Nishimura E, Nakada H, Kobayashi K, 'Surface analysis of Ti–15Zr–4Nb–4Ta alloy after implantation in rat tibia', *Biomaterials*, 2001, 22, 599–607.
54 Okazaki Y, 'Effect of friction on anodic polarization properties of metallic biomaterials', *Biomaterials*, 2002, 23, 2071–2077.
55 Okazaki Y, Gotoh E, 'Implant applications of highly corrosion-resistant Ti-15Zr-4Nb-4Ta alloy', *Mater Trans JIM*, 2002, 43, 2943–2948.
56 Okazaki Y, Gotoh E, 'Corrosion fatigue properties of metallic biomaterials in Eagle's medium', *Mater Trans JIM*, 2002, 43, 2949–2955.
57 Okazaki Y, Gotoh E, 'Comparison of metal release from various metallic biomaterials *in vitro*', *Biomaterials*, 2005, 26, 11–21.
58 Okazaki Y, Gotoh E, Nishimori M, Katsuda S, Manabe T, Kobayashi K, 'Osteocompatibility of stainless steel, Co–Cr–Mo, Ti–6Al–4V and Ti–15Zr–4Nb–4Ta alloy implants in rat bone tissue', *Mater Trans JIM*, 2005, 46, 1610–1617.
59 Okazaki Y, Gotoh E, Manabe T, Kobayashi K, 'Comparison of metal concentrations in rat tibia tissues with various metallic implants', *Biomaterials*, 2004, 25, 5913–5920.
60 Welsch G, Boyer R, Collings E W, *Materials Properties Handbook: Titanium Alloys*, ASM International, 1994.
61 Jacobs J J, Silverton C, Hallab N J, Skipor A K, Patterson L, Black J, Galante J O, 'Metal release and excretion from cementless titanium alloy total knee replacements', *Clin Orthop Relat Res*, 1999, 358, 173–180.
62 Hallab N, Merritt K, Jacobs J J, 'Metal sensitivity in patients with orthopaedic implants', *J Bone Joint Surg*, 2001, 83A, 428–436.
63 Jacobs J J, Skipor A K, Patterson L M, Hallab N J, Paprosky W G, Black J, Galante J O, 'Metal release in patients who have had a primary total hip arthroplasty. A prospective, controlled, longitudinal study', *J Bone Joint Surg*, 1998, 80A, 1447–1458.

64 Dobbs H S, Minski M J, 'Metal ion release after total hip replacement', *Biomaterials*, 1980, 1, 193–198.
65 Savarino L, Granchi D, Ciapetti G, Stea S, Donati M E, Zinghi G, Fontanesi G, Rotini R, Montanaro L, 'Effects of metal ions on white blood cells of patients with failed total joint arthroplasties', *J Biomed Mater Res*, 1999, 47, 543–550.
66 Jacobs J J, Skipor A K, Black J, Urban R M, Galante J O, 'Release and excretion of metal in patients who have a total hip-replacement component made of titanium-base alloy', *J Bone Joint Surg*, 1991, 73A, 1475–1486.
67 Jacobs J J, Skipor A K, Patterson L M, Hallab N J, Paprosky W G, Black J, Galante J O, 'Metal release in patients who have had a primary total hip arthroplasty', *J Bone Joint Surg*, 1998, 80A, 1447–1458.
68 Jacobs J J, Silverton C, Hallab N J, Skipor A K, Patterson L, Black J, Galante J O, 'Metal release and excretion from cementless titanium alloy total knee replacements', *Clinical Orthopaedics and Related Research*, 1999, 358, 173–180.
69 Agins H J, Alcock N W, Bansal M, Salvati E A, Wilson Jr P D, Pellicci P M, Bullough P G, 'Metallic wear in failed titanium-alloy total hip replacements', *J Bone Joint Surg*, 1988, 70A, 347–356.
70 Hanawa T, 'Metal ion release from metal implants', *Mater Sci Eng*, 2004, C24, 745–752.
71 Browne M, Gregson P J, 'Surface modification of titanium alloy implants', *Biomaterials*, 1994, 15, 894–898.
72 Herting G, Wallinder I O, Leygraf C, 'Metal release from various grades of stainless steel exposed to synthetic body fluids', *Corros Sci*, 2007, 49, 103–111.
73 Herting G, Wallinder I O, Leygraf C, 'Factors that influence the release of metals from stainless steels exposed to physiological media', *Corros Sci*, 2006, 48, 2120–2132.
74 Herting G, Wallinder I O, Leygraf C, 'Corrosion-induced release of chromium and iron from ferritic stainless steel grade AISI 430 in simulated food contact', *J Food Eng*, 2008, 87, 291–300.
75 Hodgson A W E, Kurz S, Virtanen S, Fervel V, Olsson C O A, Mischler S, 'Passive and transpassive behaviour of CoCrMo in simulated biological solutions', *Electrochimica Acta*, 2004, 49, 2167–2178.
76 Lewis A C, Kilburn M R, Papageorgiou I, Allen G C, Case C P, 'Effect of synovial fluid, phosphate-buffered saline solution, and water on the dissolution and corrosion properties of CoCrMo alloys as used in orthopedic implants', *J Biomed Mater Res*, 2005, 73A , 456–467.
77 Okazaki Y, Gotoh E, 'Metal release from stainless steel, Co–Cr–Mo–Ni–Fe and Ni–Ti alloys in vascular implants', *Corros Sci*, 2008, 50,
78 Haraldsson C, Cowen S, 'Characterization of Sandvik Bioline high-N-A comparison of standard grades F1314 and F1586 Stainless Steels for Medical and Surgical Applications', in: Winters G L, Nutt M J, ed. (2003) *ASTM International: ASTM STP 1438*, West Conshohocken, 3–12.
79 Cuckler J M, 'The rationale for metal-on-metal total hip arthroplasty', *Clin Orthop Relat Res*, 2005, 441, 132–136.
80 Moroni A, Savarino L, Cadossi M, Baldini N, Giannini S, 'Does ion release differ between hip resurfacing and metal-on-metal THA?', *Clin Orthop Relat Res*, 2008, 466, 700–707.
81 Savarino L, Granchi D, Ciapetti G, Cenni E, Pantoli A N, Rotini R, Veronesi C A, Baldini N, Giunti A, 'Ion release in patients with metal-on-metal hip bearings

in total joint replacement: A comparison with metal-on-polyethylene bearings', *J Biomed Mater Res*, 2002, 63, 467–474.
82 Vendittoli P-A, Mottard S, Roy A G, Dupont C, Lavigne M, 'Chromium and cobalt ion release following the Durom high carbon content, forged metal-on-metal surface replacement of the hip', *J Bone Joint Surg*, 2007, 89B, 441–448.
83 Brodner W, Bitzan P, Meisinger V, Kaider A, Gottsauner-Wolf F, Kotz R, 'Elevated serum cobalt with metal-on-metal articulating surfaces', *J Bone Joint Surg*, 1997, 79B, 316–321.
84 Dumbleton J H, Manley M T, 'Metal-on-metal total hip replacement – What does the literature say?', *J Arthrop*, 2005, 20, 174–188.
85 Massé A, Bosetti M, Buratti C, Visentin O, Bergadano D, Cannas M, 'Ion release and chromosomal damage from total hip prostheses with metal-on-metal articulation', *J Biomed Mater Res*, 2003, 67B, 750–757.
86 Savarino L, Granchi D, Ciapetti G, Cenni E, Greco M, Rotini R, Veronesi C A, Baldini N, Giunti A, 'Ion release in stable hip arthroplasties using metal-on-metal articulating surfaces: A comparison between short- and medium-term results', *J Biomed Mater Res*, 2003, 66A, 450–456
87 Hallab N J, Jacobs J J, Skipor A, Black J, Mikecz K, Galante J O, 'Serum protein carriers of chromium in patients with cobalt-base alloy total joint replacement components'. In: Disegi J A, Kennedy R L, Pilliar R, ed. (1999) *Cobalt-base Alloys for Biomedical Applications*: American Society for Testing and Materials Special Technical Publication, ASTM STP 1365, 210–219.
88 Savarino L, Greco M, Cenn E, Cavasinni L, Rotini R, Baldini N, Giunti A, 'Differences in ion release after ceramic-on-ceramic and metal-on-metal total hip replacement', *J Bone Joint Surg*, 2006, 88B, 472–476.
89 Khan M, Takahashi T, Kuiper J H, Sieniawska C H, Takagi K, Richardson J B, 'Current *in vivo* wear of metal-on-metal bearing assessed by exercise-related rise in plasma cobalt level', *J Orthop Res*, 2006, 24, 2029–2035.
90 Cobb A G, Schmalzreid T P, 'The clinical significance of metal ion release from cobalt–chromium metal-on-metal hip joint arthroplasty', *Proc Inst Mech Eng*, 2006, 220H, 385–398.
91 ASTM F 2063, Standard Specification for Wrought Nickel–Titanium Shape Memory Alloys for Medical Devices and Surgical Implants.
92 Official J European Union L 301, 27. 9. 2004, p. 51, EU 2004/96/EC Commission Directive amended Council Directive 76/769/EEC as regards restrictions on the marketing and use of nickel for piercing post assemblies for the purpose of adapting its Annex I to technical progress.
93 Machida T, 'A study of osseointegration of titanium alloy implants', *Nihon Univ J Oral Sci*, 2004, 30, 245–257.
94 Okazaki Y, Gotoh E, 'Fatigue assessment of Ti–15Zr–4Nb–4Ta alloy for enhanced biocompatible implants', *Acta Biomaterialia*, 2009, 5.
95 Okazaki Y, Gotoh E, 'Evaluation of bending properties of bone plates, intramedullary nail rods and bone screws', *Jap J of Clinical Biomechanics*, 2008, 29, 449–457.
96 Okazaki Y, Gotoh E, 'Evaluation of torsional breaking and performance properties of bone screws using sawbone', *Jap J of Clinical Biomechanics*, 2008, 29, 443–448.
97 Okazaki Y, Gotoh E, 'Evaluation of wear properties of artificial hip and knee joints with testing machines based on 4-axis control', *Jap J of Clinical Biomechanics*, 2008, 29, 433–441.

3
Mechanical properties of metallic biomaterials

T. NAKANO, Osaka University, Japan

Abstract: Almost all metallic biomaterials are crystalline, with regular atomic arrangement, and their mechanical properties are dominantly controlled by dislocation motion and twinning closely relating to the crystal structure. Their mechanical properties can be improved by control of lattice defect or phase transformation at the atomic level. In this chapter, some metallic materials applied for the biomedical field, such as stainless steel, cobalt–chromium alloys, pure titanium, titanium alloys and noble metallic alloys are taken as examples, and the basic knowledge for governing mechanical properties in metallic materials for biomedical use are described from the viewpoint of crystal structure, slip deformation, dislocation, phase diagrams and recrystallisation. Relationships between microstructure and mechanical properties, and methods for strengthening metals, are briefly mentioned. In addition, the requirements required of metallic biomaterials for implantation are discussed with respect to the bone microstructure, and strategies for improving the *in vivo* mechanical properties by combining metallic biomaterials and bones are considered.

Key words: biomaterials, mechanical property, crystal structure, phase diagram, plastic deformation, dislocation, apatite, bone microstructure, bone quality, stress shielding effect.

3.1 Introduction

Metallic materials have outstanding mechanical reliability in *in vivo* environments, and so they are the most widely used implant materials. They are particularly used in load-bearing parts in orthopedic surgery and dentistry, to support the body weight on the bones and joints and enable the reconstruction of motor functions.[1] Although there was a time when the future use of metallic biomaterials was doubted because they remain in the body, progress in regenerative medicine in recent years has indicated that it would not be possible to develop biomedical devices without taking advantage of the mechanical properties and other outstanding functions of metallic materials.

In this chapter, in order to provide a foundation for understanding and controlling the basic properties of metallic biomaterials, a general explanation of crystal structure, slip deformation and dislocation, phase diagrams and the selection of phase, and deformation and recrystallisation process is given, with a focus on the relationship between the microstructure and mechanical properties. Finally, the requirements required of metallic biomaterials for

implantation with respect to the microstructure of bones, and strategies for improving the *in vivo* mechanical properties by combining metallic biomaterials and bones are considered.

3.2 Requirements for mechanical functions *in vivo*

The mission of biomaterials is to save lives, provide medical treatment, and improve the quality of life (QOL). The advantages of metallic biomaterials include high strength, ductility, toughness, abrasion resistance, fatigue-resistance, high elastic modulus, and high electric conductivity; some metallic materials also show outstanding magnetic qualities.[2] As a result (as shown in Fig. 3.1), considering only bone-related implants, metallic biomaterials are used in a majority of devices for load-bearing parts, including artificial joints, osteosynthesis devices and spinal fixation, and they have a wide range of applications as dental restorations, artificial tooth roots, denture bases, wires for use in orthodontics, prosthetic valves, electrodes, clips, etc. Moreover, metallic stents are used to expand constricted areas in blood vessels, intestines, etc., and their use is increasing every year.

Many of these metallic biomaterials are crystalline materials with a periodic arrangement of metallic atoms, and the mechanical properties on which most importance is placed when they are being applied in load-bearing parts are governed by dislocation and twinning based on their crystal structure. Moreover, the so-called phase transformation in which the crystal structure changes, in particular the expression of superelasticity based on the martensitic transformation, has led to the application of these metallic biomaterials *in vivo* because the metal gives the appearance of behaving in a way that produces flexibility. In other words, metallic biomaterials aim to improve their mechanical properties through the control of lattice defects and phase transformation at the atomic level. Currently, typical metallic biomaterials used in clinical settings include stainless steel, cobalt-chromium (Co–Cr) alloys, pure titanium (Ti) and titanium alloys, and noble metallic alloys. All of these are crystalline materials, with their mechanical and physical properties governed by their atomic arrangement and crystal structure and the symmetry of these structures.

3.2.1 Crystals and crystal structure

Crystals are solids with long-range periodicity whose constituent atoms, ions, or molecules are arranged in an orderly repeating pattern extending in all three spatial dimensions.[3,4] Crystals are distinguished from amorphous materials, and their crystal structures are deeply related to the mechanical properties of the materials. Crystal structure does not necessarily depend on the arrangement of individual atoms, etc.; it is expressed by the distribution

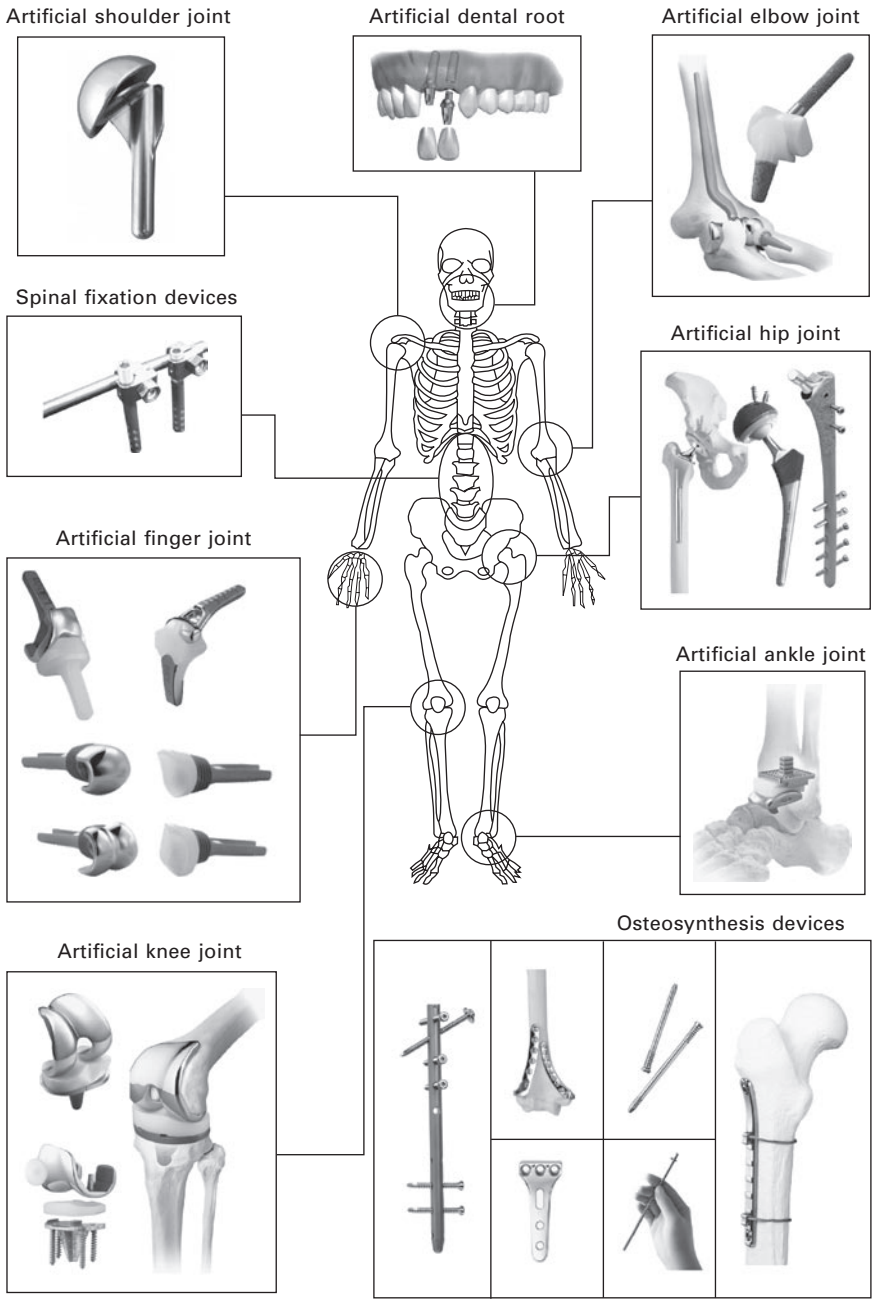

3.1 Various bone-related implants that are used *in vivo* for orthopaedic surgery and dentistry. The majority of them are made solely of metal. (Photos provided by Nakashima Medical Co. Ltd, Japan and Japan Medical Materials (JMM) Co. Ltd, Japan).

of imaginary points reflecting the periodicity in crystals, which are called the lattice points. As shown in Fig. 3.2, the arrangement of all of the lattice points is divided into seven crystal systems determined by three vectors, $\vec{a}$, $\vec{b}$, and $\vec{c}$ and the angles between them α, β, and γ, and furthermore are finally classified into 14 types of Bravais lattice on the basis of the distribution of the lattice points. Here the lattice points certainly have the same environment. It is surprising that the crystal structures are classified into only 14 types; however, the distribution of atoms, etc. to each lattice point has infinite variations, and so there is a great variety of crystal structures.

In metallic materials, most often a single metallic atom occupies the lattice points of a simple lattice, and those with a highly symmetric crystal structure are widely used in industrial applications. This is because in

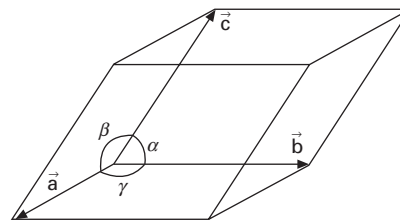

Crystal system	Axial lengths and angles	Bravais lattice
Cubic	$a = b = c$, $\alpha = \beta = \gamma = 90°$	Simple (P) Body-centered (I) Face-centered (F)
Tetragonal	$a = b \neq c$, $\alpha = \beta = \gamma = 90°$	Simple (P) Body-centered (I)
Orthorhombic	$a \neq b \neq c$, $\alpha = \beta = \gamma = 90°$	Simple (P) Body-centered (I) Base-centered (C) Face-centered (F)
Rhombohedral	$a = b = c$, $\alpha = \beta = \gamma \neq 90°$ (< 120°)	Simple (P)
Hexagonal	$a = b \neq c$, $\alpha = \beta = 90°$, $\gamma = 120°$	Simple (P)
Monoclinic	$a \neq b \neq c$, $\alpha = \gamma = 90° \neq \beta$	Simple (P) Base–centered (C)
Triclinic	$a \neq b \neq c$, $\alpha \neq \beta \neq \gamma \neq 90°$	Simple (P)

3.2 The unit cells and crystal systems that determine the crystal structure and the categories of Bravais lattices. All crystals can be classified into the seven crystal systems and the 14 Bravais lattices.

combinations of crystal grains with differing crystal orientations (in other words in polycrystals) the highly symmetric crystals easily satisfy the von Mises criterion, which are the conditions necessary for maintaining the continuity of the strain through the crystal grain boundaries. Figure 3.3 shows the typical crystal structures: the body-centered cubic (bcc) structure, the face-centered cubic (fcc) structure, and the hexagonal close-packed (hcp) structure. The symmetry of the crystal structure is lower for hcp than bcc and fcc, and the packing density of the atoms is lower in bcc than fcc and hcp. These atomic arrangements are deeply related to the mechanical properties in metallic biomaterials.

In current major metallic biomaterials, the crystal structure of the constituent phases is occupied by highly symmetric atomic arrangements. For example, stainless steel depends on alloy composition and heat treatment and generally has a bcc or fcc structure, and the SUS316L stainless steel with increased corrosion resistance, which is used as a metallic biomaterial, has fcc as its parent phase. Moreover, Co–Cr alloys for biomedical application are basically fcc, and pure titanium (Ti) has hcp (α phase) as its stable crystal structure at ambient temperature and bcc (β phase) as its stable crystal structure at a high temperature of 882.5 °C or above. Ti–6Al–4V alloys, and Ti–6Al–7Nb alloys excluding the biotoxic element vanadium (V), have an ($\alpha + \beta$) duplex microstructure, including a bcc (β phase) in addition to the hcp (α phase).

In recent years, there has been research into and development of alloys with a low Young's modulus, aimed at alleviating the stress shielding effect caused by the difference in the elastic modulus between bone tissue and metallic implants (the phenomenon in which bone mass, bone density, and bone quality decline compared to normal levels when stress is shielded). Typical examples of this are β-type Ti alloys, which have a bcc crystal

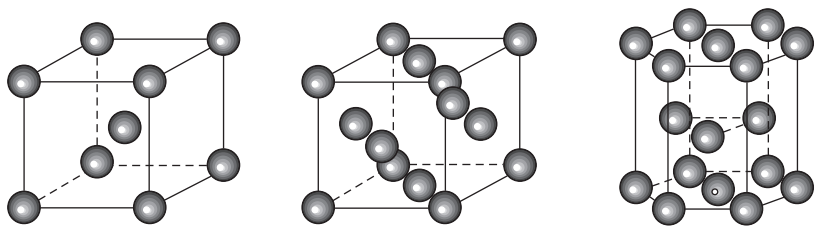

(a) Body-centered cubic structure (bcc)

(b) Face-centered cubic structure (fcc)

(c) Hexagonal close-packed structure (hcp)

3.3 The atomic arrangement in (a) the body-centered cubic (bcc) structure, (b) the face-centered cubic (fcc) structure, and (c) the hexagonal close-packed (hcp) crystal structure. These three structures are the basic crystal structures of the metallic materials that are widely used in practical applications due to their high crystal symmetry. In metallic biomaterials, most of the crystal structures of the parent phase are one of these three structures.

structure as their stable crystal structure. However, from the perspective of the improvement of mechanical properties, alloy compositions with low bcc-stability are the focus of attention, and expression of several types of martensitic phases using martensitic phase transformation and the control of precipitation using heat treatment are possible. Most of the several structures that are formed in this way belong to the hexagonal crystal systems that have an α-phase. Here, the martensitic transformation is a 'non-diffusion transformation' in which the crystal structure changes without any help from thermal activation energy and is the cause of the superelasticity and shape memory phenomenon. In particular the superelasticity derives from the fact that the crystal structure changes reversibly due to the martensitic transformation when loading and unloading stress, and creates flexibility as a rubber-like metal.

The crystal structure of noble alloys for dental use depends on the alloy composition; however, many gold and platinum series (Au–Pt) alloys have fcc as their matrix crystal structure.

3.2.2 Deformation of crystalline metallic biomaterials

The deformation of crystalline metallic materials can be classified into two types: 'elastic deformation' and 'plastic deformation'.[3,5] 'Elastic deformation' is a region governed by Hooke's law equivalent to the deformation of a spring, and unloading returns the materials to their original shape. On the other hand, if a load greater than a certain level is applied, the shape of the deformed materials does not recover to its original state even after the weight is removed. This kind of permanent deformation is called 'plastic deformation.' Figure 3.4 shows the classical stress–strain curve of a single crystal of a β-type Ti alloy for biomedical application. In the low-strain region, stress rises linearly due to elastic deformation; after reaching a certain level of stress, the gradient declines and plastic deformation starts. This stress, at which the transition from elastic deformation to plastic deformation takes place, is called the 'yield stress' or the 'elastic limit' and is an important indicator reflecting the strength of materials. However, it is important to note that even above the yield stress, elastic strain increases as stress increases.

The slope of stress–strain curves in elastic deformation is called Young's modulus, and it reflects the elastic property of materials. Generally, when metallic biomaterials are applied in implantations, etc. they are used within their elastic limit. For this reason, when they are implanted in bones the difference in the elastic modulus compared to bones is important. The elastic modulus of cortical bones is about 10–20 GPa, whereas it is higher for current metallic biomaterials. In SUS316L stainless steel, it is approximately 160 GPa, in Co–Cr alloys it is approximately 200 GPa, and in pure titanium it is approximately 110 GPa. As a result, when metallic biomaterials are introduced

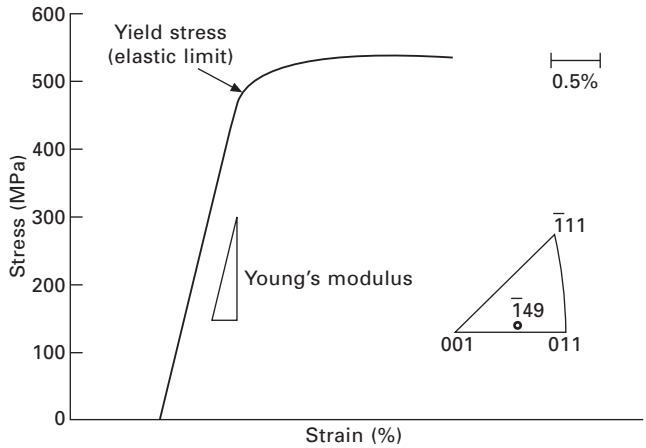

3.4 The classical stress–strain curve of a single crystal of a β-type Ti alloy used for medical applications at room temperature. After elastic deformation, macroscopic plastic deformation starts at the yield stress, and the material undergoes permanent deformation. In this case, slip deformation due to the dislocation is responsible for the plastic deformation.

in parallel into bone structure, bone tissue is absorbed by the stress shielding effect, which is based on the different elastic modulus between bone and metallic materials.[6] Therefore, in current metallic material implants, basically harm is avoided by connecting bones and implants in a series circuit with a loading direction. Nonetheless, there are inherent limitations to this kind of device design, so that an alloy with an elasticity similar to the elastic modulus of bones is thought to be necessary. For example, in the case of the newly designed Ti–niobium-tantalum-zirconium (Ti–Nb–Ta–Zr) alloys, in polycrystalline substances Young's modulus is about 60 GPa but in the [001] direction, owing to single crystallisation, it is possible to realise a Young's modulus under 40GPa, closer to that of bone tissue.[7]

In the plastic deformation region after yielding, along with an increase in the strain, the crystalline materials, in general, harden as their deformation proceeds. Metallic biomaterials are never used at the yield stress or above; however, plastic deformation behavior is extremely important with respect to fabrication to give the materials their shape, the introduction of strain for microstructure control, and the progress of deformation due to metal fatigue. Elongation up to the point of fracture in tension shows the ductility of the materials, and the larger this value, the easier the plastic deformation becomes. However, the ductility of materials tends to be in inverse proportion to the yield stress or maximum strength; therefore, it is important to adjust both accordingly for the application, and to design the materials to increase both strength and ductility.

Generally the rise in yield stress due to the decline in temperature (temperature dependence) is larger for bcc than fcc and hcp; therefore, bcc is more strongly affected by interstitial elements with small comparative atomic radii such as carbon (C) and nitrogen (N). When considering the dislocation discussed later, this is deeply related to the structures of the formation of the surrounding strain field and the dislocation core. (This is the part where the rearrangement of the atomic arrangement in the center of the dislocation occurs, a portion that cannot be described by elastic theory).

3.2.3 Slip deformation based on crystal structure

The elastic deformation and plastic deformation behaviour from a macro perspective discussed in the previous paragraph is deeply related to the crystal structure, which is a spacial atomic arrangement. Figure 3.5 shows the stylised movement of atoms in two dimensions inside crystals when first elastic deformation and subsequently plastic deformation occurs. For example, if a tensile load is added under elastic deformation (Fig. 3.5(b)), the atomic distance changes relative to that before deformation (Fig. 3.5 (a)); however, the bonding relationships among the adjacent atoms do

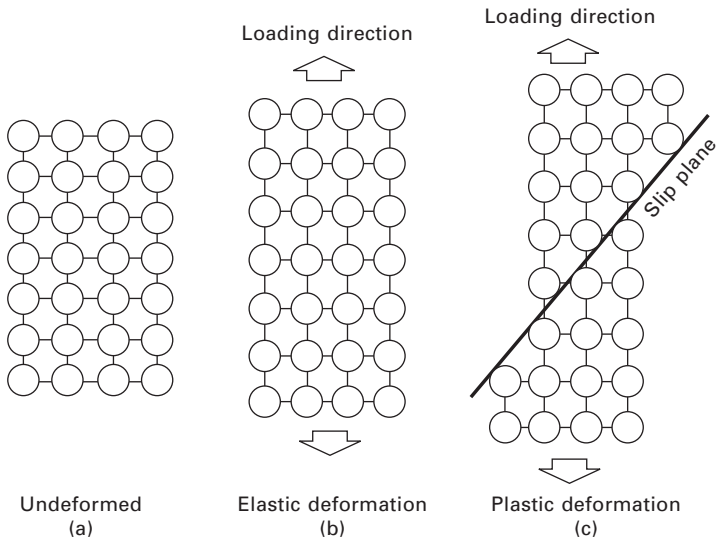

3.5 A stylised diagram showing the movements of atoms within crystals in two dimensions when elastic deformation and plastic deformation progress. With elastic deformation, after unloading, the atomic distance and external shape return to how they were originally. In plastic deformation, a slip occurs due to the atomic arrangement in crystalline metallic materials; however, the slip plane and slip direction in this case are strongly constrained.

not change. Therefore, elastic deformation is deeply related to the shape of the potential between atoms with respect to atomic distance.

On the other hand, plastic deformation progresses due to the slip deformation of the crystals, as in Fig. 3.5(c). Slip deformation is due to the relative displacement of atoms in a specific direction called the slip direction on a specific crystal plane called the slip plane.[3,5,8,9] Generally, the plane in which the separation between slip planes (lattice spacing) is large and the atoms are closely packed is selected as the slip plane, and the direction in which the atoms are most closely arranged is selected as the slip direction. This kind of deformation can be said to be a constraint condition for enabling plastic deformation to progress in metallic biomaterials and other crystalline metals while breaking down the stable crystal structure as little as possible. Therefore, there is a tendency to believe that deformation is generally easy for metallic materials; however, it is necessary to be strongly aware of the fact that actually plastic deformation progresses under constraints which result in the selection of the slip plane and slip direction based on the crystal structure. As a result, appropriate material design involves producing metallic biomaterials that combine mechanical safety and outstandingly high strength.

Figure 3.6 illustrates the typical slip systems (combinations of slip planes and slip directions) seen in bcc, fcc, and hcp, the most common structures in metallic biomaterials. The slip plane and slip direction are written in their respective separate spaces (respectively called the reciprocal lattice space and the real lattice space) using Miller indices or using Miller-Bravais indices in the hexagonal crystal system. The fcc and bcc structures are cubic crystal systems; therefore, in terms of appearance, the spaces that express the slip plane and the slip direction match, and it is possible to include them in an orthonormal coordinate system. The slip plane in the figure is displayed as

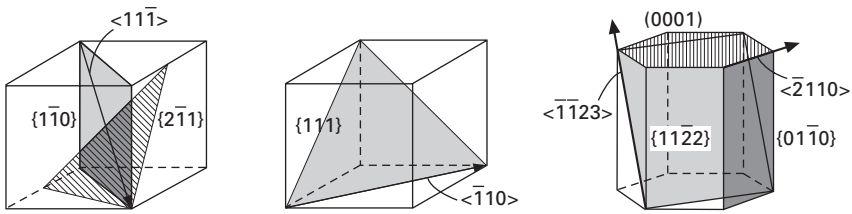

(a) Body-centerd cubic structure (bcc)

(b) Face-centered cubic structure (bcc)

(c) Hexagonal close-packed structure (hcp)

3.6 A typical slip system (the slip plane and the slip direction) in (a) the body-centered cubic (bcc) structure, (b) the face-centered cubic (fcc) structure, and (c) the hexagonal close-packed (hcp) crystal structure. Generally the plane in which the atoms are closely packed is selected as the slip plane, and the direction in which the atoms are most closely arranged is selected as the slip direction.

a vector of the slip plane normal direction and the slip direction is displayed as a vector parallel to that direction. As a result, for the fcc structure, which has the greatest packing density of atoms, the slip plane is uniquely determined to be {111} (the plane for which <111> is the normal) and the slip direction to be $<\bar{1}10>$; therefore, from the symmetry of the crystals, a total of 12 combinations of slip systems exist. On the other hand, for the bcc structure the <111> direction with the closest packed atoms is selected as the slip direction; however, the {211} plane, etc. (other than the {110} plane, the closest packed plane) can be selected as the slip plane. The selection of the slip system based on the crystal structure is extremely important when considering the strength of metallic biomaterials. This is because the degree of difficulty of slip deformation corresponds directly to the difference in the strength of the materials. In other words, resistance and impedance of slip deformation lead to high strength metallic materials.

3.2.4 Dislocation motion in crystals

In the case that shear deformation of the slip plane progresses in line with the slip direction, a relative displacement of atoms as shown in Fig. 3.7 is expected. The shear stress necessary to carry out the (a) → (b) → (c) series of atom movements in Fig. 3.7 once is called the theoretical strength.[8] This value is estimated to be about a sixth of the shear modulus of rigidity in metals; however, the actual stress for the slip is more than two or three digits smaller than this. The lattice defect that was introduced to explain the reason for this big difference is dislocation.[8] In other words, at the time of a plastic deformation, the slip does not progress all at once; rather, in the process shown in Fig. 3.7 (a) → (c), the overall slip occurs through the progress of a partial slip equivalent to the situation in (d), in other words a 'disarray of atomic arrangement' like that shown by '⊥'. The strain component due to this slip motion of the dislocation is defined as the Burgers vector ($\vec{b}$). The self-energy of the dislocation is proportionate to the square of the Burgers vector; therefore, the length of the Burgers vector has a strong effect on the formation, dissolution, and motion of the dislocation. Dislocation can be directly observed in a transmission electron microscope according to the strain field of the surrounding lattice. For example, as shown in Fig. 3.8, the dislocation can be directly observed as white lines of contrast, and the direction of the Burgers vector can be determined by using the extinguish conditions of the dislocation.

Dislocation is a partial rearrangement of atoms in the crystal structure so that a large strain field occurs in the area around the dislocation. These dislocations can be classified into three types on the basis of the relationship of the angles of the slip direction (the direction of the Burgers vector) and the direction in which the dislocation is arranged (the direction of

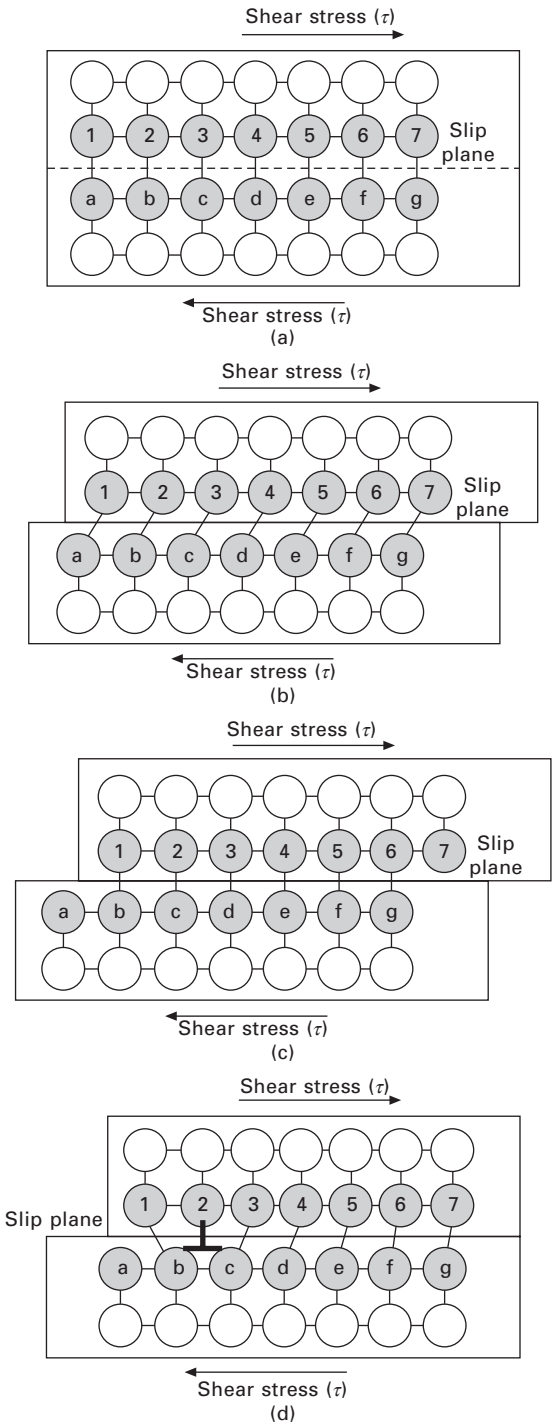

3.7 The relative displacement of atoms and the change in external shape when shear deformation on the slip plane progresses in line with the slip direction. An extremely high shear stress is thought to be necessary to carry out the series of atom movements in Figures (a) → (b) → (c) all at once, and actually the movement of the atoms is carried out in the order Figure (a) → (d) → (c). Due to the progress of a partial slip equivalent to a 'disarray of atomic arrangement' like that shown by ' ⊥' in Figure (d), an overall slip deformation occurs, which is called a 'dislocation.'

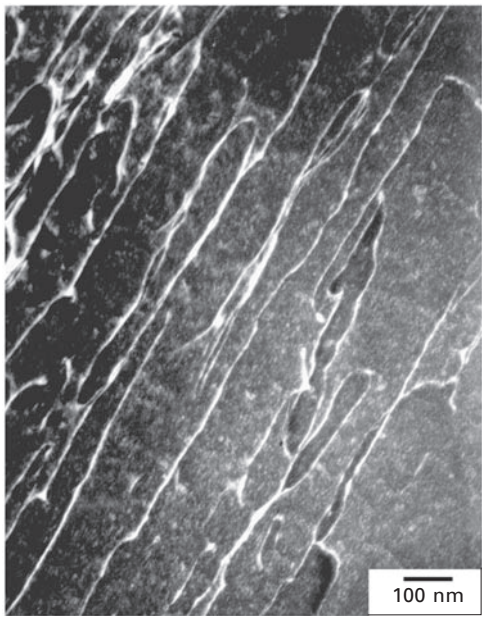

3.8 The dislocation discernible after deformation in a single crystal of a β-type Ti based alloy (the white curves). This dislocation can be directly observed in a transmission electron microscope (TEM: dark field image) on the basis of the strain field of the surrounding dislocation core.

the dislocation lines): edge dislocations, screw dislocations, and mixed dislocations. As shown in Fig. 3.9, the case in which the relationship between the slip direction (the direction of the Burgers vector) and the dislocation line is perpendicular is called edge dislocation (Fig. 3.9 (a)), the case in which that relationship is parallel is called screw dislocation (Fig. 3.9 (b)), and other cases are called mixed dislocation, in which the dislocation is composed of both an edge dislocation component and a screw dislocation component. For edge dislocation, the slip plane is uniquely determined from the relationship between the dislocation lines and the Burgers vector, whereas for screw dislocation, the motion of the identical slip plane is not inevitable. As a result, especially for the bcc structure in which the slip plane is not uniquely selected, a dislocation motion called the 'cross slip', which moves while changing the slip plane due to screw dislocation, can be observed. As a result, the curved slip traces can be discerned on the sample surface after deformation in the bcc structure. As an example of this, Fig. 3.10 (a) and (b) show the condition of the sample surface after deformation of a β-type Ti alloy single crystal newly developed for biomedical application. Wavy slip traces can be observed and the transition of the operative slip plane arising

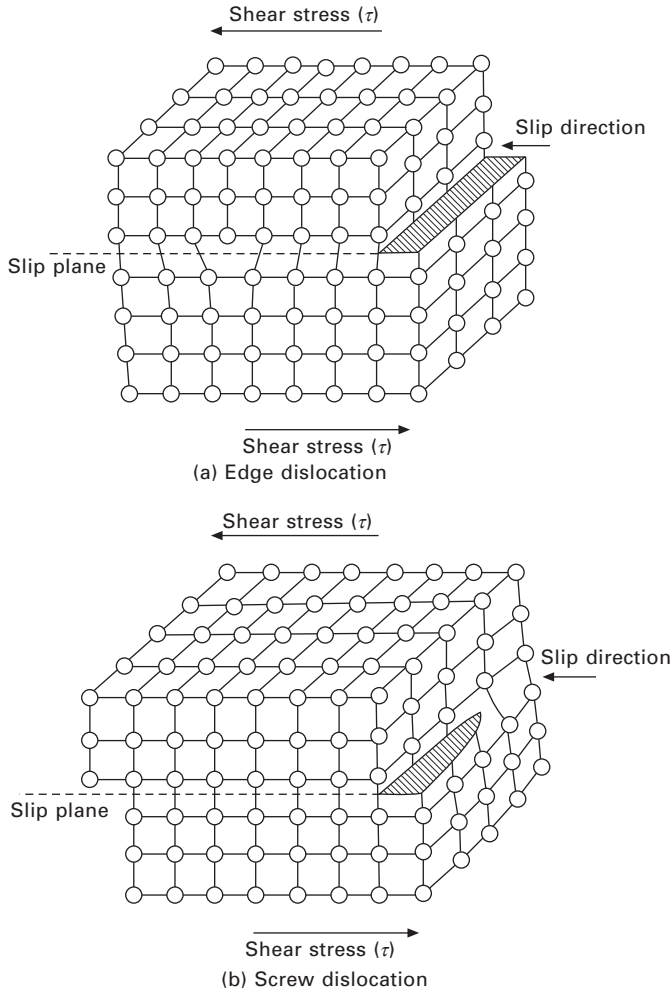

3.9 A stylised diagram of the atomic arrangement showing (a) edge dislocation and (b) screw dislocation. The relationship between the slip direction (the Burgers vector) and the dislocation lines is perpendicular (a) and parallel (b) respectively. If both components occur in combination, the dislocation is called a mixed dislocation, and the slip deformation differs depending of the respective types of dislocation.

from the change in the loading axis (corresponding to Fig. 3.10 (a) and (b)) can be discerned, and in Fig. 3.10 (a) and (b) {101} and {211} respectively are mainly selected as the slip plane. This means that the operative slip plane of the dislocation transitions while adhering to the Maximum Resolved Shear Stress Plane (MRSSP: the crystal plane in which the resolved shear stress is loaded most efficiently with respect to the external stress loading) to some

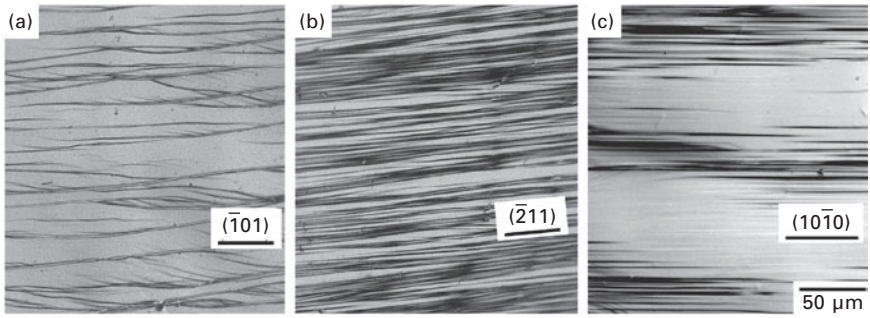

3.10 Slip traces on the sample surface after deformation of a single crystal of a β-type Ti-based alloy newly developed for biomedical application (Figure (a) and (b)) and a pure Ti single crystal (Figure (c)). With the β-type Ti alloys that have a bcc structure, a curved slip trace showing the cross slip events can be discerned; when the slip plane for which the maximum resolved shear stress plane (MRSSP) depending on the loading axis is selected, the curved slip trace of the crystal structure (Figure (a) and (b)) can be observed, and the dominant slip plane depending on the loading axis transitions from the $(\bar{1}01)$ plane (Figure (a)) to the $(\bar{2}11)$ plane (Figure (b)). On the other hand, in the pure Ti single crystal which has a hcp structure, a linear slip trace in line with the $(10\bar{1}0)$ prism plane (Figure (c)) can be discerned, and this is deeply related to the dislocation core structure based on the crystal structure.

extent.[10,11] This transition phenomenon of the slip plane differs greatly in the case of fcc and hcp due to the characteristics of the crystal structure and the dislocation core structure on the basis of the atomic arrangement. For reference, the slip line at room temperature in a pure Ti single crystal with the hcp structure is shown in Fig. 3.10(c). Unlike in the cases of Fig. 3.10 (b) and (c), a large number of slip lines that appear to be linear on the trace of the $\{10\bar{1}0\}$ prism plane can be found.

The differences in the operative slip planes depending on these crystal structures are also strongly expressed in the Critical Resolved Shear Stress (CRSS), which determines the strength of the materials. CRSS is the effective stress with respect to the slip direction on the slip plane for starting macroscopic plastic shear deformation, and in fcc structures, excluding some exceptions, it does not depend on the loading axis orientation and is largely constant. On the other hand, in bcc alloys, changes in the slip plane arising from the complexity of the dislocation core structure and even crystal orientation dependence of the CRSS frequently appear. Thus, the motion of the dislocation that determines the strength of the materials has a close relationship to the atomic arrangement within the crystals introduced by the dislocation; in other words, the dislocation mode is strongly influenced by the crystal structure of the contained constituent phase and its combinations.

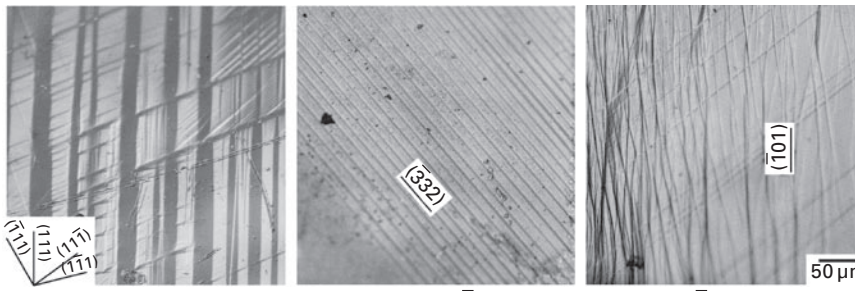

(a) Stress-induced α'' martensite (b) $\{332\}\langle 11\bar{3}\rangle$ twin (c) $\{10\bar{1}\}\langle 111\rangle$ slip (dislocation)

3.11 The stability of the bcc atomic structure depends on the deformation mode of the β-type Ti alloys used for biomedical applications. The deformation mode closely correlates with the stability of the β phase. The major deformation mode changes along with the stabilisation of the β phase from stress-induced martensitic transformation (Fig. (a)) to deformation twin (Fig. (b)) and finally to motion of dislocation (Fig. (c)).

Taking the β-type Ti alloys as an example, their deformation is closely related to the stability of β (bcc) structures. Figure 3.11 shows the trace on the specimen plane after deformation, and the deformation mode changes substantially along with stabilisation of the β phase.[12–14] The motion of the dislocation is important as the deformation mode of crystalline metallic materials; however, the deformation is frequently borne due to this deformation twin and martensitic transformation. Here, the deformation twin creates a mirror relationship (180° symmetry) with respect to the specific plane (twinning plane) with respect to the original crystals. With bcc structures generally, the {112} plane is the twinning plane, which is displaced in the <111> direction. With β-type Ti alloys, as the stability of the β phase of the parent phase increases, the deformation mode changes according to stress-induced martensitic transformation, {332} <113> deformation twin, and <111> dislocation in this order. At the same time, the mechanical properties change substantially corresponding to the variations in the deformation mode.

3.3 Methods for strengthening metallic biomaterials

Strengthening of metallic materials is basically achieved by impeding the dislocation motion.[5,15]

3.3.1 Work hardening

Work hardening is the phenomenon in which mobile dislocation undergoes interactions due to the pile-up dislocations introduced by plastic deformation,

and therefore dislocation motion becomes difficult. Generally, it rises in proportion to the square root of the dislocation density. In the case of as-wrought Co–Cr alloys, improvement of strength through work hardening is possible.

3.3.2 Solution hardening

Solution hardening is the phenomenon by which introduction of a heterogeneous solute atom to a pure metal impedes the dislocation motion resulting in hardening. In particular, hardening is promoted by differences in atomic size and the atomic modulus of rigidity. N and C in the SUS316L stainless steel for biomedical applications make a significant contribution to strengthening through solution hardening, as they are interstitial atoms between the crystal lattices; and the addition of aluminum in Ti alloys makes the same contribution to strengthening as a substitutional element.

3.3.3 Precipitation hardening

Precipitation hardening is the phenomenon in which the dislocation motion is impeded and the material is hardened by precipitating and dispersing an extremely fine precipitation in the parent phase using the differences in solubility of solute atoms at different temperatures. Hardening due to the uniform dispersion of carbide in Co–Cr alloys and the precipitation of the ordered phase of gold alloys fall into this category.

3.3.4 Particle dispersion hardening

Powder metallurgy (the method of hardening raw powder by subjecting it to pressure and heat, to mold or synthesise it as a bulk material) and other methods are used to harden the material by finely dispersing particles that harden and stabilise at high temperatures, such as alumina (Al_2O_3). Along with precipitation hardening, mobile dislocation leads to hardening by cutting particles or proceeding by an indirect route. In the case where the loop of the dislocation surrounding the particle (the Orowan loop) is left behind, owing to the resulting internal stress, there will be impedance of the motion of the dislocation which continues to move, and significant hardening will occur. It is thought that a particle distribution showing an interdistance between particles of about the order of length for a Burgers vector is necessary for hardening.

3.3.5 Composite strengthening

Compared to precipitation hardening and particle dispersion hardening, the volume fraction of the second phase for strengthening is larger, and this

approach aims to strengthen by receiving the load in accordance with the volume fraction in both the parent phase and the second phase.

3.3.6 Grain refining hardening

Deformation progresses through grain boundaries due to the multiplication of dislocation within the adjacent crystal grains after stress concentration by the pile-up dislocations in the original grain. Thus, the material gets harder if the crystal grains are smaller, and the yield stress and maximum stress change in inverse proportion to the square root of the size of the crystal grains. Grain refining is achieved through the deformation and recrystalisation process and severe plastic deformation process, etc., which are mentioned later.

3.4 Phase rule and phase diagram

In order to control the strength of crystalline metallic materials, it is essential to take into consideration the properties of the slip system on the basis of crystal structure and to have an alloying design to control the motion of the dislocation. For this reason, not only alloys comprised of single-phase but also alloy design comprised of a multi-phase of two or more phases is important. In reality, most of the metallic biomaterials that are being used in applications use the multi-phase, which allows the exclusion of pure metals such as Ti, etc. In diploidisation, it is possible to use not only the stable phase, but also the meta-stable phase. However, taking into consideration the phase rule as an indicator of whether or not multiple stable phases can coexist is extremely important when following the alloy design. Currently, under constant pressure, the degrees of freedom f′ is expressed in terms of C–P+1 (C: number of alloy components, P: number of stable phases).[15] Using this relationship, for example, an equilibrium can be achieved up to a maximum of four phases in ternary alloys (three components).

A diagram that describes this stable phase equilibrium (the situation in which free energy is at a minimum) with respect to temperature, composition, and pressure is called a phase diagram, and phase diagrams are indispensable when determining the guidelines for alloy design.[3,15] As an example, Fig. 3.12 shows a stylised binary phase diagram that can be used as the guideline when designing a Ti alloy, which is highly bio-compatible. When Ti is replaced with the secondary element (X), the transformation temperature for α (hcp)/β (bcc) fluctuates, depending on the type of element, and cases are seen where the ($\alpha + \beta$) duplex phase region exists in a stable state even at room temperature.

Fig. 3.12 (a) is useful to explain how to read and use a general binary phase diagram. The vertical axis shows the temperature (T) and the horizontal axis corresponds to the alloy composition (concentration of X). In this case,

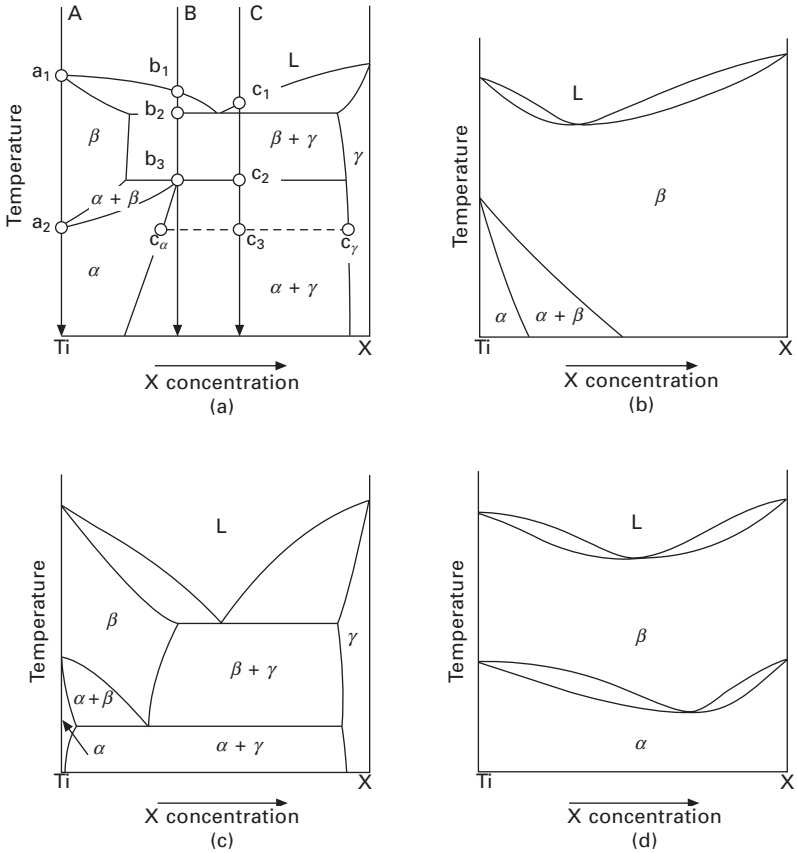

3.12 Binary phase diagrams when various second elements are added in Ti alloys. The transformation temperature for α (hcp)/β (bcc) fluctuates depending on the type of second element (X). Figure (a) shows the phase diagram for the α region expansion type (X = Al, Ga, C, N, O, etc.), Fig. (b) shows the phase diagram for the β region expansion type (X = Mo, Nb, Re, Ta, V, etc.), Fig. (c) shows the phase diagram for the β eutectoid type (X = Ag, Au, Co, Cr, H, Si, Pt, W, etc.), and Fig. (d) shows the phase diagram for the continuous solid solution type (X = Hf, Zr).

the vertical line on the extreme left means pure Ti and the vertical line on the extreme right means pure X element. Moving along the horizontal axis to the right means a greater amount of the pure Ti has been replaced with X element, and the phase state of the equilibrium condition combining the respective compositions and temperatures is shown. In other words, the phase state with the least amount of free energy for each temperature and composition is reflected. This kind of phase diagram is drawn according to the free energy–composition curve at each temperature; therefore, it is necessary

to understand the phase diagram while taking this curve into consideration at all times. Figure 3.12 (a) shows the three straight lines, A, B, and C, of different alloy compositions, and it shows the change in the equilibrium phase resulting from the decline in temperature for each of them.

$$\text{A (Pure Ti): } L\ (T > a_1) \rightarrow L + \beta\ (T = a_1) \rightarrow \beta\ (a_2 < T < a_1) \rightarrow \alpha + \beta\ (T = a_2) \rightarrow \alpha\ (T < a_2) \quad [3.1]$$

$$\text{B (Ti-X (low concentration of X) alloy): } L\ (T > b_1) \rightarrow L + \beta\ (b_2 < T \leqq b_1) \rightarrow L + \beta + \gamma\ (T = b_2) \rightarrow \beta + \gamma\ (b_3 < T < b_2) \rightarrow \alpha + \beta + \gamma\ (T = b_3) \rightarrow \alpha + \gamma\ (T < b_3) \quad [3.2]$$

$$\text{C (Ti-X (high concentration of X) alloy): } L\ (T > c_1) \rightarrow L + \beta + \gamma\ (T = c_1) \rightarrow \beta + \gamma\ (c_2 < T < c_1) \rightarrow \alpha + \beta + \gamma\ (T = c_2) \quad [3.3]$$

As can be understood from the phase rule, the maximum number of phase equilibriums in pure Ti is two ($T = a_1$: L+ β, $T = a_2$: $\alpha + \beta$); and in the binary alloys of the B and C compositions the maximum is three phase equilibriums (B composition ($T = b_2$): L + β + γ, $T = b_3$: $\alpha + \beta + \gamma$; C composition ($T = c_1$): L + β + γ, $T = c_2$: $\alpha + \beta + \gamma$), making diploidization possible due to phases having different crystal structures and different mechanical properties. In the case where the maximum number of equilibrium phases is reached, the degrees of freedom under constant pressure becomes zero and it is called an invariant reaction in which the composition and temperature required for phase equilibrium are uniquely determined. Therefore, increasing the number of elements when designing an alloy is an important method for increasing the number of degrees of freedom in the case of a multiphase equilibrium.

We can also understand the equilibrium composition and even the quantitative ratio of the equilibrium phase with the alloy phase diagram. For example, looking at C alloy (Fig. 3.12(a)), in $T = c_3$ the ($\alpha + \beta$) two phase equilibrium is maintained; however, the equilibrium compositions in that case are c_α and c_γ for the α-phase and γ-phase, respectively, and the quantitative ratio of the phases is expressed through the relationship of the values of $(c_\gamma – c_3)/(c_\gamma – c_\alpha)$ and $(c_3 – c_\alpha)/(c_\gamma – c_\alpha)$, respectively. The important point here is that even in cases where $T = c_3$, the alloy composition changed from c_α to c_γ, the compositions of the α-phase and the γ-phase are constant at c_α and c_γ, respectively, and only the quantitative ratio of the α-phase and the γ-phase changes. This reflects the fact that the free energy of the α phase and the γ phase in equilibrium is minimised in the c_α composition and the c_γ composition, respectively.

Using our basic knowledge about the above phase diagram, let us look at

the Ti-based binary phase diagram. It is classified into 'α phase stabilised elements', for which the addition of a second element raises the transformation temperature of α/β and expands the α phase region; 'β phase stabilised elements', for which conversely the transformation temperature is lowered, and the β phase region expands; and 'neutral elements', which do not belong to either of the previous categories; the respective phase diagrams have special characteristics. In Fig. 3.12(a), it is seen that X = Al, Ga, C, N, O, etc., and the α phase region expands as an α phase stabilised element. In Fig. 3.12(b), X = Mo, Nb, Re, Ta, V, etc., and the β phase region expands and in Fig. 3.12 (c) as well, the β phase region is expanded, and the β phase undergoes a solid phase transformation to the α phase and the γ phase due to the eutectoid reaction (X = Ag, Au, Co, Cr, H, Si, Pt, W, etc.). Here, the eutectoid reaction is one type of invalid reaction in the binary system, and it means the resolution from one solid phase to two different solid phases due to a decline in temperature, resulting in a three phase equilibrium. Moreover, in Fig. 3.12(d) it is seen that X = Hf, Zr, the α/β transformation temperature does not change substantially, and it behaves as a neutral element because it becomes a continuous solid solution.

If we view the history of the development of Ti and Ti alloys as metallic biomaterials in terms of phase equilibrium, pure Ti with an hcp structure (α phase) has been used often; however, owing to their lack of strength Al, V, Nb, etc. have been added to make them into ($\alpha + \beta$) duplex alloys and thus achieve precipitation hardening and solution hardening. Moreover, recently β-type Ti alloys with low Young's modulus have been gaining attention as a way to reduce the stress shielding effect on bone tissue, and alloy design using β-stabilised elements such as Ta, Nb, Mo, etc. with low toxicity is being carried out.[16]

In iron based alloys as well, the binary phase diagram is broadly classified into four (order of the change of stability from the α phase to the γ phase: γ loop formation type, γ region contraction type, γ region expansion type, γ region open type) according to the expansion and contraction of the stable region of the α phase (ferrite: bcc) and the γ phase (austenite: fcc). Cr is a γ loop formation type element, so the γ region contracts; however, with the addition of 12% or more it forms a passivated membrane as a hydrated chrome oxyhydroxide, and this increases corrosion resistance. SUS316L stainless steel, which is used as a metallic biomaterial, stabilises the γ phase by adding nickel (Ni), a γ region expansion type element, in order to improve toughness. In other words, Cr and Ni, elements with different γ phase stabilisation tendencies, are added in order to improve corrosion resistance and improve mechanical properties at the same time. In recent years, taking into consideration the allergenic properties of Ni, there has been development of Ni-free stainless steel, which adds the γ region expansion type element N instead of Ni.[17]

3.5 Deformation and recovery, recrystallisation, and grain ripening

If plastic deformation of crystalline materials is carried out at a lower temperature than the melting point, the microstructure and the mechanical properties change. Dislocations introduced owing to plastic deformation at low temperatures and other lattice defects rearrange and decrease through the processes of recovery and recrystallisation at the relatively high temperature; at the same time, the microstructure is once refined by recrystallisation, and subsequently the crystal grains become coarser through grain ripening achieved with further heat treatment.[15] In the recovery process, the extinguishing of the excess point defects that occurred in the crystal (the vacancy and interstitial atoms) and rearrangement of dislocation will not result in a change in the structure at the micron order level; however, there will be a small decline in strength and rise in ductility. Moreover, raising the temperature or the heat treatment for a long time will result in recrystallisation as the driving force reducing energy based on the extinguishment of lattice defects, especially dislocations. At this time, the new crystal grains with a low lattice defect density will nucleate, and the overall material will be covered with new crystal grains with a low density of lattice defects, and at the same time refinement will progress. During this recrystallisation process, the crystal grains with work hardening are extinguished so a marked decline in strength can be discerned; however, as a result of the crystal grains refinement, the increase in strength is greater than that of the coarse crystal grains structure before the work hardening. Moreover, if heat treatment is continued, it will be a driving force for the decrease in the total energy of the crystal grain boundaries, the crystal grains will ripen, and there will be a decline in strength corresponding to the increase in the crystal grain size. In metallic biomaterials as well, carrying out structure control through a combination of plastic deformation and heat treatment enables mechanical properties to be controlled so as to suit the application.

3.6 Microstructure and related mechanical properties in typical metallic biomaterials

SUS316L stainless steel developed for biomedical application has SUS304 (Fe–18mass%Cr–8mass%Ni), widely used as austenitic stainless steel, for its basic composition. By adding molybdenum (Mo), corrosion resistance is improved, and by reducing the amount of C, which has low solid solubility range, it is possible to keep precipitation at the grain boundary of chromium carbide ($Cr_{23}C_6$) low and thus, further improve corrosion resistance.[17,18] Through solution treatment at about 1000 °C, the carbon reaches a state of solid supersaturation, and the precipitation of the carbide is reduced. Moreover,

because the amount of carbon itself in the solid solution is kept low, it has relatively low strength properties, such as yield stress, etc., compared with SUS316 stainless steel, which has a large amount of carbon.

Co–Cr alloys for biomedical application are known as 'Vitarium' and are classified into those used for casting and for wrought.[19,20] In cast Co–Cr alloys, various defects are introduced during the solidification so their toughness is lower than for wrought alloys, and it is difficult to make them high strength. Therefore, cast defects are removed using hot isostatic pressing (HIP). When doing this, the solidification structure and crystal grain size distribution is adjusted using the molten metal temperature and the casting mold temperature to obtain certain mechanical properties. Meanwhile, wrought Co–Cr alloys have outstanding ductility compared to casting alloys because the cast defect and structure are destroyed, and the internal defects are extinguished; however, it is difficult to form them into complex shapes. For both casting and wrought materials, the carbide disperses during the Co-based parent phase so strengthening can be expected; however, in wrought alloys, the solution treatment extinguishes the carbide temporarily, plastically deforms under the recrystallisation temperature, and introduces dislocation inside the crystal grain. The following aging treatment (the process of changing the microstructure of the materials by heat treatment for a long time) creates a homogeneous dispersion of the carbide inside the parent grains; therefore, high strength is achieved through precipitation hardening without reducing toughness. As a result, Co–Cr alloys demonstrate high strength and abrasion resistance even though they have a higher Young's modulus than bone. Therefore, Co–Cr alloys are used in many artificial hips, especially, femoral head prosthesis.

Pure Ti and Ti alloys have a strong affinity for oxygen (O), and their mechanical properties tend to degrade with an increase in oxygen concentration. Furthermore, the same is true for N; therefore, these are controlled at a low concentration level.[21] Furthermore, the mechanical properties of (α + β) duplex alloys strongly depend on the amount of precipitation and the shape of precipitation of the α phase. In particular using hot forging in the duplex phase region to control the α phase from the needle shape to the equiaxed grain shape results in a decline in strength but an improvement in ductility, enabling a balance between the two to be achieved. Moreover, for β-type alloys, the microstructure and even mechanical properties can be controlled with heat treatment. The precipitation of the α-phase and ω-phase (both of which belong to a hexagonal crystal system) owing to heat treatment in the β-phase unstable region causes strength to rise; at the same time, it causes ductility to decline. Therefore, microstructural control is generally implemented so as to bring out the optimal mechanical properties by reducing the precipitation of the ω-phase and controlling the precipitation of the α-phase.

3.7 Development of metallic biomaterials based on biological bone tissues

3.7.1 Anisotropic nature of bone microstructure for optimal mechanical design

Up until the previous paragraph, the properties of metallic biomaterials and the factors that control those properties from the perspective of metal implants have been discussed. On the other hand, because most metallic implants are used by being embedded in biological structures (particularly biological bone tissues), it is necessary to develop metallic biomaterials in order to maintain the mechanical characteristics and microstructure of bone tissue and also the environment for bone cells. Since the consensus statement by the US National Institutes of Health (NIH) in 2000, bone quality factors other than the traditional indicator of bone mineral density[22] have been receiving attention regarding their governing of bone strength. In 2000, leading candidates for bone quality that were proposed included the formation and restoration of bone microstructure – typically the network structure of trabecular bone – and microcracks, the state of the collagen, bone turnover, cell viability, etc.; however, there is still not sufficient understanding of the essential bone quality control factors.

Bones possess a hierarchical structure that is precisely controlled at various levels. Their major components, excluding water, minor proteins, and bone cells, are basically type I collagen and biological apatite (BAp), with a combination of these two components giving the bones their strength and flexibility.

Of these components, BAp, as shown in Fig. 3.13, is a highly anisotropic ionic crystal with a crystal structure similar to a hexagonal column as its basic unit cell; therefore, the mechanical, chemical, and biological characteristics

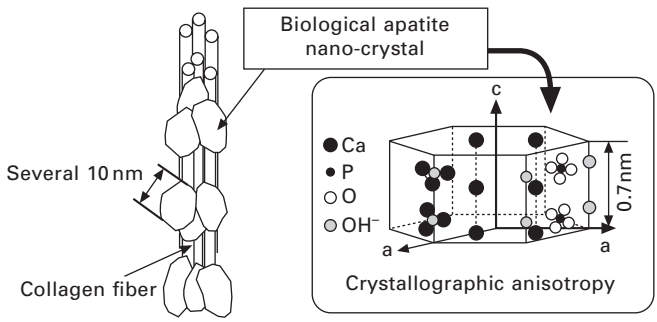

3.13 Bone structure is mainly comprised of collagen (type I) and biological apatite (BAp) crystal, and the c-axis of the BAp crystallite is arranged in the running direction of the collagen. Bone structure exhibits strongly anistropic mechanical properties crystallographically, owing to the orientation of both of these components.

of bones strongly depend on the crystallographic orientation; that is, along the a-axis and c-axis.[23] Moreover, in the bone structure, the nucleation site of the BAp crystallite seems to be inside the collagen hole zone, and it is thought that calcification (mineralisation) progresses as a result of the epitaxial nucleation and growth on the basis of the existence of the matrix vesicle. Therefore, analyses of the orientation degree of the BAp crystal also reflect collagen organisation, and orientated structure formation as BAp/collagen composite as the bone tissue is thought to be an extremely important factor for determining bone function.[24, 25]

The preferential alignment of BAp crystal in the bone structure changes substantially depending on bone pathology and bone regeneration, even in the case of normal bones, it changes considerably depending on various parameters such as species of animal, bone position, maturation, etc.[26] Figure 3.14 shows the orientation degree of BAp c-axis (relative X-ray diffraction intensity ratio) of various mature animal bones, analysed using the microbeam X-ray diffraction method (μXRD).[27] In the case of non-orientation, the figure shows a relative X-ray diffraction intensity ratio of approximately (002)/(310) of 2, meaning that in cases with higher diffraction intensity than that, it exhibits a preferential orientation degree of BAp crystal c-axis. In mature bone tissue, bone mineral density does not change substantially; however, BAp shows a uni-axial orientation structure with the c-axis arranged with the priority on the longitudinal direction, mesiodistal direction, and craniocaudal axis direction in the rabbit ulna, monkey mandible, and monkey lumbar vertebra, respectively, in cortical bone sites. On the other hand, the rabbit skull bone as a flat bone shows a two-dimensional orientation within the bone surface. This characteristic orientation distribution is deeply related to the *in vivo* stress distribution and bone growth direction normal metabolic turnover. In particular, the orientation for which the strong c axis orientation is recognised matches the maximum load orientation.[27]

The monkey mandible basically shows a BAp orientation in line with the mesiodistal direction (the C orientation in Fig. 3.14); however, just below the coronal portion it starts to show the maximum orientation with respect to the mastication load orientation (the B orientation). This tendency is strong on the buccal side which is easily exposed to the mastication load, and it controls the BAp orientation by handling the complex local changes in the *in vivo* local stress distribution due to mastication.[27]

3.7.2 Improvement of mechanical functions based on the combination of metallic biomaterials and biological bones

The orientation of collagen/BAp inside biological bones strongly depends on the *in vivo* stress distribution. In particular, the principal stress direction

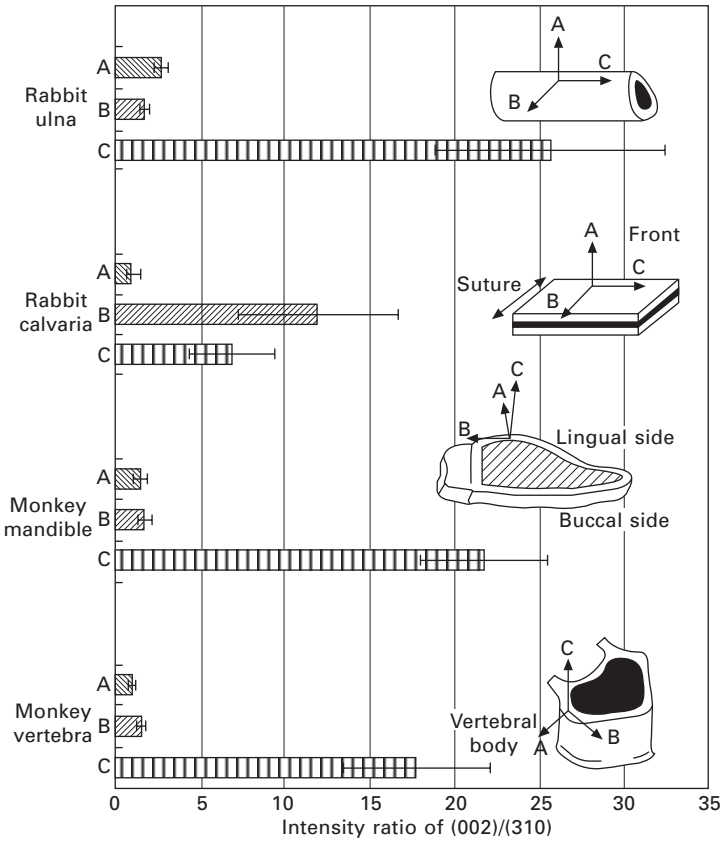

3.14 The c-axis orientation degree of BAp crystallite in mature cortical bone analysed by the microbeam X-ray diffraction method (μXRD). The bones show the characteristic anistropic microstructure for each portion, and the preferential degree of orientation can be found. In this case, when there is non-orientation, the value of 2 is shown. This figure was redrawn from ref. 27.

and the c-axis priority orientation of the BAp match well; therefore, optimal design of metallic implants to maintain the original bone microstructure should be given. Generally, the homeostasis of bone microstructure is maintained and bone remodeling progresses due to osteoblasts that form the bone, osteoclasts that resorb the bone, and osteocytes that sense the stress distribution within the bones. Making the direction of the grooves and pores match the principal stress direction gives an optimal environment to the bone cells;[28] this, in particular, enables the sensing of the stress by the osteocytes to get closer to a more normal state, resulting in formation of the appropriate microstructure containing the BAP orientation. Broadly classified, there are three necessary points required for future types of artificial joints: (i) surface

design, (ii) improvement of the properties of the materials themselves, and (iii) switching to tailor-made macro shapes. Regarding surface design, a surface shape to maintain the bone quality surrounding the metallic implants is extremely important, which encourages autonomic bone conductivity, finally making fixation over a long time feasible, and as a result leading to an improvement in the mechanical functions of metallic biomaterials and biological bones in combination. Moreover, as has already been shown in this chapter, controlling the properties of the materials is extremely effective. In particular, giving future types of metallic biomaterials a composition design and shock absorption that eliminates the difference in the elastic modulus compared to bone is an important challenge. Moreover, it is thought that the switch to tailor-made shapes that accurately fit the shape of medullary cavity in the bones of individual patients, made possible by the development of CT image construction technology, will accelerate even more in the future, along with changes to pharmaceutical approval standards.

3.8 Summary

Metallic materials have a long history as structural materials, and currently metallic biomaterials are expansively being understood and developed. On the other hand it is necessary for metallic biomaterials to have properties that can endure use in special environments; for example, it is necessary to reduce the toxic elements in these materials so they can be used *in vivo*. Moreover, structural inducibility and other interactions of metallic biomaterials with cells and biological structures are also important. In this chapter it was not possible to explain the issues fully due to space constraints. However, how the mechanical properties of metallic biomaterials are controlled at the order of atoms has been described, and also how these materials inherently have the potential to play an extremely important role as structural materials centered on the load support function in the future. Many current metallic biomaterials are materials that were developed for other applications, for example heat-resistant structural materials, etc., and have been diverted to biomedical applications. From this perspective, developmental research of metallic materials specifically for biomedical applications has only just begun, and research into implant materials for use as load-bearing parts is a field which, centered on the assigning of mechanical properties and the maintaining of intact bone microstructure, especially orientation degree of BAp crystal as a bone quality index, surrounding metallic implants, will undergo major development and building of new theories in the future.

3.9 References

1 Williams D F, Cahn R W and Bever M B (1990), *Concise Encyclopedia of Medical & Dental Materials*, Oxford, Pergamon Press.

2 Williams D F (1981), *Biocompatibility of Clinical Implant Materials*, Boca Raton, CRC Press.
3 Wert C A and Thomson R M (1970), *Physics of Solids (2nd edition)*, New York, McGraw-Hill.
4 Cullity B D and Stock S R (2001), *Elements of X-ray Diffraction (3rd edition)*, New Jersey, Prentice Hall.
5 Dieter G E (1986), *Mechanical Metallurgy (3rd edition)*, New York, McGraw-Hill.
6 Tonino A J, Davidson C L, Klopper P J and Linclau L A (1976), 'Protection from stress in bone and its effects. Experiments with stainless steel and plastic plates in dogs', *J Bone Jt Surg*, 58-B, 107–113.
7 Tane M, Akita S, Nakano T, Hagihara K, Umakoshi Y, Niinomi M and Nakajima H (2008), 'Peculiar elastic behavior of Ti–Nb–Ta–Zr single crystals', *Acta Mater*, 56, 2856–2863.
8 Hirth J P and Lothe J (1968), *Theory of Dislocations*, New York, McGraw-Hill.
9 Nabarro F R N (1979), *Dislocations in Solids*, Amsterdam, North-Holland Publishing Company.
10 Taoka T, Takeuchi S and Furubayashi E (1964), 'Slip systems and their critical shear stress in 3% silicon iron', *J Phys Soc Japan,* 19, 701–711.
11 Takeuchi S, Furubayashi E and Taoka T (1967), 'Orientation dependence of yield stress in 4.4% silicon iron single crystals', *Acta metall*, 15, 1179–1191.
12 Sakaguchi N, Niinomi M, Akahori T, Takeda J and Toda H (2005), 'Relationships between tensile deformation behavior and microstructure in Ti–Nb–Ta–Zr system alloys', *Mater Sci Eng C*, 25, 363–369.
13 Nakano T, Hagihara K, Maki H, Umakoshi Y and Niinomi M (2007), 'Crystal growth and plastic deformation behavior of Ti–29Nb–13Ta–4.6Zr bcc-based single crystal', *Ti-2007 (Proceedings of Ti-2007. The 11th World Conference on Titanium (JIMIC-5))*, 1437–1439.
14 Hagihara K, Nakano T, Sonoura A, Watanabe K, Umakoshi Y and Niinomi M (2007), 'Effect of bcc-phase stability on cyclic deformation behavior in beta-type Ti–Nb–Ta–Zr alloys single crystals with different Nb content, *Ti-2007 (Proceedings of Ti-2007. The 11th World Conference on Titanium (JIMIC-5))*, 1445–1447.
15 Cahn R W and Haasen P (1996), *Physical Metallurgy (4th edition) Vol. 1–3*, Amsterdam, Elsevier Science B.V.
16 Niinomi M (2003), 'Fatigue performance and cyto-toxicity of low rigidity titanium alloy, Ti–29Nb–13Ta–4.6Zr', *Biomaterials*, 24, 2673–2683.
17 Sumita M, Hanawa T and Teoh S H (2004), 'Development of nitrogen-containing nickel-free austenitic stainless steels for metallic biomaterials – review', *Mater Sci Eng C*, 24, 753–760.
18 Uhlig H H (1963), *Corrosion and Corrosion Control*, New York, Wiley.
19 ASTM Standards (2004), 'Standard specification for cast cobalt-28 chromium-6 molybdenum alloy castings and casting alloy for surgical implants', *Annual Book of ASTM Standards*, F75–01, 44–47.
20 ASTM Standards (2004), 'Standard specification for wrought cobalt-28 chromium-6 molybdenum alloys for surgical implants', *Annual Book of ASTM Standards*, F1537-00, 675–677.
21 Finlay W L and Snyder J A (1950), 'Effect of three interstitial solutes (nitrogen, oxygen, and carbon) on the mechanical properties of high-purity alpha titanium' *Trans AIME,* 188, 277–286.

22 NIH Consensus (2001), 'Development panel on osteoporosis prevention, diagnosis, and therapy', *JAMA*, **285**, 785–795.
23 Elliot J C (1994), *Structure and Chemistry of the Apatites and Other Calcium Phosphates*, Amsterdam, Elsevier.
24 Sasaki N, Matsushima N, Ikawa T, Yamamura H and Fukuda A (1989), 'Orientation of bone mineral and its role in the anisotropic mechanical properties of bone-transverse anisotropy', *J Biomech*, 22, 157–164.
25 Landis W J, Song M J, Leith A, McEwen L and McEwen B F (1993), 'Mineral and organic matrix interaction in three dimensions by high-voltage electron microscopic tomography and graphic image reconstruction', *J Struct Biol*, 110, 39–54.
26 Nakano T, Tabata Y and Umakoshi Y (2005), 'Texture and bone reinforcement', in *Encyclopedia of Materials: Science and Technology – Updates, Ms2061,* (ed. Buschow K H J, Cahn R W, Flemings M C, Kramer E J, Mahajan S, Veyssiere P), Oxford, Elsevier, 1–8.
27 Nakano T, Kaibara K, Tabata Y, Nagata N, Enomoto S, Marukawa E and Umakoshi Y (2002), 'Unique alignment and texture of biological apatite crystallites in typical calcified tissues analyzed by microbeam X-ray diffractometer system' *Bone*, 31, 479–487.
28 Nakano T, Kan T, Ishimoto T, Ohashi Y, Fujitani W, Umakoshi Y, Hattori T, Higuchi T, Tane M and Nakajima H (2006), 'Evaluation of bone quality near metallic implants with and without lotus-type pores for optimal biomaterial design', *Materials Transactions*, 47, 2233–2239.

4

Corrosion of metallic biomaterials

S. HIROMOTO, National Institute for Materials Science, Japan

Abstract: Corrosion of metallic biomaterials leads to a loss of their structural integrity and surface function. Because some dissolved metal ions cause allergic response and carcinogenesis, such dissolution must be within acceptable levels. Moreover, corrosion accelerates the fatigue, fretting fatigue and wear which may give rise to the deformation or the fracture of metals. Therefore, the understanding and accurate evaluation of corrosion behaviour are important to secure the reliability of metallic biomaterials. Corrosion behaviour depends on the sort of metals, the design of devices and the chemical and mechanical environment inside the body. Then, the condition and method of corrosion tests should be decided, depending on the sort of metals, the environment inside the body and the purpose of the test. This chapter therefore describes the methods for corrosion testing and their electrochemical background. Additionally, the characteristic corrosion factors inside the living body are discussed.

Key words: metallic biomaterial, corrosion, polarization test, immersion test, living cell environment.

4.1 Importance of corrosion

Corrosion is defined as the destructive attack of a metal by chemical or electrochemical reaction with water, oxygen and sulphur and so on in its environments (Revie and Uhlig, 2008). Corrosion of metals in aqueous solutions is inevitable because metal elements, except noble metal elements, are thermodynamically more stable in the oxide state than in the metal state, according to their ionization tendency.

Corrosion of metallic biomaterials causes the loss of their structural integrity and surface function. It accelerates their fatigue, fretting fatigue and wear and, conversly, such damage accelerates the corrosion. Corrosion processes of metallic biomaterials can cause alterations to bioenvironments, such as change in pH, decrease of dissolved oxygen, change in chemical components and so on. Moreover, the very small amount of released metal ions may cause allergic response and carcinogenesis in the human body. Because of these problems, the allowable amount of corrosion of metallic biomaterials is much smaller than that for the structural materials of bridges, buildings and so on. So, the corrosion process is one of the most important mediators of the tissue response to metallic biomaterials and an understanding and accurate evaluation of the corrosion behaviour of metallic biomaterials are necessary.

Titanium alloys, cobalt–chromium alloys and stainless steels are mainly used for orthopaedic and cardiovascular implants not only because of their high strength but also due to their high corrosion resistance owing to the passive surface films (oxide film). Passive films of Ti, Cr and so on show very high protectiveness against general corrosion. Noble metal alloys consisting of Au, Ag, Pt, Pd are used for dental materials and Pt is used for the electrodes of pace makers. Because of their low ionization tendency, the noble metals show relatively high thermodynamic stability, i.e. high corrosion resistance. Here, 'high corrosion resistance' means that the corrosion rate is sufficiently low from the view point of the lifetime of the materials. Release of metal ions from the passive and noble metals and alloys continues at a low level inside the human body.

Such materials as magnesium and iron alloys might be utilised for bioabsorbable (biodegradable) metallic biomaterials in stents, mini/micro plate systems and so on. Since magnesium exhibits very high ionization tendency and does not form protective film at around neutral pH, magnesium alloys are expected to be easily corroded inside the human body. The corrosion rate of bioabsorbable metallic materials needs to be precisely controlled, depending on the sort of devices and the condition of the affected parts.

As mentioned, the corrosion behaviour and the expected corrosion rate of metallic biomaterials depend on various factors in a complicated manner. The parameters of the corrosion test should be carefully considered depending on the purpose.

4.2 Principles of corrosion

4.2.1 Corrosion processes

Since corrosion processes are mostly electrochemical, an understanding of electrochemistry is very important. Furthermore, a fundamental understanding of physical metallurgy is also important because structure and composition of metallic materials often determine corrosion behaviour (Revie and Uhlig, 2008).

On the surface of metallic materials immersed in an electrolyte, an infinite number of atomic-size anodes and cathodes are formed as shown in Fig. 4.1. Short-circuit current (i) flows between local anodes and cathodes. A pair of local anodes and cathodes is called a local cell and the current flowing between them is called local current. The place of local anodes and cathodes changes every moment in the case of general corrosion. Moreover, the total anodic current is equivalent to the total cathodic current. As a result, the whole surface is uniformly attacked.

On local anodes, the dissolution (ionization) reaction of the metal M with releasing electrons (anodic reaction) (Eq. 4.1) takes place. On local cathodes, the reduction reaction of dissolved oxygen, water molecules or hydrogen

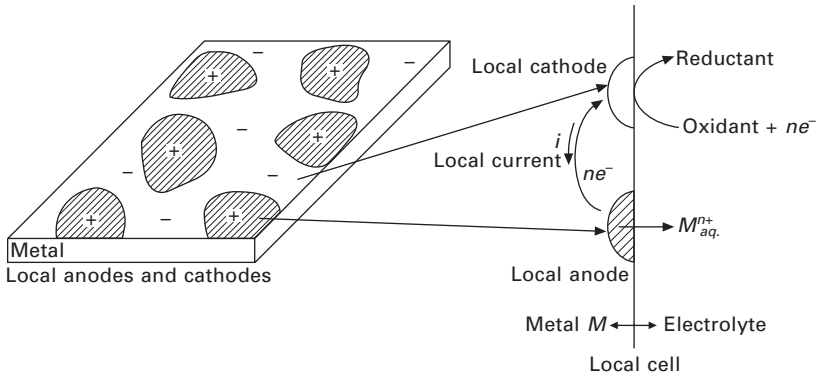

4.1 Schematic illustration of the local anodes and cathodes and a local-cell formed between them.

ions with receiving electrons (cathodic reaction) takes place. The kind of reactant in cathodic reaction depends mainly on the pH of the electrolyte. The cathodic reactant in acid and neutral electrolyte is generally hydrogen ions and dissolved oxygen, respectively (Eqs. 4.2 and 4.3).

$$M \rightarrow M^{n+} + ne^- \qquad [4.1]$$

$$2H^+ + 2e^- \rightarrow H_2 \qquad [4.2]$$

$$O_2 + 2H_2O + 4e^- \rightarrow 4OH^- \qquad [4.3]$$

When a metal M is immersed in a solution of its own salt (such as iron in iron sulphate solution), the redox reaction of Eq. 4.4 takes place as a single electrode reaction.

$$M \Leftrightarrow M^{n+} + ne^- \qquad [4.4]$$

The free energy change (ΔG) of the redox reaction is expressed by Eq. 4.5 with the standard free energy change (ΔG^0) and the activity of M^{n+} ions and metal M ([M^{n+}] and [M]).

$$\Delta G = \Delta G^0 + RT \ln \frac{[M^{n+}]}{[M]} \qquad [4.5]$$

where R and T are gas constant and absolute temperature, respectively. When the redox reaction is in an equilibrium state, $\Delta G = 0$. Then, the standard free energy change is given by Eq. 4.6.

$$-\Delta G^0 = RT \ln \frac{[M^{n+}]}{[M]} \qquad [4.6]$$

At constant temperature, $-\Delta G^0/RT$ becomes constant, so that [M^{n+}]/[M]

becomes constant. In this case $[M^{n+}]/[M]$ is called the equilibrium constant (K) of the redox reaction. The standard free energy change is then expressed as a function of the equilibrium constant (Eq. 4.7).

$$-\Delta G^0 = RT \ln K \quad [4.7]$$

Here, the free energy change gives the electrode potential (E) of the redox reaction according to Eq. 4.8.

$$\Delta G = -nFE \quad [4.8]$$

where F is the Faraday number. According to Eq. 4.5 and Eq. 4.8, the electrode potential of the redox reaction is given by Eq. 4.9.

$$E = -\frac{\Delta G^0}{nF} - \frac{RT}{nF} \ln \frac{[M^{n+}]}{[M]}$$
$$= E_0 - \frac{RT}{nF} \ln \frac{[M^{n+}]}{[M]} \quad [4.9]$$

where $\Delta G^0 = nFE^0$ and E^0 is the standard electrode potential. Equation 4.9 is called the Nernst equation and it gives the equilibrium potential of redox reactions. The tendency of the dissolution reaction of the metals can be estimated using the Nernst equation.

The equilibrium potential of elements in the standard state is called the standard electrode potential, which is expressed relative to the standard hydrogen electrode (SHE or NHE). The standard electrode potential of the elements relevant to metallic biomaterials is summarized in Table 4.1 (Revie

Table 4.1 Value of standard electrode potential of elements relevant to metallic biomaterials (298 K) (Revie and Uhlig, 2008; Kita and Uosaki, 1983)

Electrode reaction	Standard electrode potential, E^0(V vs. NHE)
$Mg \Leftrightarrow Mg^{2+} + 2e^-$	–2.36
$Al \Leftrightarrow Al^{3+} + 3e^-$	–1.66
$Ti \Leftrightarrow Ti^{2+} + 2e^-$	–1.63
$H_2 + 2OH^- \Leftrightarrow 2H_2O + 2e^-$	–0.8281
$Cr \Leftrightarrow Cr^{3+} + 3e^-$	–0.744
$Fe \Leftrightarrow Fe^{2+} + 2e^-$	–0.440
$Co \Leftrightarrow Co^{2+} + 2e^-$	–0.277
$Ni \Leftrightarrow Ni^{2+} + 2e^-$	–0.250
$H_2 \Leftrightarrow 2H^+ + 2e^-$	±0.000
$Ag \Leftrightarrow Ag^+ + e^-$	0.799
$Pd \Leftrightarrow Pd^{2+} + 2e^-$	0.987
$Pt \Leftrightarrow Pt^{2+} + 2e^-$	1.188
$2H_2O \Leftrightarrow O_2 + 4H^+ + 4e^-$	1.229
$Au \Leftrightarrow Au^{3+} + 3e^-$	1.498

and Uhlig, 2008; Kita and Uosaki, 1983). The standard electrode potential is equivalent to the electromotive force of elements; in other words, the tendency of its dissolution reaction to proceed. However, the order of the standard electrode potential of the metallic elements does not directly correspond to that of the corrosion rate because the solubility of the metal salts is limited and a protective film is often formed on the metal surface.

Because the redox reaction (electrochemical reaction) of a metal in its solution involves electrons and/or hydrogen ions, the equilibrium potential of the electrochemical reaction can be thermodynamically calculated as a function of pH based on the Nernst equation. The potential is plotted as a function of pH and the potential-pH diagram is often called Pourbaix diagram (Pourbaix, 1966). This diagram is used to estimate the corrosion behaviour of metals in aqueous solutions. For more details, please refer text books on corrosion.

When the metal M is at the equilibrium potential discussed above, the rate of anodic (oxidation) and cathodic (reduction) reaction is equal. When the potential of the metal M is shifted by η (overpotential) from the equilibrium potential, the anodic reaction is promoted and the anodic current flows externally. The apparent anodic current at the potential shifted by η is given by the Butler–Volmer equation (Eq. 4.10) as a difference between true anodic and cathodic current.

$$i = i_0 \left\{ \exp\left(\frac{\alpha n F \eta}{RT} \right) - \exp\left[- \frac{(1 - \alpha)\, nF\eta}{RT} \right] \right\} \qquad [4.10]$$

where i_0 and α are exchange current and transfer coefficient (symmetry factor), respectively. The exchange current is the anodic and cathodic current at the equilibrium potential as shown in Fig. 4.2. The magnitude of α is generally 0.3~0.7 (Sugimoto, 2009). Based on the Butler–Volmer equation, the corrosion rate of metals is estimated by electrochemical measurements since the magnitude of the current corresponds to the rate of the electrochemical reactions.

In practice, the potential of the metal M immersed in electrolytes settles at the potential at which anodic and cathodic reactions are of equal rate, but are different processes, as shown in Fig. 4.2. This 'mixed potential' is called the corrosion potential (E_{corr}), open-circuit potential (ocp) or rest potential. Note that the corrosion potential is not the equilibrium potential because it is determined by the balance between several anodic and cathodic reactions. The rate of the anodic partial reaction at the corrosion potential in Fig. 4.2 is called corrosion current (density) (I_{corr}), which corresponds to the corrosion rate.

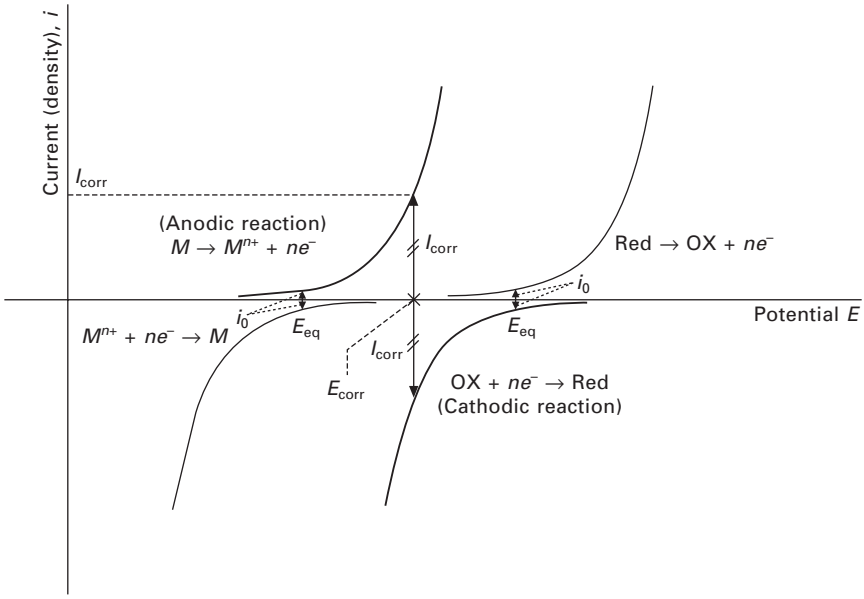

4.2 Schematic illustration of potential-current (density) curves in the corrosion system of a metal. E_{corr} = corrosion potential, E_{eq} = equilibrium potential, I_{corr} = corrosion current (density), i_o = exchange current (density).

4.2.2 Passivity

Some metals and alloys, such as titanium alloys, cobalt–chromium alloys and stainless steels, show very low corrosion rate in an environment in which a very high corrosion rate would be predicted according to the low standard electrode potential of the alloying elements. These metals and alloys are classified in passive metals and alloys. Their very low corrosion rate is due to the very thin but very protective oxide film (passive film) formed on the surface. The passive alloys include Cr, Ti, Zr and so on.

When the passive metals and alloys are anodically polarized (Fig. 4.3), the anodic current density increases with increase in overpotential (η) according to the Butler–Volmer equation (Eq. 4.10). Anodic current density achieves a critical passive current density (I_{crit}), and subsequently it suddenly drops by orders of magnitude lower to a passive current density (I_{ps}). The magnitude of passive current density represents the protectiveness of the passive film against the general corrosion. An important point for metallic biomaterials is that the release of metal ions equivalent to the magnitude of passive current density takes place continuously, although the passive alloys are in a passive state. On further increase in overpotential, the current density increases rapidly with the initiation of pitting corrosion, transpassive dissolution, and/

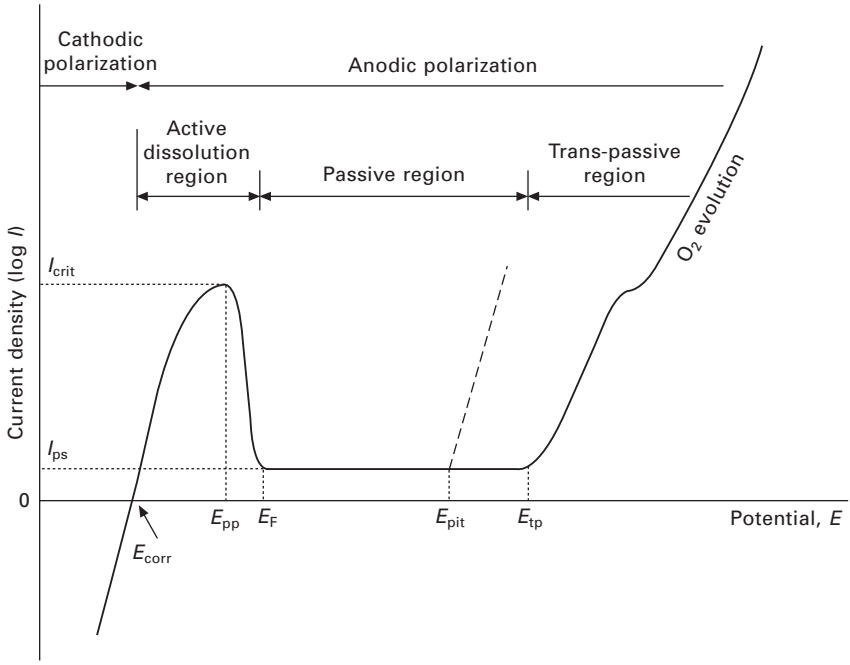

4.3 Schematic illustration of anodic polarization curve of passive metal (E_{corr} = Corrosion potential, E_{pp} = Passivation potential, E_F = Flade potential, E_{pit} = Pitting potential, E_{tp} = Transpassive potential, I_{crit} = Critical passive current density, I_{ps} = Passive current density).

or oxygen evolution. In pitting corrosion, the passive film is locally broken by halogen species such as chloride ion, fluoride ion and hydrogen fluoride. In transpassive dissolution, metal ions in the passive film are further oxidized to polyvalent metal ions and are released in the electrolyte. Oxygen evolution takes place with the electrolysis of water.

Titanium alloys, cobalt–chromium alloys and stainless steels in physiological environments generally are not in an active state but are spontaneously passivated. The passive film of stainless steels is more sensitive to chloride ion than those of titanium alloys and cobalt–chromium alloys.

4.3 Corrosion morphology

Metals show various corrosion morphologies since their corrosion behaviour is influenced by various factors such as microstructure and composition of the metal and pH, temperature and concentration of dissolved oxygen of the electrolyte. Corrosion morphology is roughly classified into general corrosion (uniform corrosion) and local corrosion (non-uniform corrosion).

4.3.1 General corrosion

The whole surface of the metal is uniformly corroded in general corrosion, as shown in Fig. 4.4(a). General corrosion of the passive alloys such as titanium alloys, cobalt–chromium alloys and stainless steels, is rarely observed in the human body. On the other hand, for the electrolytic polishing of passive alloys, general corrosion is promoted using aggressive electrolytes in which the alloys are in an active state.

4.3.2 Local corrosion

Local corrosion is sub-classified into pitting corrosion, crevice corrosion, intergranular corrosion, galvanic corrosion, selective corrosion, erosion-corrosion and stress corrosion cracking (Fontana, 1986; Revie and Uhlig, 2008). Local corrosion forms holes on the surface of metals. Corrosion holes may initiate cracks and accelerate the fracture of metals.

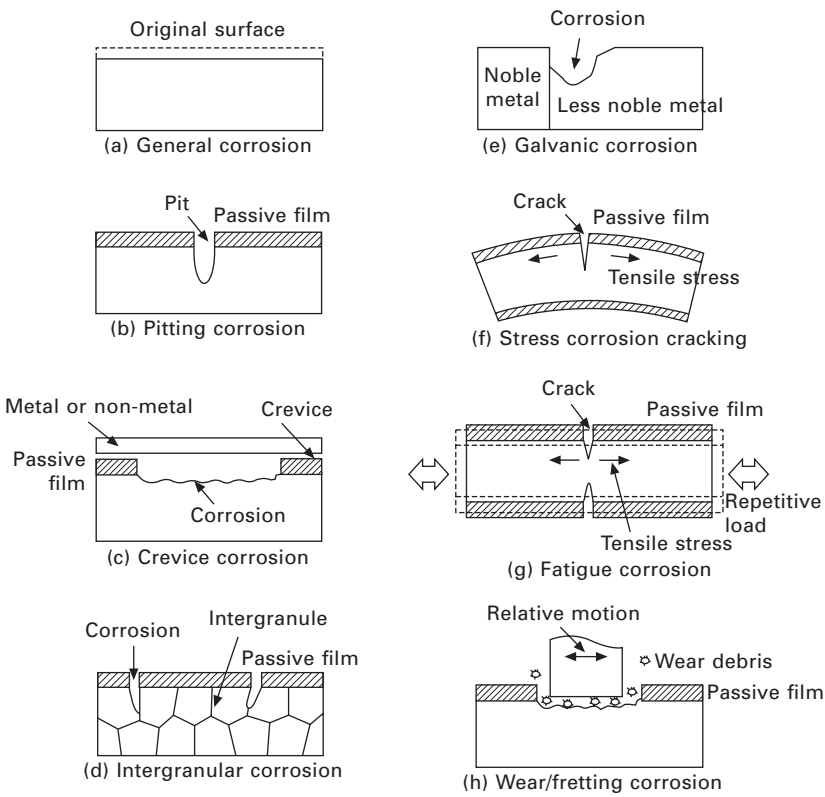

4.4 Schematic illustration of corrosion morphologies.

Pitting corrosion

Pitting corrosion is a type of local corrosion that proceeds in a very limited area while the greater part of the passivated surface is intact. Pitting corrosion is identified by the shape of the pits, of which the depth is larger than the diameter in many cases (Fig. 4.4 (b)). Pitting corrosion tends to take place on passive alloys in the presence of halogen species such as chloride, bromide and iodide ions and hydrogen fluoride. These halogen species attack the defects of passive films and locally break the film. Because the magnitude of anodic reaction inside the pits is balanced with that of the cathodic reaction outside the pits, large amount of metal ions is dissolved inside the pits. The sensitivity to pitting corrosion of the metal can be estimated based on the pitting potential obtained by electrochemical measurements. It has been reported that the austenitic stainless steels and cobalt–chromium alloys have the possibility of pitting in unfavourable conditions in physiological environments (Scharnweber, 1998). On the other hand, it is thought that the possibility of pitting corrosion of titanium alloys is low. In the case of metallic biomaterials, pitting corrosion has been observed at a screw hole of bone plates made of a stainless steel (Williams and Williams, 2004; Virtanen *et al.*, 2008).

Crevice corrosion

Crevice corrosion is a type of the local corrosion that takes place inside a metal–metal crevice and a metal–non-metal crevice (Fig. 4.4 (c)). Inside the crevice, where the mass diffusion is restricted, dissolved oxygen and pH decrease and chloride ions are enriched. Such change in the chemical environment inside the crevice causes the de-passivation of the metal surface inside the crevice. Because the rate of anodic reaction inside the crevice is balanced with that of cathodic reaction outside the crevice, corrosion inside the crevice proceeds intensively. In the case of metallic biomaterials, crevice corrosion can take place on mating interfaces such as the head/stem interface in artificial hip joints and the screw/hole interface in bone plates (Williams and Williams, 2004; Virtanen *et al.*, 2008).

Intergranular corrosion

Intergranular corrosion is a type of corrosion that selectively and deeply progresses at grain boundaries while the inside of the grains remains intact (Fig. 4.4(d)). Intergranular corrosion of stainless steels is the selective dissolution of the chromium-depleted zone formed along the grain boundaries. The chromium-depleted zone is formed with the precipitation of chromium carbides at the grain boundaries by the heat treatment.

Galvanic corrosion

When two types of metal show different corrosion potential individually and are placed in electrical contact with each other in an electrolyte, galvanic corrosion takes place on the metal at less noble potential, while cathodic protection takes place on the other metal at noble potential, as shown in Fig. 4.4(e). Some stainless steel stents are partially coated with gold as a contrast marker for an angiographic X-ray apparatus; the standard electrode potential of gold is higher than that of stainless steel indicated by Table 4.1. In the dental field, the crown is made of various noble metal alloys, and it often happens that crowns made of different sorts of alloys are used in the neighbourhood. In the case of the coupling of Ag–Pd–Cu–Au alloy and Ag alloy, the former alloy becomes the anode and the latter alloy becomes the cathode (Table 4.1). In the case of artificial joints, the coupling of a titanium alloy stem and a cobalt–chromium alloy head is often used. However, galvanic corrosion does not always take place. When the difference in corrosion potential between the coupled alloys is relatively small, galvanic corrosion may not occur.

Corrosion under mechanical loading

Under mechanical loading, such as static tensile or compressive stress, fatigue stress and wear/fretting, the surface of metallic materials is deformed and the passive film is locally and repetitively broken, as shown in Fig. 4.4(f)–4.4(h). Thus, the bare metal surface, which can be rapidly corroded, is exposed to the environment repetitively. Because the re-passivation of the bare metal surface is prevented by the repetitive removal of the passive film, local corrosion is accelerated under the mechanical loading. Corrosion under mechanical loading thus often takes place at a stress concentration area of metals. Because the progress of corrosion under mechanical loadings can promote crack initiation, fatigue, fretting fatigue and fretting/wear are accelerated, and *vice versa*. Metallic biomaterials are often subjected to mechanical loadings, so corrosion under such loadings is important. Fretting corrosion takes place on mating interfaces such as the head/stem interface in artificial joints and the screw/hole interface in bone plates (Hallab *et al.*, 2004; Rodrigues *et al.*, 2008).

4.4 Evaluation methods of corrosion behaviour

4.4.1 Electrochemical methods

Anodic polarization tests

Since the corrosion reaction is mostly electrochemical, corrosion behaviour of metals can be evaluated with electrochemical techniques. A polarization

test is one of the common techniques (ASTM F1089-02; ASTM F746-04; JIS T 0302). In anodic polarization tests, the anodic reaction of the specimen is accelerated by applying anodic overpotential and the current response is measured. According to the various parameters obtained, such as the magnitude of current density and pitting potential, the corrosion behaviour of the metals can be evaluated. In practice the anodic reaction is accelerated by applying anodic current using a potentiostat. A potentiodynamic polarization test (linear sweep voltammetry), in which the potential of the specimen is swept at a constant speed, is generally carried out. To obtain the response near the steady state, the sweep rate of potential should be as slow as possible. On the other hand, a potentiostatic polarization test is recommended to obtain the response at a steady state because the response can reach the steady state during the period when the potential is kept for several minutes.

Figure 4.5 shows a schematic illustration of electrochemical cell equipped with three electrodes; a working electrode (WE, specimen), a reference electrode (RE) and a counter electrode (CE). The potential of the working electrode is measured against the reference electrode and the current flowing between the working electrode and counter electrode is measured using a potentiostat. A saturated calomel electrode (SCE) or standard silver–silver chloride electrode (SSE) is used for a reference electrode and platinum or carbon is used for a counter electrode. The tip of the reference electrode is

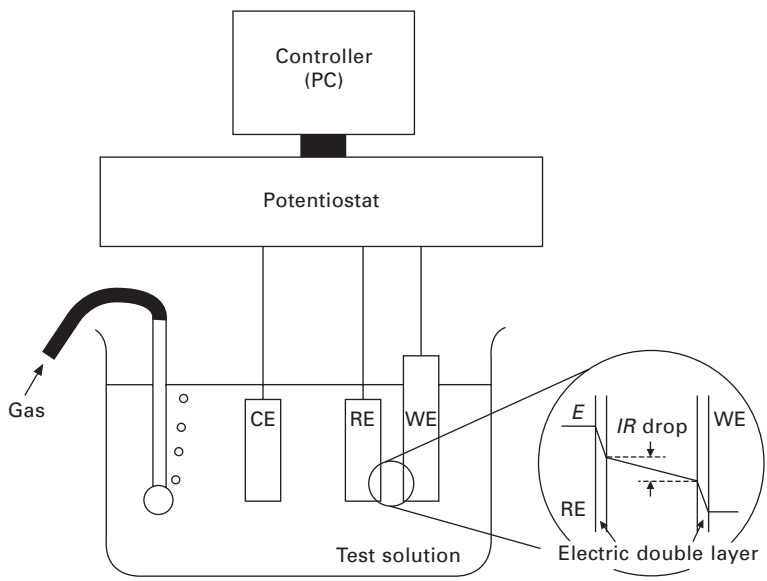

4.5 Schematic illustration of three-electrode electrochemical cell (WE: Working electrode, RE: Reference electrode, CE: Counter electrode).

set close to the surface of the working electrode to minimize the *IR* drop due to solution resistance.

The electrochemical cell is filled with a test solution. The test solution should be selected depending on the environment in the body and the purpose of the test. Saline (0.9mass% NaCl solution) is used as a simple test solution. To simulate the pH and/or the inorganic composition of body fluids, phosphate buffer saline (PBS), Hanks' solution, Ringer solution or minimum essential medium (MEM) is used. The test temperature is 310 K of body temperature and the concentration of dissolved oxygen is controlled by bubbling Ar, N_2 or O_2–N_2 gas, depending on the relevant environment and the purpose of the test.

Figure 4.6 shows anodic polarization curves for pure titanium, 316L stainless steel and cobalt–chromium alloy, measured after 1 week immersion in Hanks' solution (Hiromoto and Hanawa, 2006b), as examples. On the curve of 316L stainless steel, an abrupt increase in current density due to pitting corrosion finishes the passive region. The cobalt–chromium alloy shows an increase in current density due to transpassive dissolution following to the passive region. Pure titanium shows a constant passive current density in the potential region of this study. This result indicates that each metal shows characteristic polarization behaviour.

Tafel extrapolation method

Corrosion current density, which corresponds to the corrosion rate at the corrosion potential, can be obtained by the Tafel extrapolation method.

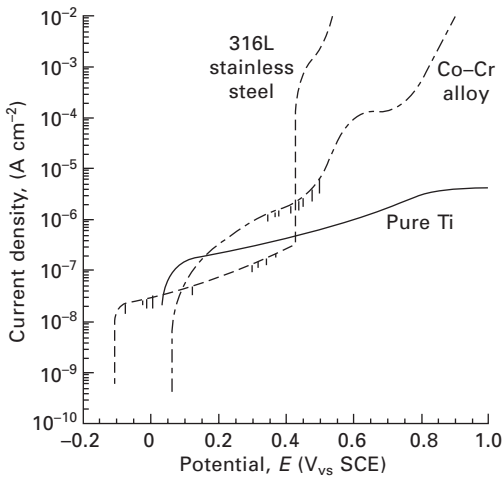

4.6 Anodic polarization curves of pure Ti, 316L stainless steel and cobalt-chromium alloy in Hanks' solution.

Sufficiently apart from the corrosion potential by ±50 mV, the current density (I) increases with the increase in overpotential, which is described by the Tafel equation (Eq. 4.11) derived from the Butlar–Volmer equation.

$$\eta = a + b \log I \qquad [4.11]$$

where b is the Tafel slope. As shown in Fig. 4.7, the intersection of the straight lines on anodic and cathodic polarization curves corresponds to the corrosion current density. Typical values of Tafel slope are 0.05~0.23 (Sugimoto, 2009). When the cathodic current is limited by diffusion of the cathodic reactant, as shown by the dashed line in Fig. 4.7, the intersection of the anodic Tafel line and the limiting current line corresponds to the corrosion current density. It should be noted that the typical anodic Tafel line does not often appear on alloys in physiological solutions because several redox reactions take place in parallel.

Linear polarization resistance method

The polarization resistance (R_p), which corresponds to corrosion resistance, is obtained by the linear polarization resistance method. Current linearly depends on the potential in a narrow potential region of E_{corr} ± 10 mV, as expressed by Eq. 4.12, called the Stern–Geary equation.

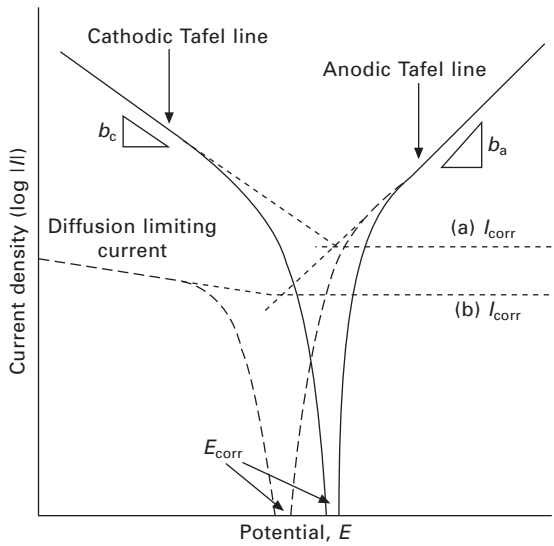

4.7 Schematic illustration of the Tafel extrapolation method (E_{corr} = Corrosion potential, I_{corr} = Corrosion current density, b_c = Cathodic Tafel slope, b_a = Anodic Tafel slope, Solid line = Both cathodic and anodic Tafel line appear on the polarization curve, Dashed line = Only anodic Tafel line appears on the polarization curve).

$$I_{\text{corr}} = \left(\frac{b_a b_c}{2.30(b_a + b_c)}\right)\left(\frac{\eta}{I}\right)^{-1} = K\, R_p^{-1} = \frac{K}{R_p} \qquad [4.12]$$

where b_a and b_c correspond to the anodic and cathodic Tafel slopes, respectively. K is called the conversion factor, and η/I, which is the slope of the polarization curve around the corrosion potential (E_{corr}), as shown in Fig. 4.8, corresponds to the polarization resistance. When the conversion factor is already known, the corrosion current density can be calculated based on the polarization resistance obtained by the linear polarization. Generally, the conversion factor is 0.02 V~0.05 V (Sugimoto, 2009).

Impedance test

The impedance test is performed by imposing an alternating potential with a small amplitude of less than 10 mV around the corrosion potential. The polarization resistance can be determined based on the impedance at low frequency around 1 mHz~10 mHz. An amplitude less than 10 mV does not disturb the corrosion system, which enables a continuous *in-situ* measurement of the impedance behaviour. The frequency is varied over a wide range, typically from 1 mHz to 1 MHz, to obtain the frequency dependence of impedance.

The corrosion interface of the metal under dissolution is simulated with the simple electrical equivalent circuit shown in Fig. 4.9. When alternating

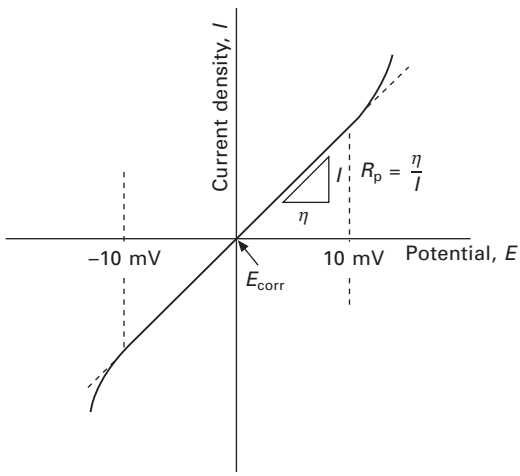

4.8 Schematic illustration of linear polarization test (R_p = Polarization resistance, E_{corr} = Corrosion potential, η = Over potential, I = Current density).

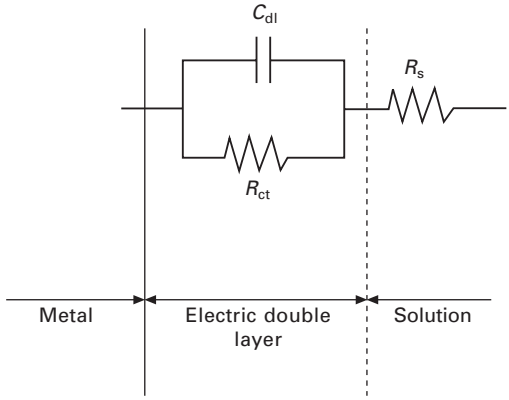

4.9 Equivalent electric circuit of the interface of the metal under dissolution (R_s = Solution resistance, R_{ct} = Polarization resistance (charge transfer resistance), C_{dl} = Capacitance of the electric double layer.

potential is imposed in this equivalent circuit, the value of impedance follows Eq. 4.13.

$$Z_{ct} = R_s + \frac{1}{j\omega C_{dl} + \frac{1}{R_{ct}}}$$

$$= R_s + \frac{R_{ct}}{1 + \omega^2 C_{dl}^2 R_{ct}^2} - j\,\frac{\omega C_{dl} R_{ct}^2}{1 + \omega^2 C_{dl}^2 R_{ct}^2} \qquad [4.13]$$

where j, ω and f are an imaginary number ($j = \sqrt{-1}$), the angular velocity ($\omega = 2\pi f$) and the frequency of the alternating potential, respectively. Additionally, R_s, R_{ct} and C_{dl} are solution resistance, polarization resistance (charge transfer resistance) and capacitance of the electric double layer, respectively. When ω is eliminated and Z_{ct} is rearranged by dividing into a real part (Z_{Re}) and an imaginary part (Z_{Im}), Eq. 4.14 is derived from Eq. 4.13.

$$\left[Z_{Re} - \left(R_s + \frac{R_{ct}}{2}\right)\right]^2 + Z_{Im}^2 = \left(\frac{R_{ct}}{2}\right)^2 \qquad [4.14]$$

The $Z_{Im} - Z_{Re}$ plot is called the Nyquist plot. The $Z_{Re} - Z_{Im}$ plot will show a semi-circle, as seen in Fig. 4.10 when the impedance measurement is carried out in a wide frequency range. The centre of this semi-circle is at [(R_s + R_{ct}/2), 0] and the radius is R_{ct}/2. Thus, the charge transfer resistance at the interface, which corresponds to polarization resistance, can be obtained from the impedance at the low frequency.

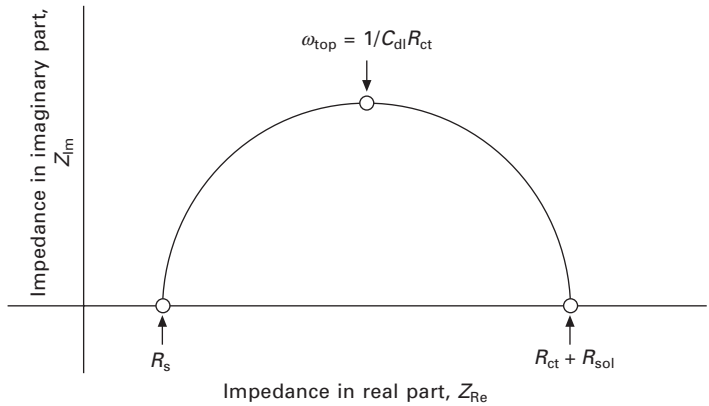

4.10 Nyquist diagram obtained from Eq. 4.14.

Monitoring of corrosion potential

Long-term change of corrosion potential (open-circuit potential) reflects a change in a corrosion system because the change in corrosion potential depends on the change in one or both of the anodic and cathodic reactions. For example, an increase in corrosion potential can be attributed to a decrease in the anodic reaction with the growth of a passive film or the increase in the cathodic reaction with an increase in dissolved oxygen. A decrease in corrosion potential can be attributed to an increase in the anodic reaction or a decrease in the cathodic reaction. The monitoring of corrosion potential is therefore often carried out (ISO 16429, 2004; JIS T 6002). For the test solution, saline, phosphate buffer saline, Ringer solution, culture medium, serum and artificial saliva are typically used. The corrosion potential of the specimen can be monitored against a reference electrode using an electrometer with high input impedance (10^{11} Ω~10^{14} Ω) or a potentiostat.

4.4.2 Immersion tests

The total amount of released metal ions in test solutions is quantified by gravimetric analysis or by solution analysis in immersion tests (dissolution tests) (ISO 10271; BS EN 1811; JIS T 0304). When the test solution is carefully selected, similar results to that in the human body can be obtained. For example, the selective dissolution of alloying elements can be reproduced *in vitro*. The test solution is selected from saline, phosphate buffer saline, Ringer solution, culture medium, serum and artificial saliva. Additionally, 0.1 mol L^{-1} lactic acid solution and 0.1 mol L^{-1} HCl solution are used for accelerated tests. The test temperature is 310 K and the test period (immersion period) is advisably longer than 7 d. The pH of the test solution should be checked before and after the immersion. The concentration of dissolved metal

ions is quantified using inductively coupled plasma (ICP), atomic absorption spectrometry and so on.

4.4.3 Other methods

The environment around the metallic biomaterial implanted in patients or immersed in test solutions is estimated from the corrosion morphology and the composition of corrosion products. Corrosion morphology is determined by the observation of surface morphology using an optical microscope and a scanning electron microscope (SEM). Corrosion products are qualified and quantified by electron dispersion spectroscopy (EDS), X-ray photoelectron spectroscopy (XPS) (JIS T 0306), auger electron spectroscopy (AES) and so on.

A tarnish test is performed for metallic dental materials because change in colour (tarnish) of the surface should be avoided for cosmetic reasons. Dental gold alloys and silver alloys are, however, easily tarnished with a slight amount of soluble sulphide in foods and drinks. The tarnish test is performed by immersion in 0.1 mol L^{-1} sodium sulphide for 3 d (ISO/TR 10271; JIS T 6002). The degree of tarnish is determined by the naked eye, comparing with the as-prepared surface.

As will be discussed in Section 4.5.4, the presence of cells on the surface of metallic biomaterials can change the chemical and/or physical environment on the surface. Electrochemical measurements under cell-culturing environments have been suggested to understand the *in vivo* corrosion reactions (Hiromoto *et al*., 2002; Lin and Bumgardmer, 2004).

When bioabsorbable metals are implanted under blood flow, their corrosion is expected to be accelerated with the promotion of mass diffusion. Flow cells or rotating disk electrodes have been suggested for electrochemical measurements and immersion tests on the bioabsorbable metals to simulate the influence of blood flow (Lévesque *et al*., 2008; Hiromoto *et al*., 2008a). Periodical replacement of the test solution is another way to simulate the circulation of body fluids (Yamamoto and Hiromoto, 2009).

4.5 Biological environments

The internal environment of a living body is maintained at a stable and constant condition (homeostasis). However, local environments have large variations in pH, concentration of dissolved oxygen, temperature and so on (Hayashi, 1987). Additionally, body fluids circulate inside the body by blood flow and natural convection.

Inside the living body, the implanted metals are firstly exposed to body fluids containing inorganic ions (chloride, carbonate, phosphate, calcium and so on), proteins, lipids and amino acids. The kind of cells that assemble

around the implanted metal varies with time. Devices made of metallic biomaterials have various designs and static and dynamic mechanical loadings are applied. These various factors affect the corrosion of metallic biomaterials in a complicated way.

4.5.1 Temperature and pH

Body temperature is kept at around 310 K (homeostasis). ISO 16428 recommends that the temperature of the test solution is kept at 310 ± 1 K. The temperature of the oral cavity varies over a wide range with eating and drinking. Because the adsorption and chelating behaviour of proteins and amino acids depends on the temperature (Ivarsson and Lundström, 1986), the temperature of test environments containing proteins and amino acids should be kept at 310 K.

While the pH of body fluids is kept around neutral by buffering with phosphate, carbonate, proteins and so on (homeostasis), it decreases to about 5.2 with inflammation (Hench and Ethridge, 1975). Inside the oral cavity, pH varies in wide range when eating and drinking, and the recovery of pH from a low value after eating and drinking sometimes takes more than 40 min (Stephan, 1943a, p. 45, 1943b, p. 53). The decrease in pH can accelerate the corrosion of metals by enhancing dissolution of the passive surface film and by cathodic reaction. When the metallic biomaterials are sensitive to chloride ions, probability of local corrosion increases with the increase in corrosion potential due to the decrease in pH. Since the test solutions, such as 0.9% NaCl and Ringer solutions, that ISO16428 recommends have a nearly neutral pH value, it is recommended that the pH value during long-term tests is recorded. On the other hand, the pH of test solution should be decided upon, depending on the purpose of the test because the pH varies in the body as has been described. To buffer test solutions, phosphate, carbonate and Good's buffer are used; however, some buffering reagents also have an effect on the corrosion behaviour of metallic biomaterials (Hiromoto and Mischler, 2006).

4.5.2 Concentration of dissolved oxygen

Since body fluids are neutral, cathodic reaction inside the body is probably the reduction of dissolved oxygen (Hayashi, 1987). The corrosion potential of metals then depends on the concentration of dissolved oxygen. The concentration of dissolved oxygen of transcellular fluids is 1/80–1/4 of that under ambient condition (Hayashi, 1987). Those of arterial blood and venous blood are 5/8 and 1/40 of that under ambient condition, respectively (Hayashi, 1987). The concentration of dissolved oxygen of the test solution is advisably controlled, depending on that inside the body. The test solution

shall be purged with pure oxygen or pure nitrogen to allow or prevent the passivation of the metal surface (ISO16428).

4.5.3 Calcium and phosphate ions, proteins and amino acids

Calcium phosphate deposits on titanium and its alloys spontaneously inside the body, while the deposition of calcium phosphate on stainless steel is relatively small (Sundgren *et al.*, 1986; Espostito *et al.*, 1999; Hiromoto and Hanawa, 2006b). The deposited calcium phosphate layer isolates the metal surface from the environment and may decelerate the corrosion. The deposition of calcium phosphate possibly affects the adsorption behaviour of proteins because calcium phosphate is a good adsorbent of proteins (MacConnell, 1973). In the case of magnesium and its alloys, the presence of calcium and phosphate ions in the test solution noticeably decelerates the dissolution of metal (Yamamoto, 2009).

Proteins and amino acids are adsorbed by metal surfaces subsequent to inorganic ions in the very initial stages of implantation. The variety of proteins adsorbed by metal surfaces changes from low molecular-weight proteins to relatively high molecular-weight proteins in the course of time (Vroman effect) (Wahlgren and Arnebrant, 1991). Because these biological molecules have carboxyl groups, amino groups and/or thiol groups, they are adsorbed by metal surfaces or form complex compounds with metal ions. Whether the corrosion of metallic biomaterials is accelerated or decelerated by proteins and amino acids, depends on their adsorption and complexation abilities. However, the influence of biological molecules on the corrosion is not systematically understood. Because the adsorption and complexation behaviour of proteins depend on the conformation of molecules, which changes by temperature and pH (Ivarsson and Lundström, 1986), it is very important to control the temperature and pH of test solutions at 310±1 K and neutral, respectively.

4.5.4 Cells and extracellular matrix

Macrophages assemble around implanted materials in the initial foreign-body reaction (inflammation) (Yoshikawa, 1993). Macrophages generate active oxygen species which dissolve and/or weaken the passive film of titanium alloys and stainless steels, forming oxyhydroxides of titanium, iron and chromium in the passive films (Hanawa, 2002). It was reported that the dissolution of pure titanium is enhanced by the presence of macrophages (Mu *et al.*, 2000). Corrosion of metallic biomaterials is expected to be enhanced under the inflammatory condition. After the initial inflammation, for a few weeks the cells of the surrounding tissues adhere to the metal

surface, generating extracellular matrix and initiating the formation of bone or soft tissue, depending on the part of body (Yoshikawa, 1993). The main components of the extracellular matrix are fibrous proteins and polysaccharides such as collagen and chondroitin sulphate. When the inflammation reaction has subsided, the pH of body fluid around the implanted materials reverts to neutral. The fibrous molecules form a gel which can retard the diffusion of ions and molecules around the metal surface. Culturing fibroblasts, which mainly generate collagen as extracellular matrix, causes an decrease in cathodic reaction of the reduction of dissolved oxygen on stainless steel and pure titanium, as shown in Fig. 4.11 (Hiromoto *et al*., 2008b). Also, the culturing of fibroblasts causes a decrease in the pitting corrosion potential of stainless steels (Hiromoto and Hanawa, 2006a; Tang, *et al*., 2006).

During long-term implantation, metallic biomaterials may be gradually degraded and release wear debris and metal ions. These wear debris and metal ions may induce macrophages around the materials which lead to post-inflammation. The corrosion of metallic biomaterials is expected to be then accelerated in the post-inflammation.

4.5.5 Circulation of body fluids

Body fluids are circulating inside the body to transport nourishment to the cells. Blood circulates inside the blood vessel by the pumping of the heart. The rate of blood flow varies from 0.1 to 1.0 m s^{-1}, depending on the diameter of blood vessel (Kaibara and Sakanishi, 1999; Sugawara and Maeda, 2003). The circulation of body fluids enhances the diffusion of released metal ions and corrosion products away from the metal surface, so

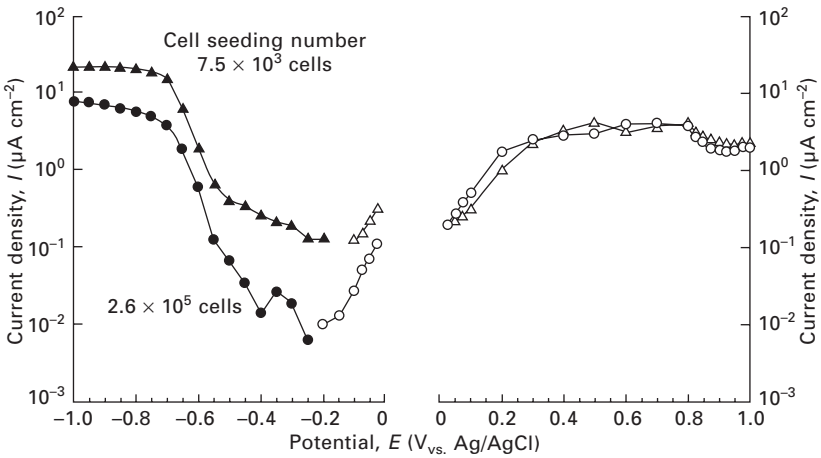

4.11 Potentiostatic polarization curves of pure titanium immersed in a medium culturing different numbers of fibroblast L929.

that it possibly accelerates the corrosion of metallic biomaterials. Especially in the case of bioabsorbable metallic biomaterials such as magnesium and iron alloys, flow rate on the surface can affect corrosion behaviour. On the other hand, agitation of the test solution in addition to the gas purge is not always recommended unless portions of the test solution are seen to stagnate at certain specimen areas (ISO16428).

4.5.6 Design of devices and mechanical loadings

The design of biomedical devices often determines the corrosion morphology of metallic biomaterials. Corrosion of metallic biomaterials is accelerated inside crevices (crevice corrosion) and at sliding parts, with repetitive removal of the passive film (wear/fretting corrosion). It is reported that fretting corrosion takes place on the surface at the screw/hole contact of bone plates and at the neck/head contact of artificial hip joints (Hallab *et al.*, 2004; Virtanen *et al.*, 2008). Repetitive load with walking, or beating of the heart, which is applied on the artificial hip joints and the bone plates or the strads of stents and the leads of pace makers, also causes fracture of the surface film and accelerates corrosion and crack initiation. Wear, fretting, fatigue and fretting fatigue are accelerated by the promotion of corrosion, and vice versa.

4.6 References

ASTM Standard F1089-02, *Standard Test Method for Corrosion of Surgical Instruments*.

ASTM Standard F746-04, *Standard Test Method for Pitting or Crevice Corrosion of Metallic Surgical Implant Materials*.

BS EN 1811:1998+A1:2008, *Reference Test Method for Release of Nickel from Products Intended to Come into Direct and Prolonged Contact with the Skin*.

Espostito M, Lausmaa J, Hirsch J M and Thomsen P (1999), 'Surface analysis of failed oral titanium implants', *J Biomed Mater Res Appl Biomater*, 48, 559–68.

Fontana M G (1987), *Corrosion Engineering*, Third Edition, New York, McGraw-Hill.

Hallab N J, Messina C, Skipor A and Jacobs J J (2004), 'Differences in the fretting corrosion of metal–metal and ceramic–metal modular junctions of total hip replacements', *J Orthopae Res*, 22, 250–259.

Hanawa T (2002), 'Evaluation techniques of metallic biomaterials *in vitro*', *Sci Tech Adv Mater*, 3, 289–295.

Hayashi K (1987), 'Biodegradation of implant materials', *JSME International J*, 30(268), 1517–1525.

Hench L L and Ethridge E C (1975), 'Biomaterials – The interfacial problem', *Adv Biomed Eng*, 5, 35–150.

Hiromoto S, Noda K and Hanawa T (2002), 'Development of Electrolytic Cell with Cell-Culture for Metallic Biomaterials', *Corr Sci*, 44, 955–965.

Hiromoto S and Hanawa T (2006a), 'Electrochemical properties of 316L stainless steel with culturing L929 fibroblasts', *J Roy Soc Interface*, 3, 495–505.

Hiromoto S and Hanawa T (2006b), 'Corrosion of Implant Metals in the Presence of Cells', *Corr Rev*, 24(5-6), 323–351.

Hiromoto S and Mischler S (2006), 'The influence of proteins on the fretting-corrosion behaviour of a Ti–6Al–4V alloy', *Wear*, 261, 1002–1011.

Hiromoto S, Yamamoto A, Maruyama N, Somekawa H and Mukai T (2008a), 'Polarization Behavior of Pure Magnesium under a Controlled Flow in a NaCl Solution', *Mater Trans*, 49(6), 1456–1461.

Hiromoto S, Ziegler J, Yamamoto A (2008b), 'Morphological Change of Fibroblast Cells on Titanium and Platinum Cultured at Anodic and Cathodic Potentials', *Zairyo-to-Kankyo*, 57(9), 400–408.

ISO 16428:2005, *Implants for surgery – Test solutions and environmental conditions for static and dynamic corrosion tests on implantable materials and medical devices*.

ISO 16429:2004, *Implants for Surgery – Measurements of Open-circuit Potential to Assess Corrosion Behaviour of Metallic Implantable Materials and Medical Devices over Extended Time Periods*.

ISO 10271:2001, *Dental Metallic Materials – Corrosion Test Methods*.

Ivarsson B and Lundström I (1986),'Physical characterization of protein adsorption on metal and metal oxide surfaces', *Critical Review in Biocompatibility*, 2(1), 1–96.

JIS T 0302:2000, *Testing Method for Corrosion Resistance of Metallic Biomaterials by Anodic Polarization Measurement*.

JIS T 0304:2002, *Testing Method for Metal Release from Metallic Biomaterials*.

JIS T 0306:2002, *Analysis of State for Passive Film Formed on Metallic Biomaterials by X-ray Photoelectron Spectroscopy*.

JIS T 6002:2005, *Dental metallic materials – Corrosion test methods*.

Kaibara M and Sakanishi A (1999), *Biorheology*, Tokyo, Sangyo-tosho, p. 78 (in Japanese).

Kita H and Uosaki K (1983), *Basic of Electrochemistry*, Tokyo, Gihodoshuppan.

Lévesque J, Hermawan H, Dube D and Mantovani D (2008), 'Design of a pseudo-physiological test bench specific to the development of biodegradable metallic biomaterials' *Acta Biomater*, 4, 284–295.

Lin H-Y and Bumgardner J D (2004), '*In vitro* biocorrosion of Co–Cr–Mo implant alloy by macrophage cells', *J Orthopaedic Res*, 22, 1231–1236.

MacConnell D (1973), *Apatite: Its Crystal Chemistry, Mineralogy, Utilization, and Geologic and Biologic Occurrences*, New York, Springer-Verlag, Ch. 5.

Mu Y, Kobayashi T, Sumita M, Yamamoto A and Hanawa T (2000), 'Metal ion release from titanium with active oxygen species generated by rat macrophages *in vitro*', *J Biomed Mater Res*, 49, 238–243.

Pourbaix M (1966), *Atlas of Electrochemical Equilibria in Aqueous Solutions*, London, Pergamon Press.

Revie R W and Uhlig H H (2008) *Corrosion and Corrosion Control, An Introduction to Corrosion Science and Engineering, Fourth Edition*, NJ, Wiley-Interscience.

Rodrigues D C, Urban R M, Jacobs J J and Bilbert J L (2008), '*In vivo* severe corrosion and hydrogen embrittlement of retrieved modular body titanium alloy hip-implants', *J Biomed Mater Res*, 88B, 206–219.

Scharnweber D (1998), 'Degradation (*in vitro–in vivo* corrosion)', in Helsen J A and Breme H J, *Metals as Biomaterials*, Chichester, John Wiley & Sons, 101–152.

Stephan R M and Miller B F (1943a), 'A Quantitative Method for Evaluating Physical and Chemical Agents which Modify Production of Acids in Bacterial Plaques on Human Teeth', *J Dent Res*, 22, 45–51.

Stephan R M and Miller B F (1943b), 'The Effect of Synthetic Detergents on pH Changes in Dental Plaques', *J Dent Res*, 22, 53–61.

Sugawara M and Maeda N (2003), *Hemorheology and Blood Flow*, Tokyo, Corona Publishing, p. 75 (in Japanese).

Sugimoto K (2009) *Kinzoku-Fushoku-Kogaku* (Corrosion Engineering of Metals), Tokyo, Uchida Rokakuho Publishing (in Japanese).

Sundgren J L, Bodo P and Lundstrom I (1986), 'Auger electron spectroscopic studies of the interface between human tissue and implants of titanium and stainless steel', *J Colloid Interface Sci*, 110, 9–20.

Tang Y-C, Katsuma S, Fujimoto S and Hiromoto S (2006), 'Electrochemical Study on Type 304 and 316L Stainless Steels in Simulated Body Fluids and Cell Cultures', *Acta Biomater*, 2(6), 709–715.

Virtanen S, Milosev I, Gomez-Barrena E, Trebse R, Salo J and Konttinen Y T (2008), 'Special modes of corrosion under physiological and simulated physiological conditions', *Acta Biomaterialia*, 4, 468–476.

Wahlgren M and Arnebrant T (1991), 'Protein adsorption to solid surfaces', *Tibtech*, 9, 201–208.

Williams D F and Williams R L (2004), 'Degradative effects of the biological environment on metals and ceramics', in Ratner B D, Hoffman A S, Schoen F J and Lemons J E, *Biomaterials Science: An Introduction to Materials in Medicine*, Second Edition, San Diego, Elsevier 430–439.

Yamamoto A and Hiromoto S (2009), 'Effect of inorganic salts, amino acids and proteins on the degradation of pure magnesium *in vitro*', *Mater Sci Eng*, C29, 1559–1568.

Yoshikawa S (1993), 'Foreign-body reaction', in Ikada Y, *Introduction to Biomaterials*, Tokyo, Japan Scientific Societies Press, 95–123 (in Japanese).

5
Fatigue failure of metallic biomaterials

M. NIINOMI, Tohoku University, Japan

Abstract: Fatigue failure is a significant problem in the usage of metallic biomaterials. Understanding the fatigue characteristics of metallic biomaterials is important for the long term usage of the implants made of metallic biomaterials. Fatigue strength including fatigue strength level, fatigue strength *in vitro* and *in vivo*, notch fatigue strength, fatigue strength and surface modification, fatigue strength and surface hardening treatment, fatigue strength and bioactive surface modification, improvement of fatigue strength including fatigue strength and heat treatment, fatigue strength and aging, fatigue strength and thermomechanical treatment, fatigue strength and unstable phase, fatigue strength and thermochemical treatment, fatigue crack propagation characteristics including short and long fatigue crack propagation in air and *in vitro*, improvement of long fatigue crack propagation resistance, fretting fatigue strength in air and *in vitro* of metallic biomaterials, and fatigue strength of wire made of new biomedical titanium alloy are described in this chapter.

Key words: fatigue strength, fatigue crack propagation, fretting fatigue, surface modification, thermomechanical treatment.

5.1 Introduction

Implants that function as bones – for example, implants that are used to replace failed hard tissue, such as artificial hip joints, artificial joints, bone plates, and dental implants – are usually used under severe cyclic loading conditions. Therefore, metallic materials that typically exhibit high strength, ductility and toughness are the main candidates for the structural biomaterials of these implants. Further, the above-mentioned implants must exhibit high biocompatibility, high performance, and reliability for long-term use.

The reliability of implants after implantation is determined by their fracture and wear after the critical period of infection. Nowadays, implants are required to exhibit much greater mechanical and biological performance. Therefore, the mechanical properties of structural biomaterials in a living body environment such as fatigue, toughness, and wear resistance need to be evaluated and improved considerably in order for these materials to be applied to implants for a long-term use.

With regard to the fracture of structural biomaterials, fatigue fracture occurs occasionally; it is considered to be a crucial problem among the various types of fractures.

Fatigue with fretting, i.e. fretting fatigue, is a type of fatigue that can occur between two bodies, such as between a bone plate and screw. Fatigue

characteristics are closely related to microstructures. The microstructures in metallic structural biomaterials change according to the processing and heat treatment employed.

Currently, the main metallic biomaterials used in practical applications are austenitic stainless steel, cobalt (Co)–chromium (Cr) alloys, and titanium (Ti) and its alloys. Among them, Ti and its alloys are receiving considerable attention for biomedical applications because of their high biocompatibility, specific strength, and corrosion resistance (Niinomi, 2001). In particular, low-modulus β-type titanium alloys composed of nontoxic and allergy-free elements have been recently developed and examined (Niinomi, 2003a). With regard to stainless steels and Co–Cr alloys, Ni-free high nitrogen austenitic stainless steel (Kuroda *et al*., 2002), and nickel (Ni)- and carbon (C)-free Co–Cr alloy (Lee *et al*., 2006) have also been developed recently and examined.

Therefore, in this chapter the fatigue characteristics of the main metallic structural biomaterials such as stainless steels, Co–Cr alloys, and Ti and its alloys, including those that are currently in use as well as those in development stage, are described.

5.2 Fatigue strength

5.2.1 Fatigue strength level of various metallic biomaterials

The fatigue life of metallic biomaterials such as Ti alloys, Co alloys and stainless steels for biomedical applications are shown in Fig. 5.1 (Niinomi, 1998): this Figure shows the fatigue limits of stainless steels, Co alloy, and Ti and its alloys as representative metallic biomaterials in air. The fatigue limits are scattered depending on factors such the fabrication process, surface condition, microstructure, and fatigue condition. The fatigue limit of bovine bone (Kim *et al*., 2005) is also shown in Fig. 5.1. The limit decreases in the following order: Co alloy ≧ Ti-6 aluminum (Al)-4 vanadium (V) ≧ 316L stainless steel. Among the titanium alloys, the fatigue limits of (α + β)-type *T*i alloys such as Ti–6Al–4V ELI and Ti–6Al–7 niobium (Nb) are greater than those of β-type titanium alloys such as Ti–13Nb–13 zirconium (Zr), Ti–15 molybdenum (Mo)–5Zr–3Al, and Ti–35.3Nb–5.1 tantalum (Ta)–5.1Zr. The fatigue limits of β-type Ti alloys increase by aging treatment after solution treatment; the fatigue limit of β-type titanium alloy such as Ti–29Nb–13Tas–4.6Zr, which is referred to as TNTZ (Kuroda *et al*., 1998), has been reported to increase and become comparable to that of Ti–6Al–4V ELI. However, the fatigue limit of each metallic biomaterial shows a fairly large scatter due to the above-mentioned factors. The fatigue limit of each metallic biomaterial is higher than that of bovine bone.

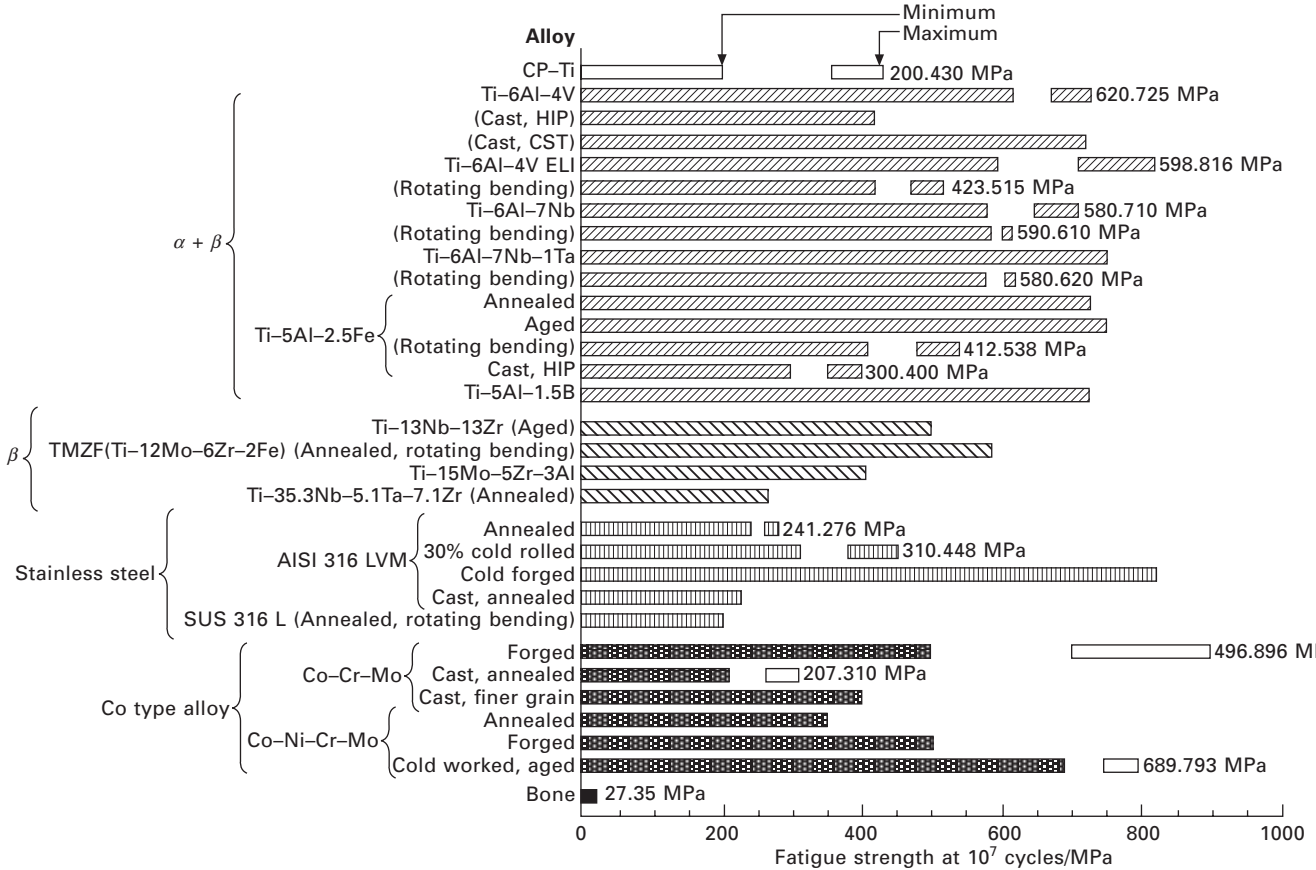

5.1 Fatigue strength at 10^7 cycles of biomedical stainless steel, Co alloys, titanium and its alloys, and bone. Data without designation of rotating bending are those obtained from uniaxial fatigue tests.

Figures 5.2 and 5.3 (Breme and Helsen, 1998; Akahori *et al.*, 2003) show the relationship between the rotating bending fatigue limit and the elongation up to fracture, and that between the fatigue strength and Young's modulus for various metallic biomaterials, respectively. The rotating bending fatigue strength increases with the elongation up to fracture. The rotating bending fatigue strength is relatively higher and the Young's modulus is relatively low in ($\alpha + \beta$)-type Ti alloys. Therefore, the BF value of Ti alloys, which is obtained by dividing the fatigue strength with Young's modulus, is high ($\simeq$ 5.2).

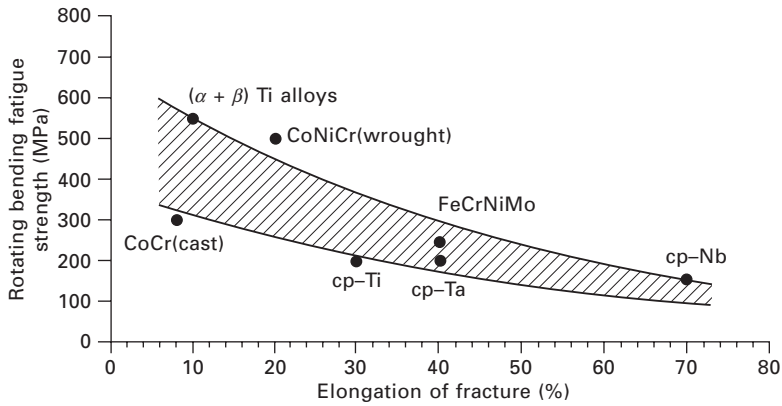

5.2 Elongation at fracture as a function of the fatigue strength of metallic biomaterials.

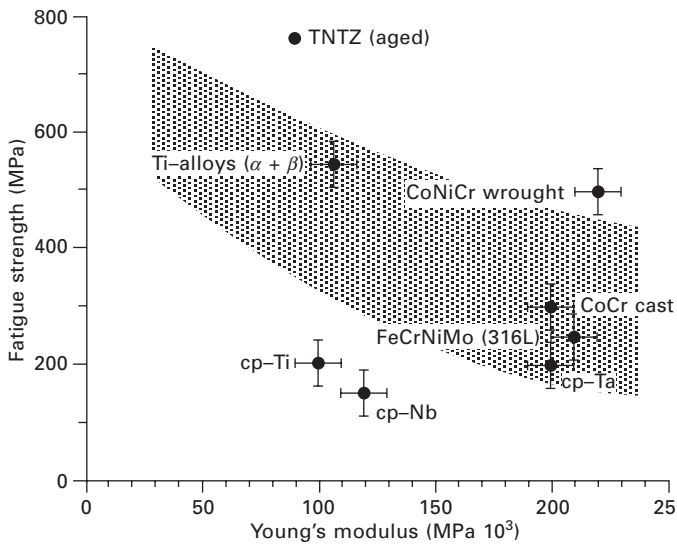

5.3 Fatigue strength and Young's modulus of metallic biomaterials.

The BF values of materials such as 316L stainless steel, Co–Cr alloy, Co–Ni–Cr alloy, pure Ti, and pure Nb, lie between 1.2 and 2.3 (Breme and Helsen, 1998). This indicates that the mechanical biocompatibility of Ti alloys is excellent in comparison with that of other metallic biomaterials. The BF value of aged TNTZ is very high (≃ 9.6) (Akahori *et al.*, 2003).

Among the Ti alloys that have received considerable attention as metallic biomaterials, the fatigue limit of pure Ti, which is an α-type, is the lowest. The fatigue limits of Ti–6Al–4V and Ti–6Al–7Nb, which are ($\alpha + \beta$)-type alloys, are among the highest. The fatigue limit of solutionized β-type alloy is low; however, it increases drastically to approximate that of an ($\alpha + \beta$)-type alloy by aging after solutionizing due to the precipitation of the α phase. The fatigue strength of ($\alpha + \beta$)- and β-type Ti alloys varies considerably with the microstructure. In ($\alpha + \beta$)-type Ti alloys, the fatigue strengths of an equiaxed α structure are, in general, higher than that of an acicular or Widmanstätten α structure (Niinomi, *et al.*, 1992).

5.2.2 Fatigue strength *in vitro* and *in vivo*

In order to estimate the fatigue strength of metallic biomaterials in a living body environment, it is essential to evaluate it in a simulated body environment. Figure 5.4 (Niinomi *et al.*, 1996) compares the rotating bending

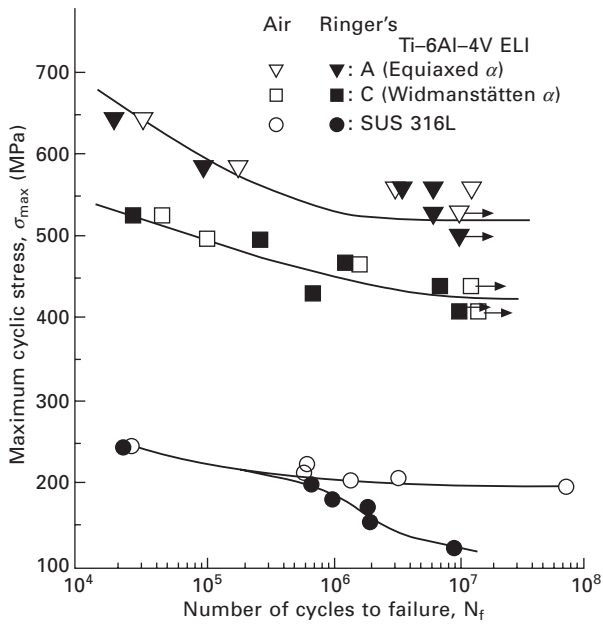

5.4 S–N curves of Ti–6Al–4V ELI and SUS 316L in air and in Ringer's solution.

fatigue strength of Ti–6Al–4V ELI and SUS 316L stainless steel in Ringer's solution with those in air. The fatigue strength of Ti–6Al–4V ELI in Ringer's solution is similar to that in air, while that of SUS 316L stainless steel in Ringer's solution is lower than that in air. Therefore, corrosion fatigue occurs in Ringer's solution for SUS 316 L stainless steel. The fatigue strength of Co–Cr–Mo is also reported to decrease in Ringer's solution, as seen in Fig. 5.5 (Kumar *et al.*, 1985).

As shown in Fig. 5.6 (Niinomi *et al.*, 1996), the fatigue strength of Ti–5Al–2.5 iron (Fe) in Ringer's solution decreases when the oxygen (O)

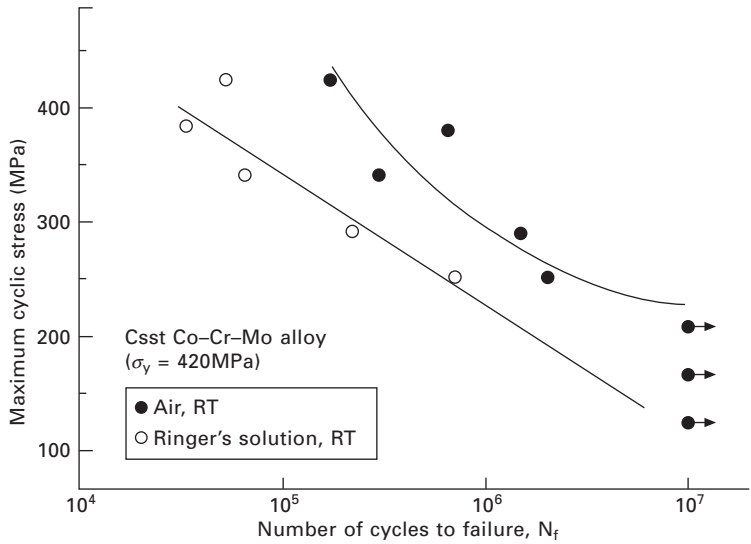

5.5 Comparison of fatigue lives for cast Co–Cr–Mo alloy (Type 1) in air and in simulated body solution.

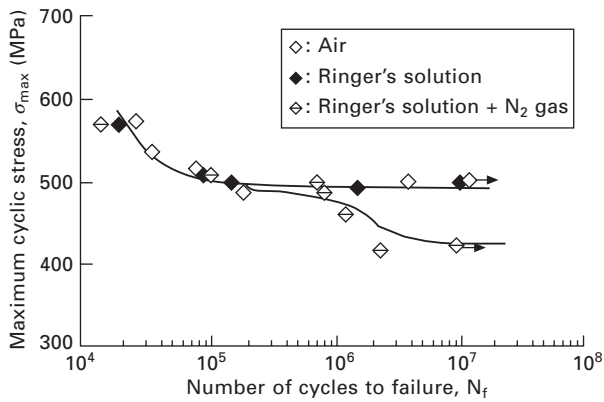

5.6 S–N curves of Ti–5Al–2.5Fe in air, in Ringer's solution, and in Ringer's solution with N_2 gas.

content is reduced by degassing with nitrogen (N) whereas it does not decrease without degassing. However, as shown in Fig. 5.7 (Niinomi, 2002a), the fatigue strength of Ti–6Al–4V ELI obtained by uni-axial fatigue tests does not degrade in a living body environment, e.g. in the body of a living rabbit, which is in contrast to the fatigue strength of Ti–6Al–4V ELI in air. Therefore, there is a higher possibility of corrosion fatigue occurring under the bending fatigue condition in Ti alloys. In other words, the passive film formed on the surface of Ti alloys is considered to fracture more easily under the bending condition, and corrosion fatigue may occur because it takes a relatively longer time for a fractured passive film to recover due to the low O content.

Figure 5.8 (Maruyama *et al.*, 1999) compares the result of the fatigue

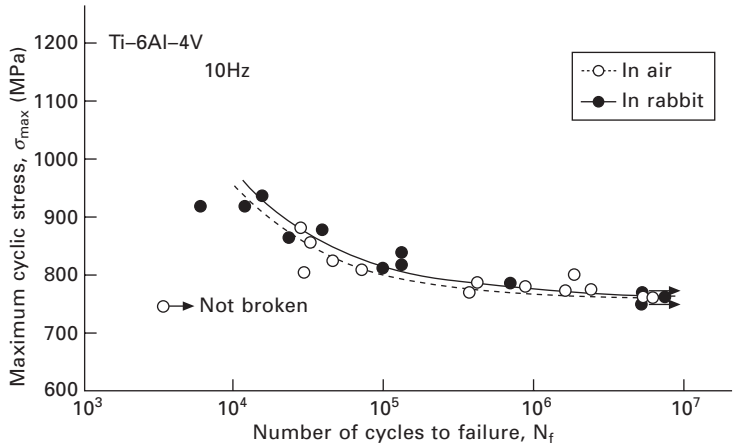

5.7 S–N curves of Ti–6Al–4V obtained from uniaxial fatigue tests in air and rabbit.

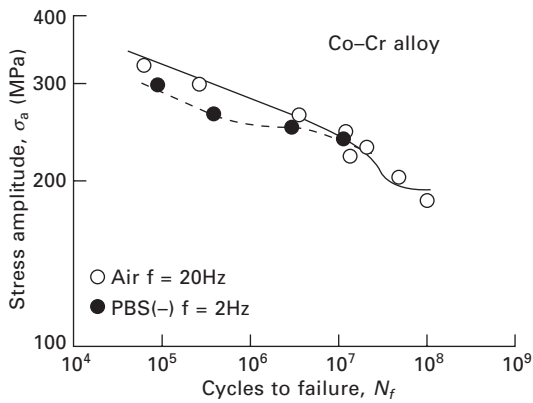

5.8 S–N curves of Co–Cr alloy in air and in PBS(–).

test of Co–Cr alloy in a physiological body simulated fluid (PBS) with that in air. The fatigue strength of Co–Cr alloy in PBS is lower than that in air in the low-cycle fatigue life region, while it is similar to that in air in the high-cycle fatigue life region.

5.2.3 Notch fatigue strength

Since implants generally have complex shapes that have stress concentration sites such as sharp corners, it is imperative that the notch fatigue strengths of medical Ti alloys be understood. Figures 5.9 and 5.10 (Akahori *et al.*, 2005a) show the S–N curves obtained from plain-fatigue and notch-fatigue tests on TNTZ subjected to AS-CRST, $CRST_{598K}$, RST_{673K}, and AS-STCR, $STCR_{598K}$, $STCR_{673K}$, and $STCR_{723K}$ indicating cold rolling by a reduction ratio of 87.6% followed by solution treatment at 1063 K for 3.6 ks, and aged at 598 K, 673 K, and 723 K, respectively for 259.2 ks after solution treatment at 1063 K for 3.6 ks and solution treatment after cold rolling by a reduction ratio of 87.6% aged at 598 K, 673 K, and 723 K, respectively after cold rolling by a reduction ratio of 87.6, respectively. The stress concentration factors (Kt = 1 + (t/ρ) 1/2, where t and ρ are the depth of the notch and the notch root radius) for plain-fatigue and notch-fatigue tests are 1 and 6, respectively. The notch fatigue strength is much smaller in comparison with the plain fatigue strength. Both the plain and notch fatigue limits of $STCR_{723}$ are the highest, where TNTZ was subjected to solutionizing (ST) and then cold

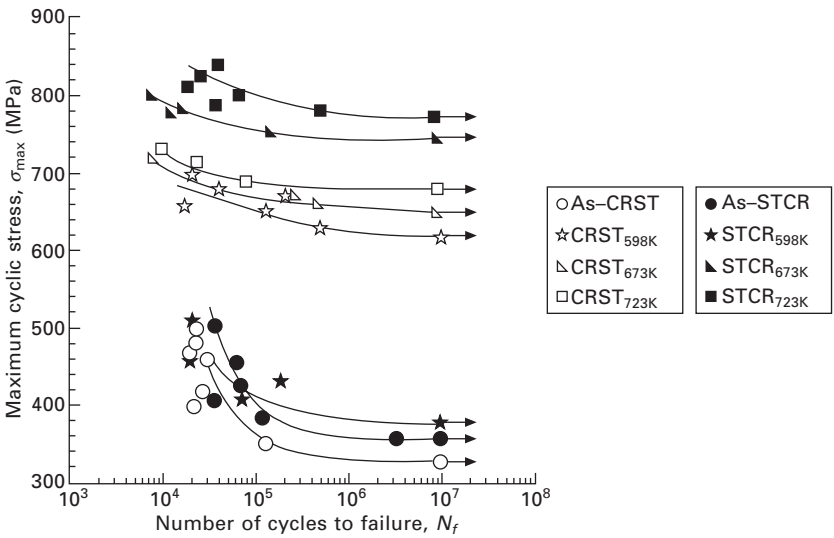

5.9 S–N curves of TNTZ subjected to various thermo-mechanical treatments obtained from plain fatigue tests (K_t = 1) in air.

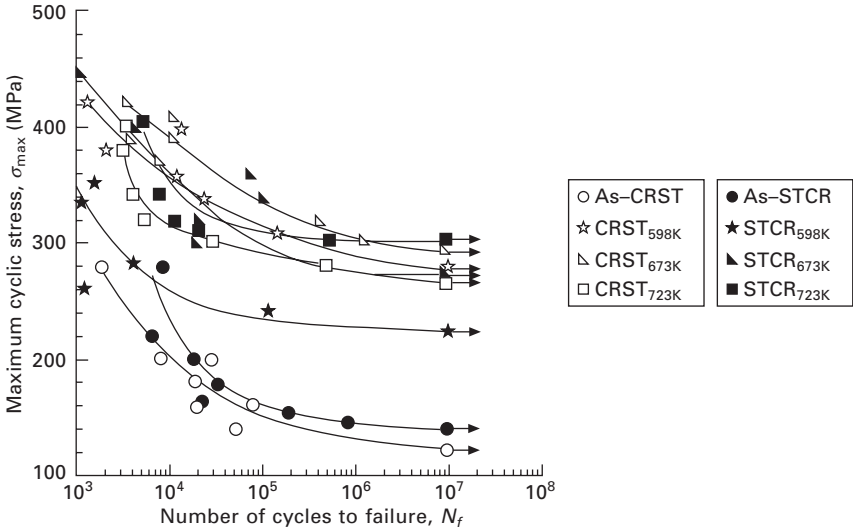

5.10 S–N curves of TNTZ subjected to various thermo-mechanical treatments obtained from notch-fatigue tests (K_t = 6) in air.

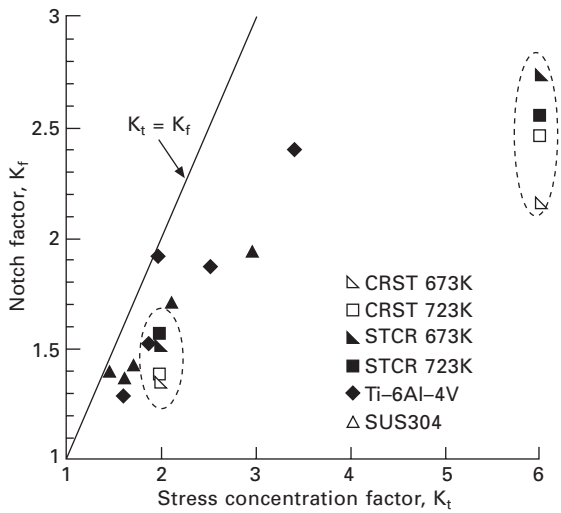

5.11 Relationships between stress concentration factor, K_t, and notch factor, K_f, of TNTZ, Ti–6Al–4V and SUS304 subjected to various thermo-mechanical treatments.

rolling followed by aging at 723 K. In this case, relatively coarse α phases are homogeneously precipitated, and the elongation is relatively higher at 10% (Akahori *et al.*, 2005a). Figure 5.11 (Akahori *et al.*, 2005a) shows the relationships between Kt and notch factor (Kf = σpf/σnf where σpf and σnf

are the fatigue limit and the notch fatigue limit) for TNTZ, Ti–6Al–4V, and SUS 316L stainless steel subjected to various thermomechanical treatments. The Kf of TNTZ subjected to each thermomechanical treatment is less than those of Ti–6Al–4V and SUS 316L stainless steel for the same Kt values. Figure 5.12 (Akahori *et al.*, 2005a) shows the relationship between the Kt and the notch sensitivity factor ($\eta = (Kf - 1)/(Kt - 1)$) of TNTZ, Ti–6Al–4V, pure Ti (CP–Ti), carbon steel (S45C), and SUS 316L stainless steel. The η of TNTZ subjected to each thermomechanical treatment is found to be less than those of the other materials.

5.2.4 Fatigue strength and surface modification

In order to improve the wear resistance of Ti alloys, surface hardening treatments such as nitriding (Nakai *et al.*, 2007) and oxidation (Niinomi *et al.*, 2002b) are applied. On the other hand, bioactive ceramic surface modifications (Kasuga *et al.*, 2003; Sato *et al.*, 2007; Hanawa *et al.*, 2001) are applied in order to improve bone conductivity because metallic biomaterials, even Ti and its alloys, are not bioactive. In these cases, understanding the effects of surface modifications on the fatigue life of metallic biomaterials is important.

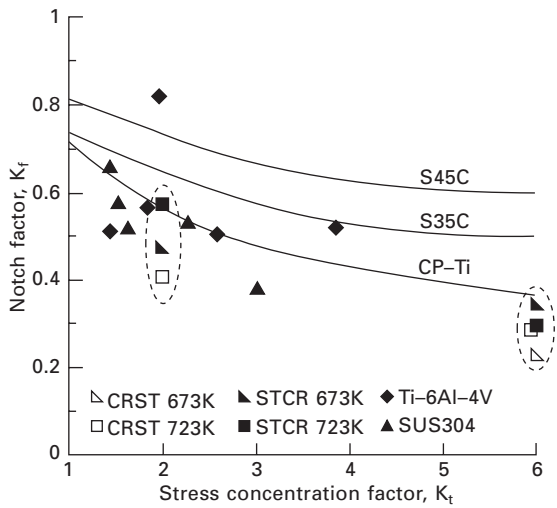

5.12 Relationships between stress concentration factor, K_t, and notch sensitivity factor, η, of TNTZ, Ti–6Al–4V, CP–Ti, S35C, S45C and SUS 304 subjected to various thermo-mechanical treatments.

Fatigue strength and surface hardening treatment

The S–N curves of titanium alloys such as Ti–6Al–4V ELI and TNTZ subjected to nitriding are shown in Fig. 5.13 (Akahori *et al.*, 2008). In this figure, $TNTZ_{ST}$, $TNTZ_{1123NP}$, $TNTZ_{1223NP}$, $Ti64_{ST}$, $Ti64_{1123NP}$, and $Ti64_{1223NP}$ indicate TNTZ subjected to solution treatment and gas nitriding at 1123 K and 1223 K, and Ti–6Al–4V ELI subjected to solution treatment and gas nitriding at 1123 K and 1223 K, respectively. The fatigue strengths of TNTZ and Ti–6Al–4V ELI are lowered by nitriding. The hard layers, TiN or Ti_2N, formed on the surface of both alloys, are brittle, leading to easy fatigue crack initiation. The intensity of the TiN peak has been found to increase with the nitriding temperature by XRD analysis. The Vickers hardness near the specimen surface of nitrided Ti–6Al–4V ELI has been reported to be greater than that of TNTZ.

The run out, which is the maximum cyclic stress that can be applied without causing fracture after 10^7 cycles, of $TNTZ_{1123NP}$ was around 300 MPa and it is nearly equal to that of $Ti64_{1123NP}$, although the tensile strength of $TNTZ_{1123NP}$ was around 200 MPa lower than that of $Ti64_{1123NP}$. This value was slightly lower than that of $TNTZ_{ST}$. The fatigue crack seems to be more easily initiated when the brittle nitrided layer (TiN or Ti_2N), is thicker as is slightly the case with nitrided Ti–6Al–4V ELI compared to nitrided TNTZ. Particularly, the elastic modulus of TiN is two or more times higher than that of the matrix (Yan *et al.*, 2001). Thus, the TiN layer of nitrided TNTZ

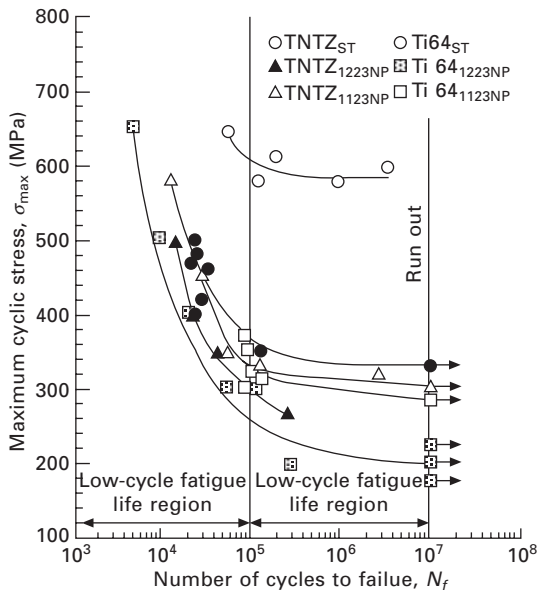

5.13 S–N curves of TNTZ and Ti 64 subjected to solution treatment and nitriding process.

and Ti–6Al–4V ELI is severely deformed under cyclic loading, wherein localized fatigue deformation could take place. This seems to result in brittle cracking and shortening of crack initiation life, in particular, with nitrided Ti–6Al–4V ELI which has a relatively high Vickers hardness and thicker nitride- and nitrogen-rich layers. In addition, the notch factor (run out of smooth specimen/run out of notch specimen), which indicates the notch sensitivity, of aged TNTZ decreases with an increase in the volume fraction of the β phase, and it is lower than that of annealed Ti–6Al4V ELI with an equiaxed β structure (Akahori *et al.*, 2008). From these points of view, it follows that by the nitriding process, the plain fatigue strength of TNTZ is not as degraded as compared to that of Ti–6Al4V ELI.

Fatigue strength and bioactive surface modification

Among the metallic biomaterials, the biocompatibility of Ti alloys is the highest, but these alloys are not bioactive as stated previously. Therefore, they are subjected to surface modification by bioactive ceramics in order to further improve their biocompatibility.

There exist many processes for bioactive ceramic surface modification. They are roughly grouped into dry process, e.g. spray method (Niinomi, 2003a), and wet processes, e.g. alkali method (Kim *et al.*, 1997) and dip-coating method (Niinomi, 2002a). The fatigue characteristics of metallic biomaterials subjected to these different surface modification processes are also significant.

For example, Fig. 5.14 (Li *et al.*, 2004) shows the results of fatigue tests for TNTZ coated with calcium phosphate invert-glass ceramic by the dip-coating method. In this method, a mixture of calcium phosphate invert-glass ceramic and distilled water is coated on the specimen by dipping the specimen into the mixture. The specimen is then fired in order to precipitate the calcium phosphate system ceramics. The firing temperature is above the β transus temperature of TNTZ; thus the fatigue strength of TNTZ cannot be maintained when the dip-coating method is employed. Therefore, it is necessary to finally age the specimen in order to improve the fatigue strength. As shown in Fig. 5.14, the fatigue strength of TNTZ coated with calcium phosphate invert-glass-ceramic increases remarkably after aging. It is possible to inhibit cracking or exfoliation of the calcium phosphate invert glass-ceramic layer or cracking between the layer and the substrate by controlling the thickness of the layer (Li, 2004; Niinomi, 2003). Figure 5.15 (Li, 2004) shows an SEM fractograph of calcium phosphate invert glass-ceramic-coated TNTZ after the fatigue test. Cracking or exfoliation of the layer cannot be observed on the SEM fractograph. It should be noted that the crack initiation sites in this case are the pits formed on the surface of the substrate by sand blasting, which is a pretreatment applied to the surface of the substrate.

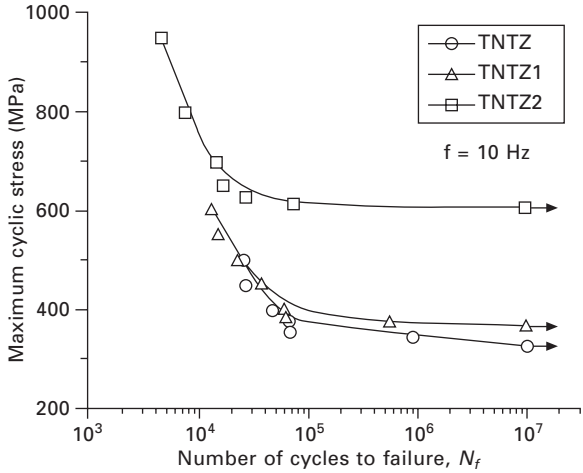

5.14 S–N curves of as solutionized TNTZ (TNTZ), glass-ceramic coated TNTZ (TNTZ1), and glass-ceramic coated TNTZ followed by aging (TNTZ2).

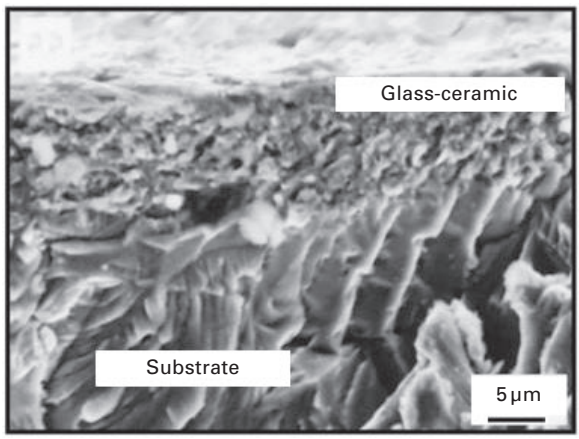

5.15 General view of fatigue fracture surface of glass-ceramic coated TNTZ (TNTZ1) (N = 557 862).

Figure 5.16 (Breme, 1998) shows the fatigue strength of SUS 316L stainless steel coated with alumina (Al_2O_3), (which is not a bioactive ceramic but is highly biocompatible) by the plasma spray method and evaluated in physiological saline. For comparison, the Figure also shows the fatigue strength of SUS 316L stainless steel without alumina coating. The fatigue strength of SUS 316L stainless steel with the alumina coating is higher than that without because corrosion of the steel is inhibited by the dense alumina-layer.

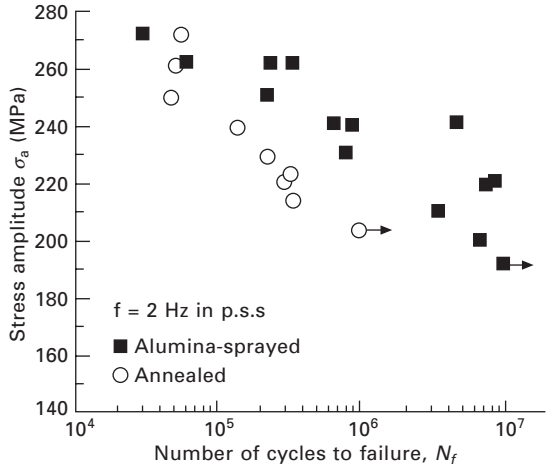

5.16 S–N curves for annealed or alumina-sprayed SUS 316L stainless steels in physiological saline solution.

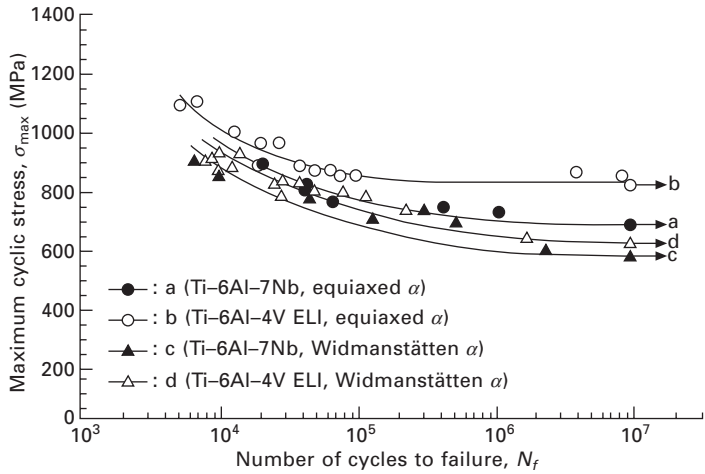

5.17 S–N-curves of Ti–6Al–7Nb and Ti–6Al–4V ELI with equiaxed α and Widmanstätten α structures.

5.2.5 Improvement of fatigue strength

Fatigue strength and heat treatment

The S–N curves of a fairly new ($\alpha + \beta$)-type biomedical Ti alloy, Ti–6Al–7Nb, solutionized beyond and below the β transus temperature, respectively followed by air cooling (AC) and aging, which yield equiaxed α and Widmanstätten α structures, respectively are shown in Fig. 5.17 in comparison with those of conventional ($\alpha + \beta$)-type biomedical Ti alloy, Ti–6Al–4V ELI, obtained by

heat treatments similar to those of Ti–6Al–7Nb (Akahori *et al*., 2000). The fatigue strength of Ti–6Al–7Nb is nearly equal to that of Ti–6Al–4V ELI when the microstructure is Widmanstätten α. However, the fatigue strength of Ti–6Al–7Nb is inferior to that of Ti–6Al–4V ELI when the microstructure is equiaxed α. This inferiority of the fatigue strength is supposed to be one of the reasons why Ti–6Al–7Nb is not widely used. The fatigue strength of Ti–6Al–7Nb with the equiaxed α structure can be controlled by changing the volume fraction of primary α. The fatigue strength of Ti–6Al–7Nb increases with the volume fraction of primary α, which leads to an increased fatigue life of Ti–6Al–7Nb. The fatigue strength of Ti–6Al–7Nb is still lower than that of Ti–6Al–4V ELI when the volume fraction of primary α is relatively greater. When a fairly high cooling rate is adopted, for example, water quenching after solutionizing in $(\alpha + \beta)$ region followed by aging, the fatigue strength of Ti–6Al–7Nb is nearly equal to that of Ti–6Al–4V ELI, as shown in Fig. 5.18 (Akahori *et al*., 2000). Further advanced microstructural control processing is expected to develop the fatigue strength of Ti–6Al–7Nb such that it exceeds the fatigue strength of Ti–6Al–4V ELI.

Fatigue strength and aging

In general, the fatigue strength of Ti alloys is improved by aging after solution treatment (ST). The fatigue strength for β-type Ti alloys is drastically improved by aging treatment after ST. Figure 5.19 (Akahori *et al*., 2006)

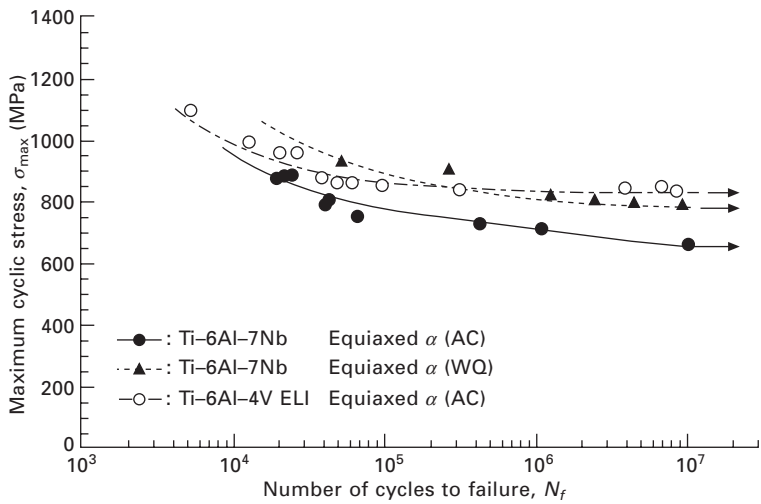

5.18 S–N curves of Ti–6Al–7Nb and Ti–6Al–4V ELI with each heat treatment. AC and WQ correspond to air cooling and water quenching, respectively after solution treatment.

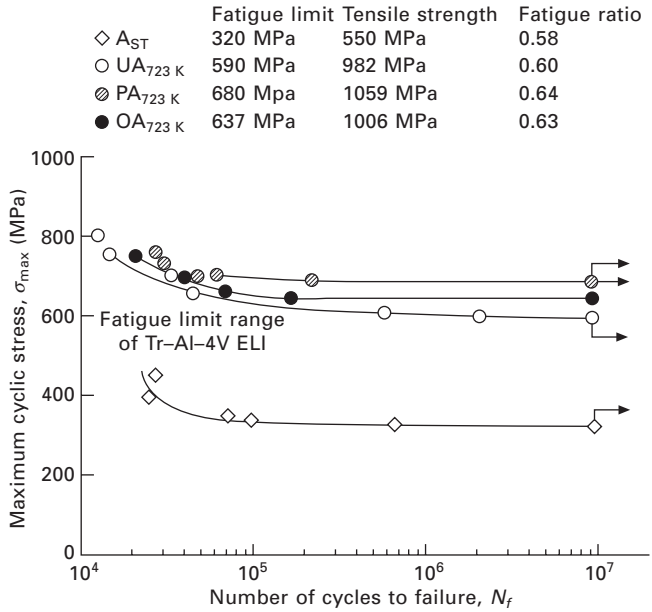

5.19 S–N curves of A_{ST}, $UA_{723\ K}$, $PA_{723\ K}$ and $OA_{723\ K}$ obtained from fatigue tests in air.

shows the S-N curves obtained from fatigue tests in air on TNTZ samples subjected to ST at 1023 K (A_{ST}) and aging treatments at 723 K for various durations after ST-under-aging ($UA_{723\ K}$), peak-aging ($PA_{723\ K}$), and over-aging ($OA_{723\ K}$); these curves were obtained from fatigue tests in air. The fatigue limit of TNTZ increases drastically by aging treatments, and the fatigue limit of peak-aged TNTZ is the highest. The fatigue limits of each aged TNTZ sample is equivalent to that of Ti–6Al–4V ELI.

Fatigue strength and thermomechanical treatment

It is possible to improve the fatigue strength of β-type Ti alloys by thermomechanical treatment involving cold working and heat treatment. Cold working can be performed very easily in β-type Ti alloys. Figure 5.20 (Akahori *et al.*, 2003) shows the fatigue strength of low-modulus TNTZ obtained after solutionizing and aging ($TNTZ_{ST}$ aged at 598 K and $TNTZ_{ST}$ aged at 673 K), and severe cold rolling and aging ($TNTZ_{CR}$ aged at 598 K and $TNTZ_{CR}$ aged at 673 K). The fatigue limits of Ti–6Al–4V ELI and Ti–6Al–7Nb are also shown in this figure. The fatigue limit of TNTZ is found to reach the upper limit of the fatigue limit range of Ti–6Al–4V ELI by aging after severe cold rolling.

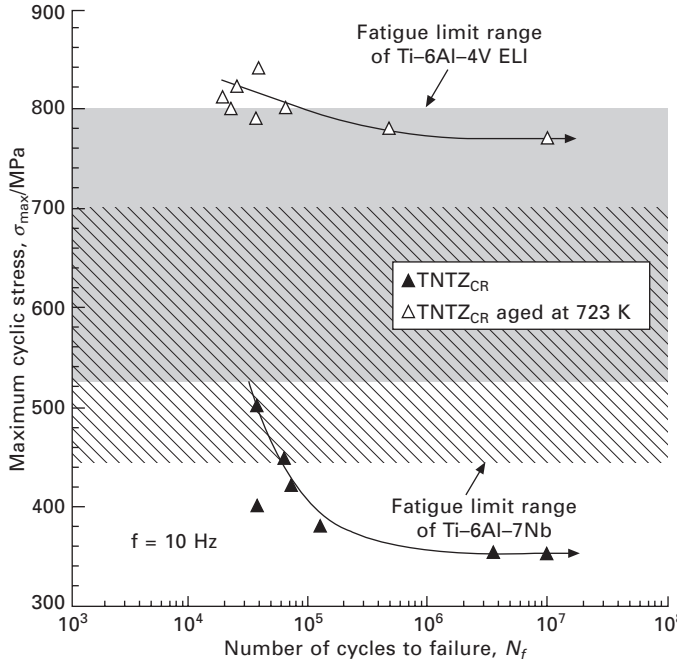

5.20 S–N curves of $TNTZ_{CR}$ and $TNTZ_{CR}$ conducted with aging at 723 K for 259.2 ks with fatigue limit ranges of Ti–6Al–4V ELI and Ti–6Al–7Nb in air. ($TNTZ_{CR}$ = severe cold rolled TNTZ.)

Fatigue strength and unstable phase

On the application of stress, martensitic transformation occurs in steels, which contain residual austenite in their microstructures. This phenomenon is called stress- or strain-induced martensitic transformation; it enhances the ductility or fracture toughness of the steels (Kobayashi and Yamamoto, 1998). Deformation-induced martensitic transformation also occurs in titanium alloys that contain the unstable β phase in their microstructures, and this transformation enhances the fatigue strength (Imam and Gilmore, 1983), fatigue crack propagation resistance (Niinomi *et al.*, 1993), fracture toughness (Niinomi *et al.*, 1990) and ductility (Gunawarman *et al.*, 2002) of the Ti alloys. In general, the unstable β phase is retained at room temperature by rapid cooling such as water quenching from a high temperature near the β transus temperature.

Figure 5.21 (Imam and Gilmore, 1983) shows the S–N curves of Ti–6Al–4V subjected to annealing treatment and ST at 1173 K followed by water quenching. The fatigue strength of Ti–6Al–4V when subjected to ST followed by water quenching is higher than that when it is subjected to subsequent annealing treatment because of the deformation-induced martensitic transformation of the unstable β phase, which is introduced by the water quenching after the ST.

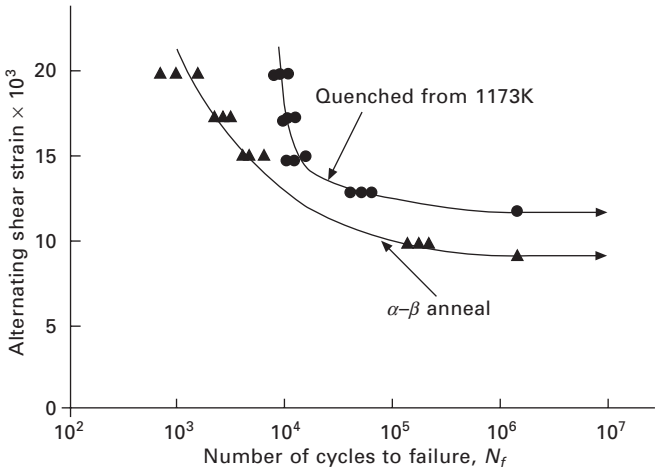

5.21 Number of cycles to failure as a function of the applied alternating shear strain for specimens α–β annealed, and heat treated at 1173K followed by a water quench.

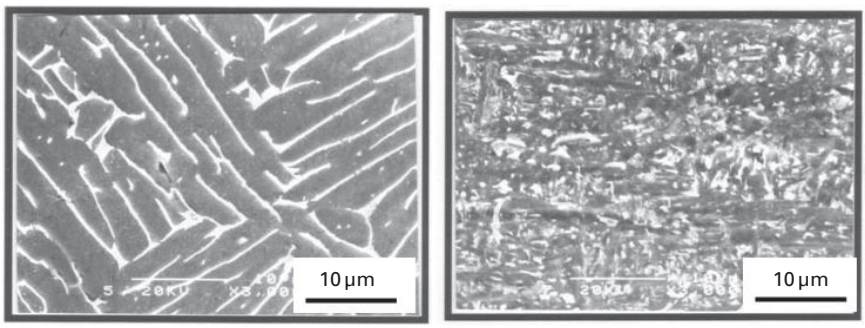

(a) as-HIP'ed (b) TCP

5.22 Scanning electron micrographs of (a) as-HIP'ed cast Ti–6Al–7Nb and (b) HIP'ed cast Ti–6Al–7Nb subjected to TCP.

Fatigue strength and thermochemical treatment

It is well known that the microstructures of (α + β)-type Ti alloys are significantly refined through the hydrogenation and dehydrogenation process, which is also referred to as thermochemical processing (TCP), as shown representatively in Fig. 5.22 (Akahori *et al.*, 2002) for the case of cast Ti–6Al–7Nb. The size of the α phase is significantly small in cast Ti–6Al–7Nb that has been subjected to TCP. In this case, the diameter of the α phase is of the order of several μm. The tensile strength and fatigue strengths of (α + β)-type Ti alloys increase significantly after they are subjected to TCP, as shown in Figures 5.23 (Akahori *et al.*, 2002) and 5.24 (Niinomi *et al.*,

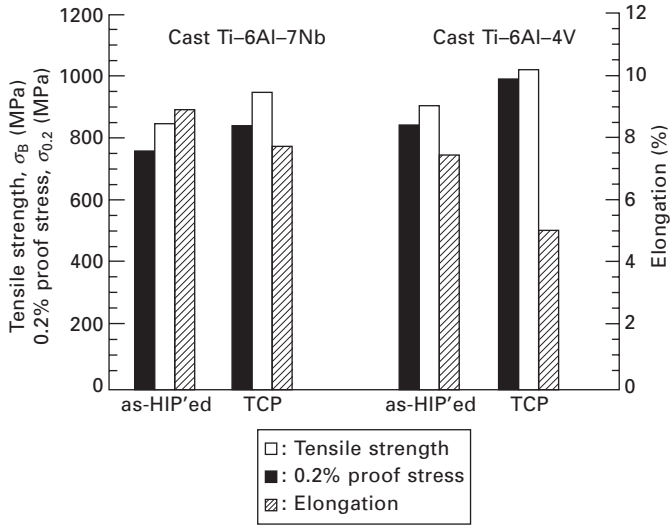

5.23 Tensile strength, 0.2% proof stress and elongation of as-HIP'ed cast Ti–6Al–7Nb and Ti–6Al–4V, and HIP'ed cast Ti–6Al–7Nb and Ti–6Al–4V conducted with TCP.

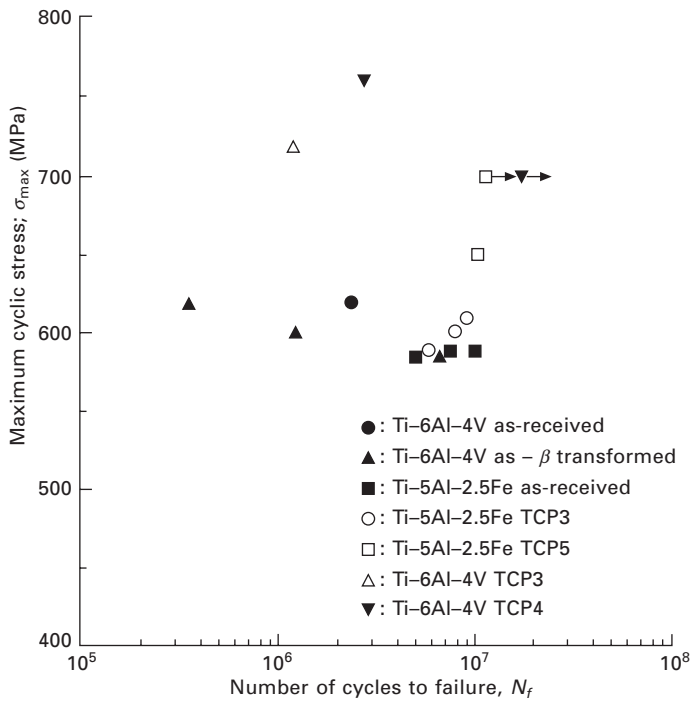

5.24 Comparison of high cycle fatigue strength of as-received, as-β transformed and TCP treated Ti–6Al–4V, as-received and TCP treated Ti–5Al–2.5Fe.

1995), respectively, with the cases of cast Ti–6Al–7Nb and Ti–6A–4V for tensile strength and Ti–6Al–4V and Ti–6Al–2.5Fe for fatigue strength. In general, contrary to the increasing trends exhibited in the cases of tensile and fatigue strengths, ductility and fracture toughness tend to decrease. In order to inhibit this decrease in ductility or fracture toughness, it is effective to perform TCP below the β-transus temperature or to perform a post-heat treatment where ST below the β-transus temperature is performed during the final stage of the TCP (Akahori *et al.*, 2002; Niinom *et al.*, 1995). By means of these treatments, relatively significant amounts of unstable β phase are retained in the microstructure at room temperature. The unstable β phase enhances the ductility or fracture toughness of the alloy.

5.3 Fatigue crack propagation

In order to inhibit the catastrophic failure of biomaterials, it is necessary to understand the fatigue crack initiation and fatigue crack propagation characteristics. The crack propagation characteristics are important for arriving at a fail-safe design for structural materials. It is considered that the catastrophic failure of these materials can be avoided by stopping the crack extension during the stable crack propagation stage, even if the crack has already been initiated.

It is important to evaluate both long and short crack (small crack) propagation characteristics. The trends in propagation rates of long and short cracks are not always similar.

5.3.1 Short fatigue crack propagation in air and *in vitro*

The relationships between the surface fatigue crack length, 2a, and the ratio of the number of cycles to the number of cycles to failure, N/Nf, in Ti–6Al–7Nb and Ti–6Al–4V ELI with an equiaxed α structure are shown in Fig. 5.25 (Akahori *et al.*, 2000). The number of cycles required for the first observation of an initial fatigue crack by light microscope is defined as the short fatigue crack initiation life; in this case, $2a < 50$ μm (approximately). The fraction of the fatigue crack initiation life in the total fatigue life that is equal to the number of cycles to failure is around 5% in Ti–6Al–7Nb and around 20% in Ti–6Al–4V ELI. Assuming that the short fatigue crack initiation and propagation life is the period for the surface crack to grow a length of five times or less than the size of the primary α grain, approximately $2a < 50$ μm, the short fatigue crack initiation and propagation life is around 50% of the total fatigue life in Ti–6Al–7Nb with an equiaxed α structure, while around 70% in Ti–6Al–4V ELI with an equiaxed α structure.

Observation of fatigue crack propagation behavior reveals that the fatigue crack in the equiaxed α structure tends to initiate mainly at the primary α

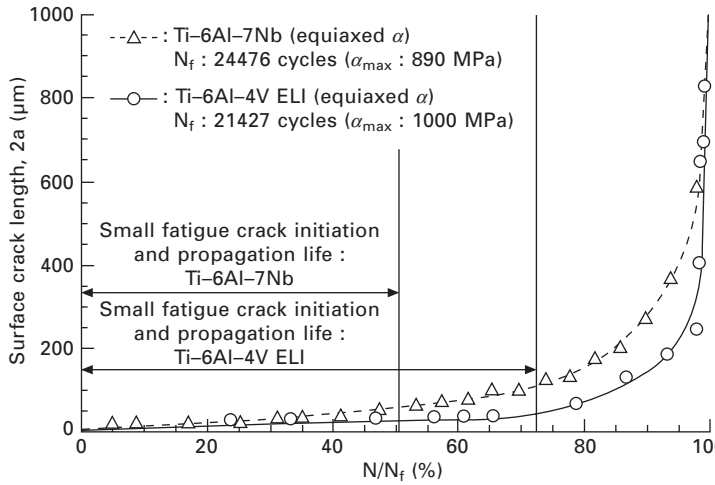

5.25 Surface crack lengths in Ti–6Al–7Nb and Ti–6Al–4V ELI with equiaxed α structure. Maximum stresses, α_{max}, are 890 and 1000MPa for Ti–6Al–7Nb and Ti–6Al–4V ELI, respectively. N_f and N are the number of cycles to failure and the number of cycles, respectively.

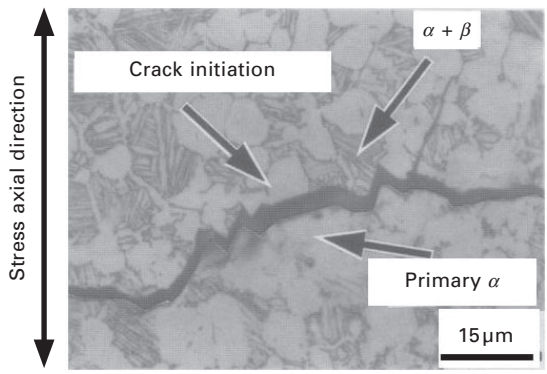

5.26 Crack initiation site and propagation path in Ti–6Al–7Nb with equiaxed α structure.

grain boundaries, while the crack tends to propagate preferentially along the β region near the interface between the primary α and β regions, as shown in Fig. 5.26 (Akahori *et al.*, 2000).

On the other hand, in the Widmanstätten α structure of both alloys, the observation of the fatigue crack behavior reveals that the fatigue crack initiates at the very early stage of the fatigue. After a few hundred cycles, the crack initiates and grows to a length that is nearly equal to the size of the α colony of the prior β grain and crack propagation is retarded at the colony boundary or at the prior β grain boundary. However, the crack propagates

in an unstable manner soon after passing through these boundaries, and this ultimately results in specimen fracture. These crack behaviors are shown in Fig. 5.27 (Akahori, 2000). The arresting period of the crack blocked in the α colony or the prior β grain boundaries occupies more than 90% of the total fatigue life in both alloys.

It is reported that the fatigue crack propagation rates of SUS 304 stainless steel, which is also austenitic stainless steel, evaluated in air and in 3% NaCl solution are clearly different in the very short fatigue crack region; the short crack propagation rate in 3% NaCl solution is higher than that in air, as shown in Fig. 5.28 (Nakajima *et al.*, 1997).

5.3.2 Long fatigue crack propagation in air and *in vitro*

Figure 5.29 (Niinomi *et al.*, 2000a) shows the relationship between the fatigue crack propagation rate, da/dN, and the nominal cyclic stress intensity factor, ΔK; and that between da/dN and the effective cyclic stress intensity factor, ΔK_{eff}, for Ti–6Al–4V ELI with Widmanstätten α and equiaxed α structures, and SUS 316L stainless steel obtained in air. When da/dN is plotted against ΔK, it is observed to decrease in the following order: Ti–6Al–4V ELI with the Widmanstätten α structure ≥ SUS 316L stainless steel ≥ Ti–6Al–4V ELI with the equiaxed α structure. On the other hand, when da/dN is plotted against ΔK_{eff}, the crack propagation rate of Ti–6Al–4V ELI with the Widmanstätten α structure is nearly the same as that of SUS 316L stainless steel. The crack

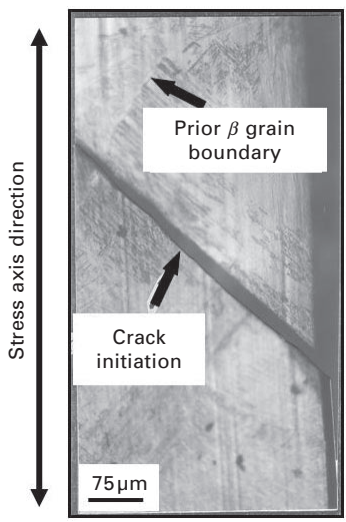

5.27 Crack initiation site of Ti–6Al–7Nb with Widmanstätten α structure.

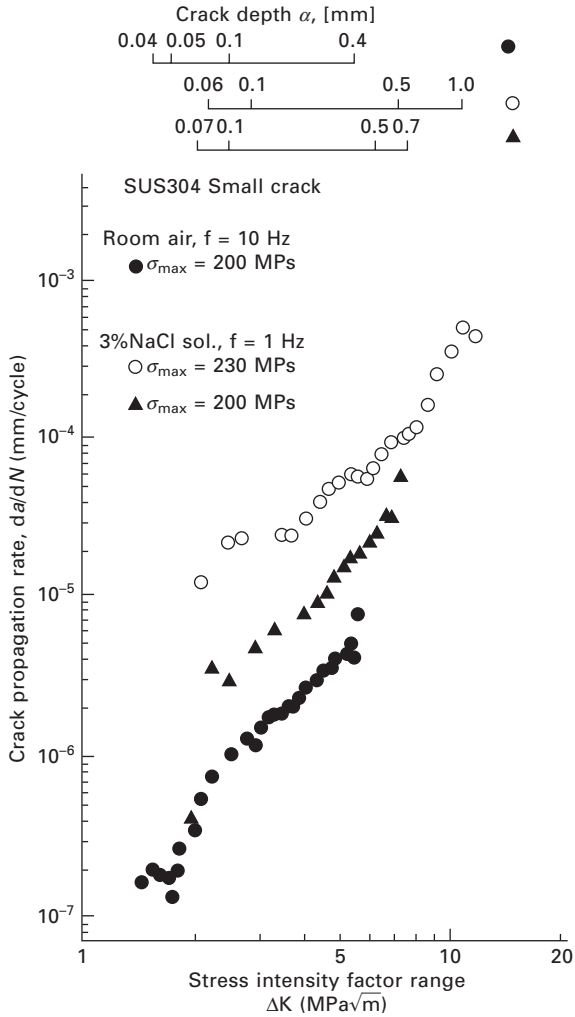

5.28 d*a*/d*N*–ΔK relationships for small cracks in SUS 304 in air and in 3% NaCl solution.

propagation rate of Ti–6Al–4V ELI with the equiaxed α structure is the highest. However, the differences in the crack propagation rates among these materials become relatively smaller. In particular, the crack propagation rate of T–6Al–4V ELI with the Widmanstätten α structure approaches that of Ti–6Al–4V ELI with the equiaxed α structure. Therefore, the crack closure effect in Ti–6Al–4V ELI with the Widmanstätten α structure is greater than that in Ti–6Al–4V ELI with the equiaxed α structure.

The microstructure strongly affects the crack propagation rate in $\alpha + \beta$ type Ti alloys. In a representative $(\alpha + \beta)$-type Ti alloy, Ti–6Al–4V, the long

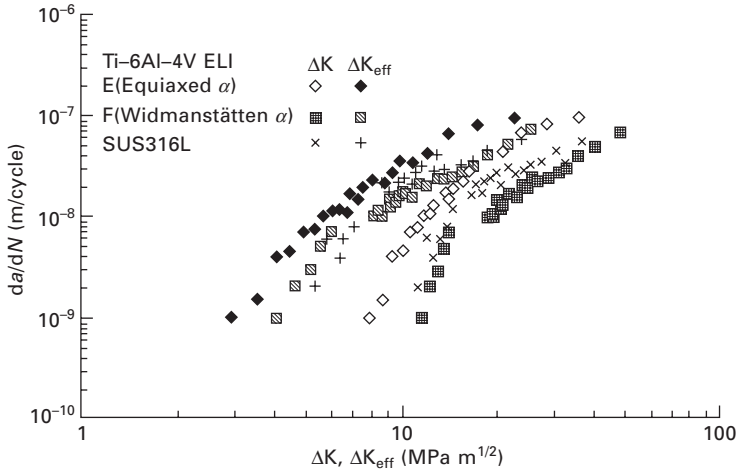

5.29 The fatigue crack propagation rate, d*a*/d*N*, as a function of the nominal cyclic stress intensity factor range, ΔK, and as a function of the effective cyclic stress intensity factor range, ΔK_{eff}, in the case of variously heat-treated Ti–6Al–4V ELI and SUS 316 L.

crack propagation rate in the Widmanstätten α structure is, in general, lower than that in the equiaxed α structure. The main reason for this phenomenon is the large crack deflection in the Widmanstätten α structure (Niinomi *et al.*, 1992). Therefore, the crack closure behavior in the Widmanstätten α structure is greater than that in the equiaxed α structure (Niinomi *et al.*, 1992).

On the other hand, the short crack propagation rate in the equiaxed α structure is, in general, lower than that in the Widmanstätten α structure as mentioned previously. The ratio of the short fatigue crack propagation life to the total fatigue life is fairly high. Therefore, improving resistance against short fatigue crack propagation is very effective in improving the total fatigue life (Akahori *et al.*, 2000a; Niinomi, 2000b).

When d*a*/d*N* is plotted against ΔK, the long fatigue crack propagation rates of Ti–6Al–4V ELI and Ti–5Al–2.5Fe in Ringer's solution are higher than those in air, as shown in Fig. 5.30, but they were nearly the same in air and Ringer's solution when d*a*/d*N* was plotted against ΔK_{eff}. In this case, it is reported that the crack closure reduces in Ringer's solution because the number of secondary cracks and the fatigue fracture surface in Ringer's solution are smaller than those in air. This suggests that the fatigue fracture surface corrodes and dissolves in Ringer's solution.

The short fatigue crack propagation rates of SUS 304 stainless steel evaluated in 3% NaCl solution are higher than those in air, as already shown in Fig. 5.28 (Nakajima *et al.*, 1997). However, the long fatigue crack propagation rate of SUS 304 stainless steel in air is almost the same as that in 3% NaCl

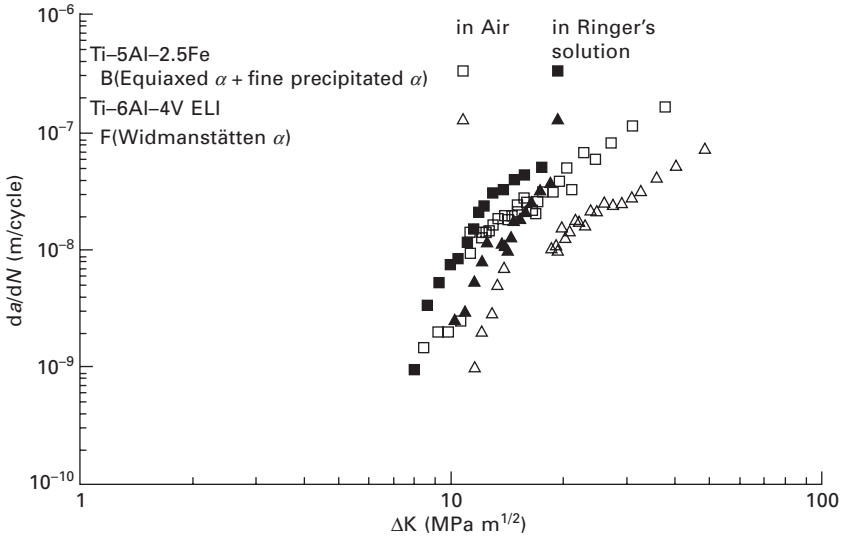

5.30 Fatigue crack propagation rate, d*a*/d*N*, as a function of nominal cyclic stress intensity factor range, ΔK, in the case of Ti–5Al–2.5Fe with (equiaxed α + fine precipitated α) and Ti–6Al–4V ELI with Widmanstätten α in air and in Ringer's solution.

solution, as shown in Fig. 5.31 (Nakajima *et al.*, 1997); however, in the range of high stress intensity factor, the crack propagation rate in 3% NaCl solution is slightly higher than that in air.

It has been reported that for Co–Cr alloy, the long fatigue crack propagation rate in Ringer's solution is higher than that in air (Hanawa *et al.*, 2000).

5.3.3 Improvement of long fatigue crack propagation resistance

The crack propagation resistance of Ti–6Al–4V is also increased due to the deformation induced transformation of the retained unstable β phase, as shown in Fig. 5.32 (Niinomi *et al.*, 1990; 1993), as well as the case of the fatigue strength as mentioned previously. This figure shows the relationship between the crack propagation rate (d*a*/d*N*) and the effective cyclic stress intensity factor divided by the Young's modulus ($\Delta K_{eff}/E$) for rolled plates of Ti–6Al–4V subjected to ST at 1173 K and at 1088 K, respectively, followed by water quenching (referred to as STQ1173R and STQ1088R) or aging treatment after water quenching (referred to as STA1173R). The d*a*/d*N* of STQ1088R in the IIb and IIc regions is the least among all the specimens. In the case of STQ1088R, the deformation-induced martensitic transformation of the retained β phase occurs as shown in Fig. 5.33 (Niinomi *et al.*, 1990; 1993).

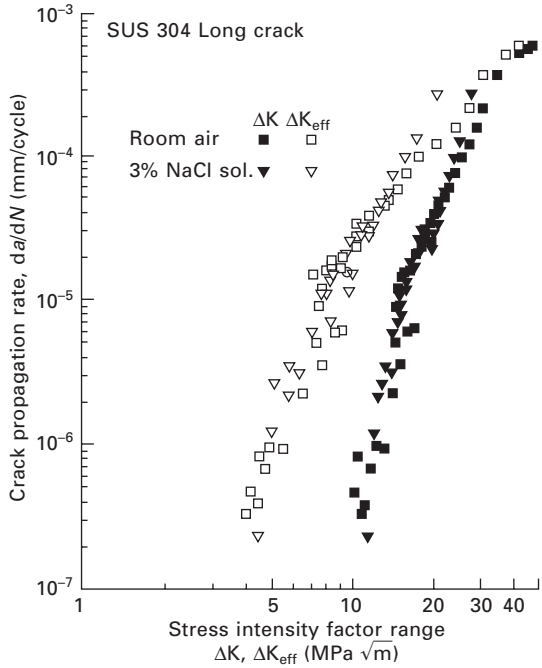

5.31 d*a*/d*N*-ΔK and ΔK_{eff} relationships for long cracks.

In order to enhance the mechanical properties of titanium alloys by using the deformation-induced martensitic transformation of the retained unstable β phase, the stability of the unstable β phase is important. If the stability of the retained β phase is considerably low, the mechanical properties may, on the contrary, be degraded because the unstable β phase transforms into martensite before crack initiation or propagation (Akmoulin *et al.*, 1993).

5.4 Fretting fatigue strength in air and *in vitro*

When fretting and fatigue occur simultaneously, the fatigue strength of biomedical Ti alloys decreases significantly. Such situations may occur in cases such as bone plate and screw, and hip joint stem and bone, where two bodies remain in contact with each other under cyclic loading conditions. This is called fretting fatigue.

The fretting fatigue strengths of biomedical Ti alloys are affected by various factors such as the contact pressure, stress amplitude, relative slip distance, friction coefficient, mean stress, frequency of cyclic stress, contact conditions, material quality, and circumstance. As an example of the effects of these factors on fretting fatigue of biomedical Ti alloys, the effect of contact pressure on the number of the cycles before failure for Ti–6Al–4V is shown

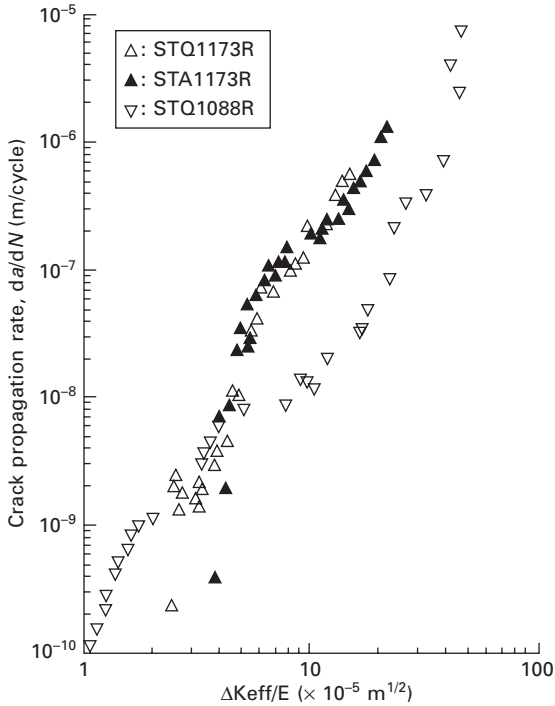

5.32 Relationships between d*a*/d*N* and $\Delta K_{eff}/E$ in solution treated specimen and aged specimens of rolled Ti–6Al–4V plates.

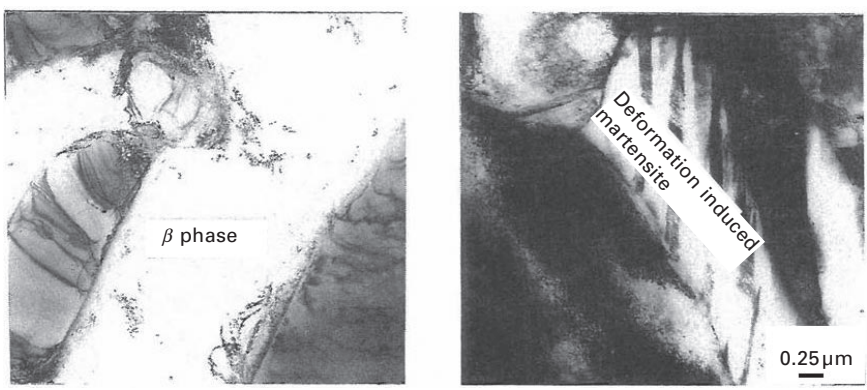

5.33 Typical TEM micrographs of β regions in (a) underformed and (b) deformed parts near the fracture surface formed in IIb region in the STQ1088R specimen.

in Fig. 5.34 (Sumita *et al.*, 1993), based on the results obtained from fretting fatigue tests. At a contact pressure of approximately 20 MPa, Ti–6Al–4V exhibits the least fretting fatigue life. This trend has also been reported for other Ti alloys such as Ti–4.5Al–3V–2Mo–2Fe (SP-700) (Takeda *et al.*, 2005), which may also be applicable in the biomedical field (Gunawarman *et al.*, 2005). In the case of steels, the fretting fatigue life decreases with an increase in the contact pressure.

Figure 5.35 (Maruyama *et al.*, 1995) shows the plain fatigue and fretting fatigue strength of Ti–6Al–4V in air and in a simulated body fluid (PBS (-)). As stated above, the fretting fatigue strength of Ti–6Al–4V is significantly lower in comparison with its plain fatigue strength in both air and in PBS (-). The plain fatigue strength of Ti–6Al–4V is nearly the same in air and PBS (-). On the other hand, the fretting fatigue strength of Ti–6Al–4V is less in PBS (-) in the low- and high-cycle fatigue life regions, but in the medium-cycle fatigue life region, it is greater in PBS (-) than in air. As shown in Fig. 5.36 (Niinomi *et al.*, 2002d), in the case of TNTZ, the trend in the fretting fatigue strength in air and in a simulated body fluid (Ringer's solution) in the low-cycle fatigue life region is different from that of Ti–6Al–4V, as stated above; the fretting fatigue strength is greater in Ringer's solution than in air. This is explained as being the result of the significantly higher lubrication effect caused by Ringer's solution.

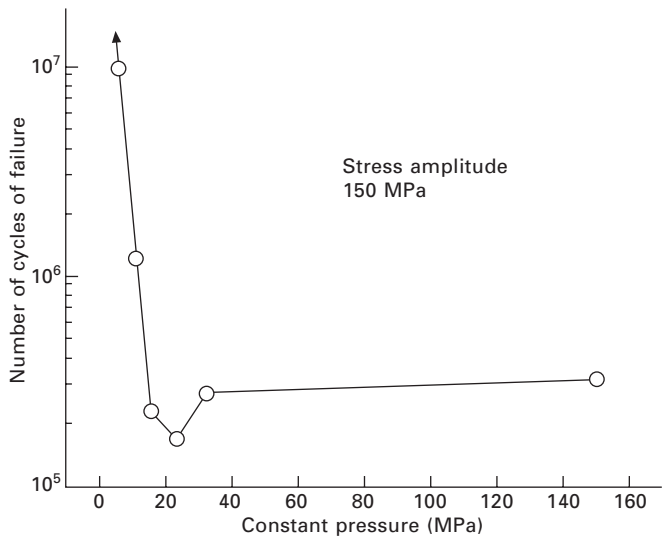

5.34 Relationship between the number of cycles to failure and constant pressure of Ti–6Al–4V.

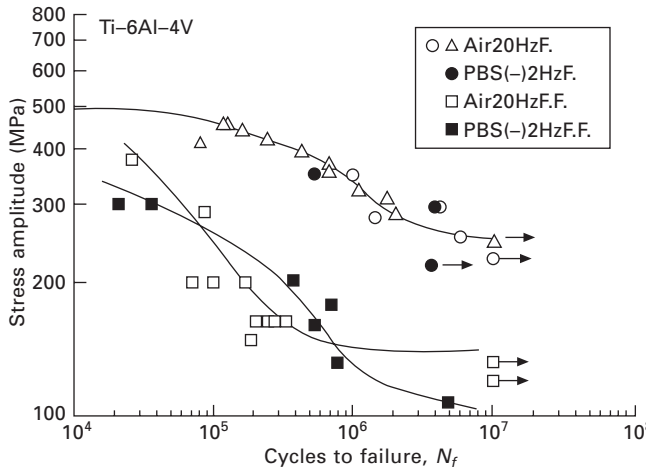

5.35 Cycles to failure as function of stress amplitude (F = fatigue, F.F. = fretting fatigue, Δ = other Ti–6Al–4V alloy data).

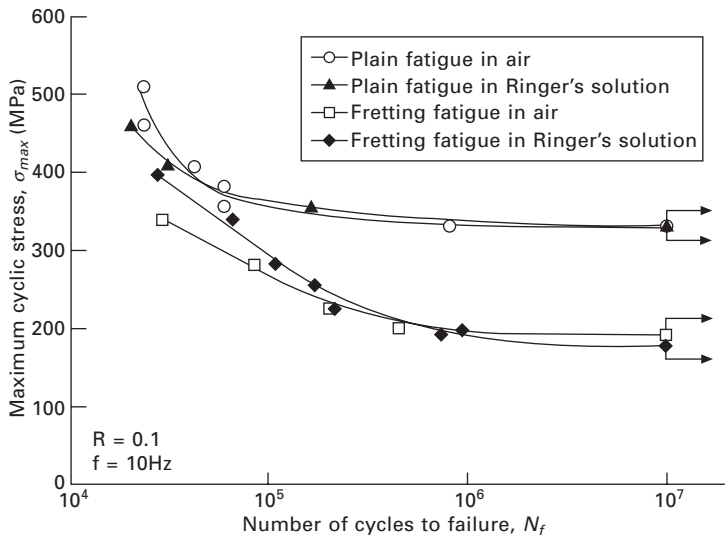

5.36 S–N curves of TNTZr conducted with solution treatment obtained from plain fatigue and fretting fatigue tests in air and in Ringer's solution.

5.5 Fatigue strength of wire

Wires composed of metallic biomaterials are useful in biomedical and dental applications, e.g. stents, guide wire of a catheter, surgical wire, and orthodontic wire.

An interesting application of metallic wires is in the high-nitrogen stainless steel wire used for the electrode of an FES (functional electrical stimulation). From the viewpoint of allergic reactions, low-Ni stainless steel wire, that is, high-nitrogen stainless steel wire (22.0% Cr, 10% Ni, 6.02% manganese (Mn), 2%Mo, 0.41% N and balance Fe) is preferred to SUS 316L stainless steel. In the case of a wire, the rotating bending fatigue strength is important. Figure 5.37 (Iguchi, 1999) shows the relationship between the number of rotations to failure, Nf, of electrode wires composed of SUS 316L stainless steel, NAS604PH (Co alloy), and NAS106N (high N stainless steel), and the distance between chucks, d, obtained from a dual–driven rotating-bending failure method in air. The rotating–bending fatigue strength of high-N stainless steel is the highest. Ti is expected to be a suitable material for this type of wire.

Low-modulus β-type Ti alloys are also used for wires for stents, catheters, and orthopedic, surgical and orthodontic equipment. The shape memory alloy TiNi is widely used for catheters or orthodontic wires. However, TiNi contains a large amount of Ni, which has been reported to be an allergen and is also brittle. Therefore, Ni-free shape memory or super elastic Ti alloys with low moduli are being developed. As orthodontic wires, β-type Ti–Mo–Zr–tin (Sn) has been put to practical use. Very recently, low modulus β-type TNTZ subjected to severe cold working and heat treatment has exhibited super elastic behavior, as shown in Fig. 5.38 (Niinomi *et al.*, 2003d). Figure 5.39

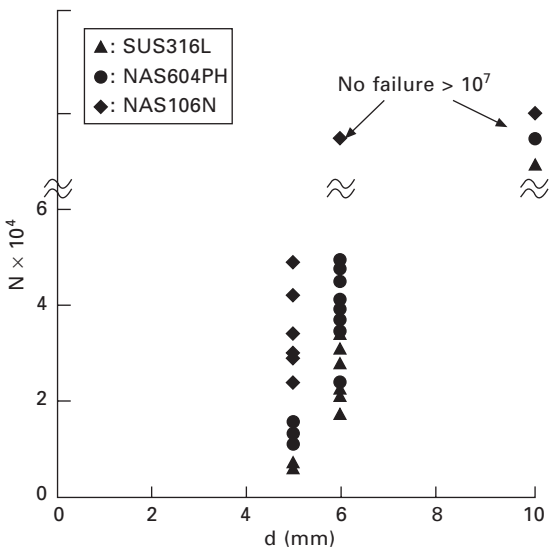

5.37 Relationship between number of rotations of electrode materials to failure, N, and distance between chucks, d, by a dual-driven rotating–bending failure method in air.

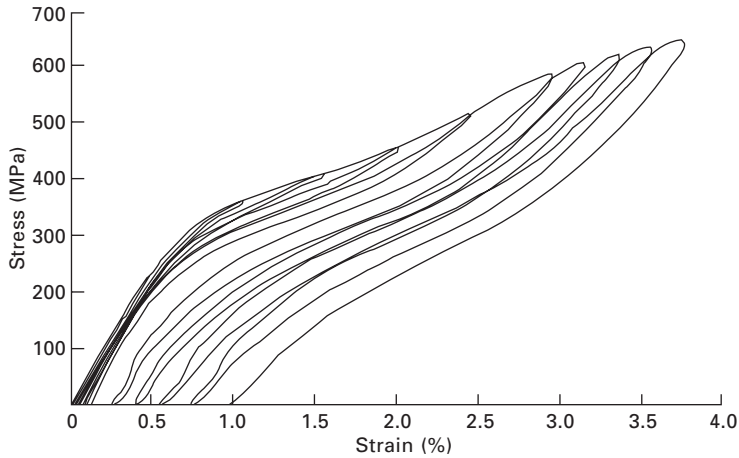

5.38 Tensile loading–unloading stress–strain curves of drawn wire of Ti–29Nb–13Ta– 4.6Zr with a diameter of 1.0 mm; total elastic strain: 2.7%.

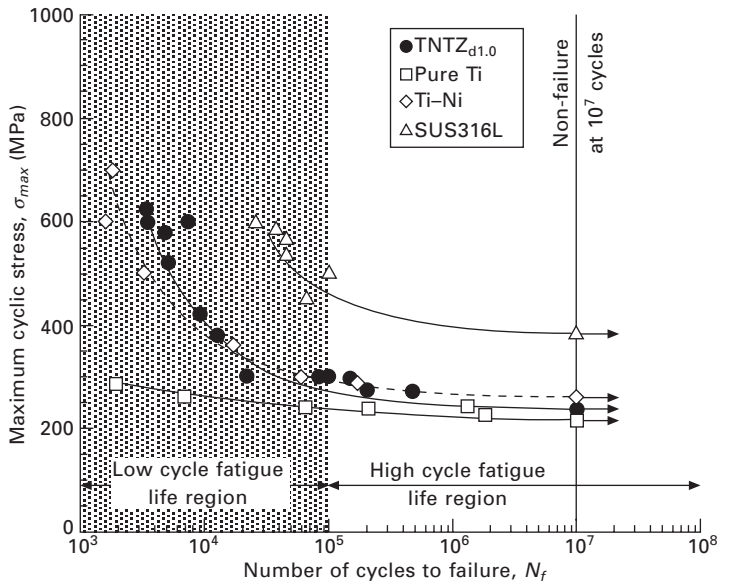

5.39 S–N curves of TNTZ (TNTZ$_{d1.0}$) and pure Ti, Ti–Ni and SUS316L stainless steel wires with a diameter of 1.0 mm obtained from notch-fatigue tests.

(Akahori, 2005b) shows the notched fatigue strength of TNTZ wire along with those of pure Ti, TiNi, and SUS 316L stainless steel wires, all with diameters of 1.0 mm. The notched fatigue strength of SUS 316L stainless

steel wire is the highest in both the low and high-cycle fatigue life regions. The notched fatigue strength of pure Ti wire is the lowest in the low-cycle fatigue life region, and that of TNTZ wire is slightly higher than that of TiNi wire. However, in the high-cycle fatigue life region, the notched fatigue strengths of pure Ti, TiNi, and TNTZ wires are nearly the same. In Japan, the official license for the application of TNTZ for orthodontic wire has been issued very recently. Thus, TNTZ wire will be put to practical use as orthodontic wire in the very near future.

5.6 Summary

With regard to the long-term usage of implants, the understanding and improvement of fatigue properties of metallic biomaterials in complexed conditions such as fretting overlapped conditions, in air, *in vitro*, and *in vivo* are significantly important. In this chapter, these fatigue properties have been described as possibilities. Because of the present trend toward the development of metallic biomaterials, the descriptions of Ti alloys has occupied a large portion of this chapter. Fatigue data on metallic biomaterials *in vivo* are lacking, although they are very important from the viewpoint of practical applications. It is desirable to report much more data of the fatigue properties *in vivo* in future.

5.7 References

Akahori, T., Niinomi, M., Fukunaga, K., Inagaki, I., 2000. Effects of Microstructure on the Short Fatigue Crack Initiation and Propagation Characteristics of Biomedical α/β Titanium Alloys. *Met. Mat. Trans.*, A 31A, 1949–1958.

Akahori, T., Niinomi, M., Matsuda, K., Suzuki, A., 2002. Microstructure and fatigue crack initiation and propagation characteristics of dental cast ($\alpha + \beta$)-type titanium alloy subjected to thermochemical treatment. *J. Japan Institute of Metals*, 66, 1098–1106.

Akahori, T., Niinomi, M., Ishimizu, K., Fukui, H., Suzuki, A., 2003. Effect of thermomechanical treatment on fatigue characteristics of Ti–29NB–13Ta–4.6Zr for biomedical applications. *J. Jpn. Inst. of Metals*, 67, 652–660.

Akahori, T., Niinomi, M., Otani, M., Toda, H., Fukui, H., Ogawa, M., 2005a. Notch fatigue properties of a Ti–29NB–13Ta–4.6Zr alloy for biomedical applications. *J. Japan Institute of Light Metals*, 55, 575–581.

Akahori, T., Niinomi, M., Toda, H., Yamauchi, K., Fukui, H., M. Ogawa, M., 2005b. Mechanical properties and deformation behavior of β-type titanium alloy (TNTZ) drawn wires. *J. Jpn. Inst. Metals*, 69, 530–535.

Akahori, T., Niinomi, M., Noda, A., Toda, H., Fukui, H., Ogawa, M., 2006. Effect of aging on mechanical properties of Ti–29NB–13Ta–4.6Zr alloy for biomedical applications. *J. Japan Institute of Metals*, 70, 295–303.

Akahori, T., Niinomi, M., Nakai, M., Nishimura, Takei, H., Fukui, H., Ogawa, M., 2008. Wear and Mechanical Properties, and Cell Viability of Gas-nitrided Beta-type Ti–Nb–Ta–Zr System Alloys for Biomedical Applications, *Mater. Trans.*, 49, 166–174.

Akmoulin, I. A., Niinomi, M., Kobayashi, T., 1993. Dynamic fracture toughness of Ti–6Al–4V alloy with various stabilities of β phase, *Metallurgical Transactions*, A 25A, 1655–1666.

Breme, H. J., Helsen, J. A., 1998. *Selection of Materials*, eds. J. A. Helsen, J. A., Breme, H. J., New York, USA, John Wiley & Sons, 1–36.

Gunawarman, Niinomi, M., Eylon, D., Fujishiro, S., Ouchi, C., 2002. Effect of β Phase Stability at Room Temperature on Mechanical Properties in β-Rich $\alpha + \beta$ Type Ti–4.5Al–3V–2Mo–2Fe Alloy. *ISIJ*, 42, 191–199.

Gunawarman, Niinomi, M., Akahori, T., Souma, T., Ikeda, M., Toda, H., Terashima, K,. 2005. Fatigue characteristics of low cost β titanium alloys for healthcare and medical applications. *Mater. Trans.*, 46, 1570–1777.

Hanawa, T., Nakazaw, K., Maruyama, N., Yamamoto, A., Hiromoto, S., Sumita, M., Ying, M., Kobayashi, T., 2000. *Study on Structural Biomaterials with Excellent Biocompatibility*, Research Report of National Inst. of Metals 22, 223–239.

Hanawa, T., Hiromoto, A., Yamamoto, A., Maruyama, N., Nakazawa, K., 2001. *Metallic Biomaterials in Body Fluid and their Surface Modification. Structural Biomaterials for the 21st Century*, eds. Niinomi, M., Okabe, T., Taleff, E. M., Lesure, D. R., Lippard, H. E., TMS, 145–156.

Iguchi, Y., 1999. Development of the implanted stainless steel electrode for functional electrical stimulation based on ultra clean refining processes. *Bull. Iron and Steel Inst. Jpn.* 4, 737–740.

Imam, M. A., Gilmore, C. M., 1983. Fatigue and microstructural properties of quenched Ti–6Al–4V. *Metallurgical Transactions*, A 14A, 233–240.

Kasuga, T., Nogami, M., Niinomi, M., Hattori, T., 2003. Bioactive Calcium Phosphate Invert Glass–Ceramic Coating on β-type Ti–29NB–13Ta–4.6Zr. *Biomaterials*, 24, 283–290.

Kim, J. H., Niinomi, M., Akahori, T., 2005. Influence of bone structure on mechanical properties of bovine and swine compact bones, *Materials Science Forum*, 475–479, 2407–2410.

Kim, H. M., Miyaji, F., T. Kokubo, T., 1995. Effect of heat treatment on apatite-forming ability of Ti metal induced by alkali treatment. *J. Materials Science Materials in Medicine*, 8, 341–347.

Kobayashi, T., Yamamoto, H., 1998. Development of high toughness in austempered type ductile cast iron and evaluation of its properties. *Metallurgical Transactions*, A 19A, 319–327.

Kumar, P., Hickl, A. J., Asphahani, A. I., Lawley, A., 1985. *Properties and characteristics of cast, wrought, and powder metallurgy (P/M) processed cobalt-chromium-molybdenum implant materials*, ASTM STP 859, 30–56.

Kuroda D., Niinomi, M., Morinaga, M., Kato, Y., Yashiro, T., 1998. Design and mechanical properties of new beta type titanium alloys for implant materials. *Materials Science and Engineering*, A A243, 244–249.

Kuroda, D., Hiromoto, S., Hanawa, T., Katada, Y., 2002. Corrosion behavior of nickel-free nitrogen austenitic stainless steel in simulated biological environments. *Materials Transactions*, 43, 3100–3104.

Lee, S. H., Takahashi, E., Nomura, N., Chiba, A., 2006. Effect of heat treatment on microstructure and mechanical properties of Ni- and C- free Co–Cr–Mo alloys for medical applications. *J. Japan Institute of Metals*, 70, 260–264.

Li, S. J. Niinomi, M., Akahori, T., Kasuga, T., Yang, R., Hao, Y. L., 2004. Fatigue characteristics of bioactive glass-ceramic-coated Ti–29NB–13Ta–4.6Zr for biomedical applications. *Biomaterials*, 25, 3341–3349.

Maruyama, N., Kobayashi, T., Sumita, M., 1995. Fretting fatigue strength of a Ti–6Al–4V alloy in a pseudo-body-fluid and quantitative analysis of the substances in the fluid. *J. Japanese Society for Biomaterials*, 13, 14–20.

Maruyama, N., Kobayashi, T., Nakazawa, K., Sumita, M., M. Sato, M., 1999. Fatigue and fretting behavior of Ni free Co–Cr alloy in a pseudo-body fluid. *J. Japan Biomaterials Soc.*, 17, 172–179.

Nakai, M., Niinomi, M., Akahori, T., Ohtsu, N., Nishimura, H., Toda, H., Fukui, H., Ogawa, M., 2007. Hard-ceramic Layer Formed on Surface of Biomedical Ti–29NB–13Ta–4.6Zr and Ti–6Al–4V ELI during Gas Nitriding. *Mater. Sci. Forum*, 561–565, 1509–1512.

Nakajima, M., Tokaji, K., Akatsuka, Y., 1995. Corrosion fatigue crack initiation and early growth behavior in stainless steel, *J. Jpn. Soc. Engineers*, A 63, 487–492.

Niinomi, M., Kobayashi, T., Inagaki, I., Thompson, A. W., 1990. The effect of deformation-induced transformation on the fracture toughness of commercial titanium alloys, *Metallurgical Transactions*, A 21A, 1733–1744.

Niinomi, M., Kobayashi, T., Akmoulin, I. A., 1992. Mechanical properties of titanium alloys, *J. Jpn. Inst. Light Metals*, 42, 605–613.

Niinomi, M., Kobayashi, T., S. Shimokawa, S., 1993. Fatigue Crack Propagation in Ti–6Al–4V Alloys, *Titanium'92*, eds. Froes, F. H., I. Caplan, I., TMS, 1835–1842.

Niinomi, M., Gong, B., Kobayashi, T., Oyabu, Y., Toriyama, O., 1995. Mechanical Properties and Fracture Characteristics of Ti–6Al–4V and Ti–5Al–2.5Fe with Refined Microstructure Using Hydrogen. *Met. Mat. Transaction*, A 26A, 1141–1151.

Niinomi, M., Kobayashi, T., Toriyama, O., Kawakami, N., Ishida, Y., Matsuyama, Y., 1996. Fracture characteristics, microstructure, and tissue reaction of Ti–5Al–2.5Fe for orthopedic surgery. *Metallurgical and Materials Transactions*, A 27A, 3925–3935.

Niinomi, M., 1998. Mechanical properties of biomedical titanium alloys. *Materials Science and Engineering*, A 243, 231–236.

Niinomi, M., Saga, A., Fukunaga, K., 2000a. Long crack growth behavior of implant materials Ti–5Al–2.5Fe in air and simulated body environment with relating microstructure. *Int. J. of Fatigue*, 22, 887–895.

Niinomi, M., 2000b. Fatigue. *Bull. Iron and Steel Inst. Jpn.*, 5, 82–88.

Niinomi, M., 2001. Recent metallic materials for biomedical applications. *Met. Mat. Trans.*, A 32A, 477–486.

Niinomi, M., 2002a. Fatigue characteristics and microstructure of titanium alloys for biomedical applications. *Proc. Fatigue 2002*, ed. Blom, A. F., EMAS, 3/5, 2073–2083.

Niinomi, M., Akahori, T., Nakamura, S., Fukui, H., Suzuki, A., 2002b. Friction wear characteristics of surface oxidized new β-type titanium alloy in simulated body environment. *Tetsu-to-Hagane*, 88, 567–574.

Niinomi,. M., Hattori, T., Morikawa, K., Kasuga, T., Suzuki, A., Fukui, H., Niwa, S., 2002c. Development of low rigidity β-type titanium alloy for biomedical applications. *Materials Transactions*, 43, 2970–2975.

Niinomi, M., Akahori., T., Yabunaka, T., Fukui, H., Suzuki, A., 2002d. Fretting fatigue characteristics of new biomedical β-type titanium alloy in air and simulated body environment. *J. Iron and Steel Institute of Japan*, 88, 553–560.

Niinomi, M., 2003a. Recent Research and Development in Titanium Alloys for Biomedical Applications and Healthcare Goods. *Science and Technology for Advanced Materials*, 4, 445–454.

Niinomi, M., Akahori, T., Yamaguchi, T., Kasuga, T., Fukui, H., Suzuki, A., 2003b.

Aging characteristics and mechanical properties of calcium phosphate invert glass-ceramic coated Ti–29Nb–13Ta–4.6Zr for biomedical applications. *J. Jpn. Inst. Metals*, 67, 604–613.

Niinomi M., Akahori T., Ishimizu K., 2003c. Fatigue and fretting fatigue of biomaterial, Ti–29Nb–13Ta–4.6Zr, in air and simulated body environment. In *Materials Lifetime Science & Engineering*, eds. Liaw P. K., Buchanan R. A., Klarstrom D. L., Wei R. P., Harlow D. G., Tortorelli P. F., TMS, 223–230.

Sato, M., Tu, R., Goto, T., Ueda, K., Narushima, T., 2005. Hydroxyapatite Formation on Calcium Phosphate Coated Titanium, *Materials Science Forum*, 561–565, 1513–1516.

Sumita, M., Kawabe Y., Nishijima, T., Fujii, T., Sitou, K., 1993. Study on improvement of fretting fatigue characteristics of high strength structural materials. *Research Reports of National Institute for Materials Science*, 14, 207–218.

Takeda, J., Niinomi, M., Akahori, T., Suzuki, Y., Toda, H., 2005, Contact pressure and fretting fatigue characteristics of highly workable titanium alloy with equiaxed α and Widmanstätten α structure, *J. Japan Institute of Light Metals*, 55, 661–667.

Yan, X., Kato, M., Nakasa, K., K. Morit, K., 2001. Evaluation of fracture strength and interfacial strength of titanium-nitride layers formed by gas-nitriding of titanium, *J. Soc. Mat. Sci. Japan*, 50, 764–771.

6

Mechanical testing of metallic biomaterials

N. MARUYAMA, National Institute for Materials Science, Japan

Abstract: Orthopedic implants such as artificial hip joints, bone plates and intramedullary nails, may fail due to the cyclic load applied by periodic motion such as walking. This chapter describes methods for fatigue and fretting fatigue tests in a simulated body fluid to evaluate mechanical properties of metallic materials to be used as fracture prostheses in the orthopedics field in particular. Next, the fatigue/fretting fatigue behavior in a simulated body fluid is discussed for 316L stainless steel, titanium-6% aluminum-4% vanadium alloy, pure titanium for industrial use, and cobalt-chromium-molybdenum alloy. Finally, a new method for fatigue tests using a living cell environment is described.

Key words: metallic biomaterial, fatigue, fretting fatigue, simulated body fluid, S–N curve, living cell environment.

6.1 Fracture of metal implants and test methods

Metallic materials are often used for implants to load-bearing parts of the living body. Metal implants used under a static load will not fail before reaching the end of their estimated lifetime except in special circumstances. On the other hand, orthopedic implants such as artificial hip joints, bone plates and intramedullary nails, may fail before reaching the end of their estimated lifetime due to the cyclic load applied by periodic motion such as walking (Sasada *et al.*, 1988). The Implant Committee of the Japanese Orthopaedic Association distributed a questionnaire survey on implant fracture to 2032 authorized organizations in 1994. A total of 950 organizations responded to the survey, and the results were as follows:

- In terms of implant type, fracture occurred to bone-connecting materials used for intramedullary nails, plates and screws, spinal-fixation materials, and artificial joints, in descending order of prevalence.
- In terms of body area, fracture occurred mainly in the femoral region, followed by spine, knee, shinbone, and hip joint.

Figure 6.1 shows a bone plate made of pure titanium (Ti) (JIS Grade 2) that failed one year after it was implanted. Failure occurred in the screw hole of the plate. The implant procedure involved screwing the plate to the bone, and fretting (contact damage process arising from surface micro-slip associated with small scale oscillatory motion of clamped structural members) occurred between the screw head and the surface around the screw hole. Subsequently,

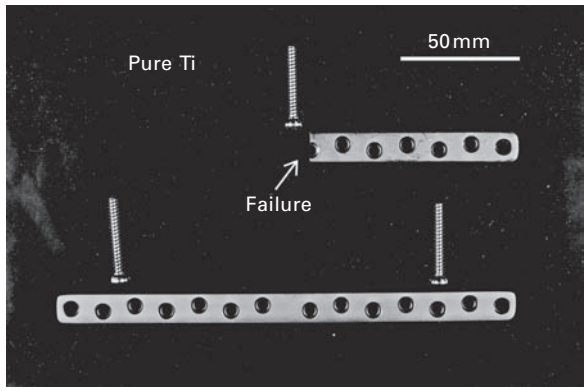

6.1 Fractured bone plate after one year of implantation.

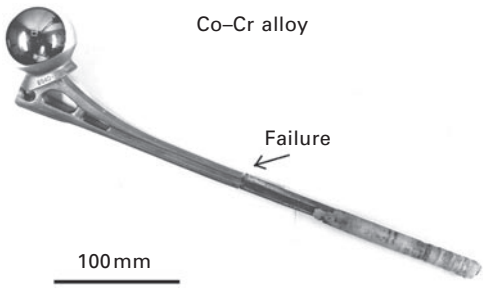

6.2 Fractured stem after nine years of implantation. (The arrow points to the crack.)

a crack nucleated and grew, presumably leading to failure. In the human body environment, it is probable that the failure was also affected by corrosion. Figure 6.2 shows a cobalt (Co)–chromium (Cr) alloy (Vitallium) stem that failed ten years after it was implanted. The stem failed in the center, where fretting occurred between the stem and the fitting mounted in the stem to prevent turning. Most of the orthopedic implants that failed were affected by cyclic loading. However, such failure is rarely caused only by plain fatigue. In most cases, the fatigue is accompanied by fretting, corrosion or both. It is known that the fatigue strength of metallic materials is significantly reduced by fretting or corrosion (Waterhouse, 1984).

Metallic materials have excellent tensile strength, fatigue strength, ductility and toughness, and the scattering in the strength is very small compared to ceramic or polymer materials. Thus, metallic materials are often used for medical implants.

For example, metallic materials are used for:

- orthodontic wires and artificial tooth roots in dentistry

- fracture prostheses such as artificial joints, bone plates and spinal fixation in orthopedics, and
- stents, catheters and guide wires in medical management.

To ensure that the above-mentioned metal implants function properly for the required period of time, sufficient durability must be provided to maintain the desired performance. Thus, different tests are employed to evaluate mechanical properties of metallic materials, because metal implants require various properties depending on the application.

These tests include, for example:

- tensile test and twist test (torque test) for orthodontic wires and guide wires
- tensile test and abrasion test for artificial joint slip parts
- tensile test, fatigue test and fretting fatigue test for bone plates and spinal fixation, and
- fatigue test and bend test for stents.

6.2 Living body environment

For mechanical testing of biomedical metallic materials, the living body environment should be considered. Generally, fatigue strength and fretting fatigue strength of metallic materials decrease in a corrosive environment.

In the living body, the salt concentration is about 1%, and the temperature is 310K (37 ºC). Oxygen (O) partial pressure in the living body is 1/4–1/5 of that in air. Between two materials or between the material and cells, however, the dissolved oxygen concentration is lowered, which is caused by crevice corrosion. Therefore, it takes longer to repair damaged oxide layers in the living body than in air. The pH level that affects corrosion of metallic materials is generally 7–7.35 in the living body. However, the level drops to 5.2 due to inflammation or foreign body reaction when an implant is inserted into the body (Hench and Ethridge, 1975). As mentioned above, the living body presents metallic materials with a severe environment.

Recently, it was clarified that the active oxygen produced by immune cells (macrophage) and organic substances in the body, such as amino acids and proteins, accelerates corrosion of titanium materials (Mu *et al.*, 2000). However, in corrosion fatigue and fretting corrosion fatigue tests for metallic biomaterials, PBS(-) (phosphate buffered saline), physiological saline, 0.9% NaCl water solution, Hank's balanced salt solution, Ringer's solution and cell culture medium are frequently used as a simulated body fluid. This chapter describes methods for fatigue and fretting fatigue tests in a simulated body fluid to evaluate mechanical properties of metallic materials to be used as fracture prostheses in the orthopedics field in particular. Next, the fatigue/fretting fatigue behavior in a simulated body fluid and in air is discussed for

316L stainless steel, titanium-6% aluminum-4% vanadium alloy, pure titanium for industrial use and cobalt–chromium–molybdenum alloy. Finally, a new method for fatigue tests using a living cell environment is also described

6.3 Tensile strength of metallic materials

Tensile properties of materials can be obtained by the following method. When a tensile specimen is loaded in a given direction until it fractures, a curve called stress–strain (S–S) curve is obtained (Fig. 6.3). The S–S curve is divided into elastic and plastic deformation regions, although the shape of the curve depends on the material. In Fig. 6.3, 0–a is the elastic deformation region where Hooke's law holds true, that is, the stress is proportional to the strain. The slope of this region is called Young's modulus. For many metallic materials, the boundary between elastic and plastic deformation is not clearly visible in the S–S curve. The stress (Point b), where plastic deformation is 0.2%, is called the 0.2% proof stress on the S–S curve and this is often regarded as the yield strength. Beyond Point b, there is a region in which macroscopic plastic deformation is observed, and the stress has a maximum value at Point c. This stress is called the ultimate tensile strength (UTS). Then the specimen fails at Point d. The configuration change of the specimen before and after the tensile test can provide the elongation and the reduction of area, which are indexes of material ductility.

Tensile properties of metallic materials are affected by the chemical compositions and microstructures, and also depend on processing or heat-treatment.

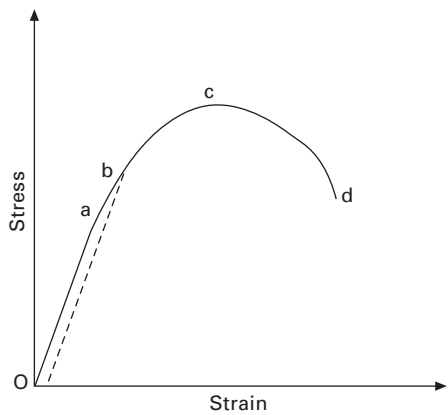

6.3 Schematic diagram of a stress–strain curve.

6.4 Fatigue and fretting fatigue of metallic materials

The corrosion fatigue test method for metal orthopedic implants is specified in ASTM F1801 (ASTM Standard F1801-97). In this standard, the recommended test environments are room temperature air and 37 °C physiological saline, and the cyclic load frequency can be accelerated up to 30Hz. However, a test at 1Hz (similar to man's walking speed) should be conducted when fatigue behavior in the living body is affected by corrosion. The number of specimens tested at each stress level should be three or more, and a stress amplitude vs. number of cycles to failure (S–N) curve up to 10^6 cycles should be obtained.

The fretting corrosion test method for metallic biomaterials is specified in F897 (ASTM Standard F897-84). As there is no standard method for the fretting corrosion fatigue test, the method proposed by Nakazawa and co-workers is often used (Nakazawa *et al*., 1992).

6.4.1 Fatigue of metallic materials

Fatigue failure is a phenomenon caused by a cyclic load equal to or lower than the tensile strength, as shown in Fig. 6.4. As shown in Fig. 6.5, fatigue failure of metallic materials is caused by localized plastic deformation on the material surface, accumulation of damage, and nucleation and growth of a crack as the number of load cycles is increased.

Metallic materials are usually composed of many crystal grains, each of which has its own slip planes and slip directions. The slip planes and directions of each crystal grain are randomly distributed in the materials. Therefore, even though the maximum stress applied to a specimen is macroscopically

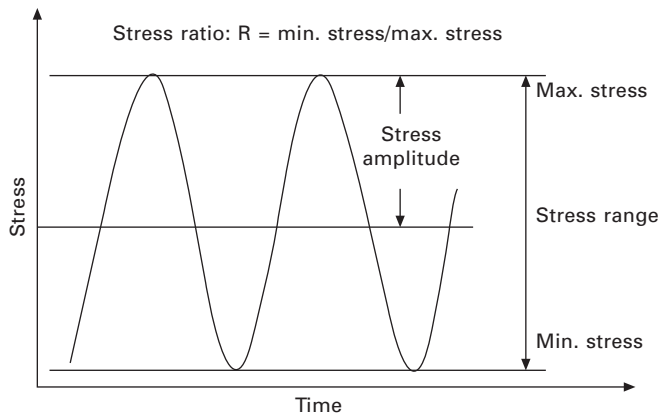

6.4 Schematic diagram of stress change with time.

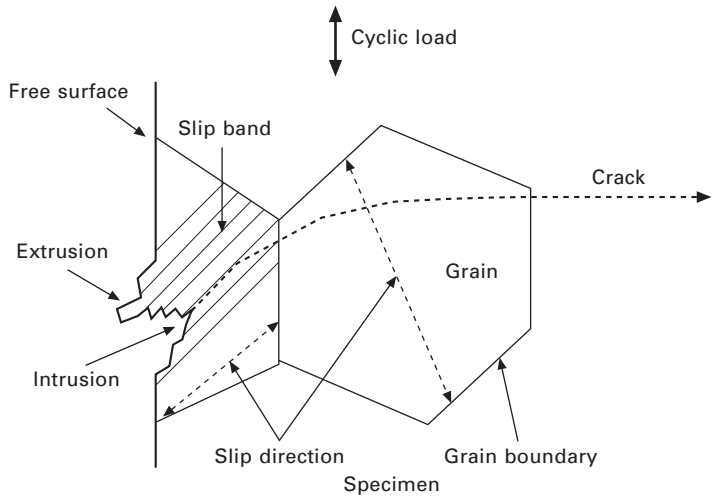

6.5 Schematic drawing of fatigue crack initiation.

within the elastic deformation region, plastically deformed grains locally exist on the specimen's surface. If the plastic deformation induced by applied load disappears when the load is removed, fatigue will not occur. In practice, however, slight plastic deformation remains in one load cycle. Thus, cyclic load causes fatigue damage. Along with an increase in the number of load cycles, this damage accumulates locally in a crystal grain, causing a crack. The number of load cycles until the material fails is called fatigue life. The fatigue life is expressed by the sum of the number of cycles until a crack nucleates and the number until the crack grows to failure.

Fatigue life test

The fatigue test can be largely classified into fatigue life test and fatigue crack propagation test. Fatigue life test results are usually given by cyclic stress amplitude vs. number of cycles to failure (S–N) curves shown in Fig. 6.6. A stress amplitude below which the specimen does not fail is called the fatigue limit or durability limit. Generally, the fatigue strength at 10^7 cycles is regarded as the fatigue limit. To obtain one S–N curve, at least ten specimens are required.

Figure 6.6 shows a schematic diagram of S–N curves for fatigue, fretting fatigue and fretting corrosion fatigue. Generally, corrosion and fretting decrease the fatigue strength of metallic materials (Waterhouse, 1984). In air, the fatigue limit is 1/2–1/3 of the tensile strength (Klesnil and Lukas, 1984, pp. 4–37). This is partly because the fatigue strength is controlled by the weakest part of the material while the tensile strength is determined

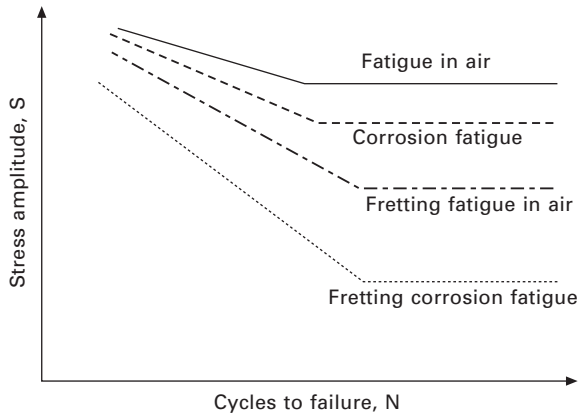

6.6 Schematic diagram of S–N curves for fatigue, fretting fatigue and fretting corrosion fatigue.

by the average properties of the whole material. Generally, as the tensile strength of materials increases, the fatigue strength increases. In materials with very high tensile strength, however, the fatigue strength is lowered in sensitive response to defects in the specimen. If there is a stress concentration site such as a bone plate hole or screw, the fatigue test is conducted using specimens with a notch with a similar stress concentration The number of cycles to crack nucleation is significantly lower for notched specimens than for smooth specimens.

Fatigue crack propagation test

As shown in Fig. 6.5, a fatigue crack nucleates in a direction inclined 45 degrees to the stress axis. Then, the crack propagates perpendicular to the stress axis. Generally, the fatigue crack propagation test is conducted with a constant stress amplitude. In this case, the fatigue crack growth rate increases exponentially with the number of stress cycles. The experimental results are typically summarized by a crack growth rate log (da/dN) – log (stress intensity factor range ΔK) curve, as shown in Fig. 6.7. Here, the stress intensity factor range ΔK is expressed by the cyclic stress range and the crack length. This Figure shows the lower limit of ΔK (ΔK_{th}), below which the crack does not propagate, the intermediate region, where log(da/dN) varies linearly with log(ΔK), and the unstable fracture region, where the crack propagates unstably and finally the specimen fractures. The stress intensity factor K, at which the specimen unstably fractures, is called the fracture toughness K_{IC}. The fracture toughness is a material constant, depending on processing or heat-treating, even though the chemical composition is the same. The linear

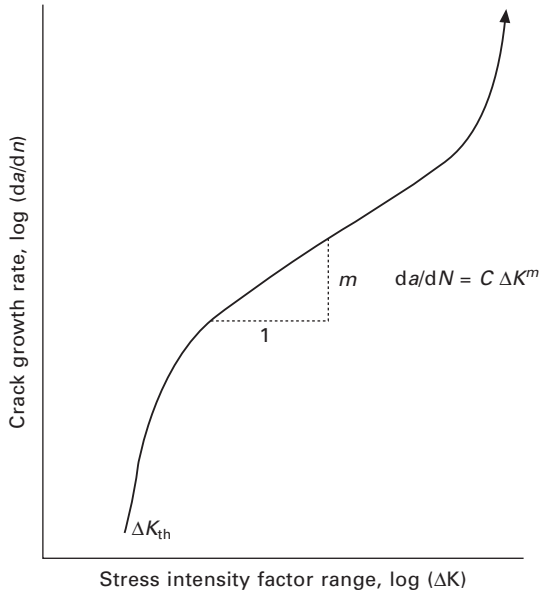

6.7 Schematic diagram of crack growth rate as a function of the stress intensity factor range.

relationship (Eq. 6.1) in the intermediate region was given by Paris (Klesnil and Lukas, 1984) and holds true for most metallic materials:

$$da/dN = C\Delta K^m, \qquad [6.1]$$

where C and m are material constants. The value of m which is experimentally obtained is between 2 and 4 for metallic materials.

A typical fracture surface of metallic materials caused by fatigue exhibits striations that show crack extension induced by cyclic stress. An example of striations in SUS 316L stainless steel is shown in Fig. 6.8. The distance between striations shows the distance that the crack grows during each stress cycle. Striations appear at a right angle to the crack propagation direction. Thus, for fatigue-failed materials, the cyclic stress applied to the material can be analyzed based on the orientation of the striations and the distance between them.

6.4.2 Fretting fatigue of metallic materials

Fretting means a contact damage process arising from surface micro-slip associated with small scale oscillatory motion of clamped structural members. The contact surfaces are worn and, at the same time, they are affected by cyclic friction stress. Fatigue with fretting is called fretting fatigue. Mechanical factors affecting the fretting properties include coefficient of friction, pressing

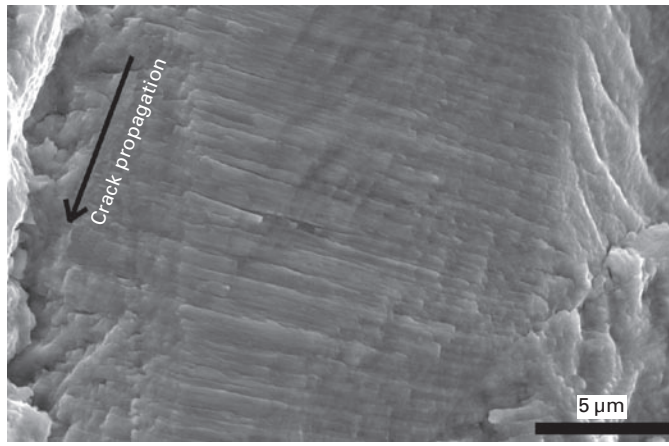

6.8 Striation on the fracture surface of SUS316L stainless steel.

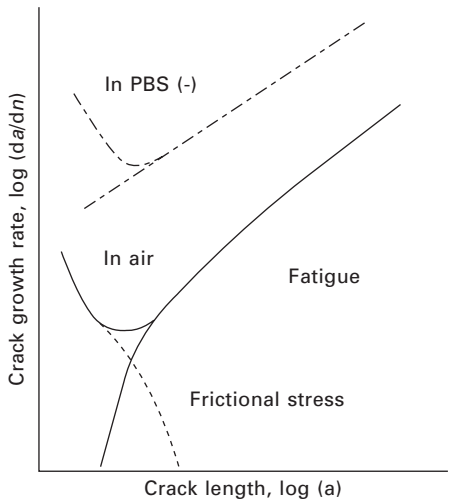

6.9 Schematic diagram of the relationship between crack growth rate and crack length in fretting fatigue test.

force, and amount of relative slip. In fretting fatigue, cyclic stress, which is the sum of cyclic applied stress and cyclic friction stress caused by fretting, is applied to the material. The friction stress is maximum on the contact surface of the material and decreases drastically toward the inside of the material. Therefore, fretting fatigue crack growth behavior differs significantly from fatigue crack growth behavior shown in Fig. 6.7. In fretting fatigue, the growth rate of a crack near the contact surface decreases drastically with increasing crack length, as shown in Fig. 6.9. Then, after showing a minimum value, it

is in accord with the plain fatigue crack growth rate. As shown in Fig. 6.6, the fretting fatigue strength is often half or less of the plain fatigue strength and it will not become higher even if the tensile strength of the material is increased (Waterhouse, 1984).

Fretting fatigue life is shorter than plain fatigue life. In fretting fatigue, a crack easily nucleates due to friction stress even at a small stress amplitude at which plain fatigue failure may not occur, and the crack grows, leading to material failure. In orthopedic implants, fretting occurs where two materials come into contact with each other; such as in bone plates or screws.

6.5 Effect of corrosion on fatigue and fretting fatigue

The fatigue strength of metallic materials in a corrosive environment varies with the effect of the corrosion on the nucleation and propagation of a fatigue crack. The effect of corrosion on crack nucleation is limited to the vicinity of the material surface. If crack nucleation is stimulated by the corrosion, in general, the crack growth rate is also increased by the corrosion.

Corrosion of metallic materials is largely classified into uniform corrosion and local corrosion by surface appearance. Fatigue failure of metallic materials is affected by whether or not local corrosion occurs. However, the surface of metallic biomaterials is always covered with dense oxide layers (passive films), which play a role as corrosion prevention films. Therefore, the plain fatigue strength is not so different between that in air and that in a simulated body fluid.

In fretting fatigue, the surface oxide layers are damaged by fretting. As a result, the newly exposed surface is largely affected by corrosion and the fretting fatigue strength is significantly lowered. However, when wear caused by fretting is heavy, cracks induced by fretting corrosion are grounded. Therefore, in some cases the effect of fretting corrosion on crack nucleation may be relatively small.

6.6 Corrosion fatigue and fretting corrosion fatigue tests in a simulated body environment

A schematic diagram of the fretting fatigue test in a simulated body fluid is shown in Fig. 6.10 (Yamamoto *et al.*, 1995). In the test, the pads that cause fretting are attached to the parallel part of the specimen. Therefore, it is necessary to provide the specimen with a parallel part for attaching the fretting pads (although various types of specimens are used in the fretting fatigue test, such as a round bar smooth specimen, an hourglass specimen, a notched specimen or a plate specimen). If a cyclic load is applied to the specimen with the bridge-shaped pad pressed on either side of the parallel

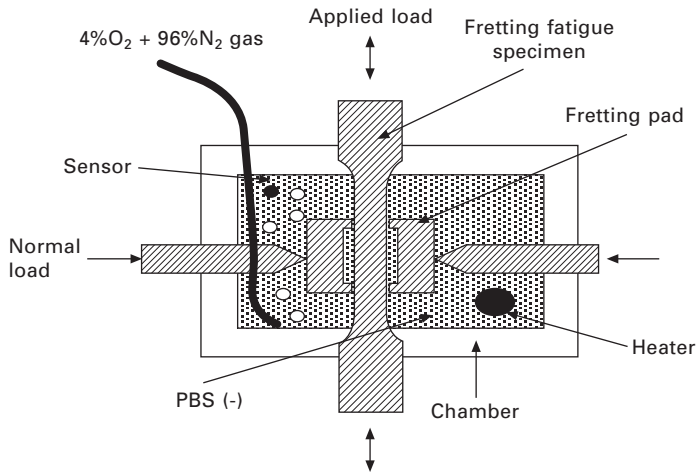

6.10 Schematic diagram of fretting fatigue test in PBS(-).

part of the specimen by a given force, relative slip is caused on the contact surface between the specimen and the pad by the expansion and contraction of the specimen, which causes fretting. The frictional force between the pad and the specimen can be measured, based on the output from a strain gage affixed inside the center of the pad. Here, it is necessary to obtain a calibration curve of the load applied to the pad and the strain in advance. If the frictional force amplitude is f, the pressing force p and the coefficient of friction μ, then μ can be defined in the following equation:

$$\mu = f/p. \qquad [6.2]$$

The relative slip distance between the specimen and the pad, S_a, is measured experimentally. In addition, as the pad can be considered a rigid body, it can be expressed as follows:

$$S_a = \sigma_a \cdot L/(2E), \qquad [6.3]$$

where σ_a is stress amplitude, E is Young's modulus, and L is the span of the pad.

The fretting fatigue life depends on the contact pressure of the pad.

From a mechanical viewpoint, cyclic shear stress on the specimen surface is a major factor that nucleates fretting fatigue cracks. Cyclic shear stress arises from the frictional force induced by the oscillatory motion of the pad. The maximum cyclic stress amplitude, σ_1, at the edge of the fretted area on the specimen surface is calculated as follows:

$$\sigma_1 = \sigma_a + 2f_a \qquad [6.4]$$

where σ_a is plain fatigue stress amplitude, and f_a is friction stress amplitude.

The region affected by fretting is limited to the shallow surface layers. Thus, fretting fatigue strength is almost equal to the fatigue strength of a specimen with short cracks (Nishioka and Hirakawa, 1969).

Generally, as the contact pressure of the pad increases, the frictional force increases and the fretting fatigue life decreases. In the low contact pressure region, however, the fretting fatigue life may show the minimum value in some cases (Maruyama *et al.*, 1990). Figure 6.11 shows the relationship between the contact pressure and the fretting fatigue life for a Ti-6 aluminum (Al)-4 vanadium (V) alloy when the applied stress amplitude is constant. This is because the contacting behavior of the area between the pad and the specimen differs depending on the contact pressure. Generally, if the contact pressure is high, the whole contact area will be the stick region. In this case, the highest stress concentration is obtained at the edge of the contact area, where a crack nucleates. If the contact pressure is low, however, the contact area is divided into a stick region to receive the contact pressure and two slip regions where wear is caused on both sides of the stick region, as shown in Fig. 6.12 (Nakazawa *et al.*, 1992). In fretting fatigue, the highest stress concentration is obtained at the boundary between the stick region and the slip region, where a crack nucleates. The behavior of the contact area changes with an increase in number of stress cycles. As the number of cycles is increased, the area of the stick region becomes smaller than the initial contact area, and thus the net contact pressure rises, although the pressing force is constant. Then, the friction stress increases with the contact pressure and the fatigue life decreases. In the orthopedic field, this contact pressure is, empirically, 20–50MPa.

The following are important points to keep in mind concerning fatigue and fretting fatigue tests in the living body environment:

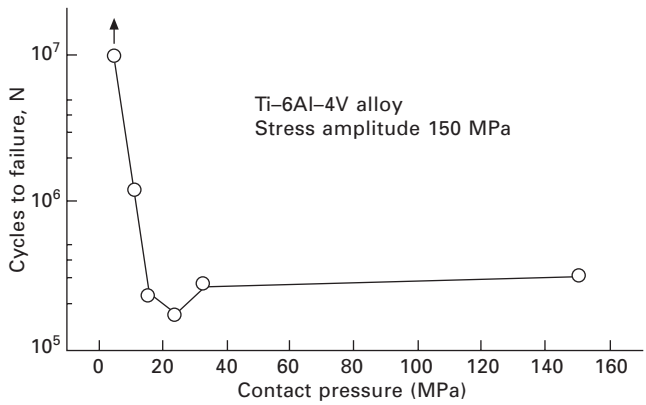

6.11 Effect of contact pressure on fretting fatigue life in air for Ti–6Al–4V alloy (Maruyama *et al.*, 1990, by courtesy of The Iron and Steel Institute of Japan).

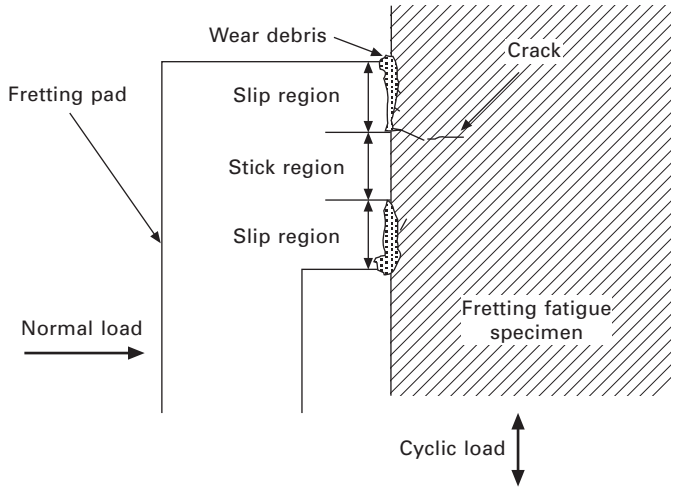

6.12 Schematic drawing of fretting damage on the contact area (Maruyama *et al.*, 1995, by courtesy of the Japanese Society for Biomaterials).

- As fatigue is a phenomenon that depends on time, it is necessary to pay close attention to the frequency of cyclic stress. A frequency of approximately 1Hz, which corresponds to man's walking speed, must be used for fatigue and fretting fatigue tests. Figure 6.13 shows the relationship between the number of cycles to failure and the frequency of the cyclic stress for Ti–6Al–4V alloy and pure titanium for industrial use, which are typical metallic biomaterials (Maruyama, 2000). Fatigue properties of titanium alloys depend on the frequency in air and the number of cycles to failure is lowered when the frequency is reduced.
- In many cases, phosphate buffered saline PBS(-), 0.9% NaCl aqueous solution, Hank's balanced salt solution, Ringer's solution and cell culture medium are used as simulated body fluids. These solutions do not contain cells producing active oxygen such as macrophage. Moreover, oxygen partial pressure in the living body is one quarter to one fifth of that in air. Therefore, repairing oxide layers damaged by fretting takes more time in a simulated body fluid than in air. The pH level, affecting corrosion of metallic materials, differs depending on the region of the human body and the presence of inflammation. Therefore, it is important to be aware that in the living body there are different factors from those in a simulated body fluid.
- In a fretting fatigue test in a simulated body fluid, it is necessary to use a pad and a pad-pressing bar made of the same material as that of the specimen, as in the case of an actual device, to prevent corrosion (galvanic corrosion) caused by the contact of different metallic materials.

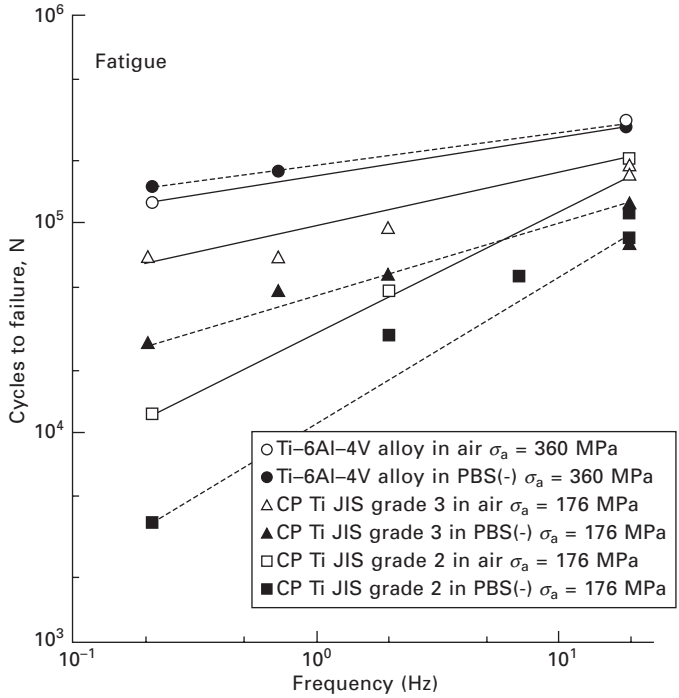

6.13 Influence of frequency of cycles to failure in fatigue tests (Maruyama *et al.*, 2000, by courtesy of the Japanese Society for Biomaterials).

6.7 Results of fatigue and fretting fatigue tests on metallic biomaterials

The following describes the S–N curve characteristics for fatigue and fretting fatigue, in air and in a simulated body fluid, of typical metallic biomaterials such as 316L stainless steel, Ti–6Al–4V alloy, pure titanium for industrial use and cobalt (Co)-chromium (Cr) alloy. Here, the test conditions are as follows: The stress ratio (ratio of the minimum stress to the maximum stress in cyclic loading) is 0.1, the cyclic stress waveform is sinusoidal, and the frequency of the cyclic stress is 20Hz in air and 2Hz in a simulated body fluid. The pad span is 20mm, and the contact pressure between the specimen and the pad is 30MPa. PBS(-) is used as a simulated body fluid. The amount of the fluid is 160mL, dissolved oxygen concentration is 4%, temperature is 310K and pH is 7.5. The components of the PBS(-) are 8000mg/L NaCl, 1150mg/L Na_2HPO_4 and 200 mg/L KH_2PO_4.

6.7.1 316L stainless steel

The S–N curve for a JIS 316L stainless steel (iron (Fe)–0.019% carbon (C)–0 0.48% silicon (Si)–1.18% manganese (Mn)–0.038% phosphorus (P)–0.013% sulfur (S)–12.10% nickel (Ni)–16.72% Cr–2.05% Mo, 0.2% Proof Stress: 328MPa, UTS: 602MPa) is shown in Fig. 6.14 (Nakazawa *et al.*, 1999). The fatigue strength at 10^7 cycles is approximately 205MPa in air and 200MPa in PBS(-). In the high stress amplitude region, the fretting fatigue strength is almost the same in air and in PBS(-). In the low stress amplitude region, however, it is lower in PBS(-) than in air. The fretting fatigue strength at 10^7 cycles is approximately 140MPa in air, and 110MPa in PBS(-). Thus, it is lowered to about two thirds to half of the plain fatigue strength.

6.7.2 Ti–6Al–4V alloy

The S–N curve for a Ti–6Al–4V alloy solution treated and aged (Ti–6.15% Al–4.19% C–0.200% Fe–0.143%-oxygen (O)–0.006% nitrogen (N)–0.005% C, 0.2% Proof Stress: 974MPa, UTS:1010MPa) is shown in Fig. 6.15 (Maruyama *et al.*, 1995). The fatigue strength at 10^7 cycles is approximately 300MPa, both in air and in PBS(-). The fretting fatigue strength is higher in PBS(-) than in air in the intermediate stress amplitude region. In the high and low stress amplitude regions, however, it tends to be lower in PBS(-) than in air. The fretting fatigue strength at 10^7 cycles is approximately 120MPa in air, and 100MPa in PBS(-). Thus, it is lowered to about one third of the plain fatigue strength.

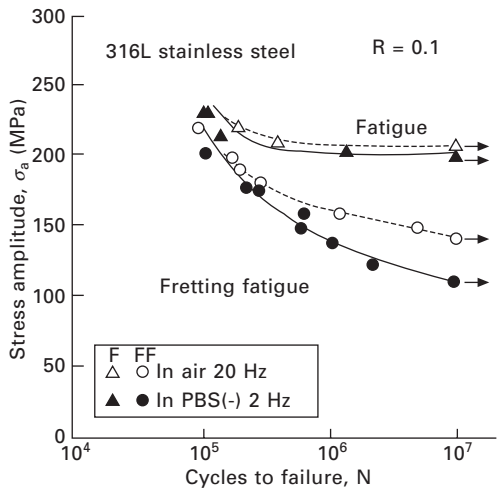

6.14 S–N curves of 316L stainless steel in air and in PBS(-) (F = fatigue and FF = fretting fatigue) (Nakazawa *et al.*, 1999, by courtesy of The Japan Institute of Metals).

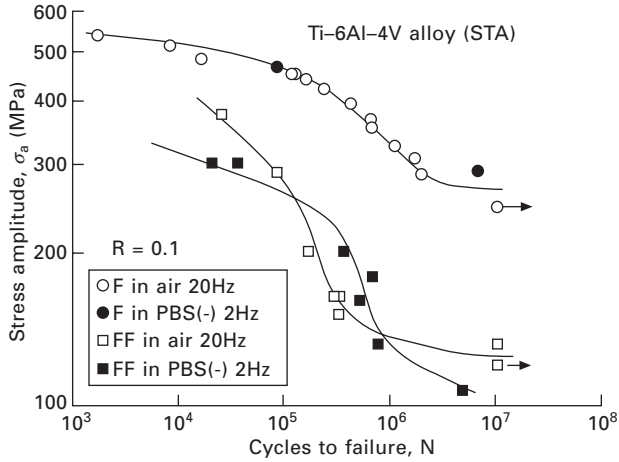

6.15 S–N curves of Ti–6Al–4V alloy in air and in PBS(-) (F = fatigue and FF = fretting fatigue) (Yamamoto *et al.*, 1995, by courtesy of The Japan Institute of Metals).

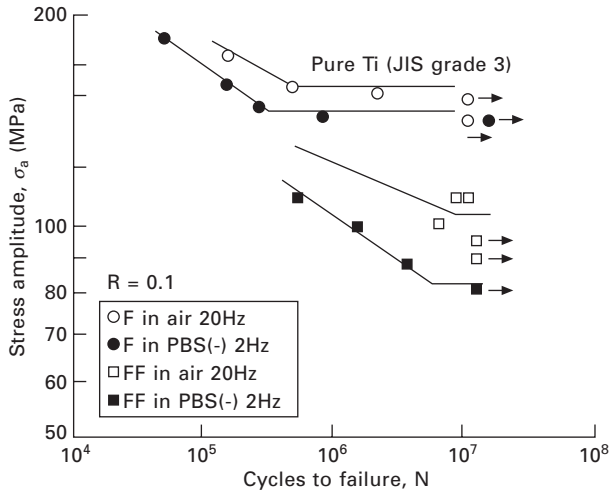

6.16 S–N curves of CP Ti (JIS grade 3) in air and in PBS(-) (F = fatigue and FF = fretting fatigue) (Maruyama *et al.*, 2000, by courtesy of the Japanese Society for Biomaterials).

6.7.3 Pure titanium for industrial use

The S-N curve for pure titanium for industrial use, JIS Grade 3 (Ti-0.123% Fe-0.144% O-0.004% N, 0.2% Proof Stress: 416MPa, UTS: 538MPa) is shown in Fig. 6.16 (Maruyama *et al.*, 1995). The fatigue strength for 10^7 cycles is approximately 150MPa in air and 140MPa in PBS(-). The fretting

fatigue strength for 10^7 cycles is approximately 100MPa in air and 85MPa in PBS(-). Therefore, it is lowered to about one third to a half of the plain fatigue strength.

6.7.4 Co–Cr alloy

The S–N curve for a forged Ni-free Co–Cr alloy (64.81% Co–28.99% Cr–5.93% Mo–0.02% Ni–0.03% Fe, 0.2% Proof Stress: 432MPa, UTS: 956MPa) is shown in Fig. 6.17 (Maruyama *et al.*, 1999). The asterisk '*' in the drawing means that in the fretting fatigue test, failure occurred in the parallel part of the specimen, not in the fretting part. For the fatigue strength in air, no fatigue limit is obtained at 10^7 cycles, and at around 10^7 cycles it drops significantly. The fatigue strength at 10^7 cycles in air is approx imately 240MPa and it is lower by 20–30MPa in PBS(-) than in air in the low-cycle region. The fatigue strength at 10^7 cycles in PBS(-) is the same as that in air. The fretting fatigue strength both in air and in PBS(-) is lower by about 30MPa than the fatigue strength. The fretting fatigue strength both in air and in PBS(-) exhibits no difference, remaining at approximately 210MPa.

Figure 6.18 shows the relationship between the tensile strength and the fatigue strength/fretting fatigue strength of metallic biomaterials at 10^7 cycles in air at room temperature and in a simulated body fluid (Maruyama *et al.*, 2000; 1995; 1999; Nakazawa *et al.*, 1999). For all of the biomaterials tested, the fatigue strength at 10^7 cycles is similar in air and in a simulated body fluid. The fatigue strength is closely correlated to the tensile strength:

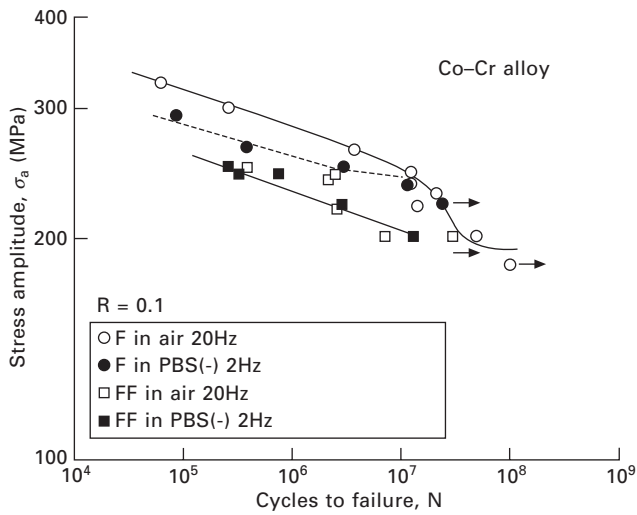

6.17 S–N curves of Co–Cr alloy in air and in PBS(-) (F = fatigue and FF = fretting fatigue). (Maruyama *et al.*, 1999, by courtesy of the Japanese Society for Biomaterials).

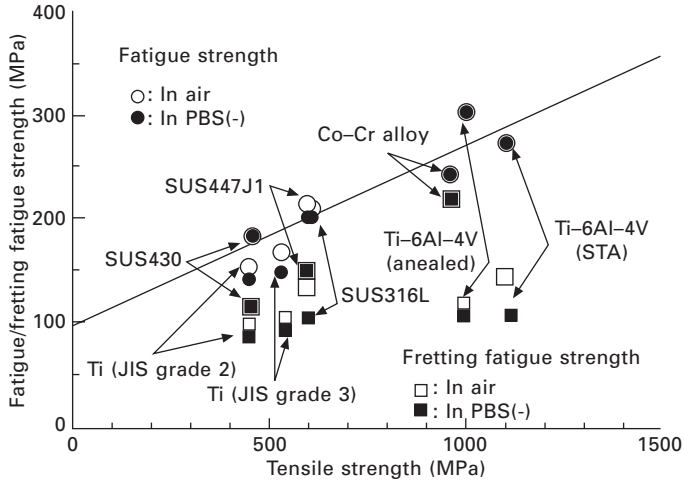

6.18 Relationship between tensile strength and fatigue strength/fretting fatigue strength at 10^7 cycles in air and PBS(-) for various alloys.

As the tensile strength is higher, the fatigue strength is higher. However, a correlation is not observed between the fretting fatigue strength at 10^7 cycles and the fatigue strength or the tensile strength.

For example, if the plain fatigue strength and the fretting fatigue strength are compared for a Ti–6Al–4V alloy and a Co–Cr alloy with the same tensile strength, approximately 1000MPa, the fretting fatigue strength of the Ti–6Al–4V alloy at 10^7 cycles is lower by half than the fatigue strength. However, the fretting fatigue strength of the Co–Cr alloy at 10^7 cycles is the same as the fatigue strength. This is because the contacting behavior of the area between the pad and the specimen differs from that of the Ti–6V–4Al alloy. On the contact area of the Ti–6Al–4V alloy in PBS(-), wear is relatively small and a crack caused by fretting fatigue grows to failure without being grounded. On the contact area of the Co–Cr alloy in PBS(-), however, significant wear is produced, as shown in Fig. 6.19. Therefore, a crack caused by fretting fatigue is grounded and it is difficult for the crack to propagate. As a result, the fretting fatigue strength is similar to the plain fatigue strength.

Therefore, for orthopedic implants with fretting parts, failure can be prevented by a design that considers the fretting fatigue strength of metallic materials to be used in a simulated body fluid, not by a design based on the required durable years or the fatigue strength. Another method for improving the fretting fatigue characteristics is to provide compressive residual stress by shot-peening treatment.

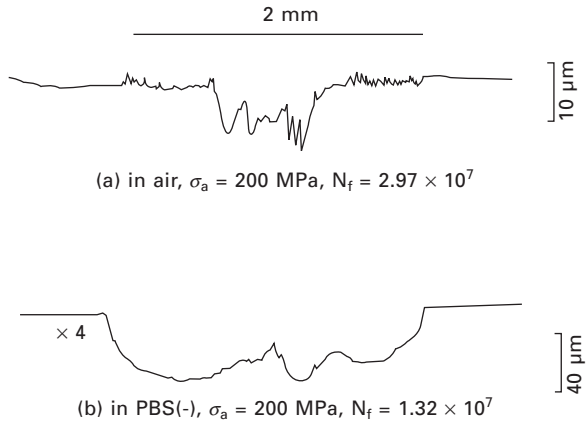

6.19 Cross-sectional profiles on fretted surface for Co–Cr alloy (Maruyama *et al.*, 1999, by courtesy of the Japanese Society for Biomaterials).

6.8 New fatigue tests for metallic biomaterials

The living body contains a large amount of amino acids and proteins. The materials implanted in the body are forced into contact with various cells and textures such as macrophage immune cells. Conventional corrosion fatigue tests for biomaterials have used a simulated body fluid such as normal saline, phosphate buffered saline, etc. Today, however, it is known that macrophage produces the active oxygen that accelerates corrosion of metallic materials through foreign body reaction immediately after insertion of the device, and the environment is more severe than in the conventional simulated body fluids of the ASTM standard (ASTM Standard, F1801–97). Actually, Hayashi and co-workers reported that for a cold-worked SUS316 stainless steel, the fatigue strength (maximum stress) at 5×10^6 cycles in air, in normal saline and in horse blood serum was approximately 850MPa and the fatigue strength of an implant in a rabbit shinbone at 5×10^6 cycles was approximately 700MPa, which is about 150MPa lower (Hayashi *et al.*, 1985).

Maruyama and co-workers developed a system for fatigue tests in a living cell environment similar to that of the living body, instead of the conventional simulated body fluids (Maruyama *et al.*, 2006). As shown in Fig. 6.20, a specimen with cells attached on the surface is inserted into a cell culture chamber kept at 310K and fatigue properties are measured over a long period by conducting cell culture through the circulation of a culture fluid bubbled by an oxygen and carbon dioxide gas mixture. The S–N curve of a SUS316L stainless steel in a macrophage culture environment obtained by this system is shown in Fig. 6.21. As shown in Figures 6.14 and 6.21, the fatigue strength of the SUS316L stainless steel does not change in air, in PBS(-) or in an osteoblast cell L929 culture environment. However, the fatigue strength in a macrophage culture

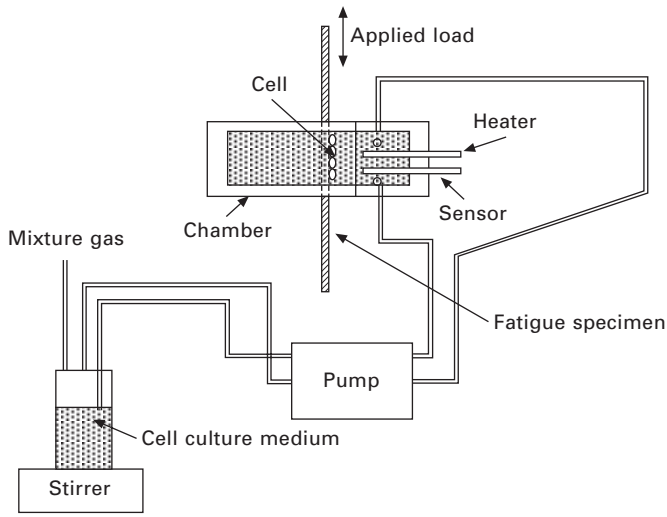

6.20 Schematic diagram of cell culture system for fatigue test.

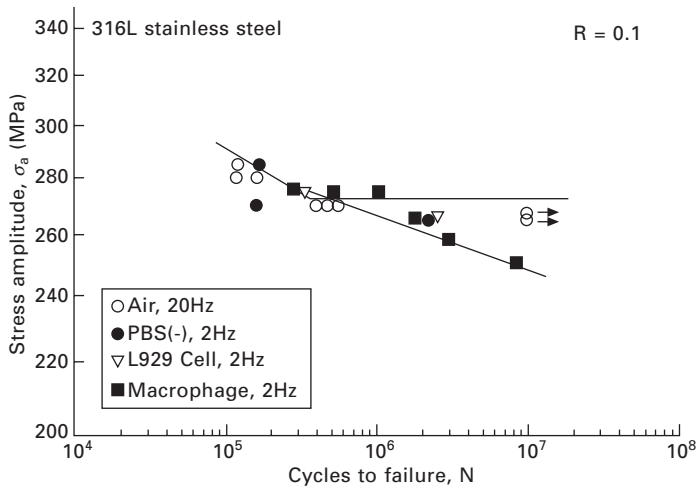

6.21 S–N curves under the various types of environment for 316L stainless steel.

environment is lowered by approximately 30MPa in the high-cycle region. As described in Section 6.6, this shows that different factors affect metallic biomaterial in the living body environment and in simulated body fluids.

6.9 Acknowledgements

The author is greatly indebted to The Iron and Steel Institute of Japan, The Japanese Society for Biomaterials and The Japan Institute of Metals for providing the figures.

6.10 References

ASTM Standard F897-84, *Standard Test Method for Measuring Fretting Corrosion of Osteosynthesis Plates and Screws*.

ASTM Standard F1801-97, *Standard Practice for Corrosion Fatigue Testing of Metallic Implant Materials*.

Hayashi H., Sasada T., Morita M., Tsukamoto Y. and Nishi H. (1985), 'Tensile fatigue test of metallic materials in living body', *Biomaterials*, 3, 143–149.

Hench L. L. and Ethridge E. C. (1975), 'Biomaterials – The interfacial problem', *Adv. Biomed. Eng,* 5, 35–150.

Klesnil M. and Lukas P. (1984), *Fatigue of Metallic Materials* (Japanese Translation by Araki, T. and Horibe, S.), Yokendo.

Maruyama N., Sumita M. and Nakazawa K. (1990), 'Fretting Fatigue Strength Analysis of Ti–6Al–4V in Air'; *Tetsu-to-Hagane*, 76, 262–269.

Maruyama M., Kobayashi T. and Sumita M. (1995), 'Fretting fatigue strength of a Ti–6Al–4V alloy in a pseudo-body-fluid and quantitative analysis of the substances in the fluids', *J Japan. Soc. Biomater.* 13, 14–20.

Maruyama N., Kobayashi T., Nakazawa K., Sumita M. and Sato M. (1999), 'Fatigue and fretting fatigue behaviour of Ni free Co–Cr alloy in a pseudo-body fluid', *J. Japan. Soc. Biomater.*,17, 172–179.

Maruyama N., Nakazawa K., Sumita M. and Sato M. (2000), 'Effect of stress frequency on fatigue and fretting life for commercially pure Ti and Ti–6Al–4V alloy in pseudo-body fluid', *J Japan. Soc. Biomater.* 18, 17–23.

Maruyama N., Yamamoto A., Kohyama Y., Hiromoto S. and Nakamura M. (2006), 'Fatigue Properties of SUS316L Stainless Steel in a Macrophage Culture Environment', *Japanese Society for Biomaterials, the 28th Conference Proceedings*.

Mu Y., Kobayashi T., Sumita M., Yamamoto A. and Hanawa T. (2000), 'Metal ion release from titanium with active oxygen species generated by rat macrophages *in vitro*', *J. Biomed, Mater Res.,* 49, 238–243.

Nakazawa K., Sumita M. and Maruyama N. (1992), 'Effect of contact pressure on fretting fatigue of high strength steel and titanium alloy', in *Standardization of Fretting Fatigue Test Methods and Equipment*, *ASTM STP 1159*, 115–125.

Nakazawa K., Sumita M. and Maruyama N. (1999), 'Fatigue and fretting fatigue of austenitic and ferritic stainless steels in pseudo-body fluid', *J Japan Inst. Metals,* 63, 1600–1608.

Nishioka I. and Hirakawa K. (1969), 'Fundamental investigation of fretting fatigue, Part 5: The effect relative slip amplitude', *Bulletin of JSME*, 52, 692–697.

Sasada T., Tsukamoto Y. and Mabuchi K. (1988), *Biotribology – Friction and Lubrication of Joints*, Sangyo Tosho, pp. 123–137.

Waterhouse R. B. (1984), *Fretting Corrosion,* (Japanese Translation by J. Sato), Yokendo, p. 191.

Yamamoto A., Kobayashi T., Maruyama N., Nakazawa K. and Sumita M. (1995), 'Fretting fatigue properties of Ti–GAL–4V alloy in pseudo-body fluid and evaluation of biocompatibility by cell culture method', *J. Japan Inst. Metals,* 59, 463–470.

7

Tribology and tribo-corrosion testing and analysis of metallic biomaterials

Y. YAN, University of Leeds, UK

Abstract: This chapter will explore the path from the field wear problem to the bench test solution. The perspective will be from that of the product designer who is experiencing a wear problem in the field. Attention will be given to extracting the necessary key information in the field problem to assist in the subsequent testing steps. A tribological code is developed to facilitate the transition from the field problem to the bench test. The impact of the selection of contact geometry will be reviewed relative to the various test machines which are available. Many special test variations have been developed over the years and these will be discussed to show the broad spectrum of testing opportunities which exists. Consideration of all the test parameters relative to accelerated tests will be reviewed. The techniques of initial exploratory tests prior to starting the test programme will be reviewed relative to the field problem and the proposed test conditions. Interpretation of the test results will be explained for several test examples.

Key words: tribology, corrosion, tribocorrosion, surface analysis, prostheses, wear, friction.

7.1 Introduction to tribology-related testing

Tribology is defined as the science and technology of interacting surfaces in relative motion. It includes the study and application of the principles of friction, lubrication and wear. The phenomena of tribology have been realized for thousands of years. In 1966, the well known 'Jost Report' was released to the British government. Since then, the word 'tribology' has been widely used and research on this area has been greatly explored. Tribology has become an interdisciplinary area. It is linked with materials, chemistry, physics and even biology.

For materials used in biomedical devices, if there are relative motions involved with interfaces, tribology contact is present. From orthopaedic implants to dental implants to ophthalmic devices, wear and friction of materials are of major importance, together with biocompability. The ultimate goals for such devices are to last longer and be safe to use. However, *in vivo* tests are normally too complicated. Various tribological testing methods and apparatus have been invented to study metallic or non-metallic materials *in vitro*. In this chapter, different testing methods are discussed. Those used to evaluate materials' tribological properties are considered in Section 7.2. For metallic materials, corrosion is also of major concern, especially for those

materials under tribological contact. Section 7.3 presents new research on interactions of tribology and corrosion, namely tribocorrosion. After testing, materials always undergo analysis processes to determine the damage and mechanisms. A brief introduction on the most commonly used surface analysis techniques is included in Section 7.4. Comments on future trends in tribology and tribocorrosion testing are presented in the last part of this chapter.

7.2 General testing methods for tribological properties

In order to increase the service life, to provide reliable performance, and to reduce cost and maintenance, wear tests are used to provide data and engineering information for specific applications, for instance, biomedical devices. They can help to improve material selection and the design of devices. The mechanisms of tribology are complex. The nature of the applications is different. There is no single or universal testing method for tribology. In a tribological system, wear, friction and lubrication are the triangle. Hence, tribology test selection and use is a key aspect in the overall consideration of wear testing. A recent survey by the National Physical Laboratory (NPL, 1997) in the UK identified over 400 wear testing standards in use around the world. A review by the American Society of Lubrication Engineers in 1973 identified 300 tests that were in use in various test laboratories (ASTM, 1992). However, many of these tests are slight variations on others, and the true number of tests available is probably less than 100. So the question is what method or methods should be chosen for a particular problem.

7.2.1 Types of wear

Failures can generally be reduced but this requires an understanding and identification of wear mechanisms involved. This is an area where experience is particularly valuable. Researchers can find useful information and data from handbooks and guidebooks. However, previous experience may not be adequate to tackle the specific problem encountered. It will then be necessary to obtain a basic knowledge of the wear performance of different materials when subjected to different types of wear. This can be obtained by carrying out comparative and controlled wear tests in laboratories. The various types of wear tests that are available therefore need to be reviewed, and matched to the various guidance on the selection of tests where they are likely to give valid information on the relative wear performance of various materials in practical applications.

Wear is progressive damage to a surface caused by relative motion with respect to another substance (ASM, 1992). One key point is that wear is

damage and it is not limited to loss of material from a surface. Sometimes it would be the change in the geometry or dimension or cracks in a surface. The main types of wear are shown in Table 7.1 and detail is decried in the following paragraphs.

Wear mechanisms can be identified by the appearance of the worn surface and the nature of the application (Williams, 1994). However, in a tribology situation, there is normally not a simple wear process. More than one mechanism can be present in a particular application.

7.2.2 Selection of wear testing

A type of wear testing is chosen in the laboratory to simulate the real conditions for tribological problems. The focus is to select a design which can achieve not only a good material selection but also general engineering information. Figure 7.1 summarizes the configuration of different test rigs.

Figure 7.1 (a) is a pin-on-plate configuration. It can provide either a plane-on-plane contact or a point-on-plane contact. Normally, a point-on-

Table 7.1 Types of wear mechanisms

Type of wear mechanism	Cause and behaviour
Abrasive wear	Abrasive wear is caused by hard particles trapped between moving surfaces, which results in grooves, scratches or indentations on a surface.
Adhesive wear	When two surfaces come into contact, they adhere to one another at localized sites. As they move relatively, wear occurs by one surface pulling the material out of the other surfaces at these sites. Transferred materials can be seen on surfaces.
Fretting	Fretting occurs when there are small oscillatory movements between two surfaces.
Erosion	Erosion involves the removal of material from the surface by impact of a liquid or a stream of hard particles.
Cavitation	Cavitation can be seen as a type of erosion. However, it arises from the intense local impact of the collapse of vapour bubbles onto the surface.
Corrosive wear	When the tribological contacts are in a corrosive environment, both chemical/electrochemical and tribology are the controlling factors. The growth and removal of oxide layers/tribofilm controls the wear rate.
Thermal wear	Material can be removed due to the result of local transient heating or recreated surface temperature.
Fatigue	Fatigue can lead to the loss of material then failure when cracks in the surface join together. Cracks can occur due to high local contact stress.

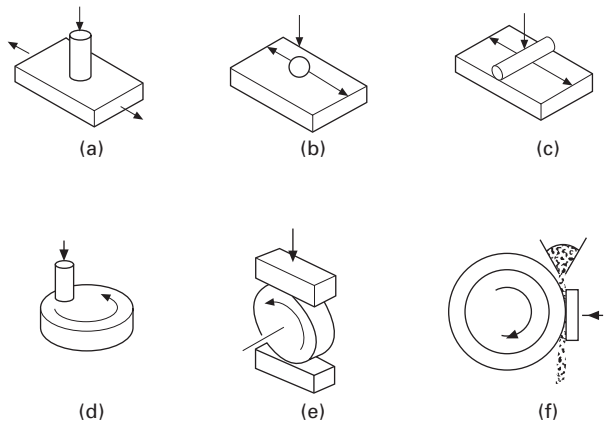

7.1 Configuration of various test rigs (a) pin-on-plate (b) ball-on-plate (c) cylinder on plate (d) pin on rotating disc (e) block on rotating wheel and (f) abrasive with plate on rotating wheel.

plane contact is chosen to have an accurate alignment of the pin, which has a spherical end. A ball-on-plate configuration is shown in Fig. 7.1 (b). It has a point-on-plane contact. Figure 7.1 (c) shows a cylinder-on-plane test. The contact is line-on-plane. A pin on a rotating disc configuration is shown in Fig. 7.1 (d), where the wear surface is a ring shape. The difference is that it involves two directional movement. A rolling and sliding motion is achieved in Fig. 7.1 (e). The wheel disc rotates with a stationary plate or a reciprocating plate. Figure 7.1 (f) presents tests of abrasive wear caused by particles. The plate is held against a rotating wheel with a feed of loose abrasive to the interface.

Before the decision of which wear testing is made, several conditions and parameters should be considered. A summary for biomedical wear testing is shown in Table 7.2.

Because of the simplicity of wear tests, they can provide very general reference data for an evaluation of materials and environmental conditions for an application. However, they are only a simulation of the real application. The critical point is to choose a similar configuration that is reasonable representation of the practical situation. The most important objective in a test is to reproduce the dominant wear mechanism (Neale and Gee, 2000).

7.2.3 Friction

Friction is the force resisting the relative motion of two surfaces in contact or a surface in contact with a fluid. When contacting surfaces move relative to each other, the friction between the two surfaces converts kinetic energy into thermal energy or heat. A widely used parameter to characterize friction is the

Table 7.2 Parameters to be considered for wear tests

Parameter/condition	Example
Materials	Metals (Ti and Ti alloys, Co alloys, stainless steel, etc.), non-metallic (ceramics, bioglass, polymer, etc.)
Lubrication	Blood, serum, synovial fluid, saliva, physiological saline (0.9% NaCl), etc.
Geometry	Point-on-plane, plane-on-plane, ball-on-socket, etc.
Motion	Unidirectional reciprocation, multidirectional, fretting (nano-, micro-motion), rotation, etc.
Loading	Value of load (body weight, etc.), constant loading, cyclic loading, etc.
Environment	Corrosive, temperature (36 °C–37 °C), etc.

Table 7.3 Typical friction coefficients for various materials

Combination	Friction coefficient
Steel on steel (dry)	0.4–0.7
Steel on steel (water)	0.2–0.4
Steel on steel (oil)	0.1–0.3
Wood on steel (dry)	0.2–0.6
Rubber on steel (dry)	0.4–0.7
Rubber on steel (water)	0.3–0.9
Contact lenses (hydrated)	0.05–0.1
Synovial joint	0.001–0.05

friction coefficient (or the coefficient of friction). It is a dimensionless scalar value (μ) to describing the ratio of the frictional force between two surfaces (F_f) and the force applied on them (F_n). It is explained in Eq. 7.1:

$$F_f = \mu F_n \qquad [7.1]$$

In a sliding and/or rolling wear situation, it is generally desirable to measure or monitor frictional behaviour during the test. The correlation of frictional changes with wear behaviour frequently provides useful information regarding mechanisms and modelling. There are two categories for friction: (a) static friction – when two objects are not moving relative to each other and (b) kinetic friction (dynamic friction) – when two objects are moving relative to each other (Loomis, 1985). In this chapter, the friction referred to is dynamic friction. Table 7.3 shows typical friction coefficients under dry and lubricated conditions. Friction can relate to the comfort or otherwise of biomedical devices, such as contact lenses. Low friction is also desirable for orthopaedic joint implants. Squeaking of hip prostheses may be associated with vibration caused by high frictional forces (Bayer, 2004; Hutchings, 1992). In tribological tests, friction force is always measured by transducers

or load cells then divided by the normal applied load to obtain the friction coefficient.

7.2.4 Lubrication and lubricant

Lubrication regime is defined by the lambda ratio (λ). The lambda ratio is the minimum film thickness (h_{min}) in relation to the composite surface roughness (R_{a1} and R_{a2}):

$$\lambda = \frac{h_{min}}{\sqrt{R_{a1}^2 + R_{a2}^2}} \qquad [7.2]$$

Stribeck (Stachowiak and Batchelor, 2001) demonstrated that the coefficient of friction is directly proportional to the viscosity of the lubricant and the difference in speed of the contact surfaces; and inversely proportional to the pressure which is exerted on the contact surfaces. Figure 7.2 shows the Stribeck curve which is the friction coefficient against the bearing number: $\mu\omega/p$ (lubricant viscosity (η), speed (ω) and contact pressure (p)). There are three regimes as defined from the Stribeck diagram: boundary lubrication, mixed lubrication and hydrodynamic lubrication.

At lambda ratio values lower than 1, it is conventionally supposed that asperity interaction becomes more severe and that the shear properties of the films on the solid surfaces, whether formed by adsorption or reaction, become significant. This regime is called boundary lubrication. In the boundary lubrication regime, the physical properties of the bulk lubricant (such as density and viscosity) are not as important as the chemical properties of the

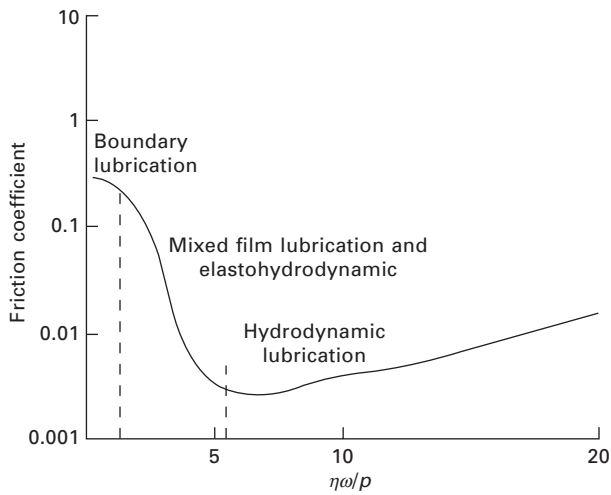

7.2 Friction coefficient as a function of the bearing number.

lubricant and the properties of the surfaces in contact. In animal or human joints and some hip replacements, the lubrication regime is in boundary lubrication (Jin *et al.*, 2000; Totten and Liang, 2004). However, for other hip replacements, the lubrication regime can be mixed lubrication (Jin *et al.*, 1997). Therefore, the boundary and mixed lubrication regimes are of primary importance in joint tribology.

If the lambda ratio is very much greater than unity, so that the film is thick, then the traction or friction force will be a function of the bulk rheological properties of the lubricant under the appropriate operating conditions of load, temperature, shear rate and so on. The influence of the surface roughness will be negligible. This regime is called full film lubrication or hydrodynamic lubrication. Full film lubrication is the most desirable form of lubrication. In this case the surfaces are not in contact so the resistance to their tangential motion, friction force, is dependent primarily on the viscosity of the lubricant (Stachowiak and Batchelor, 2001). Also since in theory there is essentially no contact between surfaces, no wear should occur.

When the film thickness and the surface roughness are of comparable dimensions ($1< \lambda <5$), then the traction will still be determined by the bulk properties of the lubricant but the local contact conditions of asperity interaction will need to be considered (Stachowiak and Batchelor, 2001). Since the lubrication is a mix of full film lubrication and some asperity contact, the regime is called the mixed lubrication regime. On further decreasing the speed and at very high specific loads, full film lubrication is difficult to maintain and, despite the presence of micro elasto-hydrodynamic-lubrication (EHL), there will be some mechanical interactions between opposing surface asperities. In this regime, the lubricant film provides partial separation (Totten and Liang, 2004). The contact load is shared between the contacting asperities and the film when mixed lubrication prevails.

As shown in Table 7.2, several lubricants can be used in simulation wear tests. It depends on the application. For contact lenses, physiological saline solution is normally employed. For dental implants, both sodium chloride solution (0.9%) and saliva solution are used. Serum and synovial fluid are studied in joint prostheses application. Table 7.4 shows the normal composition of bovine serum, which may be used in same tests. Apart from the lubricants mentioned above, wear tests and corrosion tests are also carried out in other solutions, such as Ringer's solution containing sodium ion, potassium ion, calcium ion and chloride ion.

7.3 Tribo-corrosion testing

Tribocorrosion is defined as the chemical/electrochemical and mechanical processes leading to a degradation of material under tribological contacts in a corrosive environment (Landolt *et al.*, 2001; Mischler *et al.*, 1999). It is

Table 7.4 Quality profile of bovine serum (Harlan® SERA-LAB, pH = 7.2 – 7.4)

Element	Quality profile	Element	Quality profile
Sodium	140 mmol/L	AST	32 U/L
Potassium	8.0 mmol/L	ALT	12 U/L
Glucose	6.7 mmol/L	LDH	809 U/L
Urea	6.4 mmol/L	Amylase	33 U/L
Total protein	61.83 g/L	Triglyceride	0.88 mmol/L
Albumin	32 g/L	Cholesterol	1.8 mmol/L
Calcium	1.97 mmol/L	Magnesium	1.22 mmol/L
Phosphate	3.02 mmol/L	Iron	19 μmol/L
Total bilirubin	7 μmol/L	Immunoglobulins	8.2 g/L

an irreversible transformation. Material degradation due to the combination of mechanical and electrochemical processes may occur under a variety of conditions. A sliding movement between two surfaces under two-body or three-body (i.e. with debris) contact is a common cause of tribocorrosion. With micromotion involved, fretting-corrosion is a special type of tribocorrosion. Tribocorrosion is also observed in ball bearings under rolling contact. Particle impact or impingement can also result in a combined mechanical, chemical, electrochemical attack of material.

The selection of metals in biomedical devices aims to choose materials which have very high corrosion resistance. A stable passive film on the metallic material surface can protect it from corrosion attack. Under mechanical relative movement, oxide films on passive metals can be locally or even completely destroyed. Accelerated corrosion has been found by different studies (Landolt *et al.*, 2001; Rossi *et al.*, 2000). It is generally believed that wear will enhance corrosion rate.

An electrochemical approach offers opportunities to control the surface chemistry of the material under tribological contact, as related in the next sat-Sections. The current change can be monitored by holding a certain potential. The fundamental work suggests that the passive film plays an important role on mechanical degradation.

7.3.1 Bench tests

A new material combination has to undergo stringent wear testing before being adopted as fit for use in manufacturing prosthetic joints. Simple configuration wear testing has been used extensively as an ideal method for screening novel materials, and comparing them with existing ones, for use in joint replacements, prior to more complex joint simulator tests. At a fractional cost of a full simulator wear test, the reciprocating ball-on-plate apparatus has enabled better control of the individual tribological variables, leading

to a better understanding of how these tribological factors independently influence the wear mechanisms and corrosion behaviour. These simple tests also provide important information about the relative wear and wear-corrosion performance of bearing materials.

An integrated three-electrode cell can be used to determine electrochemical behaviour under tribological contacts (Fig. 7.3). These three electrodes are:

- working electrode (WE): the specimen
- reference electrode (RE): single Ag/AgCl electrode
- counter electrode (CE): a platinum wire/mesh.

Some electrochemical techniques can be performed to understand the complex tribocorrosion behaviours.

The free corrosion potential measurement

At the free corrosion potential (E_{corr}), the anodic reaction rate is equal to the cathodic reaction rate and so there is no net current flow to or from the electrode The value of E_{corr} is often used to give a qualitative indication of the corrosion regime (active or passive) in which a material resides. It can provide a useful way to differentiate conditions of *active* corrosion from *passive* conditions. In such a study, Yan *et al.*, 2006a) measurement of E_{corr} was used to assess (a) how the action of a sliding counterface, against a passive alloy affects the passivity of the alloy and (b) how the material 'recovers' once the sliding wear ceases and passivity is re-established. In this work E_{corr} was monitored under static conditions, under the action of sliding wear and once sliding wear, ceased, as the material passivity was re-established (Fig. 7.4).

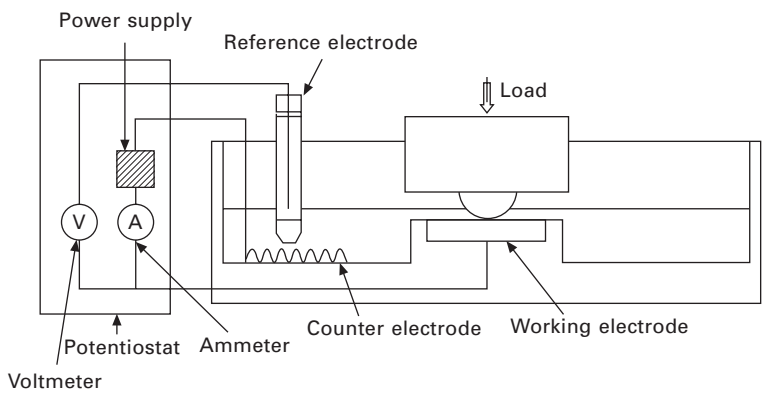

7.3 Schematic representation of integrated three-electrode cell.

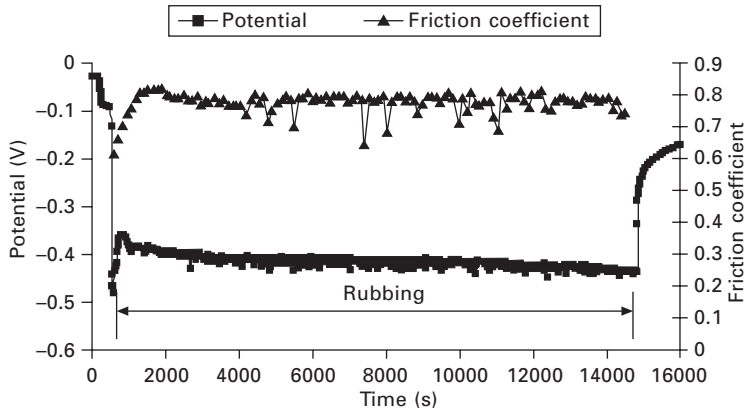

7.4 Open circuit potential as a function of sliding time for a Co–Cr–Mo alloy in serum at 37 °C.

Anodic polarization scans

In anodic polarization tests, the rate of metal dissolution (anodic) processes can be determined. In one study (Yan *et al.*, 2006b), the key purpose was to monitor the extent of passivity of the surface. This was done by using a standard 3-electrode cell and involved using a computer-controlled potentiostat to shift (at a rate of 15mV/min) the potential of the working electrode (WE) from the free corrosion potential, E_{corr}, in the positive direction. This leads to the WE (sample) becoming a net anode, and by analyzing the rate of charge transfer as a function of potential, the corrosion behaviour can be evaluated. The overpotential (the shift from E_{corr}) is the driving force for passivity breakdown and the magnitude of the breakdown potential (E_b), defined as the potential where the current in the 3-electrode cell increases rapidly, gives a measure of the resistance of the passive film to localized corrosion initiation. For passive materials, the current will stay very low in the passive region, normally less than 10 $\mu A/cm^2$, because of the protective passive film. For active materials, where there is no protective film formed on the surface, the current will increase immediately on shifting the potential from E_{corr} (Fig. 7.5).

Linear polarization resistance tests

A linear polarization resistance (LPR) test is a corrosion rate monitoring method and it can give an indication of the corrosion resistance of materials in an aqueous environment (Yan *et al.*, 2006c). LPR tests are performed both in the static condition and under reciprocating motion. With the material under sliding conditions, LPR tests are conducted every hour up to 8 hours. In LPR tests, potential is shifted from 50 mV below E_{corr} (more negative than E_{corr}) to

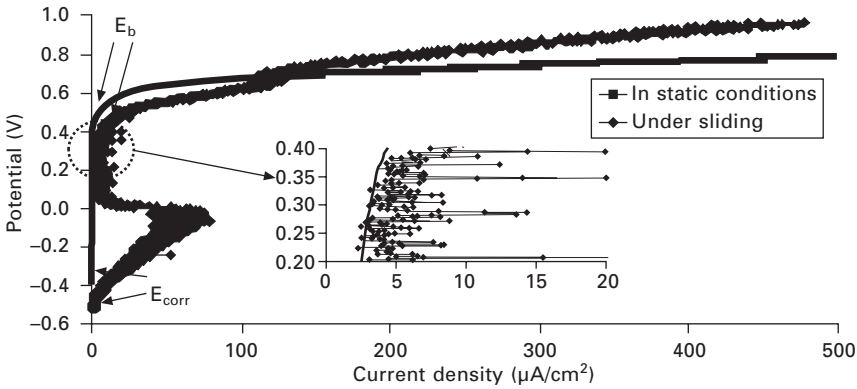

7.5 Anodic polarization curves for a Co–Cr–Mo alloy in serum in static and under sliding condition at 37 °C.

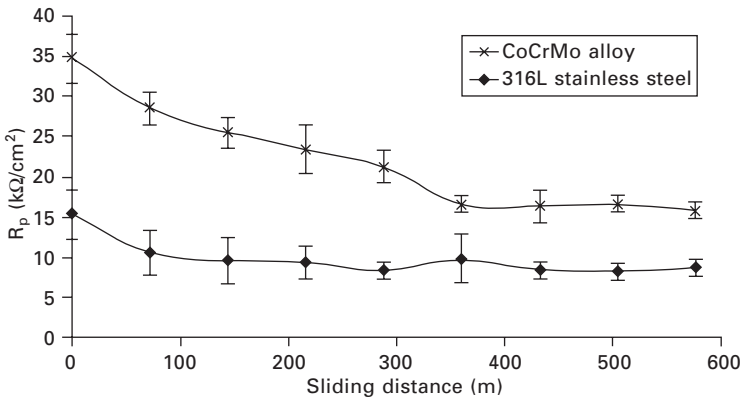

7.6 Corrosion resistance for a Co–Cr–Mo alloy and SUS 316L stainless steel in serum under sliding condition at 37 °C.

50 mV more positive than E_{corr}. Current flow between the specimen and the counter electrode is monitored. A linear relationship of potential and current values can be observed. The value of $\Delta E/\Delta i$ is calculated (Fig. 7.6).

Cathodic protection

One of the main aims of work is to establish the extent of interactions between wear and corrosion processes. The most effective means of achieving isolation of the *wear* component of degradation is to completely stop any charge transfer (corrosion) at the working electrode surface. Cathodic protection (CP), by the impressed current method, is a widely used technique to control corrosion and sliding wear tests under CP have enabled the wear material loss to be determined (Yan *et al.*, 2006c). The applied potential used can be

0.8V (Ag/AgCl), chosen to be more negative than the equilibrium electrode potential for the Co/Co^{2+} reaction yet sufficiently noble enough to prevent hydrogen-evolution at the surface which would inevitably affect the wear process. Pourbaix E-pH diagrams can assist to choose an appropriate potential value to be applied.

Quantification of corrosion-related damage

To date, there have been a few studies that attempted to quantify the contributions of material degradation (T) due to corrosion, wear and their interactions in a biotribocorrosion environment where active biological solutions or saline solutions are used (Barril *et al.*, 2004; Yan *et al.*, 2006a). This can be done by considering Eq. 7.3 which allows the quantities of corrosion, wear and corrosion-wear to be analyzed.

$$T = W + C' + S \qquad [7.3]$$

where W is the material loss in the absence of corrosion, which was measured by applying CP. C' is the material loss due to electrochemial processes (corrosion) in the absence of wear. The synergy S includes two components which are

- the effect of wear on corrosion (C_w) and
- the corrosion effect on wear (W_c).

Corrosion-related damage ($C'+ S$) can therefore be assessed. It should be remembered that this is not only the corrosion rate – it is the damage that corrosion processes do when wear–corrosion processes occur in parallel. Hence it is referred to as *corrosion-related damage* rather than corrosion damage.

7.3.2 Simulator studies

For orthopaedic implants, their movement and loading conditions are much more complicated than in bench tests. The latter provide an initial validation and view of the combination and contribution of tribological contacts and corrosion reactions. More realistic simulators have been used to determine the wear rate for hip/knee prostheses.

The phenomena of running-in state and steady state have been recognized in many applications when wear is presented (Dowson *et al.*, 2004a). Many authors have been studying metal-on-metal (MoM) total hip replacements' wear behaviour *in vivo* and *in vitro*. Two distinct wear phases were discernible for MoM joints. A running-in (or bedding-in, wearing-in) stage, followed by a lower wear rate steady-state stage (Dowson *et al.*, 2004b) (Fig. 7.7). The length of the running-in state varies depending on the different simulators

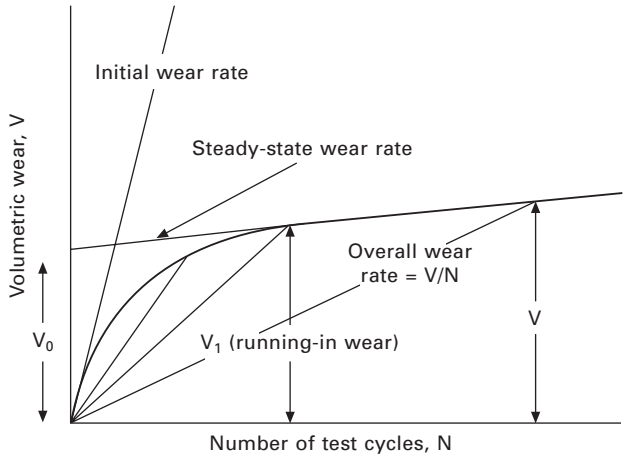

7.7 Basic features of volumetric wear for joint simulator tests.

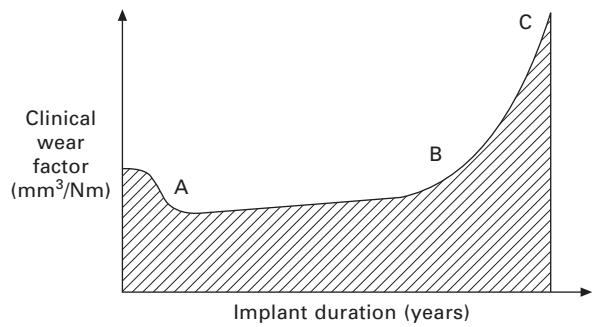

7.8 Clinical wear rate for total hip replacements.

and geometry of contacts (pin-on-plate, ball-on-plate etc.) from thousands of cycles up to about 1 million cycles (Dowson *et al.*, 1998; Katti, 2004; Stemp *et al.*, 2003). Generally, after 1 million cycles *in vitro* and 1 year *in vivo*, implants are considered to reach a steady state. Small wear debris particles are created mostly in the running-in phase and cause abrasive wear. From clinical examinations for the first few days after implantation of MoM joints, metal ions were found to increase dramatically. The metal ion levels then stabilized (Dowson *et al.*, 2004b; Lemons and Lucas, 1986), which is possibly related to the biphasic (running-in and steady-state) wear phenomena and the saturation of metal ions in the body. As shown in Fig. 7.8, from the clinical wear factor a stable wear factor was reached in region A to B after the initial relatively high wear rate (before A). It is considered that a running-in process is present before point A, as mentioned previously, the

duration being about 1 year. Then the wear dramatically accelerated (region B to C) due to the failure of devices.

Several parameters are used to quantify or evaluate material wear. Material total weight or volume loss is the most common one. The depth or width of the wear scar is also used. However, those values show no association with testing conditions. Wear factor (k) has been suggested as more appropriate. It is proportional with total wear and applied load and sliding distance. The calculation is shown in Eq. 7.4:

$$k = \frac{\text{Wear volume}}{\text{Applied load} \times \text{sliding distance}} \ (\text{mm}^3/\text{Nm}) \qquad [7.4]$$

Figure 7.9 shows the force change during a cycle of walking. A peak load of more than four times bodyweight was obtained when the action of heel strike was made. Two phases in the human hip joint are classified during a normal walking cycle. In the stance phase, the hip joint carries a very high load and the relative movement in the joint (between femoral head and socket) is small. In the swing phase, even though the load on the joint is lower than in the stance phase, the movement of the joint is greater. Some authors believe that the material degradation (wear) progresses severely in this phase (Dowson and Jin, 2006). For the Leeds hip simulators (Fig. 7.10),

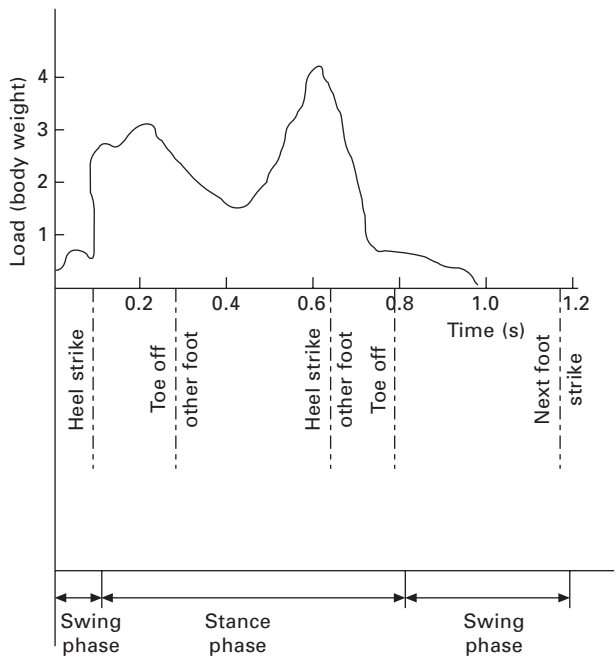

7.9 Hip joint force during one cycle of walking.

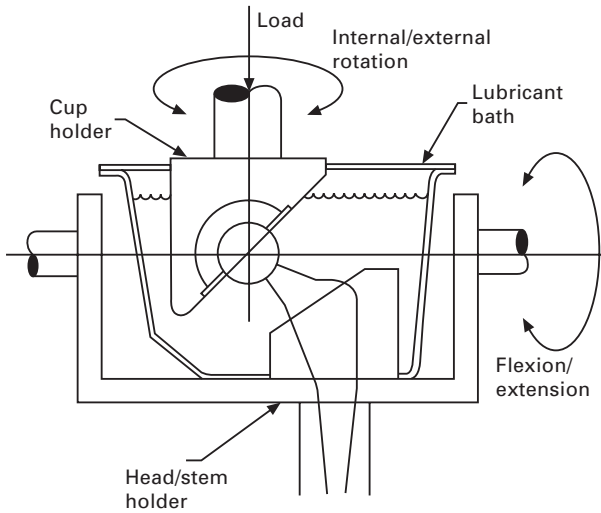

7.10 Schematic diagram for a hip simulator.

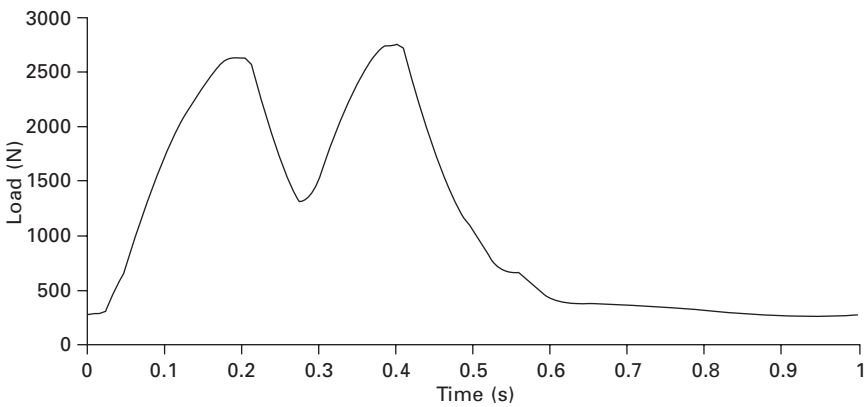

7.11 Load profile applied in hip simulators.

load is applied on the femoral head as shown in Fig. 7.11. It is very similar to the walking cycles shown in Fig. 7.9.

7.4 Surface analysis for tribology and tribo-corrosion properties

In order to understand the mechanisms and behaviour of materials' surfaces after wear tests, surface analysis techniques have been widely used. Over the years, an enormous number of techniques have been developed to probe different aspects of the physics and chemistry of surfaces. It is obvious that

the surface properties of solids are influenced to a large extent by the solid state properties of the material. After wear testing, normally there is a thin film which covers the worn area, namely a tribofilm. The thickness of the tribofilm differs over various applications and conditions. To determine the properties of the tribofilm is the goal of applying surfaces analysis.

For the examination conditions, surface analysis techniques can be divided to (a) vacuum system (including high vacuum and ultra high vacuum) and (b) normal air pressure condition. For surfaces' properties, there are two categories (a) physical properties and (b) chemical properties. To obtain the chemical composition or structure detail of surfaces, most of the techniques require the surfaces to be bombarded with photons, electrons or ions. Those techniques normally need to be operated under a vacuum condition. However, for Raman spectroscopy (RS) and Fourier transform infrared spectroscopy (FTIR), samples do not need to be placed in a vacuum chamber. Techniques for determining surfaces' mechanical properties, appearance or topography can be used in normal lab conditions, such as nano-indentation, atomic force microscopy (AFM), ellipsometry, etc. To choose which analysis technique(s) to use, the basic principles of those technique(s) need to be known prior to the sample examination. The detection limits, advantages and disadvantages of different methods should be considered. Figure 7.12 shows the lateral and depth resolution for some surface analysis techniques. In this section, some commonly used surface analysis techniques are introduced.

7.4.1 Scanning electron microscopy (SEM)

Scanning electron microscopy (SEM) images the sample surface by scanning it with a high-energy beam of electrons in a raster scan pattern. The primary

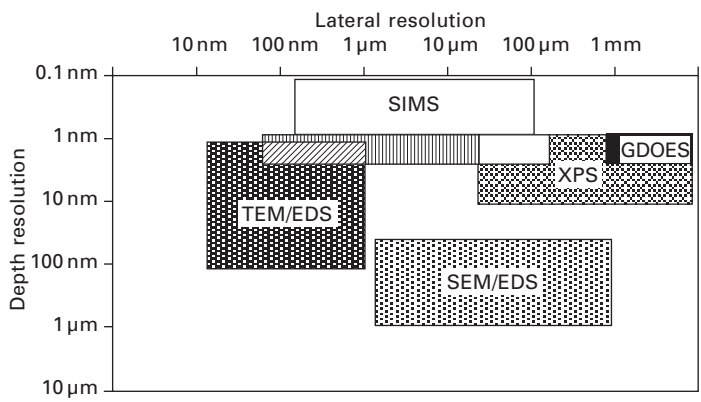

7.12 Comparison of various surface analysis techniques for their lateral resolution and depth resolution.

electron beam, which is produced under high vacuum, is scanned across the surface of a specimen. When the electrons strike the specimen, a variation of the signal produces an image of the surface, or its elemental composition together with energy dispersive X-rays (EDX). An SEM image is shown in Fig. 7.13 (a). Clear grooves can be seen at the bottom half of the image. This indicates debris generated by tribological contacts trapped in the contact. They scratch the sample surface which resulted in wear. Several functions have been developed with the principles of SEM to have a better understanding of material surfaces. Back scattered electrons (BSE) are bem electrons that are reflected from the sample by elastic scattering. BSE images can provide information about the distribution of different elements in the sample according to their atomic number. Field emission guns SEM (FEG SEM) enables a higher resolution and magnification, which is widely used in nanotechnology and biomedical fields. Figure 7.13 (b) shows a nanoparticle from FEG SEM. One of the latest innovation in SEM is environmental scanning electron microscopy (ESEM). It differs from conventional SEM in two crucial aspects. Firstly, it allows the introduction of a gaseous environment in the specimen chamber although the electron gun is kept under the standard SEM high vacuum. Secondly, non-conductive samples, such as fibers, wood, polymer, etc. do not need to be coated with a carbon or metallic layer, as is the case with conventional SEM.

7.4.2 X-ray photoelectron spectroscopy (XPS)

X-ray photoelectron spectroscopy (XPS) is a powerful technique widely used for surface analysis of materials. In one particular machine (Beamson *et al.*, 1990) a high-power monochromatized Al K_α X-ray source ($h\nu$ = 1486.6 eV), high transmission electron optics and multi-channel detector are employed. Using this machine, *survey scans* and more detailed *region scans* were run

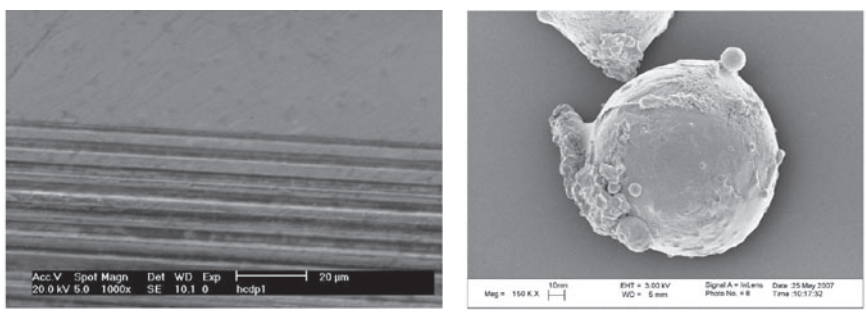

(a) (b)

7.13 SEM images for (a) wear scar on a Co–Cr–Mo alloy and (b) a nanometallic particle.

at 300 eV pass energy and 0.8 mm slit width. Although X-rays penetrate to a depth of several micrometers, ejected photoelectrons generally come from only the first several nanometres of material. In XPS, the photon is absorbed by an atom in a molecule or solid, leading to ionization and the emission of a core (inner shell) electron. The binding energy (BE) is taken to be a direct measure of the energy required to remove the electron from its initial level to the vacuum level. In order to assess the variation of composition as a function of depth, the samples were subjected to argon-ion bombardment for various times. A schematic diagram of XPS is shown in Fig. 7.14.

The high X-ray power rotating anode has a maximum power rating of 8kW, a factor of thirteen higher than a typical power of 600W for a conventional fixed anode source. A large, seven crystal, double focusing monochromator focuses the X-ray onto an area 6 mm by 0.3 mm. The beam line is then focused in the middle of the wear scar in an area of 400 μm by 300 μm. The Al K_α(1486.7 eV) line profile has a 'full width at half maximum' (FWHM) of 0.26 eV, a factor of three narrower than for an unmonochromated Al K_α source. The computer-controlled lens system has two modes of operation: a high transmission mode for optimum acceptance of photoelectrons and an imaging mode for high spatial resolution with <50 μm lateral resolution. The detection system consists of a 300 mm radius hemispherical analyser and a multi-channel detector. This gives an overall instrument resolution of 0.3 eV minimum.

In typical XPS analysis, a survey scan (Fig. 7.15 (a)) is obtained first in order to identify elements present, and then the long scans (Fig. 7.15 (b)) of the selected peaks are obtained in order to determine a more comprehensive picture of the chemical composition.

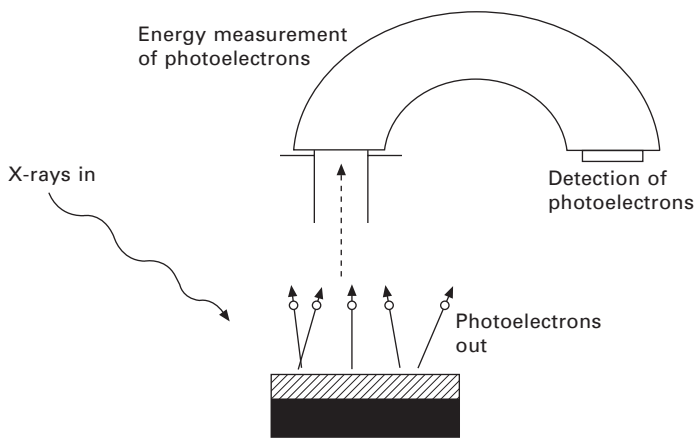

7.14 Schematic representation of XPS.

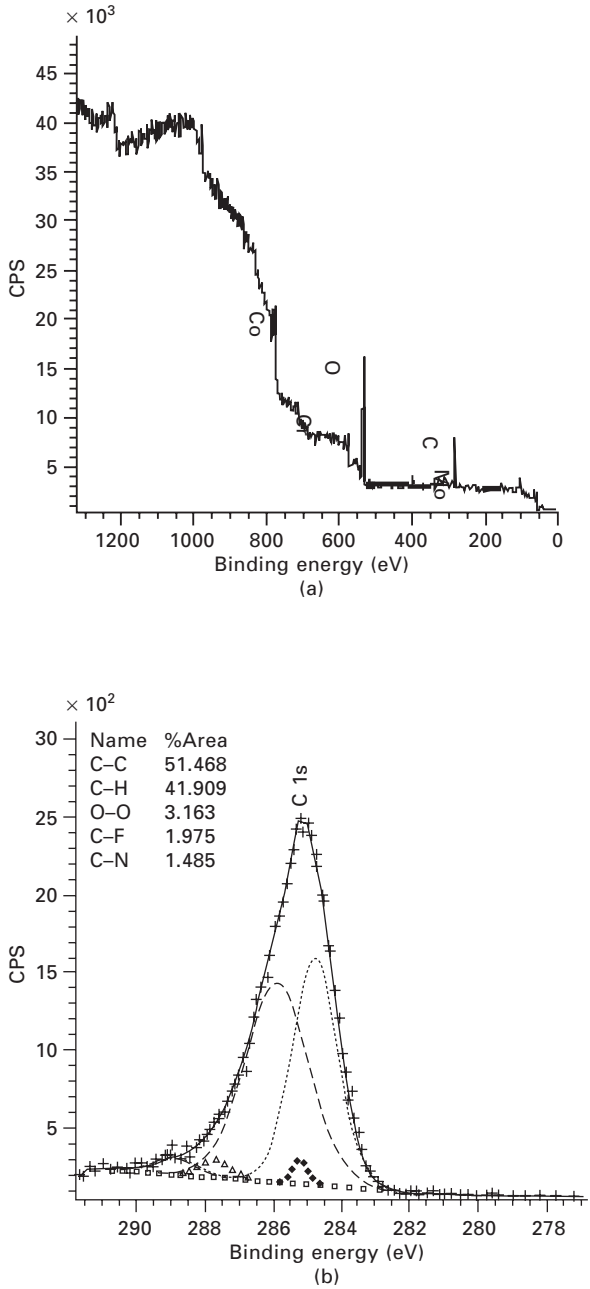

7.15 XPS spectra for the tribofilm on a Co–Cr–Mo alloy in serum (a) survey scan and (b) long scan.

7.4.3 White light interferometry (WLI)

White light interferometry (WLI) is a powerful technique for non-contact measurement of surface topography at high vertical and moderate lateral resolution. The Phase Shifting Interference (PSI) mode was used and the resolution for this mode is 0.3 nm. The Wyko machine has a range of objectives from 2X–50X and has an additional zoom from 0.5–2X called the field-of-view (FOV) objective.

7.4.4 Atomic force microscopy (AFM)

Atomic force microscopy (AFM) is in the family of scanning probe microscopy (SPM). It is very useful to study properties of material from the atomic to the micron level. AFM consists of a microscale cantilever with a sharp tip (probe) at its end that is used to scan the specimen surface. Figure 7.16 shows a schematic diagram of AFM. It is ideally suited to the investigation of topographical structure (having high resolution) along with local surface properties such as local stiffness and adhesion. AFM has normally three imaging modes: (a) contact mode (b) non-contact mode and (c) intermittent contact or tapping mode (Vickerman, 1997; O'Connor, 2003). During scanning in the contact mode, a constant bend in the cantilever is maintained. In non-contact mode, the cantilever oscillates just above the specimen. The tip–specimen separation and the oscillation amplitude are in the order of 1nm to 10nm, which is the main difference to the tapping mode, where the oscillation amplitude of the tip is in the range of 20nm to 200nm. The tapping mode is very useful for soft surfaces, especially biological samples. Figure 7.17 shows images under contact mode for tribofilm on a Co–Cr–Mo alloy.

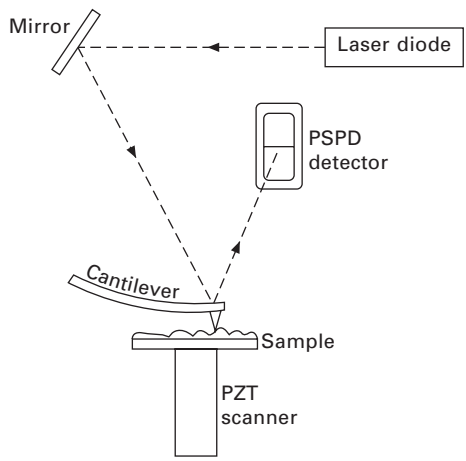

7.16 Schematic diagram of AFM.

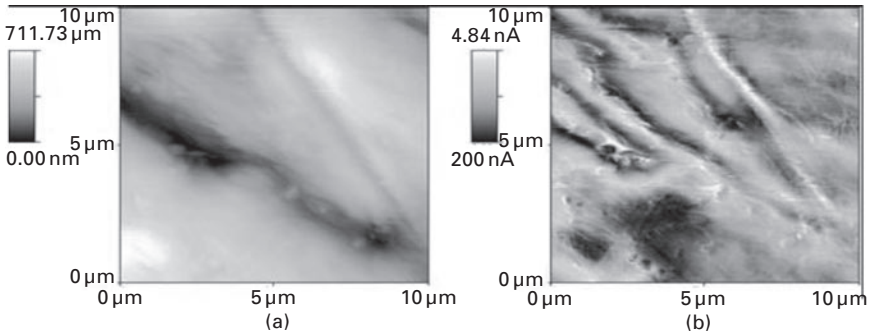

7.17 Typical AFM image of a Co–Cr–Mo alloy surface. (a) Topography and (b) lateral force.

7.4.5 Mass spectroscopy

Surface mass spectroscopy techniques consist of measuring the masses of secondary ions that are ejected, in a process known as sputtering, from the surface of a specimen when a primary beam of energetic particles bombards it. This results in the emission of a range of secondary particles, including positively and negatively charged ions. The secondary ions can provide unique information about the chemistry of the surface from which they originated. It is common practice to use electron spectroscopy in combination with surface mass spectroscopy to characterize the surface chemistry of an unknown specimen. The main methods of surface mass spectroscopy are: secondary ion mass spectroscopy (SIMS), laser ionization mass spectrometry (LIMA) and sputtered neural mass spectrometry (SNMS). SIMS is by far the most commonly used surface spectroscopic technique. It has three basic modes: (a) static SEM – used for sub-monolayer elemental analysis (b) dynamic SIMS – used for obtaining compositional information as a function of depth below the surface and (c) imaging SIMS – used for spatially-resolved elemental analysis (Briggs and Seah, 1990; Vickerman, 1997). A typical SIMS spectra is shown in Fig. 7.18.

7.5 Future trends

Wear testing methods have been developed for hundreds of years. However, with the fast development of materials and exploration of applications, some possible trends can be summarized as follows:

- *In situ, on line wear testing*: Wear tests will be integrated with surface analysis techniques, which will provide real time wear properties – how the tribofilm forms under various conditions and environments. More information will therefore be obtained from a single wear test, such as

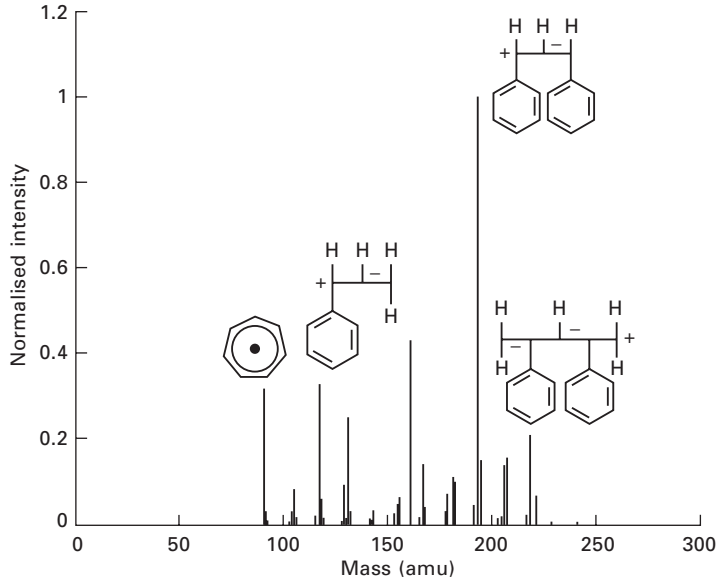

7.18 A typical SIMS spectra.

temperature, contact resistance, corrosion resistance, lubrication film properties, chemical structure changes, etc.

- *Modelling*: General property modelling, where basic mechanical properties are linked to wear behaviour (yield strength, work hardening, ductility, fracture toughness, etc.) will be developed. This is another approach to understanding tribological behaviour. Wear tests will provide a database for future modelling of different materials and conditions.
- *Micro- and nano-tribology*: This involves assemblies of atoms and molecules having at least one nano-scale dimension. Four areas at present relate to nano-tribology: probes; structure; processes; and simulation of tribological systems. Testing methods need to go smaller and smaller.
- *Coatings*: It is clear that coatings have huge potential to reduce wear and friction in a large range of applications and can provide solutions where lubricants cannot be used.
- *Specific wear testing*: More individual wear testing will come along as well as the documented standards. The family of wear testing standards will grow. Unique ways to test unique systems will be developed and invented.

7.6 References

ASM Metals handbook, Vol. 18 (1992), *Friction, Lubrication and Wear Technology*, ASM International.

ASTM STP 1167, *Wear testing of advanced materials*.
Barril S, Mischler S, and Landolt D (2004) Influence of fretting regimes on the tribocorrosion behaviour of Ti6A14V in 0.9 wt.% sodium chloride solution, *Wear*, 256, pp. 963–972.
Bayer R (2004), *Mechanical Wear Fundamentals and Testing*, Marcel Dekker, Inc.
Beamson G, Briggs D, Davies S F, Fletcher I W, Clark D T, Howard J, Gelius U, Wannberg B and Balzer P (1990), Performance and application of the Scienta ESCA300 spectrometer, *Surface and Interface Analysis*, 15, pp. 541–549.
Briggs D and Seah MP (1990), *Practical Surface Analysis*, John Wiley.
Dowson D (1998) *History of Tribology*, London, Professional Engineering Publishing.
Dowson D, Hardaker C, Flett M and Isaac G H (2004a), A hip joint simulator study of the performance of metal-on-metal joints Part I: The role of Materials, *Arthroplasty*, 19, 118–123.
Dowson D, Hardaker C, Flett M and Isaac G H (2004b), A hip joint simulator study of the performance of metal-on-metal joints Part II: Design, *Arthroplasty*, 19, pp. 124–130.
Dowson D and Jin Z M (2006), Metal-on-metal hip joint tribology, *Proc. IMechE Part H: Engineering in Medicine*, 220, pp. 107–118.
Hutchings I M (1992), *Tribology: Friction and Wear of Engineering Materials*, Edward Arnold.
Jin Z M, Dowson D and Fisher J (1997), Analysis of fluid film lubrication in artificial hip joint replacements with surfaces of high elastic modulus, *Proc Instn Mech Engrs Part H: Journal of Engineering in Medicine*, 211, pp. 247–256.
Jin Z M, Firkins P, Farrar R and Fisher J (2000), Analysis and modelling of wear of cobalt-chrome alloys in a pin-on-plate test for a metal-on-metal total hip replacement, *Proc Instn Mech Engrs H*, 214, pp. 559–568.
Katti K S (2004), Biomaterials in total joint replacement, *Colloids and Surfaces*, 39, pp. 133–142.
Landolt D, Mischler S and Stemp M (2001), Electrochemical methods in tribocorrosion: A critical appraisal, *Electrochemica Acta*, 46, pp. 3913–3929.
Lemons J E and Lucas L C (1986), Properties of biomaterials, *Arthroplasty*, 1, pp. 143–147.
Loomis W R (1985), *New Directions in Lubrication, Materials, Wear and Surface Interaction*, Noyes Publications.
Mischler S, Spiegel A and Landolt D (1999), The role of passive oxide film on the degradation of steel in tribocorrosion systems, *Wear*, 225–229, pp. 1078–1087.
Neale M J and Gee M (2000), *Guide to Wear Problems and Testing for Industry*, Professional Engineering Publishing.
NPL Report CMMT (A) 92 (1997), *Wear Testing Methods and their Relevance to Industrial Wear Problems*.
O'Connor D J (2003), *Surface Analysis Methods in Materials Science*, Springer, 31.
Rossi S, Fedrizzi L, Deflorian F and Zen M (2000), Wear-corrosion of nitrided steel: Corrosion potential monitoring to evaluate the effect of test parameters, *Materials and Corrosion*, 51, pp. 552–556.
Stachowiak G W and Batchelor A W (2001), *Engineering Tribology*, Woburn, Butterworth-Heinemann.
Stemp M, Mischler S and Landolt D (2003), The effect of mechanical and electrochemical parameters on the tribocorrosion rate of stainless steel in sulphuric acid, *Wear*, 255, pp. 466–475.

Totten G E and Liang H (2004), *Mechanical Tribology*, New York, Marcel Dekker, Inc.

Vickerman J C (1997), *Surface analysis: The Principal Techniques*. John Wiley & Sons.

Williams J A (1994), *Engineering Triblogy*, Oxford Science Publication.

Yan Y, Neville A and Dowson D (2006a), Understanding the role of corrosion in the degradation of metal-on-metal implants, *Proceeding of The Institution of Mechanical Engineers Part H: Journal of Engineering in Medicine*, 220, pp. 173–180.

Yan Y, Neville A, Dowson D and Williams S (2006b), Tribocorrosion in implants – Assessing high carbon and low carbon Co–Cr–Mo alloys by *in-situ* electrochemical measurements, *Tribology International*, 39, pp. 1509–1517.

Yan Y, Neville A and Dowson D (2006c), Biotribocorrosion – an appraisal of the time dependence of wear and corrosion interactions – Part I: The role of corrosion, *Journal of Physics D: Applied Physics*, 39, pp. 3200–3205.

8

Biocompatibility and fabrication of *in situ* bioceramic coating/titanium alloy biocomposites

C. CUI, Hebei University of Technology, China

Abstract: Ti and its alloys are superior to many other biomaterials in mechanical properties and biocompatibility. They are widely used in biomedical devices and components because of their desirable properties, such as relatively low modulus, good fatigue strength, formability, machinability, corrosion resistance, and biocompatibility. However, they cannot meet all of the clinical requirements. Therefore, in order to improve the biological, chemical, and mechanical properties, surface modification is often performed. This chapter reviews the various surface modification technologies pertaining to Ti and its alloys, including mechanical treatment, thermal spraying, sol–gel, chemical and electrochemical treatment, and ion implantation from the perspective of biomedical engineering. Recent work has shown that the wear resistance, corrosion resistance, and biological properties of Ti and its alloys can be improved selectively using appropriate surface treatment techniques while the desirable bulk attributes of the materials are retained. Some recent applications are also discussed in this chapter.

Key words: biomaterials, titanium alloys, surface treatment, biomedical devices, implants.

8.1 Introduction

As biomaterials, Ti and its alloys are superior to many materials such as stainless steel, pyrolytic carbon and so on, in terms of mechanical properties and biocompatibility. Ti and its alloys are widely used in biomedical devices and components, especially as hard tissue replacements as well as in cardiac and cardiovascular applications, because of their desirable properties, such as relatively low modulus, good fatigue strength, formability, machinability, corrosion resistance, and biocompatibility. However, Ti and its alloys cannot meet all of the clinical requirements. Therefore, in order to improve the biological, chemical, and mechanical properties, surface modification is often performed. This chapter reviews the various surface modification technologies pertaining to Ti and its alloys including mechanical treatment, thermal spraying, sol–gel, chemical and electrochemical treatment, and ion implantation from the perspective of biomedical engineering. Recent work has shown that the wear resistance, corrosion resistance, and biological properties of Ti and its alloys can be improved selectively using the

appropriate surface treatment techniques while the desirable bulk attributes of the materials are retained. Proper surface treatment expands the use of Ti and its alloys in the biomedical fields. Some recent applications are also discussed in this chapter.

8.2 Titanium and its alloys

Ti is one of the transition elements in Group IV and Period 4 of Mendeleev's periodic table. It has an atomic number of 22 and an atomic weight of 47.9. Being a transition element, Ti has an incompletely filled d shell in its electronic structure (Ogden, 1961). Some basic physical properties of unalloyed Ti are summarized in Table 8.1. The incomplete shell enables Ti to form solid solutions with most substitutional elements having a size factor within = 20%. In the elemental form, titanium has a high melting point (1668 °C) and possesses a hexagonal, closely packed crystal structure (hcp: α) up to a temperature of 882.5 °C. Ti transforms into a body centered cubic structure (bcc -β) above this temperature (Collings, 1984). Ti alloys may be classified as α, near-α, $\alpha + \beta$, metastable β, or stable β type alloys depending upon the room temperature microstructure (Polmear, 1981). In this regard, alloying elements for titanium fall into three categories: (i) α-stabilizers, such as aluminum (Al), oxygen (O), nitrogen (N), and carbon (C); (ii) β-stabilizers, such as molybdenum (Mo), vanadium (V), niobium (Nb), and tantalum (Ta)

Table 8.1 Summary of physical properties of unalloyed titanium

Property	Value
Atomic number	22
Atomic weight (g/mol)	47.9
Crystal structure	
Alpha	Hexagonal, closely packed
c (Å)	4.6832 ± 0.0004
a (Å)	2.9504 ± 0.0004
Beta	Cubic, body centered
a (Å)	3.28 ± 0.003
Density (g cm^{-3})	4.54
Coefficient of thermal expansion, α, at 20 °C (K^{-1})	8.4×10^{-6}
Thermal conductivity (W/(m K))	19.2
Melting temperature (°C)	1668
Boiling temperature (°C)	3260
Transformation temperature (°C)	882.5
Electrical resistivity	
High purity (μ Ω cm)	42
Commercial purity (μ Ω cm)	55
Modulus elasticity α, (GPa)	105
Yield strength α, (MPa)	692
Ultimate strength α, (MPa)	785

(isomorphous), and iron (Fe), tungsten (W), chromium (Cr), silicon (Si), cobalt (Co), manganese (Mn), and hydrogen (H) (eutectoid); (iii) neutrals, such as zirconium (Zr). The α and near-α Ti alloys exhibit superior corrosion resistance to the $\alpha + \beta$ alloys but have limited low temperature strength. In contrast, the $\alpha + \beta$ alloys exhibit higher strength due to the presence of both the α and β phases. The properties of the materials depend on the composition, relative proportions of the α and β phases, thermal treatment, and thermo–mechanical processing conditions.

The β alloys offer the unique characteristic of low elastic modulus and superior corrosion resistance to the α and $\alpha + \beta$ alloys (Bania, 1993; Schutz, 1993). Ti–Ni alloy is a stoichiometric compound of Ti and Ni. The equiatomic intermetallic compound TiNi exhibits the shape memory phenomenon that allows for the spontaneous recovery of shape after being subjected to macroscopic deformation higher than its elastic limit. Shape recovery may occur after heating or after release of loads. NiTi shape memory alloy with 55 wt% of Ni and 45 wt% of Ti is often called NITINOL (Ni for nickel, Ti for titanium, and NOL for Naval Ordnance Laboratory, the place where Buehler and co-workers discovered this alloy). Research activities on the application of TiNi shape memory alloys to medicine began in the late 1960s to take advantage of their unique shape memory properties. For example, tailored compressive fixation of bone fragments, and anchoring of implants and dentures to the living tissues can be more easily achieved with TiNi alloys (although Ni is poisonous to the human body if there is no coating on the alloy). In addition, flexible TiNi stents are increasingly used in surgical treatments involving constricted arteries, recurrent urethral obstructions, biliary obstructions, and malignant esophageal stenosis.

8.3 Biomedical applications and development of Ti and its alloys

Earlier applications of Ti in medical, surgical, and dental devices were based on post-World War II advances in manufacturing processes as a result of the more stringent requirements demanded by the aerospace and military industry. Increased use of Ti and its alloys as biomaterials stems from their lower modulus, superior biocompatibility and better corrosion resistance when compared to more conventional stainless steels and Co-based alloys. These attractive properties were the driving force for the early introduction of α (cpTi) and ($\alpha + \beta$)-type (Ti–6Al–4V) alloys, as well as the more recent development of modern Ti-based alloys and orthopedic metastable β-type Ti alloys. Applications of Ti and its alloys can be classified according to their biomedical functionalities.

8.3.1 Hard tissue replacements

A schematic diagram of hard tissues in the human body is shown in Fig. 8.1. Hard tissues are often damaged due to accidents, aging, and other causes. It is a common practice to surgically substitute the damaged hard tissues with artificial replacements. Depending on the regions in which the implants are inserted and the functions to be provided, the requirements of different endoprosthetic materials are different.

Because of the aforementioned desirable properties, Ti and its alloys are widely used as hard tissue replacements in artificial bones, joints, and dental implants. As a hard tissue replacement, the low elastic modulus of Ti and its alloys is generally viewed as a biomechanical advantage because the lower elastic modulus can result in less stress shielding. One of the most common applications of Ti and its alloys is artificial hip joints that consist of an articulating bearing (femoral head and cup) and stem, as depicted in Fig. 8.2. The articulating bearings must be positioned in such a way that they can reproduce the natural movement inside the hip joints whereas secure

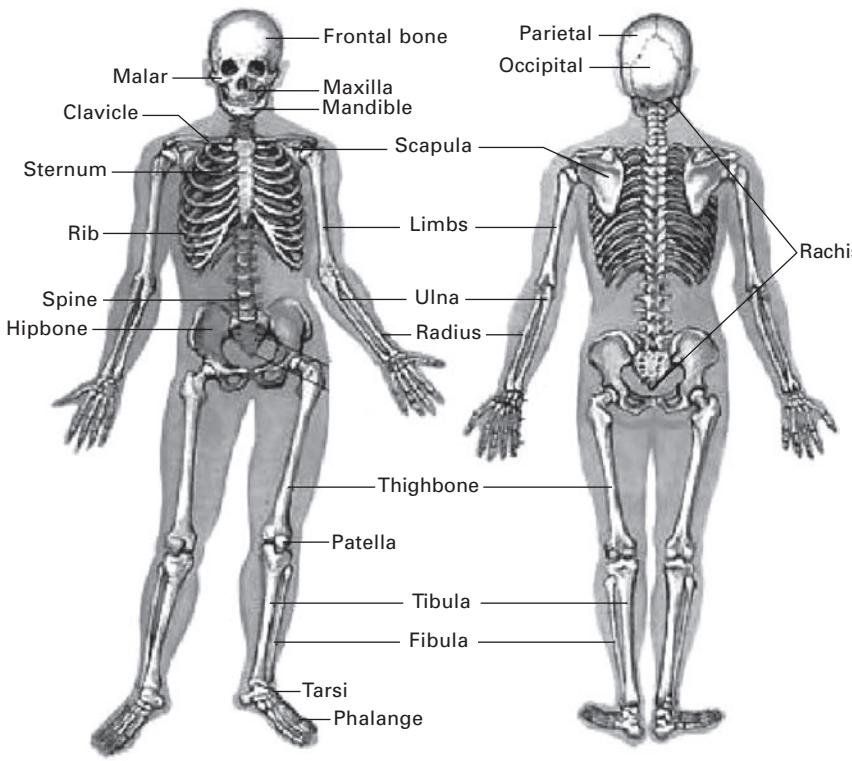

8.1 Schematic diagram of hard tissues in human body.

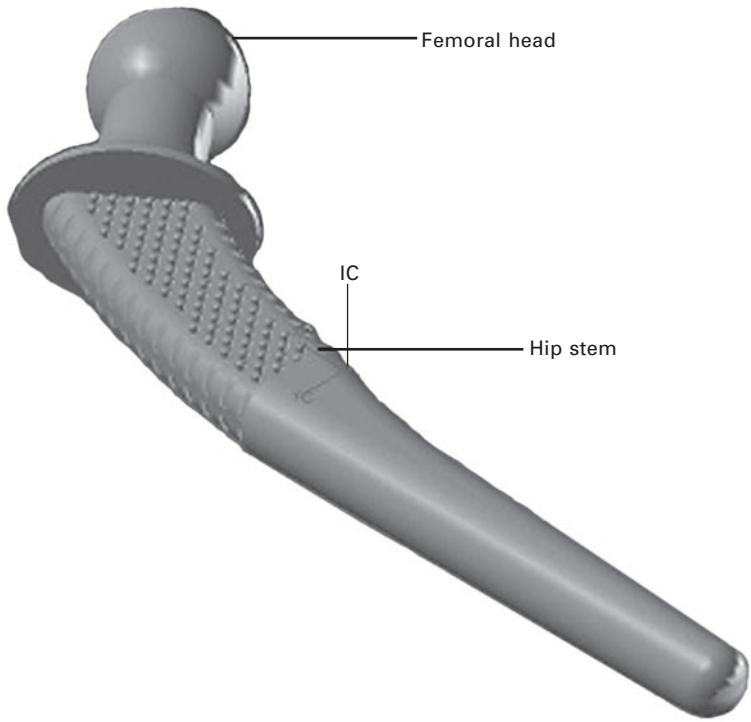

8.2 Schematic diagram of artificial hip joint.

positioning of the femoral head in relation to the other components of the joint is achieved using the stem. The hip stem is anchored permanently to the intramedullary canal of the femur. The cup, which is the articulating partner of the femoral head, is used for fixation by reaming out the natural acetabulum to fit the design. Ti and its alloys are also often used in knee joint replacements, which consist of a femoral component, tibial component, and patella.

Ti and its alloys are common in dental implants, which can be classified as subperiosteal, transosteal, and endosseous according to their position and shape. Subperiosteal implants consist of a custom-cast framework resting on the bone surface beneath the mucoperiosteum. The prosthesis is secured on posts or abutments that penetrate the mucosa into the oral cavity. Transosteal implants can be placed only in the frontal lower jaw while endosseous implants can be placed in both the upper and lower jaws via a mucoperiosteal incision. They are the most commonly used implant types and can be used in almost any situation as single implants to replace one missing tooth as well as in cases of partial and total edentulism. The most commonly used endosseous implants are root-forming analogs.

Figure 8.3 shows one of the more popular designs – a screw-shaped artificial tooth. Most dental implants are placed according to the 'osseointegration' concept, which allows dental implants to fuse with bones. Surface modification technologies, such as grist blast, chemical etching, and plasma spraying are often utilized to improve the osseointegration ability of Ti dental implants. For endosseous implant fixation in bones, such as in the case of artificial hip and knee joints, two methods are currently employed. One is bone cement fixation and the other is cementless implantation. Consequently, prostheses can be classified into cemented and cementless ones in accordance with the fixation methods in bone tissues. The requirements that are related to the properties and design of the prostheses depend closely on the type of anchoring in the human body. For cemented prostheses, the components are fixed to the bony implant bed employing bone cement based on poly(methylmethacrylate) (PMMA). The cement is usually prepared at the time of the surgery and applied with the aid of a syringe to the bony implant bed after blood and medullary fat have been removed. Penetrating into the cancellous bone structure, the cement hardens within a few minutes resulting from an exothermal reaction. This leads to a continuous cement mantle that is well anchored in the bone and lies closely against the implant (Morscher, 1995).With regard to bone cement fixation, apart from the risk of necrotic damage of the living bone by the heat liberated during polymerization of the cement, the lifetime of a cemented endoprosthesis depends on the durability of the cement as well as its tensile bond strength on the implant surface. Failure begins with loosening at the interface accompanied by micro-movements between the metal and the cement, consequently initiating the formation of metal particles and release

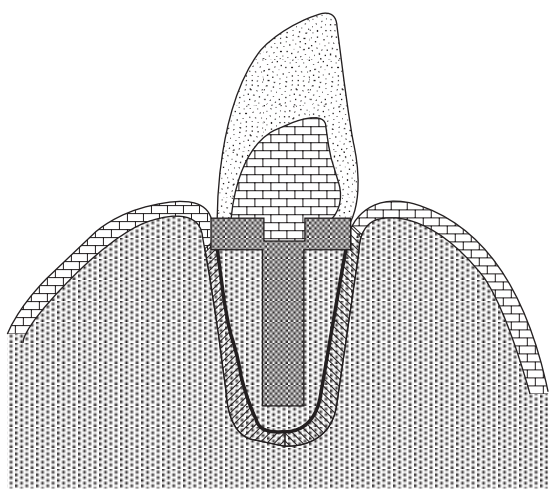

8.3 Schematic diagram of screw-shaped artificial tooth.

of metal ions. Due to its poor mechanical properties, cement is branded as the weak point in the fixation, as exemplified by the growing number of cases involving loosening of cemented prostheses since the late 1970s, regardless of prosthesis design (Jones and Hungerford, 1987). Anchoring of the prosthesis directly to the living bone is one of the solutions and the driving force for further developments. In comparison with cementing, direct cementless anchoring of the prosthesis to the bone through osseointegration is a more recent technique. Cementless prostheses with the optimal surface structure and composition to enable osseointegration can produce lasting mechanical interlocking between the implant and bone (Bobyn *et al.*, 1980; Dowson *et al.*, 1981; Howie, 1990; Jasty, 1993; Long and Rack, 1998). Rough surfaces, porous coatings and surfaces with osteoconductivity and osteoinductivity in body fluids have been shown to be good surfaces for osseointegration. Depending on the desired anchorage in the bone, partial osseointegration of the prosthetic components may be considered expedient. In such cases, the design is divided into functional zones that are optimized according to their individual functions. For a proximal anchored hip prosthesis stem, the solution may require the provision of a proximal surface that can osseointegrate with the bone.

In order to avoid adverse tissue reactions arising from hard tissue replacements, a bioinert material, which is stable in the human body and does not react with body fluids and tissues, is preferred. Bioinert materials are generally encapsulated after implantation into the living body by fibrous tissues that isolate them from the surrounding bone. Some bioactive materials, such as hydroxyapatite and bioactive glasses are increasingly used as hard tissue replacements to improve the bonding between implants and bone tissues because the materials can bond to living bones without the formation of fibrous tissues by creating a bone-like apatite layer on their surface after implantation. Apatite formation is currently believed to be the main requirement for the bone-bonding ability of materials. In this respect, Ti with its native surface oxide is known to be bioinert, but it is difficult to achieve good chemical bonding with bones and form new bones on its surface at the early stage after implantation. Hence, titanium and titanium alloys do not meet all the requirements of an ‘ideal’ material. In addition, longer human life expectancy and younger patients requiring implants have driven biomedical research from original implant concerns, such as materials strength, infection and short-term rejection to a consideration of more long-term material limitations; for instance, wear, fatigue strength, and long-term biocompatibility. The current trend is to use surface modification technologies to address a number of these ever increasing clinical demands, and the various issues are discussed later in this chapter.

8.3.2 Cardiac and cardiovascular applications

Ti and its alloys are common in cardiovascular implants because of their unique properties. Early application examples were prosthetic heart valves, protective cases in pacemakers, artificial hearts, and circulatory devices. Recently, the use of shape memory TiNi alloy (NITINOL) in intravascular devices, such as stents and occlusion coils, has received considerable attention. The advantages of Ti cardiovascular applications are that Ti is strong, inert, and non-magnetic. It also produces few artifacts under magnetic resonance imaging (MRI), which is a very powerful diagnostic tool. A disadvantage is that it is not sufficiently radio-opaque in finer structures. In artificial heart and circulatory assist devices, the materials are used both in the mechanical components of the pump and as a blood-contacting surface. Artificial hearts made entirely of titanium have, in general, not been very successful, clinically, mainly due to problems with blood-clotting occurring on the device surface (Rintoul *et al.*, 1993).

Many types of prosthetic heart valves have been used clinically. The ring and struts are made of Ti or its alloys while the disk is made of pyrolytic carbon. Around the ring is a sewing ring made of knitted Teflon (PTFE) cloth, where the sutures anchoring the prosthesis to the heart are placed. The metals in the prosthetic heart valves are often coated with a thin carbon film to enhance blood compatibility. At present, stents (Fig. 8.4) are commonly

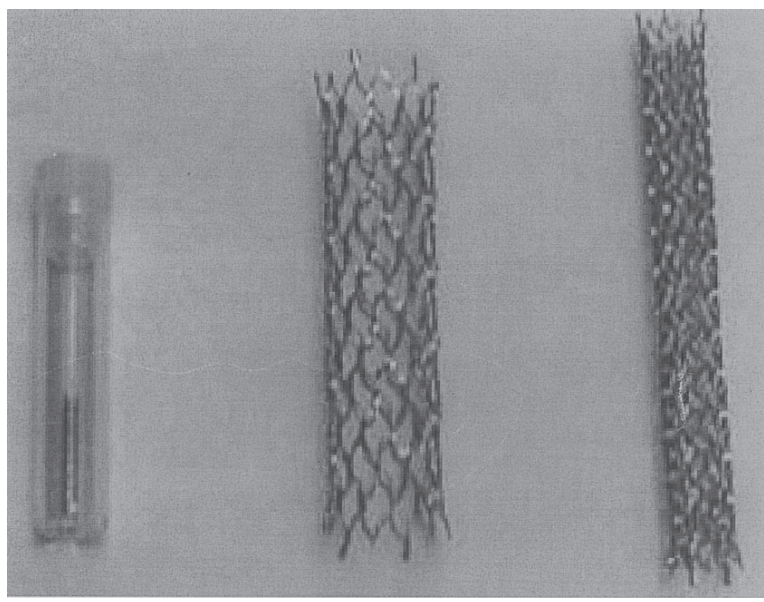

8.4 Stents commonly used in the treatment of cardiovascular disease.

used in the treatment of cardiovascular disease. They dilate and keep narrowed blood vessels open. Stents are usually mounted on balloon catheters or folded inside special delivery catheters. TiNi alloy is one of the most common materials used in vascular stents due to its special shape memory effects. Because of inevitable damage to the vessel wall in connection with placement of the stent and possible rejection by the body, there is always a risk of thrombotic occlusion of the stented vessel segment. Therefore, it is necessary to improve the antithrombogenic properties of stents.

Commercially pure titanium (Ti) and Ti alloys are preferred for dental and orthopedic implants or prostheses because of their corrosion resistance, biocompatibility, durability, and strength. However, being bioinert, the integration of such implants in bone was not good. To achieve improved osseointegration, there have been many efforts to modify the composition and topography of implant surface. Recently, the anodic oxidation treatment of Ti has attracted a great deal of attention (Ogden, 1961; Collings, 1984; Polmear, 1981; Bania, 1993; Schutz, 1993). Park *et al*. reported that an anodized titanium implant appeared to have higher removal torque values and higher percentages in both the bone-to-implant contact and the bone area in the threads than the machined implant (Collings, 1984). Meanwhile, calcium phosphate is commonly applied to metallic implants as a coating material for fast fixation and firm implant–bone attachment on account of its demonstrated bioactive and osteoconductive properties. Recently, various Ca/P ratios of thin calcium phosphate films were formed by electron beam evaporation: The films had an excellent bonding strength and showed different dissolution behaviors, depending on the Ca/P ratio (Morscher, 1995; Jones, 1987; Bobyn *et al*., 1980). Concerning the stability of the coatings, much effort has been devoted to determine the immersion behavior of calcium phosphate coatings in solutions with ionic composition similar to the inorganic fraction of blood plasma, such as phosphate buffered saline (PBS) solution, Hank's balanced salt solution (HBSS) (Howie, 1990; Jasty, 1993) and Kokubo's simulated body fluid (SBF) (Jasty, 1993; Long and Rack 1998). These *in vitro* studies are important in a practical sense in that they could give some indication of the *in vivo* behavior of the coating. Especially, thin coating layers are of interest. Consequently, these tests are practiced as a first stage to assess the bioactivity of a potential biomaterial through the formation of a bonelike apatite layer (Rintoul *et al*., 1993; Williams, 2001; Textor *et al*., 2001). It is of no doubt that the addition of certain biologically active proteins with biomaterial will improve the bioactivity of the material. Some proteins and, in particular, growth factors, have been shown to be potent osteogenic inductors. Basic fibroblast growth factor (BFGF) is one of several well-characterized growth factors which have crucial properties in bone formation processes (Boehm, 1971). Therefore, the association of BFGF with carriers would be promising in orthopedic and dental fields. So far, different scaffolds including

hydroxyapatite (HA), beta-tricalcium phosphate (β-TCP) and biodegradable polymers have been used as the carrier of BFGF (Schindler, 1990; Parfitt, 1976; Hendrich, 1985; Parks, 1965).

In a recent study (Cui *et al*., 2005), many kinds of methods to make a bioceramic coating and calcium phosphate deposition film with an excellent biocompitibility were used to be deposited on the surface Ti and Ti alloy. Some of main methods used are introduced as follows:

8.4 Biocompatibility and fabrication of *in situ* synthesized bioceramic coatings on Ti alloys

8.4.1 *In situ* synthesized potassium titanate/Ti alloys as biomedical materials

Using an *in situ* dry mixed calcination synthetic method, Cui *et al*. prepared a $K_2Ti_6O_{13}$ coating layer whose heat expansion coefficient was close to that of the matrix and its mechanical character was good. Cui *et al*. (2003) used $TiAl_xZr_ySn_zNb$ alloys as matrix materials and $K_2CO_3 + TiO_2$ as the original material for coating. The bonding of coating and matrix was improved in this study. Cui *et al*. (2005) studied theoretically the surface pattern, phase composition, bonding strength and bioactivity of the coating. The Ti alloys were produced by vacuum induction smelting furnace or non-consumable vacuum arc smelting furnace, respectively. The structure, composition and property of the Ti alloys were analyzed. The matrix was badly contaminated by carbon and oxygen in the graphite crucible or the CaO coating crucible. The contents of carbon and TiC particles were high in the Ti alloys. Using the CaO coating crucible reduced the carbon contamination of the Ti alloys. But the oxygen contamination at high temperature made it impossible to fabricate the Ti alloys with normal properties. Then the structural character of as-cast Ti alloy produced by the non-consumable vacuum arc smelting furnace was studied. The effects of the addition alloying elements on the structure and the asymmetry law of the addition elements were also analyzed.

The processing technique of potassium titanate ($K_2O{\cdot}6TiO_2$) was established in the author's laboratory. Effects of K_2CO_3/TiO_2 ratio and reaction temperature on the growth of the $K_2O{\cdot}6TiO_2$ whisker were analyzed. The results showed that: when the K_2CO_3/TiO_2 ratio was about 1:5.5~1:6, a high quality and high productivity potassium titanate whisker was synthesized by the calcination method at applicable reaction temperatures. The diameter of the whisker was about 0.1~0.3 μm and the length to diameter ratio was about 100~200. According to the processing technique of the whisker, potassium titanate coating was synthesized *in situ* on the surface of the Ti alloy. The coating was made up of potassium titanate whiskers in an orientation perpendicular to the surface of the matrix. The coating thickness was about 2~3 μm. The

action of the surface oxidized layer on the surface of the matrix in the *in situ* synthesis reaction was also studied. The effect of the reaction was that solid and liquid were the main phases and the gas phase escaped synchronously with the potassium titanate whisker's growth in orientation.

Surface micropore Ti had been fabricated, based on the principle that the growth stress and thermal stress between the high-temperature oxided layer and the base material resulted in a physical lamination, which was surface bio-activated through an acid–alkali two-step method, followed by the formation and surface bio-activation reaction of the micropore Ti. It was indicated that the orientation and shape of the micropore was related to the structure of the matrix and that a gel film was formed on the surface after the bio-activation treatment. It was found that the deposition layer, after simulation body fluid (SBF) solution cultivation, was composed of honey-comb-liked polygonal cell-shaped elements, which were constructed of randomly arranged graticule-like nanometer loops with a Ca to P atomic ratio (n(Ca)/n(P)) of 1.61:1, akin to that of HA and human bones. An analysis of the deposition mechanics suggested that the deposition of Ca and P in the liquid phase was attributed to the bioactivity of the micropore titanium surface and the ion over-saturation environment of the SBF solution.

The biological activity of the $K_2O{\cdot}6TiO_2$ coating is closely related to its specific structure and physicochemical properties, as was discovered in the research. It should be noted that the activated TiO_2 surface can adsorb physically and chemically a quantity of OH and H_2O to form Ti–OH on the surface; and that it also can act as the bioactive base for apatite heterogeneous nucleation under biological conditions, when the pores in the coating can accelerate the diffusion of the organic small molecules through the oxide networks at room temperature to form strong chemical bonds with their functional groups. For example, organic small molecules containing COOH, OH, NH_2, C=O or phosphoric acid functional groups can be fixed in this processing. So the excellent biological activity of $K_2O{\cdot}6TiO_2$ coatings is mainly attributed to their major ingredient TiO_2. Additionally, the $K_2O{\cdot}6TiO_2$ possesses excellent water compatibility, stable under certain acid–alkali conditions, and its dispersion pH value in water is comparable to that of SBF. Therefore, $K_2O{\cdot}6TiO_2$ will influence the body fluid environment less in implants. All of this makes possible the application of $K_2O{\cdot}6TiO_2$ bioactive coatings in clinical implants and reparations.

An SBF cultivation experiment was used to evaluate the biological activity of $K_2O{\cdot}6TiO_2$ functional coating. The surface properties, together with the influence of the tunnel structure of $K_2O{\cdot}6TiO_2$ crystal's ability to induce Ca /P to deposit in the liquid phase, was examined in our studies. The discovery of phenomena of the molecule self-assembling Ca/P nanometer whiskers on the $K_2O{\cdot}6TiO_2$ functional coating during SBF cultivation was very rewarding.

During research on the low-temperature deformation of *in situ* Ti-matrix

composite materials, it was found that there were the textures of $\{10\bar{1}0\}$ $<11\bar{2}0>$ and (0002) $<11\bar{2}0>$. When deformation occurred at higher temperature, multi-slip systems were operating and, moreover, the texture $\{11\bar{2}1\}$ appeared. When the temperature was higher than the recrystallization temperature, the texture was obscured.

8.4.2 Fabrication and biocompatibility of nano-TiO_2/Ti alloys as biomedical materials

As biomedical materials, Ti and its alloys are superior to many materials such as stainless steels, pyrolytic carbon, and so on, in terms of mechanical properties and biocompatibility. However, the biocompatibility of Ti and its alloys are still not sufficient for prolonged clinical use. Hence, the development of surface modification is a real necessity for the biomedical community. Ti with a biocompatible coating such as HA has been successfully studied in recent years (Kamitakahara *et al*., 2003; Rønold *et al*., 2002; Wang *et al*., 1993; Klein *et al*., 1994; Tsui *et al*., 1998; Korkusuz *et al*., 1999). Ti alloys are used for dental and orthopedic implants for their superior compatibility, which is attributed to the oxide film formed on their surface (Kamitakahara *et al*., 2003; Rønold *et al*., 2002). Surface modification recently became active in the field of implants, such as hydroxyapatite coating by plasma spraying or electrophoretic deposition (Wang *et al*., 1993; Klein *et al*., 1994; Tsui *et al*., 1998), electrochemical deposition of Ca phosphates, basification treatment, sol–gel and anodized dielectric film (Korkusuz *et al*., 1999; Wang *et al*., 1993; Haman *et al*., 1995; Kyeck *et al*., 1999; Singh *et al*., 1996; Ong *et al*., 1991; Dasarathy *et al*., 1996; Wolke *et al*., 1994; Yamashita *et al*., 1996; Montenero *et al*., 2000; Haddow *et al*., 1998; Jillavenkatesa *et al*., 1998; Hero *et al*., 1994). In this research, nanometer Ti dioxide powder was adopted as the raw material to embed Ti alloys and sinter. In this way, a new biomaterial, a nano-TiO_2 biocompatible coating on the surface of titanium alloys, was fabricated successfully. The method is a simple and adaptable technique for surface modification of Ti alloys.

Ti-2zirconium (Zr)-2niobium (Nb) alloy ingots were made in a 25 kg vacuum induction furnace by melting and casting. The ingots were machined into many specimens with a size of 20 mm × 20 mm × 8 mm. Before sintering, specimens were polished and then rinsed with distilled water and acetone, subsequently degreased with hydrofluoric acid (5%), washed with absolute alcohol and dried. Nanometer titanium dioxide powders were prepared by hydrolysis of titanium-tetrabutoxide with ethanol. The particle size of TiO_2 powder in the anatase structure is mainly between 5 nm to 10 nm, as shown in Fig. 8.1. Ti alloy specimens were embedded in nanometer TiO_2 powders, sintered at 600 °C for one hour, and annealed at 500 °C for six hours.

The preparation of the nano-TiO_2/Ti dioxide, powders by hydrolysis

of Ti-tetrabutoxide with ethanol included two processes: hydrolyzation and aggregation. Under favorable conditions the exchanges take place as follows:

$$Ti(OC_4H_9)_4 + 4H_2O \rightarrow Ti\ (OH)_4 + 4C_4H_9OH \quad [8.1]$$

$$Ti(OH)_4 \rightarrow TiO_2(s) + 2H_2O \quad [8.2]$$

The Ti dioxide powder was examined by X-ray diffraction and TEM, and the result showed that the particle size was mainly between 5nm to 10nm.

Using this kind of nanometer Ti dioxide powders, Ti alloy specimens were clad with TiO_2 and sintered at temperatures from 500 °C to 950 °C for 1h (the temperature interval was 50 °C). When the sintering temperature was low, such as at around 500 °C, the oxide film was too thin to form a coating; when the temperature was high (800 °C), the TiO_2 particles tended to grow, so the coating was not of a nanometer structure. The optimal sintering temperature was fixed at 600 °C × 1h.

The microstructure of the sintered specimen surface was examined with a Philips Tacnai F20 high resolution transmission microscopy (HREM) and Philips XL30 TMP scanning electron microscopy (SEM). X-ray diffraction (XRD) with the high–low temperature appurtenance was used to study the phase composition of the sintered coating on the surface of the Ti alloy. The specimens were cultivated in simulated body fluid (SBF) to test biocompatibility and bioactivity. Measurements of ion consistency of SBF and blood plasma were also performed with an XD685 electrolyte analyzing system. Table 8.1 gives the ion consistency of the SBF and blood plasma.

Figure 8.5a shows an HREM image of the synthesized nano-TiO_2 particles and Fig. 8.5b shows an SEM micrograph of the coating. It is indicated by

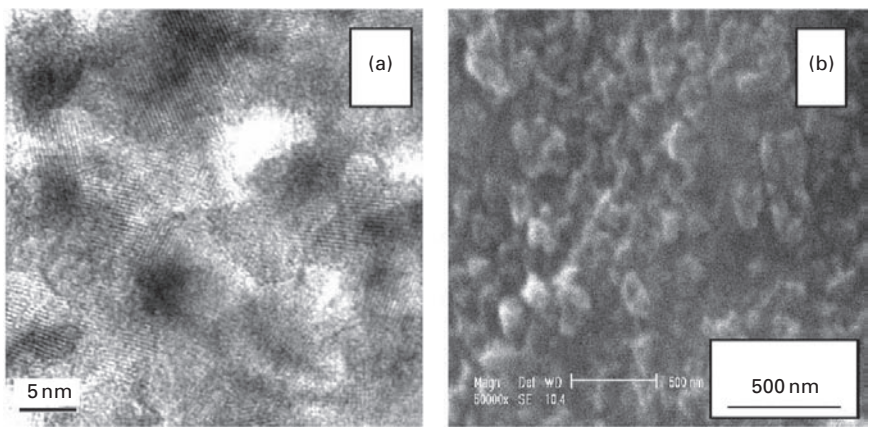

8.5 (a) HREM image and (b) SEM micrograph of nano-TiO_2 synthesized particles.

Fig, 8.5a that the particle size of TiO_2 particles is about 50 nm–90 nm. The oxide film is a very thin (<10μm) anatase-type TiO_2 (analyzed by XRD, as shown in Fig. 8.6). The titanium surface is oxidized easily in the air when the temperature is less than 500 °C. Because of the Ti dioxide powder on the surface, the noncrystal layer grows more easily by the diffusion of oxygen. As a matter of fact, there is a very thin TiO_2 film with a thickness of 3–5 nm on the surface of Ti alloy before nanometer TiO_2 powders coating is formed, and this thin TiO_2 film belongs to the two dimension nanometer material. The interface between this thin TiO_2 film and the embedded nanometer TiO_2 particles can disappear because both grow a larger crystal grain with a thickness of 50–90 nm during the sintering processing. So the coating and substrate are well knit. At the same time, the temperature is not high and this can prevent particles from growing. However, the particle size will be 4 μm–6 μm if the specimens are enwrapped by ordinary commercial Ti dioxide powders.

Theoretically speaking, nanometer materials possess much better characteristics than ordinary materials. To test the biocompatibility of nano-TiO_2/Ti alloys, we dipped the materials in SBF to cultivate the Ca/P layer, and Table 8.2 shows the ion consistency of SBF and blood plasma. After seven days, the specimens were taken out of the SBF, washed and the surface morphology observed (Fig. 8.7). From Fig. 8.7 we can see that the Ca phosphates were deposited on the surface of specimens. The Ca/P deposition layer consisted of cystiform polygons made up with irregular nanometer circles, similar to honeycomb. The energy spectrum (Fig. 8.8)

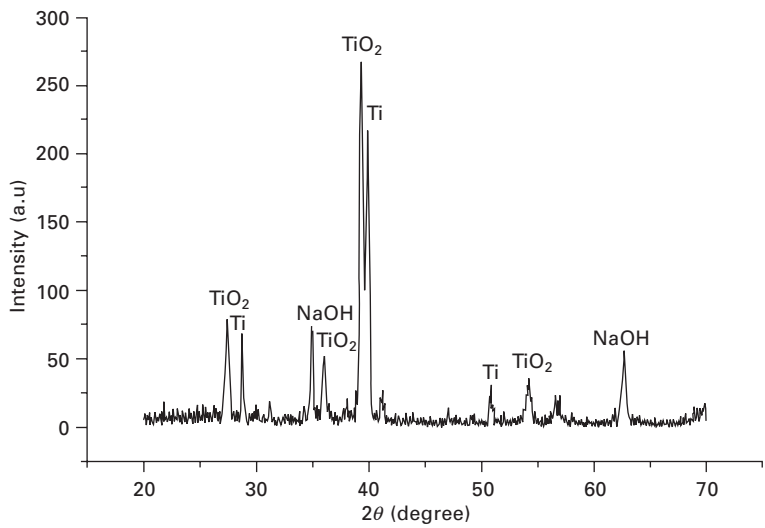

8.6 XRD pattern of nanometer TiO_2 coating.

Table 8.2 Ion consistency of simulate body fluid and blood plasma

	Na^+	K^+	Ca^{2+}	Mg^{2+}	HCO_3^-	Cl^-	HPO_4^{2-}	SO_4^{2-}
Blood plasma	142.0	5.0	2.5	1.5	27.0	103.0	1.0	0.5
SBF	142.0	5.0	2.5	1.5	4.2	148.5	1.0	0.5

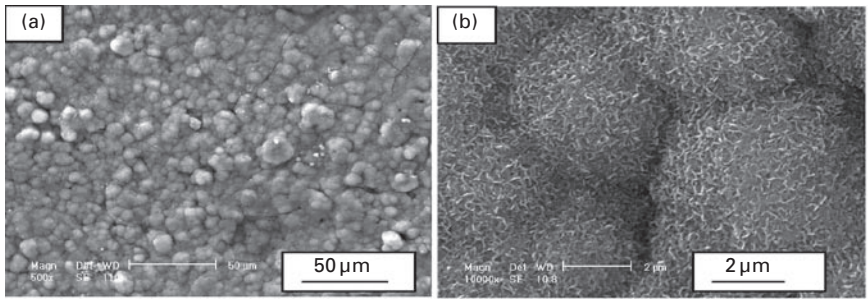

8.7 Surface morphology of nanometer TiO_2 coating after immersion in SBF for seven days and annealed under vacuum at 500 °C for six hours. (a) SEM microstructure of low-fold amplification, (b) SEM microstructure of high-fold amplification.

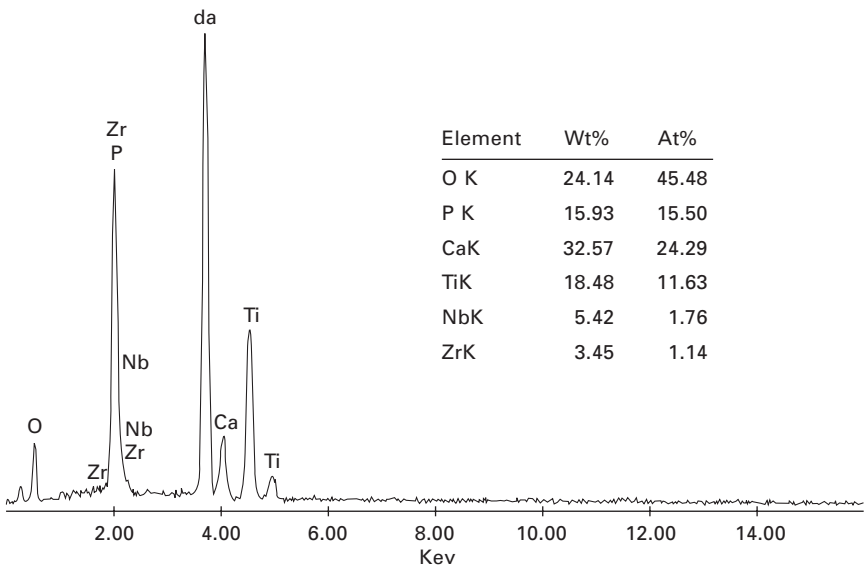

Element	Wt%	At%
O K	24.14	45.48
P K	15.93	15.50
CaK	32.57	24.29
TiK	18.48	11.63
NbK	5.42	1.76
ZrK	3.45	1.14

8.8 Element analysis of EDS for the layer of nanometer TiO_2.

shows that the n(Ca)/n(P) atomic ratio is about 1.6:1, which is very similar to that of HA and human bone. It can be concluded that nanometer TiO_2/Ti alloys possesses favorable biocompatibility.

The presence of the significant interface between nano-TiO_2 particles and

the Ti alloy matrix represents excellent biocompatibility and bioactivity. So Ca phosphates can be easily deposited on the surface of nano-TiO_2 particles. Since TiO_2 is a ceramic phase with a high melting temperature, the interface of nano-TiO_2/Ti alloys is very stable at room temperature and elevated temperatures. Analogous to the tailoring of these films through control of pH and electrochemical cell potential (Kilpadi *et al.*, 1998; Ask *et al.*, 1988–89; Pham *et al.*, 1997), the interaction between nano-TiO_2 particles and the Ti matrix during annealing causes variations in the stable oxide forms. Previous studies have specifically noted the potential toxicological benefits of low vanadium oxide content of Ti implant materials (Kilpadi *et al.*, 1998; Ask *et al.*, 1988–89), and hence the impact of the oxides evolved during heat treatment and the related topic of diffusive behavior should deserve significant attention.

Phase transformations occurring in TiO_2 particles and Ti alloy are independent of both the crystal lattice and of the physical, chemical and mechanical properties. Formation of the oxide phases of other elements such as Zr and Nb diffused into Ti requires the removal of the outer layers from cast and forged titanium products following annealing treatments, which is very difficult, so the oxides of Zr and Nb cannot be found by XRD, as shown in Fig. 8.6. Based on physical metallurgy, Zr and Nb existing in the solid solution state can prevent severe decrease in fatigue and fracture resistance (Donachie, 1988). Taken independently, the results suggest that heat treatment under vacuum eliminate the formation of oxides for other elements in Ti alloys at the interface; however, the absence of pure nano-TiO_2 particles on the surface of Ti alloy is the desired biomaterial structure. Therefore, the nano-TiO_2/titanium alloy biomedical material can be fabricated using the process whereby titanium alloys are embedded by nanometer titanium dioxide powders and sintered in the high temperature furnace. TEM observation has indicated that the particle size of TiO_2 is mainly 50 nm–90 nm. The coating layer prepared by nanometer titanium oxide powders possesses excellent biocompatibility. It is indicated by cultivation tests in simulated body fluid (SBF) that Ca phosphates are deposited on the specimen surface, and the n(Ca)/n (P) atomic ratio is about 1.6:1, which is similar to that of HA and human bone.

8.4.3 Fabrication mechanism and characteristics of surface micro-porous Ti as biomaterials

This chapter deals with the chemical fabrication technique of surface micro-porous Ti. The pure Ti clad with potassium titanate whiskers was calcined for a short time, then rapidly cooled, and then the surface micro-porous Ti was achieved. The degree of surface roughness of the Ti samples was about 3–5 μm, and this kind of surface micro-porous Ti can be used as an excellent

implanting biomaterial with good biocompatibility and bioactivity. The surface microstructure of the micro-porous Ti was observed and analyzed using SEM, EDS, XPS and XRD, and the chemical formation mechanism of the surface micro-porous Ti biomaterial has been discussed in this chapter.

As body hard-tissue implants, Ti matrix biomaterials are firstly selected among all metal materials. Although Ti and its alloy have excellent biocompatibility and mechanical properties, their surfaces are still bio-inert. At present, the surface modification has become a main research field of Ti matrix biomedical materials to improve further matrix materials' biocompatibility and bioactivity (Cui *et al*., 2003; David *et al*., 2002). Hydroxyapatite (HA), as a kind of bioactive coating material, has been widely studied; implants with plasma spray HA coating have been used in clinical orthopedics (Brown *et al*., 1994; McPherson *et al*., 1995; Cheang *et al*., 1996). Because of its low bonding-strength between coating and matrix, the HA coatings often peel off from the matrix, which leads to a failure of the implants.

In order to increase the bonding-strength at the interface of bioactive coating/matrix, surface micro-porous Ti was prepared by *in situ* reaction processing. For the fabrication process pure Ti clad with potassium titanate whiskers was calcined for a short time; this kind of surface can combine firmly with the bioactive coating. The surface, micro-porous with a homogeneous distribution of micro-apertures, is obviously different from those morphologies obtained by other modification technologies. This fabrication processing has several merits, such as low cost, simple fabrication processing, and short preparation cycle.

The samples of surface micro-porous Ti were made in three steps, as follows: (i) The first step was the preparation of the samples and their pretreatment. The sponge Ti as raw material was melted and cast into pure Ti ingots in the non-self-waste vacuum electrical arc furnace, and the ingots forged into bar shapes. The forged Ti bars were machined into 10 mm × 10 mm × 2 mm experimental samples using a SPARK FW1 electric spark line incising machine. Then the samples were burnished using a series of sand papers, such as No.280, No.400, No.600, and cleaned in acetone by an ultrasonic cleaner for 15 min. Then these samples were eroded in 10% HF liquid for a short time. Finally, they were placed into distilled water to be ultrasonic cleaned. (ii) The second step was selecting potassium titanate whiskers with perfect length–diameter ratios as cladding powders. (iii) The third step was embedding pure Ti samples in potassium titanate whisker powders that were mixed with acetone liquid; these were placed into a KSY12-16 programme controlling furnace and heated at the rate of 5 °C/min, sintered at 800~900 °C for a short time, and finally cooled rapidly. A peeling layer can be wholly peeled off from the Ti matrix at the time the surface micro-porous Ti was obtained.

The microstructure of the surface micro-pores and of the peeling layer

was examined with a Philips XL30 TMP scanning electron microscopy (SEM), with an energy dispersive X-ray spectrometer (EDS). PHI 4300 X-ray photoelectron spectrum (XPS) and Philips X'pert TMD X-ray diffraction (XRD) were used to study the surface elements and the phase composition of the peeling layer.

Figure 8.9a shows the cross-section microstructures of the titania oxided layer obtained by conventional physical delaminating of the oxide layer on the surface of a Ti matrix. It is clear that the titania layer is made up of two sub-layers which contains coarse grains of TiO_2 and fine grains of TiO_2. The layer of fine grains is between the Ti matrix and the coarse grains. Figure 8.9b shows the surface morphology of the Ti matrix after the conventional physical delaminating. Compared with general oxidation delaminating of Ti (Fig. 8.9b), Fig. 8.10 shows various morphologies of the porous surface titanium. It is obvious that these surface structures are markedly different. Thus it can be seen that the cladding layer of potassium titanate whiskers and the peeling layer, together flake away from the Ti matrix after the pure Ti cladded with the potassium titanate whiskers has been calcined for a short time, and then rapidly cooled. Finally, a micro-porous structure on the surface of the Ti sample is gained. The morphologies of the surface porous Ti were various with the change of parameters of processing, as shown in Fig. 8.10a,b,c. and d.

In this study, it was found that the cross-section microstructures of the peeling layer that made the surface micro-porous Ti (Fig. 8.11 and Fig. 8.12) were also different from those of the titania layer after conventional physical delaminating (Fig. 8.9a). Besides coarse grain TiO_2 and fine grain TiO_2, a directional layer grew on the fine grain TiO_2 and a layer of black powder was synthesized between the directional growing layer and the Ti matrix.

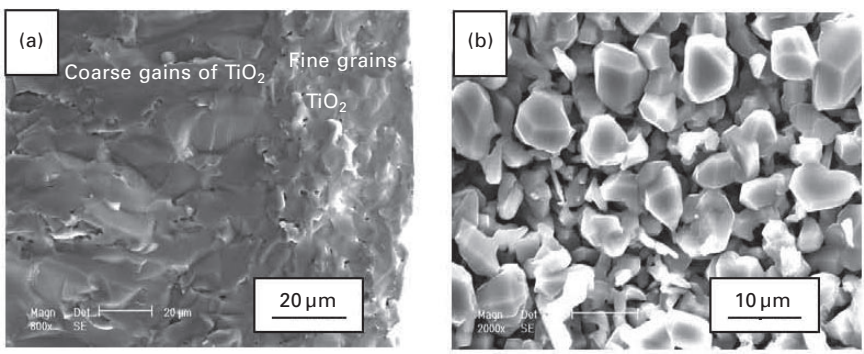

*8.9.*Microstructures of the titania layer after conventional physical delaminating. (a) Cross-section microstructures of the titania, (b) surface morphology of Ti matrix.

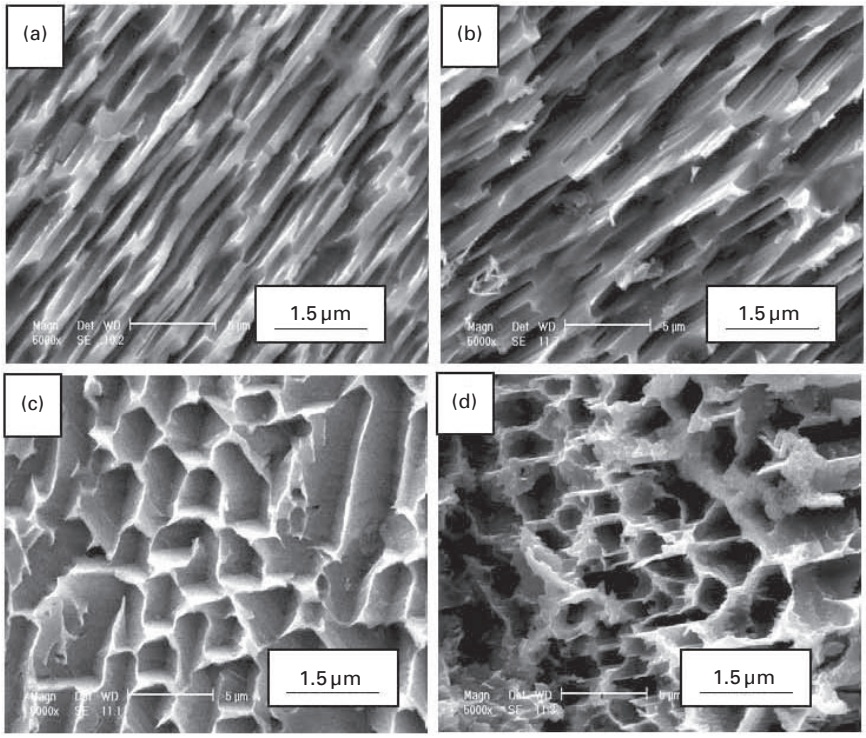

8.10 Various morphologies of the surface porous titanium (a) porous barrette surface (b) porous sandwich surface (c) porous pit surface of (d) porous hollow surface.

By XPS analysis (Fig. 8.13a) it was affirmed that the layer of black powder was TiO_2, because the Ti2p1 (binding energy) was 458.54eV, which was near to 458.5eV of TiO_2. As shown in Fig. 8.13b, the phase compositions of the interior of the peeling layer were analyzed by XRD. The results of the analysis indicated that the directional growing layer was composed of TiO_2, TiO, $KTi_8O_{16.5}$, $K_2Ti_8O_{17}$ and $K_2Ti_6O_{13}$.

Based on an analysis of the microstructure of the peeling layer described above, it is possible to discuss the formation mechanism of the surface micro-porous Ti. The process of micro-porous Ti formation includes chemical and physical delaminating. A diffusion reaction results in chemical delaminating, and in the end chemical delaminating is transformed into a physical delaminating during the processing where potassium titanate whiskers are calcined on the Ti matrix. Under the common action of growing stress and heat stress on the interface between the reacted layer and Ti matrix, the exterior reacted layer becomes separated from the Ti matrix. Figure 8.12 is a schematic diagram of the formation mechanism of the surface micro-porous

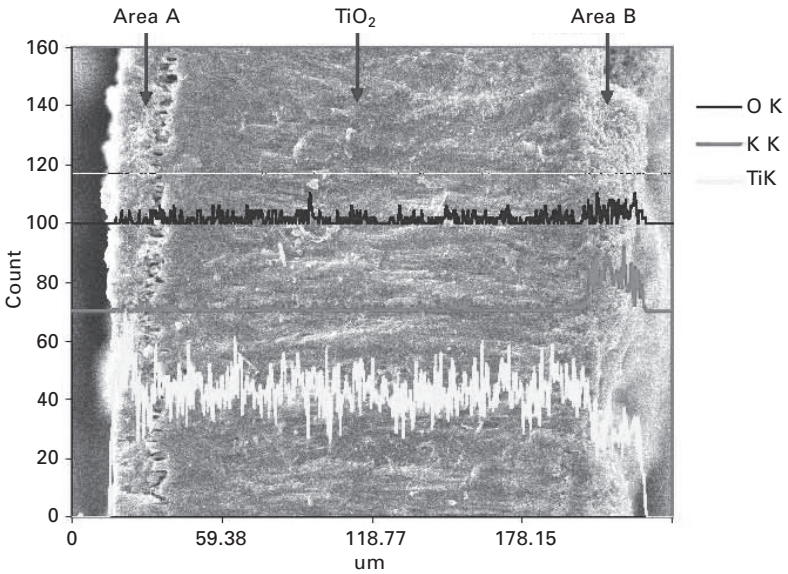

8.11 Cross-section microstructures and element linear distribution diagram of the peeling layer.

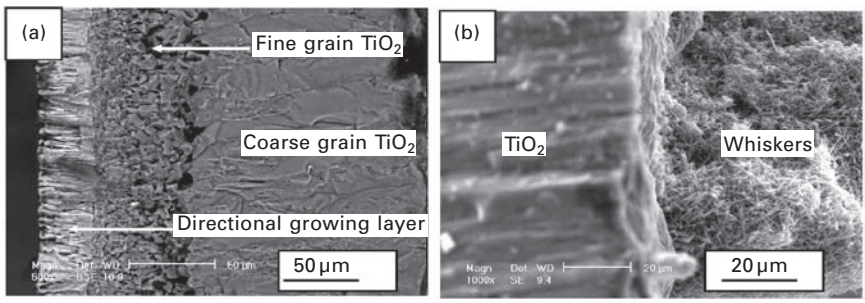

8.12 High magnification SEM images of areas A and B in Fig. 8.11. (a) Area A (b) Area B.

titanium. It is obvious that the cladding of potassium titanate whiskers has an intense effect on the sub-structures of the peeling layer. During the process of heating, for Ti is an active metal, a thin layer of TiO_2 firstly forms on the surface of the Ti matrix. Along with increase of temperature, the reactions of potassium titanate in the cladding powders and TiO_2 are as follows:

$$K_2Ti_6O_{13} + 2TiO_2 \rightarrow K_2Ti_8O_{17} \quad [8.3]$$

$$(1/2)K_2Ti_6O_{13} + 5TiO_2 \rightarrow KTi_8O_{16.5} \quad [8.4]$$

$$K_2Ti_4O_9 + 2TiO_2 \rightarrow K_2Ti_6O_{13} \quad [8.5]$$

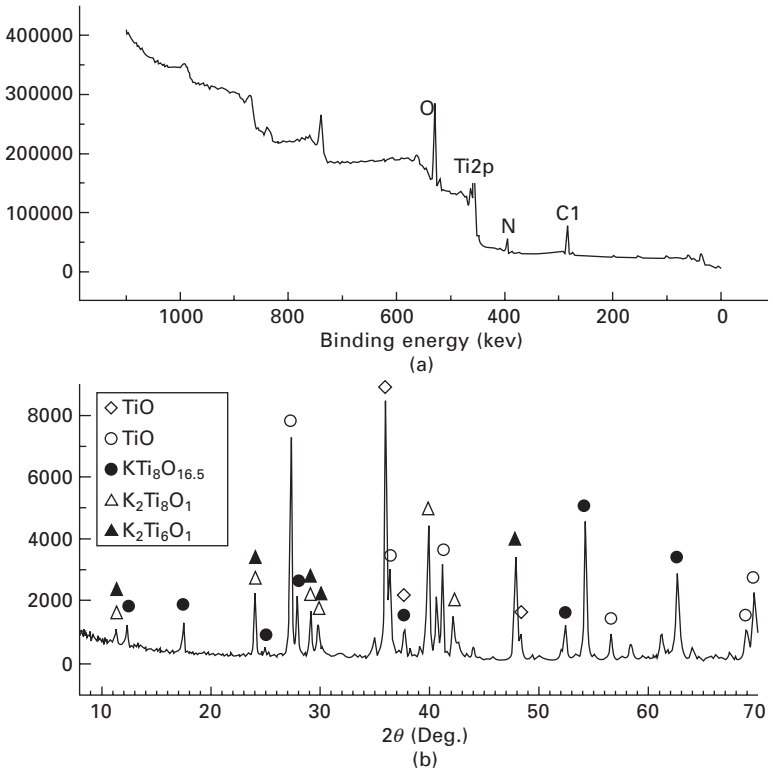

8.13 XPS and XRD analysis of the peeling layer with black powders. (a) XPS; (b) XRD.

$K_2Ti_8O_{17}$, $KTi_8O_{16.5}$, $K_2Ti_6O_{13}$ and TiO_2 form a chemical delaminating. At the same time, the diffusion of Ti ions and oxygen atoms continues at all times. During the diffusion of the ions in this system, the radius of ion is an important parameter. Here, $R(Ti^{2+}) = 0.086$ nm, $R(Ti^{3+}) = 0.067$ nm, $R(Ti^{4+}) = 0.053$ nm, $R(K^+) = 0.133$ nm, $R(O^-) = 0.093$ nm, and $R(O^{2-}) = 0.21$ nm. Because the radii of metals ion are less than that of oxygen atoms, the moving space of metal ions is bigger. So the TiO_2 formed during the *in situ* reaction grows on the outer surface of the front chemical delaminating. During the process of subsequent heat and preservation, $K_2Ti_8O_{17}$, $KTi_8O_{16.5}$ and $K_2Ti_6O_{13}$ whiskers grow up in virtue of outer TiO_2 and occur to directional growth between TiO_2 and Ti matrix, which is consistent with references (Cui *et al.*, 2005; Venezuela *et al.*, 1999; Cahn, 2001; Curry, 2001; He and Antonelli, 2001). The thicker the outer TiO_2 is, the more difficult it is for the oxygen atoms to diffuse in, so the entering diffusing oxygen atoms and the Ti ions diffusing out are transformed into Ti-rich oxide (TiO) among the $K_2Ti_8O_{17}$, $KTi_8O_{16.5}$, $K_2Ti_6O_{13}$ and TiO_2. Furthermore, we find that the

interface between the fine grain TiO_2 and the directional growing layer is distinct and bonding firmly, as shown in Fig. 8.12a. The reason can be considered as that the fine grain TiO_2 takes part in the reaction to synthesize potassium titanate whiskers. Noticeably, a thin layer of black TiO_2 powder comes into being between the Ti matrix and the directional growing layer, but the formation of this layer of black powder still needs to be further investigated. Due to the incompacted black powder, the bonding force between the directional growing layer and the Ti matrix is less than that between the fine grain TiO_2 and coarse grain TiO_2 (Tierney and Kim, 1993; Velev *et al.*, 1999; Jiang *et al.*, 2001; Erlebacher *et al.*, 2001; Bukaluk, 2001; Qu *et al.*, 2001), which leads to a physical delaminating on the interface of the former. So the microcosmic characters of the surface micro-pores are directly determined by the morphology and size of the potassium titanate whiskers in the directional growing layer. Therefore, the potassium titanate whiskers cladding the pure Ti have a great effect on the substructure of the peeling layer, which is different from that of the titania layer after conventional chemical and physical delaminating (Liang and Lian, 2003; Kokubo and Takadama, 2006; Sul and Johansson, 2001; Xuebin and Chuanxian, 2000; Cui *et al.*, 2005; Bu and Cui, 2007). The phase composition of the directional growth layer on the surface micro-porous Ti is made up of $K_2Ti_8O_{17}$, $KTi_8O_{16.5}$, $K_2Ti_6O_{13}$ and TiO_2.

8.4.4 Fabrication and biocompatibility of nano-$K_2(Ti_8O_{17})$/TiO_2 bioceramic composite coating on the surface of Ti

A $K_2(Ti_8O_{17})/TiO_2$ composite bioceramic coating on the surface of Ti was prepared successfully by an *in situ* electrochemical technique. During immersion in a simulated body liquid, the surface morphology, microstructure, composition-of-phases, and bioactivity of the coating were evaluated. The test results indicated that the $K_2(Ti_8O_{17})$/ TiO_2 bioceramic composite coating had good biocompatibility and bioactivity.

As biomedical materials, Ti and its alloys are superior to many other materials in several attributes, including biocompatibility and corrosion resistance, and have mechanical properties similar to those of bone. So they have broad application in hard tissue repair and replacement. However, Ti and its alloys appear as bio-inert because of the compact passivation layer on the surface. This character means that the Ca and P cannot be sedimentated on the surface after implantation in bodies, and the combination between the implant and the bone is only mechanical. But the surface bioactivity can be improved by surface treatment. After the treatment, a bioactive layer can be formed on the surface of Ti and its alloys. The common methods can be classified in physics, chemistry and electrochemistry. Each method has

its advantages and disadvantages. Compared to the physical method, the chemical one operates easily and can form a homogeneous layer. But its efficiency is low (Liang *et al.*, 2003). The electrochemical method not only has the advantages of the chemical one but also a high efficiency.

In this research, we fabricated a $K_2(Ti_8O_{17})/TiO_2$ composite bioceramic coating on a Ti surface by the electrochemical method, and the surface topography, microstructure, composition-of-phases, and the bioactivity of the coating were analyzed and evaluated.

The pure Ti was machined into many specimens with a size of 10 mm $\times$ 10 mm $\times$ 1 mm. Then the specimens were milled using sand paper with screen mesh 240, 400, 600 ordinally, and rinsed with acetone, absolute alcohol and distilled water, and subsequently dried. The specimens were used as the electrodes, and 0.5 mol/L K_2CO_3 electrolyte was prepared. A voltage of 20 V was applied for 20 min. After this step a TiO_2 layer was formed on the surface of the anode. And then the electrodes were put into 3 mol/L hot KOH electrolyte for 30 min and given a current density at 2 mA/cm^2. Finally the nano-$K_2(Ti_8O_{17})$ layer was synthesized *in situ* on the surface of the TiO_2 layer. In order to evaluate the bioactivity of the $K_2(Ti_8O_{17})$, the specimen was immersed in SBF (Kokubo *et al.*, 2006). Using the Philips XL30W/TMP SEM, Edax Phoenix EDS, Philips Tecnai-F20 TEM and Rigaku XRD, the surface topography, microstructure and composition-of-phases of the surface coating were analyzed.

Nano-TiO_2 layer synthesized by anode oxidation on the surface of Ti matrix

After the first step treatment in the K_2CO_3 electrolyte, a blue film was obtained on the anode. The thickness of the film was about 70 nm (Sul *et al.*, 2001). The SEM micrographs show that there were many even depressions. The TEM electron diffraction indicated the film was rutile TiO_2. From the structure and the misty diffraction ring shown in Fig. 8.14 we can learn that the TiO_2 film was nano-structured and the crystal was not fine. In other words, the film on the surface of the Ti matrix was composed of nano-particles and was amorphous TiO_2.

The reaction at the anode/electrolyte interface is:

$$Ti \rightarrow Ti^{4+} + 4e \qquad [8.6]$$

$$Ti^{4+}\,(ox) + 4H_2O(aq) \rightarrow Ti(OH)_4(ox) + 2H_2 \rightarrow TiO_{2-x}(OH)_{2x} + (2-x)H_2O \qquad [8.7]$$

After drying the gelatinous, $TiO_{2-x}(OH)_{2x}$ changed to TiO_2.

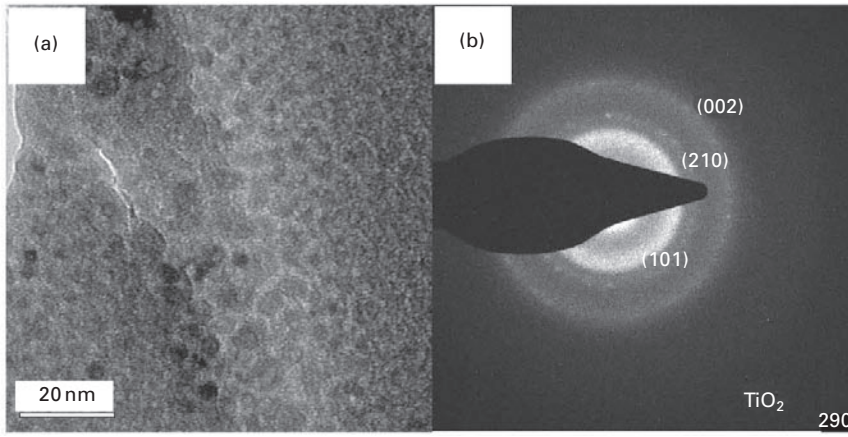

8.14 TEM micrograph (a) and diffraction pattern (b) of TiO_2.

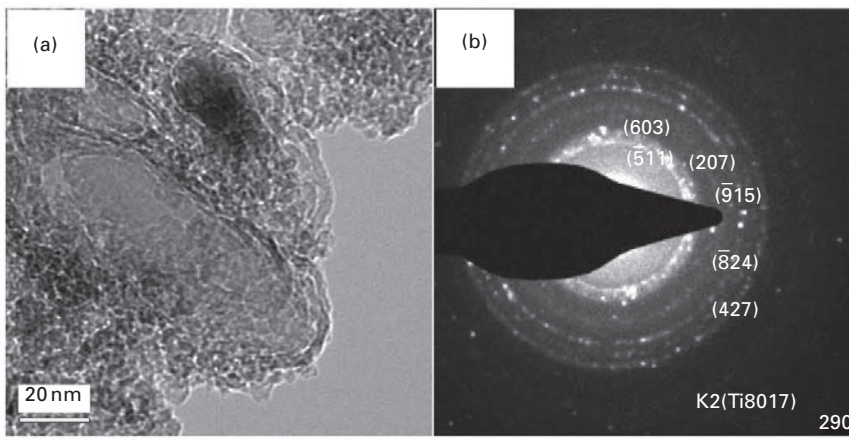

8.15 TEM micrograph (a) and diffraction pattern (b) of the surface structure after post-treatment.

Preparation by an in situ electrochemical technique

At the second step the electrodes were put into 3 mol/L hot KOH electrolyte for 30 min with a current density at $2mA/cm^2$. After that the new coating was observed and tested. Figure 8.15 shows that after the treatment, a layer of $K_2(Ti_8O_{17})$ with a nano-crystalline grain appeared on the sample. The XRD result (Fig. 8.16) indicated that this film was even and simplex. Based on the observation of the diffraction halation in Fig. 8.2b and the diffraction peaks at small angles ($2\theta < 30°$), it can be inferred that some amorphous phases are present.

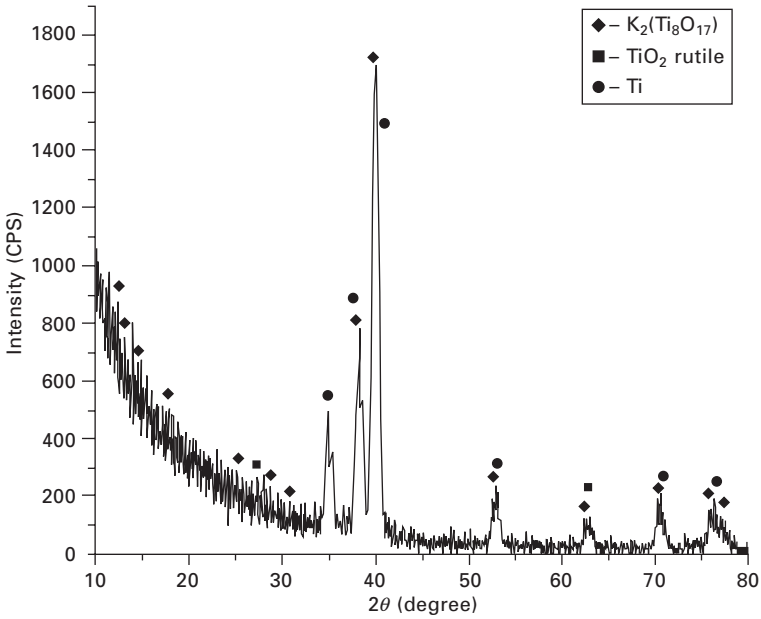

8.16 XRD pattern of the surface coating after electrochemical treatment.

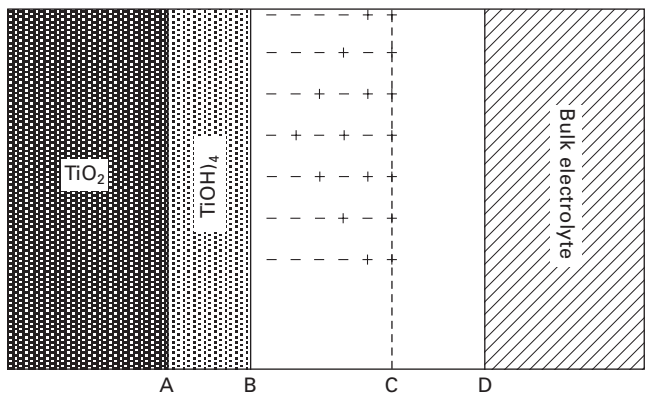

A: $TiO_2/Ti(OH)_4$ interface
B-C: Defect layer of cations
C: Gradient line of concentration distribution
C-D: Balance layer of concentration distribution
+: K^+ – : OH^-

8.17 Schematic structure of electrical double layer at anode/electrolyte interface.

Figure 8.17 is the schematic structure of the double layer at the anode/electrolyte interface. The OH^- was concentrated near the anode. The TiO_2 formed in the first step reacted with the OH^-, so a gelatinous $Ti(OH)_4$ layer

was obtained. Subsequently this united with K^+ and become $K_2Ti_8O_{17}$.

The electrode reaction is:

$$\text{Anode: } TiO_2 + 4\ OH^- \rightarrow Ti(OH)_4 + O_2 \uparrow + 4e \quad [8.8]$$

$$\text{Cathode: } 2H^+ + 2e \rightarrow H_2\uparrow \quad [8.9]$$

So the total electrode reaction is:

$$8TiO_2 + 6OH^- + 4H^+ + 2K^+ \rightarrow K_2Ti_8O_{17} + O_2 \uparrow + 2H_2 \uparrow + 3H_2O \quad [8.10]$$

Figure 8.18 is the SEM micrographs of the $K_2(Ti_8O_{17})$ coating surface. The appearance of this coating is an even and distinct reticular formation. The structure increased the roughness of the surface, and therefore the superficial area. All of these offered sites for bone growth. Thereby the combination between implant and bone was enhanced.

SBF cultivation

In order to evaluate the bioactivity of the $K_2(Ti_8O_{17})/TiO_2$ composite coating, the samples were dipped in 36.5 °C SBF in given periods. After three days, some flocculent sediments and some sheet phases (Fig. 8.19a) appeared on the coating. Seven days later, there were more distinct changes. The clear reticular formation was covered completely by the sheet phases (Fig. 8.19b). The EDS result (Fig. 8.20) showed that the phase contained Ca, P, O and the

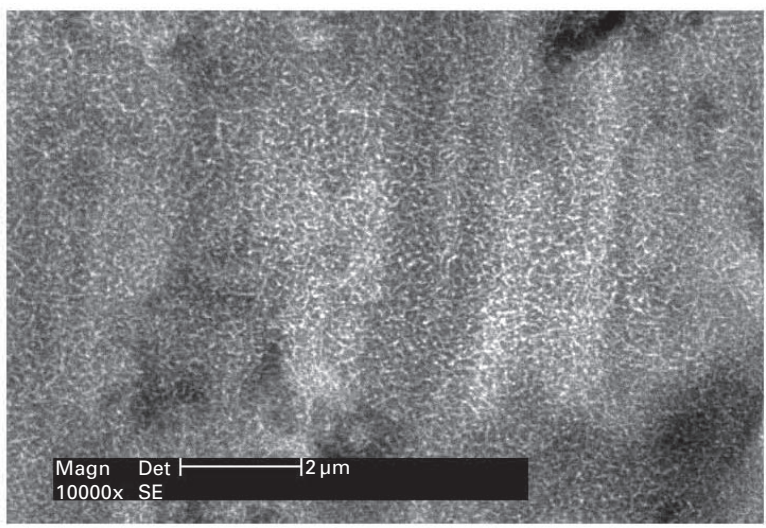

8.18 SEM micrograph of $K_2(Ti_8O_{17})$ coating.

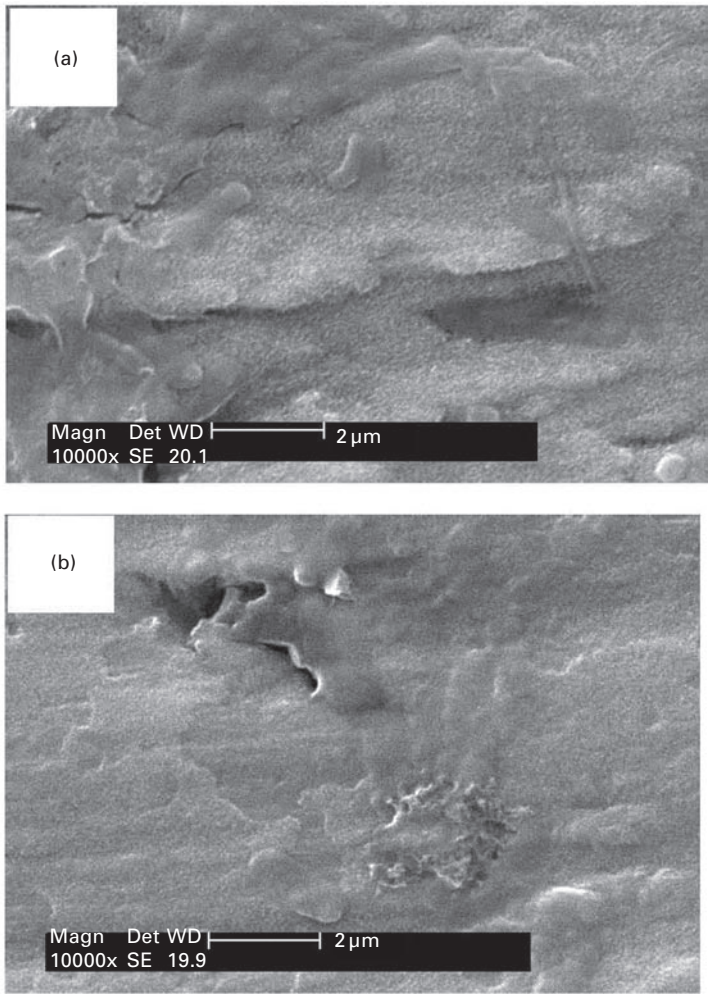

8.19 SEM micrographs of surface of $K_2(Ti_8O_{17})$ coating dipped in SBF.

ratio of Ca to P was about 1.67:1, which is similar to that of bones (Zheng *et al.*, 2000).

The structure of $K_2(Ti_8O_{17})$ is shown in Fig. 8.21. In its structure, the coordination number of the Ti is six and the TiO_6 octahedrons connect with each other at the edge and the corner to form a concatenate tunnel structure. The K^+ is inside the tunnel isolating it from the environment so that it had no chemical activity. The TiO_6 became electronegative, so the Ca^{2+} was adsorbed by the Coulomb force and could attract the HPO_4^{2-}. Therefore the Ca and P were supersaturated near the surface and it was propitious to deposit the Ca and P. In addition, the reticular formation of the $K_2(Ti_8O_{17})$

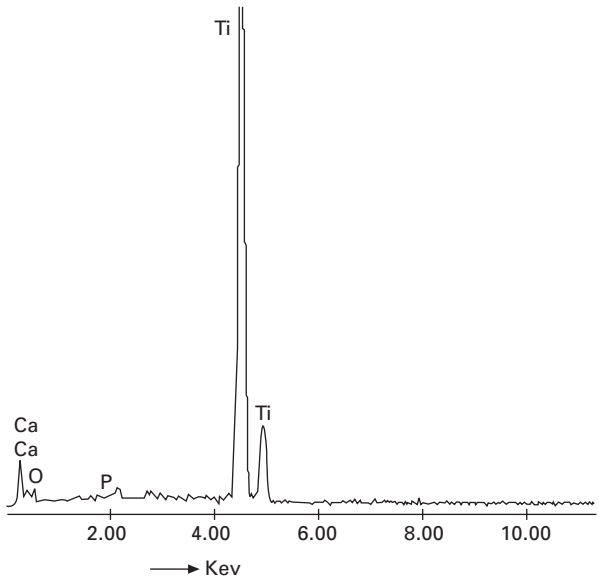

8.20 EDX spectra of titanium samples dipped in SBF.

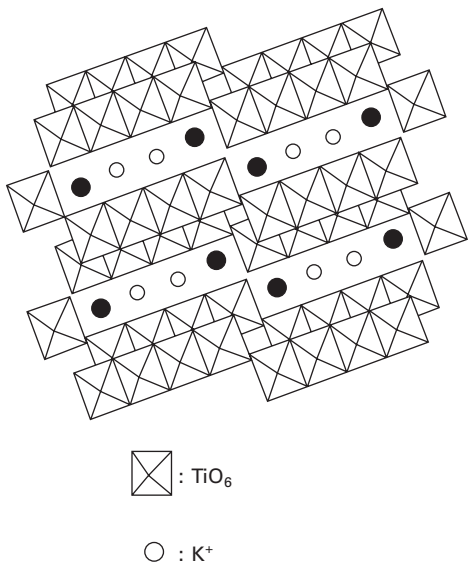

8.21 Crystal structure of $K_2(Ti_8O_{17})$.

increased the roughness, so that offered more nucleant points for the Ca and P sedimentation. The deposited layer appeared in a short time. This layer of Ca and P made the $K_2(Ti_8O_{17})$ coating better advantaged to stimulate the growth of bones and combine the bone with the implant – the coating has fine biocompatibility and bioactivity.

Therefore, a $K_2(Ti_8O_{17})/TiO_2$ bioceramic composite coating with a microstructure of nano-crystalline grain, amorphous on the surface, can be prepared successfully on Ti by an *in situ* electrochemical technique. The appearance of this composite coating is of an even and distinct reticular formation. A layer of phosphate with a Ca/P ratio similar to that of bone was deposited on the surface after the SBF cultivation in a given time. The test of SBF cultivation indicated that the $K_2(Ti_8O_{17})/TiO_2$ bioceramic composite coating has fine biocompatibility and bioactivity.

8.5 Acknowledgements

This work was supported by the programs of The Natural Science Foundation of China (Project No. 50271024), The Natural Science Foundation of Tianjin (Project No. 05YFZJC02200) and The Natural Science Foundation of Hebei Province (Project No. E2006000025).

8.6 References

Ask M., Lausmaa J., Kasemo B., *Appl Surf Sci*. **35** (1988–89) 283.

Bania P.J., in: Eylon D., Boyer R.R., Koss D.A. (Eds.), *Titanium Alloys in the 1990s*, The Mineral, Metals & Materials Society, Warrendale, PA, 1993, pp. 3–14.

Bobyn J.D., Pilliar R.M., Cameron H.U., Weatherly G.C., *Clin. Orthop*. **150** (1980) 263.

Boehm H.P., *Discuss Faraday* **52** (1971) 264.

Brown S., Turner I., Reiter H., *J. Mater. Sci*. **5** (1994) 756.

Bu Shaojing, Cui Chunxiang, Liu Xiaoxin, Bai Ling, *Journal of Sol–Gel Science and Technology* **43** (2007) 151.

Bukaluk A., *Appl. Surf. Sci*. **175–176** (2001) 790.

Cahn R.W.. *Nature* **410** (2001) 643.

Cheang P., Khor K.A., *Biomaterials* **17** (1996) 537.

Collings E.W., The physical metallurgy of titanium alloys, in: H.L. Gegel (Ed.), *ASM Series in Metal Processing*, Edward Arnold Publications, Cleveland, Metals Park, OH, 1984.

Cui Chunxiang, Liu Hua, Li Yanchun, Sun Jinbin, Wang Ru, Liu Shuangjin, Greer A.L., *Materials Letters*. **59** (2005) 3144.

Cui Chunxiang, Shen Yutian, Xu Yanji, Li Yanchun, Wang Ru, Wang Xin, Wang Chao. *Rare Metal Materials and Engineering* **32** (2003) 627.

Currey J. *Nature* **414** (2001) 699.

Dasarathy H., Riley C., Coble H.D., Lacefield W.R. and Maybee G., *J Biomed Mater Res*. **31** (1996) 81.

David G.C., Buddy D.R., *Surface Science* **500** (2002) 28.

Donachie M.J., *Titanium: A Technical Guide*. Philadelphia, PA: American Society for Testing and Materials, 1988. p. 29–34.

Dowson D., Wright V., in: D. Dowson, V. Wright (Eds.), *Introduction to the Biomechanics of Joints and Joint Replacement*, Mechanical Engineering Publications, London, 1981.

Erlebacher J., Aziz M.J., Karma A., Dimitrov N., Sieradzki K., *Nature* **410** (2001) 450.

Haddow D.B., James P.F. and Van Noort R., *J Sol–Gel Sci Technol*. **13** (1998) 261.
Haman J.D., Boulware A.A., Lucas L.C. and Crawmer D.E., *J Thermal Spray Technol*. **4** (1995)179.
He X., Antonelli D., *Angew. Chem., Intl. Ed*. **41** (2001) 214.
Hendrich V.E., *Rep. Prog. Phys*. **48** (1985) 1481.
Hero H., Wie L., Jorgensen R.B. and Ruyter I.E., *J Biomed Mater Res*. **28** (1994) 343.
Howie D.W., in: Older M.W.J. (Ed.), *Implant–Bone Interface*, Springer, London, 1990.
Jasty M., *J. Appl. Biomater*. **4** (1993) 273.
Jiang P., Bertone J.F., Colvin V.L., *Science* **291** (2001) 453.
Jillavenkatesa A. and Condrate Sr R.A., *J Mater Sci*. **33** (1998) 4111.
Jones L.C., Hungerford D.S., *Clin. Orthop*. **225** (1987) 192.
Kamitakahara M., Kawashita M., Miyata N., Kokubo T. and Nakamura T., *Biomaterials*, **24** (2003) 1357.
Kilpadi D.V., Raikar G.N., Liu J., Lemons J.E., Vohra Y. and Gregory J.C., *J Biomed Mater Res*. **40** (1998) 646.
Klein C.P.A.T., Wolke J.G.C., de BlieckñHogervorst J.M.A. and de Groot K., *J Biomed Mater Res*. **28** (1994) 909.
Korkusuz F. and Uluoglu O., *Bull Hosp Jt Dis*. **58** (1999) 86.
Kyeck S. and Remer P., *Mater Sci Forum* **308–311** (1999) 368.
Liang Fanghui, Zhou Lian, *Rare Metal Materials and Engineering* **32** (2003) 241.
Long M., Rack H.J., *Biomaterials* **19** (1998) 1621.
McPherson R., Gane N., Bastow T., *J. Mater. Sci*. **6** (1995) 327.
Montenero A., Gnappi G., Ferrari F., Cesari M., Salvioli E., Mattogno L., Kaciulis S. and Fini M., *J Mater Sci*. **35** (2000) 2791.
Morscher E., *Endoprosthetics*, Springer, Berlin, 1995.
Ogden H.R., in: Clifford A.H. (Ed.), *Rare Metals Handbook*, Reinhold Publishing Corporation, Chapman & Hall Ltd., London, 1961, pp. 559–579.
Ong J.L., Harris L.A., Lucas L.C., Lacefield W.R. and Rigney D., *J Am Ceram Soc*. **74** (1991) 2301.
Parfitt G.D., *Progress in Surface and Membrane Science, Vol. 11*, Academic Press, New York, 1976, p. 181.
Parks G.A., *Chem. Rev*. **65** (1965) 177.
Pham M.T., Zyganow I., Matz W., Reuther H., Ostwald S., Richter E. and Wieser E., *Thin Solid Films* **310** (1997) 251.
Polmear J.J., Titanium alloys, in: *Light Alloys*, Edward Arnold Publications, London, 1981 (Chapter 6).
Qu Henglei, Zhou Lian, Wei Hairong. *The Chinese Journal of Nonferrous Metals* **11** (2001) 398.
Rintoul T.C., Bulter K.C., Thomas D.C., Carriker J.W., Maher T.R., Kiraly R.J., Massiello A., Himely S.C., Chen J.F., Fukamachi K., *ASAIO J*. **39** (1993) 168.
Rønold H.J. and Ellingsen J.E., *Biomaterials*, **23** (2002) 4211.
Schindler P.W., *Rev. Mineral*. **23** (1990) 281.
Schutz R.W., in: Eylon D., R.R. Boyer R.R., Koss D.A. (Eds.), *Beta Titanium Alloys in the 1990s*, The Mineral, Metals & Materials Society, Warrendale, PA, 1993, pp. 75–91.
Singh R.K., Qian F., Damodaran R. and Moudgil S., *Mater Manuf Processes* **11** (1996) 481.
Tadashi Kokubo, Hiroaki Takadama, *Biomaterials* **27** (2006) 2907.

Textor M., Sittig C., Frauchiger V., Tosatti S., Brunette D.M., in: Brunette D.M., Tengvall P., Textor M., Thomsen P. (Eds.), *Titanium in Medicine*, Springer, Berlin, 2001, pp. 171–230.
Tierney M.J., Kim H.O.L., *Anal. Chem.* **65** (1993) 3435.
Tsui Y.C., Doyle C. and Clyne T.W., *Biomaterials* **19** (1998) 2031.
Velev O.D., Tessier P.M., Lenhoff A.M., Kaler E.W., *Nature* **140** (1999) 548.
Venezuela J.P., Tersoff J.A., Floro E., Chason D.M., *Nature*, **397** (1999) 678.
Wang B.C., Chang E., Yang C.Y., Tu D. and Tsai C.H., *Surf Coat Technol.* **58** (1993) 107 .
Williams D.F., in: Brunette D.M., Tengvall P., Textor M., Thomsen P. (Eds.), *Titanium in Medicine*, Springer, Berlin, 2001, pp. 13–24.
Wolke J.G.C., van Dijk K., Schaeken H.G., de Groot K. and Tansen J.A., *J Biomed Mater Res.* **28** (1994) 1477.
Yamashita K., Yagi T. and Umegaki T., *J Am Ceram Soc.* **79** (1996) 3313.
Young-Taeg Sul, Johansson Carina B., *Medical Engineering & Physics* **23** (2001) 329.
Zheng Xuebin, Ding Chuanxian. Plasma Sprayed HA/ZrO_2 Composite Coating, *Journal of Inorganic Materials* **15** (2000) 341.

9

Forging of metals and alloys for biomedical applications

M. CHANDRASEKARAN, Bio-scaffold International Pte Ltd, Singapore

Abstract: Processing plays a vital role in the final properties achievable in an artificial implant. The properties that are critical to an artificial implant include: comparable or higher strength and modulus to that of bone, high fatigue and wear resistance, fracture toughness and anisotropic elastic properties similar to that of bone/tissue. This chapter reviews the process of forging applied to implant materials, in particular their advantages and disadvantages in terms of achieving the desired properties. A discussion on the effect of various alloying additions on forging resistance and their impact on biocompatibility is also included, besides the various die design considerations. Finally, some of advanced methods of processing relevant to forging is discussed.

Key words: cold and hot forging, isothermal forging of titanium, titanium alloys, cobalt chromium alloys, stainless steel, die materials for forging, P/M forging.

9.1 Introduction

Metallic materials have long been used in biomedical applications and can be broadly divided into implantable and non-implantable metallic materials. In these, the properties of implantable materials are critical since they need to fulfill certain property requirements beside being biocompatible and bioinert to the physiological environment. The most common metallic materials that are used include titanium and its alloys, cobalt-chromium alloys, stainless steels, and special alloys such as nickel-titanium. Much of the properties of the end products (such as implants and fixation materials) are governed by the manufacturing method used and have a significant impact on the application design. Conventional methods of fabrication used were casting and machining to shape. However, these had limitations in the final properties achievable in the implant or the specified application. Forging of metals and alloys used in biomedical applications overcomes some of the limitations associated with other conventional methods of fabrication, especially in terms of properties achievable. A typical example is 316L stainless steel used for fixation plates, which is not heat treatable after fabrication. Cold working or forging results in improved strength. This chapter focuses on the fundamentals of forging of metallic materials and the typical forging methodology used for biomedical applications.

9.2 Fundamentals of forging and typical forging process applied to metals and alloys for biomedical applications

Forging is a process in which the work piece is shaped by compressive forces applied through various dies and tools. It is one of the oldest metalworking operations. Most forgings require a set of dies, and a press or a forging hammer.

Unlike other metal forming operations, which generally produce continuous plates, sheets, strip, or various structural cross-sections, forging is predominantly used to produce discrete parts. Forging can be broadly classified based on few factors, such as temperature, tools used for forging operation, die design in forging, etc. However, the most common classification is based on temperature and die design.

9.2.1 Cold and hot forging

Cold forging is an operation done normally at room temperature or near room temperature. Metallurgically, any forging operation done below the recovery temperature ($0.2T_m$–$0.4\ T_m$, where T_m is the melting point of the material) of the material, thereby producing a work hardening effects is termed as cold forging. On the other hand, hot forging is done at elevated temperatures, typically $> 0.4\ T_m$. Deformation at these temperatures reduces the flow stress, making the metal or alloy easier to shape and less likely to fracture. The temperature of operation is above the re-crystallization temperature of the material (typically between $0.4T_m$–$0.6T_m$) which eliminates any strain hardening effect. Warm forging is done at an intermediate temperature between room temperature and hot forging temperatures. Despite the three classifications based on temperature, the terminology of warm forging is seldom used. Alloying constituents have an important role on the forging temperature classification and can lower or rise the temperature for hot forging. Hot forging, besides eliminating the strain hardening, has many advantages that include:

- decreased yield strength and hence lower flow stress, facilitating easier plastic deformation at low loads
- increased ductility
- Reduced chemical inhomogeneities
- closure or elimination of pores during operation.

On the other hand hot forging has disadvantages such as:

- poor surface finish and dimensional control
- oxidation or undesirable reactions between the material and the surrounding atmosphere, etc.

Cold forging has certain advantages, such as:

- better surface finish and dimensional control
- increased strength due to work hardening
- minimum contamination.

Despite these advantages, cold forging suffers from disadvantages such as:

- higher yield strength and hence higher loads needed for deformation
- poor ductility compared with hot forging
- intermediate annealing requirement, sometimes needed to address work hardening
- residual stresses, sometimes produced
- Texture, sometimes formed.

Hot die and isothermal forging

One of the major problems associated with hot forging is the associated high temperature which generally requires special die materials that can withstand the temperature with a judicial compromise on the strength. However, in most forging, the die material is kept at a lower temperature compared with the forging temperature of the work-piece. A general problem associated with such a set up is the heat transfer from the work-piece to the die surfaces, causing thermal gradients in the work-piece. The cooler areas closer to the die surfaces undergo less plastic flow than in the hotter core areas, so that plastic flow is not uniform. The non-uniform plastic flow is caused by die chilling. In conventional steel forging practice, dies for forgings are heated to a maximum temperature range of 150 to 300 °C, depending on the equipment, to reduce the effects of die chilling. Another way to reduce the die chilling effect is to use lubricants that can form as thermal barrier between the work-piece and the die surfaces. Die chilling can also be reduced or eliminated by heating the dies nearer to the actual forging temperature or maintaining the die at the same temperature as that of the work-piece. The process can be classified as hot die forging when the temperature of the die is closer to the forging temperature and isothermal forging when the die is maintained at the same temperature as that of work-piece.

In general, most wrought implant materials such as alloys of titanium (Ti) and nickel (Ni) are forged in the range of 925 to 1260 °C. Conventionally, Ti and its alloys are hot forged as isothermal forging of these alloys requires special tooling materials, such as nickel-based super alloys and molybdenum alloys for dies, and lubricants that can perform adequately at these temperatures. Special attention to the surrounding atmosphere is also important, such as the use of an inert gas or vacuum to protect both the dies and the work-piece from oxidation.

Hot die and isothermal forging offer advantages and disadvantages. The primary advantages are closer forging tolerances, resulting in reduced machining and material costs, a reduction in the number of pre-forming and blocking operations, resulting in reduced processing and tooling costs, and the use of slow ram speeds, resulting in lower forging pressures and the use of smaller machines.

The primary disadvantages are the requirements for more expensive die materials, uniform and controllable die heating systems, and an inert atmosphere or vacuum around the dies and work-piece to avoid oxidation of the dies. The typical production rates are very low in order to permit proper die filling at the low forging pressures.

Warm forging

Forging operations typically carried out between the recovery temperature of the material and that of recrystallization temperatures ($0.2T_m$–$0.4T_m$) are normally termed as warm forging. This type of forging is preferred where the strength and other properties need to be either maintained within tolerable limits but not substantially higher than the initial value. Warm forging has a number of cost-saving advantages over cold or hot forging methods. Compared with cold forging, warm forging has the potential advantages of: reduced tooling loads, reduced press loads, increased ductility, elimination of need to anneal prior to forging, and favorable as-forged properties that can eliminate heat treatment. On the other hand, the temperatures used for warm forging are lower than that of hot forging operations, thus saving on energy costs as well as eliminating the need for the special tools that are required in hot forging operations. This type of metal working is limited to temperature ranges of 0.2–0.4 times the melting point of the respective material/alloy system. The operation produces a tolerable surface finish with a slightly lower energy requirement. It also normally does not require annealing in the intermediate stages of forging.

9.2.2 Open- and closed-die forging

Another major classification of forging is based on the die design and includes open-die forging, closed-die forging and flash-less forging. Medical implants are normally closed-die forged to shape.

In open die forging, Fig 9.1a, the die or punch carries the impression of the product and the material is allowed to flow under the action of a compressive load from the punch in the cavity. However, this type of forging is limited to shapes that are simple.

Closed-die forging, Fig 9.1b, however, has the forging impression on both the die and punch, with a land for flash material to flow. The material is

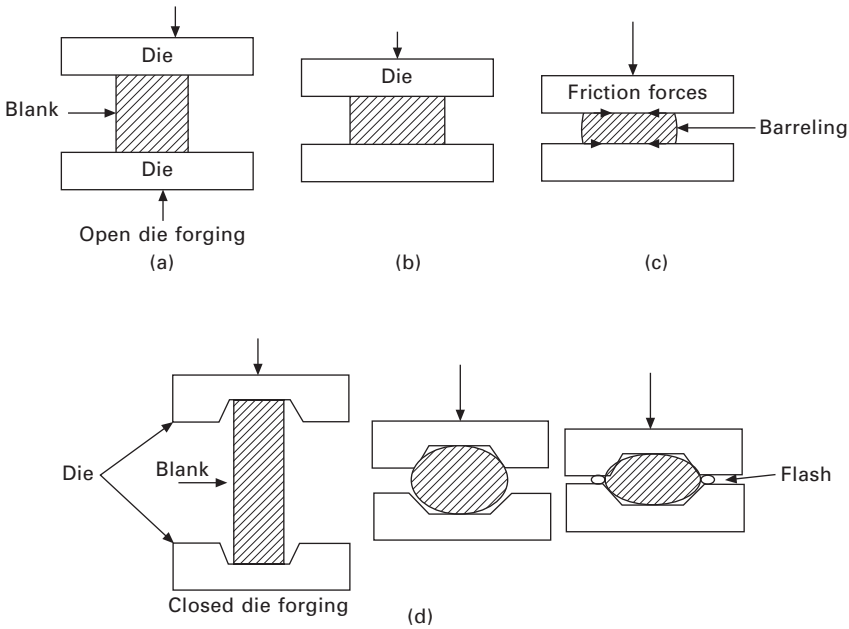

9.1 Schematic illustration of open die forging (a–c) and closed die forging (d) processes.

allowed to flow into the cavities of the punch and die to form the required shape. This results in the production of a flash. The volume of the material used in this type of forging is similar to the final volume of the product with some tolerance. Most medical implants are produced using closed-die forging followed by a finishing operation.

9.3 Properties for forgeability

The most important property that is required for good forgeability is the plasticity in the material, which governs the deformation and flow stress of the material.

The stress experienced by a work piece can be represented by equation 9.1:

$$\sigma = K\varepsilon^{n}\dot{\varepsilon}^{m}T^{T}G^{g} \qquad [9.1]$$

where K is a constant depending on the material, ε is the strain, n is the strain hardening exponent, $\dot{\varepsilon}$ is the strain rate, m is the strain rate sensitivity of the material, T is the temperature, t is the rate of change of temperature with deformation, G is the grain size, and g is the rate of change of grain size during deformation.

It can be clearly seen that as the strain hardening exponent or strain rate

sensitivity increases, the flow stress increases substantially. In other words, forgeability of the material is a function of strain, strain rate, temperature and deformation rate. Besides this, various other factors do influence the flow stress and hence the forgeability. They include, surface texture, plastic anisotropy, billet size and temperature/preprocessing history of the billet.

The crystal structure of the chosen implant material plays a significant role in the forgeability of the material because the flow stress depends on the slip systems present. Both stainless steel (SS) and cobalt (Co)-chromium (Cr) alloys exhibit FCC (face centered cubic) structure while Titanium (Ti) exhibits polymorphism of two different crystal structures at room and elevated temperature. The room temperature phase (often referred to as Alpha Ti) has an HCP (hexagonally closely packed) structure, which has only three slip systems active at room temperature; while the high temperature beta phase exhibits BCC (body centered cubic) structure which has 48 slip systems. The number of active slip systems in the alloy has a direct effect on forgeability by affecting the flow stress of the material. Typically, alloy systems having the HCP structure are the most difficult to forge, followed by FCC and then BCC. Thus, when forging an alloy with an HCP structure, it is imperative to activate more slip systems by increasing the temperature to make the alloy forgeable, and thus the forging temperature of Ti alloy systems vary from 800–1200 °C while those of Co-Cr alloys and SS require temperatures of 1100–1300 °C. Figure 9.2 shows typical crystal structures observed in common implant materials

9.4 Microstructural development and its consequences on properties

Forging results in metal that is stronger than cast or machined metal parts. This is due to the grain flow caused through forging. As the metal is pounded,

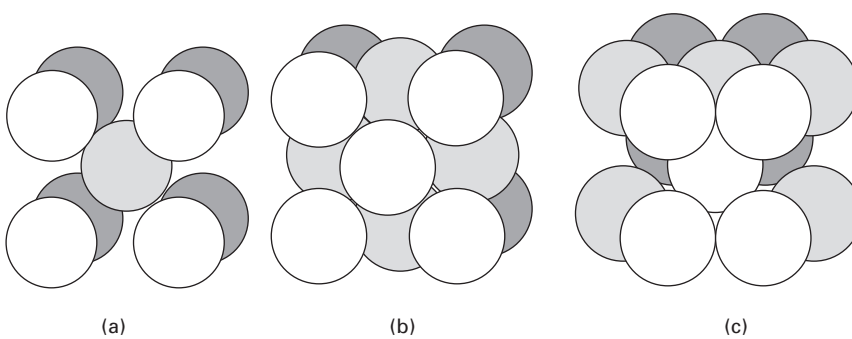

9.2 Schematic illustration of crystal structure in a unit cell of common implant materials (a) BCC (beta Ti), (b) FCC (SS and Co–Cr alloys) and (c) HCP (alpha Ti).

the grains deform to follow the shape of the part; thus the grains are unbroken throughout the part. Some modern parts take advantage of this for a high strength-to-weight ratio.

Many metals are forged cold, but iron (Fe) and its alloys are almost always forged hot. This is for two reasons: first, if work hardening were allowed to progress, hard materials such as iron and steel would become extremely difficult to work with; secondly, steel can be strengthened by other means than cold-working, thus it is more economical to hot forge and then heat treat. Alloys that are amenable to precipitation hardening, such as most alloys of aluminum and titanium, are also hot forged then hardened. Similarly cobalt-chromium is hot forged while it is preferable to perform cold working of stainless steel as strengthening is achieved by cold working. Other materials must be strengthened by the forging process itself.

9.5 Forging of metals and alloys for biomedical applications

9.5.1 Forging of titanium and its alloys

The use of Ti and its alloys in clinical applications dates back to the early 1950s owing to its excellent corrosion resistance, biocompatibility and high strength-to-weight ratio. However, the processing of Ti and its alloys has been a major challenge due to its high reactivity at elevated temperatures. The conventional method of processing includes vacuum casting followed by machining. Machining of Ti and its alloys is a major challenge due to its poor thermal conductivity, necessitating the use of high-speed machining with a suitable coolant to prevent galling. On the other hand, deforming Ti and its alloys (forging) to the required shape followed by finish machining is difficult because titanium is highly strain-rate sensitive. Moreover, Ti and its alloys exhibit polymorphism and the allotropic transformation occurs at 882.5 °C for pure Ti; this temperature varies with the alloying additions. The alloying addition can be either an alpha or beta stabilizer, depending on whether it increases or decreases the transformation temperature. Alpha/beta stabilizers can be classified as either isomorphous or eutectoid stabilizers, depending on the crystal structure of the additive. The eutectoid stabilizers result in transformation of beta phase into alpha with the corresponding alloying element upon slow cooling. Hence, in order to retain the beta phase at room temperature, quenching is preferred. In the case of alloys using isomorphous stabilizers, show cooling does not result in reverse phase transformation to alpha Ti and the respective alloying element. Hence, for eutectoid stabilizers it is recommended that the alloy be quenched from its beta transformation temperature to retain partial beta phase upon cooling. Vanadium (V) and molybdenum (Mo) are typical examples of isomorphous

beta stabilizers while Fe, Cr and silicon (Si) are eutectoid beta stabilizers. The most commonly used alloying element – aluminum (Al) – is an alpha stabilizer. Pure beta phase alloy can be rolled to about 90% reduction in thickness. Alpha and near alpha Ti are not heat treatable/weldable and have limited formability at room temperature. Alpha-beta or beta titanium alloys have reasonably good formability. Alpha or near alpha alloys are strengthened by inducing cold work or plastic deformation. Various grades of Ti and its alloys are being used in implants, including commercially pure Ti in dental implants and maxillofacial applications and specific alloy systems such as Ti–6Al–4V in hip and knee prostheses, trauma fixation devices and implants. Commercially pure Ti offers excellent corrosion resistance and biocompatibility but is restricted by its lower strength and poor wear properties. The microstructure of titanium has considerable effect on the deformation behavior and work hardening rate of titanium. This property is exploited in strengthening Ti and its alloys as well as for deformation processing of Ti and its alloys (forging). The most commonly used Ti alloy (Ti–6Al–4V) has an alpha-beta structure. The flow stress of the alloy is very high at room temperature leading to poor formability but, on the other hand, causing less contamination as the billet is maintained at room temperature. Raising the temperature of Ti and its alloys induces oxygen and hydrogen contamination, affecting the deformation despite an increase in the number of active slip systems. Thus, the deformation needs to be carried out at temperatures close to beta transus, activating more slip planes. However, Ti is highly oxidative above 600 °C since the stable Ti oxide film normally formed is broken, exposing the nascent Ti surface and increasing the rate of oxidation. Thus, the deformation of Ti and its alloys near the beta transus temperature needs to be carried out in a controlled environment in an inert atmosphere to minimize or eliminate the oxidation thus increasing the processing cost. Ti and its alloys are forged at temperatures ranging from 900 to 1200 °C, depending on the grade of pure Ti or the alloying additions used. The deformation behaviors of Ti and its alloys are much dependent on the phases present at the deformation or hot working temperature. Typically in an alpha-beta system, the deformation is controlled by either the alpha or the beta phase, depending on the temperature selected for the hot working. To improve properties such as wear resistance, surface modifications such as ion nitriding or coating are used. Some of the typical alloys which are used include Ti–6Al–4V, Ti–5Al–2.5Fe, Ti 6Al–7niobium (Nb). Ti alloys also exhibit super plasticity (elongations ranging from 200 to 2000%) if they meet certain criteria such as fine grain size and have a suitable grain refiner. Recent developments are directed towards application of super plastic forming for fabricating dental implants. The typical flow stress of Ti alloys is above 400 MPa at room temperature but this drops to <50 MPa at about 900–1100 °C. Moreover, Ti and its alloys work-harden easily, necessitating

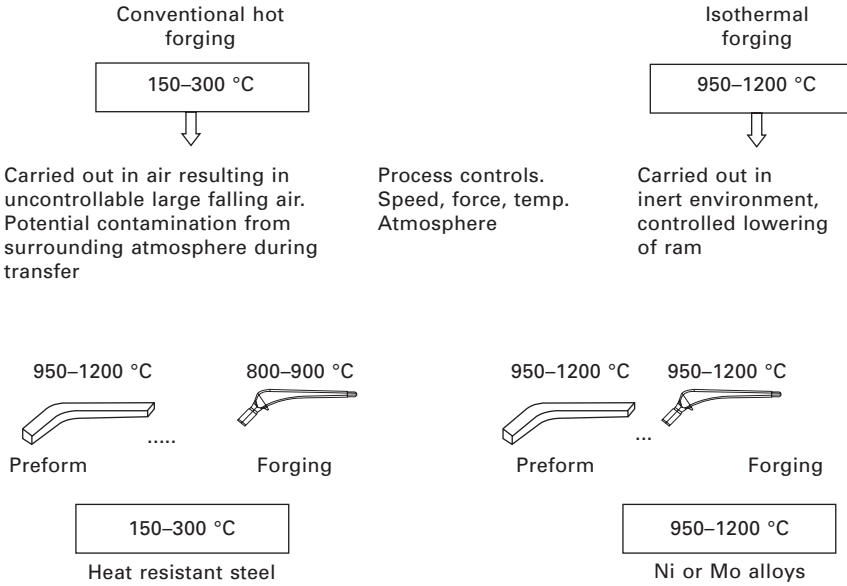

9.3 Schematic illustration of typical hot forging and isothermal forging of Ti alloy. Adapted from *Titanium in Medicine*, with kind permission from Springer Science and Business Media.

intermediate annealing steps before the final shape is arrived at, when it is either cold worked or warm forged.

Figure 9.3 illustrates the typical steps involved in hot forging and isothermal forging. Table 9.1 lists typical properties of various grades of Ti alloys.

Ti alloys are a good choice for permanent implants, due to their high corrosion resistance (spontaneous self-passivation, or development of oxide surface layer). Most Ti alloys for implants are typically fabricated by combined forging and annealing. Despite the fact that the Young's modulus of the common Ti alloy used for implants (Ti–6Al–4V) is ≈ 50% lower than stainless steel, thus reducing the stress shielding, the modulus of the alloy is still six times that of bone: this is critical, especially in wrought (forged) alloys, as mechanical properties are better than the cast alloys. Major disadvantages include reduced fatigue life, due to the presence of stress concentrations, and high wear rates.

9.5.2 Forging of Co–Cr alloys

The use of wrought Co–Cr alloys in clinical applications goes back to the early 1950s, replacing cast components owing to better mechanical properties such as fatigue life and strength. Despite the fact that there are many cobalt based biomaterials, two main alloys, namely cast Co–Cr alloys and wrought

Table 9.1 Typical properties of Ti and its alloys commonly used in implants

Material	ISO code	Ultimate tensile strength, MPa	Elongation to failure (%)
Grade-1	5832-2	240	24
Grade-2	5832-2	345	20
Grade-3	5832-2	450	18
Grade-4	5832-2	550	15
Ti–6A–l4V	5832-3	860	10
Ti–6Al–7Nb	5832-11	900	10

Note: Table consolidated from various references.

Co–Cr alloys, are used. Co–Cr alloy has an austenitic structure (FCC) which is stabilized by the presence of Ni, Fe and manganese (Mn), thus avoiding the change of crystal structure to BCT (body centred tetragonal) which is difficult to process. The presence of Ni improves the forgeability of wrought Co–Cr alloys. From a biocompatibility perspective, Co, Cr and Ni are not preferred as individual ions as Ni and Co are found to cause allergies while Cr is toxic. Though wrought Co–Cr alloy as such does not cause any toxicity, the elution of metal ions is a serious concern because Ni is also carcinogenic. Thus, the Ni content needs to be reduced or eliminated to avoid the toxicity issue. This results in a contradicting situation whereby the removal of Ni will affect the workability of the material. Wrought Co–Cr alloys are hot forged and intermediate annealing may be required before arriving at the final shape. Due to the difficulty associated with machining Co–Cr alloys, it is preferable to perform a closed die forging operation to minimize the finish machining. Forging of Co–Cr alloys normally requires a sophisticated press with heat-resistant tooling, since it is difficult to work at lower temperatures and isothermal or hot forging is desired with an intermediate annealing process.

The metallurgy of cobalt-chromium alloys is identical to that of the cobalt-based super alloys, and solid solution strengthening is produced by the presence of alloying elements. Formation of carbides also increases the strength. Therefore, the carbides should be minimized in order to be able to work the wrought alloys. The order of carbon content is about one fifth of that of the casting alloys. In addition to this, reduction of Cr content contributes to enhanced workability of Co–Cr alloys. Recommended practice is to heat treat Co–Cr alloys within 900 to 1150 °C before hot working, such as forging, is done. By controlling the forging ratio, the microstructure of Co–Cr alloys can be controlled to obtain good fatigue strength and wear resistance. The forging of Co–Cr alloys is carried out in a similar manner as that of titanium, except for the change in the working temperature, which varies typically from 1150–1300 °C.

Co–Cr–Mo alloy also is a good choice for permanent implants, due to its high corrosion resistance. Generally, cast parts have poorer mechanical properties than 316L stainless steel and the mechanical strength is enhanced by forging or hot isostatic pressing, which reduces grain size and the concentration of defects. Typical disadvantages include high cost and limitations on component complexity.

Table 9.2 lists the typical properties of Co–Cr alloys used in implants.

9.5.3 Forging of stainless steel

Stainless Steel (SS) are generally preferred for short term implants where the implant can be removed within one to two years. SS materials that are used in implants are normally not heat-treatable and thus much of their mechanical properties are tailored by performing cold work. They find use in components such as bone screws, plates and other temporary fixation devices. SS used for implants are austenitic and have good formability. Typical hot working temperatures are around 1100 to 1250 °C. Rapid cooling upon completion of hot working is not required in the case of implant materials such as 316L, since there will be no detrimental precipitation of carbides. Precipitation of carbides affects the corrosion resistance and ductility.

Table 9.3 lists the properties of various stainless steels used in implants.

9.5.4 Forging of shape memory alloys

Shape memory alloys are used in applications such as osteo-synthesis plates and dental braces. They derive the name due to their property of remembering

Table 9.2 Typical properties of Co–Cr alloy used in implants

Material	ASTM, code	Yield strength (MPa)	Ultimate tensile strength (MPa)	Ultimate elongation (%)	Hardness (HRC)	Bending strength (MPa)
Cast	F75	450	655	8	NA	300
Forged	F799	827	1172	12	35	600
Wrought and annealed	F1537	517	897	20	25	
Wrought and hot worked	F1537	700	1000	12	28	
Wrought and warm worked	F1537	827	1172	12	35	
Annealed	F562		800	40		
Annealed	F563	276	600	50		
Cold worked	F562		1200	10		
Cold worked	F563		1310	12		

Note: Table consolidated from various references.

Table 9.3 Typical properties of stainless steels used in implants

Material	ASTM code	Yield strength (MPa)	Ultimate tensile strength (MPa)	Ultimate elongation (%)
DIN 17443	5832-1		490–690	40
REX 734	5832-9		740	35
In development	P2000		980	55
316L		205	515	40
DIN 17443 CW*			860	12
REX 734 CW			1060	12
In development CW			1200	12
316L CW		690	860	12

* CW-cold worked
Note: Table consolidated from various references.

the prior shape, even if it has undergone significant deformation. One such shape memory alloy used in implants is Nitinol (Ni–Ti Alloy). Nitinol undergoes forging and rolling at elevated temperatures after the ingot is produced. Typical hot working temperatures are around 800 to 900 °C, when the workability of the material is good with minimal surface oxidation. Hot working processes improve the mechanical properties of Nitinol by adjusting its microstructure. Following hot working, Ni–Ti alloy is cold worked and heat treated to obtain the final dimensions with desired properties. Ni–Ti alloy undergoes rapid work hardening, thus necessitating multiple reductions with intermediate annealing steps at 600–800 °C until the final shape and size are obtained. A major problem associated with Ni–Ti alloy forming is the spring back, thus requiring over deformation in order to release the stress and achieve the desired shape. Another option to counteract the spring back is to heat treat the part under constraint.

9.6 Die materials and die design for forging

Hot work die steels are most commonly used in forging dies for working at temperatures of 350 to 650 °C. The hot work die steels usually contains carbide-forming elements such as Cr, tungsten (W), Mo. These alloying elements form carbides that induce hardening with high resistance to softening.

For hot forging, the die material should possess the following properties

- uniform hardenability
- good abrasion resistance
- high hardness
- toughness
- good mechanical and thermal fatigue strength.

Besides the selection of the die material, it is imperative that the die design takes into account properties such as metal flow and ensures minimal losses into flash. Thus, die design for multi-stage forging and corresponding pre-formed designs are critical for obtaining defect-free forging. Both the pre-form die design and pre-form shaping in work pieces are critical to obtain a successful and economic forging. Therefore, the pre-form shaping is done either by machining or by open die forging until the required shape for the final closed die forging operation is achieved. The pre-form shaping operation has to be carefully selected in order to avoid stress concentrations or non-uniform stress distribution in the pre-form. This will affect the flow stress of the material in different regions and thus the plasticity. Recent developments in the field of modeling help to overcome the limitations of conventional trial and error methods to obtain optimum pre-form designs and die designs. Finite element modeling helps to identify non-uniform stress states that arise due to different processing methodologies, and optimize the pre-processing conditions and the die design for pre-processing.

For Isothermal forging, the die material should possess the following properties:

- good mechanical and fatigue strengths at elevated temperature
- good abrasion resistance
- hot hardness and toughness.

Isothermal forging is typically carried out between 900 and 1100 °C, depending on the material being forged, and die steel materials do not meet the required strength criteria at elevated temperatures. Thus isothermal forging necessitates the use of Ni super alloys or Mo alloys for the die. One of the major problems associated with hot die forging and isothermal forging is the poor tool life, as opposed to closed die forging, which also affects the economics of forging.

9.7 Powder metallurgy forging of metals and alloys for biomedical applications

Powder metallurgy (PM) forging is a process whereby a sintered powdered metal part is forged using conventional closed die forging to attain the final shape. A recent development in the field of medical implants is the production of porous metallic implants by the above mentioned process using Co-based alloys or Ti alloys. This type of forging is preferred for improving the osteo-integration of the implant as well as to address the limitations associated with conventional wrought alloys such as limited plasticity and high flow stress. Especially, isothermal forging of Ti and Co based alloys require expensive tooling materials, such as Ni-based super alloys or Mo alloys for dies, and special lubricants. Moreover, use of the PM process to produce the pre-form

required for final closed die forging contributes to the cost advantage, thereby improving the economics of forging of such alloys.

9.8 Summary

Artificial implants should possess certain properties such as good dimensional tolerance, ability to be modified during surgery to fit the patient, high fracture toughness, good fatigue resistance, comparable strength and modulus to that of bone, and high wear resistance. Besides these properties, requirements for tissue biocompatibility, high purity, and reproducibility also need to be satisfied. Thus processing plays a vital role because some of the properties such as strength, modulus, fracture toughness and fatigue resistance are adjusted during the processing. Besides this, the need for anisotropic elastic properties similar to bone is an important criterion and is solely dependent on processing methodology. Forging of metals and alloys for biomedical applications has an important place in the fabrication methodologies adopted. Forging improves the strength that is critical for certain applications. However, forging has certain limitations with respect to fatigue properties, which are affected by the strength and hardness of the material. Typically, the higher the strength and hardness, the higher the resistance to fatigue, but this could lead to poor ductility and the device may fail catastrophically as crack propagation is fast. This becomes critical as the type of forging adopted prescribes the surface finish and strength. The surface finish plays a vital role in crack initiation which is therefore affected by the forging process. This becomes especially critical in Ti and its alloys, which also have poor wear properties. Thus it may be necessary to subject the metal and alloys to secondary processing such as finish machining or coating to improve surface properties. On the other hand, materials that are difficult to strengthen by heat treatment can be strengthened by cold working.

Another recent development is powder forging technology, which overcomes the limitation of having to use expensive tooling for the production of preforms, and also offers the advantage of a relatively porous material. Despite the advantages of forging, such as improved strength where heat treatment is a challenge, the cost benefits and economics of forging over other methods of fabrication need to be evaluated before designing the process to be adopted.

9.9 Sources of further information and advice

Kurt Lange, *Handbook of Metal Forming*, McGraw-Hill, (1985).

ASM, *Forging, Metals Handbook, Desk Edition*, ASM International, Metals Park Ohio.

Degarmo, E.P., Black, J.T. and Kohser, R.A., *Materials and Processes in Manufacturing* (9th ed.), Wiley, (2003).

C. Altieri, J. Flores, V. Gonzalez and A. Rodríguez, *Biomechanics of Orthopaedic Fixations*, Project on Biomechanics for Course on Mechanics of Materials- 1, GED at University of Puerto Rico, Mayaguez, December (2003).

http://www.titaniuminfogroup.co.uk/titanium.htm, *Titanium*.

http://www.steelforge.com/nonferrous/titanium.htm

http://www.azom.com.

M. Semlitsch, Titanium Alloys for hip joint replacements, in *Proc. of International Conference on Designing with Titanium*, 7–9 July, 1986, University of Bristol, UK, Institute of Metals, p 292, (1986).

D.M. Brunette, P. Tengvall, Textor, M. Thomsen, P. *Titanium in Medicine Material Science, Surface Science, Engineering, Biological Responses and Medical Applications*, Springer, Berlin, (2001).

M.A. Imam and A.C. Fraker, Titanium alloys as implant materials, in *Medical Applications of Titanium and its Alloys, The Materials and Biological Issues*, Ed. S.A. Brown, and J.E. Lemons, ASTM Special Technical Publication 1272, PA, (1996).

K.H. Kramer, Implants for Surgery, in *EUROMAT Volume 2 Materials for Medical Engineering*, Eds. H. Stallforth and P. Revell, John Wiley & Sons, Canada, Ltd, (2000).

S.V. Bhat, *Biomaterials*, Springer, Berlin, (2002).

Aly EI-Domiaty, The Effect of Strain, Strain Rate and Temperature on Forgeability of TI–6AL–4V Alloy, *Journal of Materials Processing Technology,* Vol. 32, 243–251, (1992).

Allvac® Ti–15 Mo Beta Titanium Alloy, *Technical Data Sheet*, www.allvac.com.

V. Oliveira, R.R. Chaves, R. Bertazzoli, and R. Caram, Preparation and characterization of Ti–Al–Nb alloys for orthopedic implants, *Brazilian Journal of Chemical Engineering*, Vol 15, No 4, Säo Paulo Dec. (1998).

Z.M. Hu and T.A. Dean, Aspects of forging Titanium Alloys and the production of blade forms, *Journal of Materials Processing Technology*, Vol. 111, pp 10–19, (2001).

Fengcang Ma, Weijie Lu, Jining Qin, Di Zhang, Microstructure evolution of near-alpha titanium alloys during thermomechanical processing, *Materials Science and Engineering A*, Vol 416, 59–65, (2006).

A.K. Mishra, M.A. Hamby and W.B. Kaiser, Metallurgy, Microstructure and Mechanical Properties of New Grade Cobalt Chromium Alloy before and after Porous Coating, in *Cobalt-based Alloys for Biomedical Applications* ASTM STP 1365 JA (Disegi, RL Kennedy and R Pilliar editors), American Society for Testing and Materials, West Conshohocken, PA, (1999).

S.Y. Hong, I. Markus, W. Jeong, New cooling approach and tool life improvement in cryogenic machining of titanium alloy Ti–6Al–4V, *International Journal of Machine Tools & Manufacture,* Vol. 41, 2245–2260, (2001).

E.O. Ezugwu and Z.M. Wang, Titanium alloys and their machinability – a review, *Journal of Materials Processing Technology*, Vol. 68, 262–274, (1997).

Lippard H.E. and R.L. Kennedy, Process Metallurgy of Wrought Co–Cr–Mo Alloys, *Cobalt-based Alloys for Biomedical Applications* ASTM STP 1365 (J.A. Disegi, R.L. Kennedy and R. Pilliar editors) American Society for Testing and Materials, West Conshohocken, PA, p 98, (1999).

S. Hiromotoa, E. Onoderab, A. Chibab, K. Asamic, T. Hanawaa, Microstructure and corrosion behaviour in biological environments of the new forged low-Ni Co–Cr–Mo alloys, *Biomaterials*, Vol. 26, 4912–4923, (2005).

Immarigeon J.P., Rajan Krishna and Wallace W., Microstructural Changes during

isothermal forging of Co–Cr–Mo Alloy, *Metallurgical Transactions A*, Vol. 15, Issue 2, 339–345. (1984).

Chiba, A., Kumagai, K., Takeda, H., Nomura, N., Mechanical Properties of Forged low Ni and C-containing Co–Cr–Mo Biomedical Implant Alloy, *Materials Science Forum*. Vol. 475–479, Part 3, 2317–2322, (2005).

Y. Sunami and E. Ishikawa, COP, A New Alloy for Surgical Implants, *Acta Med. Okayama*, Vol. 31, 71–80 (1977).

Peterson, C.D., Hillberry, B.M. and Heck, D.A. 1988. Component wear of total knee prostheses using Ti–6Al–4V, titanium nitride coated Ti-6Al-4V, and cobalt-chromium-molybdenum femoral components. *J. Biomed. Mater. Res*., 22, 887–903, (1988).

D. Bunea, D. Bojin, S. Zamfir, F. Miculescu, M. Miculescu, Experimental Researches Concerning the Co–Cr–Mo Alloys used in Implantology, *European Cells and Materials*, Vol. 5. Suppl. 1, 53–54 (2003).

O. Prymark, D. Bogdanski, M. Köller, S.A Esenwein, G. Muhr, F., Beckmann, T. Donath, M. Assad, M. Epple, Morphological Characterization and *in vitro* biocompatibility of a porous nickel titanium alloy, *Biomaterials*, Vol 26, 5801–5807, (2005).

10
Surface treatment

R. THULL, University of Wuerzburg, Germany

Abstract: The chapter covers surface properties of biomaterials that are essential for the interactions between implants in the human body. The interactions, of course, depend on the location, including the biological environment, the mechanical functional requirements and the duration of application. Required properties that have to be achieved by surface modifications are non-toxicity concerning eukaryotes and an antimicrobial potency against pathogenic prokaryotes. The interaction of eukaryotes and prokaryotes depends on the properties of the biomaterial's surface, the fitting tissue and the appropriate body fluid at the implantation site. The goal of the chapter is to show the possibilities of influencing the biocompatibility and the antimicrobial efficacy by physical surface modifications, namely surface structuring and modifications generated by physical vapor deposition of distinct, problem-oriented surface materials.

Key words: surface structuring, surface modification, biocompatibility, bactericidal surface.

10.1 Introduction

Metallic, polymeric, and ceramic materials are used in medical implants and comply, in most cases, with the requirements asked of functional properties at the application site with respect to biocompatibility and duration within the body. But the ambient mediums at different application sites are different, mostly extracellular fluids or blood, or the medical devices interact with different biological materials, e.g. soft or hard tissue. The function of the medical device within the body (being in contact with, generally speaking, parts of the biosystem) brings the need for particular properties of the material's surface. These are various mechanical structures, other physical properties such as high or low hardness, different electronic structures, and particular chemical functions attained, for example, certain by biomacromolecules or parts of them. The surface treatments have, in the broadest sense, the task of improving biocompatibility with respect to the desired or undesired interactions with the biosystem or to conform with the functional requirements.

Another challenge for surface modifications is achieving antimicrobial properties, which may be accomplished by inserting drugs such as antibiotics in the surface material, or by coupling biochemically active molecules or groups directly onto the surface via suitable spacers. Another way is coating with heavy metals – silver is often used.

Particular functions that have to be reached with surface treatments are

one side of the problem. The other side is the necessity to keep the treated material, including the surface modification, sterilizable and mechanically stable enough to withstand shear forces arising during the insertion of the medical device into the body.

Filling the above mentioned requirements needs scientific competence and biological knowledge, in order to communicate with the clinician, discussing therapeutic needs of the patient and requirements of the user. It simply needs bioengineers. Bioengineering is a basic research-oriented activity, closely related to physics, material sciences, chemistry, biology and medicine, designed to enable developers to understand, modify, or control human biologic systems as well as design and manufacture products that assist technically in the treatment of patients.

10.2 Surface structuring

The surface treatment of a material used in a specific medical device has to consider various factors, such as substrate mechanical origin, implant design and the manufacturing process, as well as the surgical technique used for insertion into the body and the condition and activities of the patient. Materials for applications in maxillofacial and in orthopedic surgery, in heart surgery, and for other applications of technical therapeutics within the cardiovascular or in contact with parts of the central nervous system are often surface treated, used in such implants are stainless steels, especially type 316 L, cast or forged cobalt (Co) chromium (Cr) alloys, titanium (Ti) of different grades and alloys of alpha- and beta-type. Metallic materials have the advantage of ductility and fatigue strength. In particular, titanium-based materials as pure metal or as alloys are, for many applications, the biomaterials of choice. Their unique biocompatibility is derived from the oxide layer, which arises spontaneously during passivation within the body fluids. This is true as long as the passivating oxide is dense and is not destroyed by mechanical forces arising during insertion or function. Because of the low shear resistance of the oxide layer, titanium is a candidate for a treatment to stabilize the surface against wear and tear.

Implantation site dependent metallic substrate materials, as well as polymers and even inert ceramic materials, should be provided with one or, if functionally indicated, several modifications providing, for example, wear-resistant or osteophilic or anti-thrombogenic properties or cell-proliferation inhibition *in situ*.

Minimum criteria to all surface treatments are:

- suitable for cleaning and sterilization
- locus and functionally oriented biocompatibility
- sufficiently high mechanical stability against shearing forces

- long-term chemical stability and degradation resistance.

Optionally, surface modifications should provide distinct properties of interaction with molecules or cells of the biological environment. These would promote, for example, the adaptation or in growth of cells or tissue onto the surface of fixation elements of artificial joints, or avoid cell interaction with the surface to inhibit endothelial cell proliferation to keep, e.g., stents efficient, providing them with a suitable surface for blood contact.

Based on the required properties, the treatment could be a mechanical structuring from the macro- via the micro- up to the nano-scale, or simply a hard coating, or the modification with a non-, semi- or electrically conducting surface material, applied with the aid of various processes including physical, chemical, biological, and hybrid procedures, as summarized in Fig. 10.1. Modifications have a multitude of biomaterial applications: wear resistance, prevention of substrate metal-ion release, barrier layers, and low-friction, haemocompatible, non-thrombogenic surfaces. In addition, the concept of bioactive coatings that promote certain cell responses, such as hydroxyapatite surfaces on bulk titanium or surface coatings for tissue-engineering scaffolds using titanium wires and meshes, is currently of considerable interest to the biomaterials community. PVD (physical vapor deposition) and CVD (chemical vapor deposition) coatings have played a significant role in such coating developments, along with plasma spraying, sol–gel routes and physical and chemical surface modifications. It is beyond the scope of this chapter to discuss every possible surface structuring developed. Without the restriction of universal validity, the structuring of materials will be outlined in this chapter exclusively concerning physical methods of structuring, mostly applied to titanium-based materials as substrates. CVD processes, with suitable process parameters, permit the production of similar or equivalent thin film coatings to those produced by PVD processes.

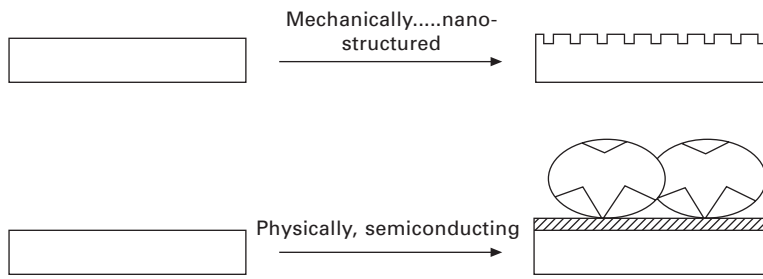

10.1 Surface modifications of materials used in implants or other medical products in contact with human tissues, mechanically or electronically structured, have to be developed with respect to application site and function.

10.3 Physical modifications

Physical methods include mechanically removing surface material, and coating techniques. Mechanical surface structuring on materials for surgical implants can be achieved through material ablation by means of machining, sandblasting or applying a liquid jet. The material can be micro-structured uniformly or quasi-fractal. Media used for sandblasting should be chosen so that contamination with materials foreign to the species are excluded. If, for instance, aluminum (Al) oxide abrasive is used for the structuring of Ti alloys, contamination of alumina in the abraded metal surface can be detected. This problem can be overcome by coating the Al oxide grains in a barrel finishing procedure with the aid of Ti oxide. The mechanical surface structuring of ceramics can be also be achieved with a sandblasting process if the ceramic is presintered in a temperature region below the finished firing temperature.

Another way to manufacture random, irregular surfaces with defined dimensional properties is by exposing the surface to a reactive plasma in a chamber wherein a reactive plasma produces a reaction product with the surface, thereby etching the surface. Of course, an etched surface can also be achieved, depending on the material, with the aid of a chemical or electrochemical etching process.

The surface can be structured in a vacuum chamber via a precipitated modifying surface material. The methods applied are, among others, PVD (physical-vapor-deposition), or PECVD (plasma-enhanced-chemical-vapor-deposition), and VPS (vacuum-plasma-spray) techniques. Derived from the latter is the FS (flame spray) technique. With PVD and PECVD, a semiconducting modification of surfaces can be achieved to enable specific adsorption reactions of biomacromolecules from the biosystem shown in Fig. 10.2.

The decreasing biocompatibility of partly-destroyed oxide films on metals require surface modifications to restrict surface damage in practice due to shearing; or to introduce specific selective adsorption/desorption mechanisms or an inhibition/promotion of electrochemical reactions between materials' surfaces and the components of the biosystem. A surface structuring should have communication properties to the biological environment.

PVD and PECVD surface modification procedures are performed mostly to achieve identical goals. Biomaterial coatings have been investigated using both PVD and CVD techniques. For example, a number of CVD and PVD techniques have been used to modify materials' surfaces with titanium nitride, titanium carbide, hydroxyapatite and diamond-like carbon for use by themselves or in multilayer coatings such as Ti/TiN/TiCN/TiC/DLC (diamond like carbon) to optimize mechanical and biological performance.[1]

Thin film modifications must have a sufficiently high connection to the

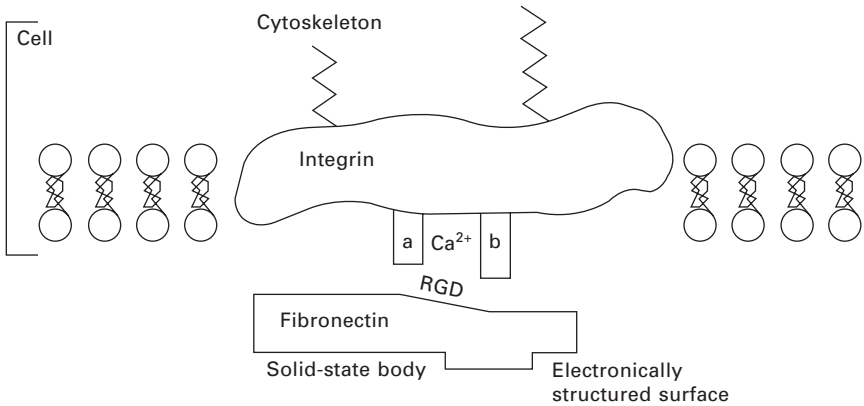

10.2 Integrin as cellular receptor for fibronectin coupled at a semiconducting electronically structured surface primarily prepared on metallic substrate materials.

substrate throughout the range of conditions to which the implant is exposed in service. Obviously, the modification has to tolerate the stress and strain variations that any particular part of the implant normally imposes on the structured surface. Conditions for the coating process must be consistent with the substrate to be coated. The process itself must not damage the substrate. For titanium, this means that any process that involves heating the substrate to high temperatures needs to be assessed carefully. The coating must not induce failure in the substrate nor introduce impurities in the surface, which may change interface properties.

PVD leads to modifications by reaction between a substrate surface and an adjacent vapor, which supplies the particles – atoms, molecules or ions – generated from a target and transported to the substrate surface, on which condensation and reaction with atoms of the surface lattice take place. Additional to the particle vapor type, particle energy, density, substrate temperature and reactive gas properties are significant parameters of the surface structuring process. Partial pressures of inert and/or reactive gases, partial vapor pressure, composition and in particular particle energy are the most important parameters distinguishing PVD from CVD.

PVD processes are characterized by high film growth rates, strong adhesion, multi-component layers, low substrate temperatures, and a wide range of possible modifications and substrate materials. Multilayers can be produced without process interruption. Important characteristic properties of PVD coatings are thickness, roughness, hardness, strength and adhesion, as well as structure, morphology, stoichiometry and internal stresses.

PVD modifications applied as functionalizations of surfaces in implants have to consider the biological environment, consisting of fluids, cells or tissues of the body – and bacterial contaminations. Furthermore, tribological

pairings in, for instance, artificial joint implants define the right choice of the surface material.

The principle of the PVD technique, which is sometimes called ion plating, is summarized in Fig. 10.3 and is characterized by energetic bombarding particles that cause changes in the substrate surface and influence the surface modification. Generally, the energetic particles are gaseous ions arising from the extraction of ions from a confined plasma and acceleration of them to a high energy. They may also be negative ions accelerated from a negatively-biased compound or alloy sputtering target, ions from vacuum or plasma arcs, or ions from special ion sources.[2] The implantation of the bombarding species results in a compaction of the near-surface region and the formation of a compressive stress in that region.

10.4 Strength of modifications

The mechanical stability of a surface modification depends on the deformation and fracture models associated with failure. Energetic particle bombardment prior to and during the initial stages of film formation may enhance adhesion by removing contaminant layers, changing the surface chemistry, generating a microscopically rough surface, increasing the nucleation density by forming nucleation site defects, implanting and recoil implanting species, increasing the surface mobility of adatoms, and creating lattice defects and introducing thermal energy directly into the surface region, thereby promoting reaction and diffusion. These effects will also improve surface coverage and thus decrease the number of interfacial voids which result in easy fracture and poor adhesion.

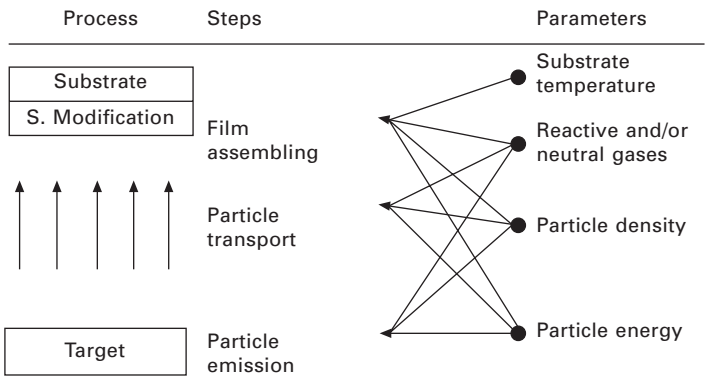

10.3 The essentials of physical vapor deposition (PVD) processes. Evaporation, sputtering and ion plating are PVD processes. Ion plating is a hybrid process with a large application range in implant surface modification.

10.5 Interface modulation and biocompatibility

ISO 10993 gives guidance on the fundamental principles governing the biological evaluation of medical devices, the definition of categories of devices based on the nature and duration of contact with the body, and the selection of appropriate tests. It covers, besides medical devices and final products, materials that are defined as any synthetic or natural polymer, metal, alloy, ceramic or other nonviable substance, including tissue rendered nonviable, used as a device or any part thereof.

In the selection of materials to be used in device manufacture, the first consideration should be fitness for purpose with respect to the characteristics and properties of the material, which include chemical, toxicological, physical, electrical, morphological and mechanical properties.

The following items should be considered for their relevance to the overall biological evaluation of the device:

- processed material(s)
- intended additives, process contaminants and residues
- leachable substances
- degradation products
- other components and their interactions during final use of the product.

For an overall assessment, the biological evaluation performed should be considered in conjunction with the nature and mobility of the ingredients in the materials used to manufacture the device, and other information, further non-clinical tests, clinical studies, and post-market experience.

If surface structuring is applied to implants, it will be in contact with tissue/bone (e.g. replacement joints, and intraosseous devices and/or blood (e.g. pacemaker electrodes, heart valves, and ventricular assist devices).

The most important properties of PVD and CVD coatings in the macro range are thickness of modification, roughness, hardness, strength and – most important of all – adhesion. In the micro range, the significant properties are structure, morphology, stoichiometry and internal stresses. Surface materials should always be considered as systems including not only the modifications themselves but also the adjacent environment where they have to perform their function.[3]

10.6 Future developments and optimizations

Modifications of interest will be described in future (beyond presently used attributes such as hardness, ductility, corrosion resistance, and aspired reactivity with parts of the biosystem) by the electronic structure and specific adhesion of distinct biomacromolecules and cells. Surface structuring will

be adapted to specific functional needs. In particular, biocompatibility of materials will no longer be discussed in general but more specifically to distinct requirements that are, for example, beyond compatibility with respect to eukaryotes to distinct applications for a defined incompatibility against procaryotes. Surface structurings of materials will be developed in the direction of specific requirements of implants, e.g. for properties to fixation elements of artificial joints to improve the contact with the surrounding hard tissue, or to inhibit the adhesion of microorganisms. Materials of cardial stents have to be structured to avoid cell proliferation provoking restenosis. Of course, for an extensive improvement of stent therapy, there needs to be a change of stent design to avoid mechanical irritations of the vessel, which are proposed another reason for cell proliferation.

Further future developments in surface structuring have to consider improvements of the inner surfaces of three-dimensional cell carriers. Outer and inner surfaces of cell carriers are identically structured. Because of the gradients of the miscellaneous ingredients of body fluids penetrating the cell carrier, best possible cell colonization requires adapted graduated surface structures, following research efforts to define the actual (up to now) not known cell type dependent micro ecology.

10.7 Summary

Surface treatments on materials improve the function and lifetime of implants. The treatments have to consider the kind of substrate material, the specific biological environment consisting of the kind of adjacent tissue, soft or hard, and ingredients of the extracellular matrix or blood. Depending on the substrate materials, specific treatment procedures have to be chosen for the modification – a biological, physical, or chemical pathway. This chapter details the physical pathway of surface modification, summarizing the production of mechanical structuring on different scales, from macro via micro to nano roughness, and physical vapor deposition (PVD) modification of surfaces. Adapted to the clinical requirements, the deposited surface material can be designed as non-conducting, semi-conducting or conducting. Aspects of materials for cell containers are discussed.

10.8 Sources of further information and advice

Werner Schatt, Hartmut Worch (edit) *Werkstoffwissenschaft*, Wiley-VCH, 9. Auflage 2003

U. Beck, R. Lange, H.-G. Neumann. Micro- and nanoscaled titanium surface structures textured by electrolytic plasma and etching methods, *Advanced Materials Research* 15–17 (2007) 141–146

U. Beck, R. Lange, H.-G. Neumann, Microplasma textured Ti-implant surfaces, *Biomolecular Engineering* 24 (2007) 1, 47–51 http://www.izbs.uni-karlsruhe.de/Biomaterials.php

The junior research group Biomaterials Interfaces is performing research activity into the chemical and physical behavior of metals and semiconductor surfaces put in contact with biological systems. http://vanha.med.utu.fi/dent/biomat/

10.9 References

1 Jones M, McColl IR, Grant DM, Parker KG, Parker TL (1999) Haemocompatibility of DLC and TiC–TiN interlayers on titanium. *Diamond and Related Materials* 8: 457–462

2 Mattox DM (1994) Ion plating. In Bunshah RF (ed) *Handbook of Deposition Technologies for Films and Coatings*. Noyes Publication, Park Ridge, NJ, USA

3 J. Breme, C.J. Kirkpatrick, R. Thull (Edit.) (2008) *Metallic Biomaterial Interfaces*. Wiley-VCH, Weinheim

11
Coatings for metallic biomaterials

T. KASUGA, Nagoya Institute of Technology, Japan

Abstract: Titanium and its alloys show the greatest biocompatibility among metallic materials for biomedical applications. They are, however, grouped within bioinert materials together with ceramics, such as alumina and zirconia, on the basis of the pattern of osteogenesis. For tight fixation and long-term use, some applications need bioactivity, which means an ability to make a bond directly to natural bone. Calcium phosphate-based ceramic materials, such as hydroxyapatite, tricalcium phosphate and so on, show bioactivity, and are often coated onto metallic biomaterials. In this chapter, some recent topics concerning bioactive ceramic coatings on metallic biomaterials are briefly reviewed. New types of coating methods on titanium and its alloys, including plasma-spraying for forming highly oriented hydroxyapatite, sputtering or vapor-deposition for inducing excellent bioactivity and phosphate glass-ceramic joining, are focused upon, as well as the chemical modifications of their surfaces.

Key words: bioactivity, ceramic, calcium phosphate, hydroxyapatite, titanium, titanium alloy, coating, plasma spraying, sputtering, CVD, biomimetic process, glass-ceramic, chemical treatment, surface modification.

11.1 Introduction

The number of aged persons demanding replacement or repair of failed tissue with biomaterials is rapidly increasing. In particular, high-performance biomaterials for replacing damaged hard tissues, such as artificial joints, bone fillers, dental implants and so on, are strongly demanded among older people. Metallic biomaterials with biological safety, such as stainless steels, cobalt (Co)-based alloys, titanium (Ti) and its alloys, are useful for replacing hard tissues at the load-bearing sections. Especially, Ti and its alloys are widely used as orthopaedic and dental implants because of their excellent biocompatibility. Recently, much attention has been paid to β-type Ti alloys because they have high mechanical strength and low modulus of elasticity. One of the current attractive metals is β-type Ti alloys containing elements sufficiently tolerated by living tissues, such as niobium (Nb), tantalum (Ta) and zirconium (Zr) (Niinomi, 2003a; Kuroda *et al.*, 1998). A Ti-29Nb-13Ta-4.6Zr (denoted by TNTZ) alloy, which has been suggested as one of the best materials, shows a high tensile strength of ~1 GPa and low Young's modulus of 60~80 GPa. However, no Ti and its alloys can make a chemical bond with living bone; that is, they are inactive.

Calcium phosphate ceramics such as hydroxyapatite ($Ca_{10}(PO_4)_6(OH)_2$; HA) and β-tricalcium phosphate (β-$Ca_3(PO_4)_2$; β-TCP) exhibit bioactivity

(Hench, 1991; Doremus, 1992). Some glasses and glass-ceramics are also well known as bioactive materials. Some portions in artificial substitutes for hard tissue may require bioactivity. Bioactive surface modification is, in general, applied to Ti and its alloys to further improve their biocompatibility. The bioactive ceramic coatings prepared using various processes have been investigated so far and some materials are clinically used as biomaterials such as dental and surgical implants.

In the present chapter, recent progress in bioactive ceramic coatings having mechanically strong bonding with Ti and its alloys is briefly reviewed.

11.2 Calcium phosphate ceramic coatings

Implants coated with calcium phosphates such as HA and β-TCP have been widely used in orthopaedics and dentistry. The cementless fixation technique combines mechanical strength, ductility and ease of fabrication with bioactivity. Calcium phosphate coatings have been applied by a variety of methods, such as dip-coating (Li *et al.*, 1996), electrophoretic deposition (EPD) (Ducheyne *et al.*, 1986), plasma spraying (Lacefield, 1993), ion-beam sputtering (Ong *et al.*, 1994), flame spraying (Berndt *et al.*, 1990), biomimetic coating (Kokubo, 1998), and so on. In this section, some recent possible coatings are briefly discussed.

11.2.1 Plasma-sprayed coatings

Plasma spraying employs a plasma or ionized gas to melt the ceramic particles and subsequently to carry them onto the surface of substrates. Two important properties of plasma sprayed coatings are (i) bonding strength between the calcium phosphate layer and the metallic substrate and (ii) dissolution behavior in body fluid. Residual stress arises at the interface between the metallic substrate and HA due to the large difference in their thermal expansions. Amorphous calcium phosphate tends to dissolve rapidly in body fluid: coatings with low crystallinity rapidly become weak and may induce inframmatory responses. A relatively high bonding strength on Ti or its alloys was reported by Tsui *et al.* (1998): the values were in the range of 20 ~ 40 MPa after optimization of the coating properties. The crystallinity of HA in the coating layers was relatively high (83 ~ 94 %). Their high crystallinity was very important for long-term benefit to the coated implants.

A radio-frequency thermal plasma spraying (rf-TPS) method was developed to obtain strong bonding between the HA coating and Ti substrate, employing an HA/Ti composite coating (Inagaki *et al.*, 2003). The HA/Ti composite coatings were prepared by controlling the starting composition using two microfeeders, which fed the HA and Ti powders at an accurate rate. The starting powders were fed so as to form the coated layer with a compositional

gradient, from a Ti-rich phase at the bottom to an HA-rich phase at the top. The composition of the plasma gas played an important role in improving the bonding strength of the coatings. Rf-TPS with nitrogen-containing plasma gas induced the formation of coatings with excellent bonding to the Ti substrate (tensile bonding strength of 65 MPa). The microstructure of the interface between deposited Ti particles in the coatings was significantly influenced by plasma gas composition during rf-TPS. By rf-TPS with nitrogen- or oxygen-containing plasma gas, titanium nitride or titanium oxide was formed in the deposited Ti particles, respectively. The bonding of the composite coatings onto the Ti substrate was suggested to be influenced by the microstructure at the interface between Ti particles.

Recently, Inagaki *et al*. (2007) prepared highly oriented HA coatings on a Ti substrate using an rf-TPS method for improving biocompatibility. HA has anisotropic properties due to its hexagonal crystal structure. HA has two major surfaces (100) and (001), with different chemical properties, such as protein absorption and dissolution behavior. Highly oriented HA coatings were sprayed onto a Ti substrate by rf-TPS. A thermal plasma of argon gas containing a small amount of nitrogen (1~6 %) was generated. The as-sprayed HA coatings were heated at 600 °C for 2 h, and then hydrothermally treated at 120 °C for 2 h in water. The resulting HA consisted of prismatic crystals having a structure with (001) preferred orientation parallel to the substrate surface, of 200~800 nm width. The formation of oriented, needle-like HA crystallites in the coatings as-sprayed with an accurate control plays an important role in obtaining both highly crystallized and highly oriented coatings using a post-heat treatment. The protein adsorption behavior of the HA coating was experimentally shown to be influenced by the preferred orientation of HA (Inagaki *et al*., 2008). Surfaces of highly (001) oriented HA coatings have a selectivity for cytochrom c (CCC). On the other hand, no selectivity in the adsorption of bovine serum albumin (BSA) or immunoglobulin G (IgG) was seen. Further investigation is in progress.

11.2.2 Thin film coatings

Physical vapor deposition (PVD) is one of the most promising methods for obtaining thin, uniform, dense coatings of calcium phosphates on metallic substrates. Radiofrequency (rf) magnetron sputtering has been widely used for coatings of thin films with excellent bonding to the substrates and has been applied to the coating of calcium phosphate films on commercially pure titanium (cpTi) (Yoshinari *et al*., 1997; Wolke *et al*., 2003) and titanium alloys (van Dijk *et al*, 1995). The method has a great advantage in that the coatings can be achieved at relatively low temperatures so that no degradation in the mechanical properties of the metallic substrate occurs.

The phases in the coatings and their surface roughness depend on the

composition and the density of the targets. Plasma sprayed HA (Wolke *et al.*, 1994) or sintered HA (Lo *et al.*, 2000) as the targets have been often used. Calcium phosphate glass targets with the Ca/P molar ratios of 0.75~0.25, which were much lower than the stoichiometric value of 1.67 for hydroxyapatite, have also been discussed (Yamashita *et al.*, 1998).

Recently, Narushima *et al.* (2005) prepared calcium phosphate films on cpTi substrates by rf magnetron sputtering using hot-pressed, dense β-TCP targets. The resulting films consisted of amorphous calcium phosphate and/or oxyapatite phases. The bonding strengths between the coatings and the cpTi substrate were estimated to be >60 MPa. When the film was soaked in Hanks' solution (Table 11.1) or phosphate buffer solution, the dissolved amount of calcium ions from the amorphous coatings was significantly larger than that from the oxyapatite coatings (Ueda *et al.*, 2007). Animal tests using beagle dogs showed that cpTi coated with the amorphous calcium phosphate film was fixed rapidly and strongly with bone (Narushima *et al.*, 2007).

Chemical vapor deposition (CVD) has also great advantages in the preparation of calcium phosphate thin films coated strongly onto metallic substrates, because of high deposition rates with excellent microstructure controllability. Some reports have been published on the preparation of β-$Ca_2P_2O_7$ film (Allen *et al.*, 1996) and its conversion to β-TCP phase by post-heat treatment. A few works on the direct preparation of bioactive calcium phosphate films such as HA or β-TCP have been reported (Darr *et al.*, 2004; Sato *et al.*, 2007a).

Bioactive calcium phosphate films have been prepared on cpTi substrates by metal–organic chemical vapor deposition (MOCVD) using bis-dipivaloylmetanato-calcium ($Ca(dpm)_2$) and triphenyl phosphate ($(C_6H_5O)_3PO$) precursors (Sato *et al.*, 2007a). Dense HA or α-TCP films were prepared by controlling the Ca/P molar ratio in the precursor at <~1 and substrate temperature at 700~800 °C. The resulting HA and α-TCP films showed (002) and (510) preferred orientation parallel to the substrate surfaces. The films could be deposited at high rates of 4~6 nm/sec. HA formed in Hanks' solution at 37 °C within 6 h on the HA films and 14 days on the α-TCP films, respectively. The HA films on cpTi are expected to show excellent bioactivity.

Calcium titanate ($CaTiO_3$) films have been also investigated as promising bioactive coatings, using a sputtering (Asami *et al.*, 2007) or CVD (Sato

Table 11.1 Chemical composition of Hanks' solution

Concentration (mg/m^3)							
NaCl	KCl	Na_2HPO_4	KH_2PO_4	$MgSO_4$	$MgCl_2$	$CaCl_2$	Glucose
8.00	0.40	4.79×10^{-2}	6.00×10^{-2}	4.88×10^{-2}	4.68×10^{-2}	0.14	1.00

et al., 2007b) method. HA forms on these films after soaking in Hanks' solution for 3~7 days. The proposed mechanism for HA formation on $CaTiO_3$ films in the solution is as follows: $CaTiO_3$ films would firstly dissolve into the solution to locally increase Ca^{2+} ion concentration, then PO_4^{3-} ions could be attracted and react with the Ca^{2+} ions, resulting in the formation of HA.

11.2.3 Biomimetic apatite coatings

At the interface between bioactive ceramics and bone in the living body, an apatite layer can be often seen: the ceramic bonds to the living bone through the apatite layer (Kitsugi *et al.*, 1986), which consists of a carbonate-containing HA with small crystallites and a defective structure. The apatite is very similar to that in bone in its composition and structure (Kokubo *et al.*, 1990). The apatite layer can form on the ceramics, metals and polymers when they are soaked in simulated body fluid (SBF) with ion concentrations nearly equal to those of human blood plasma (Kokubo, 1998), as shown in Table 11.2. A bioactive coating method utilizing this apatite-forming ability is often called a 'biomimetic method', and the apatite formed is often called 'bone-like apatite' (denoted by B-HA, hereafter). This method has an advantage over conventional coating techniques in that materials can be homogeneously coated with nano-sized apatite without heating. The method is thus applicable to polymer substrates. Two indispensable conditions needed for the formation of B-HA coatings on materials using SBF are (i) the existence of surface functional groups that induce the nucleation of apatite (e.g., Si-OH, Ti-OH, Nb-OH, Ta-OH, COOH and PO_4H_2 groups) and (ii) increase in the supersaturation concerning apatite around the surface of the materials (Kokubo, 1990; Kokubo *et al.*, 1998).

Metallic Ti and its alloys are generally covered with a passive layer of titanium oxide. Since the surface of the layer includes Ti-OH group, there exists the possibility of B-HA formation. However, relatively high supersaturation concerning B-HA is usually needed around the surface. To increase the supersaturation concerning apatite in SBF, a large amount of Ca^{2+} ions should be dissolved from the materials. Calcium carbonate has been recognized as a bioresorbable bone-filler and it has good osteoconductivity

Table 11.2 Ion concentrations of human blood plasma and SBF

	Concentration (mM)							
	Na^+	K^+	Mg^{2+}	Ca^{2+}	Cl^-	HCO_3^-	HPO_4^{2-}	SO_4^{2-}
Blood plasma	142.0	5.0	1.5	2.5	103.0	27.0	1.0	0.5
SBF*	142.0	5.0	1.5	2.5	148.8	4.2	1.0	0.5

*Buffered at pH 7.40 with tris-hydroxymethylaminomethane and 1 M HCl.

(Liao *et al*., 2000; Vago *et al*., 2002). Calcium carbonate is expected to supply both Ca^{2+} and carbonate ions when soaked in SBF. As a result, the supersaturation concerning apatite would increase and the concentration of carbonate ions in SBF would come close to that in human blood plasma. It is well known that calcium carbonate has three polymorphs; that is, calcite, aragonite, and vaterite. The solubility of vaterite is greater than that of calcite or aragonite.

Maeda *et al*. (2004) reported B-HA formation on the compacts of powder mixtures consisting of titania and calcium carbonate in SBF at 37 °C within two days. The B-HA forming ability was much higher than that of powder-compacts of titania without calcium carbonate. The plentiful amount of Ca^{2+} ion due to the dissolution of vaterite with a large specific surface area of 40 m^2/g increases the supersaturation of B-HA in SBF, resulting in the rapid formation of the B-HA layer.

Based on these backgrounds, cpTi was coated with B-HA on a TiO_2 layer (Hashimoto *et al*., 2007). The TiO_2 layer was prepared on cpTi by heat-treatment in air at 800 °C for 0.25 h. A slurry consisting of vaterite particles with a secondary particle size of ~500 nm diameter (specific surface area of ~40 m^2/g), in methanol, was dip-coated on the surface of the heat-treated cpTi. The resulting sample was soaked in SBF at 37 °C. Since the surface potential of the vaterite particles in methanol was +40 mV, the heat-treated cpTi with the negatively charged surface could control the dissociation of vaterite particles from the TiO_2 surface on the cpTi in SBF. After three days of soaking, the surface was completely coated with a leaf-like B-HA layer at ~1 μm in thickness.

Recently, a trace amount of ionic silicon species has been reported to be effective for enhancing the proliferation and differentiation of osteoblast-like cells and mesenchymal stem cells (Obata *et al*., 2008a). Xynos *et al*. (2000) reported that the proliferation of human osteoblasts was enhanced in a culture medium containing a trace amount of silicon. An HA-coating with the releasability of the silicon species is expected to show excellent bone-forming ability.

For preparing a coating with ionic silicon species releasability, B-HA was formed on a silica layer coated on a cpTi substrate by a biomimetic method (Hashimoto *et al*., 2007). A diluted water glass, $mNa_2O \cdot nSiO_2(100\text{-}m\text{-}n)H_2O$ (m = ~ 11.5, n = ~28), was dip-coated onto a cpTi substrate, and subsequently the sample was heated at 300 °C to be dehydrated. The glass-coated cpTi was soaked in dilute HCl *aq*. at 50 °C to induce the ion-exchange of sodium ions in the water glass into protons, resulting in the preparation of a silica-coating with a thickness of ~1-μm containing numerous Si–OH groups on the substrate. Calcium carbonate (vaterite) particles were placed on the SiO_2–coated substrate (Fig. 11.1(a)) and subsequently the sample was soaked in SBF. After three days of soaking, the sample surface was coated

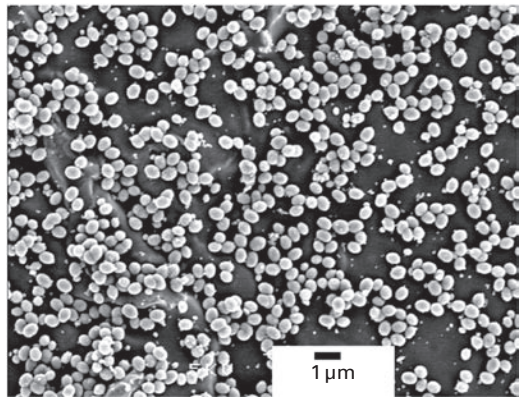

(a)

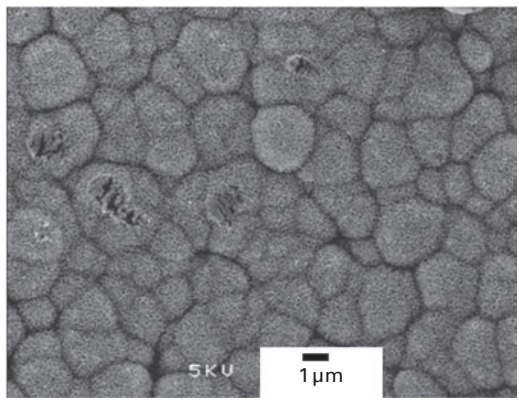

(b)

11.1 Scanning electron micrographs of (a) calcium carbonate (vaterite) particles placed on SiO_2-coated cpTi and (b) B-HA formed on the sample (a) after soaking in SBF for three days. Vaterite particles of ~500-nm diameter were placed on the surface after the dip-coating. The difference in surface potentials between the positively charged vaterite particles and the negatively charged SiO_2 coating controls the removal of them from the substrate in SBF.

with a leaf-like B-HA layer with a thickness of ~1 µm (Fig. 11.1(b)). The layer adhered tightly onto the sample surface, even after ultrasonic-treatment. Energy dispersive X-ray (EDX) analysis of the precipitate layer showed that Ca and P with a trace amount of Si were included in the precipitates. The resulting sample (10×10 mm^2) was soaked in 4 ml of α-modified minimum essential medium (α-MEM) supplemented with 10% fetal bovine serum (FBS) and incubated at 37 °C for seven days. The α-MEM was changed after one day of soaking at first, and then changed every other day. The amount of silicon ions in the α-MEM after filtration was determined by inductively coupled

plasma atomic emission spectroscopy (ICP-AES). A trace amount of ionic silicon species, 0.1 mmol/day, was continuously released from the sample.

Mouse osteoblast-like cells (MC3T3-E1 cells) were used to examine cell-proliferation on the samples. The B-HA-coated samples on the SiO_2 and TiO_2 layer on cpTi substrates are denoted by HA/SiO_2/Ti and HA/TiO_2/Ti, respectively. Figure 11.2 shows the proliferation of MC3T3-E1 cells on HA/TiO_2/Ti and HA/SiO_2/Ti. The cellular numbers on both of the samples increased during the incubation. After seven days of incubation, the cell number of HA/SiO_2/Ti was significantly higher than that of HA/TiO_2/Ti. The ionic silicon species released from HA/SiO_2/Ti may enhance the cell proliferation. This result implies a very important guide into designing the next generation of bioactive materials, since the biocompatibility of the silicon-releasable apatite layer may be significantly better than that of an apatite layer coated directly (without the silica layer) on a titanium substrate.

11.3 Calcium phosphate glass-ceramic coatings

Since glass-based materials allow some latitude of choice in composition, they have a significant advantage in that they can be controlled to improve their chemical/physical properties and microstructures after their crystallization, to attain sufficient performance as biomaterials. Silicate-based glasses and

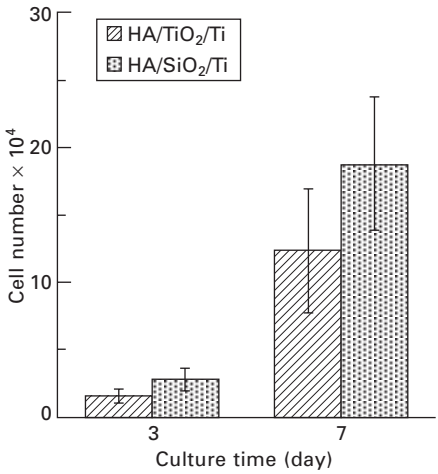

11.2 Numbers of osteoblast-like cells (MC3T3-E1 cells) cultured on HA/TiO_2/Ti and HA/SiO_2/Ti (*p <0.05). MC3T3-E1 cells were seeded at a density of 3.0×10^4 cells/well onto the sample in a 12-well culture plate, and incubated using an α-MEM supplemented with 10% FBS at 37 °C in a humidified atmosphere of 95% air and 5% CO_2 for three or seven days. At least four samples were used for cell counts by a hemocytometer.

glass-ceramics such as Bioglass® and Cerabone® A-W are known well as bioactive materials (Hench, 1992). These bioactive glasses and glass-ceramics can be coated on some metals such as 316L stainless steel, Ti alloys and Co–Cr alloys. Three kinds of methods are used to apply the glasses as coatings, as follows: (i) enamelling or glazing using glass frits, (ii) flame-spray coating and (iii) rapid-immersion coating, where the heated metal is rapidly inserted into the molten glass. These have been reviewed elsewhere (Hench *et al.*, 1993).

As described in Section 11.1, Niinomi and others have developed new β-type titanium alloys composed of elements sufficiently tolerated by living tissues, such as Nb, Ta and Zr. A Ti-29Nb-13Ta-4.6Zr (TNTZ) alloy, which has been put forward as one of the best materials, shows a high tensile strength of ~1 GPa and low Young's modulus of 60~80 GPa. As one of the most promising methods for inducing bioactivity on TNTZ, a calcium phosphate glass-ceramic coating has been investigated since it is simple and easy to attain strong joining with TNTZ. This section focuses the new type of bioactive calcium phosphate glass-ceramic coating on TNTZ.

11.3.1 Calcium phosphate invert glasses for coatings

Calcium phosphate glass-based materials have high potential for use as biomaterials because of their compositions. It is necessary to use phosphate glasses with a high Ca/P ratio for implantation. In some glasses, anionic groups can be connected through a cation, which should usually be a network modifier, to form the glassy state; such glasses can be called 'invert glasses.' New types of phosphate invert glasses with compositions of high CaO and low P_2O_5 were prepared in order to obtain bioactive materials; the glasses consisted of PO_4^{3-} (orthophosphate) and/or $P_2O_7^{4-}$ (pyrophosphate) ions without PO_3^{2-} (metaphosphate) ions, and the phosphate groups are connected through Ca^{2+} ions (Kasuga *et al.*, 1999a).

The proposed mother composition is $60CaO–30P_2O_5–3TiO_2–7Na_2O$ (in mol%) denoted by PIG hereafter). It is, usually, difficult to obtain glasses with Ca/P > 0.75 in the binary system, but they can be prepared with the addition of small amounts of TiO_2 and Na_2O. TiO_2 addition into phosphate glasses improves their glass-forming ability and chemical durability. By introducing a small amount of Na_2O, the sintering ability of glass powders of <10 μm diameter is improved (Kasuga *et al.*, 1998). The compacted powder of the PIG glass can be sintered at 800~850 °C due to viscous flow of the melt (Kasuga *et al.*, 2003a).

PIG glass was pulverized less than 10 μm in diameter (the average size; 1.0~1.5 μm) in methanol, using a zirconia ball mill. The TNTZ surface was sandblasted to a roughness of ~2 μm. The glass powder slurry was dip-coated onto TNTZ and then dried. Then the substrate with the glass powder layer

was heated in air at 800 °C for 1 h and cooled to room temperature. Figure 11.3(a) shows a cross-sectional scanning electron micrograph (SEM) of the coating obtained after heating. Due to the sintering of the glass powders, a layer with ~10-μm thickness was formed on the TNTZ. Many pores of several micrometers in size are seen. Figure 11.3(b) shows a cross-sectional SEM micrograph around the joining interface between TNTZ and the coating layer. Phase 1, which appears dark, with a thickness of ~1 μm on the substrate is seen. Phase 2 is a fine microstructure interconnecting phases 1 and 3. EDX spectra collected from portions indicated that the composition of phase 3 agrees almost with that of the mother glass, while phase 1 contains large amounts of titanium and phosphorus with a trace amount of calcium; it is

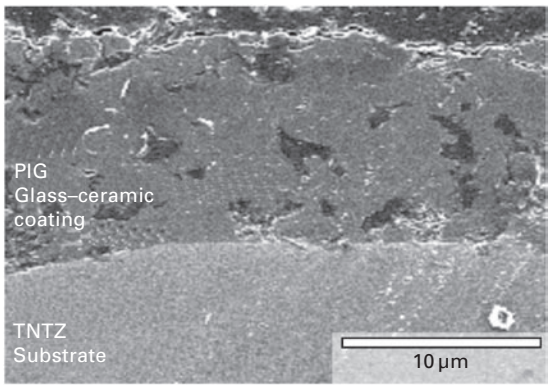

(a)

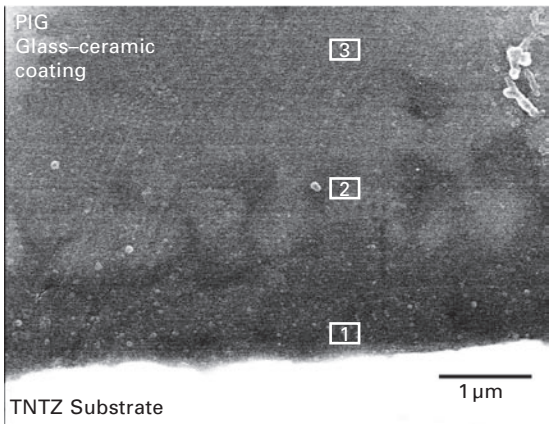

(b)

11.3 (a) Cross-sectional scanning electron micrograph around the interface between the substrate and the layer. (b) Magnified view around the interface. EDX spectra were measured from the portions labeled 1–3 in (b).

based on sodium titanium phosphate. In phase 2, the calcium content is larger and the titanium content is smaller in comparison with phase 1. That is, there exists a reaction zone of 2~4 μm in thickness between the glass-ceramic layer and the substrate. Linear thermal expansion coefficients of PIG glass-ceramic prepared by heating at 800 °C, and TNTZ, were 12×10^{-6} and 9×10^{-6} deg^{-1} (100 ~ 750 °C), respectively. The reaction layer is spontaneously developed on TNTZ by heating in air to relax the thermal stress generated in the coating layer and the substrate, resulting in the formation of the strong joint (Kasuga *et al*., 2001a).

The coating layer in the sample heated at 800 °C consists predominantly of β-$Ca_3(PO_4)_2$ (TCP) phase with trace amounts of β-$Ca_2P_2O_7$ (CPP) and TiO_2 (rutile phase) crystalline phases. When the glass powders placed on the alloy were heated at 800 °C under reduced pressure (~10 Pa), no adhesion between the glass-ceramic layer and the substrate was formed. β-CPP phase precipitated during heating the glass powders on the substrate and this reacted with residual phosphate glassy phase containing large amounts of sodium and titanium around 800 °C to form a low viscosity melt. The melt contacted the thin oxide layer formed on the TNTZ during the heating, resulting in a fine glass-ceramic/metal joining. The thin oxide layer formed on the metallic substrate plays an important role in the formation of the fine glass-ceramic coating.

When the glass-ceramic coating on the TNTZ substrate was prepared by heating at 800 °C for 1 h, the tensile bonding strength was estimated to be ~26 MPa as the highest value. The strengths of the samples prepared by heating for 0.25~0.5 h were estimated to be ~10 MPa (Kasuga *et al*., 2003b). In the latter samples, numerous pores of several micrometers in size were included due to insufficient sintering of the glass-ceramic particles. On the other hand, the tensile bonding strengths of the coating samples using Ti-6Al-4V ELI (denoted by TAV, hereafter) as the substrate were estimated to be much smaller (<5 MPa) than those of the samples using TNTZ. The strength of the sample using cpTi could not be measured since the surface layer containing a glass-ceramic coating peeled off from the substrate due to severe oxidation of the Ti during the heat-treatment (Kasuga *et al*., 2003c).

In the case of the sample using TNTZ as the substrate, a fracture occured in the glass-ceramic layer with porosity; the bonding strength at the interface layer between TNTZ and the glass-ceramic was higher than the tensile strength of the glass-ceramic. On the other hand, in the case of the sample coated on the TAV, the fracture occurs in the reaction layer between the coating and the substrate. The oxidized layer at the TNTZ surface was estimated to be <0.5 μm in depth, while that on the TAV surface was 3~5 μm in depth. Elements such as aluminum and vanadium around the surface diffused considerably to form oxides. The oxidation is suggested to lead to the generation of large tensile stresses in the surface layer of the TAV.

As a result, the layer is brittle and the bonding strength is very small. The fabrication of the fine PIG glass-ceramic coating is influenced strongly by the oxidation behavior of the metallic substrate.

11.3.2 Mechanical properties of the glass-ceramic-coated titanium alloys

An aging treatment of TNTZ at ~400 °C is effective for increasing its hardness, modulus of elasticity and strength (Niinomi *et al.*, 2002). This improvement is due to the precipitation of ω phases in the β matrix phase during the aging. After the glass-ceramic-coated TNTZ was heat-treated for aging, the tensile bonding strength of the sample with the coating layer of 5 μm thickness was not degraded, but that of 20 μm thickness was degraded due to the generation of microcracks, which originated from the formation of ω phase at the interface between the layer and the substrate (Niinomi *et al.*, 2003b).

Akahori *et al.* (2005) investigated the mechanical properties of TNTZ with a PIG glass-ceramic coating layer of 5 μm thickness. The samples were aged at 450 °C for 72 h. The tensile strengths of TNTZ and the aged TNTZ with the coating layer were estimated to be ~700 and ~900 MPa, respectively, and their elongations were 22 and 11%, respectively, which were half to quarter smaller than that of as-solutionized TNTZ. Young's modulus was estimated to be ~90 GPa. The glass-ceramic coated TNTZ showed sufficiently excellent mechanical properties (such as tensile properties and a small Young's modulus) for use as a biomaterial.

The coated samples were machined for fatigue tests according to ISO1099-75 specifications (Li *et al.*, 2004). No delaminations of the coating were observed during the fatigue test. The fatigue resistance of the samples improved due to an increase in resistance to fatigue crack initiation caused by the formation of the α phase during heating for the coating, and the precipitation of ω-phase from the substrate during the slow cooling. In addition, aging at 400 °C for 72 h greatly increased the fatigue limit of the coated TNTZ and effectively relieved the detrimental effect of sandblasting on fatigue properties.

11.3.3 Bioactivity of the glass-ceramic coatings

After 10 days of soaking in SBF, B-HA forms on the PIG glass-ceramic coating. On the other hand, B-HA formation on a $50CaO–40P_2O_5–7Na_2O–3TiO_2$ glass-ceramic-coated TNTZ does not occur (Kasuga *et al.*, 2003a). The glassy phase in the glass-ceramic may play an important role in the B-HA formation (Kasuga *et al.*, 1999b, 1999c). Chemical species such as Ti–OH and/or PO_4H_2 for inducing B-HA nucleation can be supplied from the glassy phase around the surface (Kasuga *et al.*, 2001b).

B-HA-forming ability of PIG glass-ceramic in SBF is enhanced by autoclaving in water (Kasuga *et al.*, 2003d). B-HA starts to form on the autoclaved glass-ceramic after only 3 days soaking in SBF. The surface of the treated glass-ceramic is completely covered with B-HA after 10 days of soaking. Numerous hydrated titania groups, which induce nucleation of B-HA, form around the glass-ceramic surface during the autoclaving. The B-HA-forming ability of the coating on TNTZ can be also be improved after autoclaving in distilled water (Kasuga *et al.*, 2005). Plentiful hydrated titania groups are suggested to form on the surface of the glass-ceramic coating after autoclaving, resulting in the induction of B-HA nucleation in SBF.

A rod-shaped sample of 5 mm diameter × 10 mm length was implanted into a femur removed from a Japanese rabbit. The sample was autoclaved in water at 121 °C for 1 h. Figure 11.4 shows contact microradiographs (CMR) after 4-weeks (Fig. 11.4(a)) and 52-weeks of (Fig. 11.4(b)) implantation. No significant change in the thickness of the glass-ceramic coating layer after the implantation can be seen. The observation shows new bone formation around the autoclaved glass-ceramic-coated TNTZ after 4 weeks of implantation and the bone tissue showed partial direct contact with the implants. When the samples after 52 weeks of implantation were sliced and polished for observation, crack propagation was seen to have a tendency to occur between the TNTZ (sample without the coating) and bone, while no crack occurred between the coating and bone or between the coating and TNTZ, as shown in Fig. 11.5. This result shows excellent bioactivity of the PIG glass-ceramic coating on TNTZ (Kasuga *et al.*, 2005).

This load-bearable glass-ceramic-coated-TNTZ would be applicable to surgical implants, such as Kirschner-wires and hip joints, that need to have bioactivity and low modulus of elasticity.

11.4 Bioactive surface prepared by chemical treatments

Bioactive surface modifications described in this section are not included in the category of coatings on metallic substrates. However, they are briefly reviewed, since they are quite important practical techniques for preparing bioactive surfaces on metallic substrates.

11.4.1 Surface modification by treatment with hydrogen peroxide

Titania gels can induce the formation of B-HA in SBF as described in Section 11.2.3. Gel coatings are expected to be one of the potential future surface modification techniques to improve the bioactivity of metallic implant materials (Li *et al.*, 1993). Conventional sol–gel derived coatings are usually

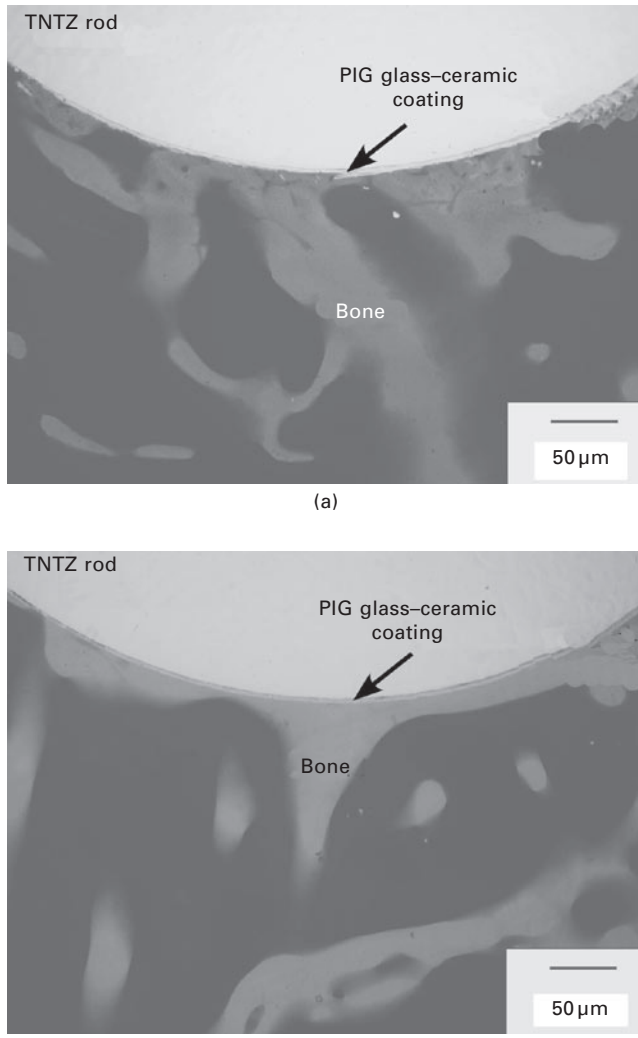

11.4 CMR images around PIG glass-ceramic-coated TNTZ rods (5 mmϕ) implanted into femurs of Japanese rabbits after (a) 4 weeks and (b) 52 weeks.

provided by a dip-coating process consisting of several coating–heating cycles for attaining the necessary thickness for B-HA formation in SBF (Jokinen *et al*., 1998). Tengvell *et al*. (1989a) reported that titanium reacts with an H_2O_2 solution, resulting in the formation of titania gel. This is one of the promising techniques for prepraring titania gel coatings on titanium substrates.

Wang *et al*. (2002) found that an acidic H_2O_2 solution containing HCl can accelerate the reaction rate and induce morphology with uniform, nano-

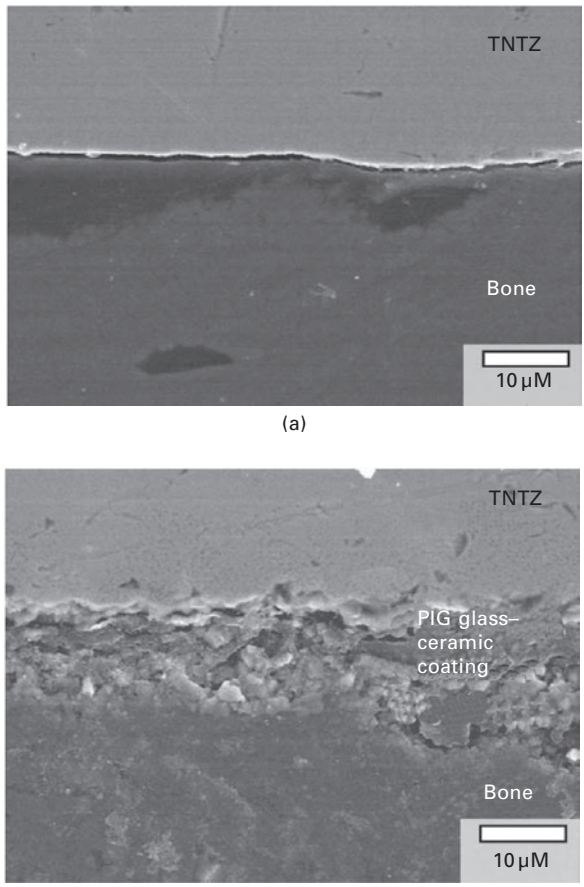

11.5 Cross-sectional scanning electron micrographs of (a) TNTZ and (b) the glass-ceramic-coated TNTZ after 52 weeks of implantation. In (a), a severe crack can be seen between the TNTZ and bone.

sized pores in the resulting gel layer. CpTi samples of $10 \times 10 \times 1$ mm in size were treated with a solution containing H_2O_2 of 8.8 M with HCl of 0.1 M at 80 °C for 0.5 h and subsequently heat-treated at various temperatures. After being chemically treated for 20 min, a porous titania gel layer of 0.5 μm thickness without cracking or chipping was formed. The pore sizes were estimated to be several hundred nanometers. By subsequent heat treatment at 300~600 °C, anatase was precipitated in the amorphous gel. When the sample was heated above 700 °C, rutile, not anatase, formed. When the samples were soaked in SBF, B-HA formed on those heated at 400~600 °C: the titania layer including an anatase phase induced B-HA formation, whereas that including a rutile phase induced no deposition.

Uchida *et al*. (2003) suggested that the anatase structure is especially effective in inducing B-HA formation in SBF. Sol–gel-derived titania gels with an amorphous structure do not induce B-HA formation on their surfaces, whereas the gels with an anatase or rutile structure via heat-treatment induce B-HA formation on their surfaces. The deposition of apatite is more enhanced on the anatase gels than on the rutile gels. The fit of the apatite (0001) plane to the anatase (110) plane or to the rutile (101) plane shows a close superposition of hydrogen-bonding groups in these crystals. These epitaxial relationships are suggested to lead to favourable B-HA formation on titania gels with anatase or rutile structures. In addition, the crystallographic matching between the apatite (0001) plane and the anatase (110) plane is better than that between the apatite (0001) plane and the rutile (101) plane. This may lead to higher B-HA-forming ability of anatase than that of rutile. These results imply that bioactivity on metallic titanium and its alloys can be induced by integrating anatase structures on their surfaces.

11.4.2 Surface modification by treatment with a concentrated alkaline solution

Ti and its alloys react with alkaline aqueous solutions. The reacted surface consists of negatively charged $HTiO_3^-$•nH_2O, which incorporates alkaline ions. Kokubo *et al*. (1996) prepared amorphous sodium titanate on cpTi by soaking the metal in an aqueous NaOH solution of 5 M at 60 °C for 24 h and subsequent heating at 600 °C for 1 h. A surface consisting of a porous layer was obtained. The sodium titanate phase was integrated with the metal substrate through a graded structure within a depth of 1.5 μm from the surface. When the treated sample was soaked in SBF, B-HA formed on the porous sodium titanate layer. Since the B-HA showed a graded structure, it achieved a tight adhesion to the metal substrate (tensile bonding strength; >30 MPa) (Kim *et al*., 1997). When titanium alloys, such as Ti–6Al–4V, Ti–6Al–2Nb–Ta and Ti–15Mo–5Zr–3Al, were treated with NaOH and subsequent heating, they also formed a sodium titanate phase, which was free of the alloying components (Kim *et al*., 1996). These treatments induced no damage to strength under tensile loading nor to fatigue strength under cyclic loading of the metals in saline solution (Kokubo *et al*., 2003).

The treated titanium metal and its alloys have been investigated in some animal models (Kokubo *et al*., 2003). When a cylindrical rod of the treated cpTi was implanted into the intramedullar canal of a rabbit femur, apatite formed on its surface within 3 weeks and it was completely covered with bone within 12 weeks. A rectangular sample implanted into a rabbit tibia formed an apatite layer on its surface and bonded to bone through the layer after 8 weeks. Surface modified titanium and titanium alloys have been clinically used as artificial hip joints since 2007.

The surface modification technique to induce bioactivity can be also applied to tantalum (Ta) metal with excellent fracture toughness and malleability (Miyazaki *et al.*, 2000). Typical treatment conditions are subjecting to aq NaOH of 0.5 M at 60 °C for 24 h and subsequently heating at 300 °C. After the treatment, an amorphous sodium tantalate phase forms on its surface. Since Na^+ ion in the phase on Ta is exchanged with the H_3O^+ ion in SBF to form Ta–OH groups for inducing apatite nucleation, B-HA forms on the treated Ta. This metal also forms apatite in the living body, and bonds tightly to bone through the apatite layer (Kato *et al.*, 2000).

11.4.3 Surface modification by treatment with a dilute alkaline solution

The surface properties, such as topography, energy and chemical composition, of biomaterials determine their compatibility with surrounding host tissues, cells and proteins. Osteogenic cells cultured on a sandblasted titanium were reported to show higher ability in differentiation than those on titanium with a smooth surface, and subsequent acid-treatment enhanced the differentiation of the cells on the sandblasted titanium (Zhao *et al.*, 2007). The topography and hydrophilicity of the titanium surface may be significantly involved in its cellular compatibility. As described in Sections 11.2.3, 11.4.1 and 11.4.2, Ti–OH groups at the surface of titania play an important role in B-HA formation. The formation of titania on titanium surfaces may induce the ability of B-HA formation *in vitro* and *in vivo*.

CpTi surfaces can be modified by hydrothermal treatment using a dilute alkaline solution (Obata *et al.*, 2008b). Some of the hydrothermal conditions used were to autoclave cpTi (e.g. 10 × 10 × 0.6 mm) in 10 ml of a dilute alkaline solution (aq NaOH of 0.05 M) for 24 h at 120 or 240 °C in a polytetrafluoroethylene vessel of internal volume 50 ml. The resulting samples were denoted by Ti-120 and Ti-240, respectively. The hydrothermal treatments might achieve the manipulation of hydrophilic groups on the surface, which were expected to be effective for inducing high cellular compatibility.

Figure 11.6 shows the surface morphologies of cpTi (Fig. 11.6(a)), Ti-120 (Fig. 11.6(b)) and Ti-240 (Fig. 11.6(c)). Leaf-like deposits with the size of ~100 nm consisting of anatase were observed on the Ti-120 surface. On the Ti-240 surface, pyramid-like anatase with the size of several hundred nanometers to several micrometers were observed. The anatase formation and its morphology were significantly related to the autoclaving temperature. The titania layers adhered strongly on the cpTi surface even after ultrasonic treatment in DW for 15 min, or a tape-test using Scotch®#6.

Figure 11.7 shows the numbers of mouse osteoblast-like cells MC3T3-E1 cultured on cpTi, Ti-120 and Ti-240 surfaces for seven days. The numbers

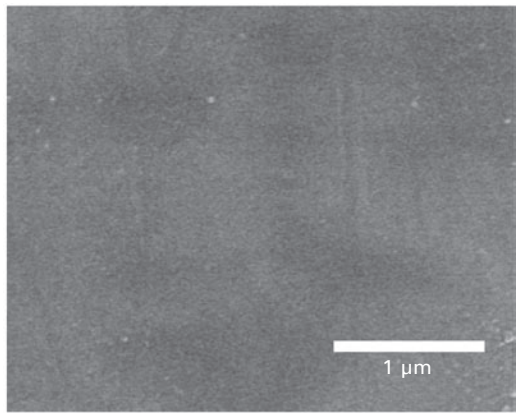

(a)

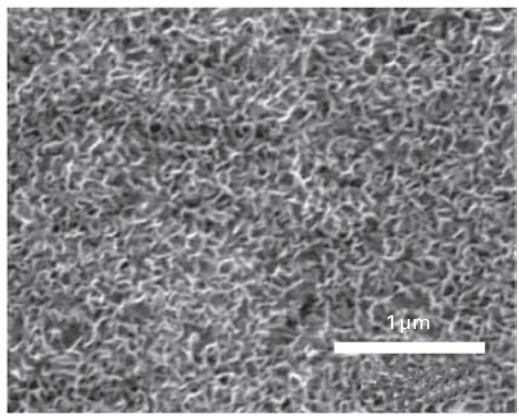

(b)

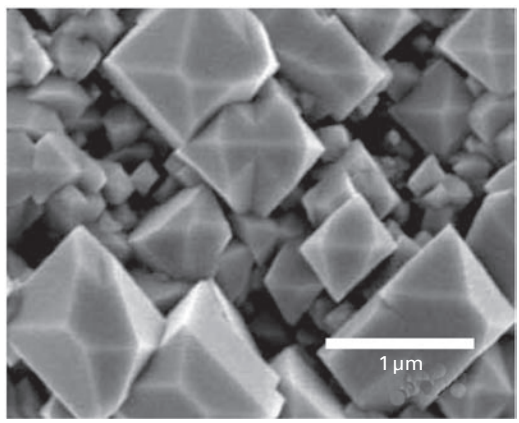

(c)

11.6 Scanning electron micrographs of the cpTi surfaces (a) before and (b, c) after hydrothermal treatments with dilute aq NaOH. (b) 120 °C (Ti–120) and (c) 240 °C (Ti–240).

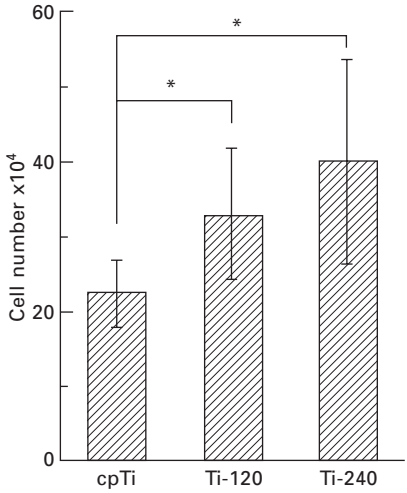

11.7 Numbers of MC3T3-E1 cells harvested from cpTi, Ti-120 and Ti-240 after seven days of culturing (*p <0.05).

of the cells harvested from Ti-120 and Ti-240 were significantly higher than that from cpTi. The titania layer formed on cpTi by autoclaving is expected to be involved in its cellular compatibility. Tengvall *et al*. (1989b, c) reported that titania shows higher biocompatibility than titanium. Zhao *et al*. (2007) reported that the differentiation of human osteoblast-like cells cultured on titanium with a hydroxylated/hydrated surface is higher than that on an untreated one. A hydrothermal treatment can achieve the manipulation of hydrophilic groups on the titanium surface. The groups formed on the autoclaved cpTi surface are expected to stimulate the cellular activity.

11.5 Summary

This chapter briefly reviewed some surface modifications, based on ceramics on Ti and its alloys, focusing on recent promising research. Some new directions, such as highly oriented hydroxyapatite coatings using plasma-spraying, and strongly-bonded, thin film coatings consisting of a single calcium phosphate phase using rf-magnetron sputtering or MOCVD, have been discussed. A bioactive coating using newly developed calcium phosphate glasses for harmonizing on β-type TNTZ for biomedical use may be a significant item for various applications. Surface modification by alkali-treatment is one of the most useful methods for preparing bioactive surfaces. The treated titanium was approved for production and sale by the Ministry of Health, Labor, and Welfare of Japan in 2007. The 'bioactive titanium' has high reliability for long-term use, since the bioactive ceramic phase is integrated with the metallic titanium.

These metallic biomaterials surface-modified by ceramics may make new progress for the next generation through their integration with bioresorbable polymers or biological substances such as proteins and/or cells. It may be feasible to design a new generation of gene-activating materials, tailored for specific patients and disease states. As described in the Section 11.2.3, some gene-activating materials are recently being designed to stimulate specific cellular responses at molecular or ionic species level (Hench *et al.*, 2002). Their releasing ability of trace amounts of ionic silicon and/or zinc species could be one of the important factors in preparing the next generation of coatings to enhance the proliferation and differentiation of cells.

11.6 References

Akahori T, Niinomi M, Koyanagi Y, Kasuga T, Roda H, Fukui H and Ogawa M (2005), 'Mechanical properties of biocompatible beta-type titanium alloy coated with calcium phosphate invert glass-ceramic layer', *Mater Trans*, **46** 1564–69.

Allen GC, Ciliberto E, Fragala I and Spoto G (1996), 'Surface and bulk study of calcium phosphate bioceramics obtained by metal organic chemical vapor deposition', *Nucl Instrum Methods Phys Res*, **B116** 457–60.

Asami K, Saito K, Ohtsu N, Nagata S and Hanawa T (2007), 'Titanium-implanted $CaTiO_3$ films and their changes in Hanks' solution', *Surf Interface Anal*, **35** 483–88.

Berndt CC, Haddad GN and Farmer AJD (1990), 'Thermal spraying for bioceramic applications', *Mater Sci Forum*, **14** 161–73.

Darr JA, Guo ZX, Raman V, Bououdina M and Rehman V (2004), 'Metal organic chemical vapour deposition (MOCVD) of bone mineral like carbonated hydroxyapatite coatings', *Chem Comm*, **62** 455–60.

Doremus RH (1992), 'Review: Bioceramics', *J Mater Sci*, **27** 285–97.

Ducheyne P, Raemdonck WV, Heughebaert JC and Heughebaert M (1986), 'Structural analysis of hydroxyapatite coating on titanium', *Biomaterials*, **7** 97–103.

Hashimoto T, Obata A and Kasuga T (2007), 'Preparation of silicon-containing apatite coating on titanium', *Proc 7th Asian BioCeram Symp (Archives of BioCeramics Vol.7)*, pp. 133–36.

Hench LL (1991), 'Bioceramics: From concept to clinic', *J Am Ceram Soc*, 1991 **74** 1487–510.

Hench LL and Wilson J (1993), '*An Introduction to Bioceramics*', Singapore, World Scientific.

Hench LL and Polak JM (2002), 'Third generation biomedical materials', *Science*, **296** 1014–17.

Inagaki M, Yokogawa Y and Kameyama T (2003), 'Bond strength and microstructure of radio-frequency thermal plasma sprayed hydroxyapatite/titanium composite coatings', *Key Eng Mater*, **240–242** 99–102.

Inagaki M and Kameyama T (2007), 'Phase transformation of plasma-sprayed hydroxyapatite coating with preferred crystalline orientation', *Biomaterials*, **28** 2923–31.

Inagaki M, Nakashima H, Saito T and Kameyama T (2008), 'Protein adsorption of highly (001) oriented hydroxyapatite coating using rf-plasma spraying', *Key Eng Mater*, **361–363** 705–08.

Jokinen M, Patsi M, Rahiala H, Peltola T, Ritala M and Rosenholm JB (1998), 'Influence

of sol and surface properties on *in vitro* bioactivity of sol–gel-derived TiO_2 and TiO_2-SiO_2 films deposited by dip-coating method', *J Biomed Mater Res*, **42** 295–302.

Kasuga T and Abe Y (1998), 'Novel calcium phosphate ceramics prepared by powder-sintering and crystallization of glasses in the pyrophosphate region', *J Mater Res*, **13** 3357–60.

Kasuga T and Abe Y (1999a), 'Calcium phosphate invert glasses with soda and titania', *J Non-Cryst Solids*, **243**, 70–74.

Kasuga T, Sawada M, Nogami M and Abe Y (1999b), 'Bioactive ceramics prepared by sintering and crystallization of calcium phosphate invert glasses', *Biomaterials*, **20** 1415–20.

Kasuga T, Nogami M and Abe Y (1999c), 'Bioactive calcium phosphate glass-ceramics in the pyrophosphate region', *Phophorus Res Bull*, **10** 534–39.

Kasuga T, Mizuno T, Watanabe M, Nogami M and Niinomi M (2001a), 'Calcium phosphate invert glass-ceramic coatings joined by self-development of compositionally gradient layers on a titanium alloy', *Biomaterials*, **22** 577–82.

Kasuga T, Hosoi Y, Nogami M and Niinomi M (2001b), 'Apatite formation on calcium phosphate invert glasses in simulated body fluid', *J Am Ceram Soc*, **84** 450–52.

Kasuga T, Nogami M and Niinomi M (2003a), 'Calcium phosphate glass-ceramics for bioactive coating on a β-type titanium alloy', *Adv Eng Mater*, **5** 498–501.

Kasuga T, Nogami M and Niinomi M (2003b), 'Joining of calcium phosphate invert glass-ceramics on a β-type titanium alloy', *J Am Ceram Soc*, **86** 1031–33.

Kasuga T, Nogami M, Niinomi M and Hattori T (2003c), 'Bioactive calcium phosphate invert glass-ceramic coating on β-type Ti-29Nb-13Ta-4.6Zr alloy', *Biomaterials*, **24** 283–90.

Kasuga T, Fujimoto T and Nogami M (2003d), 'Enhancement of biomimetic apatite forming ability of calcium phosphate glass-ceramic by a hydrothermal treatment', *J Ceram Soc Japan*, **111**, 633–35.

Kasuga T, Nogami M, Hattori, Niinomi M and Hench LL (2005), 'Enhancing effect of autoclaving on bioactivity of β-titanium alloy coated with calcium phosphate glass-ceramic', *Key Eng Mater*, **284–286** 243–46.

Kato H, Nakamura T, Nishiguchi S, Matsusue Y, Kobayashi M, Miyazaki T, Kim H-M and Kokubo T (2000), 'Bonding of alkali- and heat-treated tantalum implant to bone', *J Biomed Mater Res (Appl Biomater)*, **53** 28–35.

Kim H-M, Miyaji F, Kokubo T and Nakamura T (1996), 'Preparation of bioactive Ti and its alloys via simple chemical surface treatment', *J Biomed Mater Res*, **32** 409–17.

Kim H-M, Miyaji F, Kokubo T and Nakamura T (1997), 'Bonding strength of bonelike apatite layer to Ti metal substrate', *J Biomed Mater Res (Appl Biomater)*, **38** 121–27.

Kitsugi T, Yamamuro T, Nakamura T, Higashi S, Kotani Y, Hyakuna K, Ito S, Kokubo T, Takagi M and Shibuya T (1986), 'Bone bonding behavior of three kinds of apatite containing glass ceramics', *J Biomed Mater Res*, **20** 1295–307.

Kokubo T (1990), 'Surface chemistry of bioactive glass-ceramics', *J Non-cryst Solids*, **120** 138–51.

Kokubo T (1998), 'Apatite formation on surfaces of ceramics, metals and polymers in body environment', *Acta Mater*, **46** 2519–27.

Kokubo T, Ito S, Huang Z, Hayashi T, Sakka S, Kitsugi T and Yamamuro T (1990), 'Ca, P-rich layer formed on high-strength bioactive glass-ceramic A-W', *J Biomed Mater Res*, **24** 331–43.

Kokubo T, Miyaji F, Kim H-M and Nakamura T (1996), 'Spontaneous formation of bonelike apatite layer on chemically treated titanium metals', *J Am Ceram Soc*, **79** 1127–29.

Kokubo T, Kim H-M and Kawashita M (2003), 'Novel bioactive materials with different mechanical properties', *Biomaterials*, **24** 2161–75.

Kuroda D, Niinomi M, Morinaga M, Kato Y and Yashiro T (1998), 'Design and mechanical properties of new β type titanium alloys for implant materials', *Mater Sci Eng*, **A243** 244–49.

Lacefield WR (1993), 'Chapter 12: Hydroxyapatite Coatings' in *An Introduction to Bioceramics*, Singapore, World Scientific, 223–38.

Li P and deGroot K (1993), 'Calcium phosphate formation within sol–gel prepared titania *in vitro* and *in vivo*', *J Biomed Mater Res*, **27** 1495–500.

Li TT, Lee JH, Kobayashi T and Aoki H (1996), 'Hydroxyapatite coating by dipping method, and bone bonding strength', *J Mater Sci Mater Med*, **7** 355–57.

Li SJ, Niinomi M, Akahori T, Kasuga T, Yang R and Hao YL (2004), 'Fatigue characteristics of bioactive glass-ceramic-coated Ti-29Nb-13Tan-4.6Zr for biomedical application', *Biomaterials*, **25**, 3369–78.

Liao H, Mutvei H, Sjöström M, Hammarström L and Li J (2000), 'Tissue responses to natural aragonite (Margaritifera shell) implants *in vivo*', *Biomaterials*, **21** 457–68.

Lo WJ, Grant DM, Ball MD, Welsh BS, Howdle SM, Antonov EN, Bagratashvili VN and Popov VK (2000), 'Physical, chemical, and biological characterization of pulsed laser deposited and plasma sputtered hydroxyapatite thin films on titanium alloy', *J Biomed Mater Res*, **50**, 536–45.

Maeda H, Kasuga T and Nogami M (2004), 'Apatite formation on titania-vaterite powders in simulated body fluid', *J Euro Ceram Soc*, **24** 2125–30.

Miyazaki T, Kim HM, Miyaji F, Kokubo T and Nakamura T (2000), 'Bioactive tantalum metal prepared by NaOH treatment', *J Biomed Mater Res*, **50** 35–42.

Narushima T, Ueda K, Goto T, Masumoto H, Katsube T, Kawamura H, Ouchi C and Iguchi Y (2005), 'Preparation of calcium phosphate films by radiofrequency magnetron sputtering', *Mater Trans*, **46** 2246–52.

Narushima T, Ueda K, Goto T, Katsube T, Ouchi C and Iguchi Y (2007), 'Calcium phosphate films coated on titanium by rf magnetron sputtering for medical applications', *Mater Sci Forum*, **539–543** 551–56.

Niinomi M, Hattori T, Morikawa K, Kasuga T, Suzuki A, Fukui H and Niwa S (2002), 'Development of low rigidity beta-type titanium alloy for biomedical applications', *Mater Trans*, **43**, 2970–77.

Niinomi M (2003a), 'Cyto-toxicity and fatigue performance of low rigidity titanium alloy, Ti-29Nb-13Ta-4.6Zr, for biomedical applications and healthcare goods', *Biomaterials*, **24** 2673–83.

Niinomi M, Akahori T, Yamaguchi T, Kasuga T, Fukui H and Suzuki A (2003b), 'Aging characteristics and mechanical properties of Ti–29Nb–13Ta–4.6Zr coated with calcium phosphate invert glass-ceramic for biomedical applications', *J Japan Inst Metals*, **67** 604–13 *(in Japanese)*.

Obata A and Kasuga T (2008a), 'Cellular compatibility of bone-like apatite containing silicon species', *J Biomed Mater Res*, **85A**, 140–44.

Obata A and Kasuga T (2008b), 'Surface modification of titanium by hydrothermal treatment', *Key Eng Mater*, **361–63** 609–12.

Ong JL and Lucas LC (1994), 'Post-deposition heat treatments for ion beam sputter deposited calcium phosphate coatings', *Biomaterials*, **15** 337–41.

Sato M, Tu R, Goto T, Ueda K and Narushima T (2007a), 'Hydroxyapatite formation on calcium phosphate coated titanium', *Mater Sci Forum*, **561–565** 1513–16.

Sato M, Tu R, Goto T, Ueda K and Narushima T (2007b), 'Hydroxyapatite formation

on $CaTiO_3$ film prepared by metal–organic chemical vapor deposition', *Mater Trans*, **48** 1505–10.

Tengvell P, Elwing H and Lundstrom I (1989a), 'Titanium gel made from metallic titanium and hydrogen peroxide', *J Colloid Interface Sci*, **130** 405–13.

Tengvall P, Elwing H, Sjoqivist L, Lundwtrom I and Bjursten LM (1989b), 'Interaction between hydrogen peroxide and titanium: A possible role in the biocompatibility of titanium', *Biomaterials*, **10** 118–20.

Tengvall P, Lundstrom I, Sjoqivist L, Elwing H and Bjursten LM (1989c), 'Titanium–hydrogen peroxide interaction: Model studies of the influence of the inflammatory response on titanium implants', *Biomaterials*, **10** 166–75.

Tsui YC, Doyle C and Clyne TW (1998), 'Plasma sprayed hydroxyapatite coatings on titanium substrates, Part 1: Mechanical properties and residual stress levels', *Biomaterials*, **19** 2015–29.

Uchida M, Kim H-Mi, Kokubo T, Fujibayashi S and Nakamura T (2003), 'Structural dependence of apatite formation on titania gels in a simulated body fluid', *J Biomed Mater Res*, **64A** 164–70.

Ueda K, Narushima T, Goto T, Nakagawa H, Kawamura H and Katsube T (2007), '*In vivo* and *in vitro* evaluations of calcium phosphate films coated on titanium by rf magnetron sputtering', *Proc 11th World Conf Titanium*, Sendai, The Japan Institute of Metals, pp. 1477–80.

Vago R, Plotquin D, Bunin A, Sinelnikov I, Atar D and Itzhaki D (2002), 'Hard tissue remodeling using biofabricated coralline biomaterials', *J Biochem Biophys Methods*, **50** 253–59.

van Dijk K, Schaeken HG, Wolke JCG, Maree CHM, Habraken FHPM, Verhoeven J and Jansen JA (1995), 'Influence of discharge power level on the properties of hydroxyapatite films deposited on Ti-6A1-4V with RF magnetron sputtering', *J Biomed Mater Res*, **29** 269–76.

Wang X-X, Hayakawa S, Tsuru K and Osaka A (2002), 'Bioactive titania gel layers formed by chemical treatment of Ti substrate with a H_2O_2/HCl solution', *Biomaterials*, **23** 1353–57.

Wolke JGC, van Dijk K, Schaeken HG, de Groot K and Jansen JA (1994), 'Study of the surface characteristics of magnetron-sputter calcium phosphate coatings', *J Biomed Mater Res*, **28**, 1477–84.

Wolke JGC, van der Waerden JPCM, Schaeken HG and Jansen JA (2003), '*In vivo* dissolution behavior of various RF magnetron-sputtered Ca-P coatings on roughened titanium implants', *Biometerials*, **24** 2623–29.

Xynos ID, Edgar AJ, Buttery LDK, Hench LL and Polak JM (2000), 'Ionic products of bioactive glass dissolution increase proliferation of human osteoblasts and induce insulin-like growth factor II mRNA expression and protein synthesis', *Biochem. Biophys. Res. Comm.*, **276**, 461–65.

Yamashita K, Matsuda M, Arashi T and Umegaki T (1998), 'Crystallization, fluoridation and some properties of apatite thin films prepared through rf-sputtering from $CaO–P_2O_5$ glasses', *Biomaterials*, **19** 1239–44.

Yoshinari M, Hayakawa T, Wolke JGC, Nemoto K and Jansen JA (1997), 'Influence of rapid heating with infrared radiation on RF magnetron-sputtered calcium phosphate coatings', *J Biomed Mater Res*, **37** 60–67.

Zhao G, Raines AL, Wieland M, Schwarts Z and Boyan BD (2007), 'Requirement for both micron- and submicron scale structure for synergistic responses of osteoblasts to substrate surface energy and topography', *Biomaterials*, **28** 2821–29.

12

Biocompatible polymer assembly on metal surfaces

K. ISHIHARA and J. CHOI, The University of Tokyo, Japan

Abstract: A description is given of surface modifications to a titanium (Ti) alloy substrate by phospholipid polymers to obtain antithrombogenicity and biocompatibility. The phospholipid polymers contained 2-methacryloyloxyethyl phosphorylcholine (MPC) units, whose design was inspired by cell membrane surface structures. The MPC polymers effectively prevented platelet adhesion and thrombus formation as a result of reduced plasma protein adsorption. Silane chemistry was used to carry out surface grafting of the MPC polymer onto the Ti substrate. Long chains of MPC were much more effective in reducing protein adsorption than short ones. Another surface modification method, the integration of polymers by a layer-by-layer procedure on the Ti substrate, was introduced. The MPC polymer bearing phenylboronic acid units could form complexes covalently with poly(vinyl alcohol). This reaction was used to construct polymer integrated layers by soaking the Ti substrate alternatively in aqueous solutions of these polymers. The MPC polymer could be immobilized by this procedure on the substrate. The layer effectively prevented cell adhesion and also functioned as a drug reservoir by maintaining drugs inside the layer and controlling their release pattern. These observations clearly indicate that surface modifications using MPC polymer provide excellent functions on the Ti substrate.

Key words: phospholipid polymer, artificial cell membrane, grafting, layer-by-layer method, biocompatibility.

12.1 Introduction

Metal substrates are being used as biomaterials in medical devices, including implantable artificial organs and prostheses of hard tissues. The mechanical properties of metal biomaterials are excellent but their surface biocompatibility is not good enough, so the assistance of some pharmaceutical treatment when the metallic implantable medical devices are applied is useful. One of the methods for improving the surface biocompatibility on the metal substrate is to modify it with biocompatible materials, namely ceramics and polymers. Ceramic coatings on metal substrates have been reported (Habibovic *et al*., 2002). Polymers are also used as artificial organs because of their functionality and processability, particularly the effective surface modification of metal. However, connections between the metal and the polymer are important for stabilizing the polymer layer. Silane chemistry is suitable for this purpose,

since alkoxysilane compounds can react with the metal oxide layer which is formed on the metal substrate. Thus, these compounds with various functional groups form an intermediate layer between the polymer and the metal substrate. In this chapter, an overview is given of the grafting of polymer chains and the integration of polymers onto metal through silane chemistry. The biocompatibility evaluations from the viewpoint of protein adsorption and cell adhesion on the polymer-modified surface are also described.

12.2 Phospholipid polymers providing biocompatible surfaces on metals

12.2.1 Basic concept for constructing an artificial cell membrane structure

The development of new biomaterials was proposed based upon the mimicking of a simple component present on the extracellular surfaces of the phospholipid bilayer that forms the matrix of cell membranes; namely, the phosphorylcholine group of phosphatidylcholine and sphingomyelin. Phosphorylcholine, an electrically neutral, zwitterionic head group, which represents the dominant property of the phospholipid head groups present on the external surface of cells, is inert in coagulation assays. Several researchers have confirmed that a polymer surface coated with natural or synthetic phospholipids has good biocompatibility (Ishihara, 2000; Lewis *et al.*, 2001; Iwasaki and Ishihara, 2005). As a result of biochemical and pharmaceutical interest, phospholipid molecules, in particular phosphatidylcholines with polymerizable groups such as diene, acetylene, and acrylic, were prepared to stabilize the liposomal structure as a model cell or drug carrier. Some modification methods are described here, as shown in Fig. 12.1. The first one is the direct attachment

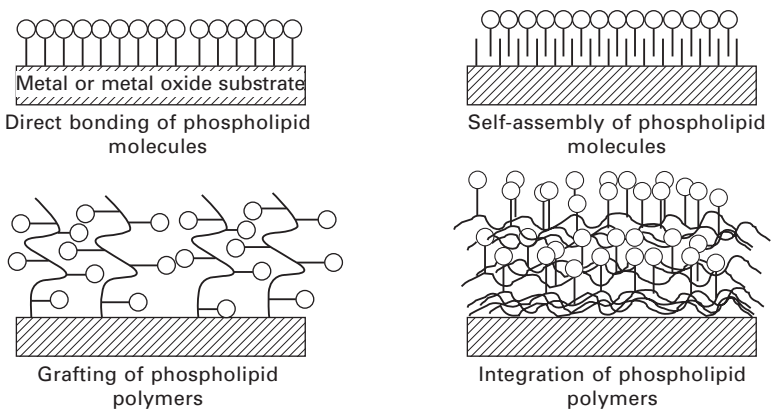

12.1 Surface modification on metal with phospholipid derivatives for making artificial cell membrane structure.

of phospholipid derivatives on the metal surface. This is a very convenient procedure; however, it requires the introduction of a specific functional group into the phospholipid molecules. The second method is the construction of monolayered phospholipid molecules on the metal surface based on self-assembly characteristics. The surface is modified with an alkyl group using silane chemistry and phospholipid molecules are applied onto the surface. These form a self-assembly monolayer by physical molecular interactions, providing a very good surface covered with phospholipids, but the monolayer has insufficient stability and mechanical properties. The third and fourth methods provide a very stable and functionally good surface, and will be described in detail in this chapter.

12.2.2 Molecular design of phospholipid polymers

Ishihara and Nakabayashi were inspired to design the materials by the cell membrane structure, a methacrylate monomer with a phospholipid polar group (phosphorylcholine group), and 2-methacryloyloxyethyl phosphorylcholine (MPC) (Fig. 12.2) (Ishihara *et al.*, 1990). The synthesis of the MPC was difficult; however, in 1987, Ishihara considered a new process for its synthesis and purification and a sufficient amount of MPC with excellent purity was obtained. It therefore became possible to prepare the MPC polymer with various other alkyl methacrylates and styrene, and carefully evaluate their biocompatibility (Ueda *et al.*, 1992). Figure 12.3 shows the chemical structures of typical MPC polymers. The solubility of the MPC polymer strongly depends on its molecular structure, the composition of the MPC and other monomer units, and its molecular weight. The homopolymer of the MPC easily dissolves in water and alcohol, but is insoluble in polar organic solvents such as acetone, acetonitrile, tetrahydrofuran and a specific composition of an aqueous solution of ethanol (60–92 vol% ethanol). The

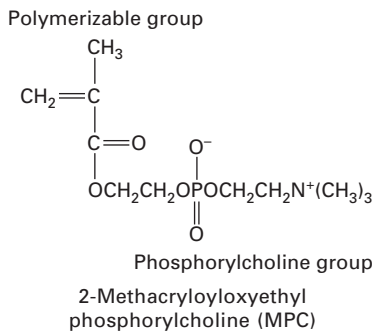

12.2 Chemical structure of 2-methacryloyloxyethyl phosphorylcholine (MPC).

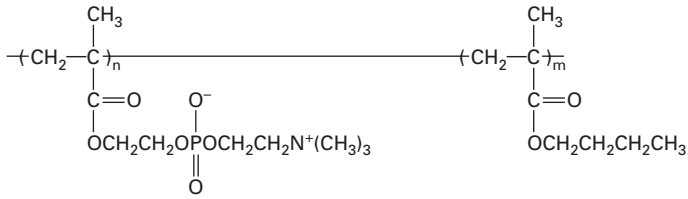

12.3 Typical chemical structure of MPC polymer (PMB) for surface modification.

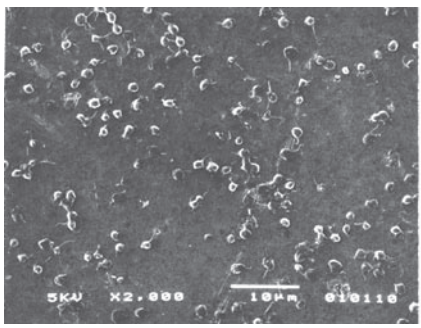

Titanium alloy substrate

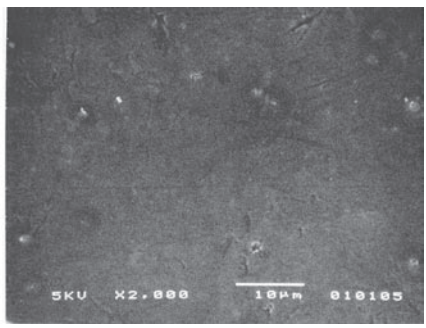

Titanium alloy substrate coated with PMB

12.4 Adhesion of platelets on Ti alloy substrate and one coated with MPC polymer (PMB).

introduction of other monomer units could change the solubility. This means it is very easy to design an MPC polymer structure to adapt to a substrate that is modified with the MPC polymer. These polymerization characteristics are very important for obtaining a suitable MPC polymer for use as a biomaterial. Controlling the monomer ratio determines the MPC unit composition in the polymer. The MPC polymer has also been prepared with other polymer architectures, such as block-type copolymers and graft-type copolymers, by a conventional radical polymerization technique. The functional MPC polymer is useful for surface modification and can convert block-type and graft-type copolymers.

12.2.3 Biocompatibility and antithrombogenicity of phospholipid polymers

Excellent antithrombogenic properties were observed when the MPC polymers came into contact with blood components (Ishihara *et al.*, 1992). Figure 12.4 shows scanning electron microscope (SEM) pictures of the polymer surfaces after contact with platelet-rich plasma. Many platelets adhered to the surface of the titanium alloy and were significantly deformed, but no cell adhesion

could be found on the surface after being coated with poly(MPC-co-*n*-butyl methacrylate(BMA)) (PMB). Moreover, even when the PMB was in contact with whole human blood without an anticoagulant, the blood coagulation was completely suppressed and a very clean surface was maintained. These results clearly show that MPC polymers have excellent antithrombogenic properties and MPC moieties in the polymers are an important element in their antithrombogenicity. Protein adsorption is one of the most important phenomena in determining the biocompatibility of materials. In general, proteins adsorb on a surface within a few minutes of the material coming into contact with body fluids such as blood, plasma or tears. Protein adsorption on the MPC polymers from human plasma, as determined by radioimmunoassay and an immunogold-colloid labeling technique, showed that the amount of adsorbed protein was quite small and decreased with an increase in the MPC moiety (Ishihara *et al.*, 1991). The proteins existing on the surfaces of the poly(BMA) and PMB that were in contact with the plasma were determined by radioimmunoassay. The major components of plasma proteins such as albumin, fibrinogen, and γ-globulin and also minor components, were observed on the surface of each material. Protein adsorption was reduced dramatically with an increase in the MPC unit composition.

12.2.4 Performance of phospholipid polymer on medical devices

As a result of these characteristics, MPC polymers are used as coating materials on various medical devices including cardiovascular stents (Whelan *et al.*, 2000), oxygenators (Myers *et al.*, 2003), and catheters (Gobeil *et al.*, 2002). In the case of stents, the metal surface is covered with self-curable MPC polymer to prevent initial thrombus formation when it is implanted into the blood vessel. The surface inhibits any cell adhesion during the first stage and then the stent is embedded into the blood vessel wall. The coating layer functions as a drug reservoir and a sustained drug release can be achieved. The next generation of stent to be developed will be a drug-eluting stent, which will prevent excess bioreactions at the interface between the stent and blood vessel after it has been embedded.

Snyder, Yamazaki *et al.* developed an implantable artificial blood pump made from titanium alloy (Snyder *et al.*, 2007), whose surface was modified with high-molecular-weight PMB with 30 mol% of MPC units. It could be physically attached to the surface, but a stable coating layer is produced by a simple dip-coating method from its solution in ethanol. The performance of the PMB layer in preventing thrombus formation was good and remained so for more than 823 days in animal tests without any anticoagulant treatment. In 2005, an artificial blood pump was implanted in a human being in clinical trials and it continues to work well up to the present time.

12.3 Surface grafting of 2-methacryloyloxyethyl phosphorylcholine (MPC) polymer on titanium alloy

12.3.1 Grafting of phospholipid polymer onto titanium alloy

The covalent attachment of organosilanes has proved to be a simple and versatile method for adjusting the properties of solid surfaces such as wettability, adhesion and surface activity. Self-assembled monolayers (SAMs) have been widely used for biofouling studies of material surfaces (Sigal *et al.*, 1998). Several functionalized SAMs on metal were prepared and the effects of the surface chemistries on protein adsorption and cell adhesion were discussed. Phosphorylcholine-assembled surfaces were of particular interest for reducing biofouling. The procedure of surface modification was classified into two approaches. One was the use of hydroxy group-terminated monolayers; the other was the chemical or physical adsorption of phospholipids or phospholipid derivatives onto alkylsilane monolayers (Orban *et al.*, 2000). A new method has been reported for the preparation of hydridosilane monolayers on various metal surfaces (Fadeev and McCarthy, 1999). Surface modification with increased hydrophilicity is believed to be a useful method for producing resistance to biofouling, and various polymers have been modified with water-soluble polymers for biomedical use (Lee, 1990). Controlled surface modification of a Ti surface with MPC polymers might be possible using a monolayer of organosilanes as the binding layer. Iwasaki and Saito carried out research on the surface modification of a Ti alloy using a well-defined MPC polymer (Iwasaki and Saito, 2003). They performed a controlled immobilization of an end-functional MPC polymer supported with a vinyldimethysilane (VDMS) monolayer on Ti (Fig. 12.5). A chemical reaction occurred between the vinyl groups immobilized on the surface and the amino group in the terminal part of the polymer, and grafting was then achieved.

The introduction of vinyl groups onto solid surfaces is made possible by varying the functionalities of the surface and improving the adhesion of the polymers and inorganic materials. Amino group terminated poly(MPC) (ATPMPC) chains with 7000 (7K-ATPMPC) and 22 000 (22K-ATPMPC) molecular weights were used for modification. After immobilization of the MPC polymers, the surface properties were characterized by atomic force microscopy (AFM), water-contact angle measurements and X-ray photoelectron spectroscopy (XPS), with particular attention being paid to the mobility of the grafted poly(MPC) chains.

The AFM image after grafting of the MPC polymer is shown in Fig. 12.6. The surface roughness was significantly increased by the immobilization of

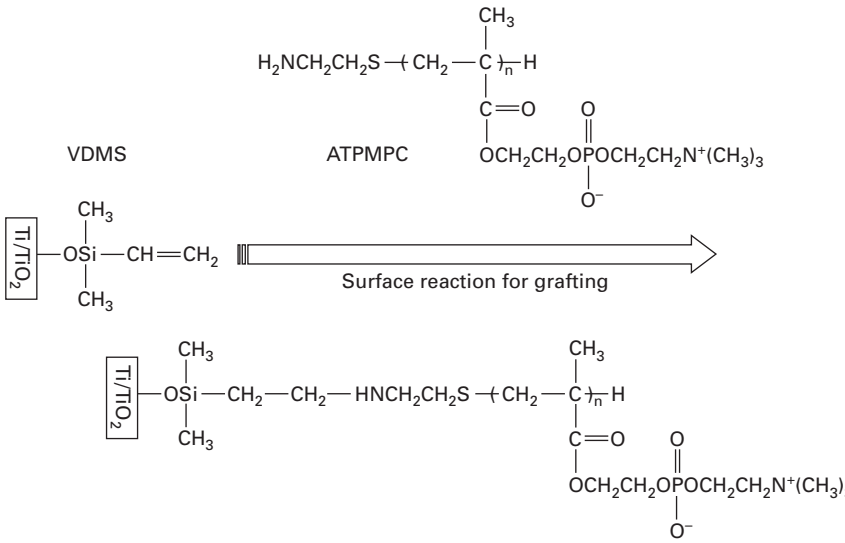

12.5 Reaction scheme for surface modification by grafting with poly(MPC).

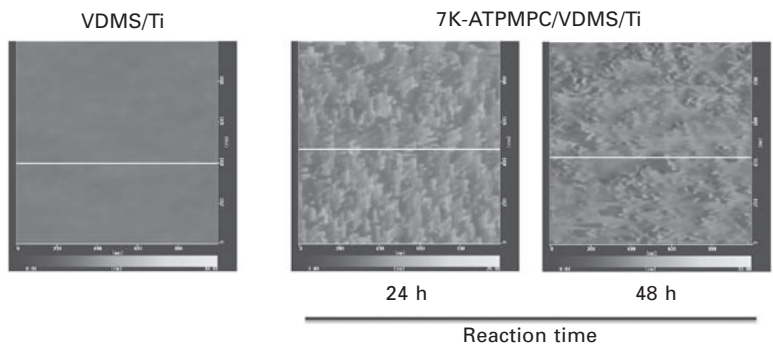

12.6 AFM images of Ti surface after grafting with poly(MPC).

the MPC polymers; therefore grafting to the surface could be confirmed. The water contact angle data showed that the hysteresis between advancing and receding contact angles on the ATPMPC-modified surface was larger than that of the VDMS monolayer surface due to the mobility of the ATPMPC. After a 24 h reaction time with 7K-ATPMPC, the advancing contact angles did not change from those of the VDMS monolayer, whereas the receding contact angles decreased. The advancing contact angles are attributed to the hydrophobic portion at the surface. Therefore the VDMS is considered to be still exposed at the surface during the 24 h reaction period. However, the advancing water contact angles decreased after a 48 h reaction time and

the size was stable for longer reaction periods. The advancing contact angle data for 22K-ATPMPC were slightly lower than those for the 7K-ATPMPC after the 48 h reaction time. The water contact angle data were in good agreement with the XPS data (Fig. 12.7). The ratio of phosphorus atoms to Ti atoms (phosphorus (P)/Ti ratio) attributed to the MPC unit for sample surfaces modified with the 7K-ATPMPC, increased with an increase in the reaction time. The P/Ti value of surfaces modified with 22K-ATPMPC was lower than those modified with 7K-ATPMPC. There was no signal on the Ti surface in direct contact with the 7K-ATPMPC. The VDMS monolayer works to immobilize the ATPMPC on the surface covalently. The surface density of the poly(MPC) on the Ti may also be controllable by changing the surface density of the VDMS.

12.3.2 Protein adsorption on phospholipid polymer graft surface

Adsorption of proteins on the graft surface was monitored by XPS analysis. When protein adsorption occurs, nitrogen (N) attributed to the amino acid residue or peptide bond in the protein may be observed (Fig. 12.8). The N/Ti ratio on the surface after contact with serum albumin increased for a few minutes. A high intensity of nitrogen was observed on the untreated Ti and VDMS surfaces due to adsorbed albumin. However, albumin adsorption was reduced on the PMPC-modified surfaces. Moreover, the surface property of high molecular weight ATPMPC, which resists albumin adsorption, became

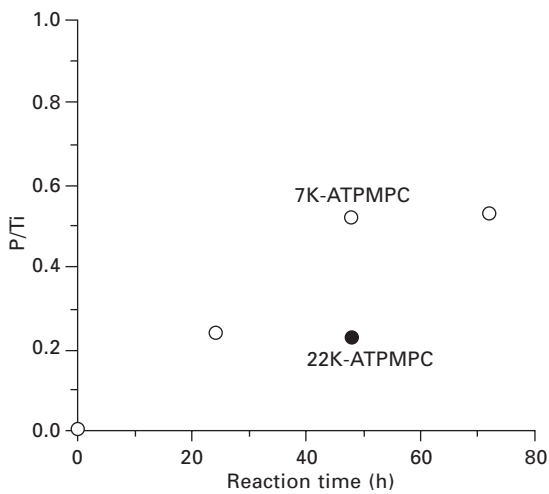

12.7 P/Ti ratio based on the surface density of poly(MPC) on Ti substrate.

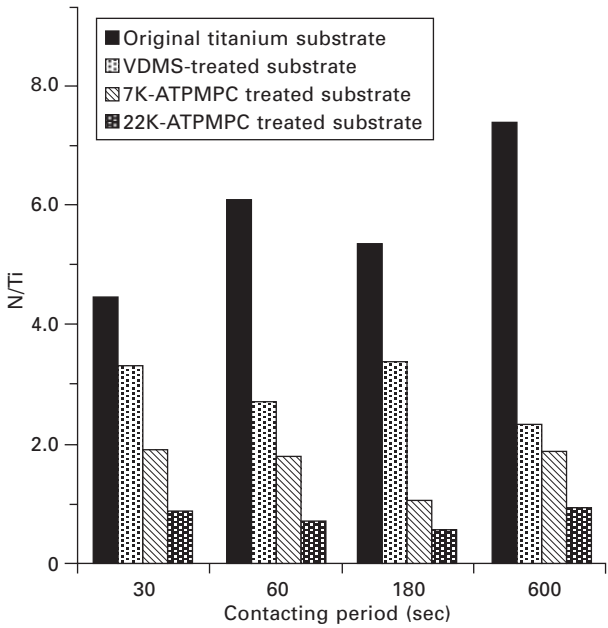

12.8 N/Ti ratio based on the albumin adsorption of the Ti substrate with various surfaces.

more effective. The order of the amounts of protein adsorbed was non-treated Ti, VDMS monolayer, 7K-ATPMPC and 22-ATPMPC.

Controlled modification of the Ti alloy substrate with poly(MPC) was carried out using the VDMS monolayer. The effect on the albumin adsorption-resistance of grafting the MPC polymer was also clarified. Using organosilane monolayers as the binding layer, precise modification of the surface with a polymer is possible. This may be a promising method of reducing biofouling on the Ti alloy substrate.

12.4 MPC polymer assembly on Ti alloy

12.4.1 Layer-by-layer molecular integration

Modifications of biomaterial surfaces have a long history in implantology and form a major area of research. Since its introduction by Decher (1997), the process of building up organic multilayer films through layer-by-layer (LbL) self-assembly has attracted a great deal of attention and allows the formation of interpolymer complexes by the deposition of oppositely charged polyelectrolytes. The LbL method is renowned for being a convenient, versatile, and efficient technique for generating biologically active surfaces. Furthermore, various important methods have been introduced for forming

multilayers by the LbL method, such as electrostatic interaction (Ren and Shen, 2006), hydrogen bonding (Sukhishvili and Granick, 2002), and covalent bonding (Brynda and Houska, 1996).

12.4.2 Surface modification by the layer-by-layer procedure based on covalent bonding

Phenylboronic acid is known to rapidly form a cyclic boronic complex with cis-diols (Yan *et al.*, 2004) such as carbohydrates and some polymers such as poly(vinyl alcohol) (PVA). It was synthesized using a new water-soluble MPC polymer (PMBV) containing MPC, BMA, and 4-vinylphenylboronic acid units (VPBA) (Fig. 12.9) (Konno and Ishihara, 2007). The interpolymer complexation of a polymer made from boronic acid with PVA has been reported to form a hydrogel due to the covalent linkage in both constituent polymers. It is thought that the LbL deposition method would allow the combination of PMBV and PVA to produce a polymer hydrogel multilayer bonded to the Ti alloy (Choi *et al.*, 2008, 2009). By constructing a multilayered hydrogel on the Ti alloy surface, the surface may become much more biocompatible and, moreover, the hydrogel layer could have a functional stage for the sustained release of biologically active molecules.

The surface modification process is described in Fig. 12.10. The Ti alloy substrates were treated with a mixture of concentrated H_2SO_4 and 30% H_2O_2 to generate hydroxy groups at the surface. A monolayer of octadecylsilane (ODS) was prepared on the Ti alloy substrate by immersion in octadecyltriethoxysilane solution. The ODS-treated Ti alloy substrates were coated with an aqueous solution of photoreactive PVA with phenylazide groups as photoreactive groups. The phenylazide groups were activated by photoirradiation to generate radicals, which attack the alkyl group and form a new covalent bonding. Thus, a PVA-modified Ti alloy substrate can be

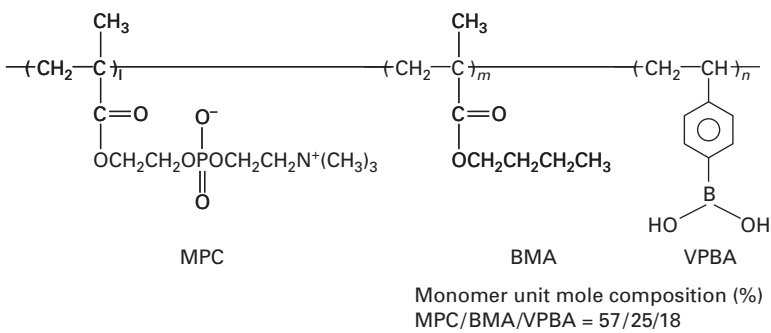

12.9 Chemical structure of the MPC polymer for preparing multilayered hydrogel (PMBV).

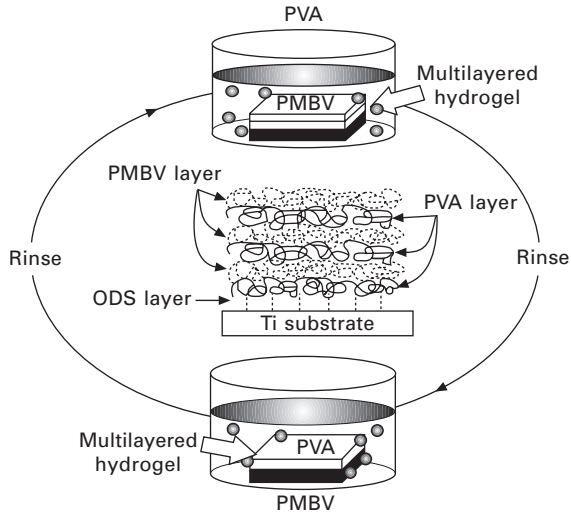

12.10 Surface modification process by polymer integration using layer-by-layer method.

obtained by this procedure. PMBV aqueous solutions were applied after the PVA modified the Ti alloy substrate. The multilayer construction was created by alternately dipping the Ti alloy substrates with bonded photoreactive PVA into the PMBV and PVA solutions for 10 min each, and subsequently rinsing them with distilled water for 1 min. Six layers (3-bilayers), terminating with a layer of PMBV, were obtained by the LbL method.

The preparation of the PMBV/PVA hydrogel layers on the Ti alloy substrates via the LbL method resulted in a change in the weight of the substrates. Weight measurements showed an increase in the multilayered hydrogel on the Ti alloy surface as a function of an even number of coating layers. The cumulative weight of PMBV/PVA after the formation of the 3-bilayers was 2.0 ± 0.2 mg and the water content in the PMBV/PVA multilayer was about 450 %.

The assembly process was followed by IR spectrum measurement (Fig. 12.11). As the specific surfaces changed gradually from Ti alloy to PMBV, each spectrum showed the particular peaks associated with the functional groups of that surface. The silanized Ti alloy surface exhibited the band corresponding to ≡Ti–O–Si≡ in the region of 970–1000 cm^{-1}. And after bonding the AWP layer to the silanized Ti surface, the spectrum exhibited characteristic vibration at 1720 cm^{-1} and 2960 cm^{-1}, corresponding to the carbonyl group and an aromatic ring, respectively. However, no azide peak was observed around 2200 cm^{-1}. After complexation with PMBV, the phosphate group in the MPC unit could be seen at 1080 and 970 cm^{-1}, and peaks at 1720 and 1460 cm^{-1} corresponding to =C=O carbonyl stretching and

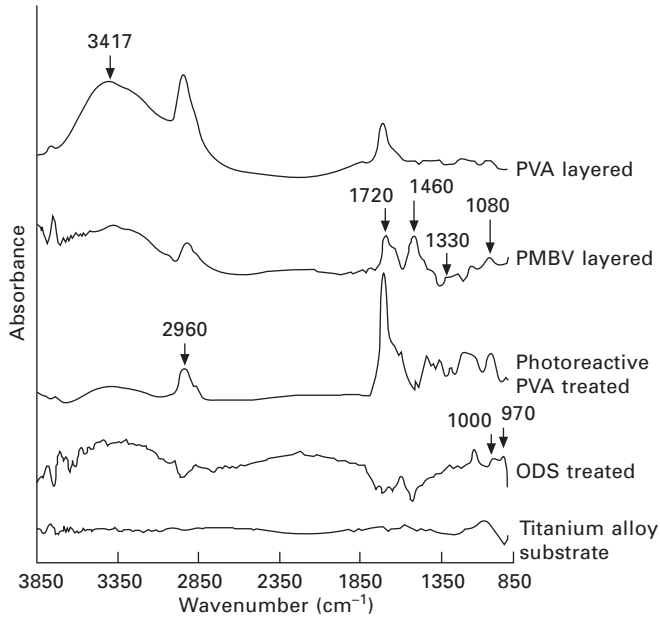

12.11 IR spectra of the surface during polymer integration.

$-CH_2-$ bending were also observed, respectively. The appearance of peaks at 1330 cm^{-1} is attributed to the B–O stretching modes in phenylboronic acid. The peak around 3417 cm^{-1} is associated with the –OH bands in PVA. The thickness of the PMBV/PVA hydrogel increased exponentially as a function of the number n of deposited layers. The final thicknesses of the PMBV/PVA multilayers were determined as 6–8 μm.

With the PMBV/PVA systems, the tendency is for an exponential increase in the thickness of the multilayered hydrogel with the number of layers during the build-up process. This phenomenon may be attributed to the diffusion behavior of the outermost polymer layers, PMBV and PVA. Moreover, the thickness and weight of the multilayered hydrogels of PMBV/PVA depends on the polymer concentration. It means that both PVA and PMBV, which contain the hydrophilic phosphorylcholine group, attract water molecules. It is thought that the contact angle data also support the hydrophilic property of these polymers.

12.4.3 Surface characterizations of the phospholipid polymer layer on Ti alloy

The contact angle depends on the nature of the surface wettability, and measurements were performed to confirm the alternate deposition of PMBV and PVA. Polymer hydrogel layers made by LbL methods on Ti alloy

surfaces are expected to alternately change surface wettability. The static water contact angle for PVA is approximately 60°, and that for PMBV is 80°. The subsequent adsorption of PMBV made the surface slightly hydrophobic compared to the PVA surface in a dry condition. However, in the case of the captive bubble method, while PVA layers are approximately 40°, most of the PMBV layers are 20° and all of the 6th layers are 0°, regardless of PMBV concentrations. This means that the outermost layers of multilayered hydrogel are totally covered with PMBV. The alternation of the static contact angle and captive bubble contact angle strongly indicates that the hydrogel layers were constructed regularly. XPS is a useful tool for obtaining qualitative and quantitative information about the different elements at a substrate surface. XPS was used to monitor each deposition step as it can provide information about the surface phosphorus/carbon ratio (P/C ratio) on the Ti alloy samples coated with different deposition layers; the results are presented in Fig. 12.12. As the deposition cycle was repeated, the P/C ratio could discriminate between the presence and absence of a PMBV layer; that is, PMBV-terminated layers (the even number) exhibited four times larger P/C values.

Both contact angle measurements revealed that the outermost layer was exchanged alternately. In particular, since the captive bubble method indicates the wettability of the surface in a wet condition, interesting information could be obtained by comparing the results from the sessile drop method. When the outermost layer was PMBV, the contact angle in a dry condition increased over that of PVA. This means that the surface of the PMBV layer was covered with a hydrophobic group; that is, phenylboronic acid and the butyl group of BMA. However, the contact angle of PMBV in a wet condition was

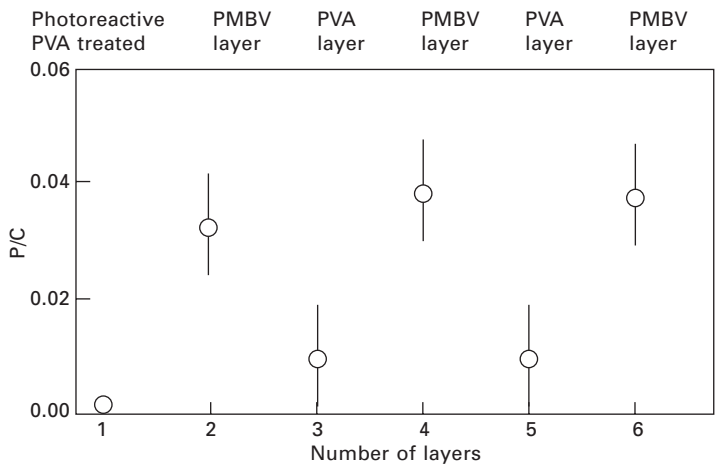

12.12 Surface density of MPC polymer during molecular integration.

very different to that in a dry condition. This is due to the rapid adsorption of the water molecules around the hydrophilic phosphorylcholine groups in the PMBV. As a result of the change of layer surface from PVA to PMBV, the P/C ratio in XPS increased because of the influence of PMBV, which contains a phosphorylcholine group.

12.4.4 Biological aspect of the phospholipid polymer layer on Ti alloy

The morphological aspects of L929 cells grown on the differently loaded multilayered hydrogel coatings were evaluated using SEM (Fig. 12.13). On a plain Ti alloy substrate and on one modified with photoreactive PVA, the adhesion and proliferation of L929 cells was observed during a one-day culture, as usual. However, apparent differences in cell morphology were found on PMBV and PVA as compared to that on the titanium alloy substrate and photoreactive PVA-modified substrate. The number of L929 cells that adhered to the PMBV and PVA surfaces was significantly lower than the number on the Ti alloy substrate and photoreactive PVA. In addition, the L929 cells did not preserve their normal spindle-like shape, but exhibited circular shapes.

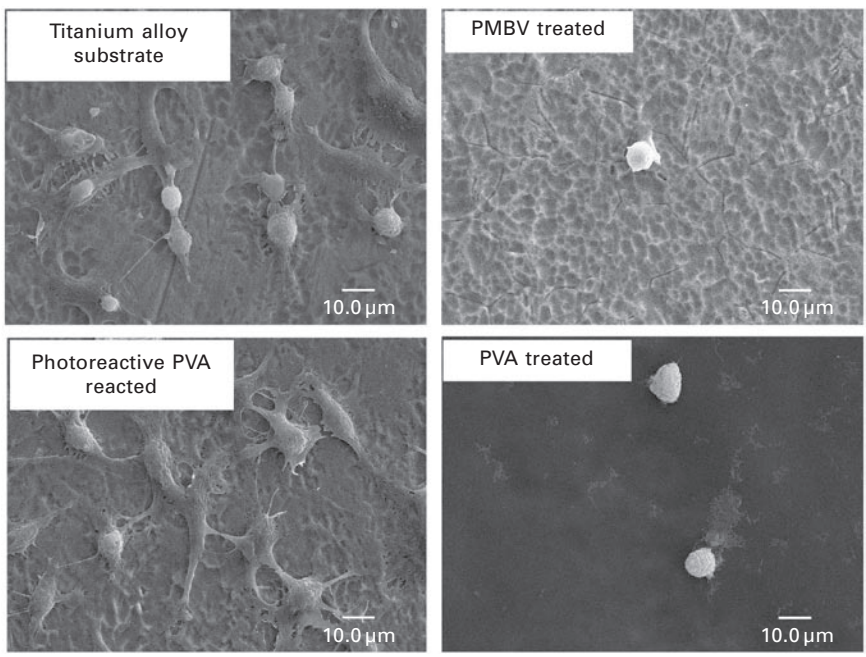

12.13 Platelet adhesion on Ti alloy substrate and one modified by polymer integration.

Cellular behavior is an important factor in interpreting the biocompatibility of biomaterial. The cell morphology images revealed that Ti alloy and photoreactive PVA surfaces permitted the adhesion, spreading, and migration of L929 cells to a degree that PVA and PMBV surfaces did not. The adhesion of cells to surfaces is dependent on the adsorption of highly adhesive proteins such as fibronetin and vitronectin, which link cells to the biomaterial surface. It is generally accepted that hydrophilic polymers such as poly(ethylene oxide)-based polymers and phosphorylcholine group functioned polymers do not allow protein adsorption at their surface (Iwasaki, 1997). Thus, they can reduce the adhesion of cells, including fibroblasts, platelets, and macrophages. The MPC polymer-hybridized Ti alloy substrates and multilayered hydrogels offer the potential for preparing blood-contacting materials via the incorporation of the outmost layer, PMBV, which inhibits the adsorption of proteins and the adhesion of cells.

12.4.5 Functionalization of the phospholipid polymer layer as a drug reservoir on Ti alloy

Much attention is currently being paid to drug delivery systems that can regulate the rate of drug release and release pattern over time. In the case of cardiovascular stents, drug release can help the healing process of the blood vessel after embedding the stent. A polymer coating may be suitable for maintaining and controlling the release of drugs with various properties. Therefore, the drug-releasing property of multilayered hydrogels formed on the Ti alloy substrate was examined.

One of the anticancer drugs, paclitaxel (PTX), was used as a model drug. The solubility of PTX in water is quite low, even if it contains PVA, but it can be dissolved in PMBV aqueous solution. From this, a multilayered hydrogel containing PTX could be made. To determine the time when PTX starts to be released from different locations, three samples, with PTX at different locations in the PMBV layer, were built up and the release experiments were performed. The results of PTX release are illustrated in Fig. 12.14, which shows cumulative concentration vs. time. The PTX in the top layer (upper side) started releasing after 10 min, the middle layer started releasing after 30 min, and the PTX at the bottom of the multilayer started releasing after 180 min. It was confirmed that the location of the layer with PTX caused the differences in the releasing profile.

The basic mechanism for the construction of multilayered hydrogels is the selective reactions between the boronic acid moiety in PMBV and the hydroxyl groups in PVA. To initiate the LbL process, a silane coupling reaction was used to introduce an alkyl group onto the Ti alloy substrates. Thus, photoreactive PVA could bind covalently to the substrate surface by photoirradiation. Subsequently, the PMBV/PVA hydrogel system was

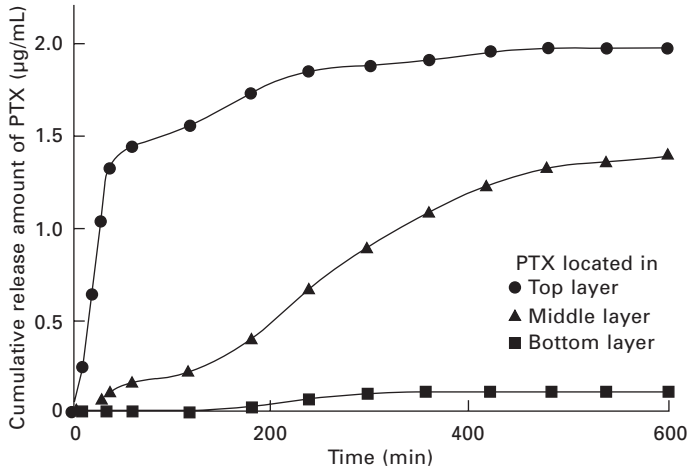

12.14 Release pattern of PTX from multilayered hydrogel prepared on Ti alloy substrate.

fabricated. The process was followed by contact angle measurements and XPS analyses; these results indicated that the surface properties changed alternately, reflecting the nature of the polymer on the outer surface. The thickness of the hydrogel increased with the number of layers. These data suggested that PMBV/PVA successfully covered the Ti alloy substrate surface. Furthermore, PMBV, the outmost layer, was found to inhibit cell attachment. The hydrogel layer can also entrap bioactive reagents effectively and control their diffusivity.

It was concluded that Ti alloy substrates with multilayered polymer hydrogels could be useful in applications such implantable devices and local drug delivery systems.

12.5 Future trends

Metal biomaterials are needed to make not only implantable medical devices but also bio-related devices including nano-needles, nanoparticles, nanowire, and so on. The characteristics of the metal biomaterials are their essential mechanical properties and processability. However, their surface biocompatibility is not good enough and should be improved. Conventional modification is performed using other materials, such as surface coatings with bioceramics and biocompatible polymers. The polymers have a good potential to provide surface functionality on metal biomaterials. Therefore, we should pay much more attention to metal/polymer hybrid-type materials. From this point of view, regulation between the metal and polymer layer will be important in obtaining a stable and high-performance metal/polymer hybrid.

This chapter has described several examples of modifying a metal surface using a phospholipid polymer. The surface modification occurred only for a very thin layer and it did not affect the original mechanical properties of the metal biomaterials. Other functions based on the hydrogel-like structure, such as the controlled release of bioactive molecules, super-hydrophilicity, and excellent lubrication properties, could also be added. Recent progress in bioscience provides us with many biomolecules with high bioactive functions. When tissue-activating proteins or inducing proteins can be incorporated into the polymer layer formed on the metal biomaterials, these proteins can be slowly released from the polymer layer. Thus, new tissue formation may take place and finally metal biomaterials may be tightly adhered to tissue.

Metal-on-metal bearings have been used mainly because of their very low long-term clinical wear rate. In a survey of the orthopedic field, orthopedic researchers generally agreed that metal-on-metal bearings wear clinically at a rate of 1–5 mm^3/year, which is 10–100 times lower than the typical wear rate for a conventional metal-on-ultrahigh molecular weight polyethylene (UHMWPE) bearing couple. However, even in metal-on-metal bearings, aseptic loosening induced by wear particles and metallosis remains a serious issue in revision surgeries. In addition to metallosis, electrochemical corrosion and carcinogenesis occurring due to the dissemination of wear particles to other parts of the body have been reported. The size of wear particles in metal-on-metal bearings is between 6 nm and 5 mm. The nanometer-sized metallic wear debris is more easily digested by cells, bound into proteins, and/or dissolved into body fluids than is the larger UHMWPE wear debris. Several improvements to the bearing materials and surface modifications of the metal have been attempted in order to reduce such wear particles. Surface modifications of the metal surface with hydrophilic polymers may be suitable for reducing wear due to the formation of a thin water layer at the interface between the metal bearings. Kyomoto *et al.* (2009) performed fundamental experiments to prepare a highly lubricious metal bearing material in which the biocompatible MPC polymer was grafted onto the surface of a Co–Cr–Mo alloy. The excellent functions of MPC polymer-modified Co–Cr–Mo alloy might avoid the activation of cell systems by the wear particles, thus entirely preventing aseptic loosening and metallosis. In view of its greatly superior lubricious and biological advantages, the metal/polymer hybrid is widely expected to be the next-generation bearing material for artificial hip joints. This will be beneficial in preventing many of the problems observed at the interface between medical devices and tissues.

12.6 Summary

The fabrication of well-controlled polymer layers on a metal substrate has been described. First, the modification of metal surfaces with phospholipid

derivatives was described. The self-assembly properties of phospholipid analogues were applied to obtain a protein-adsorption-resistant surface. The basic chemistry used for the immobilization of the phospholipid analogues was a silane-coupling reaction with a hydroxy group generated on the metal. Following this, the construction of an artificial cell membrane surface was described. A phospholipid polymer platform was constructed on the metal substrate and then functionalized. The phospholipid polymer chains were grafted onto the surface of the Ti by chemical reactions. The surface density and thickness of the phospholipid polymer could be controlled. Another method for modification that was described was the construction of a multilayered polymer on a Ti alloy substrate via layer-by-layer self-assembly deposition. Phospholipid polymers bearing a phenylboronic acid moiety (PMBV) and poly(vinyl alcohol) (PVA) were used as polymer components. The hydrogel layer growth on the Ti surface was initialized by the deposition of one layer of PVA onto the Ti alloy substrate. The multilayered hydrogel was built up by alternating the deposition of the PMBV and PVA. The phospholipid polymer platform prepared on the Ti alloy substrate reduced the adhesion and morphology of cells compared with those on an untreated Ti alloy substrate. Moreover, the multilayered hydrogel could play an excellent role in regulating the drug release profile. Therefore, a new controlled-release system from the metal surface may be achieved. Thus, it could be concluded that the formation of an artificial cell membrane structure by the phospholipid polymer was effective in improving the biocompatibility of Ti alloy-based medical devices.

12.7 Acknowledgement

The authors express their appreciation to Dr Madoka Takai, Dr Tomohiro Konno, Dr Ryosuke Matsuno, and Dr Masayuki Kyomoto, The University of Tokyo, for helping in the preparation of the manuscript. Also, the authors would like to give special thanks to Dr Yasuhiko Iwasaki, Kansai University for providing figures and photos for the manuscript.

12.8 References

Brynda E, Houska M (1996), 'Interactions of proteins with polyelectrolytes at solid/liquid interfaces: Sequential adsorption of albumin and heparin' *J Colloid Interface Sci*, 183, 18–25 DOI:10.1006/jcis.1996.0514

Choi J, Matsuno R, Konno T, Takai M, Ishihara, K (2008), 'Surface immobilization of biocompatible phospholipid polymer multilayered hydrogel on titanium alloy', *Colloid Surf, B:Biointerfaces*, 67, 216–223. DOI:10.1016/j.colsurfb.2008.08.025

Choi J, Konno T, Takai M, Ishihara, K (2009), 'Controlled drug release from multilayered phospholipid polymer hydrogel on titanium alloy surface', *Biomaterials*, 30, 5201–5208. DOI:10.1016/j.biomaterials.2009.06.003

Decher G (1997), 'Fuzzy nanoassemblies: Toward layered polymeric multicomposites', *Science*, 277, 1232–1237. DOI: 10.1126/science.277.5330.1232

Fadeev AY, McCarthy TJ (1999), 'A new route to covalently attached monolayers: Reaction of hydridosilanes with titanium and other metal surfaces', *J Am Chem Soc*, 121, 12184–12185 DOI: 10.1021/ja9931269

Gobeil F, Juneau C, Plante S (2002), 'Thrombus formation on guide wires during routine PTCA procedures: A scanning electron microscopic evaluation', *Can J Cardiol*, 18, 263–269.

Habibovic P, Barrère F, Blitterswijk CA, Groot K, Layrolle P (2002), 'Biomimetic hydroxyapatite coating on metal implants', *J Am Ceramic Soc*, 85, 517–522. DOI: 10.1111/j.1151-2916.2002.tb00126.x

Ishihara K, Ueda T, Nakabayashi N (1990), 'Preparation of phospholipid polymers and their properties as hydrogel membrane', *Polym J*, 22, 355–360. DOI: 10.1295/polymj.22.355

Ishihara K, Ziats NP, Tierney BP, Nakabayashi N, Anderson JM (1991), 'Protein adsorption from human plasma is reduced on phospholipid polymers', *J Biomed Mater Res*, 25, 1397–1407. DOI: 10.1002/jbm.820251107

Ishihara K, Oshida H, Endo Y, Ueda T, Watanabe A, Nakabayashi N (1992), 'Hemocompatibility of human whole blood on polymers with a phospholipid polar group and its mechanism', *J Biomed Mater Res*, 26, 1543–1552. DOI: 10.1002/jbm.820261202

Ishihara K (2000), 'New polymeric biomaterials – phospholipid polymers with a biocompatible surface', *Front Med Biol Eng*, 10, 83–95. DOI: 10.1163/15685570052061946

Iwasaki Y, Mikami A, Yui N, Ishihara K, Nakabayashi N (1997), 'Reduction of surface-induced platelet activation on phospholipid polymer', *J Biomed Mater Res*, 36, 508–515. DOI: 10.1002/(SICI)1097-4636(19970915)36:4<508::AID-JBM8>3.0.CO;2-I

Iwasaki Y, Saito N (2003), 'Immobilization of phosphorylcholine polymers to Ti-supported vinyldimethylsilyl monolayers and reduction of albumin adsorption', *Colloid Surf, B:Biointerfaces*, 32, 77–84. DOI: 10.1016/S0927-7765(03)00147-4

Iwasaki Y, Ishihara K (2005), 'Phosphorylcholine-containing polymers for biomedical applications', *Anal Bioanal Chem*, 381, 534–546. DOI: 10.1007/s00216-004-2805-9

Konno T, Ishihara K (2007), 'Temporal and spatially controllable cell encapsulation using a water-soluble phospholipid polymer with phenylboronic acid moiety', *Biomaterials*, 28, 1770–1777. DOI: 10.1016/j.biomaterials.2006.12.017

Kyomoto M, Moro T, Iwasaki Y, Miyaji F, Kawaguchi H, Takatori Y, Nakamura K, Ishihara K (2009), 'Superlubricious surface mimicking articular cartilage by grafting poly(2-methacryloyloxyethyl phosphorylcholine) on orthopaedic metal bearings', *J Biomed Mater Res*, 91A 730–741.

Lee JH, Kopeckova P, Kopecheck J, Andrade JD (1990), 'Surface properties of copolymers of alkyl methacrylates with methoxy (polyethylene oxide) methacrylates and their application as protein-resistant coatings', *Biomaterials*, 11, 455–464. DOI: 10.1016/0142-9612(90)90058-X

Lewis AL, Cumming ZL, Goreish HH, Kirkwood LC, Tolhurst LA, Stratford PW (2001), 'Crosslinkable coatings from phosphorylcholine-based polymers', *Biomaterials*, 22, 99–111. DOI: 10.1016/S0142-9612(00)00083-1

Myers GJ, Johnstone DR, Swyer WJ, McTeer S, Maxwell SL, Squires C, Ditmore SN, Power CV, Mitchell LB, Ditmore JE, Aniuk LD, Hirsch GM, Buth KJ (2003), 'Evaluation of mimesys phosphorylcholine (PC)-coated oxygenators during cardiopulmonary bypass in adults', *J Extra Corpor Technol* 2003, 35, 6–12.

Orban J, Faucher KM, Diuhy RA, Chaikof EL (2000), 'Cytomimetic biomaterials. 4. *In-situ* photopolymerization of phospholipids on an alkylated surface', *Macromolecules*, 33, 4205–4212. DOI: 10.1021/ma9915780

Ren K, Ji J, Shen J (2006), 'Construction and enzymatic degradation of multilayered poly-l-lysine/DNA films', *Biomaterials*, 27, 1152–1159. DOI: 10.1016/j.biomaterials.2005.07.021

Sigal GB, Mrksics M, Whitesides GM (1998), 'Effect of surface wettability on the adsorption of proteins and detergents', *J Am Chem Soc*, 120, 3464–3473. DOI: 10.1021/ja970819l

Snyder AT, Tsukui H, Kihara S, Akimoto T, Litwak KN, Yamazaki K, Kameneva MV, Yamazaki K, Wagner WR (2007), 'Preclinical biocompatibility assessment of the EVAHEART ventricular assist device: Coating comparison and platelet activation', *J Biomed Mater Res*, 81A, 85–92. DOI: 10.1002/jbm.a.31006

Sukhishvili SA, Granick S (2002), 'Layered, erasable polymer multilayers formed by hydrogen-bonded sequential self-assembly', *Macromolecules*, 35, 301–310. DOI: 10.1021/ma011346c

Ueda T, Oshida H, Kurita K, Ishihara K, Nakabayashi N (1992), 'Preparation of 2-methacryloyloxyethyl phosphorylcholine copolymers with alkyl methacrylate and their blood compatibility', *Polym J*, 24, 1259–1269 Doi:10.1295/polymj.24.1259

Whelan DM, van der Giessen WJ, Krabbendam SC, van Vliet EA, Verdouw PD, Serruys PW, van Beusekom HM (2000), 'Biocompatibility of phosphorylcholine coated stents in normal porcine coronary arteries', *Heart*, 83, 338–345. DOI:10.1136/heart.83.3.338

Yan J, Springsteen G, Deeter S, Wang B (2004), 'The relationship among pK_a, pH, and binding constants in the interactions between boronic acids and diols – it is not as simple as it appears', *Tetrahedron*, 60, 11205–11209. DOI :10.1016/j.tet.2004.08.051

13

Sterilisation and cleaning of metallic biomaterials

S. LEROUGE, Ecole de Technologie Supérieure, Canada

Abstract: Sterilisation should be considered at the earliest stages of design of any new medical device intended for use in contact with sterile tissues, mucous or breached skin, to ensure that the final product can be sterilised effectively and safely. This chapter defines sterilisation concepts and challenges. It then presents the main sterilisation techniques available, with their advantages and limitations. Although this book focuses on metallic implants, which are little prone to damage by sterilisation processes, polymer alteration by the various sterilisation techniques are discussed since nowadays most devices include polymeric compounds or packaging which may be sensitive to high temperatures and radiation.

Key words: sterilisation, ethylene oxide, steam, radiation sterilisation, Sterrad®, safety, efficiency, security assurance level (SAL), cleaning.

13.1 Introduction

Sterilisation is an important step in manufacturing implants or biomedical devices to prevent the spread of infection. Failures in adequate sterilisation of medical devices (MDs) result in significant institutional costs related to patient nosocomial infections and mortality/morbidity concerns. It is important to consider sterilisation issues and requirements at the earliest stages of development of any new medical devices, to ensure that the final product can be sterilised effectively and safely, with the most cost-effective and environment-friendly procedures. Except for the rare instances when sterilisation can take place where the sterile products are to be used, MDs must be packaged to preserve their sterility during storage, handling, and transport. The majority of sterile MDs are terminally sterilised – that is, they are sterilised already packaged. If reusable, the device must sustain several cycles of cleaning and sterilisation in clinical settings.

In the next section, the main concepts of sterilisation will be defined, such as sterilisation efficiency and safety, which are the two most important aspects to consider when choosing a biomaterial, designing the device and choosing the packaging and sterilisation technique. When deciding on a sterilisation method, one of the first considerations should be product compatibility. All type of materials can be degraded to some extent by one or more sterilisation processes. Sterilisation can also leave toxic products that may impair device biocompatibility. For these reasons, functional and

biocompatibility testing for US Food and Drug Administration (FDA) or European Community (EC) approval must be performed on the final packaged and sterilised products.

An overview of the main sterilisation processes and more recent alternatives will be presented in Sections 13.3 and 13.4, with emphasis on their main advantages and limitations. The most widely used MD sterilisation technologies are gamma and electron beam irradiation, hot steam and ethylene oxide (EO). Alternatives include low-temperature hydrogen peroxide gas plasma (LTHPGP), vapour-phase hydrogen peroxide, ozone, liquid peracetic acid, X-rays and chlorine dioxide. Although this book focuses on metallic implants, which are resistant to heat and are little prone to damage by sterilisation processes, it should be kept in mind that many metallic devices nowadays include small polymeric parts (adhesives, interconnectors, liners, protective layers and so on) and are packaged with materials that may be sensitive to high temperatures and radiation.

In Section 13.5, prion and endotoxin deactivation will be briefly discussed, as this represents an important challenge due to their high resistance to sterilisation techniques. Cleaning methods will be presented in Section 13.6. Finally, Section 13.7 will briefly present the many regulations and standards related to sterilisation and will propose other useful sources of information.

13.2 Concepts and definitions

13.2.1 Sterilisation efficiency

Sterilisation efficiency is defined as the ability to remove or destroy all forms of microbial life, including viruses, bacteria and fungi, in the vegetative state or as spores (Crow, 1993). Since absolute sterility cannot be verified, the statistical definition of sterility is used in practice, by using the Security Assurance Level (SAL), defined as 'the probability of a single viable micro-organism occurring in or on a product after sterilisation.' The worldwide accepted definition of sterility of medical devices is defined as the chance of finding a viable organism in or on a medical device to be, at most, 1 in 1 000 000 or a SAL of, at most, 10^{-6} (Block, 2000).

13.2.2 Sterilisation versus disinfection

It is important to distinguish sterilisation from disinfection, which does not ensure the same security level and does not necessarily inactivate all forms of micro-organisms – bacterial spores for instance. The choice between sterilisation and disinfection must be done according to the risk of spreading infection. Thus, according to the Spaulding Classification (1972), sterilisation

is required for all critical medical devices, i.e. those intended to be used in contact with sterile tissues, and is *recommended* for semi-critical devices, e.g. those intended to be in contact with mucous tissues or breached tissues, such as endoscopes. A high level of disinfection is, however, acceptable for the latter (Spaulding, 1972).

Sterilisation should not be confused with cleaning, which is defined as the removal of all foreign material (dust, soil and organic debris). Yet cleaning devices is an important step before sterilisation, especially in healthcare centres, since it has been demonstrated that it is more difficult to sterilise devices where micro-organisms hide behind proteineous or greasy matter.

13.2.3 Sterilisation validation

Sterilisation validation studies must document that the product attains the required SAL after exposure to the proposed process. In the industry, sterilisation validation is evaluated by determining the typical bioburden (type and number of viable microorganisms on the implant just prior to sterilisation) after the manufacturing process and using fractional-run sterilisation studies to determine the rate of killing. In a fractional sterilisation run, product samples (in packages) are exposed to various fractions of the desired sterilisation process or dose. The number of survival microorganisms is reported graphically on a semi-logarithmic scale to extrapolate the exposure time or dose required to achieve a 10^{-6} SAL (Fig. 13.1). A security factor is then generally applied.

As seen in Fig. 13.1, microorganism inactivation does not follow a linear curve but generally a semi-logarithmic function. At a certain temperature

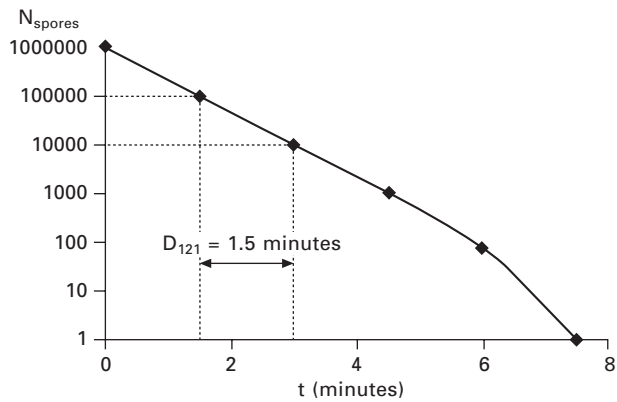

13.1 Typical deactivation curve of bacterial spores during steam sterilisation, which allows the calculation of the D-value (D_{121}) as the time required to decrease the number of spores by 90% at 121 °C.

(here 121°C), the same exposure time is required to decrease the number of microorganisms from 10^6 to 10^5 as from 10^2 to 10^1. This exposure time (or dose, in the case of radiation sterilisation) required to kill 90% of the microorganism burden is called the D-value (the decimal reduction time) and is very useful in calculating the exposure time required to achieve SAL from a known bioburden. Such a parameter does however not exist for every sterilisation process.

Validation studies must be done on product samples prepared under actual manufacturing conditions and exposed to the sterilisation process under its final packaging configuration. Device geometry (small lumen or cavities) can be of concern when sterilisation agents have limited penetration. More details about sterilisation process validation can be found in the specific ISO documents (ISO11134, 1994; ISO11135, 1994; ISO11137, 1993)

It is important to differentiate between industrial sterilisation and resterilisation of reusable devices achieved in healthcare centres. In the latter cases, the bioburden cannot be easily determined since it can be influenced by several factors and a more drastic sterilisation called 'overcharge' sterilisation is therefore generally used, considering an initial microbial charge of 10^6 per device. Moreover, cleanliness is another important parameter for reusable devices, and this must be taken into account when designing the device, to avoid unreachable cavities.

Even once the process has been validated, its efficiency must be verified on each sterilisation load. With an increasing number of sterilisation processes, product release can be based on dosimetric release, parametric control, or process control. As discussed later, monitoring the delivered radiation dose is sufficient to allow product release after gamma sterilisation. In contrast, EO process control is more complex since several parameters such as EO concentration, humidity rate, time, temperature, and vacuum/pressure influence process efficiency. In many cases, monitoring sterilisation efficiency requires biological indicators (BI) containing bacterial spores. While conventional BI requires 24 to 48 h spore incubation before reading results and releasing sterilised products, a new generation of BI, using spore-associated enzymes, is now able to detect sterilisation failure in only a few hours (McCormick *et al.*, 2003; Rutala *et al.*, 1996; Leventon, 2002; Rutala and Weber, 2001).

Finally, an expiration date must be labelled on sterilised products given that packaging materials cannot indefinitely prevent recontamination with micro-organisms. The time allowed between sterilisation and clinical use mostly depends on the type of packaging material used. For costly single-use devices such as implants, manufacturers should take this matter into account to avoid withdrawal of unused and expired sterilised products from the market.

13.2.4 Sterilisation safety

Safety of sterilisation is a broad term including concerns for patients, sterilisation personnel and the environment. The first concern with the choice of a sterilisation process is the demonstration that the product is compatible with the sterilisation process; the integrity of the product and of the packaging which maintains its sterility after the process must be demonstrated since most sterilisation conditions can degrade materials. This could lead to a significant loss of functionality or biocompatibility of the device. For instance, toxic residues or by-products may be formed on devices during sterilisation. It is then essential to ensure that patient exposure to these residuals stays below safe limits. Metallic biomaterials are generally resistant to most processes but packaging materials are often polymers and most new devices now incorporate also small amounts of polymeric compounds, which are more sensitive to sterilisation conditions. Moreover, metallic reusable devices can also be damaged by multiple sterilisation exposures such as corrosion of carbon steels after steam sterilisation. These issues will be specifically addressed when discussing each sterilisation process. One should also be aware of the possible direct harm of the sterilisation process towards manufacturing personnel and the environment, as will be discussed in the ethylene oxide sterilisation section. National or international regulations may also lead to progressive proscription of a sterilisation method with time, as has already been done for chlorofluorocarbon gas (CFC), an ozone-layer depletion agent commonly used to stabilise ethylene oxide, now forbidden in EO sterilisers in most countries (Jorkasky, 1993).

13.3 Principal sterilisation methods for biomaterials; advantages and limitations

13.3.1 Overview of sterilisation processes

Gamma radiation and ethylene oxide are still the main industrial sterilisation processes of medical devices but several other processes, such as moist heat (steam autoclave), dry heat, electron beam radiation and, more recently, low-temperature hydrogen peroxide gas plasma, ozone or peracetic acid are available and are increasingly used in healthcare facilities. Process principles and inactivation mechanisms, as well as main advantages and disadvantages, of each of these processes will be described in the following section. Main parameters, as well as advantages and disadvantages are reviewed in Table 13.1.

13.3.2 Radiation sterilisation

Radiation sterilisation is still the main industrial sterilisation process for single-use medical devices. Sterilisation processes using radiation include

Table 13.1 Parameters, advantages and limits of the main sterilisation processes

Technique	Main parameters	Advantages	Limits
Steam sterilisation (autoclave)	121 °C, 5–20 min High humidity level	Simple, safe, rapid and efficient Good penetrability Easy to monitor No toxic residues Can sterilise liquids Low cost	High temperature and moisture Incompatible with many thermosensitive polymers. Metals may corrode Requires breathable packaging
	Options:		
	Flash autoclave 134 °C, 3–6 min in vacuum with steam pulses	Rapid	Incompatible to many materials due to very high temperature and moisture
	Low temperature steam (110–115 °C, 35–40 min)	Allows sterilisation of more heat sensitive materials	Longer exposure Efficiency subject to some controversy
Dry heat	160–170 °C 1–2 hours	Generally avoids metal corrosion	Longer exposure than steam
Gamma radiations	10–40 kGy (most common 25 kGy) Ambient temperature A few hours	Excellent penetrability, efficiency and reliability Dosimetric release Large product volumes Cost effective Compatible with many materials No residues Environmentally safe, except for the disposal of radioactive waste	Isotope containment requires costly facilities for safety reasons Only available in a few industrial centres Some polymer damage, increasing with increased doses Limited to single industrial sterilisation
Electron-beam	11–40 kGy	Very rapid (seconds/minutes) Compatible with more materials than gamma rays	Lower penetrability than gamma rays Less penetration than gamma
Ethylene oxide (EO)	25–65 °C (generally 55 °C) High humidity EO: 400–1500 mg/L 2–4 hours + aeration	Compatible with most materials Efficiency, relatively good penetrability	Long cycle and safety risks EO toxicity and mutagenicity: Safety risks for sterilisation personnel Toxic EO residues and reaction products in polymers: requires aeration EO may be banned by regulations Difficult to monitor

gamma rays, electron-beam process, and, more recently, X-rays. Gamma rays from a Cobalt (Co) or Cesium (Cs) isotope source are by far the most popular and widespread agent (Block, 2000; Booth, 2001).

Gamma radiation

Gamma rays have an energy of about 1.2 MeV and are highly penetrating, thus allowing sterilisation of large amounts of densely packaged materials but requiring highly specialised facilities to protect workers from radiation. Figure 13.2 presents a typical industrial ^{60}Co irradiator, where the radioisotope is contained in sealed 'pencils' around which medical products are moved. Gamma radiation requires bulky shielding for the safety of the operators; it also requires storage of the radioisotope, which continuously emits gamma rays. A water-filled pool is therefore used to immerse the source when personnel require to enter the radiation cell. For safety reason, gamma ray sterilisation cannot be performed in clinical facilities and takes place only in a few industrial centres.

Gamma rays cause ionisation of key cellular components, especially nucleic acids, which results in the death of micro-organisms (Hutchinson, 1961). DNA is also altered by oxidoreduction reactions due to water radiolysis into H^+ and OH^- radicals under ionising radiations. These radiations are highly effective in killing micro-organisms, but they do not have sufficient energy to impart radioactivity to the sterilised material

Gamma sterilisation is performed at ambient temperature and allows sterilisation of temperature-sensitive material. The high penetrability of gamma rays permits large sterilisation loads and reliability, even in complex geometries and densely packaged materials. Other benefits include precise dosing, rapid processing, uniform dose distribution, and FDA dosimetric release. This last point means that control of the dose of radiation delivered to the product (by dosimeters placed in containers, read after the process) is sufficient to ensure efficiency. It allows elimination of sterility tests using BI and permits immediate availability of product after processing, both of these allowing cost savings. The most commonly validated dose used to sterilise medical devices is 25 kGy (kilograys). While steam and EO sterilisation require packages that are permeable to the gases and vapours, radiation sterilisation is compatible with nonbreathable packaging. This allows for a wider selection of materials of choice for the package.

Gamma radiation is compatible with many materials, including all metallic alloys which are very stable to radiation. While all polymers are affected in some degree by ionising radiation, many have a natural tolerance for sterilising radiation doses of up to and beyond 50 kGy, with the notable exceptions of acetal, unstabilised polypropylene (PP) and polytetrafluoroethylene (PTFE or Teflon) (Fig. 13.3). Polymer irradiation can lead to molecular-chain

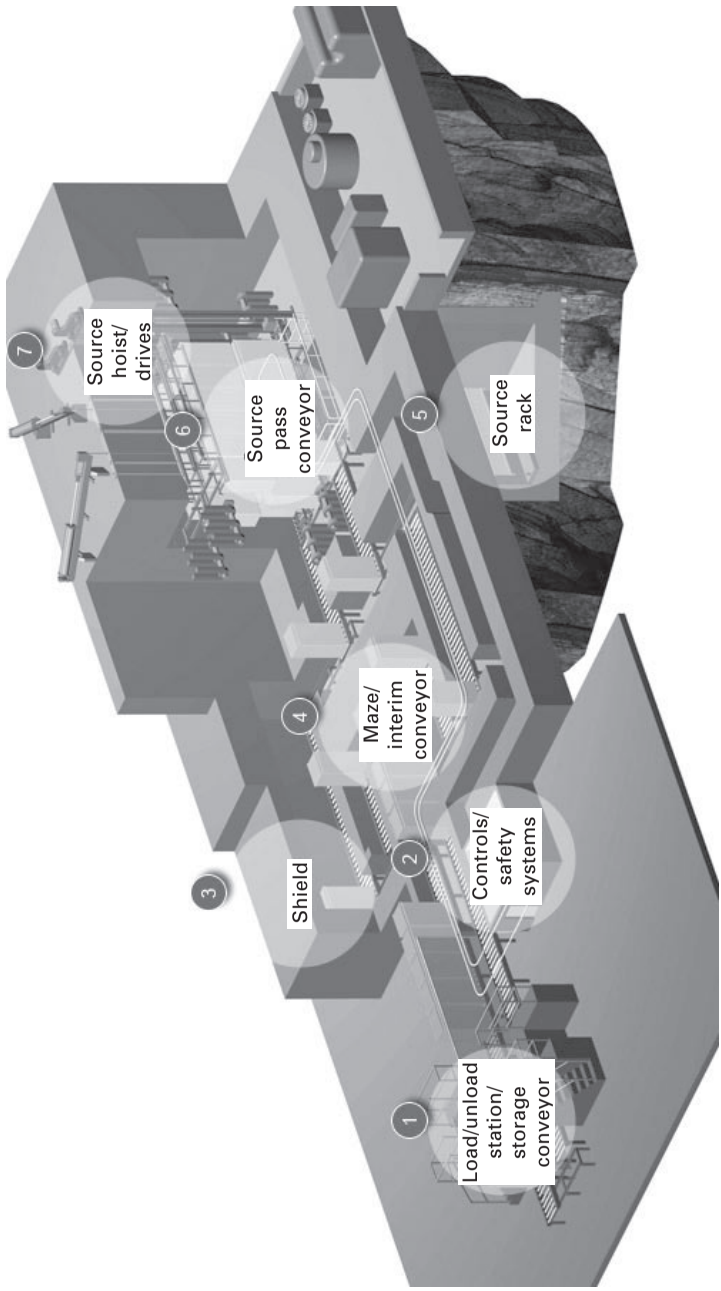

13.2 An industrial gamma sterilisation irradiator (©MDS Nordion; www.mdsnordion.com).

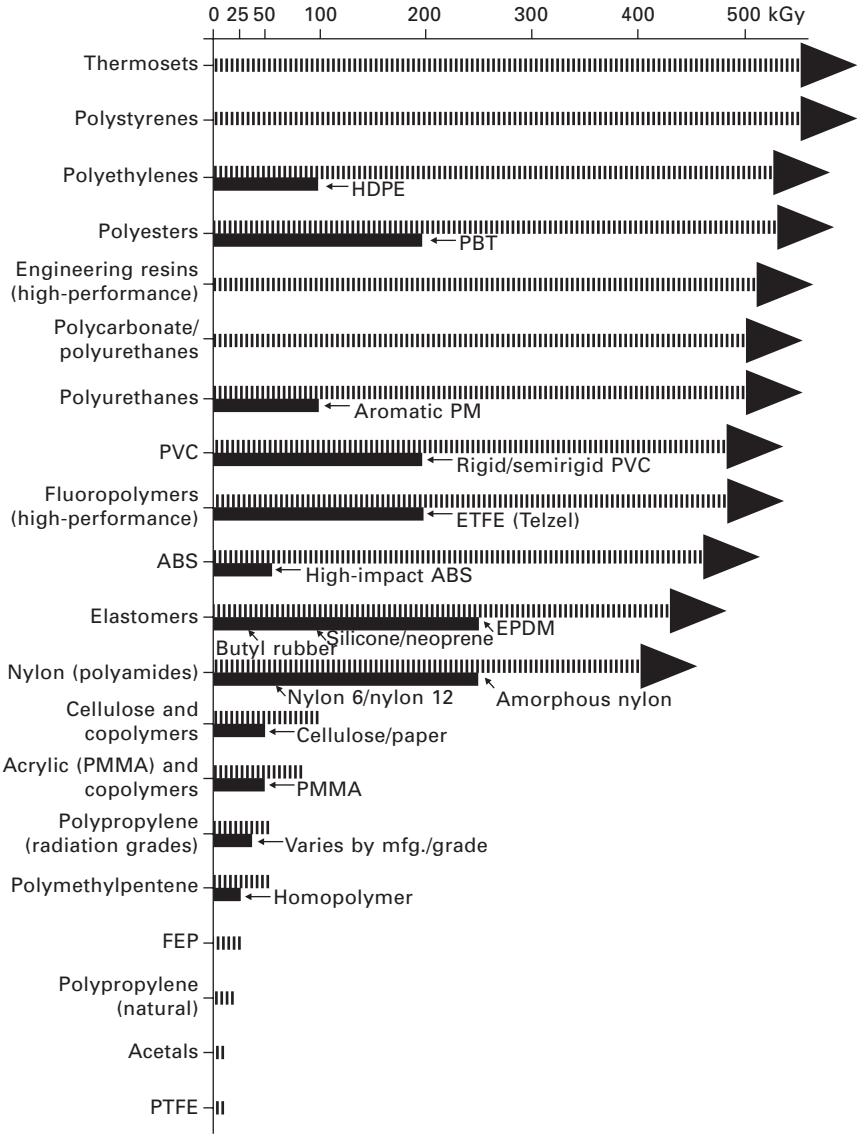

13.3 Relative stability of medical polymer families after radiation sterilisation, indicating the dose at which elongation decreases by 25%. Reprinted with permission from Medical Device and Diagnostic Industry 'Radiation Sterilization-Polymer Materials Selection for Radiation-sterilized Products,' Feb 2000. Copyright ©2000 Canon communications LLC.

crosslinking or scission, and possible alteration of mechanical properties (Bruck and Mueller, 1988; Collier *et al.*, 1996; Nair, 1995; Plester, 1970; Premnath *et al.*, 1996; Yagoubi *et al.*, 1997; Ries *et al.*, 1996). While polymers with cyclic groups such as polystyrene (PS) are highly resistant to radiation, others such as PTFE, nylon, acetal and cyanoacrylates have high radiation sensitivity (Kowalski and Morrissey, 2004; Morrissey and Ratner, 1998). More complete data on various polymers' compatibility with radiation can be found in other books (Massey, 2005; Hill, 1998; Rogers, 2005). Most bioresorbable polymers are also too sensitive to radiation to be sterilised by this process. It has also been shown than gamma radiation provides an environment conducive to the oxidation of UHMWPE used in load-bearing joints. Gamma sterilisation processes in inert environments (argon, nitrogen or vacuum) instead of ambient air are now commonly used to reduce oxidation and improve wear resistance of UHMWPE for such applications. Colour change is common in PVC, PC, PS, ABS and acrylics, before any physical change can be detected. Irradiated polymers (such as polyurethanes) can also be the source of strong odours. For more sensitive polymers, the first and most significant change in mechanical properties is the loss of elongation to break. This is due to molecular shortening by scission and is one reason to start with high molecular weight materials. It should be noted that gamma compatibility is less an issue than before since suppliers have introduced a variety of radiation-compatible materials that are now being specified by device manufacturers.

While ideal for the sterilisation of many single use devices, gamma radiation is not very appropriate for resterilisation of medical devices. Reasons are that this method cannot be performed in clinical settings and that repeated irradiation may cause important damage to polymers.

Electron-beam, X-ray and ultraviolet light radiation

Electron beam (e-beam) processing is commonly used for industrial MD sterilisation (Reich *et al.*, 2005; Block, 2000). Similar ionising mechanisms are involved to those encountered with gamma rays, but high energy electrons are here machine-generated using an accelerator. The electron energy is then higher than with gamma rays (between 4 and 6 MeV) (Massey, 2005; Woo and Sandford, 2002). While these installations must also be installed in a concrete room to contain electrons, they use an on–off technology (no radiation is emitted once the accelerator is turned off and personnel can then safely enter the sterilisation room) which decrease costs and give this process wider use than gamma sterilisation.

Due to the higher dose rate, less exposure time is needed and thereby potential degradation of polymers is reduced, making e-beam compatible with more materials than gamma radiation. It can degrade rubber and

polypropylene but these materials now come in grades that are e-beam compatible. The process can also be harmful to electronic components or batteries. The main limitations of electron beam processing are however the much lower penetration of electrons compared to either gamma or X-rays, and the shadowing effect, which make this method unsuitable for thick or densely package products, and more risky for devices with complex geometries. Penetration of electrons is directly related to their kinetic energy and to the acceleration voltage used.

X-ray sterilisation is growing as a result of recent increases in the beam power ratings of industrial electron accelerators, which can generate intense X-ray beams. X-rays are more penetrating than e-beams, but less than gamma rays. They are more costly than gamma processes but will decrease exposure times, require less shielding and shorten turnaround times. X-ray sterilisation is still in the experimental phase but standards already exist and several electron beam facilities in Europe, Japan and North America are already equipped for both electron beam and X-ray sterilisation (Stichelbaut *et al*., 2007) (ISO/ASTM 51608:2002).

In contrast, ultraviolet (UV) light radiation has very low penetrability and is limited to the treatment of surfaces. UV irradiation by germicidal lamps is routinely used to sterilise the interiors of biological hoods between uses, but is ineffective in shaded areas, including areas under dirt.

13.3.3 Moist and dry heat sterilisation

Steam sterilisation

Steam sterilisation has limited industrial application but is very commonly used in healthcare facilities. A steam steriliser, also known as an 'autoclave', uses saturated steam at 121–132 °C. A typical standard for steam sterilisation is achieved after 15 to 30 minutes under a pressure of 106 kPa (1 atm) once all surfaces have reached a temperature of 121 °C (Block, 2000). To insure reliability of this sterilisation method, the critical factors are: (i) proper temperature and time; and (ii) the complete replacement of the air with steam (i.e. no entrapment of air). Some autoclaves use a pre-cycle vacuum to remove air prior to steam introduction. Others utilise a steam activated exhaust valve that remains open during the replacement of air by live steam until the steam triggers the valve to close.

Moist heat sterilisation kills microorganisms by destroying structural and metabolic components essential to their replication. The coagulation of essential enzymes and the disruption of proteins and lipids are the main lethal events (Kowalski and Morrissey, 2004). The advantage of wet heat is a better heat transfer to, and into, the cell, resulting in needing an overall shorter exposure time and a lower temperature (Block, 2000).

Steam sterilisation has many advantages. It is a simple, rapid, effective, safe, environment-friendly and low-cost sterilisation method. It yields little waste (entropy is its only by-product). Monitoring physical parameters (moisture, temperature, time, etc.) can be used to ensure efficiency of sterilisation, although biological indicators are still commonly used in several countries. It can also sterilise liquids. It is therefore commonly used in healthcare centres for the sterilisation of reusable metallic devices and instruments, hospital linen, various solutions, etc.

Its main limitation is clearly that it is incompatible with many materials. Steam sterilisation damages most polymers. It can also cause corrosion of some metallic devices, in particular high carbon steels used for surgical and dental instruments, and cause unprotected cutting edges to dull. Moisture also can adversely affect electronics. To avoid this, it is of utmost importance to clean and thoroughly dry the instruments before sterilising by autoclave. One way to reduce progressive corrosion of carbon steel instruments is to dip them in an anticorrosive solution prior to autoclaving (Stach *et al.*, 1995; Holmlund, 1965). In surgical trays, contact between instruments of dissimilar metals should be avoided to prevent galvanic corrosion.

Damage on polymers can vary from a little oxidation to complete distortion and melting, depending on polymer composition and properties. It is not possible here to do a complete review of polymers regarding steam sterilisation. More information can be found in handbooks. It is important to mention that some polymers can be safely sterilised by steam. This is the case of polypropylene (PP), PTFE, aromatic polyurethanes, nylons, Tyvec, polycarbonate, etc. Others will undergo mild to severe changes. Steam sterilisation of certain polyurethanes may result in a toxic hydrolytic by-product, dimethyl aniline (Shintani, 1995). The number of plastic materials capable of being steam sterilised will vary considerably with the selected temperature of sterilisation. To accommodate more heat-sensitive polymers, so-called 'low-temperature' steam sterilisation is sometimes used, but is subject to controversy. The process then takes place at 110–115 °C, but during 35–40 minutes instead of 10–15 minutes once temperature is obtained. In contrast, fewer materials can be sterilised by *flash sterilisation*, which uses higher temperatures (134 °C, 3–6 min in vacuum with steam pulses). Flash sterilisation is used in a clinical setting when an instrument or device is needed urgently (Carlo, 2007).

Dry heat sterilisation

To avoid metallic corrosion, *dry heat sterilisation* can be used as an alternative, but it is less efficient than wet heat and requires longer times and/or higher temperatures. In order to accomplish the same effect with dry heat in an oven, the temperature needs to be increased to 140 ºC for 3 hours or 160–170 °C

(320–338 °F) for 1 or 2 hours (Block, 2000; Kowalski and Morrissey, 2004). Dry heat can sterilise some electrical components without damaging them, and it can sterilise metals without producing corrosion.

13.3.4 Ethylene oxide gas sterilisation

Ethylene oxide (EO) gas sterilisation is widely used in the biomedical industry as well as in health-care centres, especially for temperature-sensitive materials. However, due to potential hazards of EO to patients, staff, and the environment, regulations have tended to decrease its use in several countries and may even ban it within a few years or decades.

EO gas (Fig. 13.4) is an alkylating agent that reacts with the cellular constituents of organisms, such as nucleic acid and functional proteins, including enzymes, which leads to consequent denaturation. The addition of alkyl groups to proteins, DNA, and RNA in micro-organisms prevents normal cellular metabolism and the ability to reproduce, which render micro-organisms nonviable. EO sterilisation takes place in a sterilisation chamber under vacuum to prevent EO leakage outflow. Gas concentration, moisture level (between 30–80%), and temperature (between 40–55 ºC) must be carefully controlled throughout the process (around 2 hours) to ensure efficiency. This process is preceded by a preconditioning phase during which time the products are heated and humidified (humidity is synergistic for EO inactivation of spores), and followed by an aeration phase to remove EO residues.

The main advantages of this low-temperature chemical sterilisation process are its effectiveness, its reliability and more especially its compatibility with most materials, including all metals, ceramics and most polymers. A few polymers can be, however, altered by this alkylating agent.

Unfortunately, EO gas has also been shown to be toxic, haemolytic, and mutagenic, and is classified as a potential carcinogen (A2). The United States Occupational Safety and Health Administration (USOSHA) permissible exposure limit is 1 part per million over an 8-hour shift. Safety procedures must be taken to prevent exposure of personnel to EO. Toxic EO residues or by-products (ethylene chlorohydrin, and the less toxic ethylene glycol) can also stay on medical devices and desorb during their clinical use (Page, 1993). The aeration phase which must follow the sterilisation process can last only a few hours for metallic devices but up to several weeks for some polymers that easily absorb EO and slowly desorb it (Handlos, 1980). This time period can be significantly shorter when using the new generation EO

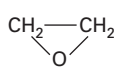

13.4 Ethylene oxide molecule.

sterilisers designed to allow aeration within the sterilisation chamber. An EO sterilisation cycle duration is typically of 12 hours to several days. While this is not a big issue for industrial sterilisation, it requires hospital centres to buy several batches of similar devices to ensure their availability. Regulations and ISO10993 standards for evaluation of EO residues on medical devices have been created to prevent safety problems associated with EO.

Another safety concern is that EO, mixed with air at a ratio of at least 3% EO gas, forms an explosive mixture. Commonly used to stabilise EO in the past, chlorofluorocarbon gas (CFC) is now forbidden by regulations due to the ozone depleting nature of CFCs. Hydrochlorofluorocarbons (HCFC) with smaller ozone depletion potential will also soon be banned in many countries. Many industrial sterilisation settings now use 100% EO, which requires intrinsically explosion-safe equipment and instrumentation. EO can also be mixed with CO_2, but this requires a high-pressure process.

Finally, since EO is also toxic for the environment, guidelines for the reduction of ethylene oxide emissions from sterilisation facilities are limiting its use in several countries such as Canada, Europe and the USA, and may lead to the abandonment of this technique within a few decades (EnvironmentCanada, 2005). This situation requires a safe alternative to ethylene oxide for reprocessing heat-sensitive medical devices.

13.4 Alternative sterilisation methods

The main low-temperature alternatives to EO include low-temperature hydrogen peroxide gas plasma sterilisation (LTHPGP), ozone, vapour hydrogen peroxide, chlorine dioxide, and immersion into liquids such as peracetic acid or formaldehyde solution.

13.4.1 Low-temperature hydrogen peroxide gas plasma sterilisation

Low-temperature hydrogen peroxide gas plasma sterilisation (LTHPGP), marketed under the trade name Sterrad® (Advanced Sterilisation Products (ASP), Johnson and Johnson, Irvine, CA) is the most widespread novel technology in North America and Europe. This process combines an oxidative chemical phase (vaporised hydrogen peroxide, a strong antimicrobial agent), followed by low-temperature plasma. The five phases or stages of the LTHPGP sterilisation process consist of vacuum, H_2O_2 injection, diffusion, plasma, and vent (Fig. 13.5) (Rutala *et al.*, 1999). Briefly, after vacuum and diffusion of H_2O_2, an electromagnetic field is created in which the hydrogen peroxide vapour breaks apart, producing a low-temperature plasma cloud, a partially ionised gas that contains ultraviolet light and free radicals. Following the reaction, the activated components lose their high energy and recombine to

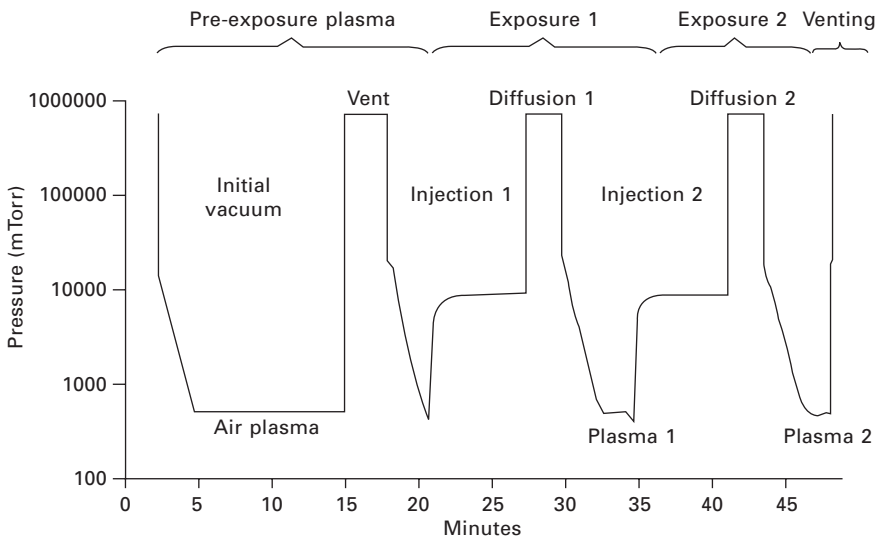

13.5 Sterrad® 100S steriliser process diagram (with the permission of Johnson & Johnson).

form oxygen and water. Although most inactivation efficiency is provided by the chemical phase, gas plasma can further kill micro-organisms and helps in eliminating H_2O_2 residues (Lerouge *et al.*, 2002c).

The first Sterrad® system was cleared in 1993 as an alternative to ethylene oxide and has known wide success with several thousand systems in clinical facilities. In many countries it has become the most common low-temperature alternative to EO. Several systems of different load size are presently available (Rutala and Weber, 2001); the cycle duration ranges from about 38 min for the smallest (Sterrad®NX, 30L, conceived for operating rooms and small facilities) to 75 min for the largest chamber (150L) (Sterrad®200).

More generally, low-pressure plasmas have been shown to kill micro-organisms very rapidly (Lerouge *et al.*, 2000b); other sterilisation processes based on gas plasma processes are under development (Kylian *et al.*, 2006, 2008; Baxter *et al.*, 2005; Halfmann *et al.*, 2007). It is a promising technology in that it acts rapidly, does not leave toxic residuals on processed parts or in the exhaust gas, and the temperature of a substrate usually does not exceed 60 °C. This field is rapidly moving forwards, for sterilisation as well as for cleaning processes.

Sterrad® sterilisation is an interesting technology since it is a fast, low-temperature process, in which chemical active species disappear practically immediately after the plasma power is turned off; by-products are water vapour and oxygen. It is therefore potentially safer for healthcare workers, patients and for the environment, and this eliminates the need for aeration

or ventilation. In hospital centres, the quick instrument turnaround decreases the need for duplicate inventories and associated costs.

The limited penetrability of vaporized and plasma reactive species into the innermost areas, lumens and packaging materials is the main limitation of this technology. This limits the size of each sterilisation load, and impairs the efficiency for some devices, especially those with small diameter/length ratio of lumens. Moreover, Sterrad® sterilisation systems and operation are relatively expensive.

Finally, material damage, especially to polymers, can be induced by oxidative species (Lerouge *et al.*, 2000a). Little is known about this issue compared to the numerous data acquired regarding alterations by radiation or heat sterilisation. Polyacetal and nylons may have limited life. Paper, cellulose, and linen absorb H_2O_2 and cannot be processed by this technique. Despite these limitations, Sterrad® systems' efficiency and safety have been tested on hundreds of devices from many different manufacturers.

13.4.2 Ozone sterilisation

Another interesting alternative to EO is ozone (O_3) sterilisation. Ozone has been already used for decades for water decontamination (Dufresne *et al.*, 2008; Murphy, 2006). Ozone sterilisers for medical devices, such as the 125L system marketed by Technologies of Sterilisation with Ozone Inc. (TSO_3, Québec, Canada), have been recently approved by the FDA and HealthCanada. Ozone is an oxidative gas, which quickly and effectively deactivates microorganisms by denaturing cell membranes. It can be created in an enclosed ozone generator by passing oxygen through an electrical field that converts the oxygen (O_2) into O_3. In the 125L system, the sterilisation cycle lasts about 4.5 hours and is divided into two identical half-sterilisation periods, where vacuum is created, following by humidification of devices and generation of ozone. The ozone produced is measured by an in-line ozone monitor, ensuring proper sterilant quality.

The main advantages of ozone sterilisation are low-temperature (temperature range of 30 °C–36 °C), safe and easy use, and absence of toxic by-products or residues. Moreover, since operation requires only water, oxygen and electricity, operation costs are low.

The main disadvantage is the limited number of devices for which this sterilisation process has been cleared to date, partly because of its recent development and partly inherent to the process itself. O_3 is a very strong oxidiser. The humidity within the sterilisation chamber is high, a factor that may cause natural rubber and some plastics to degrade. Metals may also corrode using this technique. Moreover, easy recombination of O_3 in O_2 on materials surfaces limits its efficiency in complex geometries and long lumens. The TSO_3 ozone steriliser has gained FDA clearance for stainless steel

devices with rigid lumens. The system is not intended for use in processing any flexible endoscopes, glass or plastic ampoules or liquids. To date, it has not been cleared for implants or devices intended to be in contact with the human body for more than 24 h. Latex and textile fabrics should also not be processed.

13.4.3 Other sterilisation techniques

Other sterilisation techniques for healthcare centres are under decline or in development. For example, low-temperature steam formaldehyde is used in European countries (UK, Sweden, Holland, Germany) instead of EO (Rogers, 2006). It shares many characteristics of steam sterilisation but at lower compatible temperatures (65–85 ºC). Formaldehyde is, however, toxic and a potential carcinogen. Gaseous formaldehyde has been around for many years but is used less than it was previously because of toxicity, odour and carcinogenicity. It is still used in several countries, mainly in Asia.

Another available alternative for chemical sterilisation is chlorine dioxide gas (ClO_2), an oxidative gas, which is best efficient at temperatures ranging from 25–30 °C (Kowalski and Morrissey, 2004). The process has been shown to be effective for the sterilisation of medical products. It is relatively rapid (1.5 to 3 hours) in duration, and there is little or no need for post-sterilisation. However, this strong oxidative gas also requires prehumidification and may corrode some materials.

Liquid sterilisation, consisting of immersing devices in peracetic acid or glutaraldehyde, is also commonly used for reusable endoscopes but should be considered as a high level disinfection owing to the efficiency limits and the inability to conserve sterility after sterilisation (Rutala *et al*., 1998). The System 1 Sterile Processing System (Steris) uses a liquid peracetic acid solution with a proprietary anti-corrosion formulation to sterilise metallic endoscopes, cameras or other long lumen instruments.

Pulsed high-intensity light sterilisation and microwave sterilisation have also been the subject of a number of patents.

13.5 New challenges for sterilisation

13.5.1 Prions

Healthcare resterilisation is challenged by the risk of transmission of prions (short for proteinaceous infectious particle). Stanley Pruisner, winner of the Nobel Prize in Physiology or Medicine in 1997, determined that a prion is neither bacterial nor fungal nor viral, and contains no genetic material. It is a protein that occurs normally in a harmless form but can fold into an aberrant shape, able to self-replicate and to be the agent of infection in a

variety of degenerative brain diseases, such as Creutzfeldt-Jakob disease (CJD), fatal familial insomnia, an unusual form of hereditary dementia known as Gertsmann–Straeussler–Scheinker disease, or the well-known bovine spongiform encephalopathy (BSE) in animals (Prusiner, 1995; Rosenberg, 1997).

Prions have been shown to be transmissible via several routes, including transplantation and contaminated medical products. They are notoriously resistant to processes known to inactivate bacteria, spores and viruses (Steelman, 1999; Taylor, 2000; Zobeley *et al*., 1999). None of the conventional sterilisation procedures has been shown to be completely efficient. Since these diseases are progressive and cannot be diagnosed efficiently, preventing their transmission is a real challenge. To prevent accidental transmission of CJD, various decontamination procedures have been adopted for re-usable medical devices in contact with high risk tissues, such as instruments for brain, spinal cord and eye surgeries. For patients with known or suspected Creutzfeldt-Jakob disease, it is even recommended to discard instruments used for surgery, since no proven technique is available. In terms of practical application, autoclaving at 134 °C for 18 min or 121°C for 30 min, and 1N sodium hydroxide for 15 min strongly reduces infectivity but not completely. Moreover, most materials do not sustain such aggressive conditions. Recently promising results showed elimination of detectable levels of infectivity after using an alkaline cleaner followed by autoclaving (Fichet *et al*., 2004; Lawson *et al*., 2007; Lemmer *et al*., 2008) or when using an enzymatic cleaning preparation in conjunction with gaseous hydrogen peroxide (Fichet *et al*., 2007). In contrast to the gas form, liquid peroxide was not effective. Other novel sterilisation methods have shown promising preliminary results and are under assay, such as LTHPGP, pure plasma processes, and ozone (Baxter *et al*., 2005).

13.5.2 Endotoxins

Endotoxins are another challenge for sterilisation. Endotoxins are lipopolysaccharides found in the cell wall of Gram-negative bacteria, which can induce inflammation and fever as an immune response in higher organisms. Reaction to endotoxins can lead to anaphylactic shock and death of patients. This risk has been illustrated in rare but serious clinical cases (Cookson *et al*., 1997). Endotoxins can be present on 'sterile' biomedical devices since sterilisation processes do not remove micro-organisms but simply deactivate them or partly destroy them. They are highly resistant to sterilisation processes. Presently, the only procedure recommended by the United States Pharmacopeia (USP) is dry heat at 250 °C during 30 minutes, or 180 °C during 3 hours, which is completely impractical for polymeric, and even metallic materials (Cookson *et al*., 1997; Nakata, 1993). Recent

studies showed that plasma technique may have an interesting potential for depyrogenisation, with a fast (10 s to a few minutes) removal rate of the immune-stimulating competence of these molecules (Kylian *et al.*, 2006; Tessarolo *et al.*, 2006).

13.5.3 Anti-microbial coatings

Despite device adequate sterilisation and aseptic procedures, device infection can appear as a result of bacterial adhesion and subsequent biofilm formation after implantation. This is a major clinical problem, especially with urethral catheters, subcutaneous sensors and implants. Although this is not directly the topic of this chapter, the importance of developing biomaterials that resist bacterial adhesion should be emphasised. Several bioactive coatings are in development that release antimicrobial agents, such as antibiotics, silver ions, antibodies, and nitric oxide, for reducing the incidence of implant-associated infection (Hetrick and Schoenfisch, 2006; Ramritu *et al.*, 2008; Darouiche, 2007).

13.6 Cleaning

Surface cleaning is also an important manufacturing step, not only useful to decrease the bioburden (living organisms) before sterilisation but also to eliminate contaminants originating from manufacturing processes, such as cutting or polishing fluids and particles, mould release agents, polymer processing aids, airborne contamination, etc. These can negatively impact on device biocompatibility and further processing, such as coating adhesion or bonding between two surfaces and corrosion resistance.

Conventional cleaning methods generally employ wet chemical techniques, such as the use of an aqueous surfactant solution with/without acids or organic solvents to dissolve and eliminate contaminant. Ultrasound can also be used as adjunct. However, these methods have several limitations, for example aqueous surfactants may leave residues, even after several rinses. Organic solvents can also leave toxic residues and may degrade polymeric devices. Low-temperature plasma processes have a high potential for these kinds of applications and several processes have been patented. Plasma reactive species (UV and VUV emissions, oxygen or hydrogen radicals, etc.) are known to be able to etch surfaces without altering bulk properties and can remove contaminants. As mentioned, protein removal is also an important issue in a clinical setting, for reusable devices, since protein adsorbed on the device surface may alter its biocompatibility and prevent efficient resterilisation. The use of plasma discharge for these applications is also under investigation (Kylian *et al.*, 2008). Ozone is another possible process for surface cleaning by oxidising surface dirt.

13.7 Standards and other sources of further information

Many regulations and standards provided by non-governmental international organisations (e.g. the International Organization for Standardization, ISO (ISO/TC 198, Sterilisation of Healthcare Products), or the European Community for Normalisation, CEN (CEN/TC 204, Sterilisation of Medical Devices)), pharmaceutical compendiums, private organisations (such as the Association for the Advancement of Medical Instrumentation AAMI) and governmental agencies (e.g. US Food and Drug Administration, FDA) have been developed regarding sterilisation issues, such as safety, validation, and evaluation of toxic residues (Reich *et al.,* 2005). In the United States, the FDA is responsible for approving sterilisation methods. In the UK, it is the Department of Health Sciences. Concerning standards, an attempt to harmonise some of the AAMI and CEN standards has resulted in many ISO standards, which are too numerous to describe in this chapter. Briefly, the main standards are ISO11134 for industrial moist heat sterilisation, ISO 11135 for EO, and ISO11137 for radiation sterilisation. The updated ISO 11137: 2006 gives specific requirements and guidance for radiation sterilisation including the use of X-rays as the sterilisation agent. Standards regarding biological and chemical indicators are ISO11138 and 11140, respectively. An interesting although non-exhaustive description of standards is provided in Sterilisation of Polymer Healthcare Products (Rogers, 2005, Chapter 2, Table 2.2). The reader can also refer directly to ISO. More information on sterilisation can also be found in two interesting books focused on sterilisation (Block, 2000; Booth, 2001)

13.8 Summary

Sterilisation is an important and problematic step that should be considered as early as possible in the design of any new medical device intended for use in contact with sterile tissues, mucous membranes or breached skin, in order to save money, time, and trouble. There is no singular sterilisation method that is compatible with all healthcare products including drugs, polymers, devices, and materials, because of the severity of a process to meet the sterilisation criteria and definitions. An ideal sterilisation method (i) should be efficient and highly reliable (this can be achieved when the sterilant is highly penetrating and can be homogeneously distributed within the load; (ii) should be able to deactivate prions and endotoxins; (iii) should be easy to monitor, by checking that the required physical or chemical conditions were achieved within each package; (iv) should be easy, cheap and safe to operate; (v) should be safe for patients and not leave any toxic residues on biomedical devices or in the environment; and (vi) should be compatible

with all materials. As discussed, metallic alloys are generally compatible with most sterilisation processes. However, devices are getting smaller and more fragile, with complex geometries, and often include polymeric compounds (such as coatings or adhesives) that require low-heat sterilisation processes. The increasing use of drugs or biological products with synthetic materials, for example in coated stents or tissue engineering applications, is also challenging.

The growing importance of polymers, on the one hand, and the hazardous nature of EO on the other hand, has led to the development of novel sterilisation methods. However, these have their own limitations. Therefore, no ideal sterilisation technique presently exists. The parameters and effects of different sterilisation methods must thus be evaluated and reviewed before selecting the best method for each application. As discussed earlier, a high variation of resistance to sterilisation techniques is observed in biomaterials, particularly for polymers. It is recommended, when possible, to choose materials that are compatible with radiations. Manufacturers should take advantage of the new medical grade materials compatible with radiation sterilisation. In the case of reusable devices, their design should take into account that they must be cleaned and dried before they can be resterilised and that other sterilisation methods than radiation will be used. Materials that are compatible with steam sterilisation should then be favoured when possible. Devices should be designed to avoid regions sealed off from the cleaning or sterilisation process or allow the device to be disassembled to expose all parts. The efficiency and safety of sterilisation will have to be demonstrated before device approval. Due to the increasing number and complexity of regulations and standards, many industrial manufacturers are going to outside contract sterilisation.

13.9 References

Baxter, H. C., Campbell, G. A., Whittaker, A. G., Jones, A. C., Aitken, A., Simpson, A. H., Casey, M., Bountiff, L., Gibbard, L. and Baxter, R. L. (2005) Elimination of transmissible spongiform encephalopathy infectivity and decontamination of surgical instruments by using radio-frequency gas-plasma treatment. *J Gen Virol*, 86, 2393–9.

Block, S. S. (2000) *Disinfection, Sterilization and Preservation, 5th ed.*, Lippincott, Williams & Wilkins.

Booth, A. (2001) *Sterilization Validation and Routine Operation Handbook: Radiation* Technomics Publishing Company.

Bruck, S. D. and Mueller, E. P. (1988) Radiation sterilization of polymeric implant materials. *J Biomed Mater Res,* 22, 133–44.

Carlo, A. (2007) The new era of flash sterilization. *Aorn J*, 86, 58–68; quiz 69–72.

Collier, J. P., Sutula, L. C., Currier, B. H., Currier, J. H., Wooding, R. E., Williams, I. R., Farber, K. B. and Mayor, M. B. (1996) Overview of polyethylene as a bearing material: Comparison of sterilization methods. *Clin Orthop Relat Res*, 76–86.

Cookson, S. T., Nora, J. J., Jr., Kithas, J. A., Arduino, M. J., Bond, W. W., Miller, P. H., Monahan, J., Hoffman, R. E., Curiel, T., Kaufman, D., Groves, B. M. and Jarvis, W. R. (1997) Pyrogenic reactions in patients undergoing cardiac catheterization associated with contaminated glass medicine cups. *Cathet Cardiovasc Diagn,* 42, 12–8.

Crow, S. (1993) Sterilization processes. Meeting the demands of today's health care technology. *Nurs Clin North Am*, 28, 687–95.

Darouiche, R. O. (2007) Antimicrobial coating of devices for prevention of infection: Principles and protection. *Int J Artif Organs*, 30, 820–7.

Dufresne, S., Leblond, H. and Chaunet, M. (2008) Relationship between lumen diameter and length sterilized in the 125L ozone sterilizer. *Am J Infect Control*, 36, 2917.

Environment Canada (2005) Guidelines for the reduction of ethylene oxide releases from sterilisation applications. In Environment, C. D. O. T. (Ed.). Government of Canada, Ottawa.

Fichet, G., Antloga, K., Comoy, E., Deslys, J. P. and McDonnell, G. (2007) Prion inactivation using a new gaseous hydrogen peroxide sterilisation process. *J Hosp Infect*, 67, 278–86.

Fichet, G., Comoy, E., Duval, C., Antloga, K., Dehen, C., Charbonnier, A., McDonnell, G., Brown, P., Lasmezas, C. I. and Deslys, J. P. (2004) Novel methods for disinfection of prion-contaminated medical devices. *Lancet*, 364, 521–6.

Halfmann, H., Bibinov, N., Wunderlich, J. and Awakowicz, P. (2007) A double inductively coupled plasma for sterilization of medical devices. *Journal of Physics D: Applied Physics* 40, 4145–4154.

Handlos, V. (1980) Kinetics of the aeration of ethylene oxide sterilized plastics. *Biomaterials*, 1, 149–57.

Hetrick, E. M. and Schoenfisch, M. H. (2006) Reducing implant-related infections: Active release strategies. *Chem Soc Rev*, 35, 780–9.

Hill, D. (1998) *Design Engineering of Biomaterial for Medical Devices*, Chichester; John Wiley.

Holmlund, L. G. (1965) Steam corrosion and inhibition in autoclave sterilization of dental and surgical steel materials. *Biotechnology and Bioengineering*, 7, 177–198.

Hutchinson, F. (1961) Molecular basis for action of ionizing radiations. *Science*, 134, 533–8.

Jorkasky, J. (1993) Special considerations for ethylene oxide: Chlorofluorocarbons (CFCs). In Morrissey, R. F., Phillips, G.B. (ed.) *Sterilization Technology: A Practical Guide for Manufacturers and Users of Health Care Products*. Van Nostrand Reinhold.

Kowalski, J. B., Morrissey, R. F. (2004) Sterilization of implants. In Ratner, B. D., Hoffman A. S., Schoen, F. J., Lemons, J. E. (eds) *Biomaterials Science: An Introduction to Materials in Medicine* Academic Press.

Kylian, O., Rauscher, H, Gilliland, D., Bretagnol, F. and Rossi, F. (2008) Removal of model proteins by means of low-pressure inductively coupled plasma discharge. *J Phys D: Appl. Phys.*, 41, 8.

Kylian, O. H., Hasiwa, M and Rossi, F (2006) 'Plasma based De-pyrogenization' *Plasma Processes and Polymers*, 3 (3), 272–5.

Lawson, V. A., Stewart, J. D. and Masters, C. L. (2007) Enzymatic detergent treatment protocol that reduces protease-resistant prion protein load and infectivity from surgical-steel monofilaments contaminated with a human-derived prion strain. *J Gen Virol*, 88, 2905–14.

Lemmer, K., Mielke, M., Kratzel, C., Joncic, M., Oezel, M., Pauli, G. and Beekes, M. (2008) Decontamination of surgical instruments from prions. II. *In vivo* findings with

a model system for testing the removal of scrapie infectivity from steel surfaces. *J Gen Virol*, 89, 348–58.

Lerouge, S., Guignot, C., Tabrizian, M., Ferrier, D., Yagoubi, N. and Yahia, L. (2000a) Plasma-based sterilization: Effect on surface and bulk properties and hydrolytic stability of reprocessed polyurethane electrophysiology catheters. *J Biomed Mater Res*, 52, 774–82.

Lerouge, S., Tabrizian, M., Wertheimer, M. R., Marchand, R. and Yahia, L. (2002c) Safety of plasma-based sterilization: Surface modifications of polymeric medical devices induced by Sterrad and Plazlyte processes. *Biomed Mater Eng*, 12, 3–13.

Lerouge, S., Wertheimer, M. R., Marchand, R., Tabrizian, M. and Yahia, L. (2000b) Effect of gas composition on spore mortality and etching during low-pressure plasma sterilization. *J Biomed Mater Res*, 51, 128–35.

Leventon, W. (2002) Medical Device Sterilization: What manufacturers need to know. *MD&DI*, Sept., p 52.

Massey, L. (2005) *The Effects of Sterilization Methods on Plastics and Elastomers*, William Andrew Publishing/Plastics Design Library PDL

McCormick, P., Finocchario, C., Manchester, R., Glasgow, L. and Costanzo, S. (2003) Qualification of a rapid readout biological indicator with moist heat sterilization. *PDA J Pharm Sci Technol*, 57, 25–31.

Morrissey, F., Ratner, B. D. (1998) Sterilization. In Hill, C. H. (ed.) *Design Engineering of Biomaterials for Medical use*, Chichester: John Wiley.

Murphy, L. (2006) Ozone – The latest advance in sterilization of medical devices. *Can Oper Room Nurs J*, 24, 28, 30–2, 37–8.

Nair, P. D. (1995) Currently practised sterilization methods – some inadvertent consequences. *J Biomater Appl*, 10, 121–35.

Nakata, T. (1993) Destruction of typical endotoxins by dry heat as determined using LAL assay and pyrogen assay. *J Parenter Sci Technol*, 47, 258–64.

Page, B. F. J. (1993) Special considerations of ethylene oxide: Product residues. In Morrissey, R. F., Phillips, G. B., (ed.) *Sterlization Technology: A Practical Guide for Manufacturers and Users of Health Care Products*. New York, Van Nostrand Reinhold.

Plester, D. W. (1970) The effects of sterilising processes on plastics. *Biomed Eng*, 5, 443–7.

Premnath, V., Harris, W. H., Jasty, M. and Merrill, E. W. (1996) Gamma sterilization of UHMWPE articular implants: An analysis of the oxidation problem. *Biomaterials*, 17, 1741–53.

Prusiner, S. B. (1995) The prion diseases. *Sci Am*, 272, 48–51, 54–7.

Ramritu, P., Halton, K., Collignon, P., Cook, D., Fraenkel, D., Battistutta, D., Whitby, M. and Graves, N. (2008) A systematic review comparing the relative effectiveness of antimicrobial-coated catheters in intensive care units. *Am J Infect Control*, 36, 104–17.

Reich, R. S., Schneider, P. M. and Kinsley, C. (2005) Global sterilization: Making the standards standard. *MD&DI*, March, p 78.

Ries, M. D., Weaver, K., Rose, R. M., Gunther, J., Sauer, W. and Beals, N. (1996) Fatigue strength of polyethylene after sterilization by gamma irradiation or ethylene oxide. *Clin Orthop Relat Res*, 87–95.

Rogers, W. (2005) *Sterilisation of Polymer Healthcare Products*, Smithers Rapra.

Rogers, W. (2006) Steam: Uses and challenges for device sterilization. *MD&DI*. March, p 80.

Rosenberg, R. N. (1997) Nobel Prize in Physiology or Medicine for 1997 Awarded to Stanley B. Prusiner, MD. *Arch Neurol*, 54, 1456.

Rutala, W. A., Gergen, M. F. and Weber, D. J. (1998) Comparative evaluation of the sporicidal activity of new low-temperature sterilization technologies: Ethylene oxide, two plasma sterilization systems, and liquid peracetic acid. *Am J Infect Control*, 26, 393–8.

Rutala, W. A., Gergen, M. F. and Weber, D. J. (1999) Sporicidal activity of a new low-temperature sterilization technology: The Sterrad 50 sterilizer. *Infect Control Hosp Epidemiol*, 20, 514–16.

Rutala, W. A., Jones, S. M. and Weber, D. J. (1996) Comparison of a rapid readout biological indicator for steam sterilization with four conventional biological indicators and five chemical indicators. *Infect Control Hosp Epidemiol*, 17, 423–8.

Rutala, W. A. and Weber, D. J. (2001) New disinfection and sterilization methods. *Emerg Infect Dis*, 7, 348–53.

Shintani, H. (1995) Formation and elution of toxic compounds from sterilized medical products: Methylenedianiline formation in polyurethane. *J Biomater Appl*, 10, 23–58.

Spaulding, E. H. (1972) Chemical disinfection and antisepsis in the hospital. *Journal Hospital Research*, 9, 5–31.

Stach, D. J., Cross-Poline, G. N., Newman, S. M. and Tilliss, T. S. (1995) Effect of repeated sterilization and ultrasonic cleaning on curet blades. *J Dent Hyg*, 69, 31–9.

Steelman, V. M. (1999) Prion diseases – An evidence-based protocol for infection control. *Aorn J*, 69, 946–54, 956–67 passim; quiz 968–76.

Stichelbaut, F. Bol, J. L., Cleland, M. R. *et al*. (2007) A high performance X-ray system for medical device irradiation. *Radiation Physics and Chemistry*, 76, 1775–1778.

Taylor, D. M. (2000) Inactivation of transmissible degenerative encephalopathy agents: A review. *Vet J*, 159, 10–17.

Tessarolo, F., Caola, I., Nollo, G., Antolini, R., Guarrera, G. M. and Caciagli, P. (2006) Efficiency in endotoxin removal by a reprocessing protocol for electrophysiology catheters based on hydrogen peroxide plasma sterilization. *Int J Hyg Environ Health*, 209, 557–65.

Woo, L., Sandford, C. L. (2002) Comparison of electron beam irradiation with gamma processing for medical packaging materials. *Radiation Physics & Chemistry*., 63, 845–850.

Yagoubi, N. B., Boucherie, P. and Ferrier, D (1997) Radiosterilization and steam autoclaving sterilization effects on phosphite antioxidant stability. *Nuclear Instruments & Methods in Physics Research: Section B – Beam Interactions with Materials & Atoms*, 131, 398–404.

Zobeley, E., Flechsig, E., Cozzio, A., Enari, M. and Weissmann, C. (1999) Infectivity of scrapie prions bound to a stainless steel surface. *Mol Med*, 5, 240–3.

14

Orthopaedic applications of metallic biomaterials

T. MATSUSHITA, Chubu University, Japan

Abstract: The chapter discusses various metallic implants used in orthopaedic surgery. It first describes artificial hip replacement arthroplasty related with metallic biomaterial, stem design, fixation methods and joint bearing surface. The chapter then discusses features of typical artificial joints such as knee, shoulder and elbow. The chapter further describes metallic implants for bone fractures related with their structures, functions and breakages.

Key words: hip joint, knee joint, elbow joint, shoulder joint, cement fixation, cementless fixation, joint bearing surface, mobile knee, bisurface knee, triple tapered stem, bone cement. Co–Cr–Mo alloy, titanium alloy, vanadium-free titanium alloy, ultra high molecular weight polyethylene, hydroxyapatite, plasma spraying, wear debris, bone fracture, compression hip screw, bioactivity.

14.1 Introduction

We human beings are able to walk and pick up something because our joints move smoothly. If bone is broken in an accident, we cannot move at all. If arthritis is growing worse, walking becomes virtually impossible. Bone fractures can be healed by performing a surgical operation using metallic plates and screws. Sometimes, tubular and stick-type metal pieces, such as intramedullary nails and γ-nails are used to treat a subtrochanteric fracture. Artificial joint replacement is performed for severe cases of articular diseases. As bones and joints are necessary to bear our body weight and make movement possible, materials used for orthopaedic surgery must have a high strength, toughness and wear resistance. Therefore, metallic biomaterials are unavoidably employed as implant materials with a combination of ceramics and polymer materials. Figure 14.1 shows examples of orthopaedic implants used for repairing the diseases of various skeletal site structures.

Typical metallic materials for orthopaedic applications are stainless steel, cobalt-chromium-molybdenum alloy and pure titanium and its alloys. These materials were originally developed for industrial uses, then were later turned over for medical usage. Since metallic implants are exposed to a strong corrosive environment inside the body, metallic ions are released. The living body contains almost all the metallic elements. If the amount exceeds the adequate level, these elements become toxic. Therefore, metallic biomaterials

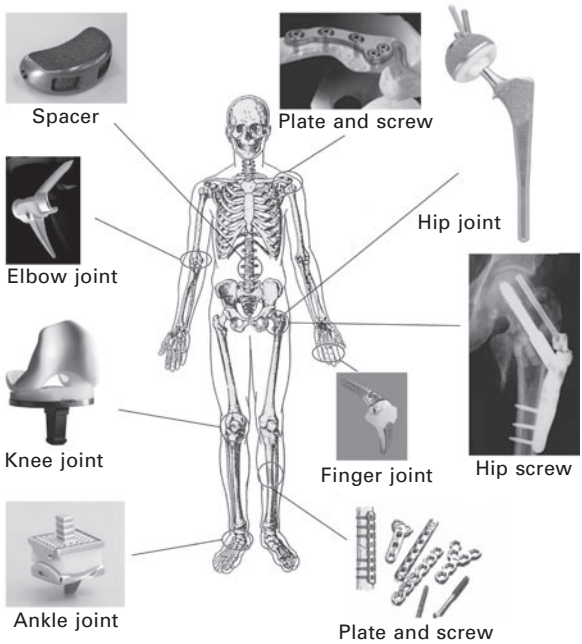

14.1 Various implants made of metallic biomaterials for orthopaedic surgery (with permissions from Japan Medical Materials Corp., Nakashima Medical Corp., and Mizuho Ikakogyou Co. Ltd).

Table 14.1 Development of metallic biomaterials

Materials	Subjects	Examples of alloys
Stainless steel	Corrosion resistance ⇒ reducing C content Skin allergy ⇒ Ni free	Fe–18Cr–8Ni–0.03C Fe–18Cr–12Ni–2.5Mo–0.03C Fe–23Cr–2Mo–1.4N
Co–Cr–Mo alloy	Wear resistance, high strength and Ni allergy	Co–29Cr–6Mo
Ti-alloy	Cyto-toxity ⇒ V free High strength & low elasticity ⇒ β alloy High biocompatibility	Ti–6Al–7Nb Ti–6Al–2Nb–1Ta–0.8Mo Ti–15Mo–5Zr–3Al Ti–12Mo–6Zr–2Fe Ti–15Zr–4Nb–4Ta Ti–29Nb–13Ta–4.6Zr

have been empirically improved to be suited to the living body, based on clinical experience over a long period. Table 14.1 shows examples of new alloys that have been developed from the perspective of solving conventional shortcomings. Examples of applications of these metallic biomaterials to orthopaedic surgery will be introduced in this chapter.

14.2 Total hip replacement

14.2.1 Materials for total hip replacement

A hip joint consists of a sphere and a socket. It allows the joint to be mobile in omnidirection under low friction and is extremely important to human support activities. Approximately 50 years have passed since artificial hip joints began to be used clinically. This technique became widespread after an artificial total hip prosthesis was developed by Charnley during the 1960s (Charnley, 1970). Hip arthroplasty alleviates pain and improves function in the patient and he/she becomes able to walk and to enjoy quality of life. Numerous people all over the world have benefited from hip replacement arthroplasty. Artificial hip joints can ordinarily serve for twenty years or more after surgery (Ilchmann *et al*., 1998, Meding *et al*., 2000). Recently, advanced materials have been used in order to achieve a long life of over thirty years. They require (i) avoidance of materials causing inflammations or cancer, (ii) high strength and ductility, (iii) early fixation and long-term stability and (iv) reduced wear debris on the sliding surfaces.

Figure 14.2 illustrates a typical example of an artificial hip joint. The stem is fixed to the femur. A load totally about three times the body weight consistently acts on it, so the stem needs to have high fatigue strength. Historically, stainless steel consisting of steel, chromium and nickel was first used due to the corrosion resistance provided by chromium. However,

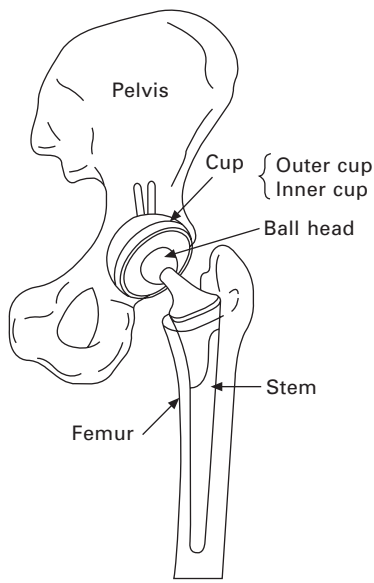

14.2 Structure of artificial total hip joint.

it was not able to bear the high stress and had a risk of causing skin allergy, a cobalt-chromium alloy was adopted due to its higher strength and superior corrosion resistance. A cast material was initially used. Since it did not have sufficient strength, elements such as tungsten (W) and nickel (Ni) were added to enhance the plastic deformability of the alloy when hot forged. Recently, thanks to the improvement of materials processing technology, the cobalt-chromium-molybdenum (Co–Cr–Mo) alloys shown in Table 14.1 have been used. Titanium (Ti) metal, which has high biocompatibility, is also useful as a metallic biomaterial. Ti-6aluminum (Al)-4vanadium (V) alloy is a particularly versatile material with high mechanical strength in conjunction with corrosion resistance. As a result of the concern about vanadium's cytotoxicity, the titanium alloys shown in Table 14.1 are applied clinically as a vanadium-free alloy. In future, Ti alloys composed of elements harmless to the human body, such as tantalum (Ta), niobium (Nb) and zirconium (Zr), are expected to be useful metallic biomaterials (Okazaki *et al.*, 1998; Kuroda *et al.*, 1998).

There are two ways to integrate the stem and cup with bone. The first method is to use bone cement made of PMMA (polymethyl methacrylate). Numerous clinical reports have been released to indicate clinical outcomes which showed the effects of the bone cement thickness, surface roughness of the stem and a combination with implant materials on clinical results (Morscher and Wirz, 2002). The other method is to apply bioactive treatment on the implant surface, and directly bind the bone and the implant. These two methods will be described later in more detail.

Wear debris from the sliding surfaces of the ball head and the acetabular cup is a serious concern in artificial hip arthroplasty. In order to suppress the generation of wear debris, some novel materials have been developed. High density polyethylene was first used for an acetabular cup. Then UHMWPE (ultra high molecular weight polyethylene) was applied to improve the performance of the cup. For ten years, cross-linked UHMWPE cups have been thought to be advantageous for decreasing wear debris in conjunction with mirror finished ball heads made of Co–Cr–Mo alloy or alumina ceramic. A combination of a hard ball on a hard cup, such as ceramic on ceramic or metal on metal, is also effective in reducing wear debris. Alumina ceramic (Hamadouche *et al.*, 2002) and Co–Cr–Mo alloy are available for this articulation. As described, many kinds of materials are used to demonstrate functions in total hip replacement. In this section, each function is discussed in more detail.

14.2.2 Stem design using V-free Ti alloys

For total hip replacement arthroplasty, the material to use for the stem and how to design the shape to fit the patient's bone structure are important

factors. There are numerous reports on the presence of metal ions released from the implants in the body (Dobbs and Minski, 1980, Hallab *et al.*, 2001). Although Ti–6Al–4V alloy is a well-known metallic biomaterial due to its superior properties, it contains vanadium, showing cytotoxicity (Steinemann, 1980). To avoid this concern, Ti–6Al–7Nb (Semlitsh *et al.*, 1985) and Ti–12Mo–6Zr–2Fe have been developed and clinically used as vanadium-free titanium alloys. The author and co-workers have applied Ti–15Mo–5Zr–3Al to an artificial hip joint (Matsuda *et al.*, 1997, Maehara *et al.*, 2002); this alloy is registered in ISO as a metallic biomaterial. It possesses a tensile strength of 980 MPa and a fatigue strength of 600 MPa under annealed condition. When the heat treatment condition is selected, it presents a markedly high strength, as much as 1500 MPa, with 14% elongation, as shown in Fig. 14.3. It also has novel biocompatibility as shown in Fig. 14.4 (Isama and Tsuchiya, 2002), in conjunction with much better corrosion resistance than Ti–6Al–4V. Because of its high strength, it was possible to design a slender stem neck of 9 mm diameter, and to expand the range of movement without impingement with the cup.

In the case of cementless artificial hip joints, the stem is generally exposed to high temperature to endow a bone-bonding ability on its surface. This treatment reduces the strength of a stem made of β-type titanium alloy and Ti–6Al–4V alloy. The author and co-workers have proposed Ti–6Al–2Nb–1Ta–0.8Mo as a biomaterial which contains no vanadium and has heat resistance (Anon., 1994). This alloy presents high corrosion resistance and superior biocompatibility. Its fatigue strength at room temperature after heat treating up to 1000 °C remains the same as that before heating. This alloy

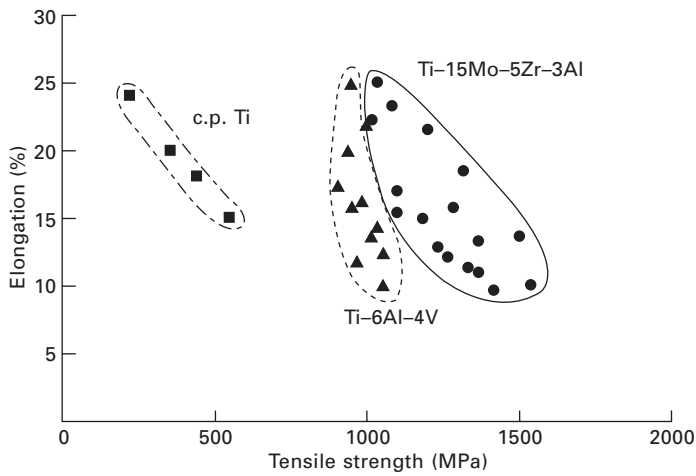

14.3 Tensile strength and elongation of Ti–15Mo–5Zr–3Al alloy compared with those of Ti–6Al–4V alloy.

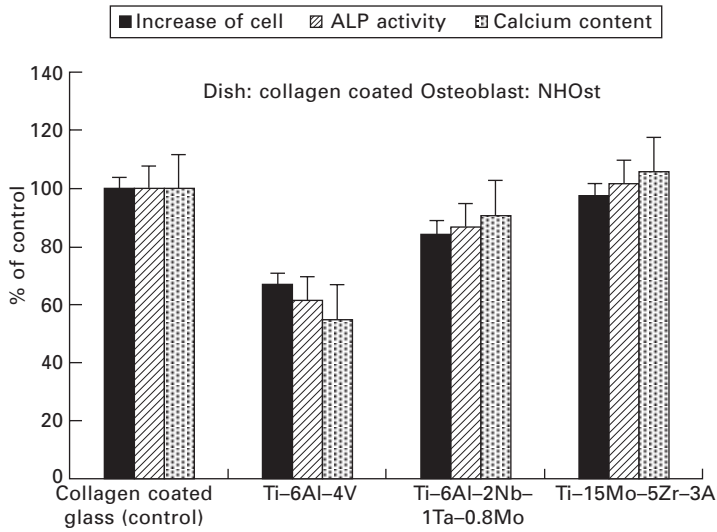

14.4 Comparison of biocompatibility of vanadium-free titanium alloys with that of Ti–6Al–4V.

was standardized in 2002 as JIS T 7401-3. To fabricate a porous layer on the surface of the stem and shell in order to attain bone-ingrowth, titanium powders were plasma-sprayed and given diffusion heat treatment. If these heat treatments are applied to Ti-6Al–4V alloy, however, the strength of the alloy is markedly reduced, so the stem loses its long life. This suggests that by using Ti–6Al–2Nb–1Ta–0.8Mo it would become possible to design a higher-functional stem for cementless hip replacement.

The optimal design of stem shape depends on the patient's bone structure, as well as clinical experience. This is the reason why a few hundred types of stem shape have been developed throughout the world, and are supplied by manufacturers. Figure 14.5 shows a cementless artificial hip joint designed using Ti–6Al–2Nb–1Ta–0.8Mo. The proximal portion of this stem is designed to be relatively thinner. This intends to preserve, as much as possible, the cancellous bone in the proximal portion of the femur. As a result of the cancellous bone binding with the stem's porous surface, the force acting on the femur head disperses into the femoral cortex to prevent stress shielding. The middle portion of the stem is designed with a trapezoidal cross-section to prevent rotation of the stem.

Another type of artificial hip joint designed using Ti–6Al–2Nb–1Ta–0.8Mo is shown in Fig 14.5. This has a double tapered shape, which is intended to support the load at the medial proximal and to secure fixation for extended periods. This stem shape matches Asian people's femoral medullary cavity.

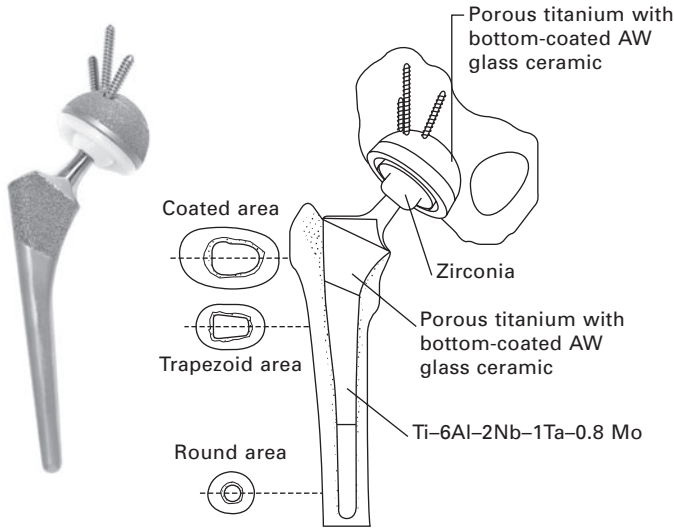

14.5 Designs of cementless type artificial hip joint using Ti–6Al–2Nb–1Ta–0.8Mo alloy. Right: Originally designed with trapezoid area by Prof. Yamamuro, Left: Designed with straight back by Prof. Ninomiya.

14.2.3 Cement fixation

In the cement fixation, bone cement penetrates the uneven surface formed by rasping to bind strongly with the bone. However, bone cement does not bind with the metallic implant (Barker *et al.*, 2000). Generally speaking, it is believed that a roughened surface is more effective in binding strongly at the stem-to-cement interface. In this condition, the strain in the stem and the cement is the same at the interface, and the cement has a risk of fracture when the stress within the cement exceeds the strength of the cement. However, some researchers have reported that a polished surface produced better clinical performance since a subsidence of the stem generates compressive stress within the cement mantle (Collis and Mohler, 2002; Justin *et al.*, 2006). The thickness of the bone cement layer and its combination with the stem materials were examined to extend the life of fixation. It was found that, if there is insufficient thickness, the bone cement is liable to break and that a thickness of around 2 mm is clinically preferable (Skinner *et al.*, 2003). In stem material terms, on the other hand, Co–Cr–Mo alloy is reported to be preferable to Ti–6Al–4V (Issack *et al.*, 2003). Otherwise, a Charnley-type stem made of Ti–15Mo–5Zr–3Al, introduced in the previous section, was used clinically by many surgeons. Its surface roughness was about Ra 0.3 μm, achieved by shot blasting, and the bone cement was made 0.5 mm thick – the prosthesis showed the favorable performance for more than ten years. This is attributed to the fact that the condition of the surface of the stem and its material are related to the friction with the bone cement.

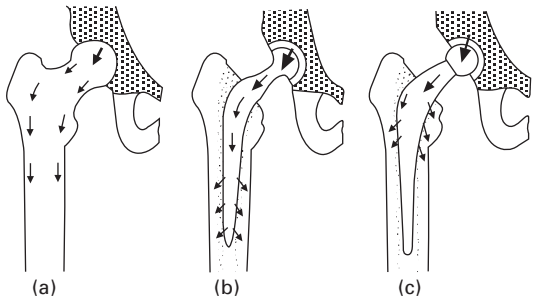

14.6 Three types of load transmission patterns. (a) Normal femur; load transmission through cortex, (b) conventional tapered stem; load transmission through the center axis and distal of stem, (c) triple tapered stem; load transmission through proximal of stem.

A conventional cemented stem gives stress shielding to the proximal femor. A mirror finished stem is advantageous for effective load transmission from the stem to the bone by allowing subsidence of the stem when a load is applied to the stem. If the cross-section of the stem is given a triple taper, subsidence of the stem creates compressive stress within the cement mantle and transmission of the load occurs at the proximal of the femur (Wroblewski *et al.*, 2001). This prevents the proximal femoral stress shielding, as is the case with the cementless type of stem. Figure 14.6 shows the difference of load transmission between a double and triple tapered stem with a polished surface.

14.2.4 Surface treatment for cementless fixation

Various designs have been attempted for a cementless artificial hip joint to bind with the bone using sintered beads, fiber mesh and spraying hydroxyapatite. They have shown favorable clinical results. In the case of a stem, a porous layer formed along the whole circumference of the proximal stem generates a strong binding force with the bone and prevents stress shielding. It also prevents the invasion of wear debris to the interface, so it leads to favorable clinical performance. The second method is to coat the roughened metal surface with hydroxyapatite. This also presents favorable clinical results (Coathap *et al.*, 2001). If hydroxyapatite is plasma-sprayed, the temperature during treatment reportedly becomes too high, which causes deterioration of the bioactivity of hydroxyapatite (Gross *et al.*, 1998). As a way to reduce this deterioration, a flame spray coating process has been developed and applied to a stem and cup made of Ti–6Al–4V (Fujisawa *et al.*, 1995). The implants using this process are shown in Fig. 14.7.

The author and co-workers have used heat-resistant vanadium-free titanium alloy Ti–6Al–2Nb–1Ta–0.8Mo (referred to previously) to overcome the

14.7 Stem and cup coated with hydroxyapatite using PROARC HA process, which is an inert-gas shield, arc-spray method originally developed by Japan Medical Materials Co. Ltd. Pure titanium is arc-sprayed to roughen the surfaces of stem and cup and then hydroxyapatite is flame-sprayed (with permission from Japan Medical Materials Corp.).

problem of decreasing strength on heating. A plasma-sprayed porous layer had about 50% porosity, the pore size ranged from 200 to 400 μm and its tensile strength was 17 MPa. The tensile strength increased to 70 MPa after heat-treating at a temperature close to 1000 °C under vacuum. This was followed by coating only the bottom areas of the titanium porous layer with AWGC (apatite and wollastanite containing glass ceramic) to allow the bone to grow into the pores (Yamamuro *et al*., 1991). An animal experiment verified that a high bonding strength with the bone could be obtained, and an artificial hip prosthesis employing this type of surface treatment is already commercialized in Japan.

Titanium metal does not have any bone-bonding properties without surface treatment. In 1995, however, Kokubo *et al*. (1996) invented a simple

treating process to provide bioactivity to titanium metal. In this process, a sodium titanate layer is formed by soaking titanium metal in NaOH solution at 60 °C for 24 h and heating at 600 °C for 1 h. The sodium titanate layer induces apatite formation on its surface when it is soaked in a solution with ions that have the same concentration as that of the body fluid's inorganic ions (simulated body fluid, or SBF) and the titanium metal binds with the living bone through the apatite layer. This novel method has been applied to a porous layer of titanium, plasma-sprayed on the stem and cup. As shown in Fig. 14.8, a fine nano-structured network consisting of sodium titanate can be formed on the surface of the porous layer after the treatment. It is so bioactive that apatite grains precipitate and cover the entire surface of the treated titanium metal within a few days in the SBF. Experiments also showed that when a porous body given such treatment is implanted in a dog's femur, rapid bone ingrowth is observed and that it has a higher bonding strength than when an AWGC bottom coating is used (Nishiguchi *et al.*, 2001). Based on these research findings, a clinical test on the artificial hip joint was conducted (Kawanabe *et al.*, 2009). The outcome of the clinical tests was that, four years after surgery, the system shows favorable performance. In particular, bone ingrowth to the porous section was observed at an early stage, and little or no thigh pain was induced. This NaOH- and heat-treated artificial hip joint has been used clinically in Japan since 2007.

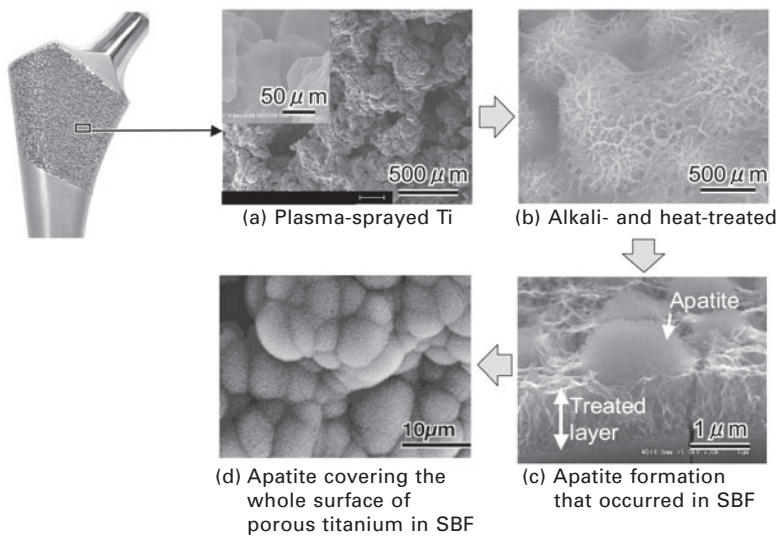

14.8 Bioactivity of alkali- and heat-treated titanium porous layer plasma-sprayed on the stem.

14.2.5 Joint bearing surface

Since the debut of Charnley's low-friction arthroplasty, polyethylene has been used for the acetabular cup. Wear debris generated by the friction between a polyethylene cup and a ball head induces aseptic loosening, so some way had to be developed to reduce the volume of wear debris. One of them is to polish the ball head to a smooth surface. As shown in Fig. 14.9, it is effective in decreasing an average surface roughness Ra to less than 0.02 μm (Weightman and Light, 1986). Thanks to advancements in the technology of polishing, it is now possible to finish the ball head surface roughness to Ra 0.01 μm. With those made of metal, however, it is difficult to maintain the ultra-mirror surface for long periods because of the invasion of a third body to the sliding surfaces. Alumina has higher hardness, so it can better maintain a mirror surface to reduce wear debris (Saikko *et al.*, 1993; Dowson, 1995). The disadvantage of alumina is that it sometimes causes breakage due to its brittleness. As zirconia ceramic is tougher than alumina, it would be expected to be suitable for the ball head. However, it causes a greater amount of wear debris than one made of alumina or Co–Cr–Mo alloy. This is attributed to the frictionally induced heat which is accumulated inside because of the low heat conductivity of zirconia (Lu and McKellop, 1997), and the low temperature phase transformation that may occur at temperatures close to 100 °C under wet conditions. An effective method to suppress zirconia's transformation is to add trace amounts of aluminum and to control the fine crystal grains. The manufacturing process must therefore be rigorously and thoroughly controlled.

As a way to enhance wear resistance capability, the structure of UHMWPE can be changed to be highly-crystallized by using high-pressure treatment

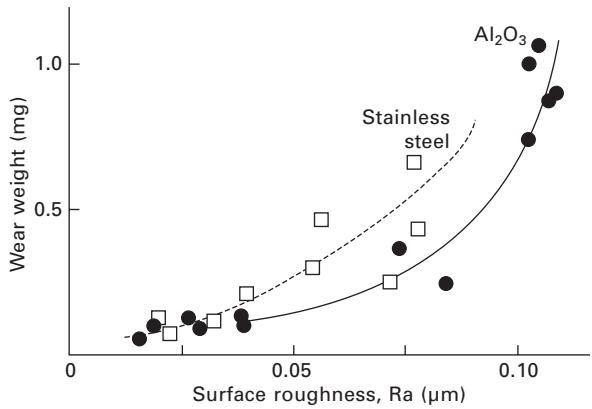

14.9 Effect of surface roughness of ball head on wear weight of polyethylene cup at 10^6 cycles. Reproduced from the table of Weightman and Light (1986).

(Hylamer). In one case of this material, an *in vitro* wear test showed a small volume of wear debris, so it was expected to be a promising means of suppressing the generation of wear debris. When used clinically, however, Hylamer produced a greater volume of wear debris than ordinary UHMWPE (Livingston *et al.*, 1997, Iwase *et al.*, 2003). An acetabular cup made from *cross-linked* UHMWPE has currently become predominant. Irradiating with about 25 kGy of γ-rays is a standard procedure in sterilizing medical products. During this process, however, free radicals are generated inside the polymer material, and a part of it becomes cross-linked. During the 1970s, Oonishi *et al.* clinically adopted a HDPE (high density polyethylene) cup irradiated with 1000 kGy of γ-rays, and showed that it produced an extremely small volume of wear debris (Oonishi *et al.*, 2001). However, because the irradiation dose is large, the polymer material becomes hard, with poor elasticity. When 10–50 kGy of γ-rays is irradiated, this amount of cross-linkage enhances the wear resistance while maintaining elasticity.

Nowadays, UHMWPE cups are heated to just below the melting point after irradiation and are kept in a nitrogen atmosphere for longevity (Muruatoglu *et al.*, 2001).

A metal-on-metal articulation is also effective to reduce wear debris. This method was first attempted by McKee-Farrar. With subsequent improvements of metallic composition and super polishing technology, the method is now widely used in clinical application. Figure 14.10 shows a typical artificial hip joint of this type. A follow-up study has been made, to confirm the effects on health of metallic ions released from wear debris. Alumina ceramic on alumina articulation is also an attractive method to reduce wear debris. Just as in the case of metal-on-metal, the generation of wear debris is low. Unfortunately, there are some complications due to breakage, since alumina ceramic is a fragile material. In order to overcome this disadvantage, adoption of a structure combining an alumina ceramic cup with a metallic shell is effective. A tougher and harder ceramic such as zirconia-toughened alumina is also applicable.

Recently, a new method to extend the longevity of a cross-linked UHMWPE cup has been developed. This method is one of surface modifications using photo-induced graft polymerization, which is induced by ultraviolet irradiation onto the surface of polymer cup soaked in an aqueous MPC(2-methacryloyloxyethyl phosphorylcholine) solution (Moro *et al.*, 2004). After such treatment of the cross-linked UHMWPE, brush-like structures of hydrophilic macromolecules are formed on the surface, as shown in Fig. 14.11, giving rise to hydration lubrication. Although its thickness varies depending on the treatment conditions, it is roughly 100 nm, and the surface layer is characterized by an extremely small water-contact angle (Kyomoto, 2009). Figure 14.12 shows the gravimetric wear in a hip joint simulator of cross-linked UHMWPE cups with and without MPC grafting. The weight

14.10 Example of artificial hip joint with metal-on-metal articulation (with permission from Kobayashi Medical Corp.).

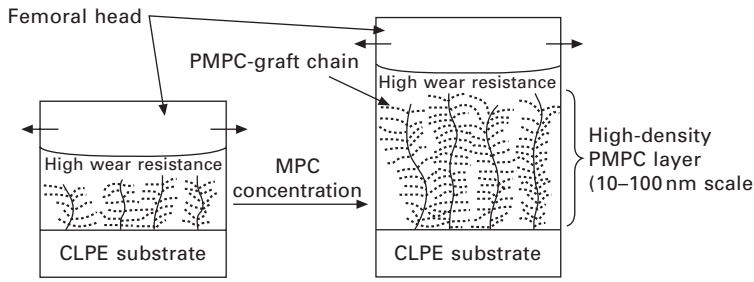

14.11 Schematic illustration of the MPC-grafted layer with increasing MPC concentration (Kyomoto, 2009).

loss of the MPC-grafted cup is significantly less than that of the untreated cup (Moro *et al.*, 2004).

14.3 Total knee replacement

14.3.1 Materials for total knee replacement

Figure 14.13 shows the structure of an artificial total knee joint forming the condyloid joint. This consists of a femoral component, a tibial component and

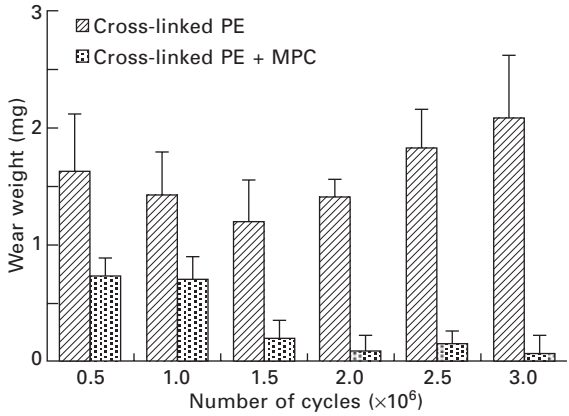

14.12 Wear of MPC-grafted cross-linked UHMWPE cup in hip joint simulator compared with untreated cross-linked UHMWPE cup (Moro *et al.*, 2004).

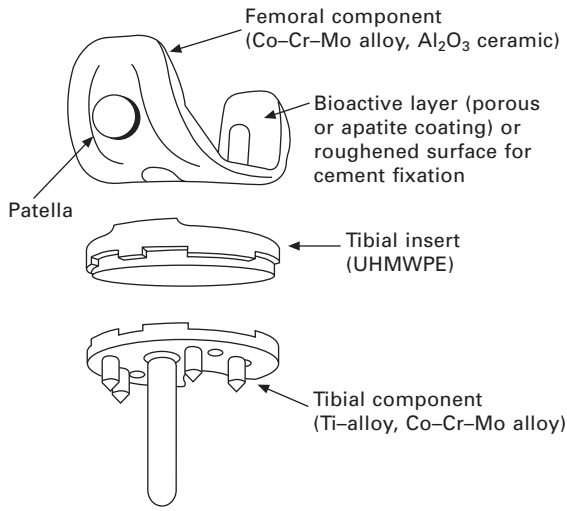

14.13 Structure of an artificial total knee joint.

a patella. The majority of the femoral components are made of Co–Cr–Mo alloys, but sometimes, alumina ceramic or titanium alloys are used for patients with allergies to these metals. In most cases, a tibial-side tray is made of titanium alloy and the insert is made of UHMWPE. The insert has grooves corresponding to the configurations of lateral and medial condyles. The patella, which is made of UHMWPE, slides on the surface of the femoral component. The same two alternatives to anchor implants to the bone are used as in the case of the artificial hip joint, with and without bone cement.

14.3.2 Joint bearing surface

As the knee joint is a condyloid joint, rotation of lateral and medial condyles occurs in conjunction with sliding over the insert surface made of UHMWPE. This brings about the generation of wear debris. Considerable contact pressure is induced by the contact between the two condyles and the UHMWPE, and it is at a maximum slightly inside the UHMWPE surface, so delamination occurs. If the UHMWPE insert is hard, a higher concentration of stress is induced in the area of contact between the insert and the femoral condyle, and makes it more likely for delamination to occur. In view of this, increasing the contact area between the UHMWPE and the femoral condyle may be advantageous for reducing the stress generated in the UHMWPE insert. A vitamin E-addition to the UHMWPE enables it to retain strength while remaining soft and flexible; hence it shows decreased wear debris (Tomita *et al.*, 1999).

When a femoral component made of Co–Cr–Mo alloy slides over a UHMWPE surface, the roughness of the component surface determines the amount of wear on the UHMWPE. If a titanium alloy is used as a femoral component, the surface may be markedly scratched or damaged by a third body, such as fragments of bone cement, which accelerates the generation of wear debris. Although Co–Cr–Mo alloy is hard and its surface is finished with a super mirror, roughening of condyles occurs clinically and wear of the UHMWPE is increased. When a femoral component made of alumina ceramic is used, scratches are minimized and wear debris of UHMWPE is reduced, although a fracture of the alumina ceramic component may occur.

The above suggests that a harder surface suppresses the scratches and provides low friction with UHMWPE. An oxidized zirconium femoral component was developed. It is made of wrought zirconium alloy, Zr-2.5%Nb, and its sliding surface is oxidized by thermal diffusion (Spector *et al.*, 2001). The surface is layered by zirconia ceramic at about 4 μm thickness. This material has advantages of resistance to scratches and low friction, while the toughness of femoral component is maintained due to the use of the wrought metallic alloy.

14.3.3 Design of knee joint with a large flexion angle

The knee joint has a sliding surface on the femorotibial joint consisting of the femoral condyle and the tibial condyle, and on the patellofemoral joint comprising the patella and the intercondylar fossa. The former joint lacks the ball-and-socket stability, and creates articular movements with the support of ligaments and muscles. This movement is accompanied by rolling and sliding of the convex-shaped femoral condyle over the concave surface of the tibial condyle. In addition, the tibia rotates outwardly against the femur during

flexion. This fact was recently taken into consideration when designing an artificial knee joint with a large flexion angle. Figure 14.14 shows a novel total knee joint with the ball-and-socket joint in the mid-posterior portion of the femoral and tibial component. The surface 'A' is the same as that of the conventional femoral component. When the flexion angle reaches a larger angle than 70 degrees, the hemispheric surface 'B' starts to work as a ball-and-socket joint to enlarge the flexion angle. This system provides a large flexion angle of around 140 degrees (Akagi *et al.*, 2002).

The 'mobile knee' realizes the natural movement of the knee described above. In this method, the UHMWPE insert can rotate around the pivot installed on the tray. As a result, the patient can bend the knee easily, even up to large flexion angles (Callaghan *et al.*, 2000, Price *et al.*, 2003). In employing such a structure, it became possible to enlarge the area of contact between the femoral component and the UHMWPE insert, up to several times greater than conventional artificial knee articulation. The structure, moreover, helped to reduce the contact pressure induced in the UHMWPE insert and allowed stable articular movement. A concern with this method is that the dual sliding surfaces may produce an abundance of wear debris. It is necessary, therefore, to provide a super-mirror finish on the surfaces of the tray and femoral component.

A third method is to design the shape of the femoral condyle to allow a movement similar to the natural human knee joint. Figure 14.15 shows the shape of the femoral component and its movement opposite the UHMWPE insert. The lateral condyle of the femoral component is shaped to a flat surface, while the medial condyle is given a convex surface, then a difference in

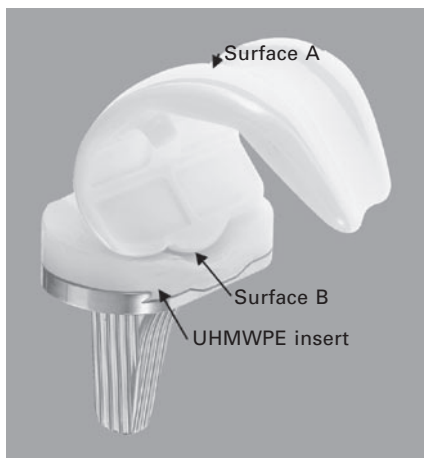

14.14 Artificial knee joint with bisurface femoral component enlarging flexion angle. Femoral component cited here is made of a ceramic (with permission from Japan Medical Materials Corp.).

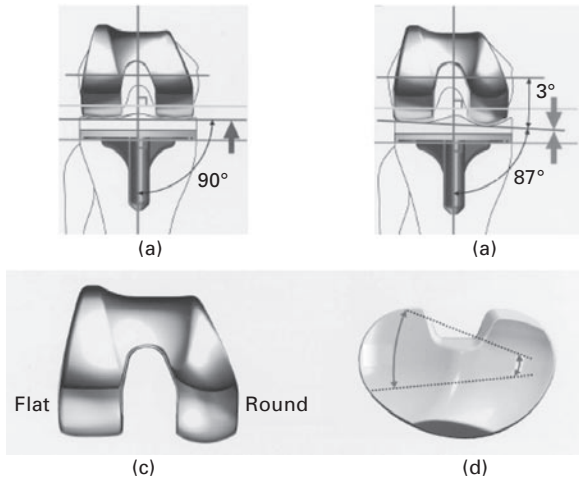

14.15 New design of femoral component providing the anatomical motion of a natural knee. (a) Conventional type of femoral component, (b) new type of femoral component; height difference of lateral and medial condyles, (c) asymmetrical shape of condyle, (d) external rotation of femoral component centering on medial condyle (with permission from Nakashima Medical Corp.).

height of about 2 mm is designed between the medial and lateral condyles. This design facilitates the generation of rotations centering on the medial condyle, making it possible to obtain a large flexion angle (Anon., 2009).

14.4 Miscellaneous joint replacement

In addition to hip and knee joints, the human skeletal structure has numerous kinds of articulation in the shoulder, elbow, wrist and hand. These joints are suited to their functions, as shown in Fig. 14.16. Hip and shoulder joints are of the ball-and-socket type, enabling movements such as bending and rotating in all directions. The elbow joint, on the other hand, is a hinge type, whose primary movement is to bend in one direction. This movement may also be assisted by a slight rotation to increase the flexion angle. The wrist joint is a so-called 'oval joint' type, making two-way movements possible. The thumb has a saddle joint, allowing it to move in two directions.

Figure 14.17 shows various kinds of artificial joints. The artificial shoulder joint (a) consists of a hemispheric head anchored to the tip of a stem and a socket. The stem is made of titanium alloy and its surface is coated with hydroxyapatite. The hemispheric head is made of either alumina ceramic or Co–Cr–Mo alloy and the socket is made of UHMWPE. The artificial elbow joint (b) has a hinge-type sliding surface. On the humeral side, the stem,

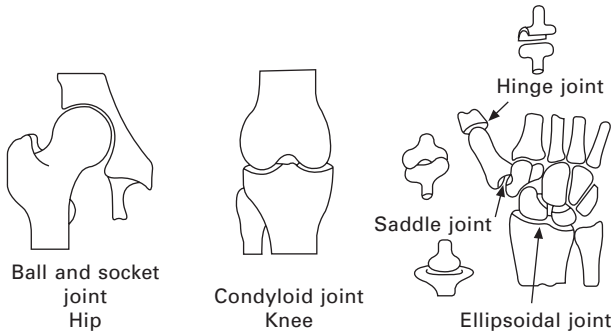

14.16 Illustration of various types of diarthrodial joints.

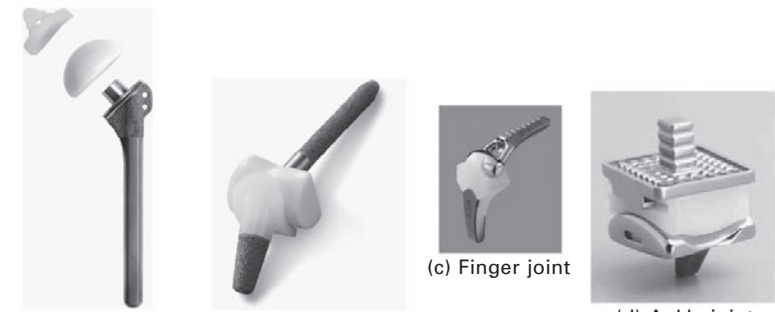

14.17 Examples of various artificial joints, (a) shoulder joint, (b) elbow joint (with permission from Japan Medical Materials Corp.), (c) finger joint, (d) ankle joint (with permission from Nakashima Medical Corp.).

made of a Co–Cr–Mo alloy, is integrated with a drum-shaped cylinder. On the ulnar side, a receiver made of UHMWPE is attached to the tip of the Co–Cr–Mo alloy stem. Using this joint system, a flexion angle ranging from 0 to 100° enables it to move accompanied with a small relative rotation of both. The artificial finger joint (c) has a structure resembling the artificial elbow joint. The sliding surfaces are a Co–Cr–Mo alloy and UHMWPE. Figure 14.17 (d) shows an example of a total ankle system. The system consists of a talar component attached to the talus side, a socket holder attached to the tibial side, and a tibial socket made of UHMWPE. In this system, the metal portion is also made of a Co–Cr–Mo alloy. The tibial socket is joined with the grooves of the socket holder; it can allow back and forth movement and medial–lateral rotation at an angle of 10 degrees without dislocation.

14.5 Implants for bone fractures

14.5.1 Materials

Human bone tissue is a composite material of apatite and collagen fibers, and has anisotropic properties. The strength and elasticity of cortical bone are at a maximum in the direction of the long bone axis, and at a minimum in the traverse direction to the bone axis. Because of these structural characteristics, bone tissue has strong resistance to compression, but not to tension or torsion. If an excessive force is applied to the arm or leg, the bone breaks; in osteoporosis the bone fractures easily. In general, implants made of stainless steel and titanium alloy are used to repair such fractures. When the bone fracture is repaired by plates, nails and screws, the rigidity of the implant material should ideally be high to incorporate bone fragments. If the cross-sectional shape is the same, stainless steel has higher rigidity than titanium alloy. This difference is taken into consideration to design implants. In view of corrosion resistance and biocompatibility, however, titanium alloy is superior to stainless steel. Since titanium materials characteristically have high affinity with the bone, a mirror finished surface is advantageous to prevent binding of bone to the implant, compared with a rough surface.

14.5.2 Compression hip nail and hip screw

When an intertrochanteric fracture occurs, a compression hip nail or compression hip screw, as shown in Fig. 14.18, is used. In the case of compression hip nail shown in Fig. 14.18, its basic structure is similar to that of the γ nail except that a lag screw slides inside the lag screw supporter attached to an intramedullary nail. This structure enables the use of a shorter lag screw.

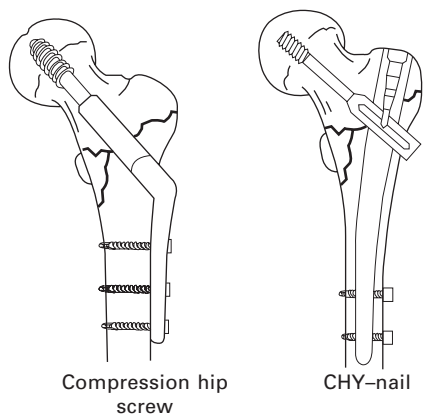

14.18 Compression hip screw and hip nail for intertrochanteric fracture.

Even if a lag screw slides during postoperative walking training, the end of the screw remains stored inside the lag screw supporter. The sliding screw therefore causes no subcutaneous irritations (Matsui *et al.*, 2001).

In the case of a compression hip screw, the plate is fixed to the femur with a screw; and the lag screw to the femoral head through a barrel integrated to the plate. Since the fixed angle of the barrel (lag screw)-plate is given in manufacturing (such as 125 degrees), the surgeon sometimes fails to join the intertrochanteric fracture, and a 'cut-off' of an internal lag screw from the femoral head sometimes occurs. A novel type of compression hip screw (CHS) has been developed to solve these problems. The angle can be continuously changed within the range of 125 to 145 degrees. Figure 14.19 shows the structure and appearance of the CHS. The angle is adjusted by applying a cam-slide mechanism. After the lag screw is pierced into an appropriate location of the femoral head, the plate is closely fixed with screws onto the femur and the crossing angle is permanently settled by using a fixing screw (Nakayama *et al.*, 2000).

14.5.3 Plate and screw

When a bone fracture occurs in diaphysis, epiphysis and metaphysis of the bone, it is repaired using a plate and screw. A plate needs to match the configuration of bone. In the case of a simple fracture of a long bone, a flat plate is set on the fractured site and fixed with a screw. In the case of a comminuted fracture, however, it is necessary to carefully gather the dispersed bone fragments and fix them. Therefore, a multiple number of mini-plates may be used for the repair (Ikeda *et al.*, 2003). To reconstruct the fractured bone to its original shape, it may also be necessary to fix it

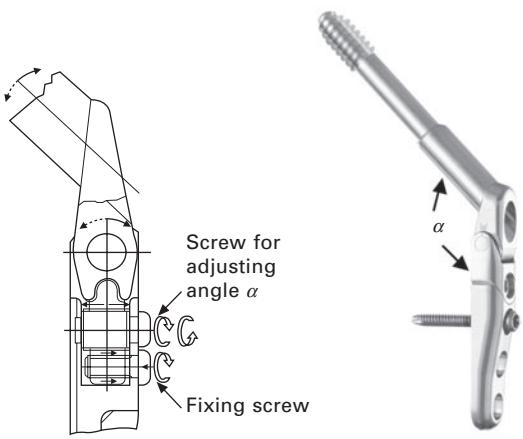

14.19 A hip screw with cam-sliding mechanism to adjust angle α.

using an anatomically-shaped plate. Figure 14.20 shows examples of various plates used for bone fractures.

14.6 Failure of orthopaedic implants

Orthopaedic implants sometimes fail due to the large force acting on the bone and the implant (Barrack, 2000). When an implant is fractured, the patient is operated on again to repair it and must tolerate excruciating pain once again. The Japanese Orthopaedic Association has investigated the failure of implants caused in 1998 in orthopaedic surgery (Anon., 2000). The surveyed results showed that breakage occurred in 1.39% of the all surveyed cases, with 46% pertaining to artificial joints, 40% to fracture repairing implants, 13% to spinal fusions and 1% to others. Failure of the implant is usually attributed to inappropriate selection of materials and inadequate considerations in designing. From the cases of failure that occurred between 1992 and 2001, as surveyed by the FDA (US Food and Drug Administration), those for artificial hip joints were extracted and the sites of failure investigated. It was found that breakage occurred in 52% of the cases in the stem, 20% in the inner cup, 14% in the ceramic ball head, 6% in the outer cup, and 8% in other components. Wear and tear was the main cause of failure of the inner cup, while the majority of other failure/breakage cases showed a fatigue breakdown. Figure 14.21 shows a typical SEM observation of a fatigue failure that occurred in the intramedullary tube. This photograph reveals that the origin of a crack near the outer surface

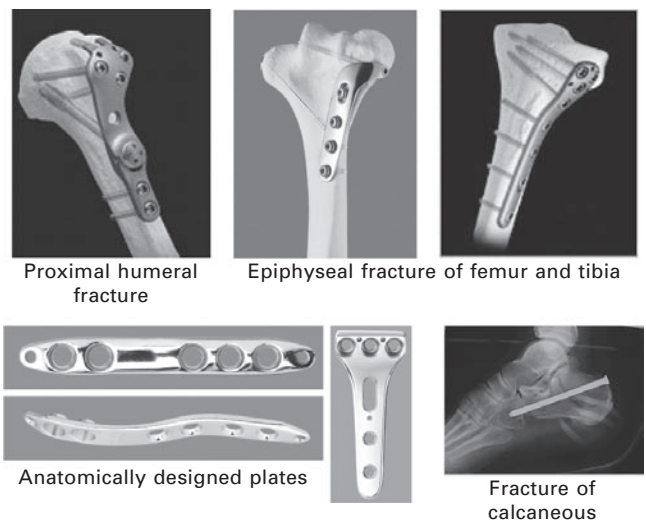

14.20 Examples of plate and screw for fractures (with permission from Nakashima Medical Corp. and Mizuho Ikakogyo Co. Ltd).

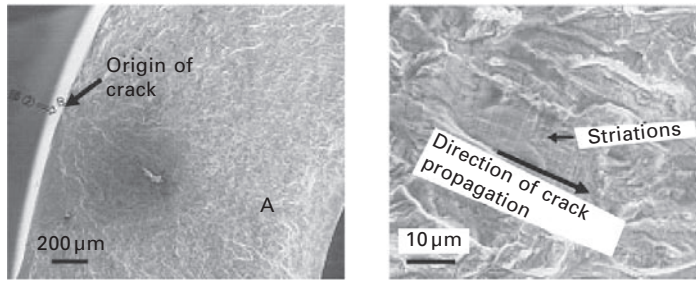

Origin of crack near the outer surface

Crack propagation through the wall observed at A

14.21 SEM observation of fracture occurring in the intramedullary tube.

Table 14.2 Causes of fracture occurring in implants

Category	Major causes
Design	Insufficient strength (material selection) Inadequate microstructure, Poor shape design, Lack of assessment Prediction of lower working force
Manufacture	Surface defects (scar, crack, dent, etc.) Degradation caused by heat treatment Sharp edge and notch in machining Poor cleaning
Clinical operation and patient	Poor filling and fracture of bone cement Unsuitable selection of implant Large load on repaired bone before healing Violent action of patient after operation

propagated into the inside of the wall due to repeated stress, as indicated by the striations. In general, fatigue is localized structural damage when an implant is subjected to cyclic loading. Therefore, fatigue life is influenced by various factors such as surface finish including notches, the microstructure of metal subjected to heat treatment in manufacturing, residual stress, and over-loading after implantation. Taking these facts into consideration, the genesis of fatigue breakdown can be classified into different groups such as (i) problems related to the design, (ii) problems related to manufacturing and (iii) clinical problems, as shown in Table 14.2.

In order to prevent an occurrence of implant failure, prior evaluation is important based on various standards such as ISO, ASTM and JIS. A variety of evaluation methods has been established, including fatigue tests of the femoral components, bending tests of plates and nails, and a twisting test for screws. Recently, it has become possible to use numerical simulations to predict the amount of stress that occurs on the implant. This method

has advantages such as time and cost saving and prediction of the stress distribution generated inside of implant when boundary conditions are appropriately selected.

14.7 Summary

As described in this chapter, numerous implants made of metallic biomaterials have been developed by the co-operation of surgeons and medical engineers for repairing diseases in the patient. Generally, metallic implants release ions and generate wear debris, and sometimes fail accidentally because the implant is exposed to a high bearing load, severe sliding motion or highly corrosive environment. To settle these problems and obtain improved longevity of implants, biocompatible metals, ceramics and polymers have been developed and devised to meet the needs of each orthopaedic disease in the last three decades. However, these are not sufficient for the future because of the increasing number of patients due to the increase of people over seventy across the world. Topics for further improvement are considered to be as follows: (i) advanced metallic materials with high strength, consisting of non-cytotoxic elements such as Ti, Zr, Ta and Nb. (ii) Designs of implants with appropriate shape and structure to fit the diseased site and with mechanical properties similar to living bone. A porous body is one of the possible available materials, and a prototyping process such as laser melting is attractive to produce the arbitrary shape and structure. (iii) Implants with dual properties such as a bioactive metal coated alumina ceramic for a sliding part. (iv) Improved longevity of implants to more than thirty years. (v) Low manufacturing costs. These objectives will be attained when surgeon and medical engineer work co-operatively.

14.8 References

Akagi M, Ueo T, Takagi H, Hamanishi C and Nakamura T (2002), 'A mechanical comparison of two posterior-stabilizing designs', *J Arthroplasty*, **17**, 627–634.

Anon. (1994), Materials Properties Handbook: Titanium Alloys. In Boyer R, Welsch G and Collings E W (eds) *Materials Properties Handbook*, ASM International, 321–336.

Anon. (2000), 'Report of failure of implants', *J Jpn Orthop Assoc*, **74**, 525–534.

Anon. (2009), *FINE total Knee System*, Catalogue of Nakashima Medical Corp.

Barker D S, Wang A W, Yeo M F, Nawana N S, Brumby S A, Pearcy M J and Howie D W (2000), 'The skeletal response to matt and polished cemented femoral stems', *J Bone Joint Surg*, **82**-B, 1182–1188.

Barrack R L (2000), 'Early Failure of Modern Cemented Stems', *J Arthroplasty*, **15**, 1036–1050.

Callaghan J J, Insall J J, Greenwald A S, Dennis D A, Komistek R D Murray D W, Bourne R B, Rorabeck C H and Dorr L D (2000), 'Mobile-bearing Knee Replacement', *J Bone Joint Surg*, **82**-A, 1020–1041.

Charnley J (1970), 'Total Hip Replacement by Low-friction Arthroplasty', *Clinical Orthopaedics and Related Research*, No.72, September–October, 7–21.

Coathap M J, Blunn G W, Flynn N, Wiliams C and Thomas N P (2001), 'A comparison of bone remodeling around hydroxyapatite-coated, porous-coated and grit-blasted hip replacements retrieved at post-mortem', *J Bone Joint Surg*, **83**-B, 118–123.

Collis D K and Mohler C G (2002), 'Comparison of Clinical Outcomes in Total Hip Arthroplasty Using Rough and Polished Cemented Stems with Essentially the Same Geometry', *J Bone Joint Surg*, **84**-A, 586–592.

Dobbs H S and Minski M J (1980), 'Metal ion release after total hip replacement', *Biomaterials*, **1**, 193–198.

Dowson D (1995), 'A comparative study of the performance of metallic and ceramic femoral head components in total replacement hip joints', *Wear*, **190**, 171–183.

Fujisawa A, Noda I, Nishio Y and Okimatsu H (1995), 'The development of new titanium arc-sprayed artificial joints', *Mater Sci Engng C2*, 151–157.

Gross K A, Berndt C C and Herman H (1998), 'Amorphous phase formation in plasma-sprayed hydroxyapatite coatings', *J Biomed Mater Res*, **39**, 407–414.

Hallab N, Merritt K and Jacobs J (2001), 'Metal sensitivity in patients with orthopaedic implants', *J Bone Joint Surg*, **80**-B, 377–381.

Hamadouche M, Boutin P, Daussange M E and Sedel L (2002), 'Alumina-on-alumina total hip arthroplasty', *J Bone Joint Surg*, **84**-A, 69–77.

Ikeda M, Yamashita Y, Kamimoto M and Oka Y (2003), 'Open reduction and internal fixation of comminuted fractures of radial head using low-profile mini-plates', *J Bone Joint Surg*, **85**-B, 1040–1044.

Ilchmann T, Markovic L, Joshi A, Hardinge K, Murphy J and Wingstrand H (1998), 'Migration and wear of long-term successful Charnley total hip replacement', *J Bone Joint Surg*, **80**-B, 377–381.

Isama K and Tsuchiya K (2002), 'Biocompatibility of titanium alloys', *Proc. 24th Annual Meeting of The Japanese Society for Biomaterials*, 194.

Issack P S, Botero H G, Hibert R N Bong M R, Stuchin S A, Zuckerman J D and DiCesare P E (2003), 'Sixteen-year follow-up of the cemented spectron femoral stem for hip arthroplasty', *J Arthroplasty*, **18**, 925–930.

Iwase T, Warashina H, Yamauchi K, Sugiura S and Hasegawa Y (2003), 'Early head penetration into cemented Hylamer Ogee socket', *J Arthroplasty*, **18**, 920–925.

Justin J, Sherfey D O and Richard W M (2006), 'Mid-term results of Exeter vs Endurance Cemented Stems', *J Arthroplasty*, **21**, 1118–1123.

Kawanabe K, Ise K, Goto K, Akiyama H, Nakamura T, *et al.* (2009), 'A new cementless total hip arthroplasty with bioactive titanium porous-coating by alkaline and heat treatment: Average 4.8-year results, *J Biomed Mater Res, Appl Biomater*, **90B**, 476–481.

Kokubo T, Miyaji F, Kim H M, Nakamura T (1996), 'Spontaneous Formation of Bonelike Apatite Layer on Chemically Treated Titanium Metals', *Am Ceram Soc*, **79–4**, 1127–1129.

Kuroda D, Niinomi M, Morinaga M, Kato Y and Yashiro T (1998), 'Design and mechanical properties of β-type titanium alloys for implant materials', *Mater Sci Eng A*, 243, 244–249.

Kyomoto M (2009), *Design of surface with hydration lubrication by phospholipid polymers for extending longevity of artificial joints*, Doctorial Dissertation, The University of Tokyo.

Livingston B J, Chemell M J, Spector M. and Poss R (1997), 'Complications of total hip arthroplasty associated with use of an acetabular component with Hylamer liner', *J Bone Joint Surg*, **79**-A, 1080–1090.

Lu Z and McKellop H (1997), 'Frictional heating of bearing materials tested in a hip joint wear simulator', *Proc Instn Mech Engrs*, **211**, Part H, 101–107.

Maehara K, Doi K, Matsushita T and Sasaki Y (2002), 'Application of vanadium-free titanium alloys to artificial hip joint', *Materials Transaction*, **43**, 2936–2942.

Matsui T, Oota Y, Saito S, Ishii J and Hasuike N (2001), 'Treatment of femoral neck fractures using compression hip Y(CHY)-nail: Analysis of lag screw sliding' (Japanese), *Orthopedic Surgery*, **52**, 768–771.

Matsuda Y, Nakamura T, Ido K, Matsushita T, Oka M (1997), 'Femoral component made of Ti–15Mo-5Zr-3Al alloy in total hip arthroplasty', *J Orthopaedic Sci*, 2, 166–170.

Meding J B, Nassif J H and Ritter M A (2000), 'Long-term survival the T-28 versus the TR-28 cemented total hip anthroplasties', *J Arthroplasty*, **15**, 928–933.

Moro T, Takatori Y, Ishihara K, Konno T, Takigawa Y, Matsushita T, Chung Ung-Il, Nakamura K and Kawaguchi H (2004), 'Surface grafting of artificial joints with a biocompatible polymer for preventing periprosthetic osteolysis', *Nature Materials Advance Online Publication*, 24-Oct.

Morscher E M and Wirz D (2002), 'Current state of cement fixation in THR', *Acta Orthopaedica Belgica*, **68**, 1–12.

Muruatoglu O K, Bragdon C R, O'Connor D O, Jasty M and Harris W H (2001), 'A Novel Method of Cross-linking Ultra-High-Molecular-Weight Polyethylene to Improve Wear, Reduce Oxidation, and Retain Mechanical Properties', *J. Arthroplasty*, **16**, 149–160.

Nakayama I, Kobori M, Kamisato S, Yoshida M, *et al*. (2000), 'Development and clinical results of the adjustable sliding hip screw' (Japanese), *Orthopedic Surgery (separated volume)*, 37, 122–126.

Nishiguchi S, Kato H, Fujita H, Oka M, Kim H M, Kokubo T and Nakamura T (2001), 'Titanium metals form direct bonding to bone after alkali and heat treatments', *Biomaterials*, **22**, 2525–2533.

Okazaki Y, Rao S, Ito Y and Tateishi T (1998), 'Corrosion resistance, mechanical properties, corrosion fatigue strength and cytocompatibility of new Ti alloys without Al and V', *Biomaterials*, **19**, 1197–1215.

Oonishi H, Kadoya Y and Masuda S (2001), 'Gamma-irradiated cross-linked polyethylene in total hip replacement: Analysis of retrieved sockets after long term implantation', *J. Biomed Mater Res (Appl Biomat)*, **58**, 176–171.

Price A J, Rees J L, Beard D, Juszczk E, Carter S, White S, Steiger R, Dodd, C A F, Gibbons M, Smith P M, Goodfellow J W and Murray D W (2003), 'A mobile- bearing total knee prothesis compared with a fixed-bearing prosthesis', *J Bone Joint Surg*, **85**-B, 62–67.

Saikko V S, Pavolainen P O and Slatis P (1993), 'Wear of the polyethylene acetabular cup – metallic and ceramic heads compared in hip simulator', *Acta Orthop Scand*, **64**, 391–402.

Semlitsh M, Staub F and Weber H (1985), 'Titanium–Aluminum–Niobium Alloy, Development for Biocompatible, High Strength Surgical Implant', *Biomed Tech*, **30**, 334–339.

Skinner J A, Todo S, Talor M, Wang J S, Pinskerova V and Scott A (2003), 'Should the cement mantle around the femoral component be thick or thin', *J Bone Joint Surg*, **85**-B, 45–52.

Spector M, Reis M D, Boune R B, Sauer W S, Long M and Hunter G (2001), 'Wear Performance of Ultra-High Molecular Weight Polyethylene on Oxidized Zirconium Total Knee Femoral Components', *J Bone Joint Surg*, **83**-A, Supplement 2, Part 2, 80–86.

Steinemann S G (1980), *Evaluation of Biomaterials*, John Wiley & Sons Ltd.
Tomita N, Kitakura T, Onmori N, Ikeda Y and Aoyama E (1999), 'Prevention of Fatigue Cracks in UHMWPE Joint Components by Addition of Vitamin E', *J Biomed Mater Res (Appl Biomater)*, **48**, 474–478.
Weightman B and Light D (1986), 'The effects of the surface finish of alumina and stainless steel on the wear rate of UHMW polyethylene', *Biomaterials*, **7**, 20–24.
Wroblewski B M, Siney P D and Fleming P A (2001), 'Triple Taper Polished Cemented Stem in Total Hip Arthroplasty', *J Arthroplasty*, **16**, No. 8 Suppl, 37–41.
Yamamuro T and Takagi H (1991), 'Bone bonding behaviour of biomaterials with different surface characteristics under load-bearing conditions'. In J. E. Davies (ed.) *The Bone–Material Interface*, University of Toronto, 406–414.

15
New-generation metallic biomaterials

T. NARUSHIMA, Tohoku University, Japan

Abstract: In this chapter, the current status of metallic biomaterials and the research and development of new-generation metallic biomaterials are discussed. First, the traditional metallic biomaterials are reviewed. The alloy design and properties of the new metallic biomaterials and the new processing technologies used in fabricating porous metallic biomaterials and in grain refining are then discussed. This chapter focuses on the following metallic biomaterials: stainless steels, cobalt (Co)-chromium (Cr) alloys, titanium (Ti) and its alloys, magnesium (Mg) alloys, and bulk metallic glasses. Finally, the future trends in new-generation metallic biomaterials are presented.

Key words: stainless steel, Co–Cr alloy, titanium, Mg alloy, processing technology.

15.1 Introduction

The proportion of aged people in the population is rapidly growing in advanced countries, as well as in developing countries. It is predicted that the numbers of patients suffering due to injuries sustained during falls and deterioration of body functions will increase in this super-aged society. In order to improve the quality of life of these patients, dental and medical technologies have to improve further to enable reconstruction of the human body. Highly functional and safe biomaterials can contribute to the development of dental and medical technologies and tissue engineering. Owing to the mechanical strength and ductility of metallic biomaterials, they can replace damaged hard tissue (Niinomi, 2002). It is known that more than 70% of medical implants are made of metallic biomaterials such as stainless steels, Co–Cr alloys, and Ti and its alloys.

Figure 15.1 shows the weight of biomaterials used in orthopaedics in Japan in recent years (Narushima, 2005). Co–Cr alloys and Ti alloys have been mainly used in orthopaedics; biomaterials of high mechanical strength and excellent ductility are required in this field. Metallic biomaterials have been widely used as implants in medical and dental fields, and cannot be equalled by ceramic or polymer biomaterials from the point of view of mechanical properties. Almost all metals are thermodynamically unstable under biological conditions. The corrosion of metallic biomaterials cannot be avoided; oxide films are formed as corrosion products under biological conditions (Blackwood, 2003). Oxide films, such as Cr oxide and Ti oxide, are uniform and dense, and act as protective passive films with excellent

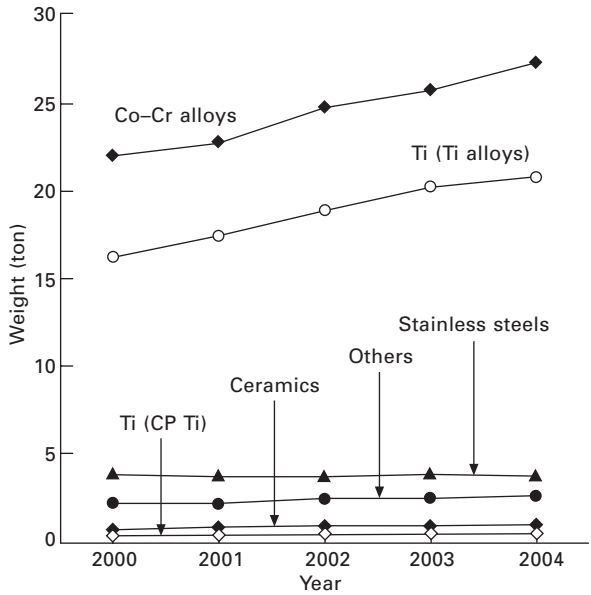

15.1 Biomaterial usage (by weight) in orthopaedics in Japan.

adhesion to metallic biomaterials. However, there is the possibility of scratching and deterioration of sliding or load-bearing parts in implants, such as artificial hip and knee joints (Hanawa, 2004). This means that the bulk metallic biomaterials should be durable and safe.

With improvements in medical and dental technologies and tissue engineering, properties such as low elastic modulus, shape memory effect/superelasticity, wear resistance, superplasticity, and hot/cold workability are desirable in biomaterials. These properties should be achieved in practical devices of various shapes under a range of biological and economic conditions.

In this chapter, the current status of metallic biomaterials and the research and development of new-generation metallic biomaterials are discussed.

15.2 Brief overview of traditional metallic biomaterials

Table 15.1 shows the chemical compositions of the stainless steels, Co–Cr alloys, and Ti and its alloys registered in the ASTM (American Society for Testing and Materials) standards for surgical implant applications. The contents of alloying elements are hereafter expressed as percentage masses. These metallic biomaterials are used as substitutes in hard-tissue replacements such as artificial hip and knee joints, fracture healing aids, spinal fixation

Table 15.1 Chemical composition of metallic biomaterials registered in the ASTM standards (mass%)

Stainless steels	Co–Cr alloys	Ti and its alloys
Fe–18Cr–14Ni–2.5Mo (C<0.03) F138–08, wrought (bar and wire) F139–08, wrought (sheet and strip) F1350–08, wrought (wire) F2257–03, wrought (tube)	Co–28Cr–6Mo F75–07, castings	CP Ti, α type F67–06 Grade 1 Grade 2 Grade 3 Grade 4
Fe–18Cr–12.5Ni–2.5Mo F745–07, cast and solution-annealed	Co–28Cr–6Mo F1537–07, wrought H799–06, wrought (forgings)	Ti–6Al–4V, $\alpha + \beta$ type F1108–04, castings F1472–02, wrought
Fe–22Cr–13Ni–5Mn–2.5Mo (C<0.03, 0.2<N<0.4) F1314–07, wrought (bar and wire)	Co–20Cr–15W–10Ni F90–07, wrought F1091–08, wrought (wire)	Ti–6Al–4V ELI*, $\alpha + \beta$ type F136–02, wrought
Fe–21Cr–10Ni–3Mn–2.5Mo (0.25<N<0.5) F1586–08, wrought (bar)	Co–35Ni–20Cr–10Mo F562–07, wrought F688–05, wrought (plate, sheet, and foil) F961–03, wrought (forgings)	Ti–6Al–7Nb, $\alpha + \beta$ type F1295–05, wrought
Fe–23Mn–21Cr–1Mo (0.85<N<1.10) F2229–07, wrought (bar and wire)	40Co–20Cr–16Fe–15Ni–7Mo F1058–08, wrought (wire and strip)	Ti–3Al–2.5V, $\alpha + \beta$ type F2146–07, wrought (seamless tube)
Fe–11Mn–17Cr–3Mo (0.45<N<0.55) F2581–07, wrought (bar and wire)		Ti–13Nb–13Zr, near β type F1713–08, wrought
		Ti–12Mo–6Zr–2Fe, β type F1813–06, wrought
		Ti–15Mo, β type F2066–07, wrought
		NiTi, intermetallics F2063–05, wrought

*ELI: extra low interstitial

devices, dental implants, vascular stents, catheter guide wires, orthodontic dental archwires, and cochlea implants, because of their excellent mechanical and functional properties (Park and Kim, 2003). Figure 15.2 summarizes the minimum requirements in the ASTM standards for tensile strength and total elongation for metallic biomaterials. Stainless steels exhibit excellent hot/cold workability and are relatively low-cost biomaterials. Co–Cr alloys generally exhibit high mechanical strength and excellent wear resistance, but their hot/cold workability is low if nickel (Ni) is not added. Although the mechanical strength and ductility and wear resistance of Ti and its alloys are inferior to stainless steels and Co–Cr alloys, their corrosion resistance and biocompatibility are exceptional.

15.2.1 Stainless steels

Austenitic stainless steels are registered in the ASTM standards for surgical implant applications, as listed in Table 15.1. The main alloying elements are Cr, Ni, molybdenum (Mo), manganese (Mn), and nitrogen (N). Cr accelerates passivation and improves corrosion resistance in oxidizing acid solutions and pitting corrosion resistance in chloride solutions, but it is a ferrite-stabilizing element. Ni stabilizes the austenitic phase and improves corrosion resistance in nonoxidizing acid solutions by stabilizing the passive film. However, Ni has been pointed out to be highly associated with metal allergy and toxicity when Ni ions elute from the implants into the human

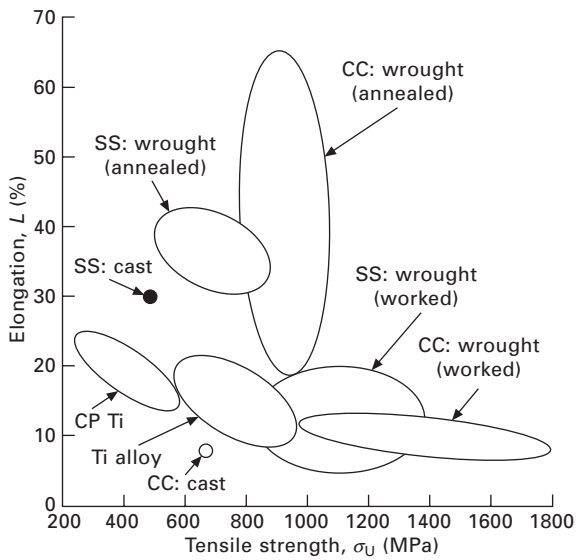

15.2 Tensile strength and elongation of stainless steels (SS), Co–Cr alloys (CC), and CP Ti and Ti alloys registered in the ASTM standards.

body. Mo contributes to the stability of the passive film and improves the corrosion resistance in chloride solutions. Mn stabilizes the austenitic phase, increases the N solubility and lowers the magnetic susceptibility; however, it lowers the corrosion resistance. Increasing the N content is preferred from the point of view of stabilization of the austenitic phase, strengthening, and corrosion resistance; however, Cr_2N may precipitate during heat treatment when the N content is higher than the solubility value at the heat treatment temperature. Cr_2N precipitation results in a decrease in ductility and corrosion resistance. Therefore, the maximum N content in biomedical stainless steels is limited to 1mass%. The addition of Cr and Mn is known to increase N solubility in stainless steels.

The wrought stainless steels are low carbon (C) iron (Fe)–Ni–Cr–Mo alloy (type 316L), high N Fe–Cr–Ni–Mn–Mo alloy and high N and Ni-free Fe–Cr–Mn–Mo alloys. Type 316 L stainless steel has been mainly used in implants. Reduction of C content to less than 0.03mass% minimizes sensitization; the sensitization is caused by the formation of a Cr-depleted zone due to the grain-boundary precipitation of $Cr_{23}C_6$, lowering the corrosion resistance.

15.2.2 Co–Cr alloys

Since the 1900s, it has been known that Co-based alloys exhibit excellent wear resistance. In the 1930s, cast Co–Cr–Mo alloy (Vitallium) was developed for dental applications. Cast and wrought Co–Cr alloys have been recognized as the most suitable biomaterials for sliding parts in artificial joints because of their higher wear resistance compared to stainless steels and Ti materials.

Cast Co–28Cr–6Mo alloy (ASTM F75) has been used in the stem, ball and cup of artificial hip joints of both metal-on-UHMWPE (ultrahigh molecular weight polyethylene) and metal-on-metal types, and sliding components of artificial knee joints. The F75 alloys usually contain approximately 0.25mass% C; the carbide precipitates lead to an increase in the wear resistance. The carbide is mainly the $M_{23}C_6$ type. Since the carbides are formed during the cast process, the effects of the investment cast conditions such as mould temperature and pouring temperature on the microstructure of the as-cast F75 alloys have been studied (Gómez *et al.*, 1997). As-cast F75 alloys are subjected to heat treatments such as hot isostatic pressing (HIP) to remove cast defects and improve ductility. The phase and dissolution behaviour of precipitates in as-cast alloys during heat treatment has been investigated (Caudillo *et al.*, 2002).

The Co–Cr alloys in Co–Cr-tungsten (W)–Ni (ASTM F90, F1091), Co–Ni–Cr–Mo (ASTM F562), and Co–Cr–Fe–Ni–Mo (ASTM F1058) systems, which contain Ni as an alloying element, are used as wrought materials. Since they exhibit excellent hot/cold workability and can be strengthened by

cold working, they have been used in vascular stents, intracranial aneurysm clips, orthodontic dental archwires, and fracture healing aids such as bone plates and wires. The workability of Co–Cr–Mo alloys without Ni addition is considered to be inferior to that of Ni-containing alloys. Low Ni and low C Co–29Cr–6Mo alloy can be forged at temperatures above 1273 K; this temperature has to be strictly maintained during forging (Chiba *et al.*, 2005).

15.2.3 Ti and its alloys

Titanium (Ti) and its alloys are lightweight, nonmagnetic materials that exhibit excellent corrosion and mechanical properties. They show very good biocompatibility, producing few allergic reactions. In addition, Ti possesses a unique property known as osseointegration (Brånemark *et al.*, 1977). Osseointegration refers to the direct bonding between Ti and bone at an optical microscopic level; due to this property, Ti materials exhibit excellent biocompatibility with bone. Because of their excellent properties as biomaterials, Ti and its alloys have been widely used to manufacture medical and dental implants for hard-tissue replacements, especially for parts where long-term contact with bone is expected.

Among the Ti materials, α type commercially pure (CP) Ti and $\alpha + \beta$ type Ti–6 aluminium (Al)-4 vanadium (V) alloy are the most widely used for biomedical applications. The Ti–6Al–4V alloy possesses higher mechanical strength than CP Ti. Because of concerns about potential cytotoxicity of V and potential neurotoxicity of Al, research regarding alloy designs of V-free and Al-free $\alpha + \beta$ type Ti alloys has been conducted since the 1980s (Okazaki *et al.*, 1998). In the 1990s, finite element studies and animal studies suggested the effectiveness of low elastic modulus biomaterials in hip prostheses (Wang, 1996). The mismatch between the elastic moduli of the biomaterials and the surrounding bone has been considered to be the main reason for implant loosening and stress shielding of bone. The development of metallic biomaterials with a lower elastic modulus has been conducted in β type Ti alloys in Ti–niobium (Nb) and Ti–Mo systems.

It is well known that NiTi exhibits shape memory effect and superelasticity, and is practically applied to orthodontic dental archwires, catheter guide wires, intracranial aneurysm clips, orthopaedic staples, and vascular stents. Recently, Ni-free Ti- based alloys with shape memory effect and superelasticity have been developed in Ti–Nb and Ti–Mo systems (Chai *et al.*, 2008). Since the reversible and thermoelastic transformation between β phase and α'' phase in β type Ti alloys is associated with the shape memory effect and superelasticity, the shape memory and superelastic Ti-based alloys in the composition range close to that of the low elastic modulus β type Ti alloys have been investigated.

15.3 Newer alloys as metallic biomaterials

New alloys as metallic biomaterials and their fabrication processes are described here, focusing on stainless steels, Co–Cr alloys, and Ti and its alloys. Other metallic biomaterials will be discussed in Section 15.5.

15.3.1 Stainless steels

In order to avoid possible Ni allergy problems, the development of Ni-free stainless steels has been studied. Table 15.2 lists the chemical composition, manufacturing processes, and mechanical properties of the Ni-free stainless steels developed thus far. Ni-free stainless steels such as Fe–(15–18)Cr–(10–12)Mn–(3–6)Mo–0.9N (Uggowitzer *et al.*, 1996), Fe–18Cr–18Mn–2Mo–0.9N (Menzel *et al.*, 1996), and Fe–(19–23)Cr–(21–24)Mn–(0.5–1.5)Mo–(0.85–1.1)N (Gebeau and Brown, 2001) in the Fe–Cr–Mn–Mo–N system have been developed. The significant aspects of the alloy design are the stability of the austenitic phase, corrosion resistance, and mechanical properties. Ni-free stainless steels are expected to be used in wires, bone screws, and bone plates, which are fabricated by cold working processes. Therefore, the stability of the austenitic phase with a lower magnetic susceptibility for excellent MRI compatibility is required, even after the cold working process. During the cold working process, a stress-induced martensitic transformation might occur.

As described in Section 15.2, the addition of Mn to stainless steels lowers their corrosion resistance. Ni–free stainless steels in the Fe–Cr–N and Fe–Cr–Mo–N systems have been developed using the processes consisting of forming and N-absorption treatment (Kuroda *et al.*, 2003). N-absorption treatment was conducted at 1473 K in an N_2 gas pressure of 1 atm for ferritic Fe–24Cr and Fe–24Cr–2Mo alloys. After treatment for 86.4 ks, an austenized region with a thickness of 1.5 mm was obtained in these alloys. The N content in the region was reported to be approximately 0.9mass%. Grain growth was noted during the heat treatment process.

The alloy design and manufacturing of Ni-free stainless steels for biomedical applications will be carried out from the point of view of stability of the austenitic phase, corrosion resistance, magnetism and workability. N seems to be an essential alloying element for Ni-free stainless steels. A cost-effective N-addition process, removal of impurities, and suppression of grain growth are important for fabrication of new-generation Ni-free stainless steels.

15.3.2 Co–Cr alloys

Co–Cr alloys are the main metallic biomaterials used in orthopaedics, as shown in Fig. 15.1. Both cast and wrought Co–Cr alloys have been noted in the use of artificial hip joints.

Table 15.2 Ni-free stainless steels for biomedical applications

Chemical composition (mass%)	Manufacturing process	Tensile strength (MPa)	Elongation (%)	Ref.
Fe–(15–18)Cr–(10–12)Mn–(3–6)Mo–0.9N	Pressure electroslag remelting and counter pressure casting	981–1110 (Forged and solution annealed)	53–70 (Forged and solution annealed)	Uggowitzer *et al.*, 1996
Fe–18Cr–18Mn–2Mo–0.9N	Pressure electroslag remelting	(0.2% proof stress) 600 (annealed) 2100 (50% cold worked)		Menzel *et al.*, 1996
Fe–(19–23)Cr–(21–24)Mn –(0.5–1.5)Mo–(0.85–1.1)N	Electroslag remelting	931 (annealed) 2206 (80% cold worked)	49 (annealed) 3 (80% cold worked)	Gebeau and Brown, 2001
Fe–24Cr–1N	Forming and nitrogen absorption, (1473K, 1atm, ~129.6ks)	800	25	Kuroda *et al.*, 2003
Fe–24Cr–2Mo–1N	Forming and nitrogen absorption, (1473K, 1atm, ~129.6ks)	1000	45	Kuroda *et al.*, 2003

Cast Co–Cr alloy

The strength, wear resistance, and corrosion resistance in cast Co–Cr–Mo alloys can be improved by optimization of their chemical compositions and microstructures. ASTM F75 standards allow the addition of C up to 0.35mass%. The carbides formed during the cast process affect not only the wear resistance, but also the mechanical properties and corrosion resistance. Therefore, it is important to understand the effects of the alloying elements, heat treatment, and cast conditions on the phase, size, shape, and distribution of carbides in the Co–Cr alloy matrix. An understanding of the reaction of carbides in the Co–Cr–Mo–C system is also required to produce high-performance cast F75 Co–Cr alloys (Ramírez-Vidaurri *et al.*, 2009).

Fine distribution of hard carbide appears to be effective in cast Co–Cr alloys because of the precipitation strengthening. $M_{23}C_6$ type carbide and intermetallic σ phase are usually observed as precipitates in as-cast ASTM F75 Co–Cr alloys (Caudillo *et al.*, 2002). The precipitate of the hard carbide, such as the M_7C_3 type, and suppression of the formation of the σ phase will improve the wear and mechanical properties of the alloy. The addition of a small amount of alloying element to F75 Co–Cr alloys is an effective way of controlling the microstructure. The addition of Zr (Lee *et al.*, 2007) or boron (B) (Chiba and Nomura, 2009) to F75 Co–Cr alloys has been reported to be effective in producing a fine microstructure under as-cast conditions. The addition of N is know to be effective for improvement of mechanical properties in as-cast F75 Co–Cr alloys, though the function of solute N in Co–Cr alloys has not been clarified in detail. In F75 Co–Cr alloys, an N content of up to 0.2mass% is permissible. Increase in the Cr content up to 34mass%, which is greater than that in the F75 composition range, was reported to be effective in increasing the N solubility in Co–Cr alloys and in improving mechanical strength and ductility (Lee *et al.*, 2008).

Wrought Co–Cr alloy

The main topic in the research and development of wrought Co–Cr alloys is the improvement of its hot/cold workability without addition of Ni. The suppression of the grain-boundary precipitation of carbides and intermetallics and the stabilization of the γ phase, which exhibits considerably better plastic deformability than the ε phase, are required. Lower C content, as compared with cast Co–Cr alloys, is preferred for wrought Co–Cr alloys in order to suppress the carbide formation to achieve workability. On the other hand, C is known to be a γ-stabilizing element, so that the solute C, not precipitated, may contribute to the improvement of workability. Consequently, studies on the utilization of solute C in wrought Co–Cr alloys might be important. N is also a γ-stabilizing element. It has been reported that the addition of N

improves the hot-working properties of Co–28Cr–6Mo–0.16N at temperatures in the range of 1273–1473 K (Chiba *et al.*, 2009). Excellent hot/cold workability similar to ASTM F90, F562, and F1058 alloys is desirable for the new-generation wrought Ni-free Co–Cr alloys.

15.3.3 Ti and its alloys

β type Ti alloys

The elastic moduli of stainless steels and Co–Cr alloys are more than 200 GPa, and α type and α + β type Ti materials have elastic moduli of 90–110 GPa, which are much larger than that of cortical bones (10–30 GPa). β type Ti alloy is known to exhibit a lower elastic modulus than α type and α + β type Ti materials; therefore, the β type Ti alloy is considered to be the first candidate for low elastic modulus metallic biomaterials.

Alloy design in the case of Ti–Mo and Ti–Nb systems, including other biocompatible alloying elements such as tantalum (Ta) and zirconium (Zr), has been studied. Figure 15.3 shows the post-annealing elastic modulus, tensile strength, and total elongation of the β type Ti alloys that have been developed thus far (Narushima, 2005). Elastic moduli of approximately 80 GPa were reported in the Ti–Mo systems, such as Ti–12Mo–6Zr–2Fe (Wang *et al.*, 1993), Ti–15Mo–2.8Nb–0.2 silicon (Si)–0.28 oxygen (O) (Fanning, 1996), and Ti–15Mo (Zardiackas *et al.*, 1996), and elastic moduli of 50–60 GPa were achieved in the Ti–Nb systems such as Ti–35.3Nb–5.1 Ta–7.1Zr

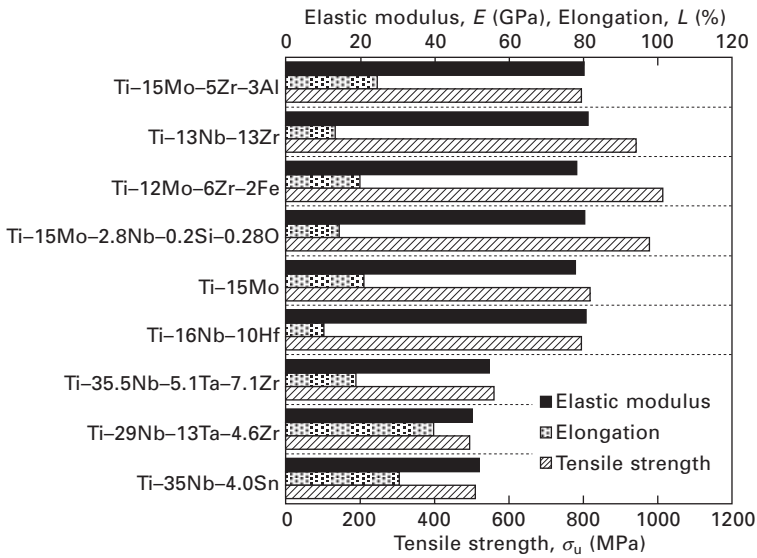

15.3 Mechanical properties of low elastic modulus β-type Ti alloys.

(Ahmed *et al*., 1996), Ti–29Nb–13Ta–4.6Zr (Kuroda *et al*., 1998), and Ti–35Nb–4.0 tin (Sn) (Matsumoto *et al*., 2005). As seen in Fig. 15.3, the β type Ti alloys with low elastic moduli tend to have lower mechanical strength after annealing. However, both low elastic modulus and high mechanical strength could be achieved after cold rolling of the β type Ti alloys in the Ti–Nb system (Saito *et al*., 2003; Matsumoto *et al*., 2005).

Recently, the anisotropy of the elastic modulus in the β type Ti alloy single crystal has been studied. Figure 15.4 shows the crystallographic anisotropy of the elastic moduli of β type Ti–29Nb–13Ta–4.6Zr alloy single crystal (Tane *et al*., 2008). The elastic modulus of β type Ti alloy single crystal strongly depends on the crystallographic orientation, where that in the <100>-direction is the lowest of all crystallographic orientations and that in the <111>-direction is the highest. The elastic modulus in the <100>-direction is approximately 35 GPa; which is half that in the <111>-direction and is similar to that of human cortical bones. These results imply that polycrystals with a texture in which the crystallographic <100> directions are oriented or single crystals whose <100> directions are oriented along the loading direction in human bones are promising candidates for biomedical implants with elastic moduli comparable to the elastic modulus of human bones.

Ti alloys with shape memory effect and superelasticity

Shape memory and superelastic Ti-based alloys for biomedical applications have been developed in Ti–Nb–Sn, Ti–Nb–Al, Ti–Mo–gallium (Ga), Ti–Mo–Sn, Ti–Nb–O, and Ti–Nb–Zr systems. It has been noted that the elastic

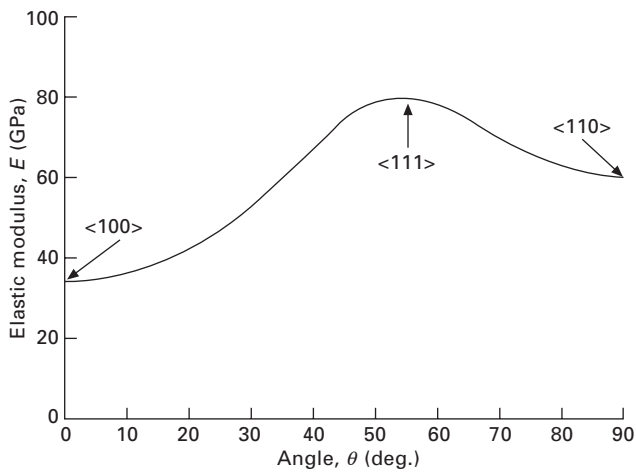

15.4 Orientation dependence of elastic moduli of Ti–29Nb–13Ta–4.6Zr single crystal in directions between <100> and <110>.

strain of these alloys was approximately 3%, which is much less than that of NiTi. Texture control by cold rolling and heat treatment in Ti–22Nb–6Al alloys (Kim *et al.*, 2006) and an increase in the critical stress for permanent deformation by the addition of interstitial solute elements in Ti–22Nb alloys (Kim *et al.*, 2005) were reported to be effective in improving their shape memory and superelastic properties.

Low-cost Ti alloys

Although not originally developed as biomaterials, the $\alpha + \beta$ type Ti–Fe–O–N alloys represented by Ti–1Fe–0.35O–0.01N alloy (Fujii, 2003) have been evaluated for dental applications because of their higher strength compared to CP Ti and lower fabrication cost compared to Ti–6Al–4V alloy (Koike *et al.*, 2005). Their strength and ductility are in the intermediate range between CP Ti and Ti–6Al–4V alloy. Their fabrication cost is relatively low because they do not contain expensive rare metals, such as Ta, Nb, Zr, Mo, or scandium (Sc). They contain Fe and O, which are the main impurity elements in sponge Ti produced by the Kroll process. In addition, the concerns of possible toxicity with Fe and O are considered to be very low. Therefore, the $\alpha + \beta$ type Ti–Fe–O–N alloys are promising low-cost metallic biomaterials.

Thus far, the use of low-cost elements for fabrication of low elastic moduli or shape memory and superelastic β type Ti alloys has not significantly progressed. High chemical affinity with many other elements and their high solubility are unique properties in Ti. The utilization of inexpensive, common β-stabilizing elements such as Mn, Si, Cr, or Fe is a key issue for research and development of low-cost β type Ti alloys with high mechanical and biological performance. The low-cost β type Ti–13Cr–1Fe–3Al alloy (Ogawa *et al.*, 2007), developed for welfare goods, such as wheelchairs, was reported to have excellent biocompatibility. This alloy could be applied in the biomedical field.

15.4 Novel processing technologies for metallic biomaterials

The new processing technologies for fabricating porous metallic biomaterials and grain refining are discussed with the focus on Ti and its alloys.

15.4.1 Porous metallic biomaterials

Many fabrication methods, such as sintering metal powder, space holder methods, combustion synthesis, plasma spraying, decomposition of foaming agents, and rapid prototyping (Ryan *et al.*, 2006) for porous metallic

biomaterials have been proposed. A low elastic modulus is one of the advantages of porous metallic biomaterials. Porous CP Ti (Oh *et al.*, 2003) and β type Ti–15Mo–5Zr–3Al alloy (Nomura *et al.*, 2005) exhibit elastic moduli similar to cortical bone at a porosity of approximately 25–30%, as shown in Fig. 15.5. The appropriate balance between elastic modulus and mechanical strength has to be established in bulk porous biomaterials because introducing pores into the bulk body lowers the tensile and fatigue strengths. Porous Ti has been considered to be the scaffold for bone regeneration and tissue engineering (Karageorgiou and Kaplan, 2005). Controlling the porosity, and the size, shape, and distribution of pores in bulk porous Ti, is essential for a scaffold with the proper strength and biocompatibility. In addition, since osteogenesis is known to be affected by the direction of pores in bulk porous materials (Nakano *et al.*, 2006), the pore direction should be considered in the design of the scaffolds.

Rapid prototyping technology has received much attention for fabricating porous biomaterials. Since rapid prototyping can create complex three-dimensional components from a computer model of the parts using layer-by-layer construction (Ryan *et al.*, 2006), it allows precise control of porosity and size, shape, distribution, and direction of pores in the parts. Bulk porous Ti implants and scaffolds have been fabricated using rapid prototyping technology in combination with the investment cast process (Lopez-Heredia *et al.*, 2008), the powder metallurgy technique (Ryan *et al.*, 2008), and 3D

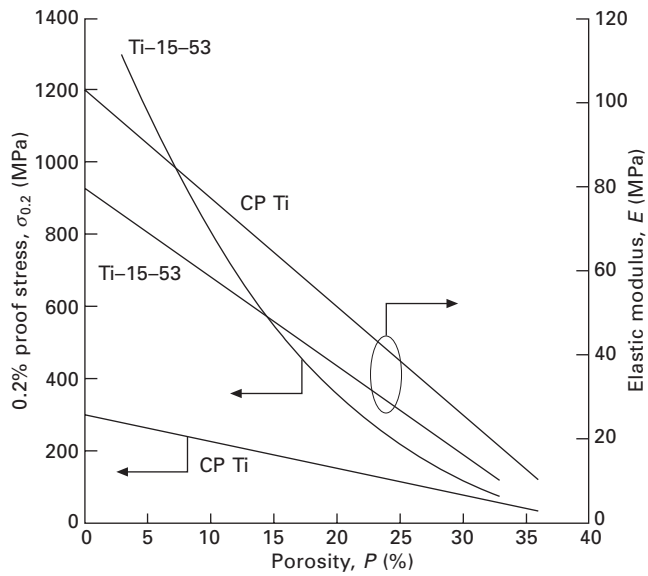

15.5 0.2% proof stress in three-point bending tests, and elastic modulus of porous CP Ti and Ti–15Mo–5Zr–3Al (Ti–15–53).

fibre deposition (Li *et al.*, 2007). The biological performances of these methods are being studied. Rapid prototyping in combination with laser or electron beam melting/sintering is another promising process that does not involve post casting or sintering. In this process, bulk porous Ti implants can be directly fabricated using layer-by-layer selective melting/sintering of Ti powder (Hollander *et al.*, 2006). Figure 15.6 shows the appearance of porous Ti–6Al–4V alloy blocks with various sizes of pores, directly fabricated by rapid prototyping in combination with electron beam melting (Nakano and Ishimoto, 2009). Rapid prototyping technologies can also be applied to other metallic biomaterials. A Co–Cr alloy implant with controlled surface topography has been produced by rapid prototyping in combination with investment casting and laser sintering (Hunt *et al.*, 2005).

The surface treatment of bulk porous Ti is related to its bone formation ability. Calcium phosphate coating (Lopez-Heredia *et al.*, 2008) and NaOH-treatment + heating (Fujibayashi *et al.*, 2004) have been examined as methods of surface treatment of porous Ti. Bone formation on the surface of porous CP Ti blocks, fabricated by plasma spraying, was observed in the dorsal muscles of mature beagle dogs twelve months after implantation (Fujibayashi *et al.*, 2004). The acceleration of bone formation on the surface of porous Ti blocks was achieved by optimization of the processes in NaOH-treatment +

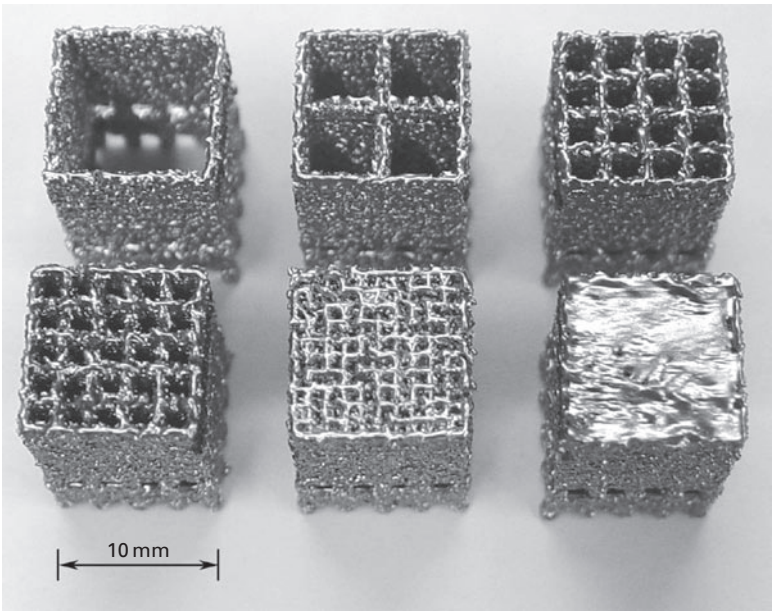

15.6 Appearance of porous Ti–6Al–4V alloy blocks (courtesy of Prof. Nakano, Osaka University, Japan).

heating; that is, bone formation was observed within three months (Takemoto *et al.*, 2006). Bone formation on a porous Ti–6Al–4V alloy cylinder produced by a positive replica technique with and without an octacalcium phosphate ($Ca_8H_2(PO_4)_6 \bullet 5H_2O$, OCP) coating was studied both in the back muscle and in the femur of goats. The OCP was coated on the porous Ti by immersion in simulated body fluids. Bone formation on both the back muscle and femur was found in OCP-coated porous Ti–6Al–4V alloy implants after 6 and 12 weeks (Habibovic *et al.*, 2005). These results show that osteoinductivity can be introduced in Ti by achieving a proper porous structure and by surface treatment; osteoinductivity is an added advantage of using Ti materials in artificial bones and scaffolds.

15.4.2 Crystal-grain refinement

Crystal-grain refinement in metallic materials is a common method of improving the balance of strength and ductility. In this section, recent advances in the processes of grain refining of $\alpha + \beta$ type and β type Ti alloys are discussed. Since a microstructure with a grain size of 1–2 μm can be obtained in biomedical $\alpha + \beta$ type Ti alloys by thermomechanical treatments (Hirano *et al.*, 2007), a microstructure with submicron-sized grains is targeted.

Hydrogen treatment

Hydrogen treatment, wherein hydrogen is used as a temporary alloying element, is an interesting method for grain refinement in $\alpha + \beta$ type Ti alloys. This treatment consists of three processes: (i) hydrogen absorption in a hydrogen atmosphere, (ii) martensitic transformation and heat treatment/hot working to cause finely dispersed hydride precipitates, and (iii) hydrogen desorption and recrystallization in a vacuum. It is known that absorption and desorption of hydrogen in a hydrogen atmosphere and in a vacuum, respectively, are completed within a very short period of time. The main mechanisms of microstructure refinement in the hydrogen treatment are as follows: (i) martensitic transformation makes the microstructure fine and homogeneous by division of the β-grains, and (ii) hydride precipitation promotes homogeneous and equiaxed precipitation of the α phase.

It has been reported that superplastic elongation values reaching 9000% were observed in hydrogen-treated Ti–6Al–4V and Ti–1Fe–0.35O alloys, obtained in tensile tests at 1123 K and 1098 K, respectively. Denture bases were fabricated by superplastic formation of hydrogen-treated Ti–6Al–4V alloy (Nakahigashi and Yoshimura, 2002). Hydrogen treatment of $\alpha + \beta$ type Ti alloys in combination with superplastic forming is a suitable technique to fabricate implants with complicated shapes and small production mass. As described above, hydrogen treatment is effective in the grain refinement of

$\alpha + \beta$ type Ti alloys, but not in CP Ti. Investigation into grain refinement in single-phase Ti materials may be a future research subject.

Severe plastic deformation

Severe plastic deformation techniques, such as high-pressure torsion (HPT), equal-channel angular pressuring (ECAP), and accumulative roll bonding (ARB), have been widely used to prepare submicron-grained materials in order to improve their mechanical properties. Grain refinement of CP Ti and $\alpha + \beta$ type Ti alloys by severe plastic deformation has been studied and improvements in tensile strength, fatigue properties, and superplastic properties have been observed.

The effects of severe plastic deformation in ECAP and multicycle extension on the mechanical properties of Ti–6Al–4V ELI alloy have been investigated for implant applications (Saitova *et al.*, 2009) and an improvement in fatigue strength was achieved.

Microalloying

The grain growth rate in the single β phase of Ti materials during reheating and hot working is very high, yielding a very coarse β-grain microstructure and a resultant transformed microstructure, which cannot be refined even by post-heat treatment after hot working. The very coarse acicular microstructure formed by transformation from the very coarse β microstructure is favourable for further improvement of fracture toughness or creep property at an elevated temperature, but the ductility or fatigue property markedly deteriorates at ambient temperature.

It is known that the addition of a small amount of yttrium (Y), less than 0.1mass%, into $\alpha + \beta$ type Ti alloy (microalloying) effectively suppresses the grain growth in the β region (Hotta *et al.*, 2006). Figure 15.7 shows a variation of β-grain size with the heating temperature for biomedical $\alpha + \beta$ type Ti–4.5Al–6Nb–2Fe–2Mo alloys containing small amounts (approximately 0.1 mass%) of various rare earth metals (RE). The β transus of the alloys is approximately 1160 K. Grain size in the alloys with the addition of RE is much smaller and grain coarsening is largely suppressed in the low temperature region of the β phase, as compared with the alloy without addition. β-grain size in the RE-added alloys rapidly increases from a particular temperature which depends on the added RE and is highest in the Y-added alloy. In the case of the Y-added alloy, the pinning of the grain boundary by fine Y_2O_3 precipitates formed in the reaction represented in Eq. 15.1 suppresses β-grain growth of the alloys.

$$2\underline{Y} + 3\underline{O} = Y_2O_3(s) \qquad [15.1]$$

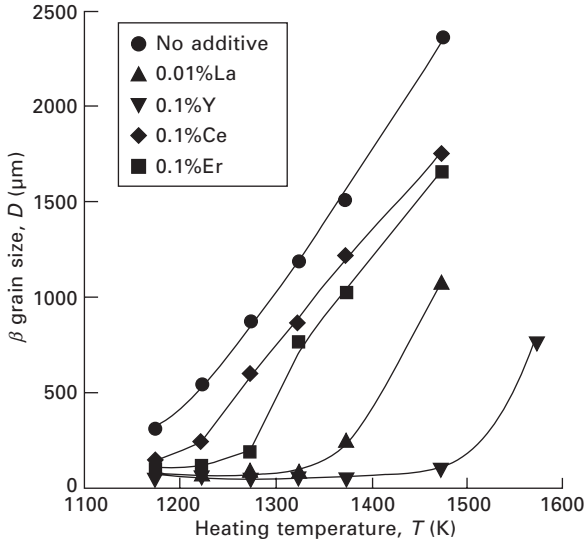

15.7 Variation of β-grain size with heating temperature for Ti–4.5Al–6Nb–2Fe–2Mo alloys containing rare earth metals.

Appearance of rapid grain growth at a particular temperature, as shown in Fig. 15.7, seems to be caused by the dissolution of Y_2O_3 precipitates into the β matrix or coarsening of Y_2O_3 precipitates. The suppression of grain growth in the β region contributes to the freedom in selection of the processing temperatures of surface treatment and heat treatment.

15.5 Other metallic biomaterials

Recent advances in Mg alloys and bulk metallic glasses for biomedical applications are discussed.

15.5.1 Mg alloys

Biodegradable polymers and ceramic materials are widely applied to implants such as plates, screws, pins, and interbody fusion cages. Biodegradable implants eliminate the need for a second operation for implant removal. However, replacing metallic biomaterials with biodegradable polymer and ceramic materials is considered to be difficult. Biodegradable metallic materials with excellent mechanical properties are required.

Mg alloys are expected to be candidates for biodegradable metallic biomaterials. The elastic moduli of Mg materials are 40–45 GPa. Mg is essential for human metabolism and is naturally found in bone tissue. Mg is harmlessly excreted in the urine as a soluble and nontoxic oxide (Staiger

et al., 2006). Since the corrosion rate of highly pure Mg in the human body is too high and its mechanical properties are inferior to other metallic biomaterials, improvements in corrosion resistance and mechanical properties through alloying and surface modification are being pursued.

Commercially available Mg alloys, such as Mg–4Y–3RE (WE43, RE: rare earth metals) (Waksman *et al.*, 2006), Mg–3Al–1 zinc (Zn) (AZ31), Mg–9Al–1Zn (AZ91), and Mg–4 lithium (Li)–4Al–2RE (LAE442) (Witte *et al.*, 2005), are used in coronary stents and hard-tissue replacements. *In vivo* evaluations of porous Mg–9Al–1Zn-(0.15–0.5)Mn (AZ91D) scaffolds were reported (Witte *et al.*, 2007). New Mg alloys in Mg-calcium (Ca) (Pietak *et al.*, 2008), Mg–Al–Zn–Ca (Kannan and Raman, 2008) and Mg–Mn–Zn (Xu *et al.*, 2008) systems have been developed for biomedical applications. The development of commercially available and newly designed Mg alloys is still a debatable issue because the safety, corrosion resistance, and mechanical strength are insufficient for use in stents and implants. The effect of alloying elements on the biological properties of Mg alloys is being systematically investigated.

Surface modification of Mg alloys is an effective way to control the corrosion rates in the human body (Yamamoto, 2008). Chemical conversion treatment, anodic oxidation, air oxidation, alkali treatment, and hydroxyapatite coating (Hiromoto and Yamamoto, 2009) have been studied thus far.

15.5.2 Bulk metallic glasses

Amorphous alloys usually show higher tensile strength and lower elastic moduli than crystalline alloys of the same composition (Inoue, 2000). Amorphous alloys also show higher corrosion resistance than crystalline alloys. Recently, Ti-based bulk metallic glasses in Ti–Zr–copper (Cu)-palladium (Pd) (Zhu *et al.*, 2007) and Ti–Zr–Cu–Pd–Nb (Qin *et al.*, 2008) systems have been developed. An elastic modulus of approximately 80 GPa, a tensile strength of 2050 MPa, and a plastic strain of over 6.5% were obtained in the bulk metallic glass of $(Ti_{40}Zr_{10}Cu_{36}Pd_{14})_{100-X}Nb_X$ (X = 1 and 3).

15.6 Future trends

The research and development of new-generation metallic biomaterials and their novel fabrication processes will continue. The research aims at functional and economical improvement of biomedical devices to expand their applications to soft-tissue replacement and tissue engineering, in addition to hard-tissue replacement.

The addition of N for improving mechanical and corrosion resistance might be a key issue in designing new stainless steels and Co–Cr alloys, considering the effect of other alloying elements such as Cr, Mo, C, and

Mn on the properties of the N-added alloys. The goal of stainless steels and Co–Cr alloys without Ni addition is to improve biocompatibility and hot/cold workability. As for the Ti materials, the development of the β type Ti alloys for controlling elastic modulus and shape memory effect/superelasticity is still considered to be still a major issue. Mg alloys with controlled corrosion rates and Ti-based bulk metallic glasses without Ni and Cu are to be developed.

In addition to the development of new metallic biomaterials, the alloy design and fabrication of highly functional metallic biomaterials under the present standards are issues to be considered. One example of development in the fabrication of highly functional metallic biomaterials under the present standards is the improvement of wear properties and hot/cold workability in Co–Cr–Mo alloys in ASTM F75 and F1537 standards, optimizing the contents of the minor alloying elements such as C, N, Si or Mn.

Since mechanical stress is anisotropically induced in biomedical devices in the human body, a consideration of the anisotropic effects of the devices is interesting. New processes in the fabrication of highly anisotropic metallic biomaterials need to be developed. In Co–Cr alloys and Ti alloys, microstructure control by thermomechanical and thermochemical treatments may be effective in the future. The fundamental thermodynamic data on the phase and stability of precipitates, phase relation, and activity and solubility of alloying elements in Co–Cr alloys and Ti alloys at high temperatures have become important; hence, these data have to be derived and assessed. For applications in tissue engineering, porous structures made of Mg alloys or Ti alloys are being developed.

Although biocompatibility is the priority while considering metallic biomaterials, the cost of production processes is another important aspect.

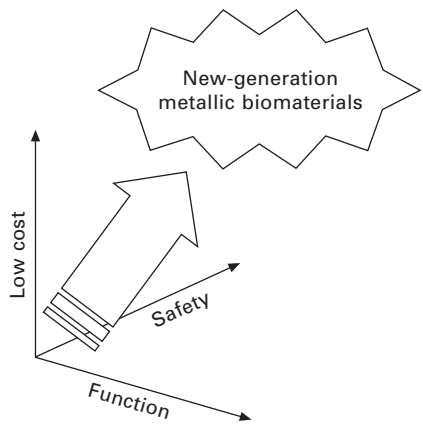

15.8 Future trends in fabricating metallic biomaterials.

Low-cost production processes can be achieved by using low-cost alloying elements and reasonable processes for desired texture, grain size, and precipitates. The common metal elements, such as Si, Al, Fe, or Mn, and interstitial elements, such as C, N, and O, are candidate low-cost alloying elements. Alloy design and processing using these elements need to be investigated and further developed. New-generation metallic biomaterials will be created to achieve a balance of function, safety, and cost (Fig. 15.8).

15.7 Sources of further information and advice

Metallic biomaterials

Park J and Lakes RS (2007), *Biomaterials: An Introduction*, New York, Springer.

Mayer VA (2008), *2008 Annual Book of ASTM Standards, Section Thirteen, Medical Devices and Services, Vol.13.01*, West Conshohocken, ASTM International.

Wnek GE and Bowlin GL (2008), *Encyclopedia of Biomaterials and Biomedical Engineering*, New York, Informa Healthcare USA.

Co–Cr alloys

Sims CT, Stoloff NS and Hagel WC (1987), *Superalloys II*, New York, Wiley.

Ti and its alloys

Boyer R, Welsch G and Collings EW (1994), *Materials Properties Handbook: Titanium Alloys*, Materials Park, ASM International.

Brunette DM, Tengvall P, Textor M and Thomsen P (2001), *Titanium in Medicine: Material Science, Surface Science, Engineering, Biological Responses and Medical Applications*, Berlin, Springer.

Lütjering G and Williams JC (2007), *Titanium, Second edition*, Berlin, Springer.

15.8 References

Ahmed T, Long M, Silvestri J, Ruiz C and Rack HJ (1996), 'A new low modulus, biocompatible titanium alloy', in Blenkinsop PA, Evans WJ and Flower HM, *Titanium'95: Science and Technology, Proc. 8th Int. Conf. Titanium*, The University Press, London, 1760–1767.

Blackwood DJ (2003), 'Biomaterials: Past successes and future problems', *Corr Rev*, 21, 97–124.

Brånemark P-I, Hansson BO, Adell R, Breine U, Lindström J, Hallén O and Öhman A (1977), 'Osseointegrated implants in the treatment of the edentulous jaw, experience from a 10-year period', *Scand J Plast Reconstr Surg*, 11 Suppl 16, 1–132.

Caudillo M, Herrera-Trejo M, Castro MR, Ramírez E, González CR and Juárez JI (2002), 'On carbide dissolution in an as-cast ASTM F-75 alloy', *J Biomed Mater Res*, 59, 378–385.

Chai YW, Kim HY, Hosoda H and Miyazaki S (2008), 'Interfacial defects in Ti–Nb shape memory alloys', *Acta Mater*, 56, 3088–3097.

Chiba A, Kumagai K, Takeda H and Nomura N (2005), 'Mechanical properties of forged low Ni and C-containing Co–Cr–Mo biomedical implant alloy', *Mater Sci Forum*, 475–479, 2317–2322.

Chiba A, Lee S-H, Matsumoto H and Nakamura M (2009), 'Construction of processing map for biomedical Co–28Cr–6Mo–0.16N alloy by studying its hot deformation behavior using compression tests', *Mat Sci Eng A*, 513–514, 286–293.

Chiba A and Nomura N (2009), *Biomedical Implant Materials*, Japan Patent, P2008–69394A.

Fanning JC (1996), 'Properties and processing of a new metastable beta titanium alloy for surgical implant applications: TIMETAL 21SRx', in Blenkinsop PA, Evans WJ and Flower HM, *Titanium'95: Science and Technology, Proc. 8th Int. Conf. Titanium*, The University Press, London, 1800–1807.

Fujibayashi S, Neo M, Kim H-M, Kokubo T and Nakamura T (2004), 'Osteoinduction of porous bioactive titanium metal', *Biomaterials*, 25, 443–450.

Fujii H (2003), 'Control of mechanical properties of Ti–Fe–O–N based titanium alloys by thermomechanical processing', *Mat Sci Forum*, 426–432, 661–666.

Gebeau RC and Brown RS (2001), 'Biomedical implant alloy', *Ad Mater Process*, 159, 46–48.

Gómez M, Mancha H, Salinas A, Rodríguez JL, Escobedo J, Castro M and Méndez M (1997), 'Relationship between microstructure and ductility of investment cast ASTM F-75 implant alloy', *J Biomed Mater Res*, 34, 157–163.

Habibovic P, Li J, van der Valk CM, Meijer G, Layrolle P, van Blitterswijk CA and de Groot K (2005), 'Biological performance of uncoated and octacalcium phosphate-coated Ti6Al4V', *Biomaterials*, 26, 23–36.

Hanawa T (2004), 'Metal ion release from metal implants', *Mat Sci Eng C*, 24, 745–752.

Hirano T, Murakami T, Taira M, Narushima T and Ouchi C (2007), 'Alloy design and properties of new $\alpha + \beta$ titanium alloy with excellent cold workability, superplasticity and cytocompatibility', *ISIJ Int*, 47, 745–752.

Hiromoto S and Yamamoto A (2009), 'High corrosion resistance of magnesium coated with hydroxyapatite directly synthesized in an aqueous solution', *Electrochim Acta*, in press. doi:10.1016/j.electacta.2009.07.033

Hollander DA, von Walter M, Wirtz T, Sellei R, Schmidt-Rohlfing B, Paar O and Erli H-J (2006), 'Structural, mechanical and *in vitro* characterization of individually structured Ti–6Al–4V produced by direct laser forming', *Biomaterials*, 27, 955–963.

Hotta S, Yamada K, Murakami T, Narushima T, Iguchi Y and Ouchi C (2006), 'β grain refinement due to small amounts of yttrium addition in $\alpha + \beta$ type titanium alloy, SP–700', *ISIJ Int*, 46, 129–137.

Hunt JA, Callaghan JT, Sutcliffe CJ, Morgan RH, Halford B and Black RA (2005), 'The design and production of Co–Cr alloy implants with controlled surface topography by CAD–CAM method and their effects on osseointegration', *Biomaterials*, 26, 5890–5897.

Inoue A (2000), 'Stabilization of metallic supercooled liquid and bulk amorphous alloys', *Acta Mater*, 48, 279–306.

Kannan MB and Raman RKS (2008), '*In vitro* degradation and mechanical integrity of calcium-containing magnesium alloys in modified-simulated body fluid', *Biomaterials*, 29, 2306–2314.

Karageorgiou V and Kaplan D (2005), 'Porosity of 3D biomaterial scaffolds and osteogenesis', *Biomaterials*, 26, 5474–5491.

Kim HY, Sasaki T, Okutsu K, Kim JI, Inamura T, Hosoda H and Miyazaki S (2006), 'Texture and shape memory behavior of Ti–22Nb–6Ta alloy', *Acta Mater*, 54, 423–433.

Kim JI, Kim HY, Hosoda H and Miyazaki S (2005), 'Shape memory behavior of Ti–22Nb–(0.5–2.0)O(at%) biomedical alloys', *Mater Trans*, 46, 852–857.

Koike M, Ohkubo C, Sato H, Fujii H and Okabe T (2005), 'Evaluation of cast Ti–Fe–O–N alloys for dental applications', *Mat Sci Eng C*, 25, 349–356.

Kuroda D, Niinomi M, Norinaga M, Kato Y and Yashiro T (1998), 'Design and mechanical properties of new β type titanium alloys for implant materials', *Mat Sci Eng A*, 243, 244–249.

Kuroda D, Hanawa T, Hibaru T, Kuroda S, Kobayashi M and Kobayashi T (2003), 'New manufacturing process of nickel-free austenitic stainless steel with nitrogen absorption treatment', *Mater Trans*, 44, 414–420.

Lee S-H, Uchikanezaki T, Nomura N, Nakamura M and Chiba A (2007), 'Effects of zirconium addition on microstructures and mechanical properties of Co–29Cr–6Mo Alloy', *Mater Trans*, 48, 1084–1088.

Lee S-H, Nomura N and Chiba A (2008), 'Significant improvement in mechanical properties of biomedical Co–Cr–Mo alloys with combination of N addition and Cr-enrichment', *Mater Trans*, 49, 260–264.

Li JP, Habibovic P, van den Doel M, Wilson CE, de Wijn JR, van Blitterswijk CA and de Groot K (2007), 'Bone ingrowth in porous titanium implants produced by 3D fiber deposition', *Biomaterials*, 28, 2810–2820.

Lopez-Heredia MA, Sohier J, Gaillard C, Quillard S, Dorget M and Layrolle P (2008), 'Rapid prototyped porous titanium coated with calcium phosphate as a scaffold for bone tissue engineering', *Biomaterials*, 29, 2608–2615.

Matsumoto H, Watanabe S and Hanada S (2005), 'Beta TiNbSn alloys with low Young's modulus and high strength', *Mater Trans*, 46, 1070–1078.

Menzel J, Kirschner W and Stein G (1996), 'High nitrogen containing Ni-free austenitic steels for medical applications', *ISIJ Int*, 36, 893–900.

Nakahigashi J and Yoshimura H (2002), 'Superplasticity and its application of ultra-fine grained Ti–6Al–4V alloy obtained through protium treatment', *Mater Trans*, 43, 2768–2772.

Nakano T, Kan T, Ishimoto T, Ohashi Y, Fujitani W, Umakoshi Y, Hattori T, Higuchi Y, Tane M and Nakajima H (2006), 'Evaluation of bone quality near metallic implants with and without lotus-type pores for optimal biomaterial design', *Mater Trans*, 47, 2233–2239.

Nakano T and Ishimoto T (2009), 'Porous metals', in Tabata Y, *Modern Scientific Technology in Growing Role of Surrounding Environment for Cells – From Control of Existence, Proliferation and Function of Cells to Regenerative Medicine*, Medical Do, Osaka, 179–184.

Narushima T (2005), 'Titanium and its alloys as biomaterials', *J Jpn Inst Light Metals*, 55, 561–565.

Niinomi M (2002), 'Recent metallic materials for biomedical applications', *Metall Mater Trans A*, 33, 477–486.

Nomura N, Kohama T, Oh IH, Hanada S, Chiba A, Kanehira M and Sasaki K (2005), 'Mechanical properties of porous Ti–15Mo–5Zr–3Al compacts prepared by powder sintering', *Mat Sci Eng C*, 25, 330–335.

Ogawa M, Shimizu T, Noda T and Ikeda M (2007), 'The effect of Al content on tensile and fatigue properties of solution-treated and quenched Ti–13Cr–1Fe alloys', *Mater Trans*, 48, 390–394.

Oh I-H, Nomura N, Masahashi N and Hanada S (2003), 'Mechanical properties of porous titanium compacts prepared by powder sintering', *Scripta Materialia*, 49, 1197–1202.

Okazaki Y, Rao S, Ito Y and Tateishi T (1998), 'Corrosion resistance, mechanical properties, corrosion fatigue strength and cytocompatibility of new Ti alloys without Al and V', *Biomaterials*, 19, 1197–1215.

Park JB and Kim YK (2003), 'Metallic biomaterials', in Park JB and Bronzino JD, *Biomaterials: Principles and Applications*, Boca Raton, CRC Press, 1–20.

Pietak A, Mahoney P, Dias GJ and Staiger MP (2008), 'Bone-like matrix formation on magnesium and magnesium alloys', *J Mater Sci: Mater Med*, 19, 407–415.

Qin FX, Wang XM, Xie GQ and Inoue A (2008), 'Distinct plastic strain of Ni–free Ti–Zr–Cu–Pd–Nb bulk metallic glasses with potential for biomedical applications', *Intermetallics*, 16, 1026–1030.

Ramírez-Vidaurri LE, Castro-Román M, Herrera-Trejo M, García-López CV and Almanza-Casas E (2009), 'Cooling rate and carbon content effect on the fraction of secondary phases precipitate in as-cast microstructure of ASTM F75 alloy', *J Mater Process Tech*, 209, 1681–1687.

Ryan G, Pandit A and Apatsidis DP (2006), 'Fabrication methods of porous metals for use in orthopaedic applications', *Biomaterials*, 27, 2651–2670.

Ryan GE, Pandit AS and Apatsidis DP (2008), 'Porous titanium scaffolds fabricated using a rapid prototyping and powder metallurgy technique', *Biomaterials*, 29, 3625–3635.

Saito T *et al*. (2003), 'Multi functional titanium alloy "GUM METAL"', *Mat Sci Forum*, 426–432, 681–688.

Saitova LR, Höppel HW, Göken M, Semenova IP, Raab GI and Valiev RZ (2009), 'Fatigue behavior of ultrafine-grained Ti–6Al–4V "ELI" alloy for medical applications', *Mat Sci Eng A*, 503, 145–147.

Staiger MP, Pietak AM, Huadmai J and Dias G (2006), 'Magnesium and its alloys as orthopedic biomaterials: A review', *Biomaterials*, 27, 1728–1734.

Takemoto M, Fujibayashi S, Neo M, Suzuki J, Matsushita T, Kokubo T and Nakamura T (2006), 'Osteoinductive porous titanium implants: Effect of sodium removal by dilute HCl treatment', *Biomaterials*, 27, 2682–2691.

Tane M, Akita S, Nakano T, Hagihara K, Umakoshi Y, Niinomi M and Nakajima H (2008), 'Peculiar elastic behavior of Ti–Nb–Ta–Zr single crystals', *Acta Mater*, 56, 2856–2863.

Uggowitzer PJ, Magdowski R and Speidel MO (1996), 'Nickel free high nitrogen austenitic steels', *ISIJ Int*, 36, 901–908.

Waksman R *et al*. (2006), 'Safety and efficacy of bioabsorbable magnesium alloy stents in porcine coronary arteries', *Catheterization and Cardiovascular Interventions*, 68, 607–617.

Wang K, Gustavson L and Dumbleton J (1993), 'Low modulus, high strength, biocompatible titanium alloy for medical implants', in Froes FH and Caplan IL, *Titanium'92: Science and Technology*, TMS, Warrendale, PA, 2697–2704.

Wang K (1996), 'The use of titanium for medical applications in the USA', *Mat Sci Eng A*, 213, 134–137.

Witte F, Kaese V, Haferkamp H, Switzer E, Meyer-Lindenberg A, Wirth CJ and Windhagen H (2005), '*In vivo* corrosion of four magnesium alloys and the associated bone response', *Biomaterials*, 26, 3557–3563.

Witte F, Ulrich H, Palm C and Willbold E (2007), 'Biodegradable magnesium scaffolds: Part II: Peri-implant bone remodeling', *J Biomed Mater Res*, 81A, 757–765.

Xu L, Zhang E, Yin D, Zeng S and Yang K (2008), '*In vitro* corrosion behaviour of Mg alloys in a phosphate buffered solution for bone implant application', *J Mater Sci: Mater Med*, 19, 1017–1025.

Yamamoto A (2008), 'Biomedical application of magnesium alloys', *J Jpn Inst Light Metals*, 58, 570–576.

Zardiackas LD, Mitchell DW and Disegi JA (1996), 'Characterization of Ti–15Mo beta titanium alloy for orthopaedic implant applications', in Brown SA and Lemons JE, *Medical Applications of Titanium and Its Alloys*, ASTM, West Conshohocken, PA, 60–75.

Zhu SL, Wang XM, Qin FX and Inoue A (2007), 'A new Ti-based bulk glassy alloy with potential for biomedical application', *Mat Sci Eng A*, 459, 233–237.

16

Degradable metallic biomaterials for cardiovascular applications

H. HERMAWAN, D. DUBÉ and D. MANTOVANI,
Laval University, Canada

Abstract: The use of degradable materials for modern biomedical applications was introduced in the late 1980s. Nowadays, the study of degradable biomaterials has become one of the most interesting research topics for biomaterials. A high increase in publications in this research field has been recorded in Medline for the last decade. Degradable biomaterials are expected to support an undergoing healing process of diseased tissues and to progressively disappear thereafter. Cardiovascular, orthopaedic and paediatric are three promising fields of applications for this new class of biomaterials. In cardiovascular applications, the coronary artery stent is one of the interesting degradable implants. This tiny implant provides a temporary scaffolding function to open a narrowed arterial vessel until the vessel remodels. Introduced in 2001, biodegradable stents raised interest among researchers, clinicians and industrialists. Although there are not yet any available for clinical use, a few models are presently undergoing pre-clinical tests in humans.

Improvements toward ideal degradable metallic biomaterials still need to be addressed. In this chapter, studies on degradable metallic biomaterials are reviewed. Properties of ideal degradable metallic biomaterials are elaborated and strategies to develop them are also proposed. Finally, their possible future direction is summarised.

Key words: degradable biomaterials, metal, cardiovascular, degradation, stent.

16.1 Introduction

Degradable polymers applied as biomaterials have been investigated for decades since their introduction in 1988 (Stack *et al.*, 1988). Among the polymers which have been proposed are poly-l-lactic acid (PLLA) (Stack *et al.*, 1988; Tamai *et al.*, 2000), polyglycolic acid/polylactic acid and polycaprolactone (van der Giessen *et al.*, 1996). In 2000, PLLA stents were tested for implantation in human coronary obstructions (Tsuji *et al.*, 2001) but no follow-up report was ever published. Degradable polymers decompose in the human body after 12 to 24 months for the lactic-acid family, whereas degradation takes more than 24 months for polycaprolactone (Waksman, 2006). Degradable polymers have a major drawback because of their limited mechanical performance. Stents made of polymers have shown high incident of recoil (Tsuji *et al.*, 2001). They need to be thicker in order to compete

with metals (Venkatraman *et al.*, 2003). Especially for load bearing implants such as stents, metals, which offer an excellent combination of strength and ductility, still constitute the principal choice of biomaterials.

Research on metals as degradable biomaterials is much more recent than that on polymers. In fact, corrosion *resistance* has always constituted one of the main requirements for metallic biomaterials, as is reported worldwide in most biomaterial textbooks. This was a paradigm. In this sense, the idea of considering degradable metals to fabricate temporary implants required some sort of break for this paradigm.

Introduced in 1938, magnesium (Mg) was the first metal used for biodegradable implants (McBride, 1938). However, at that time, the degradation behaviour of Mg was not well known and the booming of stainless steel caused this metal to be abandoned. Nowadays, as Mg technology has advanced, Mg has regained the attention of biomaterialists as a basic material for biodegradable implants. Currently, two classes of metals have been proposed: magnesium (Mg)– and iron (Fe)–based alloys. Several Mg alloys have been investigated, including AE21 alloy, which contains 2 wt% aluminum (Al) and 1 wt% rare earth elements (RE) (Heublein *et al.*, 2003), AM60 alloy with 6 wt% Al and 0.3 wt% manganese (Mn) (Levesque *et al.*, 2003), AZ91 alloy with 9 wt% Al and 1 wt% zinc (Zn) (Witte *et al.*, 2005; Xin *et al.*, 2007), and WE43 alloy with 4 wt% yttrium (Y) and 3 wt% RE (Di Mario *et al.*, 2004; Peeters *et al.*, 2005; Witte *et al.*, 2005; Waksman *et al.*, 2006). More recently, biodegradable Mg stents have advanced to a multi-center clinical trial involving 63 patients, with some encouraging initial results (Erbel *et al.*, 2007). The potential of Fe for cardiovascular application has also been investigated (Peuster *et al.*, 2001, 2006b; Waksman *et al.*, 2008).

Nowadays, the study of innovative degradable biomaterials is one of the most interesting research topics at the forefront of biomaterials. This enthusiasm is driven by three main factors:

- The advancement of materials science and engineering which allows us to better control the structure and properties of metallic materials, as well as their processing.
- Knowledge about tissue-implant interactions, which raises the new concept of bioactive biomaterials, rather than the conventional concept of inert biomaterials. A bioactive biomaterial should promote positive interactions with the physiological site where it is implanted.
- Increasing life expectancy, which strongly influences society's expectation (demand) for a better quality of life, and pushes biomaterialists to develop new technologies to provide better implants.

16.2 Clinical needs for using degradable metallic biomaterials

One of the main goals and interests for degradable biomaterials is that they are expected to fulfill functions for only temporary, short-term periods. During this time, the normal body pathways are expected to strongly participate in the healing of the diseased sites while the degradable materials are expected to support the undergoing regenerative process and to progressively disappear thereafter. Stents are a good example of a temporary implant application in this new replacement philosophy. They are tiny tubular mesh-like structures, currently made from corrosion resistant alloys, such as stainless steel 316L (SS316L), cobalt (Co)-chromium (Cr) alloys and nickel (Ni)–titanium (Ti) alloys, implanted in conditions as described in Table 16.1. Stents provide

Table 16.1 Environmental conditions of implanted coronary stents

Parameters	Values	References
Implantation condition		
Inflation pressure	10–14 atm (1.0–1.4 MPa)	(Colombo *et al.*, 1995)
Stent's plastic deformation induced during inflation	Up to 20%	(Migliavacca *et al.*, 2005)
Coronary artery environment		
Blood plasma main composition	Protein: albumin, globulin, fibrinogen Ions: chloride, sodium, bicarbonate, etc. Lipid: cholesterol, phospholipid, triglyceride	(Schneck, 2000)
Blood density	1.06 g/cm^3	(Doriot *et al.*,
Blood viscosity	3–4 mPa.s	2000, Muller-
Blood pH	7.4	Hulsbeck
Blood average peak velocity	7–25 cm/s	*et al.*, 2001)
Temperature	37 °C	
Shear stress	0.3–1.2 Pa	
Arterial vessel diameter	2–5 mm	(Schneck, 2000)
Arterial vessel wall thickness	0.5–1 mm	
Dynamic load cycle	10^8 cycles for a 10 year life	(Marrey
Heart beating pressure	Systole: 80 mmHg (~10 kPa) Diastole: 120 mmHg (~16 kPa)	*et al.*, 2006)
Frequency of heart beating and artery pulse	1.17 Hz	
Other condition		
Magnetic field generated during MRI (if applicable)	0.2–3 Tesla	(Roberts and Macgowan, 2004)

a mechanical scaffolding support and prevent early recoil and late vascular remodelling, the two major limitations of balloon angioplasty (Serruys *et al.*, 1994; Fischman *et al.*, 1994).

Stenting has become a proven procedure for the treatment of coronary artery occlusions (Serruys *et al.*, 2006). During 2002–2003, more than half a million hospital discharges with at least one coronary stent insertion procedure performed among adults were reported in the USA (Leavitt *et al.*, 2005). Since its first introduction in 1987 (Sigwart *et al.*, 1987), stent technology has progressively advanced from the conventional bare metal stents to drug eluting stents and, recently, biodegradable stents (Elliot *et al.*, 2006; Waksman, 2007). Stent have become a product in which the technology pulls and the market pushes. The stents market is growing rapidly. In the USA (Figure 16.1), drug eluting stents have enjoyed a growth from approximately 405 000 implanted stents in 2003 to more than 1.5 million estimated for 2008 (Medtech, 2004). Between 2003 and 2008, the market has grown from $1.2 million to $4.1 million (Medtech, 2004).

However, the role of stenting is temporary. Remodelling of the arterial wall is expected as a consequence of the mechanical stresses generated by the stent after deployment (Grewe *et al.*, 2000). The remodelling process can take up to 6–12 months (Grewe *et al.*, 2000; König *et al.*, 2002; Willfort-Ehringer *et al.*, 2004). Thereafter, the continued presence of the stent is not necessary, since in some way, the tissue finds a new equilibrium after remodelling. The long-term presence of the stent could provoke late thrombosis and chronic inflammation (Virmani *et al.*, 2004) and may inhibit the ongoing arterial remodelling, leading to in-stent restenosis problems (Hoffmann *et al.*, 1996). In paediatric intervention, after a congenital heart disease has been treated, the disappearance of the stent easily enables further vessel growth and avoids the need for further serial stent dilatation to adulthood (Zartner *et al.*, 2005, Schranz *et al.*, 2006). Therefore, biodegradable stents are envisaged to support the arterial wall during the remodelling and progressively degrade thereafter. The problem of late stent thrombosis is unlikely and the prolonged antiplatelet therapy is not required (Waksman, 2006).

16.3 Studies on degradable metallic biomaterials for cardiovascular applications

16.3.1 Rationale

The use of two proposed base metals for biodegradable implants, Fe and Mg, are justified by their implantation safety based on their essentiality and their well known influence on metabolism (Peuster *et al.*, 2001; Heublein *et al.*, 2003). They possess a low toxicity (Table 16.2) and the transport

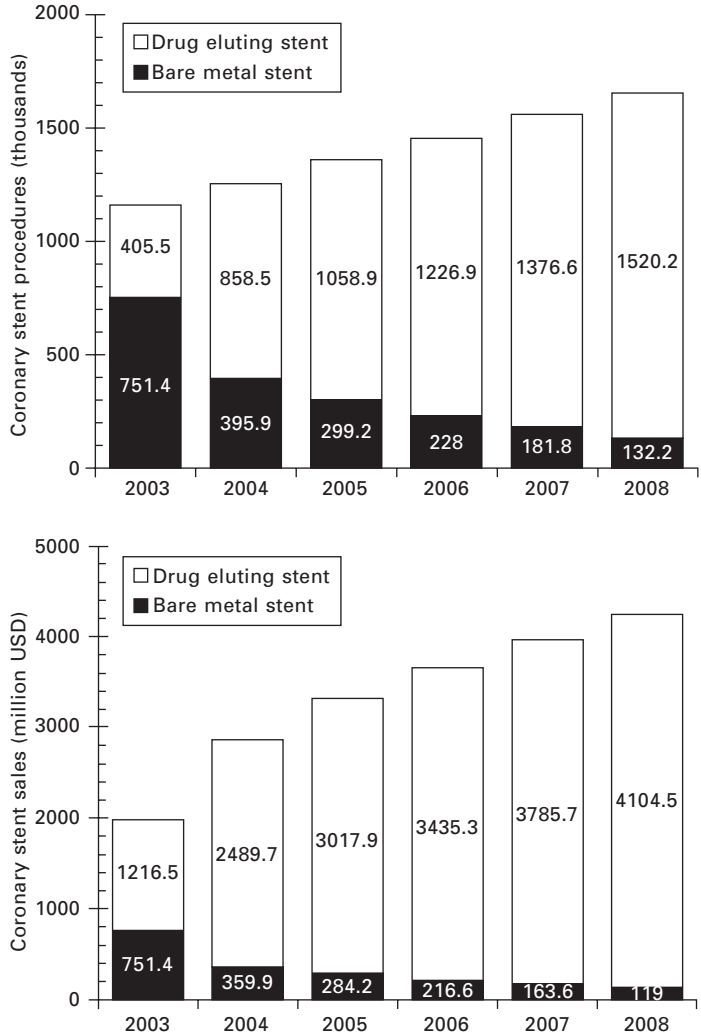

16.1 US procedure volume and market forecast for bare metal and drug eluting stents. Data compiled from Medtech Insight report (Medtech, 2004).

systems for clearance of their degradation products are well-defined. Their biocompatibility is assumed to be good.

Fe can interconvert between ferric (Fe^{2+}) and ferrous (Fe^{3+}) forms by accepting and donating electrons quite readily, which makes it a useful component for cytochromes, oxygen-binding molecules (hemoglobin and myoglobin), and many enzymes (Andrews, 1999). Fe ions are bound to transferrin (the Fe-transporting protein) during circulation and bound to

Table 16.2 Toxicity values for Fe and Mg in humans

	Fe	Mg
Biological role	Essential component of hemoproteins	Essential trace element for many enzyme cofactors
IARC evaluation (Boffetta, 1993).	Fe(III) =3	N/L
Dietary intake (mg/day) (Emsley, 1998)	6–40	250–380
Level in whole blood (mg/L) (Emsley, 1998)	447	37.8
Blood toxic level (mg/L)	3.5–5 (in serum) (Frey, 1999)	85–121 (in plasma) (Saris *et al.*, 2000)

Note: IARC classification: 1 = carcinogenic to humans, 2A = probably carcinogenic to humans, 2B = possibly carcinogenic to humans, 3 = not classifiable as carcinogenic to humans, N/L = not listed in IARC monograph.

ferritin (the Fe-storaging protein) when accumulated within cells (Aisen *et al.*, 1999). Even though Fe is essential to life, its excess or deficiency can be deleterious (Andrews, 1999). However, the insignificance of cytotoxic effect of Fe and its degradation products *in vivo* has been argued as follows. The *in vivo* degradation rate of pure Fe is slow and its toxicity is also low (Peuster *et al.*, 2001). The slow degradation rate and the small amount of Fe in a stent (approximately 40 mg) compared to the high Fe-load of blood, 447 mg/L (Emsley, 1998), make any systemic toxicity rather unlikely (Mueller *et al.*, 2006). The mechanical properties of Fe are excellent due to a good combination of strength and ductility (Brandes and Brook, 1992). Fe is an important base metal for a rich selection of structural alloys, such as stainless steels, fulfilling the needs of various applications. Their structure and properties can be further adjusted by alloying and by using thermo-mechanical treatments.

Mg^{2+} is the fourth major cation of the human body, with 50% of the total Mg content in bones and only 1% in the extracellular fluid (Okuma, 2001). Mg is a co-factor for many enzymes, and it stabilizes the structures of DNA and RNA (Hartwig, 2001). The toxicity of Mg is low (Emsley, 1998), and early signs of toxicity during intravenous Mg treatment usually occur at a total concentration of 85–121 mg/L in plasma (Saris *et al.*, 2000). The incidence of hyper-Mg is rare, due to the efficient excretion of Mg in the urine (Vormann, 2003; Saris *et al.*, 2000). From physical and mechanical points of view, the density and stiffness of Mg (ρ = 1.74 g/cm^3 and E = 45 GPa) are the most similar to cortical bone (ρ =1.99 g/cm^3 and E = 11.7–18.2 GPa) (Currey, 1998) when compared to Al (ρ = 2.70 g/cm^3, E = 70 GPa) and Ti (ρ = 4.51 g/cm^3, E = 110 GPa) (Brandes and Brook, 1992). Its very low density gives

it an interestingly high strength-to-weight ratio (Mordike and Ebert, 2001), which in turn would significantly reduce the weight of medical implants. Its low Young's modulus would give benefit in reducing the stress shielding at the bone-implant interface, which is still the main problem of currently used non-degradable bone implants (Karachalios *et al.*, 2004).

In addition, it was recently found that *in vivo* corrosion products of Mg have a positive effect on osteoblastic activity, leading to a complete replacement of the implant by bone tissue (Witte *et al.*, 2005). These unique features make biodegradable Mg alloys suitable for orthopaedic applications; for example, internal bone fixation implants such as plates, pins and screws. Their use would avoid second surgery to expel the implant, which is the case for non-biodegradable implants, after sufficient healing. Therefore, it would prevent the increasing costs and reduce morbidity rates. Alloying, purification and surface treatment are continuously advanced as strategies to improve current Mg performance (Song, 2007).

16.3.2 Mechanical properties

Currently, metallic biomaterials used for long-term implantation are corrosion resistant alloys. Stainless steel 316L, as the most widely used alloy, is often considered as the standard reference for mechanical properties in developing new biomaterials (Balcon *et al.*, 1997). Table 16.3 compares the mechanical properties of already implanted degradable metals with SS316L.

The mechanical properties of pure Fe are closer to those of SS316L than Mg alloys, making Fe more suitable for applications that require high strength and ductility such as coronary stents. Nevertheless unlike most metallic nonmagnetic biomaterials, Fe is ferromagnetic substance, an important characteristic which can influence its compatibility with Magnetic Resonance Imaging (MRI). MRI will eventually become the default noninvasive imaging modality for coronary investigation. An attempt has been made to alter the ferromagnetic properties of Fe and improve its mechanical properties by alloying it with Mn (Hermawan *et al.*, 2008). A composition of Fe with 35 wt% Mn, produced through mechanical alloying, results into a nonmagnetic austenitic alloy with a yield strength reaching 230 MPa and maximum elongation up to 32% (Hermawan *et al.*, 2008).

The ductility of Mg alloys is limited, compared to most Fe alloys (Mordike and Ebert, 2001). The alloy used in stents which are implanted in babies, the WE43 alloy (Zartner *et al.*, 2005; Schranz *et al.*, 2006), has only 4% maximum elongation (Table 16.3). A specific stent design was therefore implemented (Figure 16.2). The circumferential noose-shaped structures connected by unbowed cross-links along the longitudinal stent axis optimise the flexibility for optimal delivery and radial expansion during stent implantation (Di Mario *et al.*, 2004; Erbel *et al.*, 2007).

Table 16.3 Properties of already implanted degradable metals compared to SS316L

Metal	Metallurgical condition	Main alloying composition (wt%)	Density (g/cm^3)	Magnetic/non-magnetic	Yield strength (MPa)	Ultimate strength (MPa)	Young's modulus (GPa)	Maximum elongation (%)
SS316L (ASTM, 2003)	Annealed plate	Fe, 16–18.5Cr, 10–14Ni, 2–3Mo, <2Mn, <1Si, <0.03C	8.00	Non-magnetic	190	490	193	40
Iron*	Annealed plate	99.8Fe	7.87	Magnetic	150	210	200	40
WE43 magnesium alloy (ASTM, 2007)	Extruded bar	Mg, 3.7–4.3Y, 2.4–4.4Nd, 0.4-1Zr	1.84	Non-magnetic	150	250	44	4

*Data provided by Goodfellow Corporation, Oakdale, PA, USA.

(a) (b)

16.2 WE43 magnesium alloy stent (a) before (electron microscopy image) and (b) after being inflated (photograph). Adapted from (Erbel *et al.*, 2007). Reprinted with permission from Elsevier.

The ductility of Mg alloys can be improved by alloying and employing advanced processing techniques. For example, alloying Mg with lithium (Li) can change the crystal structure from hexagonal to body centered cubic and produces a large increase in ductility. Mg alloyed with 8.7 wt% Li showed 52% elongation, but tensile strength dropped to 132 MPa (Sanschagrin *et al.*, 1996). A hot extruded Mg alloyed with 1 wt% calcium (Ca) showed a good combination of strength and ductility, where tensile strength reached 240 MPa with 11% elongation (Li *et al.*, 2008). A hot extrusion process was also employed to improve the strength of Mg–Li–Al alloy, resulting in a combination of tensile strength of 239 MPa with 33% elongation (Sanschagrin *et al.*, 1996). Other processes have reported to improve ductility of Mg alloys including grain refinement (Mukai *et al.*, 2001) and texturing through an equal channel angular processing (Agnew *et al.*, 2004). Nevertheless, the choice of alloying elements for Mg is limited from a medical point of view. A simple toxicological analysis arrives at few elements that can be tolerated in the human body, comprising Ca, Zn, Mn and perhaps a very small amount of low toxicity RE elements (Song, 2007).

16.3.3 *In vitro* investigation

In order to understand the degradation behaviour of the proposed alloys, a series of investigations has been conducted involving both *in vitro* and *in vivo* methods. Some of the *in vitro* tests dedicated to understanding the degradation mechanism and rate without contact with cells were reported (Kuwahara *et al.*, 2000, 2003; Peuster *et al.*, 2001; Levesque *et al.*, 2003, 2008; Witte *et al.*, 2006; Hermawan *et al.*, 2007; Kannan and Raman, 2008a, 2008b). Meanwhile, there are few reports about *in vitro* tests involving cells or cytotoxicity assays (Li *et al.*, 2004, 2008). The *in vitro* investigation method without contact with cells can be divided into three categories: (i) immersion test, (ii) electrochemical test and (iii) specialised immersion test.

- *Immersion test*: The closest standard generally used for conducting a laboratory immersion test is ASTM G 31 (ASTM, 2001a). Specimens are simply immersed in the test solution for a determined period, varying from hours to weeks. The test solution can be based on a Ringer-lactate solution (Peuster *et al.*, 2001), an artificial seawater solution (Witte *et al.*, 2006, 2007) or a Hank's solution (Kuwahara *et al.*, 2000; Hermawan *et al.*, 2007). Corrosion rates (CR) can be determined by measuring the ion release using an atomic absorption spectrometer (Peuster *et al.*, 2001) or by calculating the weight loss of specimens (ASTM, 2001a).
- *Electrochemical test*: The most used electrochemical method is a potentiodynamic polarisation test, according to two available standards: ASTM G 59 (ASTM, 2001b) and ASTM F 2129 (ASTM, 2004). The

set-up for a potentiodynamic polarisation test is illustrated in Figure 16.3. Specimens are usually mounted in an acrylic resin, having had 1 cm^2 of the exposed surface polished before the tests. The test solution can be prepared from a Hank's solution (Hermawan *et al.*, 2007), a borax-phosphate buffer (Witte *et al.*, 2006), artificial seawater (Witte *et al.*, 2007), or a specific simulated body fluid (Xin *et al.*, 2007; Kannan and Raman, 2008b). The CR is calculated from the measured corrosion current density (ASTM, 2001b). Recently a new electrochemical method, the slow strain rate test (SSRT), was introduced to investigate the mechanical integrity of metals (AZ91Ca magnesium alloy) during degradation (Kannan and Raman, 2008b).

- *Specialised immersion test*: One example of a specialised immersion test is a pseudo-physiological test which employs a test-bench (Fig. 16.4) to reproduce conditions similar to those in the human coronary artery (Table 16.1) (Levesque *et al.*, 2003, 2008). This test has shown the important role of shear stress on the degradation rate, as well as on the degradation mechanism, which cannot be assessed with the immersion or electrochemical test method. It is suggested that the test-bench will be useful in further investigation for the development of metallic alloys for biodegradable stents (Levesque *et al.*, 2008).

Even though the ASTM standards give guidance for conducting *in vitro* degradation tests, they are not specifically designed for testing degradable biomaterials. Some adjustments in test parameters should be made to make

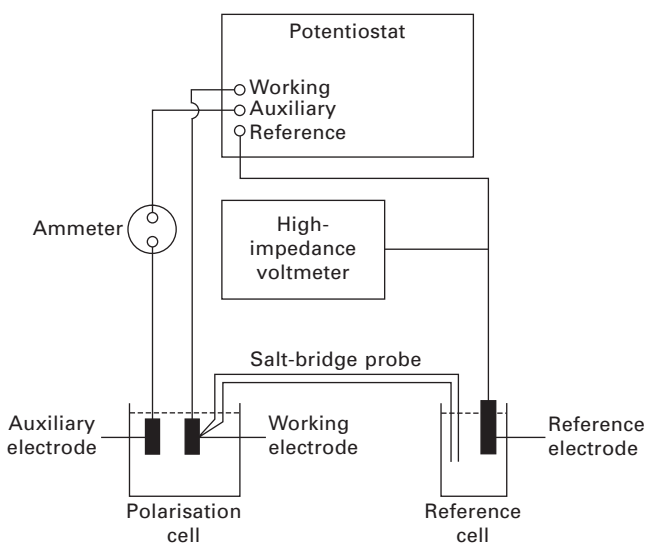

16.3 A potentiodynamic polarisation test set-up. Adapted from Scully and Taylor (1992).

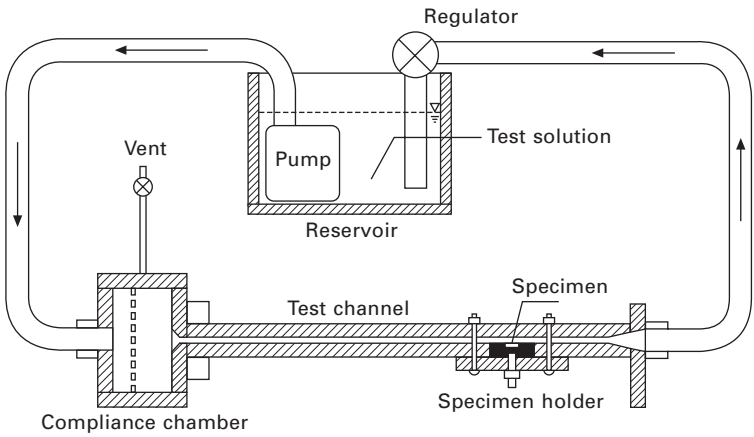

16.4 A pseudo-physiological test-bench. Adapted from Levesque *et al.* (2008).

Table 16.4 Comparison of *in vitro* degradation rates of Fe and Mg alloys

Material	Degradation rate (mm/year) Immersion	Electrochemical	Reference
Pure iron	0.21	N/A	(Peuster *et al.*, 2001)
	0.23	0.19	(Hermawan *et al.*, 2007)
AM60 magnesium alloy	2.78	8.97	(Hermawan *et al.*, 2007)
AZ91 magnesium alloy	10.39	147.68	(Hermawan *et al.*, 2007)
	–0.27	2.8	(Witte *et al.*, 2006)
LAE442* magnesium alloy	5.53	6.9	(Witte *et al.*, 2006)

*A non-commercial magnesium alloy composed of 4 wt% lithium (Li), 4wt% aluminum and 2 wt% rare earth (RE). The RE consisted mainly of 51 wt% cerium (Ce), 22 wt% lanthanum (La), 16 wt% neodymium (Nd) and 8 wt% praseodymium (Pr) (Witte *et al.*, 2006).

the test as close as possible to the *in vivo* conditions, such as temperature, test solution and pH. The difference in determining test parameters produces different results, for instance, in degradation rate. Table 16.4 presents a comparison on degradation rates, determined by immersion and electrochemical test methods on Fe and Mg alloys. The degradation rates of Fe were similar in both investigations due to the use of rather similar test parameters. Large differences were found for the AZ91 magnesium alloy by the two investigators. The differences in test solution (artificial seawater vs. Hank's solution), test temperature (room temperature vs. 37 °C) and specimen's preparation (sterilised vs. non-sterilised surface) probably constituted the main cause of these divergences.

In vitro tests in the presence of cells are carried out in order to assess early signs of cell compatibility (for example cell viability) in contact with the proposed alloys. The ISO 10993-5:1999 standard provides a suitable method for conducting such tests (ISO, 1999). One *in vitro* study reported the response of human umbilical venous smooth muscle cells (SMCs) to an excess of ferrous ions in which the ions reduced the cell growth rate (Mueller *et al.*, 2006). More cytotoxicity studies were carried out for Mg alloys mostly proposed for orthopaedic applications (Heublein *et al.*, 2003; Li *et al.*, 2004, 2008; Witte *et al.*, 2007).

A cell viability assay (indirect contact cytotoxicity) involves depositing samples of sterilised pure Mg ($2 \times 2 \times 2$ mm^3) in 96-multiwell plates, seeded with 1×10^6 cells/mL marrow cells, followed by incubation up to 72 hours in a humidified atmosphere with 5% CO_2 at 37 ºC (Li *et al.*, 2004). The same method was carried out for Mg–Ca alloys using L-929 cells (Li *et al.*, 2008). Other cytocompatibility tests were performed on biodegradable Mg–hydroxyapatite metal matrix composite using human bone derived cells and MG-63 plus RAW 264.7 cells (Witte *et al.*, 2007). Although those studies were conducted for Mg alloys proposed for bone implants, the method can be adapted for other alloys proposed for biodegradable stent applications.

16.3.4 *In vivo* investigation

There were two initial *in vivo* investigations of metallic biodegradable stents, published in early 2000 – first, the implantation of Fe stents into the descending aorta of New Zealand white rabbits (Peuster *et al.*, 2001) and second, the implantation of AE21 magnesium alloy stents into the coronary artery of domestic pigs (Heublein *et al.*, 2003). These pioneering works have proved the potential for degradable metals to be used in cardiovascular applications. Recently, at least four studies of metallic biodegradable stents implanted in animals have been published (Table 16.5).

The long-term biocompatibility of Fe stents was evaluated in a study involving the implantation of Fe stents (Fig. 16.5), and SS316L stents as a control, in the descending aorta of minipigs. The results showed that there was no difference in the amount of neointimal proliferation between 316L and Fe stents. There was no sign of Fe overload or Fe-related organ toxicity as well as no evidence for local toxicity due to corrosion products. It was concluded that Fe is a suitable metal for the production of a large-size degradable stent, although a faster degradation rate was desirable (Peuster *et al.*, 2006b). Another study to assess the safety and efficacy of Fe stents was conducted by the implantation of Fe and Co–Cr (control) stents in the coronary arteries of juvenile domestic pigs. The results of this short-term study showed that there was a trend in favour of the Fe stents compared to the Co–Cr stents for the intimal thickness, intimal area, and percentage of

Table 16.5 In vivo investigations on Fe and Mg alloys for cardiovascular stent applications

Material	Implantation site	Implantation time	Findings	Reference
Fe stents				
Fe	Descending aorta of New Zealand rabbits	18 months	▪ Low thrombogenicity ▪ Mild inflammatory response ▪ Lack of local or systemic toxicity ▪ Accelerated degradation is warranted	(Peuster *et al.*, 2001)
Fe	Descending aorta of minipigs	12 months	▪ No local or systemic toxicity ▪ Neointimal proliferation is comparable to AISI 316L stent ▪ A faster degradation rate is desirable	(Peuster *et al.*, 2006b)
Fe	Coronary arteries of porcines	28 days	▪ Fe stents are safe	(Waksman *et al.*, 2008)
Mg alloys stents				
AE21	Coronary artery of pigs	56 days	▪ Mg alloy stents are promising ▪ Prolonged degradation is desired	(Heublein *et al.*, 2003)
WE43	Coronary artery of domestic or minipigs	3 months	▪ Mg alloy stents are safe and are associated with less neointima formation ▪ Long-term studies (>3 months) are needed to prove positive remodelling	(Waksman *et al.*, 2006)
WE43	Coronary artery of domestic pigs with VBT	28 days	▪ VBT as adjunct to stenting further reduces intimal hyperplasia and improves lumen area when compared to stenting alone	(Waksman *et al.*, 2007)

occlusion. It was then concluded that stents made of Fe were relatively safe (Waksman *et al.*, 2008). The advantage of Fe stents was also mentioned in a study on the influence of ions released from Fe stents because the ions could reduce the proliferation of vascular smooth muscle cells, an event associated with the problem of in-stent restenosis (Mueller *et al.*, 2006).

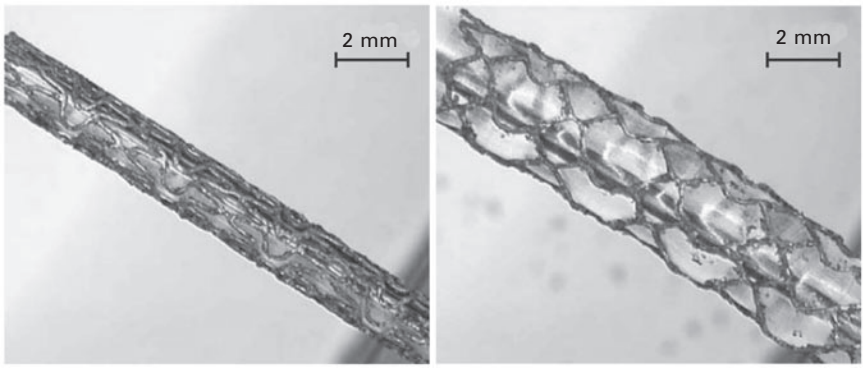

16.5 The NOR-1 iron stent (a) before and (b) after being inflated. Adapted from (Peuster *et al.* (2006a). Reprinted with permission from Cambridge University Press.

A study to determine the safety and efficacy of Mg alloy stents was carried out involving the implantation of stents in porcine coronary arteries. The results led to a conclusion that Mg alloy stents were safe and were associated with less neointima formation compared to stainless steel stents. However, they were associated with a modest degree of late recoil and intimal hyperplasia (Waksman *et al.*, 2006). A follow-up study was then conducted involving the use of adjunct vascular brachytherapy (VBT) to overcome these limitations. It was concluded that VBT as an adjunct to Mg alloy stents further reduced the intimal hyperplasia and improved the lumen area when compared to the stent alone, but did not have any impact on late recoil (Waksman *et al.*, 2007).

16.3.5 Implantation trials in humans

Today, biodegradable stents are no longer just a concept as they are already implanted in humans. Table 16.6 summarises the conclusions of published reports on implantation trials of Mg alloy stents. The first report described a preliminary three-month follow-up of critical limb ischemia (CLI) treatment in 19 adults. It was reported that the primary clinical patency was as high as 89.5%, with no major or minor amputation necessary in any of the patients, yielding a limb salvage rate of 100%. This trial suggested promising performance of the devices in the treatment of CLI patients (Peeters *et al.*, 2005).

The Mg alloy stent was used for the first time to treat a congenital heart disease in a preterm baby. The implantation was performed using a hybrid procedure when the baby weighed 1.7 kg, and successfully re-established the left lung reperfusion. During the four months of follow-up, the degradation

Table 16.6 Implantation trials of WE43 magnesium alloy stents in humans

Trial	Findings	Reference
Pre-clinical testing of stents for critical limb ischemia (CLI) in adult patients	Three months primary clinical patency and limb salvage rates suggest the potential of Mg alloys stents for CLI treatment	(Peeters *et al.*, 2005)
Implantation of stents to treat critical recoarctation of the aorta in a newborn	Biodegradable metal stent can be used for the treatment of aortic coarctation in a newborn	(Schranz *et al.*, 2006)
Implantation of stents to open an occlusion in the left pulmonary artery of a preterm baby	– Biodegradable Mg stent implantation has rescued a child from an extremely severe clinical problem – Completed degradation of the Mg stent led to minimal changes within the arterial wall	(Zartner *et al.*, 2005, 2007)
Implantation of stents to treat stenotic aorto-pulmonary collateral in a two-months-old baby girl	There was an initial significant increase in vessel diameter but four months after stent placement significant restenosis occurred	(McMahon *et al.*, 2007)
Clinical performance and angiographic results of coronary stenting with absorbable metal stents (PROGRESS-AMS) clinical trial involving implantation of 71 stents in 63 patients	– The immediate angiographic result is similar to the result is similar to the result of other metal stents – The stents are safely degraded after four months	(Erbel *et al.*, 2007)

process was clinically well tolerated and the mechanical characteristics proved to be adequate to secure the reperfusion (Zartner *et al.*, 2005). However, after five months of implantation, the baby died from multiple organ failure. It was an interesting finding that histo-pathological tests conducted during the autopsy confirmed that the stent had completely disappeared. A jelly-like calcium phosphate and fibrotic structure substituted the stent struts, which allowed a slight increase of the intraluminal diameter over the original stent diameter (Zartner *et al.*, 2007).

The Mg alloy stent was used for the second time to treat a newborn baby with severely impaired heart function due to a long segment recoarctation following a complex surgical repair (Schranz *et al.*, 2006). The stent was able to sustain perfusion without measurable recoil after implantation but, due to a rapid degradation process, the operated vessel backslid into its previous course and required the implantation of a second stent. However, pathological Mg levels in serum were not detected, despite the use of two stents.

An encouraging report comes from a multi-centre, non-randomised prospective study, the PROGRESS-AMS (Clinical Performance and

Angiographic Results of Coronary Stenting with Absorbable Metal Stents) (Erbel *et al.*, 2007). The trial successfully implanted 71 stents in 63 patients. After 4 months, the ischaemia-driven target lesion revascularisation (TLR) rate was 23.8% and the overall TLR rate was 45% after one year. This study revealed that Mg alloy stents can achieve an immediate angiographic response similar to that of other metallic stents and be safely degraded after four months. However, the current stent still shows limitation where the restenosis and incidence of TLR were higher than reported for the bare metal stents (Morice *et al.*, 2002). The study suggested that it is necessary to modify the stent characteristics with a prolonged degradation time.

Very recently, a published report revealed an early restenosis following Mg alloy stent implantation in aortopulmonary collateral of a two-month-old girl with pulmonary atresia and hypoplastic pulmonary arteries (McMahon *et al.*, 2007). At the beginning there was a significant increase in vessel diameter, but four months after stent placement, a significant restenosis occurred. This study stresses once again the need for further refinements in the Mg alloy stent technology, which yields a very promising potential for the intervention in children previously deemed unsuitable for permanent stent placement.

16.4 Lessons from the first ten years of investigation in degradable metallic biomaterials

16.4.1 Ideal degradable metallic biomaterials

Biodegradable stents should possess at least two main characteristics:

- *Good mechanical properties*: The mechanical properties of SS316L, which has been considered as a gold standard material for stents, can be used as a reference for developing new biodegradable stent materials. Figure 16.6 illustrates the relative mechanical properties of metals proposed for biodegradable stents to the minimum requirement for ASTM F138 (SS316L). It is shown that Mg alloys have the lowest value for both strength and ductility compared to Fe-based alloys. Ideally, the mechanical properties of metals for biodegradable stents should pass the minimum value of SS316L. This will ensure that developed stents display the excellent performance shown by SS316L stents.
- *Controlled degradation process*: It is expected that a complete degradation will occur after the vessel remodelling process has taken place. In addition, during the degradation process, the stent material should not release substances causing toxic effects. The ideal compromise between degradation and mechanical integrity during *in vivo* implantation of a biodegradable stent is illustrated in Fig. 16.7. It begins with a very slow degradation rate to keep the optimal mechanical integrity during arterial

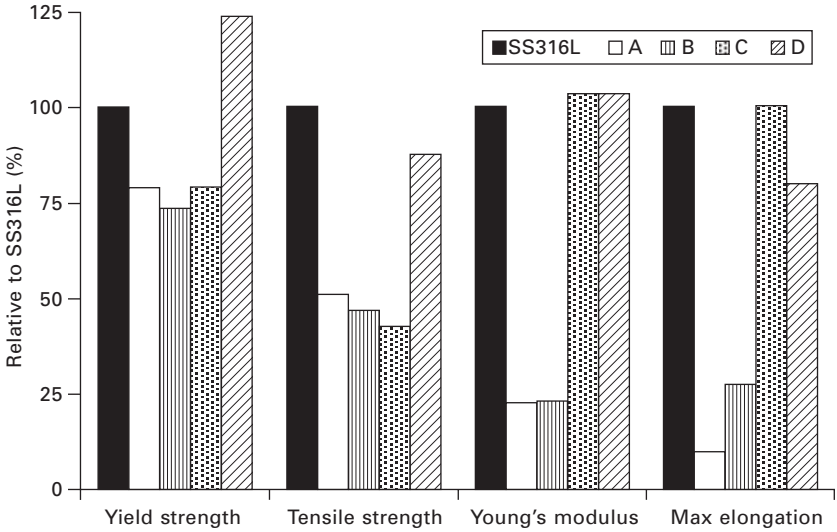

16.6 Mechanical properties of proposed biodegradable metals compared to stainless steel 316L (ASTM, 2003). A = extruded WE43 magnesium alloy (ASTM, 2007), B = extruded Mg–1Ca magnesium alloy (Li *et al.*, 2008), C = annealed Fe, D = mechanically alloyed Fe–35Mn alloy (Hermawan *et al.*, 2008).

vessel remodelling. This can be achieved, for example, by coating the stent with a degradable polymer. Thereafter, the degradation progresses while the mechanical integrity decreases. The degradation ideally occurs at a sufficient rate that will not cause an intolerable accumulation of degradation product around the implantation site. Figure 16.7 also shows that the Mg alloy stent degrades completely before the remodelling period; conversely, polymeric stents continue their presence thereafter. The degradation of Fe stents, which completes after the remodelling period but is not as long as that of polymeric stents, could be considered as approaching the ideal degradation time.

Besides degradation rate, the degradation mechanism is also of importance where a uniform corrosion is expected. Ideally, degradation of the stents begins from the surface to the bulk, in order to maintain their mechanical integrity. Localised corrosion such as pitting should be avoided since this could lead to the stent cracking or fragmenting, leading to blood vessel injuries.

16.4.2 Strategies to develop the ideal degradable metallic biomaterials

The ideal features of degradable stents can be approached by implementing the following strategies:

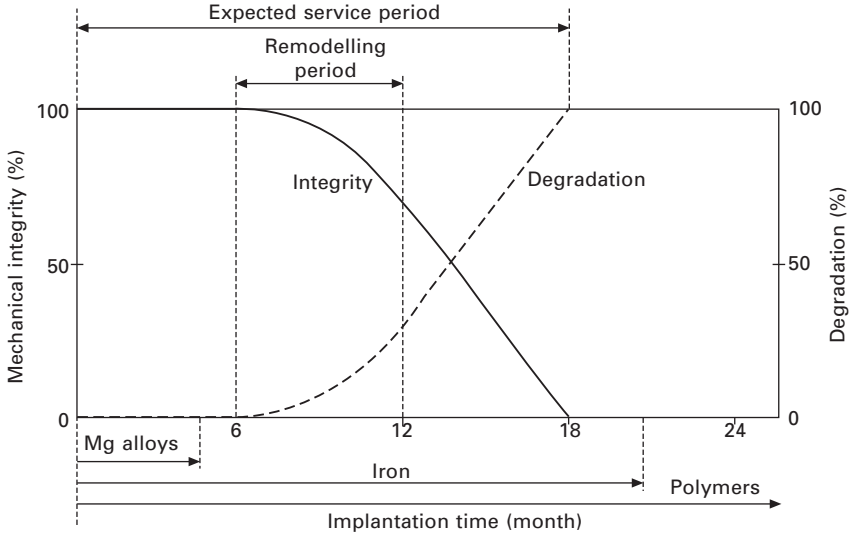

16.7 Illustration of an ideal compromise between degradation and mechanical integrity of a biodegradable stent. Times for complete *in vivo* degradation of current biodegradable stents are mapped at the bottom.

- *Developing new classes of metallic alloys with new chemical compositions*: This strategy could introduce a broad range of new alloy compositions; however, this is limited by toxicological considerations in choosing the different elements. There are two elements having the highest toxicity limit in the human body, which can be used as the base metal, namely Fe and Mg (Emsley, 1998). Then, only a few elements can be tolerated in the human body and can be used as alloying elements, including Ca, Zn, Mn and a very small amount of RE elements (Song, 2007). Accordingly, new alloys have been proposed recently, including Fe–Mn alloys (Hermawan *et al.*, 2008), Mg–Ca alloys (Li *et al.*, 2008, Kannan and Raman, 2008b) and Mg–Zn/Mn alloys (Song, 2007). In general, those newly developed alloys show improved features in both mechanical properties and degradation behaviour, but are not yet tested *in vivo*. Finally, it has to be emphasised that degradable metals might also be coated with degradable polymers, as appropriate strategies to target the starting time of the degradation process of the metal. Furthermore, the polymeric coatings can eventually be charged with drugs providing specific targeting effects.
- *Improving properties through non-conventional processing techniques*: Traditionally, alloys are made through melting processes. The major drawbacks of these are compositional segregation and non-uniform grain structure, leading to inferior mechanical properties and degradation

behaviour. Two non-conventional processing techniques can be used to produce new alloys: powder metallurgy and electrodeposition. Powder metallurgy was used to develop Fe–Mn alloys, resulting in faster degradation rates than pure Fe. The presence of porosity in the alloy contributes to this acceleration, but without sacrificing the mechanical properties (Hermawan *et al.*, 2008). The electrodeposition method offers an advantage in producing metals with high purity. This purity eliminates the problem of impurities as is the case with cast Mg alloys; these lead to faster and localised degradation. Finally, heat treatments, thermo-mechanical processes and surface modifications constitute more conventional (and industrially adopted) processes applicable to target the mechanical properties and degradation behaviour of degradable metals.

16.4.3 Summary

The last ten years have witnessed the rapid evolution of a new class of biomaterials: the degradable metallic biomaterials. Their specificity consists in providing a structural mechanical support for a limited time after implantation, and then disappearing within a reasonable time by being adsorbed or resorbed by physiological metabolic reactions. The strength of the mechanical support and the time required to disappear are strongly linked to the site of implantation. For example, orthopaedic applications are rather different from cardiovascular applications.

A number of fundamental questions have been raised by the introduction of these degradable metals, including:

- The mechanisms of degradation and of adsorption/resorption.
- The physiological pathways by which the degradation products will be stored or expelled by the body.
- The effects of the implantation on the metabolic organs initially, and the rest of the body after; and these at short, medium and long terms, for example weeks to months, months to years and years to decades.

All the above questions should be answered before proceeding with clinical trials. Despite the fact that the industrial and marketing potentials are extremely high, the intrinsic risks of these degradable metals are also dramatically important. Specific standards and regulatory approaches have to be introduced, in particular by governmental agencies such as the Food and Drug Administration (FDA). These standards and rules have to be oriented in order to protect the patients, health and welfare while encouraging industrialists and researchers to dare to develop a new class of biomaterials. A truly ethical approach is required, although this is not easy to implement and assess. In this context, the approach tends to be the following: all the *in vitro* and *in*

vivo experiments that can be imagined and that show reasonable chances to open new horizons should be pursued and be welcomed. However, extreme prudence and pro-active criticism must be used prior to any clinical application. At the present time, human implantations are not realistic, mainly because too little is known concerning the above described critical questions.

The introduction of degradable metals is going to break the paradigm established with the first metallic biomaterials introduced more than fifty years ago – the paradigm in which metallic biomaterials must be 'corrosion-resistant' which is written in scholarly textbooks and described in a number of scientific papers. Although fifty years ago it was unbelievable to imagine that a metal could be expected to degrade in the body, today this is a reality. The evolution of the field fully justifies the pioneering approach required to further develop degradable metallic biomaterials.

Even if the list of envisaged medical applications of degradable metals seemingly is limited at the moment, this work hopefully has shown their obvious potential in the medical field. In the coming years, a true revolution will occur in some medical specialties. Revolutionary advancements towards paediatric surgery have already injected new challenges. The history of biomaterials shows that new and extremely bright horizons have been opened when clinicians, scientists, and industrialists start to interact together to master the complexity of the interfacial field of biomaterials through a truly multidisciplinary approach. As a partial result, numerous applications have been raised, but many more can be envisaged. Degradable metals are expected to provide a new insight in the biomaterials field for a number of surgeries, including paediatric, orthopaedic and cardiovascular. Considering their revolutionary potential, these materials will represent a stimulus for developing new devices which were not possible before, and will be focused to break some scientific barriers and accomplish technological challenges.

Very recently, some attempts have been reported in the literature to implant degradable metals in new-born babies and in clinical studies in humans as well. This is absolutely premature, and is not visionary at all: we invite industrialists to be prudent in the future. The history of biomaterials already reported catastrophic and irreversible effects following the implantation of biomaterials issuing from immature technologies. Industrial applications have risen too fast without allowing scientists to fully develop the science behind the technology, including understanding mechanisms and assessing the effects. Today, a more rational and less emotional approach must be adopted. Understanding should be privileged and misunderstanding must be avoided to ethically gain the full confidence of the potential patients that we all are.

Applications must respond to the specific social requirements of our age: the medical surgical services must be adapted to a progressively ageing population at the lowest cost. The safety question of degradable metals placed in the body requires particular attention, and all implants must have

the required qualities of biocompatibility, biofunctionality, and biodurability over short, medium and long terms.

16.5 References

Agnew, S. R., Horton, J. A., Lillo, T. M. and Brown, D. W. (2004) Enhanced ductility in strongly textured Mg produced by equal channel angular processing. *Scr Mater*, 50, 377–81.

Aisen, P., Wessling-Resnick, M. and Leibold, E. A. (1999) Iron metabolism. *Curr Opin Chem Biol*, 3, 200–6.

Andrews, N. C. (1999) Disorders of iron metabolism. *N Engl J Med*, 341, 1986–95.

ASTM (2001a) *ASTM G 31: Standard Practice for Laboratory Immersion Corrosion Testing of Metals*, West Conshohocken, ASTM International.

ASTM (2001b) *ASTM G 59: Standard Test Method for Conducting Potentiodynamic Polarization Resistance Measurements*, West Conshohocken, ASTM International.

ASTM (2003) *ASTM F 138: Standard Specification for Wrought 18Chromium-14Nickel-2.5Molybdenum Stainless Steel Bar and Wire for Surgical Implants (UNS S31673)*, West Conshohocken, ASTM International.

ASTM (2004) *ASTM F 2129: Standard Test Method for Conducting Potentiodynamic Measurement to Determine the Corrosion Susceptibility of Small Implant Devices*, West Conshohocken, ASTM International.

ASTM (2007) *ASTM B 107/B 107M: Specification for Magnesium-Alloy Extruded Bars, Rods, Profiles, Tubes, and Wire*, West Conshohocken, ASTM International.

Balcon, R., Beyar, R., Chierchia, S., De Scheerder, I., Hugenholtz, P. G., Kiemeneij, F., Meier, B., Meyer, J., Monassier, J. P. and Wijns, W. (1997) Recommendations on stent manufacture, implantation and utilization. *Eur Heart J*, 18, 1536–47.

Boffetta, P. (1993) Carcinogenicity of trace elements with reference to evaluations made by the International Agency for Research on Cancer. *Scand J Work Environ Health*, 19 Suppl 1, 67–70.

Brandes, E. A. and Brook, G. B. (1992) *Smithells Metals Reference Book*, Oxford, Butterworth-Heinemann.

Colombo, A., Hall, P., Nakamura, S., Almagor, Y., Maiello, L., Martini, G., Gaglione, A., Goldberg, S. L. and Tobis, J. M. (1995) Intracoronary stenting without anticoagulation accomplished with intravascular ultrasound guidance. *Circulation*, 91, 1676–88.

Currey, J. (1998) Cortical bone. In Black, J. and Hastings, G. (Eds) *Handbook of Biomaterial Properties*. London, Chapman and Hall.

Di Mario, C., Griffiths, H., Goktekin, O., Peeters, N., Verbist, J., Bosiers, M., Deloose, K., Heublein, B., Rohde, R., Kasese, V., Ilsley, C. and Erbel, R. (2004) Drug-eluting bioabsorbable magnesium stent. *J Interv Cardiol*, 17, 391–5.

Doriot, P. A., Dorsaz, P. A., Dorsaz, L., De Benedetti, E., Chatelain, P. and Delafontaine, P. (2000) *In-vivo* measurements of wall shear stress in human coronary arteries. *Coron Artery Dis*, 11, 495–502.

Elliot, J. S., Ajay, K. and Martin, T. R. (2006) New developments in coronary stent technology. *J Interv Cardiol*, 19, 493–9.

Emsley, J. (1998) *The Elements*, Oxford, Clarendon Press.

Erbel, R., Di Mario, C., Bartunek, J., Bonnier, J., De Bruyne, B., Eberli, F. R., Erne, P., Haude, M., Heublein, B., Horrigan, M., Ilsley, C., Bose, D., Koolen, J., Luscher, T. F., Weissman, N. and Waksman, R. (2007) Temporary scaffolding of coronary arteries

with bioabsorbable magnesium stents: A prospective, non-randomised multicentre trial. *Lancet*, 369, 1869–75.

Fischman, D. L., Leon, M. B., Baim, D. S., Schatz, R. A., Savage, M. P., Penn, I., Detre, K., Veltri, L., Ricci, D., Nobuyoshi, M. *et al*. (1994) A randomized comparison of coronary-stent placement and balloon angioplasty in the treatment of coronary artery disease. *N Engl J Med*, 331, 496–501.

Frey, R. J. (1999) Iron tests. *Gale Encyclopaedia of Medicine*. Gale Research.

Grewe, P. H., Thomas, D., Machraoui, A., Barmeyer, J. and Muller, K. M. (2000) Coronary morphologic findings after stent implantation. *Am J Cardiol*, 85, 554–8.

Hartwig, A. (2001) Role of magnesium in genomic stability. *Mutat Res*, 475, 113–21.

Hermawan, H., Alamdari, H., Mantovani, D. and Dubé, D. (2008) Iron-manganese: New class of degradable metallic biomaterials prepared by powder metallurgy. *Powder Metall*, 51, 38–45.

Hermawan, H., Moravej, M., Dubé, D. and Mantovani, D. (2007) Degradation behaviour of metallic biomaterials for degradable stents. *Adv Mater Res*, 15–17, 113–18.

Heublein, B., Rohde, R., Kaese, V., Niemeyer, M., Hartung, W. and Haverich, A. (2003) Biocorrosion of magnesium alloys: A new principle in cardiovascular implant technology? *Heart*, 89, 651–6.

Hoffmann, R., Mintz, G. S., Dussaillant, G. R., Popma, J. J., Pichard, A. D., Satler, L. F., Kent, K. M., Griffin, J. and Leon, M. B. (1996) Patterns and mechanisms of in-stent restenosis. A serial intravascular ultrasound study. *Circulation*, 94, 1247–54.

ISO (1999) *The ISO 10993-5: Biological Evaluation of Medical Devices – Part 5: Tests for in vitro Cytotoxicity*, Arlington, VA, ANSI/AAMI.

Kannan, M. B. and Raman, R. K. S. (2008a) Evaluating the stress corrosion cracking susceptibility of Mg–Al–Zn alloy in modified-simulated body fluid for orthopaedic implant application. *Scr Mater*, 59, 175–8.

Kannan, M. B. and Raman, R. K. S. (2008b) *In vitro* degradation and mechanical integrity of calcium-containing magnesium alloys in modified-simulated body fluid. *Biomaterials*, 29, 2306–14.

Karachalios, T., Tsatsaronis, C., Efraimis, G., Papadelis, P., Lyritis, G. and Diakoumopoulos, G. (2004) The long-term clinical relevance of calcar atrophy caused by stress shielding in total hip arthroplasty: A 10-year, prospective, randomized study. *J Arthroplast*, 19, 469–75.

König, A., Schiele, T. M., Rieber, J., Theisen, K., Mudra, H. and Klauss, V. (2002) Influence of stent design and deployment technique on neointima formation and vascular remodeling. *Z Kardiol*, 91, 98–102.

Kuwahara, H., Al-Abdullat, Y., Ohta, M., Tsutsumi, S., Ikeuchi, K., Mazaki, N. and Aizawa, T. (2000) Surface reaction of magnesium in Hank's solution. *Mater Sci Forum*, 350–351, 349–58.

Kuwahara, H., Mazaki, N., Mabuchi, M., Wein, C. and Aizawa, T. (2003) Behavior of magnesium in Hank's solution aimed to trabecular pattern of natural bone. *Mater Sci Forum* 419–422, 1007–12.

Leavitt, M. O., Gerberding, J. L. and Sondik, E. J. (2005) *Health United States 2005*, Hyattsville, US Dept of Health and Human Services.

Levesque, J., Dubé, D., Fiset, M. and Mantovani, D. (2003) Investigation of corrosion behaviour of magnesium alloy AM60B-F under pseudo-physiological conditions. *Mater Sci Forum*, 426–432, 521–6.

Levesque, J., Hermawan, H., Dubé, D. and Mantovani, D. (2008) Design of a pseudo-physiological test bench specific to the development of biodegradable metallic biomaterials. *Acta Biomater*, 4, 284–95.

Li, L., Gao, J. and Wang, Y. (2004) Evaluation of cyto-toxicity and corrosion behavior of alkali-heat-treated magnesium in simulated body fluid. *Surf Coat Technol*, 185, 92–8.

Li, Z., Gu, X., Lou, S. and Zheng, Y. (2008) The development of binary Mg–Ca alloys for use as biodegradable materials within bone. *Biomaterials*, 29, 1329–44.

Marrey, R. V., Burgermeister, R., Grishaber, R. B. and Ritchie, R. O. (2006) Fatigue and life prediction for cobalt-chromium stents: A fracture mechanics analysis. *Biomaterials*, 27, 1988–2000.

McBride, E. D. (1938) Absorbable metal in bone surgery. *J Am Med Assoc*, 111, 2464–7.

McMahon, C. J., Oslizlok, P. and Walsh, K. P. (2007) Early restenosis following biodegradable stent implantation in an aortopulmonary collateral of a patient with pulmonary atresia and hypoplastic pulmonary arteries. *Catheter Cardiovasc Interv*, 69, 735–8.

Medtech (2004) Emerging U.S. Markets for Myocardial Revascularization, Repair and Regeneration Products and Technologies. Newport Beach, Medtech Insight.

Migliavacca, F., Petrini, L., Montanari, V., Quagliana, I., Auricchio, F. and Dubini, G. (2005) A predictive study of the mechanical behaviour of coronary stents by computer modelling. *Med Eng and Physics*, 27, 13–8.

Mordike, B. L. and Ebert, T. (2001) Magnesium properties, applications and potential. *Mater Sci Eng: A*, 302, 37–45.

Morice, M. C., Serruys, P. W., Sousa, J. E., Fajadet, J., Ban Hayashi, E., Perin, M., Colombo, A., Schuler, G., Barragan, P., Guagliumi, G., Molnar, F. and Falotico, R. (2002) A randomized comparison of a sirolimus-eluting stent with a standard stent for coronary revascularization. *N Engl J Med*, 346, 1773–80.

Mueller, P. P., May, T., Perz, A., Hauser, H. and Peuster, M. (2006) Control of smooth muscle cell proliferation by ferrous iron. *Biomaterials*, 27, 2193–200.

Mukai, T., Yamanoi, M., Watanabe, H. and Higashi, K. (2001) Ductility enhancement in AZ31 magnesium alloy by controlling its grain structure. *Scr Mater*, 45, 89–94.

Muller-Hulsbeck, S., Grimm, J., Jahnke, T., Haselbarth, G. and Heller, M. (2001) Flow patterns from metallic vascular endoprostheses: *In vitro* results. *Eur Radiol*, 11, 893–901.

Okuma, T. (2001) Magnesium and bone strength. *Nutrition*, 17, 679–80.

Peeters, P., Bosiers, M., Verbist, J., Deloose, K. and Heublein, B. (2005) Preliminary results after application of absorbable metal stents in patients with critical limb ischemia. *J Endovasc Ther*, 12, 1–5.

Peuster, M., Beerbaum, P., Bach, F. W. and Hauser, H. (2006a) Are resorbable implants about to become a reality? *Cardiol Young*, 16, 107–16. Cambridge University Press.

Peuster, M., Hesse, C., Schloo, T., Fink, C., Beerbaum, P. and Von Schnakenburg, C. (2006b) Long-term biocompatibility of a corrodible peripheral iron stent in the porcine descending aorta. *Biomaterials*, 27, 4955–62.

Peuster, M., Wohlsein, P., Brugmann, M., Ehlerding, M., Seidler, K., Fink, C., Brauer, H., Fischer, A. and Hausdorf, G. (2001) A novel approach to temporary stenting: Degradable cardiovascular stents produced from corrodible metal. Results 6–18 months after implantation into New Zealand white rabbits. *Heart*, 86, 563–9.

Roberts, T. P. L. and Macgowan, C. K. (2004) Magnetic resonance imaging. In Moore, J. and Zouridakis, G. (Eds) *Biomedical Technology and Devices Handbook*. Boca Raton, CRC Press LLC.

Sanschagrin, A., Tremblay, R. and Angers, R. (1996) Mechanical properties and microstructure of new magnesium–lithium base alloys. *Mater Sci Eng*, 220, 69–77.

Saris, N. E., Mervaala, E., Karppanen, H., Khawaja, J. A. and Lewenstam, A. (2000) Magnesium. An update on physiological, clinical and analytical aspects. *Clin Chim Acta*, 294, 1–26.

Schneck, D. J. (2000) An outline of cardiovascular structure and function. In Bronzino, J. D. (Ed.) *The Biomedical Engineering Handbook*. Boca Raton, CRC Press LLC.

Schranz, D., Zartner, P., Michel-Behnke, I. and Akinturk, H. (2006) Bioabsorbable metal stents for percutaneous treatment of critical recoarctation of the aorta in a newborn. *Catheter Cardiovasc Interv*, 67, 671–3.

Scully, J. R. and Taylor, D. W. (1992) Electrochemical methods of corrosion testing. In Korb, L. J. and Olson, D. L. (Eds) *ASM Handbook Volume 13: Corrosion*. Materials Park, ASM.

Serruys, P. W., De Jaegere, P., Kiemeneij, F., Macaya, C., Rutsch, W., Heyndrickx, G., Emanuelsson, H., Marco, J., Legrand, V., Materne, P. *et al*. (1994) A comparison of balloon-expandable-stent implantation with balloon angioplasty in patients with coronary artery disease. Benestent Study Group. *N Engl J Med*, 331, 489–95.

Serruys, P. W., Kutryk, M. J. and Ong, A. T. (2006) Coronary-artery stents. *N Engl J Med*, 354, 483–95.

Sigwart, U., Puel, J., Mirkovitch, V., Joffre, F. and Kappenberger, L. (1987) Intravascular stents to prevent occlusion and restenosis after transluminal angioplasty. *N Engl J Med*, 316, 701–6.

Song, G. (2007) Control of biodegradation of biocompatible magnesium alloys *Corr Sci*, 49, 1696–701.

Stack, R. S., Califf, R. M., Phillips, H. R., Pryor, D. B., Quigley, P. J., Bauman, R. P., Tcheng, J. E. and Greenfield, J. C., Jr. (1988) Interventional cardiac catheterization at Duke Medical Center. *Am J Cardiol*, 62, 3F–24F.

Tamai, H., Igaki, K., Kyo, E., Kosuga, K., Kawashima, A., Matsui, S., Komori, H., Tsuji, T., Motohara, S. and Uehata, H. (2000) Initial and 6-month results of biodegradable poly-l-lactic acid coronary stents in humans. *Circulation*, 102, 399–404.

Tsuji, T., Tamai, H., Igaki, K., Kyo, E., Kosuga, K., Hata, T., Okada, M., Nakamura, T., Komori, H., Motohara, S. and Uehata, H. (2001) Biodegradable polymeric stents. *Curr Interv Cardiol Rep*, 3, 10–7.

Van Der Giessen, W. J., Lincoff, A. M., Schwartz, R. S., Van Beusekom, H. M., Serruys, P. W., Holmes, D. R., Jr., Ellis, S. G. and Topol, E. J. (1996) Marked inflammatory sequelae to implantation of biodegradable and nonbiodegradable polymers in porcine coronary arteries. *Circulation*, 94, 1690–7.

Venkatraman, S., Poh, T. L., Vinalia, T., Mak, K. H. and Boey, F. (2003) Collapse pressures of biodegradable stents. *Biomaterials*, 24, 2105–11.

Virmani, R., Farb, A., Guagliumi, G. and Kolodgie, F. D. (2004) Drug-eluting stents: Caution and concerns for long-term outcome. *Coron Artery Dis*, 15, 313–18.

Vormann, J. (2003) Magnesium: Nutrition and metabolism. *Mol Aspects Med*, 24, 27–37.

Waksman, R. (2006) Update on bioabsorbable stents: From bench to clinical. *J Interv Cardiol* 19, 414–21.

Waksman, R. (2007) Promise and challenges of bioabsorbable stents. *Catheter Cardiovasc Interv*, 70, 407–14.

Waksman, R., Pakala, R., Baffour, R., Seabron, R., Hellinga, D. and Tio, F. O. (2008) Short-term effects of biocorrodible iron stents in porcine coronary arteries. *J Interv Cardiol*, 21, 15–20.

Waksman, R., Pakala, R., Kuchulakanti, P. K., Baffour, R., Hellinga, D., Seabron, R.,

Tio, F. O., Wittchow, E., Hartwig, S., Harder, C., Rohde, R., Heublein, B., Andreae, A., Waldmann, K.-H. and Haverich, A. (2006) Safety and efficacy of bioabsorbable magnesium alloy stents in porcine coronary arteries. *Catheter Cardiovasc Interv*, 68, 606–17.

Waksman, R., Pakala, R., Okabe, T., Hellinga, D., Chan, R., Tio, M. O., Wittchow, E., Hartwig, S., Waldmann, K. H. and Harder, C. (2007) Efficacy and safety of absorbable metallic stents with adjunct intracoronary beta radiation in porcine coronary arteries. *J Interv Cardiol*, 20, 367–72.

Willfort-Ehringer, A., Ahmadi, R., Gruber, D., Gschwandtner, M. E., Haumer, A., Haumer, M. and Ehringer, H. (2004) Arterial remodeling and hemodynamics in carotid stents: A prospective duplex ultrasound study over two years. *J Vasc Surg*, 39, 728–34.

Witte, F., Feyerabend, F., Maier, P., Fischer, J., Störmer, M., Blawert, C., Dietzel, W. and Hort, N. (2007) Biodegradable magnesium–hydroxyapatite metal matrix composites. *Biomaterials*, 28, 2163–74.

Witte, F., Fischer, J., Nellesen, J., Crostack, H.-A., Kaese, V., Pisch, A., Beckmann, F. and Windhagen, H. (2006) *In vitro* and *in vivo* corrosion measurements of magnesium alloys. *Biomaterials*, 27, 1013–18.

Witte, F., Kaese, V., Haferkamp, H., Switzer, E., Meyer-Lindenberg, A., Wirth, C. J. and Windhagen, H. (2005) *In vivo* corrosion of four magnesium alloys and the associated bone response. *Biomaterials*, 26, 3557–63.

Xin, Y., Liu, C., Zhang, X., Tang, G., Tian, X. and Chu, P. K. (2007) Corrosion behavior of biomedical AZ91 magnesium alloy in simulated body fluids. *J Mater Res*, 22, 2004–11.

Zartner, P., Buettner, M., Singer, H. and Sigler, M. (2007) First biodegradable metal stent in a child with congenital heart disease: Evaluation of macro and histopathology. *Catheter Cardiovasc Interv* 69, 443–6.

Zartner, P., Cesnjevar, R., Singer, H. and Weyand, M. (2005) First successful implantation of a biodegradable metal stent into the left pulmonary artery of a preterm baby. *Catheter Cardiovasc Interv* 66, 590–4.

Index